JOINT SPECIAL ISSUE:
ADVANCES IN CONSTRUCTION PRACTICES FOR ADDITIVE CONSTRUCTION

V. 121, NO. 2, MARCH 2024

ACI MATERIALS JOURNAL

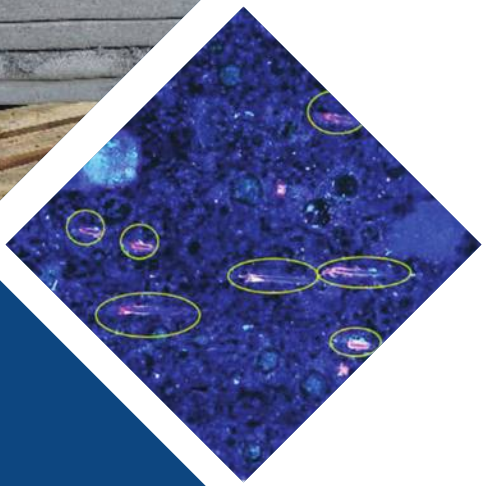

American Concrete Institute

CONTENTS

ACI MATERIALS JOURNAL

MARCH 2024, V. 121, NO. 2

A JOURNAL OF THE AMERICAN CONCRETE INSTITUTE
AN INTERNATIONAL TECHNICAL SOCIETY

SPECIAL ISSUE: Advances in Construction Practices for Additive Construction

ALSO FEATURING:

Discussion is welcomed for all materials published in this issue and will appear ten months from this journal's date if the discussion is received within four months of the paper's print publication. Discussion of material received after specified dates will be considered individually for publication or private response. ACI Standards published in ACI Journals for public comment have discussion due dates printed with the Standard.

The *ACI Materials Journal* (ISSN 0889-325x) is published bimonthly by the American Concrete Institute. Publication office: 38800 Country Club Drive, Farmington Hills, MI 48331. Periodicals postage paid at Farmington, MI, and at additional mailing offices. Subscription rates: $199 per year, payable in advance. POSTMASTER: Send address changes to: *ACI Materials Journal*, 38800 Country Club Drive, Farmington Hills, MI 48331.

Canadian GST: R 1226213149.

Direct correspondence to 38800 Country Club Drive, Farmington Hills, MI 48331. Telephone: +1.248.848.3700.
Website: http://www.concrete.org.

MEETINGS

APRIL 2024

10-26—The Masonry Society's 2024 Spring Meeting, Virtual, https://masonrysociety.org/event/2024-spring-meeting-virtual

14-17—2024 PTI Convention, Indianapolis, IN, www.post-tensioning.org/events/conventions.aspx

15-18—CRSI 2024 Spring Business & Technical Meeting, Anaheim, CA, www.crsi.org/event/2024-spring-business-technical-meeting

16-17—1st RILEM International Conference on Mineral Carbonation for Cement and Concrete, Aachen, Germany, www.rilem.net/agenda/1st-international-rilem-conference-onmineral-carbonation-for-cement-and-concrete-1569

18-19—Cementitious Materials International Technical and Trade Congress, Casablanca, Morocco, https://industrylink.eu/event/cementitious-2024

21-24—2024 ICRI Spring Convention, Boston, MA, www.icri.org/news-events/2024-icri-spring-convention/

MAY 2024

6-7—International Geotechnical Innovation Conference (IGIC 2024), Jeddah, Saudi Arabia, https://geotechnicalinnovationconference.com

13-16—World of Coal Ash 2024, Grand Rapids, MI, https://worldofcoalash.org

13-18—The Fifth European and Mediterranean Structural Engineering and Construction Conference (EURO MED SEC 5), Vilnius, Lithuania, www.isec-society.org/EURO_MED_SEC_05

14-16—ACI Foundation CIC Technology Forum, Santa Fe, NM, www.acifoundation.org/technology/forums.aspx

14-17—International Conference on Iron Sulfide Reactions in Concrete, Quebec City, QC, Canada, https://icisr.ca

18-24—The 17th International Conference on Alkali-Aggregate Reaction in Concrete (17th ICAAR), Ottawa, ON, Canada, https://www.icaar.ca

20-24—ICSF 2024: 31st International Conference on Structural Failures (Awarie Budowlane XXXI), Międzyzdroje, Poland, www.awarie.zut.edu.pl

JUNE 2024

5-7—ConCreep12, Delft, the Netherlands, www.aanmelder.nl/129439

ACI CONCRETE CONVENTION: FUTURE DATES

2024—November 3-6, Philadelphia Marriott Downtown, Philadelphia, PA
2025—Mar. 30-Apr. 2, Sheraton Centre Toronto Hotel, Toronto, ON, Canada
2025—October 26-30, Hilton Baltimore & Baltimore Marriott Inner Harbor, Baltimore, MD
2026—Mar. 29-Apr. 1, Hyatt Regency O'Hare, Rosemont/Chicago, IL

For additional information, contact:
Event Services, ACI
38800 Country Club Drive
Farmington Hills, MI 48331
Telephone: +1.248.848.3795
email: conventions@concrete.org

ON FRONT COVER: 121-M14, Fig. 12—Examples of structures and techniques implemented by novel dry-forming technology: (a) pillar coral 3D-printed structures (left); **121-S17**, Fig. 10—(b) manufactured demonstrator (center); **121-M13**, Fig. 7—(e) Optical microscope image of surface of three-dimensionally printed specimen with polyvinyl alcohol fibers (right).

ON BACK COVER: 121-S19, Fig. 1—Additive construction process: (a) machine.

Contributions to *ACI Materials Journal*

The *ACI Materials Journal* is an open forum on concrete technology and papers related to this field are always welcome. All material submitted for possible publication must meet the requirements of the "American Concrete Institute Publication Policy" and "Author Guidelines and Submission Procedures." Prospective authors should request a copy of the Policy and Guidelines from ACI or visit ACI's website at **www.concrete.org** prior to submitting contributions.

Papers reporting research must include a statement indicating the significance of the research.

The Institute reserves the right to return, without review, contributions not meeting the requirements of the Publication Policy.

All materials conforming to the Policy requirements will be reviewed for editorial quality and technical content, and every effort will be made to put all acceptable papers into the information channel. However, potentially good papers may be returned to authors when it is not possible to publish them in a reasonable time.

Discussion

All technical material appearing in the *ACI Materials Journal* may be discussed. If the deadline indicated on the contents page is observed, discussion can appear in the designated issue. Discussion should be complete and ready for publication, including finished, reproducible illustrations. Discussion must be confined to the scope of the paper and meet the ACI Publication Policy.

Follow the style of the current issue. Be brief—1800 words of double spaced, typewritten copy, including illustrations and tables, is maximum. Count illustrations and tables as 300 words each and submit them on individual sheets. As an approximation, 1 page of text is about 300 words. Submit one original typescript on 8-1/2 x 11 plain white paper, use 1 in. margins, and include two good quality copies of the entire discussion. References should be complete. Do not repeat references cited in original paper; cite them by original number. Closures responding to a single discussion should not exceed 1800-word equivalents in length, and to multiple discussions, approximately one half of the combined lengths of all discussions. Closures are published together with the discussions.

Discuss the paper, not some new or outside work on the same subject. Use references wherever possible instead of repeating available information.

Discussion offered for publication should offer some benefit to the general reader. Discussion which does not meet this requirement will be returned or referred to the author for private reply.

Send manuscripts to:
http://mc.manuscriptcentral.com/aci

Send discussions to:
Journals.manuscripts@concrete.org

LETTER FROM THE GUEST EDITORS

Additive construction (that is, three-dimensional [3-D] construction printing) has gained significant momentum in a short time frame, with the the first major publication on materials in 2012 and the first buildings being completed in 2014/2015. While there are several potential options, the field of additive construction (AC) has been dominated by mortar/concrete materials. This method of construction places material without formwork present, resulting in a unique relationship between material and structural performance during construction that is not considered in traditional concrete construction. The popularity is a result of the potential of the technology to improve productivity and cost of construction, as well as improving structural performance through geometrical freedom, the ability to mobilize, and the ability to produce structures in dangerous or remote places. As a result, the number of high-visibility and high-risk projects being executed and proposed has become more common, while the industry is left without a general knowledge of the construction practices and structural performance or a structural code/guidance to assist designers, contractors, and inspectors. Therefore, it is imperative that the concrete industry be educated in the current state and limitations of the technology.

The intent of this joint special issue is to provide awareness to professionals in the concrete industry to the technical construction aspects (materials and structural) of the technology. This joint special issue of the *ACI Structural Journal* and *ACI Materials Journal* contains nine manuscripts focused on construction aspects of additive construction using cement-based materials. It should be highlighted that the number of manuscripts received/accepted for this joint special issue is indicative of the difference in the amount of research or publicly shared information on structural and construction aspects of AC compared to the amount of research on materials, as showcased in the November 2021 special issue of the *ACI Materials Journal*. The papers in these joint special issues cover a wide range of topics including structural topics on testing reinforced beams and modeling the construction process, and materials topics on the characterizing extrusion, enhancing, and testing mechanical properties; shoreline resiliency; fracture behavior; and quality control methods. It is the hope of the editors that this brief introduction will help to provide the readers with insight to the current state of research on structural/materials performance and the construction process, the structural/materials considerations that come into play when considering this technology, and how research in this area can benefit the concrete construction industry as a whole.

Liberato Ferrara
Eric L. Kreiger

REGISTER TODAY

TECHNOLOGY FORUM

MAY 14-16, 2024, SANTA FE, NM, USA

Hilton Santa Fe - Historic Plaza, 100 Sandoval Street

The **Technology Forum** is an innovation-focused educational and networking event for concrete professionals **powered by the ACI Foundation's Concrete Innovation Council**.

Whether you are an emerging professional or a seasoned veteran, the ACI Foundation Technology Forum is the place to learn about **current trends, emerging technologies, and discoveries within the concrete industry**.

Join us for an exciting and insightful event featuring thought leaders and technology innovators to discuss the future of the concrete industry.

aci Foundation
Building the Future

acifoundation.org

ACI MATERIALS JOURNAL TECHNICAL PAPER

Title No. 121-M11

Characterization of Extrudability Using Rheology and Desorptivity

by Kavya Vallurupalli, Nicolas Ali Libre, and Kamal H. Khayat

*Successful implementation of extrusion-based three-dimensional (3-D) printing requires the development of print materials with adapted rheology. In this study, filtration characteristics coupled with rheological properties of mortar mixtures are investigated to characterize the extrudability of print materials and establish a "printability window" (that is, the acceptable range of material properties for successful extrusion and shape stability). The extrudability was measured as the maximum force needed for the ram extrusion of the material. The fluid filtration rate was assessed in terms of desorptivity of the fresh mixture under pressure. The yield stress, plastic viscosity, and desorptivity were varied by changing the water-cement ratio (*w/c*), high-range water-reducing admixture (HRWRA) dosage, and welan gum (WG) content. Regression analysis indicated that during extrusion-based printing, the yield stress and desorptivity values can exhibit a more significant effect on extrudability than plastic viscosity.*

Keywords: extrudability; fluid filtration; printability window; rheology; three-dimensional (3-D) printing.

INTRODUCTION

Over the past decade, there has been a growing interest in three-dimensional (3-D) printing (3DP) of cement-based materials in concrete construction. The main advantage of 3DP over conventional construction is the elimination of formwork and the ability to print topologically optimized structures. This has the potential to lower construction costs, reduce material use, and enhance sustainability.[1-3] Two different 3DP techniques are mainly applied for cement-based materials: particle-bed binding and material extrusion.[4,5] Particle-bed binding involves selectively depositing binder liquid onto a bulk material bed laid in layers. The constituents of the binder liquid phase and the bulk material vary with the type of cement system selected (that is, paste, mortar, or concrete). The bulk material hardens upon contact with the ink, and at the end of the printing, the hardened element needs to be taken out of the loose bulk material bed.[6-8] This additional step can limit the use of binder-jetting techniques for in-place and large-scale 3DP applications. The extrusion-based 3DP involves the extrusion of print material through a nozzle into filaments that are deposited layer-by-layer at a controlled speed.[9-11] Compared to particle-bed binding, there is little need for post-processing work and use of formwork in case of material extrusion. Due to these advantages, extrusion-based 3DP has been successfully implemented in 3DP of large-scale structures.[12,13] The current work focuses on the extrusion-based 3DP using a ram extruder setup.

During extrusion-based 3DP, the print material is usually pumped into an extruder, and this requires the print material to have high flowability (that is, low yield stress). The absence of formwork necessitates that the extruded material resists plastic deformation to retain its initial shape (that is, shape stability). This requires the yield stress of the extruded material to be higher than the shear stress exerted by gravity, which is a function of the density of the material and the height of the printed layer.[14] The opposing requirements of high flowability before extrusion and shape stability after extrusion pose a challenge during the development of the material.[15] Furthermore, the material can undergo process-induced variation during printing, and these flow-induced changes in material properties can hamper the shape stability of extruded material.[16] For a given 3DP setup, the print material is selected based on the rheological properties (that is, yield stress [τ_y] and plastic viscosity [μ_p]),[11,17-19] with limited emphasis on the process-induced behavior of the material.

In this study, in addition to rheological properties, the flow behavior of the print material during the ram extrusion process and the key material properties affecting the flow behavior are evaluated. These material properties of mortar mixtures are varied by changing the water-cement ratio (*w/c*), high-range water-reducing admixture (HRWRA) dosage, and welan gum (WG) content. The influence of these mixture proportioning parameters and material properties on the extrudability was examined. The study aims to define a printability window for the successful extrusion of the mortar based on its rheology and fluid filtration characteristics. The printability window refers to the acceptable range of material properties within which the material can be extruded into shape-stable layers.

RESEARCH SIGNIFICANCE

Three-dimensional printing (3DP) offers numerous benefits in terms of structural, environmental, and safety aspects of construction. The development of printable materials is necessary for exploiting these benefits. The current study evaluates the importance of both rheology and desorptivity on printability, which is currently missing in the literature. The printability window proposed in this paper can be used

ACI Materials Journal, V. 121, No. 2, March 2024.

MS No. M-2022-076.R3, doi: 10.14359/51740301, received November 18, 2023, and reviewed under Institute publication policies.

as a practical guideline for material properties during the selection and optimization of mixtures for 3DP.

RAM EXTRUSION PROCESS—MATERIAL FLOW BEHAVIOR

Figure 1(a) illustrates the extrusion process of 3DP using a ram extruder. The ram extrusion involves the filling of the print material in a barrel and the application of force (F_E) on the ram to push the material into a nozzle located at the end of the barrel. During ram extrusion, the application of F_E results in different material flow behaviors (that is, plastic, viscoplastic, and frictional-plastic) that depend on the material rheology and fluid filtration. For plastic and viscoplastic flow behaviors, the material stays homogenous. However, the extent of shearing in the material varies. In the case of plastic flow behavior, only the print material close to the barrel wall undergoes shearing, and the remaining material moves along the extruder unsheared, as shown in green in Fig. 1(b). For viscoplastic flow in Fig. 1(c), most of the print material is sheared during the extrusion. Frictional-plastic flow behavior occurs when the application of F_E results in the migration of the fluid toward the nozzle. This causes the formation of dry and consolidated material near the ram, as shown in Fig. 1(d), and can lead to blockage during extrusion. The flow behavior within the extruder has a significant effect on extrudability. The extrudability in this study is assessed as maximum F_E (that is, high extrudability implied a lower value of F_E).[20-22] The influence of τ_y, μ_p, and fluid filtration characteristics on flow behavior and extrudability are summarized in Table 1.

Perrot et al.[23] noted that during the extrusion of a homogenous material, the flow behavior is affected by τ_y, μ_p, extrusion speed (V_R), and barrel diameter (D_B). The influence of these parameters can be assessed using the Bingham number (B_N), as shown in Eq. (1).[16]

$$B_N = \frac{\tau_y D_B}{8\mu_p V_R} \quad (1)$$

The high and low values of τ_y/μ_p for plastic and viscoplastic flow behaviors in Table 1 correspond to B_N values of >100 and ≤100, respectively. The fluid filtration needs to be significantly low to reduce water migration and avoid the formation of dry and consolidated material during the extrusion. The degree of fluid filtration is a function of the filtration characteristics of the print material, extruder dimensions, and V_R.[23] The fluid filtration characteristics of the print material can be assessed in terms of desorptivity (D_e).[24,25] The D_e is the measurement of the rate of forced bleeding of the material under a given pressure gradient. Unlike B_N, no acceptable ranges of D_e are available in the literature to ensure material homogeneity during extrusion. In this study, the influence of the τ_y, μ_p, and D_e on the maximum F_E (extrudability) was examined, and suitable ranges of τ_y, μ_p, and D_e parameters are established for successful 3DP.

MATERIALS AND EXPERIMENTAL PROCEDURES

Materials and mixture proportions

In this study, a Type I/II portland cement conforming to ASTM C150 was used. The specific gravity and Blaine fineness of the cement were 3.14 and 390 m^2/kg (1900 ft^2/lb), respectively. The nominal maximum size of aggregate and relative content of the sand were 2 mm and 40%, by volume of mortar, respectively. The specific gravity and absorption values of the sand were 2.58 and 2.24%, respectively. A polysaccharide-based WG powder with a specific gravity of 0.8 was used to modify rheology and reduce the risk of fluid filtration. A polycarboxylate-based HRWRA with 23% solid mass content and 1.05 specific gravity was also used to enhance flow. The mini-slump cone with a height of 60 mm (2.36 in.), upper diameter of 70 mm (2.75 in.), and lower diameter of 100 mm (3.94 in.) without any jolting was used

Table 1—Influence of print material properties on flow behavior and extrudability[16]

Flow behavior	Print material property		Extrudability†
	τ_y/μ_p*	Fluid filtration	
Plastic	High	Low	High
Viscoplastic	Low	Low	Medium
Frictional-plastic	—	High	Poor

*High and low values correspond to B_N of >100 and ≤100, respectively.

†High extrudability implies lower F_E needed for extrusion of print material.

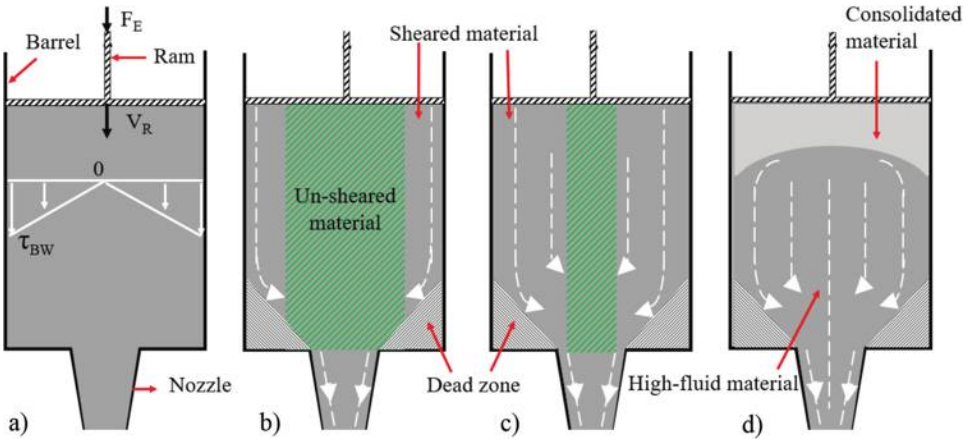

Fig. 1—Ram extrusion process: (a) ram extruder setup; (b) plastic flow behavior; (c) viscoplastic flow behavior; and (d) frictional-plastic flow behavior (adapted from Vallurupalli et al.[16]).

Table 2—Mixture proportions and initial mini-slump flow

Mixture*	Cement, kg/m^3	Water, kg/m^3	Sand, kg/m^3	HRWRA, kg/m^3	WG, kg/m^3	Initial mini-slump flow, mm (in.)
0.35W	899	315	1032	—	—	120 (4.7)
0.25W0.09SP	1049	266	1031	0.9	—	120 (4.7)
0.25W0.11SP	1049	266	1031	1.1	—	170 (6.7)
0.25W0.22SP	1048	266	1030	2.3	—	280 (11.0)
0.25W0.43SP	1045	266	1028	4.5	—	340 (13.4)
0.25W0.7SP0.1WG	1041	264	1024	7.2	1.0	170 (6.7)
0.25W1.3SP0.2WG	1034	263	1016	13.5	2.1	170 (6.7)
0.25W1.8SP0.3WG	1027	261	1010	18.8	3.1	170 (6.7)

*0.25W1.8SP0.3WG indicates 0.25 *w/c* and HRWRA dosage and WG content of 1.8% and 0.3%, by mass of cement, respectively.

Note: 1 kg/m^3 = 1.68 lb/yd^3.

to measure flow. The dosage rate of the HRWRA was varied to maintain an initial mini-slump flow of 170 ± 10 mm (6.7 ± 0.4 in.) for the mixtures made with WG. For other mixtures, the HRWRA dosage was varied to secure mini-slump flow values in the range of 120 ± 10 mm (4.7 ± 0.4 in.) to 340 ± 10 mm (13.4 ± 0.4 in.).

Eight mortar mixtures with *w/c* varying between 0.25 and 0.35; HRWRA dosages of 0, 0.09, 0.11, 0.22, and 0.43%, by mass of binder; and WG contents of 0, 0.1, 0.2, and 0.3%, by mass of binder, were prepared. The mixture proportions and initial flow values determined right before the extrusion of the print materials are shown in Table 2. The time corresponds to approximately 20 minutes after the contact of cement and water. The mixing procedure of the mortars involved: 1) dry mixing of the sand and cement at 1 rps for 2 minutes; 2) gradual addition of water along with HRWRA to the dry materials and mixing at 2 rps for 3 minutes; and 3) resting the material for 1 minute, followed by final mixing at 2 rps for 3 minutes. In the case of mixtures with WG, WG was premixed with water and HRWRA for 3 minutes using a blender and was added to the dry materials in Step 2 of the mixing process. After the end of mixing, the material was left to rest (protected from water evaporation) until 20 minutes from cement and water contact. After 20 minutes, the slump flow, rheology, and extrusion tests were carried out, as all three tests are time-sensitive and require time for setting up—that is, filling the slump cone, rheometer cylinder, and extruder. The time interval of 20 minutes was selected to ensure all tests were set up correctly and carried out concurrently.

Rheology

The τ_y and μ_p values of mortar mixtures were measured using a coaxial cylinder rheometer with inner and outer radii of 50 and 60 mm (2 and 2.4 in.), respectively. The rheometer cylinder was filled with the mortar sample in two layers, and each layer was rodded 25 times with a tamping rod. The rheology testing protocol involved pre-shearing of mortar at 0.5 rps for 25 seconds, followed by a stepwise drop in the shear rate from 0.5 to 0.025 rps in 10 steps, with each shear rate applied for 5 seconds. The average value of torque at each shear rate was recorded, and the τ_y and μ_p values were estimated using the Reiner-Riwlin equations for the Bingham model.[26] The rheological measurements were determined initially at 20 minutes, and thereafter at 30-minute intervals up to 220 minutes. Between each test, the sample was hand-mixed for 30 seconds and covered.

Fluid filtration

The D_e of the mortar mixtures was assessed using a filtration cell test setup, shown in Fig. 2(a). The test consisted of a metallic cylinder fitted with a metal screen and filter paper of pore size 2 µm placed at the bottom against the draining surface. The cylinder was filled with approximately 750 g (1.6 lb) (approximately 580 mL [35 in.^{3}]) of mortar sample in two layers, with each layer rodded 25 times with a tamping rod. The cylinder assembly was placed in the test frame, and an overhead pressure was applied on the mortar using CO_2 gas. The overhead pressure was applied for 5 minutes, and the forced bleed water was collected using a 10 mL (0.6 in.^{3}) graduated cylinder. The mortar samples were tested at different ages, starting from 20 minutes to up to 220 minutes (±10 minutes). At each age, the filtration test was conducted at five different overhead pressures of 120, 180, 240, 300, and 360 kPa (±10 kPa) (17, 26, 35, 44, and 52 psi [±1.4 psi]) using a separate sample of mortar for each pressure value. Three pressure cells were available to conduct the pressure filtration tests simultaneously. The D_e at each overhead pressure was estimated by plotting the relative amount of filtrated water to the square root of time, as shown in Fig. 2(b). The relative amount of filtrated water corresponds to the volume of collected forced bleed water divided by the total water content in the mortar sample. A high value of D_e implies a high fluid filtration rate that can lead to frictional-plastic flow behavior during the extrusion of the mortar.

Ram extrusion

The extrudability of a mortar sample is defined as the ability of the material to be extruded without any blockage.[17,27] The extrudability of mortar mixtures was evaluated using a custom-designed displacement-controlled ram extrusion setup (Fig. 3(a)) with D_B of 39 mm (1.5 in.) and D_N of 9 mm (0.4 in.), as shown in Fig. 3(b).[28] The extruder was powered by a stepper motor calibrated to apply a maximum load of 135 N (30 lbf) to avoid failure of the extruder. The mortar mixtures were extruded with a constant V_R of 2.5 mm/s (0.1 in./s). Before each test, the inner surface

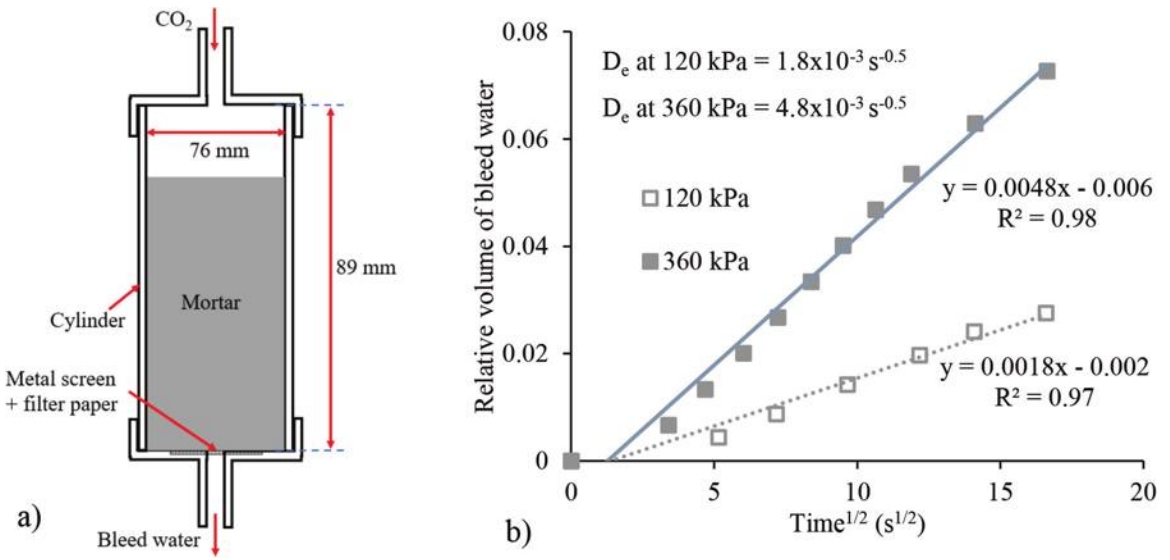

Fig. 2—Filtration test: (a) schematic of filtration cell test setup; and (b) typical variations in relative volume of forced bleed water as function of time (up to 5 minutes) for two overhead pressures of 120 and 360 kPa (17 and 52 psi).

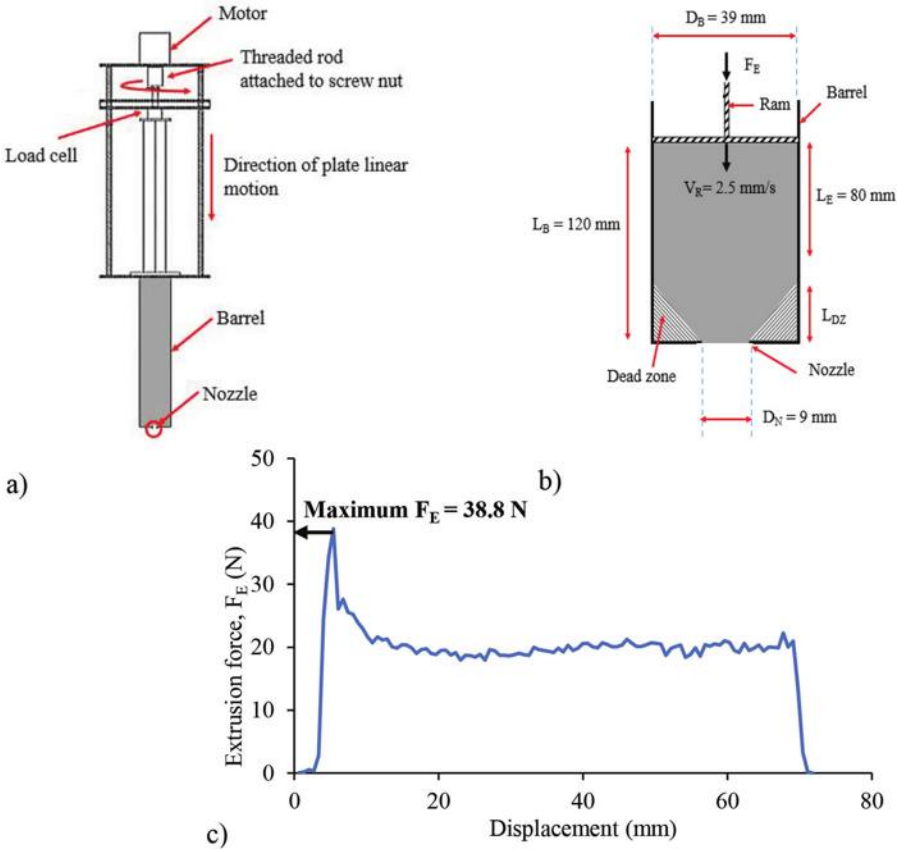

Fig. 3—Extrusion test: (a) schematic of ram extruder setup; (b) close-up of barrel and nozzle; and (c) typical load-versus-displacement data from ram extrusion test. (Note: 1 mm = 0.04 in.)

of the barrel and ram were lubricated using silicone oil to minimize the wall friction. Additionally, the extrusion test was carried out on an empty ram to determine the F_E needed for pushing an empty ram extruder. A mortar sample of 140 mL (8.5 in.^{3}) (approximately 180 g [0.4 lb]) was added to the barrel, which corresponded to the barrel length (L_B) of 120 mm (4.7 in.) (Fig. 3(b)). A drastic increase in F_E was reported by Perrot et al.[29,30] when the ram approached the dead-zone length (L_{DZ}). To minimize the effect of the dead zone on F_E, only a portion of mortar within the extruder was extruded. The extruded portion of the material corresponded to the extruder length (L_E) of 80 mm (4.9 in.). The extrudability was assessed at different ages of mortar starting from 20 minutes after water and cement contact. The extrudability of the mortar is evaluated by determining the maximum F_E needed to extrude the material, as shown in Fig. 3(c).[28] A

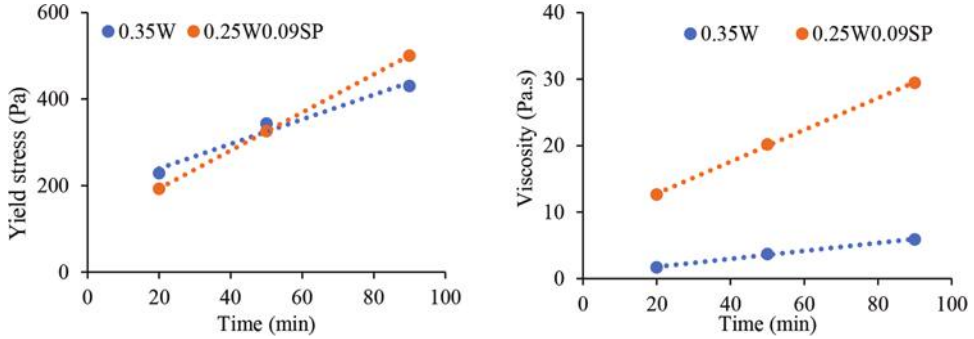

Fig. 4—Influence of w/c *on: (left)* τ_y*; and (right)* μ_p*. (Note: 1 Pa = 0.02 lb/ft*^{2}*.)*

high maximum F_E implies low extrudability. Additionally, the open time was determined as the age of the print material beyond which the material could not be extruded without risk of blockage. The blockage of the print material implied that the F_E needed to extrude the material exceeds the load limit (135 N [30 lbf]) of the extruder setup. In this study, the D_B and V_R were fixed at 39 mm (1.5 in.) and 2.5 mm/s (0.1 in./s), so B_N was primarily a function of τ_y and μ_p, as shown in Eq. (2).[16]

$$B_N = \frac{\tau_{dy} D_B}{8\mu_p V_R} = \frac{\tau_{dy}\,(39\text{ mm})}{8\mu_p\,(2.5\text{ mm/s})} = \frac{\tau_{dy}\,(1.5\text{ in.})}{8\mu_p\,(0.1\text{ in./s})} \quad (2)$$

EXPERIMENTAL RESULTS AND DISCUSSION

Influence of *w/c* and WG content on HRWRA demand

The influence of *w/c* and WG content on rheology and fluid filtration characteristics of the mortar mixtures was examined by comparing the results of the mortars proportioned with identical initial flow values. As indicated in Table 2, the mixture prepared with a 0.35 *w/c* required no HRWRA to achieve the target initial flow of 120 mm (4.7 in.). However, with the reduction in the *w/c* to 0.25, 0.09% of HRWRA was required to secure the targeted mini-slump flow. The HRWRA demand increased to 0.7%, 1.3%, and 1.8% for the mixtures made with 0.1%, 0.2%, and 0.3% of WG, respectively, for mortars made with a 0.25 *w/c*. A similar increase in HRWRA demand was observed in previous studies[31-34] with an increase in WG content for grout and ultra-high-performance mortar mixtures.

Influence of mixture proportioning parameters on material properties

Effect of w/c—The influence of *w/c* on rheology and D_e was evaluated by comparing the results for 0.35W (mixture with a 0.35 *w/c*) and 0.25W0.09SP (mixture with a 0.25 *w/c* and 0.09% HRWRA ["SP" refers to superplasticizer]). The τ_y and μ_p values are shown in Fig. 4. In terms of τ_y, no significant difference was observed for either mixture at 20, 50, and 90 minutes. Conversely, a 400 to 650% increase in μ_p occurred with the decrease in *w/c*, despite the fixed mini-slump flow values. The high μ_p values for the 0.25W0.09SP mixture at different times were due to the lower amount of water content.[35] However, the lack of such influence on τ_y was due to the opposing effect of a low *w/c* and HRWRA addition.[36] The lowering of the *w/c* from 0.35 to 0.25 resulted in a fourfold increase in the rate of increase in μ_p with time. Such a significant increment can be attributed to the increased rate of flocculation due to the lower interparticle distance between the cement particles of the lower-*w/c* mixture.[37,38]

The B_N values were calculated using Eq. (2) and ranged from 142 to 264 for the 0.35W mixture and 30 to 33 for the 0.25W0.09SP mixture. Such a decrease in B_N from values >100 to <100 with the decrease in the *w/c* from 0.35 to 0.25 suggests a change in the material flow behavior from plastic to viscoplastic. As per Table 1, such a change in flow behavior results in a decrease in extrudability.

Figure 5 shows variations in D_e with applied overhead pressure for the 0.35W and 0.25W0.09SP mixtures after 20 and 90 minutes of water addition. These results indicate an increase in D_e with the increase in overhead pressure from 120 to 360 kPa (17 to 52 psi). Approximately 80% lower D_e values were observed for the 0.25W0.09SP mixture compared to the 0.35W mixture. The low D_e can be attributed to the lower amount of free water available for filtration and higher μ_p. The high D_e results for the 0.35W mixture suggest the possibility of fluid filtration and poor extrudability.

Based on the aforementioned results, the decrease in B_N to below 100 with the reduction of the *w/c* from 0.35 to 0.25 suggests a lower level of extrudability. On the other hand, the decrease in D_e with the decrease in *w/c* suggests an improvement in extrudability. These contradicting effects of rheology and D_e on extrudability indicate that the assessment of rheological properties alone is not sufficient to characterize the extrudability of the print material during extrusion-based 3DP.

Effect of HRWRA dosage—The influence of HRWRA dosage on material properties was evaluated by comparing the results of the 0.25W0.09SP, 0.25W0.11SP, 0.25W0.22SP, and 0.25W0.43SP mixtures prepared with a 0.25 *w/c*, different HRWRA dosages, and initial mini-slump flow values. The increase in HRWRA dosage can enhance the deflocculation of cement particles and increase the amount of free water.[39] The increase in HRWRA dosage from 0.09 to 0.43% led to an over 200% increase in mini-slump flow (Table 2) and an over 90% drop in τ_y and μ_p, as shown in Fig. 6. The increase in HRWRA dosage also reduced the rate of increase of τ_y and μ_p with time. These changes are due to the decrease in the rate of flocculation because of the

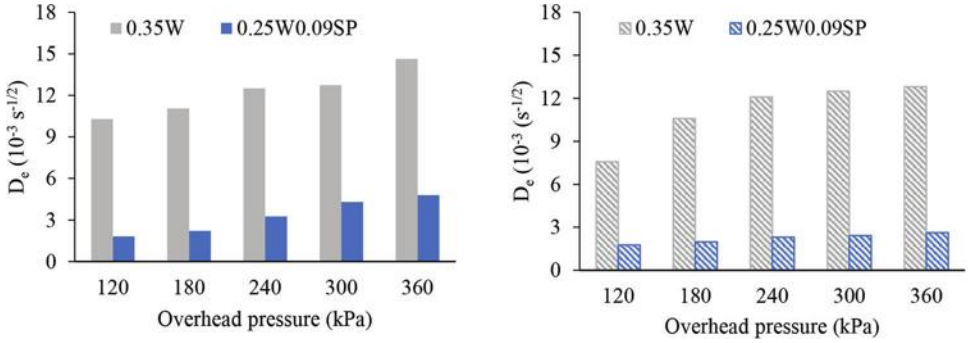

Fig. 5—Influence of w/c *on* D_e *at: (left) 20 minutes; and (right) 90 minutes. (Note: 1 kPa = 0.14 psi.)*

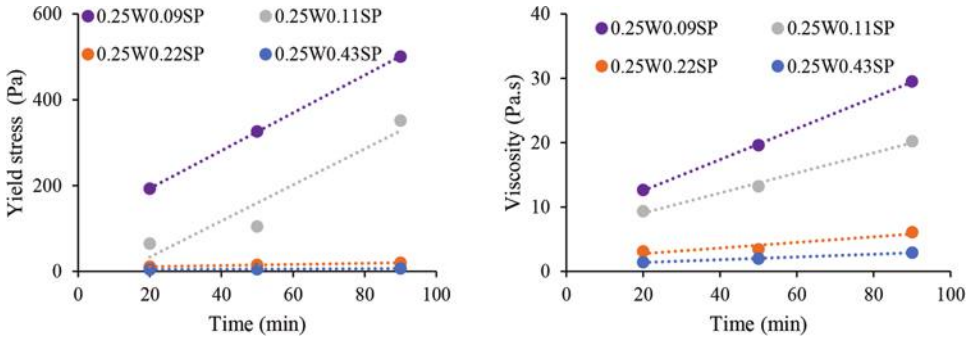

Fig. 6—Influence of HRWRA dosage on: (left) τ_y*; and (right)* μ_p*. (Note: 1 Pa = 0.02 lb/ft².)*

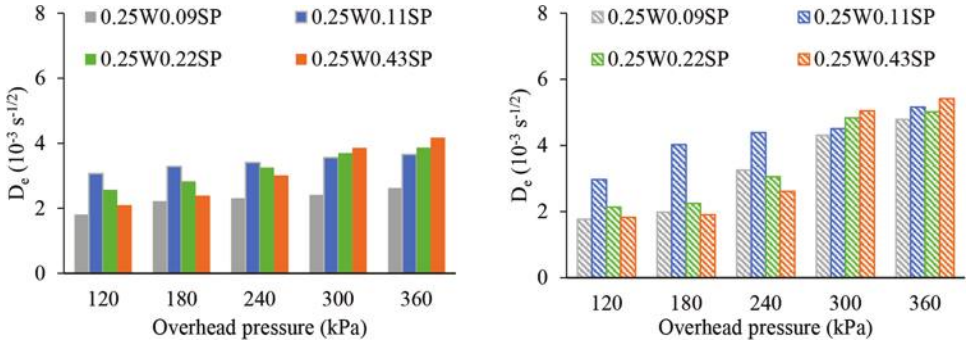

Fig. 7—Influence of HRWRA dosage on D_e *at: (left) 20 minutes; and (right) 90 minutes. (Note: 1 kPa = 0.14 psi.)*

increased interparticle distance between cement particles in the presence of HRWRA.[40,41]

The B_N values for the 0.25W0.09SP, 0.25W0.11SP, 0.25W0.22SP, and 0.25W0.43SP mixtures were in the ranges of 30 to 33, 14 to 34, 5 to 8, and 4 to 6, respectively. The relatively low values of B_N (<100) suggest viscoplastic flow behavior during ram extrusion. Additionally, the 25 to 90% reduction in B_N with the increase in HRWRA dosage from 0.09 to 0.43% suggests an increase in viscosity contribution to the extrusion force. The low B_N value reflects that a higher volume of the material within the extruder is sheared during the extrusion process.[42,43]

Figure 7 shows variation in D_e with overhead pressure for mixtures with different HRWRA dosages. The influence of HRWRA dosage on D_e varied depending on the pressure. At low pressures (that is, 120, 180, and 240 kPa [17, 26, and 35 psi]), the increase in HRWRA dosage from 0.09 to 0.11% increased the D_e by 70%. However, further increases in HRWRA dosage to 0.22 and 0.43% had the opposite effect. The increase in HRWRA dosage leads to increased dispersion of the cement and increased free water in the mixture.[25] As a result, with the application of overhead pressure, more water is available to filter through, which can increase D_e. At the same time, the increased dispersion of cement particles reduces the permeability of the mortar against the drainage surface, which can contribute to reduced D_e.[31] These contradicting effects of HRWRA resulted in nonlinear variation in D_e with increased HRWRA and pressure.[31] At 0.22 and 0.43% HRWRA dosages, the low permeability of the mortar mixtures resulted in lower D_e values.[25,31] However, at high pressure (that is, 300 and 360 kPa [44 and 52 psi]), no decrease in D_e was observed with an increase in HRWRA dosage. This suggests that the D_e at high pressure values is less sensitive to the permeability characteristics of the material.[44]

For mixtures made with different HRWRA dosages, low B_N values indicate viscoplastic behavior. Additionally, the decrease in τ_y and μ_p with the increase in HRWRA dosage suggests that a lower F_E is needed to extrude the mixture with high HRWRA (that is, increased extrudability).[23,45]

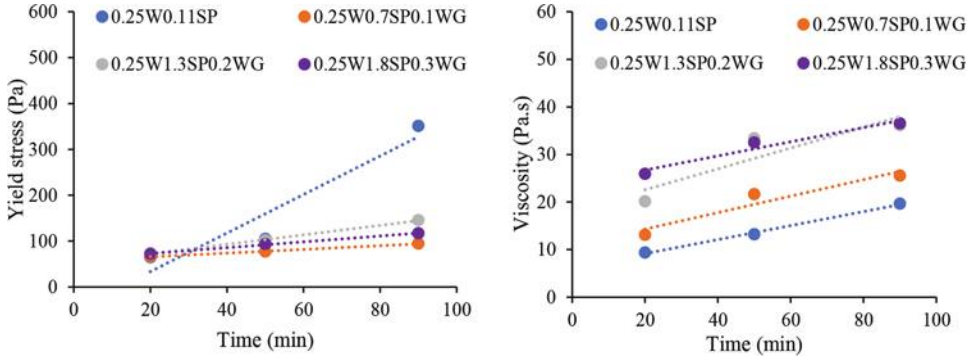

Fig. 8—Influence of WG content on: (left) τ_y; and (right) μ_p. (Note: 1 Pa = 0.02 lb/ft^2.)

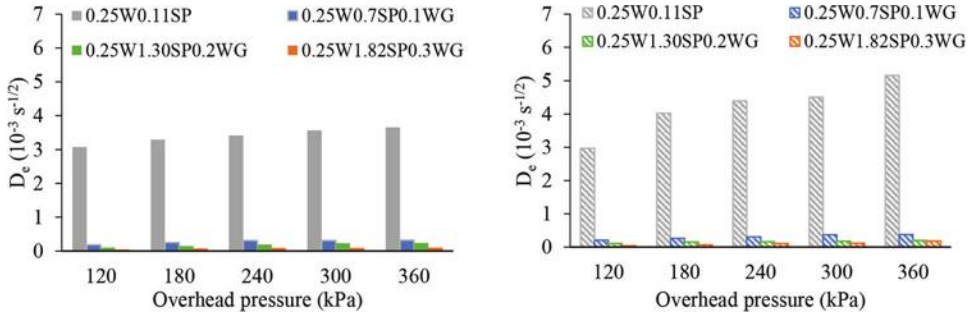

Fig. 9—Influence of WG content on D_e *at: (left) 20 minutes; and (right) 90 minutes. (Note: 1 kPa = 0.14 psi.)*

However, the influence of HRWRA dosage on D_e varied depending on the amount of HRWRA and the overhead pressure. Such D_e results suggest that the influence of HRWRA on extrudability is not straightforward, and that increasing the HRWRA dosage does not guarantee improvement in the extrudability.

Effect of WG content—The rheology and D_e results of mortars prepared with different WG contents are shown in Fig. 8 and 9, respectively. The increase in WG content necessitated greater HRWRA demand to maintain an initial mini-slump flow of 170 ± 10 mm (6.7 ± 0.4 in.). As a result, the rheology and D_e results presented were due to the combined action of WG and HRWRA. In Fig. 8, the rate of increase in τ_y with time dropped by 90% with the increase in WG content from 0 to 0.1% and the consequent increase in HRWRA dosage from 0.11 to 0.7%, respectively. However, a significant increase (30 to 190%) in μ_p was observed with the addition of WG, despite the higher HRWRA demand. The addition of 0.1 and 0.2% WG increased the rate of increase in μ_p, while no such increase occurred at 0.3% WG due to the high HRWRA demand.[31] The values of B_N for the 0.25W0.11SP, 0.25W0.7SP0.1WG, 0.25W1.3SP0.2WG, and 0.25W1.8SP0.3WG mixtures were in the ranges of 14 to 34, 7 to 10, 6 to 8, and 5 to 6, respectively. The significantly lower B_N values for mixtures made with WG (that is, lower than 100) reflect a viscoplastic flow behavior. Moreover, the drastic increase in μ_p with the addition of WG suggests a higher F_E may be needed to shear the mortar during extrusion (that is, decreased extrudability).

The D_e results in Fig. 9 indicate that a small addition of WG is sufficient to remarkably reduce the D_e from approximately 3×10^{-3} s$^{-0.5}$ to up to 0.04×10^{-3} s$^{-0.5}$. These results are in agreement with the low fluid filtration and high water retention reported by Wang et al.[34] and Khayat and Saric-Coric[46] for cement paste mixtures with WG. Such a drop can be partly attributed to the reduction in free water available for filtration[31] and an increase in the pore-solution viscosity, which could reduce the rate of fluid filtration.[46,47] Desbrieres[48] and Brumaud et al.[49] observed that the long-chain polymers (such as WG) can aggregate and partially fill the pores in the mortar matrix during fluid filtration, consequently reducing D_e. In the present study, the low D_e of WG mixtures can also be partly attributed to the decreased permeability of the mortar with increased HRWRA demand. The low D_e of WG mixtures indicates low migration of the fluid and homogenous shearing of the material during extrusion (that is, viscoplastic due to low B_N as opposed to frictional-plastic flow behavior).

Table 3 summarizes observed results stemming from the influence of *w*/*c*, HRWRA dosage, and WG content on material properties and extrudability. The increase in *w*/*c* at fixed flow had a limited effect on τ_y but reduced μ_p and increased D_e. The drop in the μ_p led to a change in B_N values from <100 to >100, suggesting improved extrudability. On the other hand, the increase in D_e with *w*/*c* indicates a high rate of forced bleeding and a drop in extrudability. The increase in the HRWRA reduced both τ_y and μ_p and had a varied effect on D_e. The use of WG at a fixed mini-slump flow increased μ_p, had a limited effect on τ_y (suggesting a drop in extrudability), and drastically reduced D_e (increase in extrudability). Such opposing effects of rheology and fluid filtration on extrudability highlight the importance of measuring both properties to assess the suitability of materials for 3DP.

Table 3—Influence of mixture parameters on material properties and extrudability

Increase in parameter	Rheology			Fluid filtration	
	τ_y	μ_p	Effect on extrudability	D_e	Effect on extrudability
w/c	Fixed*	Decrease	Improve	Increase	Deteriorate
HRWRA dosage	Decrease	Decrease	Improve	Increase/Decrease	Deteriorate/Improve
WG content	Fixed*	Increase	Deteriorate	Decrease	Improve

*For mixtures with different *w/c* and WG contents, τ_y and mini-slump flow values were fixed.

Table 4—Material properties and maximum extrusion force

Mixtures	Time, minutes	τ_y, Pa	μ_p, Pa·s	D_e at 120 kPa (10^{-3} $s^{-0.5}$)	B_N	Maximum F_E, N (lbf)
0.35W	20	229	2	10.33	223	>135 (30)
	50	343	4	9.87	167	>135 (30)
	90	431	6	7.58	140	>135 (30)
0.25W0.09SP	20	193	13	1.81	29	45 (10)
	50	326	20	1.78	32	95 (21)
	90	501	29	1.77	34	>135 (30)
0.25W0.11SP	50	105	13	3.01	16	41 (9)
	90	351	20	2.97	34	105 (24)
0.25W0.7SP0.1WG	130	100	28	0.21	7	28 (7)
	180	118	32	0.20	7	34 (8)
	220	174	48	0.18	7	46 (10)
0.25W1.3SP0.2WG	90	145	36	0.12	8	30 (7)
	130	185	37	0.10	10	39 (9)
	180	340	39	0.09	17	45 (10)
	220	470	44	0.05	21	63 (14)
0.25W1.8SP0.3WG	90	117	37	0.06	6	31 (7)
	130	150	44	0.05	7	35 (8)
	180	196	47	0.04	8	41 (9)
	220	346	58	0.04	12	70 (16)

Note: 1 Pa = 0.02 lb/ft².

Relationship between material properties and extrudability

During the ram extrusion, the print materials with a low τ_y were able to flow out of the nozzle due to gravity without the need to apply any F_E. However, the shape stability was not adequate. A τ_y of >100 Pa (2 lb/ft²) was required to extrude shape-retaining filaments. As mentioned, the load capacity of the ram extruder was 135 N (30 lbf), which corresponds to a pressure value of 113 kPa (16 psi) for D_B of 39 mm (1.5 in.), as indicated in Fig. 3(b). This means that for the print material, the maximum rate of fluid filtration during the ram extrusion is equivalent to D_e values measured at an overhead pressure of 120 ± 10 kPa (17 ± 1.4 psi) during the fluid filtration test. Table 4 summarizes the material properties, along with B_N and maximum F_E results at different ages where τ_y > 100 Pa (2 lb/ft²).

For the mixture prepared with a 0.35 *w/c* (0.35W), the material could not be extruded at 20, 50, or 90 minutes. This was because the F_E needed exceeded the load capacity (135 N [30 lbf]) of the extruder. On the other hand, the mixture with a 0.25 *w/c* and 0.09% HRWRA (0.25W0.09SP) was extrudable, with a maximum F_E of 45 and 95 N (10 and 21 lbf) at 20 and 50 minutes, respectively. These results indicate an improvement in the extrudability with the decrease in *w/c* from 0.35 to 0.25 and the addition of HRWRA dosage. Such improvement, despite the drop in B_N from over 100 to below 100, can be attributed to the lower D_e and consequent change in flow behavior from frictional-plastic to viscoplastic.

For mixtures made with a 0.25 *w/c*, the increase in HRWRA dosage from 0.09 to 0.11% reduced τ_y. As a result, the 0.25W0.11SP mixture was too flowable and not suitable for extrusion at 20 minutes. However, at 50 and 90 minutes, the τ_y increased beyond 100 Pa (2 lb/ft²), and the material became extrudable. The rheological properties were identical for the 0.25W0.09SP mixture at 50 minutes and the 0.25W0.11SP mixture at 90 minutes (τ_y = 330 to 340 Pa [6.9 to 7.1 lb/ft²] and μ_p = 20 Pa·s [0.42 lb/ft²·s]). However, the D_e was 67% higher for the 0.25W0.11SP mixture, resulting in an 11% increase in maximum F_E. For mixtures prepared with higher HRWRA (0.25W0.22SP and 0.25W0.43SP mixtures), τ_y was lower than 100 Pa (2 lb/ft²) until 220 minutes of age, and the extrudability could not be assessed.

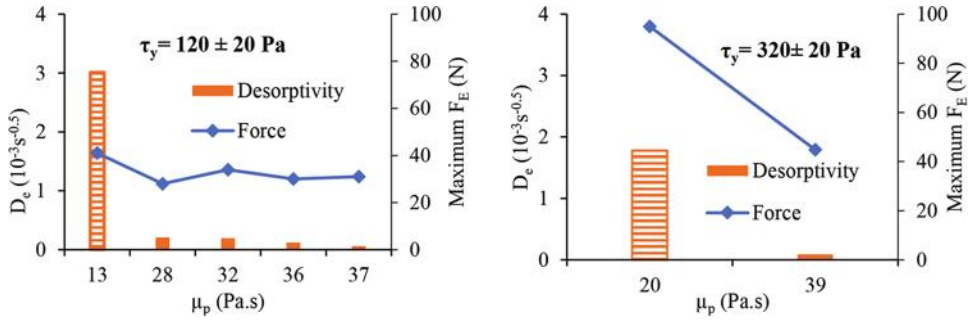

Fig. 10—Relationship between material properties and extrudability of mortar with τ_y of: (left) 120 Pa; and (right) 320 Pa. Dashed bar indicates D_e of mixtures without WG. (Note: 1 Pa = 0.02 lb/ft²; 1 N = 0.22 lbf.)

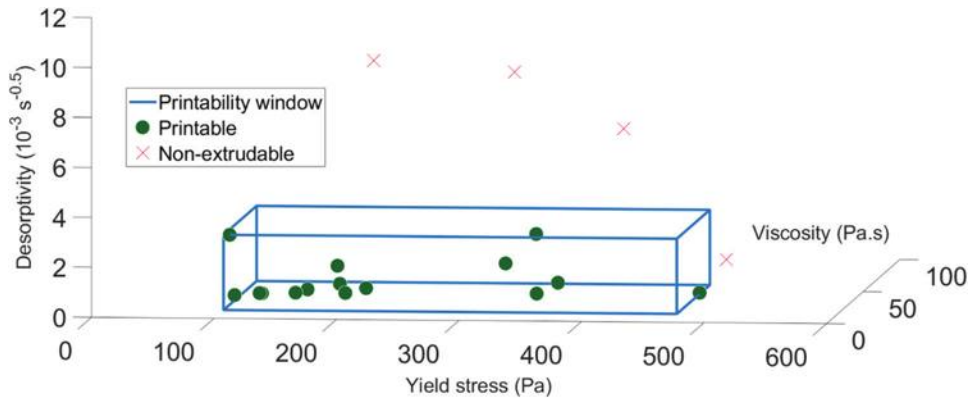

Fig. 11—Printability window of mortar encompassing yield stress (100 to 470 Pa), plastic viscosity (10 to 60 Pa·s), and desorptivity ($<3 \times 10^{-3}$ $s^{-0.5}$).

The mixtures prepared with WG were too flowable at 20 and 50 minutes, but they became extrudable at later ages. Compared to the mixtures without any WG, mixtures containing WG were extrudable for a longer time, indicating an increased open time with the combined use of WG and HRWRA. The higher μ_p, and consequently lower B_N values for mixtures with WG, suggest that the print material undergoes a viscoplastic flow during extrusion. Additionally, for a given τ_y, the maximum F_E needed to extrude the material was lower for mixtures made with WG due to the reduction in D_e. As shown in Fig. 10, the enhanced extrudability was especially significant for mixtures with high τ_y values. Furthermore, the addition of WG enabled the extrusion of print mortars having high $\tau_y > 400$ Pa (8.4 lb/ft²). The ability to extrude print materials with such high τ_y values can lead to the printing of shape-retaining layers of larger heights. It also facilitates faster printing by reducing the time gap required between successive layers to ensure the shape stability of printed elements.[14]

The material properties and extrudability results of the investigated mixtures were used for the development of a "printability window," as shown in Fig. 11. The printability window, indicated as a blue box, encompasses the range of material properties where the print material is extrudable into shape-stable layers. The lower limits for τ_y and μ_p correspond to the minimum values needed to extrude shape-stable layers and limit fluid filtration during extrusion, respectively, while the upper limits for τ_y and μ_p correspond to the maximum shear the extruder can exert on the material, beyond which the load capacity of the extruder is exceeded. The upper limit for D_e limits the fluid filtration and frictional-plastic flow behavior during extrusion. The printability window for the mortar mixtures tested was: τ_y: 100 to 470 Pa (2 to 10 lb/ft²); μ_p: 10 to 60 Pa·s (0.2 to 1.2 lb/ft²·s); and D_e at 120 kPa overhead pressure $<3 \times 10^{-3}$ $s^{-0.5}$. These material ranges are valid for the ram extrusion parameters of $D_B = 39$ mm, $D_N = 9$ mm, $L_E = 80$ mm, and $V_R = 2.5$ mm/s that are used in this study. The printability window can vary depending on V_R, dimensions, and load capacity of the extruder.

Statistical modeling of material properties and extrudability

Multiple linear regression was used for modeling the maximum F_E as a function of τ_y, μ_p, and D_e. Considering the limited number of data points available in this study (Table 4), the proposed regression equation is used for explanatory modeling (that is, for assessing the significance of τ_y, μ_p, and D_e on extrudability) instead of the estimation of the maximum F_E.

The multiple regression model for the maximum F_E was initially fit using τ_y, μ_p, and D_e. The adjusted R^2 values and estimates, along with the p-values of partial tests for τ_y, μ_p, and D_e, are shown in Table 5. The p-values indicate the significance of the test parameters (τ_y, μ_p, and D_e) on the output (maximum F_E). The p-values lower than 0.05 indicate that the parameter has a significant effect on the output. The p-values are lower than 0.05 for τ_y and D_e, hence indicating that these properties have a significant effect on the maximum F_E. Conversely, the high p-value for μ_p indicates that the viscosity does not have a significant effect on the maximum F_E, given

Table 5—Multiple regression analysis of extrudability results

Property	Maximum F_E = $f(\tau_y, \mu_p$, and $D_e)$		Maximum F_E = $f(\tau_y$ and $D_e)$	
	Estimate	*p*-value	Estimate	*p*-value
τ_y, Pa	0.13	0.0013	0.14	0.0002
μ_p, Pa·s	0.48	0.3127*	—	—
D_e (10^{-3} $s^{-0.5}$)	15.39	0.0155	10.55	0.0029
Adjusted R^2	0.76		0.76	

*p-value > 0.05 implies that influence of specific parameter is insignificant.

Note: 1 Pa = 0.02 lb/ft^2.

certain values of τ_y and D_e. Therefore, a second regression model was established using τ_y and D_e, and these results are also reported in Table 5. The *p*-values lower than 0.05 indicate that τ_y and D_e have a significant effect on extrudability. Additionally, the positive values of the estimates for both properties indicate that an increase in τ_y and D_e can lead to a higher F_E or a lower level of extrudability.

CONCLUSIONS

In this study, the rheology and fluid filtration characteristics of mortar mixtures were varied by changing the water-cement ratio (*w*/*c*), high-range water-reducing admixture (HRWRA) dosage, and welan gum (WG) content. The influence of these properties on extrudability was evaluated. The fluid filtration was measured in terms of desorptivity (D_e), while the extrudability was assessed as the maximum application of force (F_E) needed during extrusion. A printability window was proposed for the extrusion of mortar based on the rheology and fluid filtration characteristics. Additionally, regression analysis was carried out to evaluate the significance of the effect of material properties on extrudability. Based on the findings of this investigation, the following conclusions can be made:

1. For a ram extruder with D_N of 9 mm (0.4 in.) and extrusion speed (V_R) of 2.5 mm/s (0.1 in./s), the suitable ranges of material properties for successful three-dimensional (3-D) printing (3DP) 3DP consist of yield stress (τ_y) of 100 to 470 Pa (2 to 10 lb/ft^2), plastic viscosity (μ_p) of 10 to 60 Pa·s (0.2 to 1.2 lb/ft^2·s), and $D_e < 3 \times 10^{-3}$ $s^{-0.5}$ at an overhead pressure of 120 kPa (17 psi).

2. For the investigated rheology and filtration characteristics, the influence of μ_p on extrudability is insignificant compared to τ_y and D_e. The extrudability can be improved by reducing τ_y and D_e. However, a lower limit of 100 Pa (2 lb/ft^2) for τ_y is needed to ensure shape stability.

3. The decrease in *w*/*c* from 0.35 to 0.25 required an increase in HRWRA dosage from 0 to 0.09%, by mass of cement, to maintain an initial mini-slump flow of 120 mm (4.7 in.). The decrease in *w*/*c* led to a 400 to 650% increase in μ_p and reduced the D_e by 80%. It also improved the extrudability due to a change in flow behavior during extrusion from frictional-plastic (at 0.35 *w*/*c* and no HRWRA) to viscoplastic (at 0.25 *w*/*c* and 0.09% HRWRA).

4. The increase in HRWRA dosage from 0.09 to 0.43% increased initial mini-slump flow by 200% and reduced τ_y and μ_p by over 90%. The influence of HRWRA on D_e varied depending on the overhead pressure in the forced bleeding cell and the HRWRA dosage. The increase in HRWRA from 0.09 to 0.11% resulted in improved extrudability due to the reduction in the material rheological properties. Mixtures with higher HRWRA dosages (that is, 0.22 and 0.43%) were not suitable for extrusion owing to the low τ_y and poor shape stability.

5. At a fixed initial mini-slump flow of 170 mm (6.7 in.), the addition of WG at 0.1, 0.2, and 0.3%, by mass of cement, significantly increased μ_p, by up to 180%, and reduced the rate of increase in τ_y with time. The use of WG also drastically reduced the D_e by up to two orders of magnitude. The use of WG improved the extrudability due to low fluid filtration and open time given the high HRWRA demand. The use of WG also enabled the extrusion of print material with high τ_y (>400 Pa [8.4 lb/ft^2]) at lower F_E.

6. Overall, the use of WG enabled the development of print materials that are most suitable for extrusion-based 3DP (that is, higher τ_y needed for shape stability, lower D_e needed for homogeneous extrusion, and increased open time).

AUTHOR BIOS

ACI member **Kavya Vallurupalli** *is a Scientist at Master Builders Solutions Construction Systems. She received her PhD in civil engineering from Missouri University of Science and Technology (Missouri S&T), Rolla, MO, in 2022. The current work was part of her PhD.*

ACI member **Nicolas Ali Libre** *is an Associate Teaching Professor of civil engineering at Missouri S&T. He is a member of ACI Committees 211, Proportioning Concrete Mixtures, and 238, Workability of Fresh Concrete.*

Kamal H. Khayat, *FACI, is a Professor of civil engineering and Vice Chancellor for Research and Innovation at Missouri S&T. He is a member of the ACI Board of Direction, the* ACI Materials Journal *Editorial Board, the ACI Technical Activities Committee, and several other ACI committees, including ACI Committee 564, 3-D Printing with Cementitious Materials.*

REFERENCES

1. Hack, N., and Lauer, W. V., "Mesh-Mould: Robotically Fabricated Spatial Meshes as Reinforced Concrete Formwork," *Architectural Design*, V. 84, No. 3, May/June 2014, pp. 44-53. doi: 10.1002/ad.1753

2. Jagoda, J.; Diggs-McGee, B.; Kreiger, M.; and Schuldt, S., "The Viability and Simplicity of 3D-Printed Construction: A Military Case Study," *Infrastructures*, V. 5, No. 4, Apr. 2020, Article No. 35. doi: 10.3390/infrastructures5040035

3. Zhang, J.; Wang, J.; Dong, S.; Yu, X.; and Han, B., "A Review of the Current Progress and Application of 3D Printed Concrete," *Composites Part A: Applied Science and Manufacturing*, V. 125, Oct. 2019, Article No. 105533. doi: 10.1016/j.compositesa.2019.105533

4. Bhardwaj, A.; Jones, S. Z.; Kalantar, N.; Pei, Z.; Vickers, J.; Wangler, T.; Zavattieri, P.; and Zou, N., "Additive Manufacturing Processes for Infrastructure Construction: A Review," *Journal of Manufacturing Science and Engineering*, V. 141, No. 9, Sept. 2019, Article No. 091010.

5. Buswell, R. A.; Leal da Silva, W. R.; Bos, F. P.; Schipper, H. R.; Lowke, D.; Hack, N.; Kloft, H.; Mechtcherine, V.; Wangler, T.; and Roussel, N., "A Process Classification Framework for Defining and Describing Digital Fabrication with Concrete," *Cement and Concrete Research*, V. 134, Aug. 2020, Article No. 106068. doi: 10.1016/j.cemconres.2020.106068

6. Gibbons, G. J.; Williams, R.; Purnell, P.; and Farahi, E., "3D Printing of Cement Composites," *Advances in Applied Ceramics*, V. 109, No. 5, 2010, pp. 287-290. doi: 10.1179/174367509X12472364600878

7. Xia, M., and Sanjayan, J., "Method of Formulating Geopolymer for 3D Printing for Construction Applications," *Materials & Design*, V. 110, Nov. 2016, pp. 382-390. doi: 10.1016/j.matdes.2016.07.136

8. Utela, B.; Storti, D.; Anderson, R.; and Ganter, M., "A Review of Process Development Steps for New Material Systems in Three Dimensional Printing (3DP)," *Journal of Manufacturing Processes*, V. 10, No. 2, July 2008, pp. 96-104. doi: 10.1016/j.jmapro.2009.03.002

9. Khoshnevis, B., "Automated Construction by Contour Crafting—Related Robotics and Information Technologies,"

Automation in Construction, V. 13, No. 1, Jan. 2004, pp. 5-19. doi: 10.1016/j.autcon.2003.08.012

10. Khoshnevis, B.; Hwang, D.; Yao, K.-T.; and Yeh, Z., "Mega-Scale Fabrication by Contour Crafting," *International Journal of Industrial and Systems Engineering*, V. 1, No. 3, 2006, pp. 301-320. doi: 10.1504/IJISE.2006.009791

11. Le, T. T.; Austin, S. A.; Lim, S.; Buswell, R. A.; Gibb, A. G. F.; and Thorpe, T., "Mix Design and Fresh Properties for High-Performance Printing Concrete," *Materials and Structures*, V. 45, No. 8, Aug. 2012, pp. 1221-1232. doi: 10.1617/s11527-012-9828-z

12. Salet, T. A. M.; Ahmed, Z. Y.; Bos, F. P.; and Laagland, H. L. M., "Design of a 3D Printed Concrete Bridge by Testing," *Virtual and Physical Prototyping*, V. 13, No. 3, 2018, pp. 222-236. doi: 10.1080/17452759.2018.1476064

13. Meisenzahl, M., "This Building in Dubai Is the Largest 3D-Printed Structure in the World — and It Took Just 3 Workers and a Printer to Build It," *Business Insider*, New York, Dec. 30, 2019, https://www.businessinsider.com/dubai-largest-3d-printed-building-apis-cor-photos-2019-12. (last accessed Feb. 7, 2024)

14. Roussel, N., "Rheological Requirements for Printable Concretes," *Cement and Concrete Research*, V. 112, Oct. 2018, pp. 76-85. doi: 10.1016/j.cemconres.2018.04.005

15. Wi, K.; Hong, J.; and Wang, K., "Determining Printable Zone of Three-Dimensional-Printable Mortar Using Flow Table Tests," *ACI Materials Journal*, V. 118, No. 6, Nov. 2021, pp. 75-85.

16. Vallurupalli, K.; Farzadnia, N.; and Khayat, K. H., "Effect of Flow Behavior and Process-Induced Variations on Shape Stability of 3D Printed Elements – A Review," *Cement and Concrete Composites*, V. 118, Apr. 2021, Article No. 103952. doi: 10.1016/j.cemconcomp.2021.103952

17. Alghamdi, H.; Nair, S. A. O.; and Neithalath, N., "Insights into Material Design, Extrusion Rheology, and Properties of 3D-Printable Alkali-Activated Fly Ash-Based Binders," *Materials & Design*, V. 167, Apr. 2019, Article No. 107634. doi: 10.1016/j.matdes.2019.107634

18. Bentz, D. P.; Jones, S. Z.; Bentz, I. R.; and Peltz, M. A., "Towards the Formulation of Robust and Sustainable Cementitious Binders for 3-D Additive Construction by Extrusion," *Construction and Building Materials*, V. 175, June 2018, pp. 215-224. doi: 10.1016/j.conbuildmat.2018.04.167

19. Panda, B., and Tan, M. J., "Experimental Study on Mix Proportion and Fresh Properties of Fly Ash Based Geopolymer for 3D Concrete Printing," *Ceramics International*, V. 44, No. 9, June 2018, pp. 10258-10265. doi: 10.1016/j.ceramint.2018.03.031

20. Kuder, K. G., and Shah, S. P., "Rheology of Extruded Cement-Based Materials," *ACI Materials Journal*, V. 104, No. 3, May-June 2007, pp. 283-290.

21. Srinivasan, R.; DeFord, D.; and Shah, S. P., "The Use of Extrusion Rheometry in the Development of Extruded Fiber-Reinforced Cement Composites," *Concrete Science and Engineering*, V. 1, No. 1, 1999, pp. 26-36.

22. Zhou, X., and Li, Z., "Characterization of Rheology of Fresh Fiber Reinforced Cementitious Composites through Ram Extrusion," *Materials and Structures*, V. 38, No. 1, Jan. 2005, pp. 17-24. doi: 10.1007/BF02480570

23. Perrot, A.; Rangeard, D.; and Mélinge, Y., "Prediction of the Ram Extrusion Force of Cement-Based Materials," *Applied Rheology*, V. 24, No. 5, Oct. 2014, pp. 34-40.

24. Ince, C.; Carter, M. A.; Wilson, M. A.; Collier, N. C.; El-Turki, A.; Ball, R. J.; and Allen, G. C., "Factors Affecting the Water Retaining Characteristics of Lime and Cement Mortars in the Freshly-Mixed State," *Materials and Structures*, V. 44, No. 2, Mar. 2011, pp. 509-516. doi: 10.1617/s11527-010-9645-1

25. Rahul, A. V.; Sharma, A.; and Santhanam, M., "A Desorptivity-Based Approach for the Assessment of Phase Separation during Extrusion of Cementitious Materials," *Cement and Concrete Composites*, V. 108, Apr. 2020, Article No. 103546. doi: 10.1016/j.cemconcomp.2020.103546

26. Feys, D.; Wallevik, J. E.; Yahia, A.; Khayat, K. H.; and Wallevik, O. H., "Extension of the Reiner–Riwlin Equation to Determine Modified Bingham Parameters Measured in Coaxial Cylinders Rheometers," *Materials and Structures*, V. 46, No. 1-2, Jan. 2013, pp. 289-311. doi: 10.1617/s11527-012-9902-6

27. Nerella, V. N.; Näther, M.; Iqbal, A.; Butler, M.; and Mechtcherine, V., "Inline Quantification of Extrudability of Cementitious Materials for Digital Construction," *Cement and Concrete Composites*, V. 95, Jan. 2019, pp. 260-270. doi: 10.1016/j.cemconcomp.2018.09.015

28. Kuchem, J. T., "Development of Test Methods for Characterizing Extrudability of Cement-Based Materials for Use in 3D Printing," master's thesis, Missouri University of Science and Technology, Rolla, MO, 2019, 190 pp.

29. Perrot, A.; Lanos, C.; Melinge, Y.; and Estellé, P., "Mortar Physical Properties Evolution in Extrusion Flow," *Rheologica Acta*, V. 46, No. 8, Oct. 2007, pp. 1065-1073. doi: 10.1007/s00397-007-0195-6

30. Perrot, A.; Rangeard, D.; Nerella, V. N.; and Mechtcherine, V., "Extrusion of Cement-Based Materials - An Overview," *RILEM Technical Letters*, V. 3, 2018, pp. 91-97. doi: 10.21809/rilemtechlett.2018.75

31. Khayat, K. H., and Yahia, A., "Effect of Welan Gum-High-Range Water Reducer Combinations on Rheology of Cement Grout," *ACI Materials Journal*, V. 94, No. 5, Sept.-Oct. 1997, pp. 365-372.

32. Teng, L.; Zhu, J.; Khayat, K. H.; and Liu, J., "Effect of Welan Gum and Nanoclay on Thixotropy of UHPC," *Cement and Concrete Research*, V. 138, Dec. 2020, Article No. 106238. doi: 10.1016/j.cemconres.2020.106238

33. Üzer, E., and Plank, J., "Impact of Welan Gum Stabilizer on the Dispersing Performance of Polycarboxylate Superplasticizers," *Cement and Concrete Research*, V. 82, Apr. 2016, pp. 100-106. doi: 10.1016/j.cemconres.2015.12.009

34. Wang, F.; Wang, D.; Wang, Q.; Yu, J.; and Shi, J., "Impact of Welan Gum on Cement Paste Containing PCE Superplasticizers with Different Charge Densities," *ChemistrySelect*, V. 4, No. 5, 2019, pp. 1722-1726. doi: 10.1002/slct.201803307

35. Wallevik, O. H., and Wallevik, J. E., "Rheology as a Tool in Concrete Science: The Use of Rheographs and Workability Boxes," *Cement and Concrete Research*, V. 41, No. 12, Dec. 2011, pp. 1279-1288. doi: 10.1016/j.cemconres.2011.01.009

36. Tay, Y. W. D.; Qian, Y.; and Tan, M. J., "Printability Region for 3D Concrete Printing Using Slump and Slump Flow Test," *Composites Part B: Engineering*, V. 174, Oct. 2019, Article No. 106968. doi: 10.1016/j.compositesb.2019.106968

37. Bentz, D. P.; Peltz, M. A.; and Winpigler, J., "Early-Age Properties of Cement-Based Materials. II: Influence of Water-to-Cement Ratio," *Journal of Materials in Civil Engineering*, ASCE, V. 21, No. 9, Sept. 2009, pp. 512-517. doi: 10.1061/(ASCE)0899-1561(2009)21:9(512)

38. Libre, N. A.; Khoshnazar, R.; and Shekarchi, M., "Relationship between Fluidity and Stability of Self-Consolidating Mortar Incorporating Chemical and Mineral Admixtures," *Construction and Building Materials*, V. 24, No. 7, July 2010, pp. 1262-1271. doi: 10.1016/j.conbuildmat.2009.12.009

39. Sakai, E.; Kasuga, T.; Sugiyama, T.; Asaga, K.; and Daimon, M., "Influence of Superplasticizers on the Hydration of Cement and the Pore Structure of Hardened Cement," *Cement and Concrete Research*, V. 36, No. 11, Nov. 2006, pp. 2049-2053. doi: 10.1016/j.cemconres.2006.08.003

40. Kirby, G. H., and Lewis, J. A., "Comb Polymer Architecture Effects on the Rheological Property Evolution of Concentrated Cement Suspensions," *Journal of the American Ceramic Society*, V. 87, No. 9, Sept. 2004, pp. 1643-1652. doi: 10.1111/j.1551-2916.2004.01643.x

41. Yahia, A.; Mantellato, S.; and Flatt, R. J., "Concrete Rheology: A Basis for Understanding Chemical Admixtures," *Science and Technology of Concrete Admixtures*, P.-C. Aïtcin and R. J. Flatt, eds., Woodhead Publishing, Sawston, UK, 2016, pp. 97-127.

42. Basterfield, R. A.; Lawrence, C. J.; and Adams, M. J., "On the Interpretation of Orifice Extrusion Data for Viscoplastic Materials," *Chemical Engineering Science*, V. 60, No. 10, May 2005, pp. 2599-2607. doi: 10.1016/j.ces.2004.12.019

43. Perrot, A.; Mélinge, Y.; Rangeard, D.; Micaelli, F.; Estellé, P.; and Lanos, C., "Use of Ram Extruder as a Combined Rheo-Tribometer to Study the Behaviour of High Yield Stress Fluids at Low Strain Rate," *Rheologica Acta*, V. 51, No. 8, Aug. 2012, pp. 743-754. doi: 10.1007/s00397-012-0638-6

44. Vanhove, Y., and Khayat, K. H., "Forced Bleeding Test to Assess Stability of Flowable Concrete," *ACI Materials Journal*, V. 113, No. 6, Nov.-Dec. 2016, pp. 753-758. doi: 10.14359/51689240

45. Nair, S. A. O.; Panda, S.; Santhanam, M.; Sant, G.; and Neithalath, N., "A Critical Examination of the Influence of Material Characteristics and Extruder Geometry on 3D Printing of Cementitious Binders," *Cement and Concrete Composites*, V. 112, Sept. 2020, Article No. 103671. doi: 10.1016/j.cemconcomp.2020.103671

46. Khayat, K. H., and Saric-Coric, M., "Effect of Welan Gum-Superplasticizer Combinations on Properties of Cement Grouts," *The Sixth Canmet/ACI Conference on Superplasticizers and Other Chemical Admixtures in Concrete*, SP-195, V. M. Malhotra, ed., American Concrete Institute, Farmington Hills, MI, 2000, pp. 249-268.

47. Khayat, K. H., and Guizani, Z., "Use of Viscosity-Modifying Admixture to Enhance Stability of Fluid Concrete," *ACI Materials Journal*, V. 94, No. 4, July-Aug. 1997, pp. 332-339.

48. Desbrieres, J., "Cement Cake Properties in Static Filtration. On the Role of Fluid Loss Control Additives on the Cake Porosity," *Cement and Concrete Research*, V. 23, No. 6, Nov. 1993, pp. 1431-1442. doi: 10.1016/0008-8846(93)90080-S

49. Brumaud, C.; Bessaies-Bey, H.; Mohler, C.; Baumann, R.; Schmitz, M.; Radler, M.; and Roussel, N., "Cellulose Ethers and Water Retention," *Cement and Concrete Research*, V. 53, Nov. 2013, pp. 176-184. doi: 10.1016/j.cemconres.2013.06.010

JOIN AN ACI Chapter!

The American Concrete Institute has Chapters and Student Chapters located throughout the world. Participation in a local chapter can be extremely rewarding in terms of gaining greater technical knowledge and networking with leaders in the concrete community.

Because chapters are distinct and independent legal entities, membership includes both ACI members and non-ACI members and is made up of a diverse blend of architects, engineers, consultants, contractors, educators, material suppliers, equipment suppliers, owners, and students—basically anyone interested in concrete. Many active ACI members initially became involved in ACI through their local chapter. In addition to technical programs and publications, many chapters sponsor ACI Certification programs, ACI educational seminars, project award recognition programs, and social events with the goal of advancing concrete knowledge.

Check out the Chapters Special Section from the November 2020 *Concrete International*: www.concrete.org/publications/concreteinternational.aspx

---

Student Chapters

Join or form an ACI Student Chapter to maximize your influence, knowledge sharing, and camaraderie! ACI has 240+ student chapters located throughout the world, each providing opportunities for students to:

- Connect with their peers and participate in concrete-related activities such as: student competitions, ACI Conventions, ACI Certification Programs, ACI Educational Seminars, local chapter meetings, social events, and community service projects;
- Network with members of local chapters, many of whom have been in the industry for decades and can help to develop professional relationships and offer career advice;
- Win recognition for their universities through the University Award; and
- Learn about the many scholarships and fellowships offered by the ACI Foundation and by ACI's local chapters.

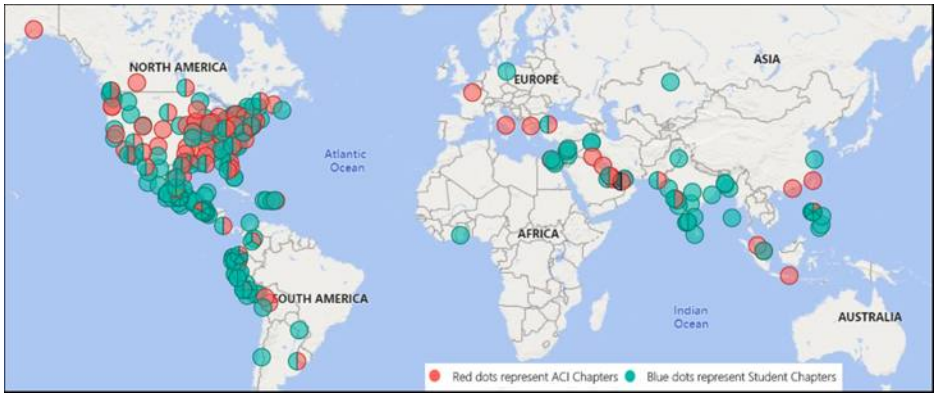

ACI MATERIALS JOURNAL TECHNICAL PAPER

Title No. 121-M12

Print Geometry Alterations and Layer Staggering to Enhance Mechanical Properties of Plain and Fiber-Reinforced Three-Dimensional-Printed Concrete

by Avinaya Tripathi, Sooraj A. O. Nair, Harshitsinh Chauhan, and Narayanan Neithalath

Conventional approaches to concrete three-dimensional (3-D) printing relies on printing concrete in a straight (linear) print path, with layers overlaid on top of each other. This results in interlayer and interfilament joints being potential weak spots that compromise the mechanical performance. This paper evaluates simple alterations to the print geometry to mitigate some of these effects. A printable mixture with 30% of limestone powder replacing cement (by mass), with a 28-day compressive strength of approximately 70 MPa in the strongest direction is used. S- and 3-shaped print paths are evaluated as alternatives to the linear print path. Staggering of the layers ensures that the interfilament joints do not lie on the same plane along the depth. Flexural strength enhancement is observed when print geometries are changed and/or layers are staggered. The study shows that print geometry modifications mitigate mechanical property reductions attributed to interfilament defects in 3-D concrete printing.

Keywords: anisotropy; compressive strength; flexural strength; layer geometry; three-dimensional (3-D) concrete printing.

INTRODUCTION

Three-dimensional (3-D) concrete printing is attracting a lot of interest in the construction industry due to its numerous advantages such as freedom to create complex architectures, optimized material use, ability to print on-demand structures, and reduced labor requirements.[1-5] This has resulted in concurrent advances in novel materials that satisfy stringent rheology and strength development requirements, and printing systems capable of executing complex geometries in an efficient manner. However, several challenges from a materials standpoint still exist. The combined attainment of pumpability, extrudability, and buildability, which sometimes necessitates contradictory material properties, is still a challenge. However, through careful material design, admixtures for rheology control, and print path planning, efforts are ongoing to address these impediments.[6-10] While attention has rightly been focused on rheology and consequent printability of concrete, mechanical properties of 3-D-printed concrete has been treated, for the most part, like those of conventional concrete, except for allowances for the layered construction method that induces anisotropy in properties. It has been reported that the mechanical properties of 3-D-printed concrete structures can likely be inferior to those fabricated using traditional casting techniques.[10-12]

Because the 3-D-printing process involves laying individual filaments side-by-side and stacking layers of filaments one over the other, there are several likely zones of weakness in the overall structure, which results in reduced mechanical performance.[13-17] The compressive strengths of 3-D-printed specimens are generally reported for the three orthogonal directions.[11,18,19] The direction of maximum strength is dependent on the method of casting and the process aspects involved in 3-D printing, including the nozzle standoff distance, which makes generalizing the results rather difficult. While higher strengths can be achieved through changes in material design,[20,21] the effects of planes of weakness that are introduced through layering cannot be overcome using improved materials alone. It is in this context that there is a need to investigate the arrangement of interfilamentous and interlayer joints that results in different levels of anisotropy in a 3-D-printed structural element. Changing the direction of printing of individual filaments within a layer, or layers within a component, will change the direction-dependent mechanical properties, thereby providing an option to optimize the desired performance.

For instance, filaments of rectangular cross section (with or without bullnosed edges) are printed in straight lines (unless it is an architectural structure with a nonlinear geometry) and subsequent layers are overlaid symmetrically on top of the lower layers. This results in the interfilamentous joints in each layer aligning along the entire depth of the structure. When tested in flexure, if there is only one filament width that is tested, this effect will not be captured, but when samples with multiple filaments are tested, this effect will dominate. Instead of printing the filaments in a straight path, curving of the print paths in a prismatic specimen will result in non-alignment of regions of weakness along the direction of loading, thereby likely enhancing the strength. This aspect is evaluated in this work. Furthermore, based on the nozzle type used (circular or rectangular), the extent of discontinuity at locations where the filaments meet in the horizontal and vertical directions can result in reduced mechanical performance. A potential workaround is to stagger the filaments in each layer so that the interfilamentous joints do not occur in different layers exactly above one another. This aspect is also explored in this paper. In addition to linear or straight filament printing,

ACI Materials Journal, V. 121, No. 2, March 2024.

MS No. M-2022-164.R1, doi: 10.14359/51740262, received January 26, 2023, and reviewed under Institute publication policies.

Table 1—Chemical composition and physical properties of mortar components

Components of binders	Chemical composition, % by mass							d_{50}, µm	Specific gravity
	SiO_2	Al_2O_3	Fe_2O_3	CaO	MgO	SO_3	LOI		
OPC	19.60	4.09	3.39	63.21	3.37	3.17	2.54	10.4	3.15
Limestone (L)	$CaCO_3 > 99\%$							1.5	2.70
Medium sand (M)	$SiO_2 > 99\%$							200	2.40

Note: LOI is loss on ignition.

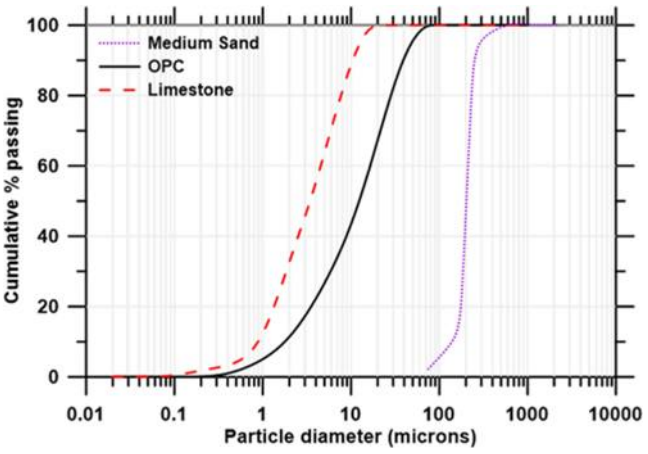

Fig. 1—PSD of mortar components.

this paper explores S-shaped and 3-shaped printing paths to evaluate their influence on the flexural performance when the layers are perpendicular to the direction of loading, and cube compressive strengths in the three orthogonal directions. The synergistic effects of fiber reinforcement—either steel or basalt—along with the aforementioned geometric modifications are also studied in this paper.

RESEARCH SIGNIFICANCE

The rationale behind this study is to demonstrate that the mechanical performance of 3-D-printed concrete elements can be enhanced by simple variations in the print geometry. In this work, S-shaped and 3-shaped (top-view) filament prints are compared to linear filament prints, and the effect of staggering of filament layers is compared to the conventional method where the filaments are overlaid one on top of the other in an ordered fashion. It is shown that the introduced modifications help enhance the flexural strength of 3-D-printed concrete, while not influencing the compressive strength in any significant manner. The paper provides experimental results that can motivate the field printing of different shapes (including curved shapes using S- or 3-shaped geometries) or different layering types (for example, staggered) of 3-D-printed concretes without the concern for property loss.

EXPERIMENTAL PROGRAM

Materials and mixtures

The mortar mixtures in this study were proportioned using Type I/II ordinary portland cement (OPC) conforming to ASTM C150, fine limestone (L) powder conforming to ASTM C568, and commercial sand (M), having a median particle size of 0.20 mm, conforming to ASTM C778. The chemical and physical properties of the mortar components are provided in Table 1 and their particle size distributions (PSDs) in Fig. 1. Chopped steel fibers (SFs) and chopped basalt fibers (BFs), the properties of which are shown in Table 2, were used as fiber reinforcement. A polycarboxylate ether-based high-range water-reducing admixture (HRWRA) (at a dosage of 0.20 to 0.35% by mass of the binder) was used in all the mixtures. The mortar mixture proportions shown in Table 3 were derived from authors' earlier work that considered particle packing and rheological characteristics that are necessary for printability (that is, extrudability and buildability).[22] The selected mortar mixture (L_{30}, containing 30% of fine limestone powder by mass as cement replacement) has also been used by the authors to evaluate the influence of different layer heights on the compressive, flexural, and fracture response of 3-D-printed specimens.[23] All mixtures contained 50% sand by mass of the total solids in the mortar, as shown in Table 3.

Table 2—Properties of fibers used in study

Type of fibers	Diameter, mm	Length, mm	Specific gravity	Tensile strength, GPa	Young's modulus, GPa
Chopped SF	0.20	13	6.80	3.0	210
Chopped BF	0.04 to 0.06	15	2.36	0.28	18

3-D printing of mortars

A gantry-based 3-D printer equipped with a screw extrusion system (shown in Fig. 2) was used to print the selected mortars shown in Table 3. To obtain consistent filament cross-section dimensions (that is, invariant layer widths for non-orthogonal prints), a circular nozzle of diameter (ND) 20 mm was used instead of a rectangular nozzle. Mortar slabs of size 400 x 400 x 60 mm were printed at an in-plane print speed of 50 mm/s. To obtain uniform filaments of layer height (LH) 10 mm (0.5 × ND) and layer width (LW) of 20 mm (equal to ND), the stepper for the screw extruder was calibrated for a flow rate of approximately 10 mL/s. An LH of 10 mm was selected based on authors' previous work,[23] which showed that lower LH is beneficial for plain mixtures because a non-zero standoff distance, resulting in some consolidation, will mitigate the likely adverse effects of layer interfaces. For fiber-reinforced mixtures designed using stiff fibers such as chopped steel fibers, an LH that is close to the fiber length is preferable, as otherwise, defects due to scratching of fibers and fibers not being totally confined in layers become significant.[23] For these reasons, an LH of 10 mm was selected for all the studies in this paper. The LH

Table 3—Mortar mixture proportions used in study

Mixture ID	Mass fraction of ingredients			Chopped steel fiber (SF)*	Chopped basalt fiber (BF)*	Water-binder ratio (w/b) by mass	HRWRA-binder ratio (HRWRA%) by mass of binder
	OPC	Limestone (L)	Sand (M)				
L_{30}	0.35	0.15	0.5	—	—	0.35	0.25
$L_{30\text{-}SF}$	0.35	0.15	0.5	0.27	—	0.35	0.35
$L_{30\text{-}BF}$	0.35	0.15	0.5	—	0.27	0.35	0.35

*Percentage by volume of mixture.

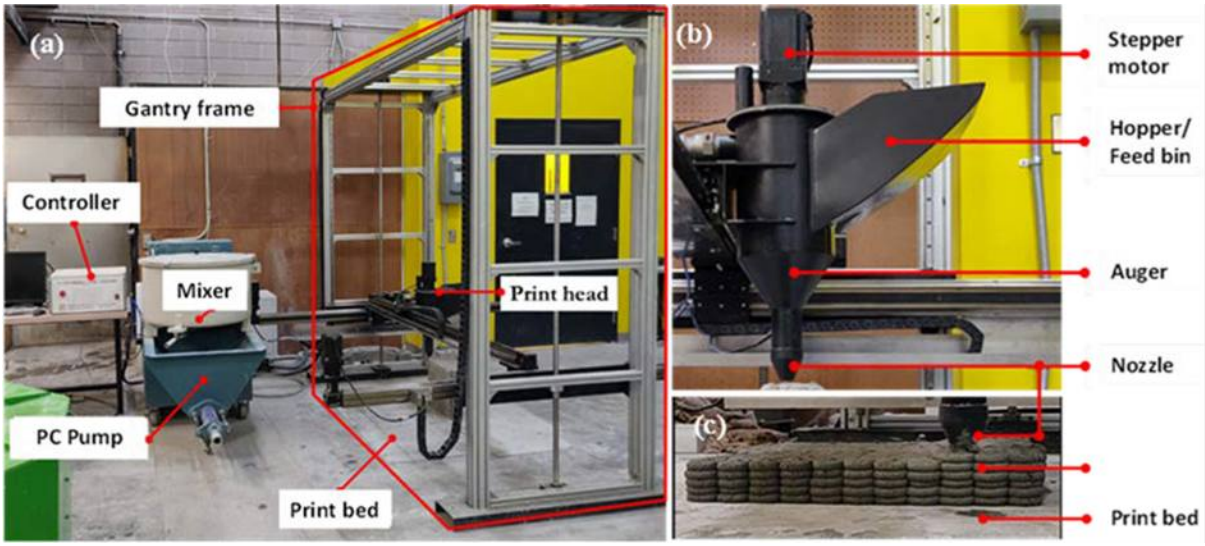

Fig. 2—Printer setup showing: (a) gantry printer with controller and mixer; (b) close-up of print head; and (c) S-shaped conventional (S-C) print in progress.

was not varied to ensure efficient comparisons, because it has been shown that the flexural strength varies with LH.[23]

The print filament layouts (note that these are the plan geometries; the cross section always remains rectangular) chosen for this study were straight line (or linear), S-shaped, and 3-shaped. Detailed descriptions of the dimensions for different filament types are provided in Fig. 3. S-shaped and 3-shaped filaments consist of arcs of chord length 100 mm formed on a circle of radius 120 mm laid side-by-side. For the S-shaped prints, the arc alternates between convex and concave (that is, changes direction alternatively), while for the 3-shaped prints, the arcs are in the same direction (that is, always convex), as shown in Fig. 3. These three chosen filament layouts (linear, S-shaped, and 3-shaped) were printed in two different ways—first, conventional printing, where filaments of the new layer were laid exactly above the corresponding filament on the lower layer; and second, staggered printing, where filaments of the new layer were staggered by half the layer width. Three-dimensional representations of the conventional (C) and staggered (S) printing types for linear, S-shaped, and 3-shaped prints are shown in Fig. 4. The letters 'C' or 'S' following the print geometry type—linear (L), S-shaped (S), or 3-shaped (3)—indicate the configuration. Note that the 3-shaped filament printing was only done for the conventional arrangement and not for the staggered one, as the 3-shaped print demonstrated a reduced mechanical performance than the S-shaped print in preliminary studies. Moreover, the S-shaped prints were found to be more effective in enabling a smoother printing because of the easy transition between the convex and concave arcs, as opposed to transition from one convex to another convex arc. Slabs were 3-D printed (refer to Fig. 5) and moist-cured in a curing chamber, at 23 ± 2°C and >98% reltive humidity (RH), for 28 days. After the curing duration, they were cut into cubes and beams (as shown in Fig. 6) for compression and flexural tests.

Flexure testing

After 28 days of moist curing, the 3-D-printed slabs were cut into beams (60 x 60 x 300 mm in size) such that the filament print direction is oriented parallel to the longer side of the beam. One of the longer 300 mm faces perpendicular to the filament direction was speckled with black paint to enable the use of digital image correlation (DIC) to track surface displacements and crack initiation and propagation. Flexural response of the beams was obtained in accordance with ASTM C78/C78M-18[24] under four-point bending. A servo-controlled universal testing machine (MTS 810) with a capacity of 100 kN was used. The test was carried out under midpoint deflection control using linear variable differential transformers (LVDTs) at a rate of 0.02 mm/min until either failure occurred or the load capacity dropped to 500 N or the total deflection at center of the beam reached 0.8 mm, whichever happened first. These endpoints were determined based on several trial experiments, especially on SF-reinforced specimens, to enable accurate determination of specimen ductility. Figure 7(a) shows the general test setup and the corresponding components.

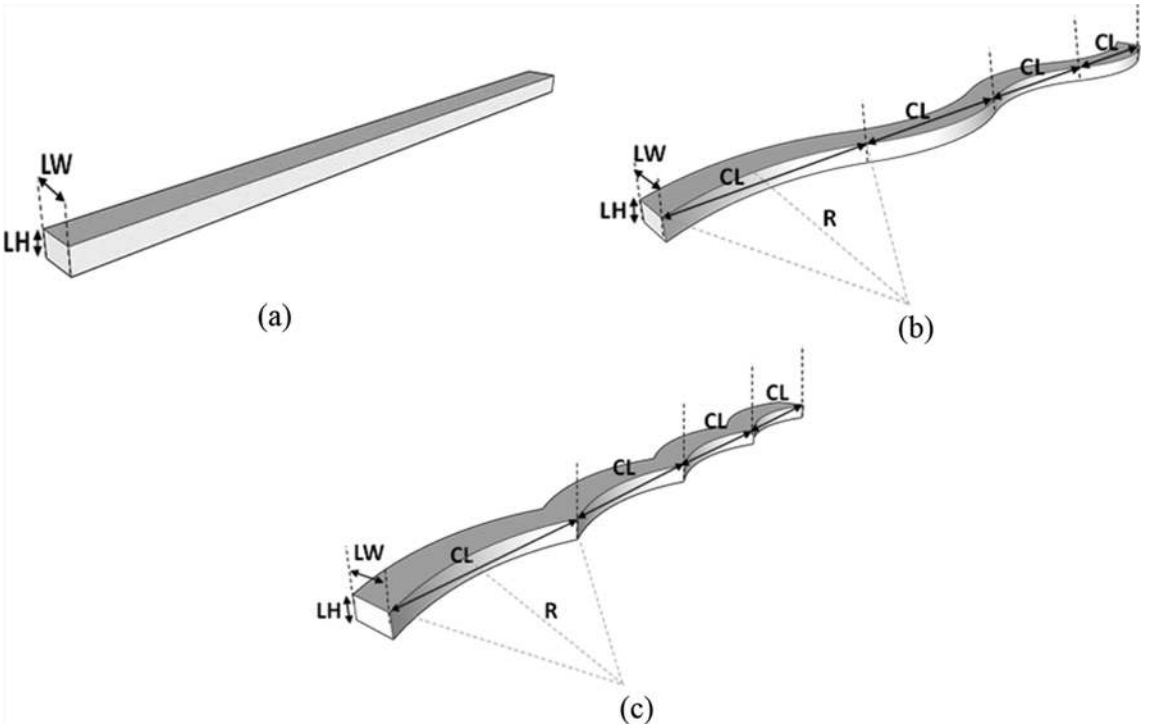

Fig. 3—Filament geometries used in this study: (a) linear (L); (b) S-shaped (S); and (c) 3-shaped (3). LH used was 10 mm, LW was 20 mm, chord length (CL) was 100 mm, and radius of arc (R) was 120 mm.

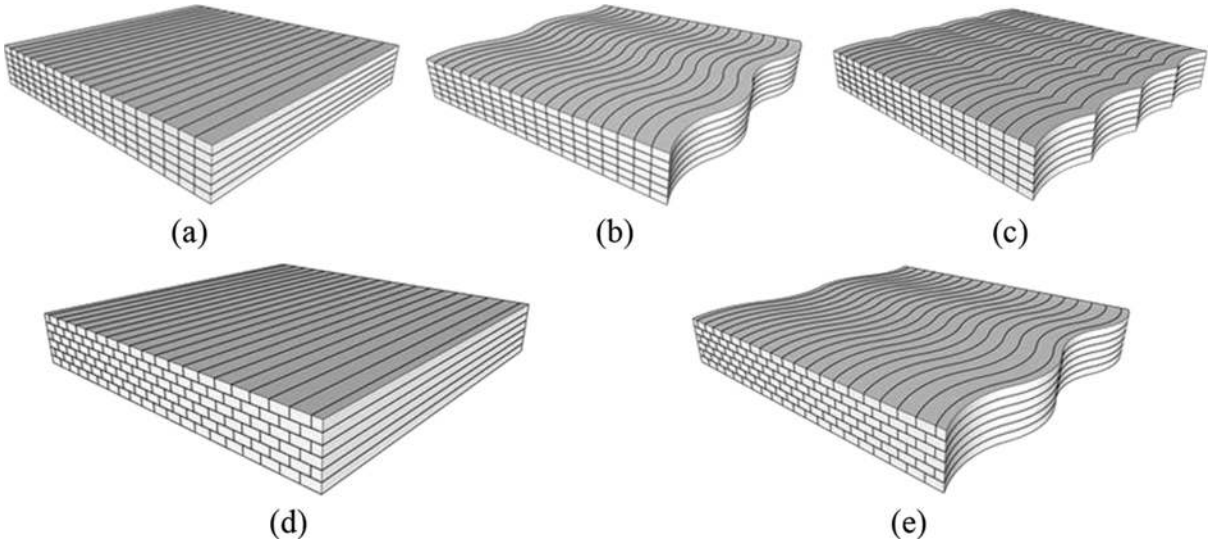

Fig. 4—Three-dimensional representation of printed slabs using different geometries of filaments and their configuration: (a) linear conventional (L-C); (b) S-shaped conventional (S-C); (c) 3-shaped conventional (3-C); (d) linear staggered (L-S); and (e) S-shaped staggered (S-S). Note that in nomenclature use, first letter/number indicates filament geometry (linear, S-shaped, or 3-shaped), and second letter indicates configuration in which it is printed (conventional or staggered).

Compression testing

Cubes of 60 x 60 x 60 mm (shown in Fig. 8(a)) were prepared by cutting the slab. These cubes were then subjected to uniaxial compression using a servo-controlled universal testing machine with a maximum capacity of 489 kN. Compression tests were carried out in all three orthogonal directions for the different print layouts and configurations. Direction-1 represents the case where load is applied along the x-axis (perpendicular to the faces lying in y-z plane, where printing happens along the x-direction), Direction-2 along the z-axis (perpendicular to the faces lying in x-y plane), and Direction-3 along the y-axis (perpendicular to the faces lying in x-z plane), as shown in Fig. 8(b) to (d). Loading was done at a stroke displacement rate of 0.15 mm/min corresponding to an initial strain rate of 0.25%/min. The test setup is shown in Fig. 7(b).

DIC for visualizing strain fields and crack propagation

DIC is used as a non-contact means to acquire the surface displacements and strain fields in the specimens during the flexural testing. Strain profiles extracted from the DIC data

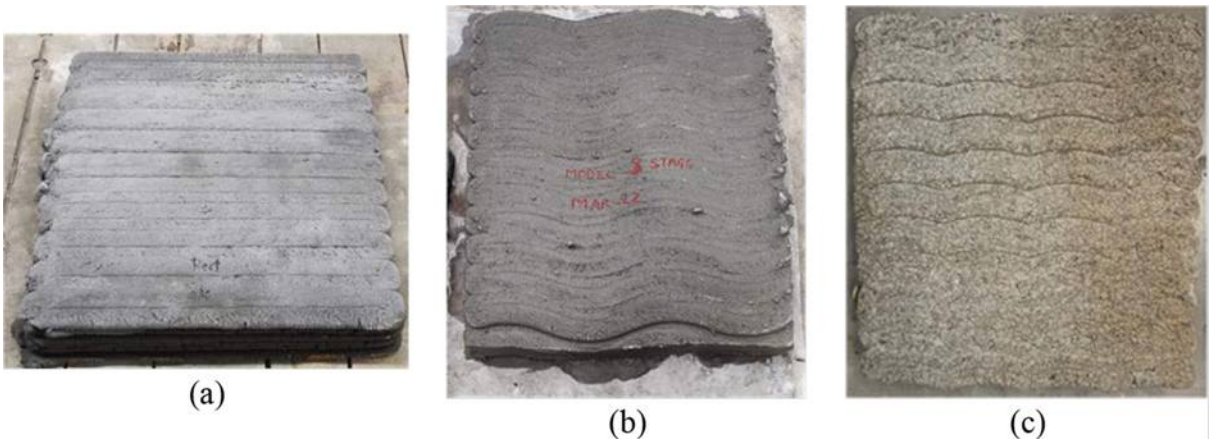

Fig. 5—Printed slab: (a) linear conventional (L-C); (b) S-shaped staggered (S-S); and (c) 3-shaped conventional (3-C).

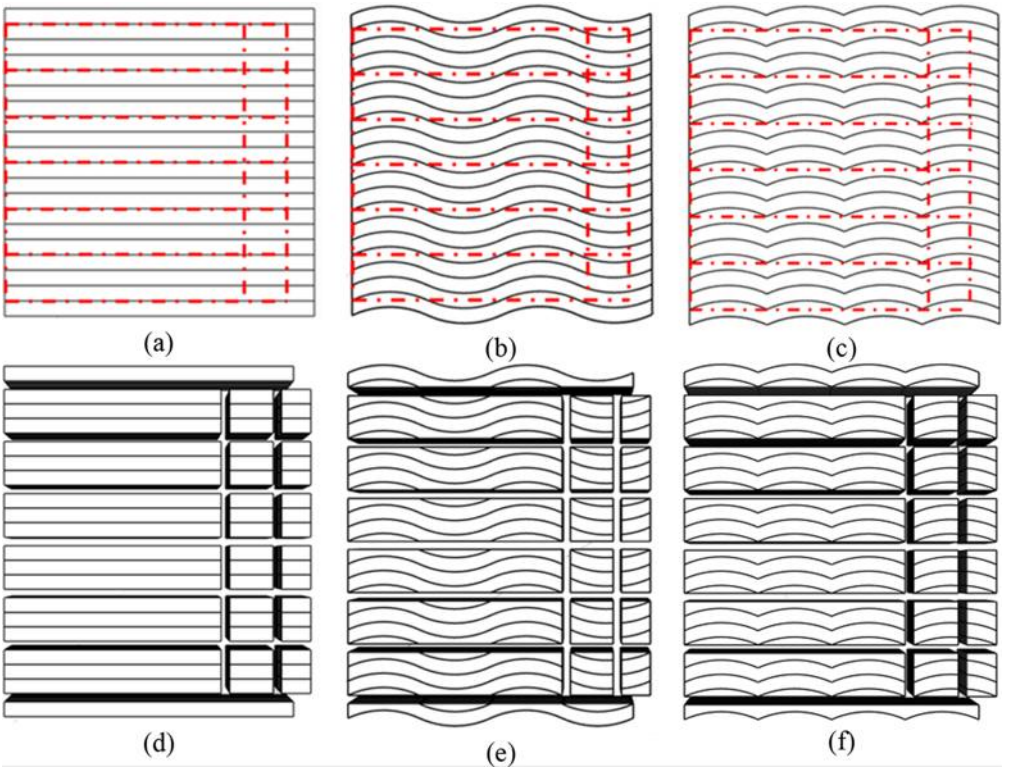

Fig. 6—Top view of: (a) R-C; (b) S-C; and (c) 3-C slabs with dotted lines showing region of cut to obtain beams and cubes shown in (d), (e), and (f), respectively.

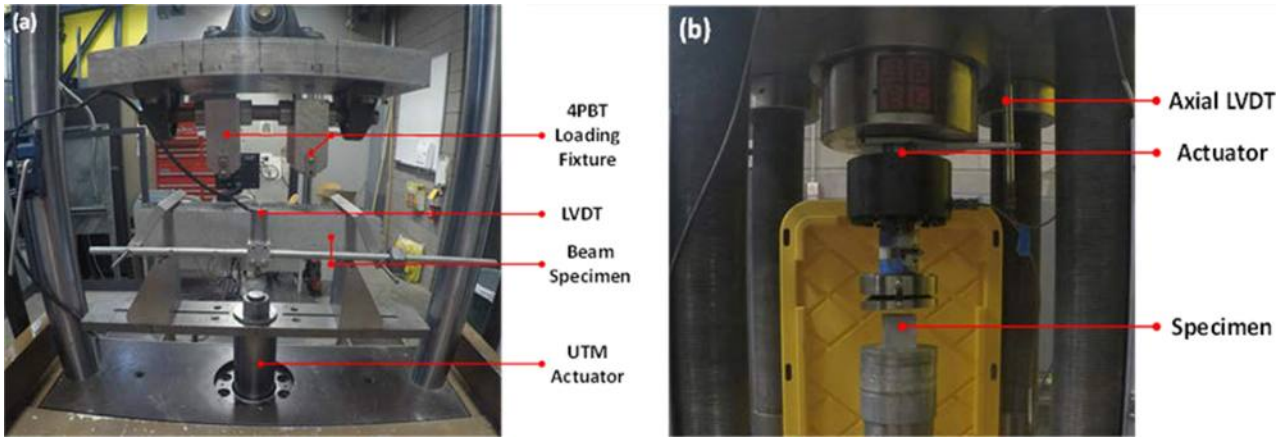

Fig. 7—(a) Flexure test setup; and (b) uniaxial compression test setup, showing different components.

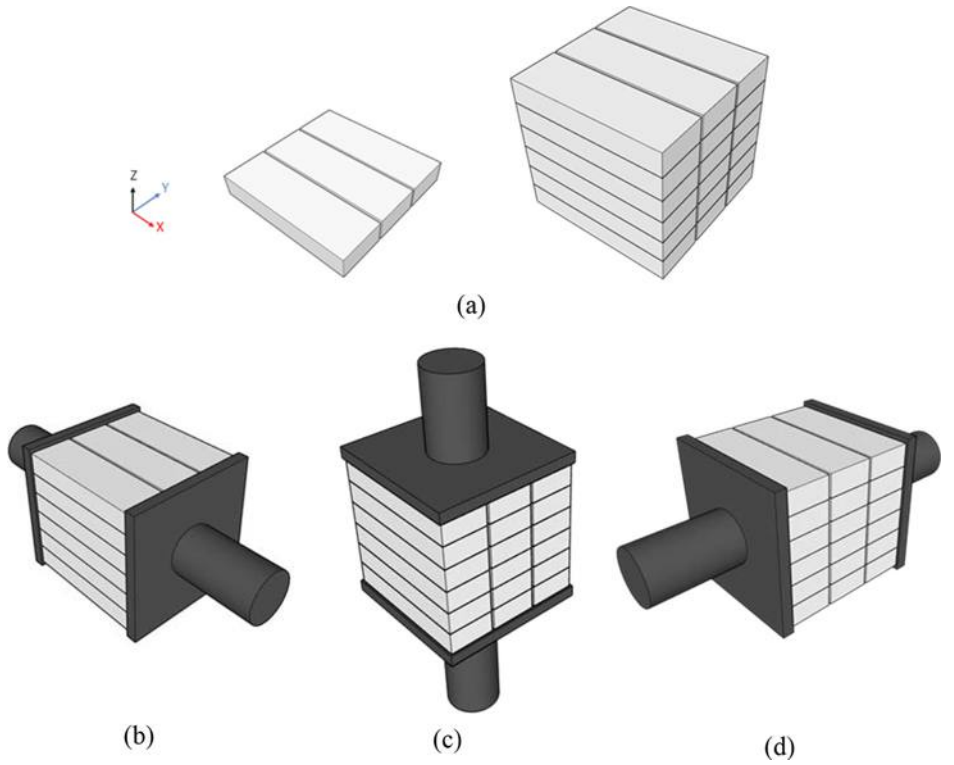

Fig. 8—(a) Representative single layer and complete cube showing three filaments and six layers; print direction is parallel to x-axis; and compression testing along (b) Direction-1, (c) Direction-2, and (d) Direction-3.

are used to identify and track crack initiation and propagation. The DIC setup shown in Fig. 9(a) consists of two cameras focused on a speckled area of interest on the beam, which is illuminated by high-intensity flood lights; the data acquisition (DAQ) unit controls the cameras. The frequency of image capture is fixed at 1 Hz. Figure 9(b) shows a typical Lagrangian strain field in the beam subjected to four-point bending. The process of obtaining Lagrangian strain fields from the displacement field captured by DIC is described in detail elsewhere.[25,26]

RESULTS AND DISCUSSIONS

Effect of filament print layout and configuration on flexural strength of unreinforced specimens

As discussed earlier, three different print layouts were used in this work. The effect of print layout (L, S, and 3) on the flexural strengths of the conventionally laid (not staggered) unreinforced 3-D-printed beams (denoted as L-C, S-C, and 3-C) are reported first. The flexural specimens (60 x 60 x 300 mm) were tested such that the filaments were oriented along the length direction. The span length used for testing was 240 mm. The average flexural strengths for beams printed using L-, S-, and 3-shaped geometries are shown in Fig. 10(a). It is clearly noticed that by changing the individual filament print layout (plan geometry), flexural strengths of the printed beams can be enhanced. Among the three layouts, the S-shaped layout (S-C) gives the highest average flexural strength, which is about 15% higher than that of the regular linear geometry (L-C), which is the most common print (plan) geometry. The use of a 3-shaped printing layout also increases the flexural strength by approximately 10% or more compared to the L-C case. The enhancements in flexural strength can be explained based on the nature of interfilament joints present in 3-D-printed elements. Interfilament joints are the joints present between two adjacent filaments in the plan view (as opposed to interlayer joints, which are present between the adjacent layers in the cross-sectional view). The 3-D-printing process and the nozzle standoff distance used typically results in some amount of layer consolidation, resulting in densification of the interlayer joints, while the interfilament joints do not benefit from such consolidation and are generally weaker.[15-17] In a beam conventionally printed using straight filaments (L-C), the weaker interfilament joints run parallel to the length direction, while in the S-C and 3-C print layouts, the interfilament joints are curved (refer to Fig. 6(d) to (f)), creating more contact area between the filaments for the same length of the beam (300 mm). Moreover, the curved paths also ensure that the stress required to separate the adjacent filaments is higher since the interfilament contact path is more tortuous. It is possible to note from the S-C and 3-C geometries (shown in Fig. 3, 4(a) to (c), and 6) that the 3-C geometry induces more interfilament stress concentrations than the S-C geometry because of the sharp changes in path needed to keep the arcs convex always, thereby resulting in slightly lower strengths. However, the flexural strengths are still higher than those of the conventional case. The results shown herein indicate that it is possible to alter the print plan layout, while maintaining the other parameters the same, to obtain higher flexural strengths. In the forthcoming sections of the paper, the comparisons are restricted to the straight linear (L) and S-shaped print layouts. Even though the 3-shaped prints showed better strengths than the linear prints, it was observed that the S-shaped prints

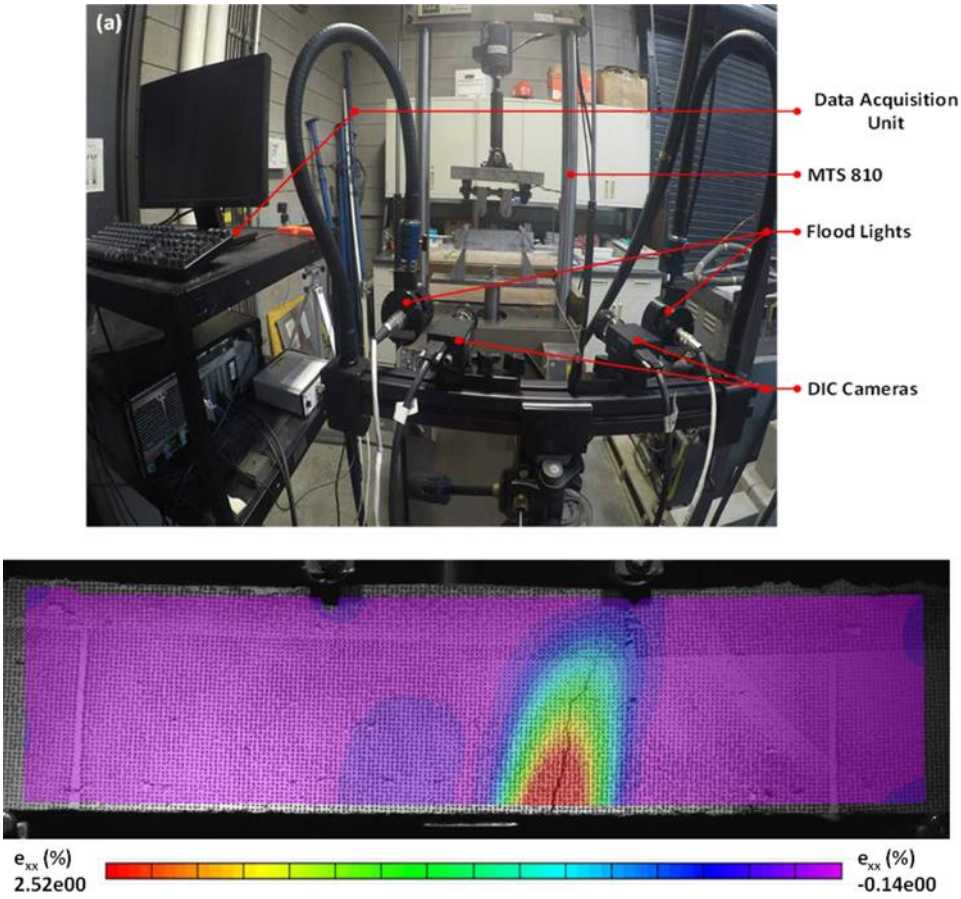

Fig. 9—(a) DIC setup; and (b) representative Lagrangian strain field (just before end of test in S-S-SF beam) subjected to four-point bending.

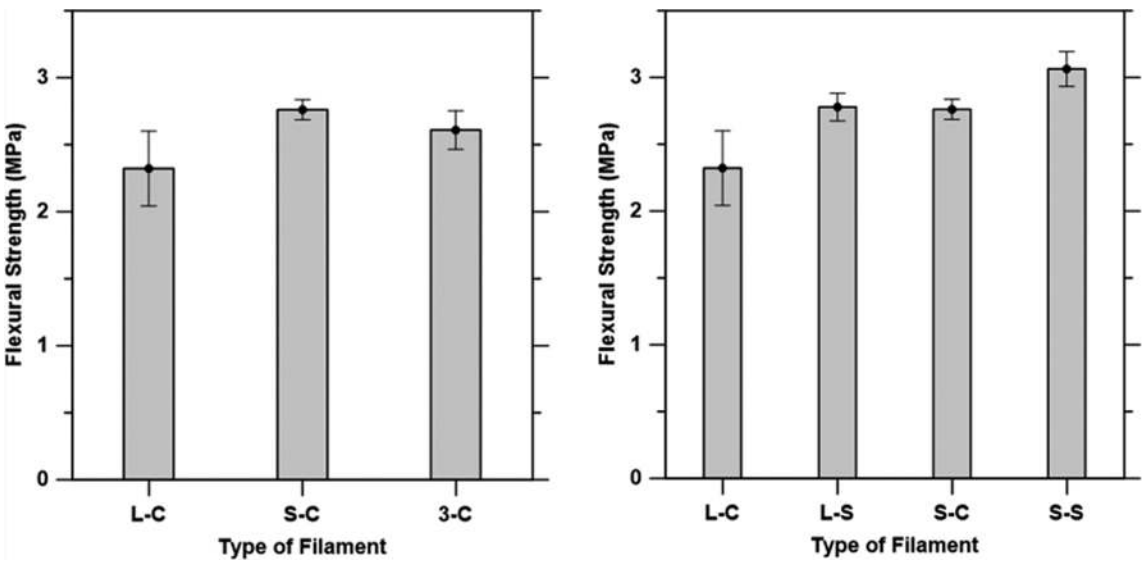

Fig. 10—Flexural strengths of beams printed using different layouts: (a) L-C, S-C, and 3-C; and (b) L-C, L-S, S-C, and S-S geometries. All beams were subjected to four-point bending test. Error bars correspond to standard deviation from three or more replicate specimens.

enable smoother printing, and consequently fewer defects, the reasons for which were explained earlier.

It was observed in authors' previous work[23] that, despite adjusting the flow rate and print speed to reduce the chances of formation of interfilament voids, this was not always feasible (more prominent at larger layer heights). Using a circular nozzle (instead of a rectangular one) also increased this effect because in that case, the filaments tend to have curved side edges, which also results in the formation of a gap at the interfilament joints. To mitigate this concern to a certain extent, a staggered printing configuration is adopted in this work where the filaments in the

upper layer are staggered by half a layer width in the plane of printing. Figure 10(b) shows the flexural strengths of the staggered L and S prints along with those of their non-staggered (conventional) counterparts. Staggering the layers in an S-shaped print geometry (S-S) results in an increase in flexural strength of approximately 25% as compared to the conventional linear mode of printing that is commonly adopted (L-C), and more than 10% as compared to the linear layout in the staggered configuration (L-S). Changing the print configuration from conventional to staggered results in interfilament defects not lining up perfectly—in other words, some tortuosity in the crack path that likely follows the interfilament contacts is introduced, which helps enhance the load-carrying capacity. When compared to its non-staggered counterpart (S-C), the strength enhancement is seen to be approximately 10%. The flexural strength results reported here shows that it is indeed beneficial to consider alternate printing layouts (in plan geometry) and layer configurations to mitigate the mechanical property reduction associated with some of the common defects encountered in 3-D concrete printing.

Effect of fiber reinforcement on flexural strength

Because the staggered print configuration performed better than the conventional print configuration (as shown in Fig. 10), the influence of fiber reinforcement is evaluated here only for the staggered print configuration. It is shown in many recent publications that fibers (metallic or polymeric) added to a 3-D-printed matrix helps in crack control and/or enhances the strength and toughness, based on the fiber type.[27,28] Figure 11 shows the flexural strengths of mixtures reinforced with either steel or basalt fibers, and the comparison with unreinforced mixtures printed with different filament layouts. Note that both basalt and steel fibers have similar lengths, but the basalt fibers have significantly smaller diameters. The volume fractions of the fibers used are the same for both fiber types (0.27% by volume of the mortar; refer to Table 3), adopted from authors' previous work.[23] The flexural strength results indicate clear enhancement in flexural strengths due to fiber incorporation, which is expected. An increase in flexural strength by approximately 10 to 30% is noted when either of the two types of fibers are incorporated into the specimens printed in the L and S-shaped layouts, with a more noticeable enhancement for the staggered linear (L-S) print type. The reason for reduced efficiency of fibers in the S-shaped mixtures, especially for stiff fibers, is that the print direction changes in a wavy pattern and the fibers cannot consistently be oriented in the length direction of the overall filament. Using image analysis of printed sections, it is possible to estimate the efficiency of fibers in the print direction based on their angle of dispersion; such a detailed quantification is not attempted here because the objective is to simply compare the efficiencies of different print geometries. Moreover, for the linear geometry, as explained earlier, the interfilament defects are more, which the enhanced capacity through the use of fibers overcomes to a certain extent. Thus, fibers—which orient along the direction of print—are seen to benefit the linear print geometry better.[29-32]

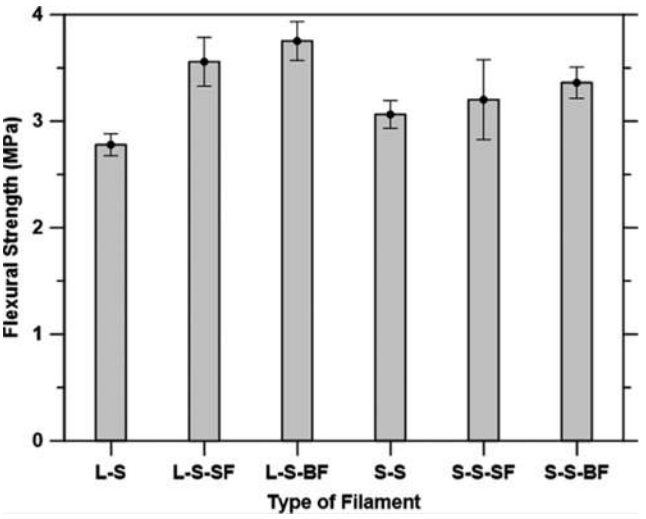

Fig. 11—Flexural strength of unreinforced and fiber-reinforced beams printed using different layout with staggered configuration (L-S, L-S-SF, L-S-BF, S-S, S-S-SF, and S-S-BF). All beams were subjected to four-point bending test. Error bars correspond to standard deviation from three or more replicate specimens.

For both the linear and S-shaped filament layouts, the BF-reinforced mixture is observed to slightly outperform the SF-reinforced mixture from a flexural strength standpoint. As shown in the authors' previous work,[23] stiffer SFs, when introduced in a layer that has a lower LH than the fiber length, result in scratching of the surface of the layer during the printing process. This causes surface defects that lead to the total effect of fibers not being realized with respect to flexural strength. This shows that less-stiff fibers such as BFs (E lower by an order of magnitude as compared to SFs; refer to Table 2) could be used to obtain enhanced flexural strengths in 3-D-printed concrete elements. More importantly, a lower LH (than the fiber length) can be used because it has been shown that a lower layer height is beneficial in enhanced mechanical performance,[23] even though the speed of construction could somewhat be compromised. It also needs to be recognized that, for a given volume fraction of fibers, there are approximately 13 times the number of BFs in the mixture as compared to SFs, based on their diameter difference. A higher number of fibers in a unit volume enables the matrix to efficiently transfer stresses. Higher fiber density in the matrix also enhances the crack path tortuosity, which extends the load-carrying capacity in this case. While a layered printing process will always encounter issues related to interlayer and interfilament strength, the aforementioned discussions demonstrate that geometric modifications, along with material modifications (such as the use of fiber reinforcement) can be suitably used to mitigate some of these effects from a viewpoint of flexural strength.

Post-peak response, in flexure, as function of print geometry and configuration, and fiber reinforcement

Representative load-midpoint deflection responses of the beams from the four-point bending tests are shown in

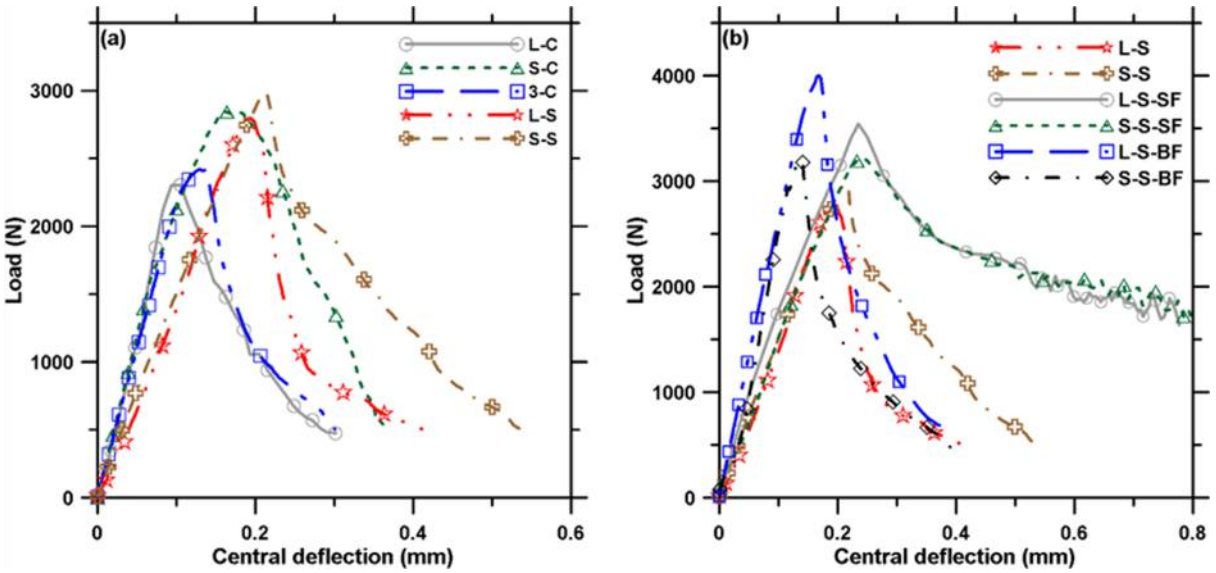

Fig. 12—Load-deflection response of: (a) unreinforced beams, printed with different layouts and configuration; and (b) unreinforced and fiber-reinforced beams printed using different layouts with staggered configuration.

Fig. 12. The tests were carried out until the beams failed completely, or the load in the post-peak regime dropped to 500 N, or a total test run-time of 40 minutes (equivalent to a midpoint deflection of 0.8 mm) from the start of the test, whichever occurred earlier. The load-deflection responses, rather than the stress-strain curves, are shown here because the beams were cut from slabs and slight dimensional inaccuracies could be present. The load-deflection responses of the unreinforced beams are shown in Fig. 12(a). All the specimens show a rather brittle behavior, as expected. However, an important observation from this figure is that, when alternate print layouts and configurations are attempted, the midpoint deflection (indicative of the strain) at the peak load increases. From approximately 0.1 mm at the peak load for a conventionally printed specimen (L-C), the midpoint deflection increases to approximately 0.15 mm for S-shaped conventional (S-C), and to approximately 0.12 mm for the 3-shaped layout (3-C). Staggering the layers also results in enhanced deflections at the peak load. Increase in midpoint deflection is also correlated with increased load capacity (or failure stress), as mentioned in an earlier section. The effect of fiber reinforcement on the load-deflection response of the beams printed in the staggered configuration is shown in Fig. 12(b). For the same volume of fibers, the stiff SFs are shown to provide a considerable degree of post-peak toughness. Between the linear and S-shaped layouts for the SF-reinforced mixtures, the S-shaped layout shows a higher midpoint deflection at the peak load as explained earlier, but the post-peak response at higher deflections is found to be invariant of the layout. The BFs do not provide the same degree of toughness enhancement, even though the peak strength is enhanced for reasons described earlier.

Layout- and configuration-induced changes in strain profile

DIC is used to obtain the strain profiles of the beams tested under flexure. DIC analysis of representative surface strain profiles in the middle-third portion of the beam span, under four-point bending, at or very close to the peak load, are shown in Fig. 13 for all the layout and fiber type combinations. The Lagrangian strain fields were extracted from the displacement fields determined from DIC. The Lagrangian strain ranges in each of the cases are also shown along with the representative images as their magnitude changes based on the chosen combination.

Figures 13(a) to (c) depict the strain fields for the conventional orientation of the L-, S-, and 3-shaped configurations. The maximum strain at failure is higher for the S-C beam, while the L-C beam has the least strain at failure. Note that both the S-C and 3-C configurations also have higher peak stresses as well, as shown in Fig. 10. Because the material and printing parameters, including the layer height, are the same for all these cases, it can be concluded that the enhancement in strain at the peak load is a result of changed print layout, the effects of which was reported earlier in the section on flexural strengths. It is important to mention here that the discussions are based on the strains observed at the peak load alone; this typically occurs at the point of crack formation or localization. Redistribution of strains occurs in the specimen when a crack forms and thus, the strains at peak stress shown here are not indicators of the average strain that will be measured across the depth or a gauge length when LVDTs or strain gauges are used. It is also not necessary that the average strains follow the trends indicated by the value at peak stress. This important distinction should be considered when comparing strains determined using DIC.

When the layers are staggered (Fig. 13(a) and (d), which compare L-C and L-S beams), it is noticed that there is a more than 50% enhancement in the maximum strain at the peak stress because of the staggering of alternate layers along the height of the beam. The enhancement in peak strains as a result of print layout changes (S- and 3-shapes) and staggering indicates that the failure at lower strains (a more brittle behavior) in conventional prints (straight lines, layers laid one on top of the other) is a result of combined effects of interfilament and interlayer defects. While changing the

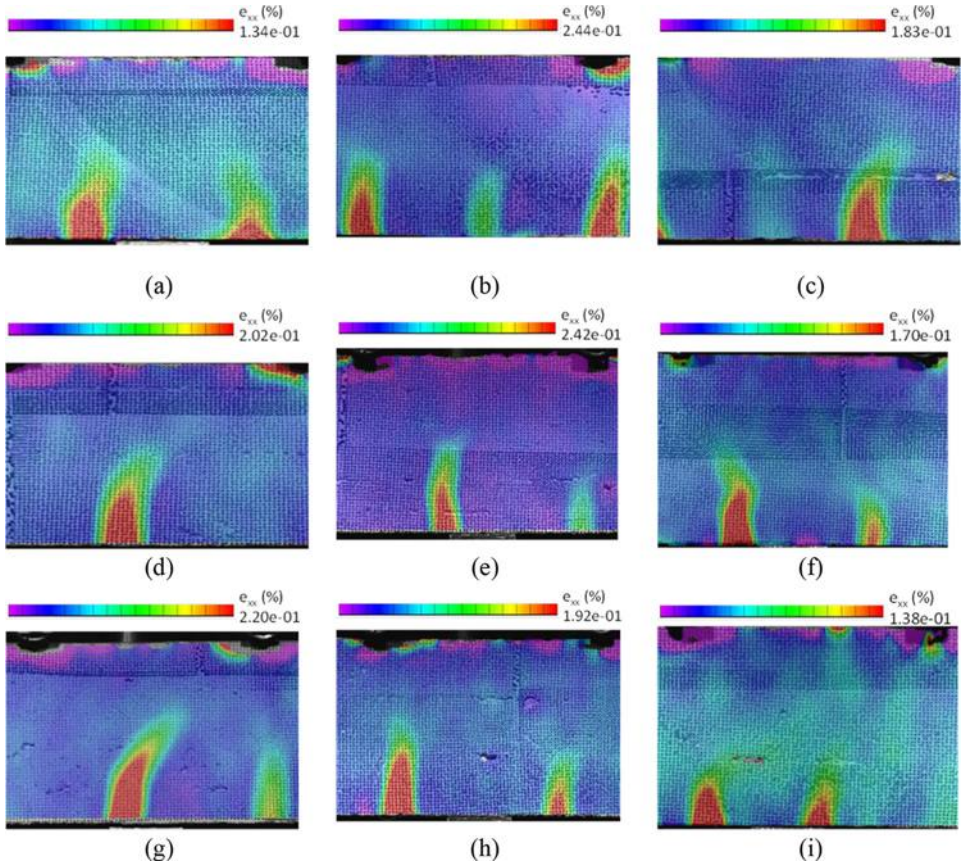

Fig. 13—Lagrangian strain profile at peak load for different layouts and configurations: (a) L-C; (b) S-C; (c) 3-C; (d) L-S; (e) L-S-SF; (f) L-S-BF; (g) S-S; (h) S-S-SF; and (i) S-S-BF. Note that lowest strain value is set to –6.00 × 10^{-2} for all figures.

print layout enables curving of the filaments and thus minimizes stress concentrations, staggering of layers introduces tortuosity in the defect path (all the interfilament joints are not on top of each other); both resulting in the specimens being able to tolerate higher maximum strains (and stresses) before failure. Figures 13(d) and (g) enable comparison between the L- and S-shaped beams where the layers are in a staggered configuration for both the beams. Here, the S-S beam shows a slightly higher maximum strain at peak stress than the L-S beam, but the effect is not as significant as that between a conventional and staggered case. This result shows that staggering of layers has a more significant effect than changing the print layout with respect to peak strains. A similar but less-conspicuous effect is noticed for the peak stresses as well.

The influence of fibers on the strains at peak stress are also shown in Fig. 13(e) to (f) and (h) to (i) for the L-S and S-S beams. As discussed earlier, only the staggered configuration is shown here. Even until the peak load, the steel fiber reinforced specimens show significantly higher maximum strains, commensurate with the enhancement in peak stress. Between the L-S-SF and S-S-SF specimens—that is, in the L- and S-shaped staggered configurations (Fig. 13(e) and (h))—there is a reduction in the maximum strain for the staggered S-shaped configuration as the fibers are not oriented along the isostrain lines in the tensile region because of the curved layer layout. The SF-reinforced specimens demonstrate higher maximum strains as compared to the BF-reinforced specimens at the peak stress as shown in Fig. 13(e) to (f) and (h) to (i). The BFs are more brittle than the SFs, have a lower stiffness, and their strain capacity is also lower (1% failure strain compared to 11% for steel fibers). As mentioned earlier, between the L- and S-shapes when layers are staggered, there is no significant difference between the peak strains for specimens reinforced with a particular fiber type, indicating that staggering creates a more dominant effect in the pre-peak (both stress and strain) mechanical response than the chosen layouts alone.

Because the unreinforced beams do not carry significant strains after the peak load (even though changes in layout and configuration seem to define better performance than conventionally layered systems), the post-peak strain distributions in fiber-reinforced beams are only reported here. Figures 14(a) and (b) depict the strain distributions in the L-S-SF and L-S-BF beams, while Fig. 14(c) and (d) show the strain distributions in the S-shaped configurations, that is, S-S-SF and S-S-BF. Because the SF-reinforced beams showed a very gradual load reduction in the post-peak region because of the ductility provided by the presence of SFs, the strain profiles are recorded for a midpoint deflection of 0.8 mm, when the test was ended. This corresponded to residual loads slightly higher than 50% of the peak load. The maximum strain values recorded at end of the test for both the SF-reinforced specimens—that is, L-S-SF and S-S-SF (Fig. 14(a) and (c), respectively)—are much higher than the strains at peak load for the unreinforced beams. While a cursory look at the load-deflection response (Fig. 12) shows that the midpoint deflections at the end of the test are

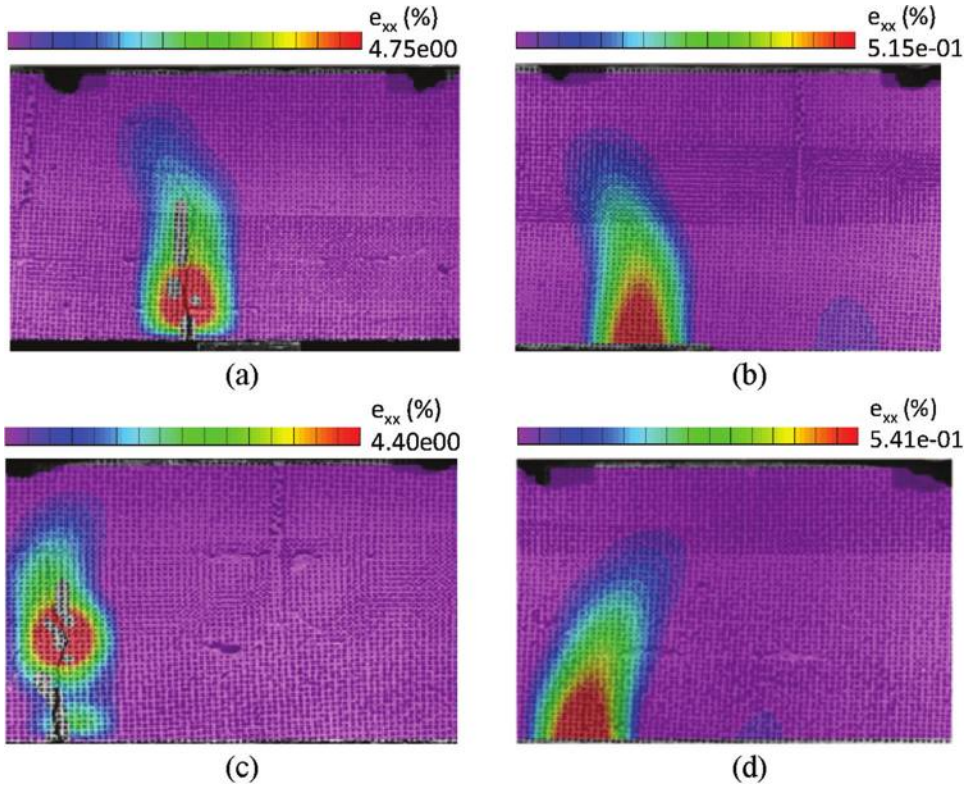

Fig. 14—Lagrangian strain profile at 50% of peak load in post-peak region for: (a) L-S-SF; (b) L-S-BF; (c) S-S-SF; and (d) S-S-BF. (Note: For L-S-SF and S-S-SF, residual load did not drop to 50% of peak until end of test [refer to Fig. 12], and last frame before end of test [midpoint deflection of 0.8 mm] is shown. Lowest strain value is set to 0 for all figures.)

approximately four times that at the peak load, the recorded strains are approximately 20 times that of the maximum strain at the peak for the corresponding specimens (shown in Fig. 13(e) and (h)). This is because the post-peak maximum strains reported are close to the extreme tension fibers of the beams, rather than at the crack tips. As the crack initiates and surface separation occurs, the strain on the extreme fibers tends to increase rapidly, but is arrested to some extent by the SFs. The propagation of a single crack is shown in these figures, which is the dominant crack for SF-reinforced specimens (note multiple locations of larger strains are seen in the strain distribution image at peak load). The volume of fibers is small enough that multiple cracking (as is noted for ultra-high-performance concrete [UHPC] beams[21,33]) is not mobilized in these specimens. BF-reinforced beams did not have such a noticeable post-peak response as the SF-reinforced specimens because of the lower stiffness and ductility of BFs.[10,34] Also, due to the higher aspect ratio of BFs (250 to 375) and their relatively brittle nature, the bridging effect of fibers is reduced, and fiber breakage rather than fiber pullout could have occurred (as noticed through microscopy observations of fracture surfaces), resulting in a less-ductile response. Thus, the maximum strains recorded are also lower, even though they help achieve similar or slightly higher strengths than SF-reinforced specimens because of reasons described earlier.

Compressive strength

As explained in a previous section, 60 mm cubes were used for compression strength testing. Because 3-D-printed samples are anisotropic, the compressive strength was evaluated in all the three directions, as shown in Fig. 8. At least three samples were tested on each direction and the compressive strength results are shown in Fig. 15. The results for the straight filament layout prints (L series) are shown in Fig. 15(a), whereas the results for the S-shaped layouts are shown in Fig. 15(b); in both the figures, two orientations (conventional and staggered) and two fiber types (steel and basalt) are also considered. As explained earlier, fiber reinforcement is used only in the staggered configuration. As has been previously reported,[10,11,18,35] the inherent anisotropy in compression of 3-D-printed components is brought out. It can be noticed that Direction-2 is the weakest among the three directions, while Directions-1 and -3 demonstrate relatively similar strengths for all the cases considered in this study. The weak zones formed by the interfilament and interlayer joints influence the flexural and tensile response significantly, while they seem to have a lesser effect on the compressive strength. The maximum compressive strength at 28 days is almost 75 MPa for many of the cases, indicating that 3-D-printed mixtures with up to 30% cement replacement with limestone can attain high compressive strengths for many structural applications.

From Fig. 15(a) and (b), it can be noticed that the differences in compressive strength between mixtures printed with different layouts, configurations, or fiber reinforcement types are not very significant, unlike the case for flexure reported earlier in this paper. However, anisotropy in compression is evident based on the obtained lower strength when tested in Direction-2. There are conflicting

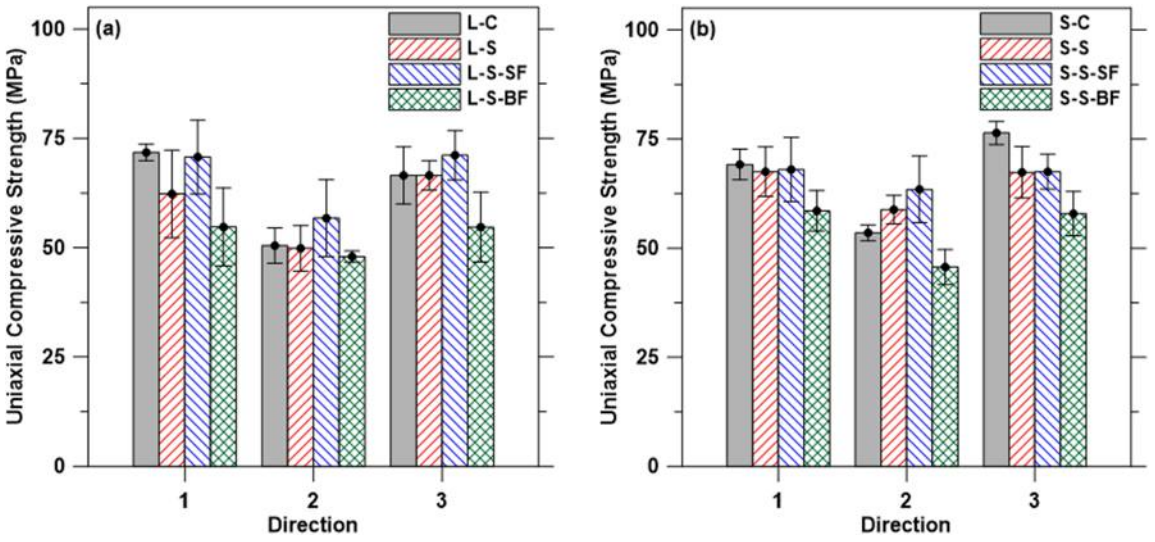

Fig. 15—Uniaxial compressive strength in three orthogonal directions for: (a) L-C versus L-S versus L-S-SF versus L-S-BF; and (b) S-C versus S-S versus S-S-SF versus S-S-BF.

results reported in this regard. For example, it is shown[18] that Direction-3 is the strongest and Direction-1 the weakest; however, this is likely because only a single filament was incorporated in each layer of the cube in those tests, while the current work uses a cut portion from a printed slab, which comprises multiple filaments. On the other hand, similar work done by other authors[19] also uses cubes with each layer consisting of a single filament and reports that Direction-2 is usually the strongest while Direction-3 is the weakest. Similarly, another work[36] reports that Direction-1 is stronger than Direction-2. Nevertheless, as interfilamentous joints corresponding to layers in X-Y plane (refer to Fig. 8(a)) are locations of potential weakness, evaluating anisotropy with test specimens having multiple filaments in the same layer is important. While a typical 60 mm cube for all the different print types used in this study has the same interlayer (horizontal) joint area (of approximately 18,000 mm^2), a straight (linear) conventionally printed cube has approximately 7200 mm^2 of interfilamentous vertical joint area compared to approximately 9000 mm^2 for a linear staggered print cube. Thus, the linear staggered configuration shows somewhat lower strength in compression in Direction-1 than its conventionally printed counterparts. In Directions-2 and -3, this effect is not dominant, resulting in comparable strengths for the conventional and staggered configurations. For the S-shaped prints shown in Fig. 15(b), staggering slightly reduces the strength in Direction-3 for the unreinforced mixture, though it is unclear if it is just an experimental artifact. While SF-reinforced mixtures display comparable compressive strengths to their unreinforced counterparts with similar layer geometry and orientation, the BF-reinforced mixtures show reduced compressive strengths. This contrasts with the behavior in flexure noted earlier. It was mentioned that the scratching of the layer surface by stiff and long steel fibers leads to interlayer defects, which are detrimental in flexure, but such defects are not critical in compression. Chopped BFs are generally reported to result in some enhancement in compressive strength of concrete at volume fractions comparable to those used in this work. However, it is possible that, with larger number of fibers per unit volume, BFs likely could influence the sampling volume under compression (the entire specimen volume is under compression) more than steel fibers. Here, due to: (i) fiber-matrix interface defects; and (ii) the increased number of BFs reducing the packing density of the matrix,[37] the compressive strength is reduced. Under flexure, the sampling volume under tension is much smaller, and hence it is feasible that there is a higher statistical possibility of encountering a larger defect in a fine fiber reinforced matrix under compression. This aspect requires further investigation, using a range of fiber volume fractions, which is beyond the scope of this work, the focus of which is the evaluation of property differences with layout, configuration, and fiber type.

SUMMARY AND CONCLUSIONS

This study examined the influence of print geometry and configuration on the flexural and compressive response of three-dimensional (3-D)-printed concrete elements. In the conventional printing approach, straight filaments are overlaid in different layers (resulting in interlayer joints) and several such filaments are laid side-by-side to obtain desired member thicknesses (resulting in interfilament joints). In this study, S- and 3-shaped print patterns and staggering of the layers were studied to reduce the impact of interfilament joints on mechanical properties. Flexural and compressive strength tests were carried out on the specimens, along with digital image correlation (DIC) on the flexural specimens. Steel (SFs) or basalt fibers (BFs) were also used in some of the mixtures.

- Among the different print geometries, the S-shaped (in plan) print geometry provided flexural strengths that were 10% higher than the conventional (straight line [L]) print path. Staggering the layers by half a layer width as compared to the top and bottom layers further enhanced the flexural strengths, resulting in approximately 25% enhancement in strength as compared to the conventional print type. An increase in flexural strength

by approximately 10 to 30% was observed when steel or basalt fibers were incorporated into the specimens printed in the L and S-shaped staggered layouts. The enhancement was more noticeable for the staggered linear (L-S) print type.

- SFs provided enhanced flexural ductility at the same replacement volume as compared to BFs, though BFs provided slightly higher strengths. The use of less-stiff fibers is preferable when using longer fibers or when the layer height needs to be limited because stiffer SFs might contribute to slight strength reduction by layer scratching. A hybrid combination of SFs and BFs that could enhance both the microscale and macroscale response is a possible approach that needs investigation. Between the linear and S-shaped layouts for the SF-reinforced mixtures, the S-shaped layout showed a higher midpoint deflection at the peak load, indicating the efficiency of changing geometry in strain capacities as well.
- The peak strains determined using DIC were lower for the conventional prints (straight lines, layered one on top of the other), while they were higher when the print layout changed (S- and 3-shapes) or when the layers were staggered. This demonstrates that a more brittle behavior in conventional prints is a result of combined effects of interfilament and interlayer defects. Changes in the print layout minimized stress concentrations, while staggering of layers introduced tortuosity in the defect path, resulting in the specimens being able to tolerate higher maximum strains (and stresses) before failure.
- Direction-2 was found to be the weakest in compression among the three directions, while Directions-1 and -3 showed similar strengths. The need to use multiple filaments in a single layer to evaluate the anisotropic behavior, because interfilament joints within a layer are potential regions of weakness and hence a cause of anisotropy, was also brought out.

This study has shown that modifications in print geometry (shapes and orientation) as well as material characteristics (using fiber reinforcement) can be used to mitigate some of the undesirable strength-related effects of interfilament joints in layered 3-D printing of concrete.

AUTHOR BIOS

ACI member **Avinaya Tripathi** *is a PhD Candidate in the School of Sustainable Engineering and the Built Environment at Arizona State University, Tempe, AZ. He received his undergraduate degree from Western Regional Campus, Tribhuvan University, Kirtipur, Nepal. His research interests include additive manufacturing, material and process optimization in three-dimensional (3-D) concrete printing, structural testing, and computer-aided designing.*

Sooraj A. O. Nair *is a Senior Researcher at Corporate Innovation Center, USG Corporation, Libertyville, IL. He received his doctoral degree from the School of Sustainable Engineering and the Built Environment at Arizona State University in 2021. His research interests include additive manufacturing, soft matter mechanics, and connecting microlevel to macrolevel properties of construction materials.*

Harshitsinh Chauhan *is a Project Engineer at Coreslab Structures (ARIZ) Inc., Phoenix, AZ. He received his graduate degree from the School of Sustainable Engineering and the Built Environment at Arizona State University in 2021. His research interests include sustainable construction materials and additive manufacturing.*

Narayanan Neithalath, *FACI, is a Professor in the School of Sustainable Engineering and the Built Environment at Arizona State University. He is a member of ACI Committee 564, 3-D Printing with Cementitious Materials. His research interests include material design of novel and sustainable multifunctional cement-based materials, rheology of cementitious suspensions, and materials and process aspects related to 3-D concrete printing.*

ACKNOWLEDGMENTS

The authors sincerely acknowledge support from the U.S. National Science Foundation (NSF) (CMMI: 1727445; OISE: 2020095) towards this project. The contents of this paper reflect the views of the authors who are responsible for the facts and accuracy of the data presented herein, and do not necessarily reflect the views and policies of the NSF, nor do the contents constitute a standard, specification, or regulation. The authors acknowledge support from Salt River Materials Group, Omya, BASF, Bekaert, and ROCKFIBER for donating materials. The authors acknowledge the use of 3-D printing and material characterization facilities within the Laboratory for the Science of Sustainable Infrastructural Materials (LS-SIM) at Arizona State University.

REFERENCES

1. Chen, Y.; Veer, F.; and Çopuro, O., "A Critical Review of 3D Concrete Printing as a Low CO_2 Concrete Approach," *HERON*, V. 62, No. 3, 2017, pp. 167-194.

2. Vantyghem, G.; De Corte, W.; Shakour, E.; and Amir, O., "3D Printing of a Post-Tensioned Concrete Girder Designed by Topology Optimization," *Automation in Construction*, V. 112, 2020, p. 103084. doi: 10.1016/j.autcon.2020.103084

3. Wu, P.; Wang, J.; and Wang, X., "A Critical Review of the Use of 3-D Printing in the Construction Industry," *Automation in Construction*, V. 68, 2016, pp. 21-31. doi: 10.1016/j.autcon.2016.04.005

4. Nematollahi, B., Xia, M., and Sanjayan, J., "Current Progress of 3D Concrete Printing Technologies," *Proceedings of the 34rd ISARC*, Taipei, Taiwan, 2017, pp. 260-267.

5. Holt, C.; Edwards, L.; Keyte, L.; Moghaddam, F.; and Townsend, B., "Chapter 17 - Construction 3D Printing," *3D Concrete Printing Technology*, 2019, pp. 349-370.

6. Jones, S. Z.; Bentz, D. P.; Martys, N. S.; George, W.; and Thomas, A., "Rheological Control of 3D Printable Cement Paste and Mortars," *First RILEM International Conference on Concrete and Digital Fabrication—Digital Concrete 2018*, V. 19, 2019, pp. 70-80.

7. Chen, Y.; Chaves Figueiredo, S.; Li, Z.; Chang, Z.; Jansen, K.; Çopuroğlu, O.; and Schlangen, E., "Improving Printability of Limestone-Calcined Clay-Based Cementitious Materials by Using Viscosity-Modifying Admixture," *Cement and Concrete Research*, V. 132, 2020, p. 106040. doi: 10.1016/j.cemconres.2020.106040

8. Eugenin, C.; Navarrete, I.; Brevis, W.; and Lopez, M., "Air Bubbles as an Admixture for Printable Concrete: A Review of the Rheological Effect of Entrained Air," *3D Printing and Additive Manufacturing*, 2021.

9. Vantyghem, G.; Boel, V.; De Corte, W.; and Steeman, M., "Compliance, Stress-Based and Multi-physics Topology Optimization for 3D-Printed Concrete Structures," *First RILEM International Conference on Concrete and Digital Fabrication—Digital Concrete 2018*, V. 19, 2019. pp. 323-332.

10. Kristombu Baduge, S.; Navaratnam, S.; Abu-Zidan, Y.; McCormack, T.; Nguyen, K.; Mendis, P.; Zhang, G.; and Aye, L., "Improving Performance of Additive Manufactured (3D Printed) Concrete: A Review on Material Mix Design, Processing, Interlayer Bonding, and Reinforcing Methods," *Structures*, V. 29, 2021, pp. 1597-1609. doi: 10.1016/j.istruc.2020.12.061

11. Wolfs, R. J. M.; Bos, F. P.; and Salet, T. A. M., "Hardened Properties of 3D Printed Concrete: The Influence of Process Parameters on Interlayer Adhesion," *Cement and Concrete Research*, V. 119, 2019, pp. 132-140. doi: 10.1016/j.cemconres.2019.02.017

12. Alchaar, A. S., and Al-Tamimi, A. K., "Mechanical Properties of 3D Printed Concrete in Hot Temperatures," *Construction and Building Materials*, V. 266, 2021, p. 120991. doi: 10.1016/j.conbuildmat.2020.120991

13. Perrot, A.; Rangeard, D.; and Pierre, A., "Structural Built-Up of Cement-Based Materials Used for 3D-Printing Extrusion Techniques," *Materials and Structures*, V. 49, No. 4, 2016, pp. 1213-1220. doi: 10.1617/s11527-015-0571-0

14. Roussel, N., "Rheological Requirements for Printable Concretes," *Cement and Concrete Research*, V. 112, 2018, pp. 76-85. doi: 10.1016/j.cemconres.2018.04.005

15. Zareiyan, B., and Khoshnevis, B., "Effects of Interlocking on Interlayer Adhesion and Strength of Structures in 3D Printing of Concrete,"

Automation in Construction, V. 83, 2017, pp. 212-221. doi: 10.1016/j.autcon.2017.08.019

16. Salman, N. M.; Ma, G.; Ijaz, N.; and Wang, L., "Weak Interlayer Bonding in Extrusion 3D Concrete Printing: A Comparative Analysis of Mitigation Techniques," *IOP Conference Series: Materials Science and Engineering*, V. 1028, 2021, p. 012003. doi: 10.1088/1757-899X/1028/1/012003

17. Keita, E.; Bessaies-Bey, H.; Zuo, W.; Belin, P.; and Roussel, N., "Weak Bond Strength Between Successive Layers in Extrusion-Based Additive Manufacturing: Measurement and Physical Origin," *Cement and Concrete Research*, V. 123, 2019, p. 105787. doi: 10.1016/j.cemconres.2019.105787

18. Panda, B.; Chandra Paul, S.; and Jen Tan, M., "Anisotropic Mechanical Performance of 3D Printed Fiber Reinforced Sustainable Construction Material," *Materials Letters*, V. 209, 2017, pp. 146-149. doi: 10.1016/j.matlet.2017.07.123

19. Ye, J.; Cui, C.; Yu, J.; Yu, K.; and Dong, F., "Effect of Polyethylene Fiber Content on Workability and Mechanical-Anisotropic Properties of 3D Printed Ultra-High Ductile Concrete," *Construction and Building Materials*, V. 281, 2021, p. 122586. doi: 10.1016/j.conbuildmat.2021.122586

20. Yu, R.; Spiesz, P.; and Brouwers, H. J. H., "Development of an Eco-Friendly Ultra-High Performance Concrete (UHPC) with Efficient Cement and Mineral Admixtures Uses," *Cement and Concrete Composites*, V. 55, 2015, pp. 383-394. doi: 10.1016/j.cemconcomp.2014.09.024

21. Arora, A.; Yao, Y.; Mobasher, B.; and Neithalath, N., "Fundamental Insights into the Compressive and Flexural Response of Binder- and Aggregate-Optimized Ultra-High Performance Concrete (UHPC)," *Cement and Concrete Composites*, V. 98, 2019, pp. 1-13. doi: 10.1016/j.cemconcomp.2019.01.015

22. Nair, S. A. O.; Alghamdi, H.; Arora, A.; Mehdipour, I.; Sant, G.; and Neithalath, N., "Linking Fresh Paste Microstructure, Rheology and Extrusion Characteristics of Cementitious Binders for 3D Printing," *Journal of the American Ceramic Society*, V. 102, No. 7, 2019, pp. 3951-3964. doi: 10.1111/jace.16305

23. Nair, S. A. O.; Tripathi, A.; and Neithalath, N., "Examining Layer Height Effects on the Flexural and Fracture Response of Plain and Fiber-Reinforced 3D-Printed Beams," *Cement and Concrete Composites*, V. 124, 2021, p. 104254. doi: 10.1016/j.cemconcomp.2021.104254

24. ASTM C78/C78M-18, "Standard Test Method for Flexural Strength of Concrete (Using Simple Beam with Third-Point Loading)," ASTM International, West Conshohocken, PA, 2018.

25. Das, S.; Kizilkanat, A.; and Neithalath, N., "Crack Propagation and Strain Localization in Metallic Particulate-Reinforced Cementitious Mortars," *Materials & Design*, V. 79, 2015, pp. 15-25. doi: 10.1016/j.matdes.2015.04.038

26. Zhang, D.; Eggleton, C. D.; and Arola, D. D., "Evaluating the Mechanical Behavior of Arterial Tissue Using Digital Image Correlation," *Experimental Mechanics*, V. 42, 2002, pp. 409-416.

27. Marković, I., "High-Performance Hybrid-Fibre Concrete: Development and Utilisation," doctoral thesis, Technical University of Delft, Delft, the Netherlands, 2006, 232 pp.

28. Bester, F.; van den Heever, M.; Kruger, J.; Cho, S.; and van Zigl, G., "Steel Fiber Links in 3D Printed Concrete," *Second RILEM International Conference on Concrete and Digital Fabrication*, V. 28, 2020. pp. 398-406.

29. Arunothayan, A. R.; Nematollahi, B.; Sanjayan, J.; Ranade, R.; Hau Bong, S.; and Khayat, K., "Quantitative Evaluation of Orientation of Steel Fibers in 3D-Printed Ultra-High Performance Concrete," *Second RILEM International Conference on Concrete and Digital Fabrication*, V. 28, 2020, pp. 389-397.

30. Bos, F. P.; Bosco, E.; and Salet, T. A. M., "Ductility of 3D Printed Concrete Reinforced with Short Straight Steel Fibers," *Virtual and Physical Prototyping*, V. 14, No. 2, 2019, pp. 160-174. doi: 10.1080/17452759.2018.1548069

31. Nematollahi, B.; Vijay, P.; Sanjayan, J.; Nazari, A.; Xia, M.; Naidu Nerella, V.; and Mechtcherine, V., "Effect of Polypropylene Fibre Addition on Properties of Geopolymers Made by 3D Printing for Digital Construction," *Materials (Basel)*, V. 11, No. 12, 2018, p. 2352. doi: 10.3390/ma11122352

32. Hambach, M.; Rutzen, M.; and Volkmer, D., "Chapter 5 - Properties of 3D-Printed Fiber-Reinforced Portland Cement Paste," *3D Concrete Printing Technology*, 2019, pp. 73-113.

33. Mobasher, B.; Li, A.; Yao, Y.; Arora, A.; and Neithalath, N., "Characterization of Toughening Mechanisms in UHPC Through Image Correlation and Inverse Analysis of Flexural Results," *Cement and Concrete Composites*, V. 122, 2021, p. 104157. doi: 10.1016/j.cemconcomp.2021.104157

34. Sim, J.; Park, C.; and Moon, D. Y., "Characteristics of Basalt Fiber as a Strengthening Material for Concrete Structures," *Composites Part B: Engineering*, V. 36, No. 6-7, 2005, pp. 504-512. doi: 10.1016/j.compositesb.2005.02.002

35. Pham, L.; Lu, G.; and Tran, P., "Influences of Printing Pattern on Mechanical Performance of Three-Dimensional-Printed Fiber-Reinforced Concrete," *3D Printing and Additive Manufacturing*, 2020, p. 1-18.

36. van den Heever, M.; Bester, F.; Kruger, J.; and van Zijl, G., "Mechanical Characterisation for Numerical Simulation of Extrusion-Based 3D Concrete Printing," *Journal of Building Engineering*, V. 44, 2021, p. 102944. doi: 10.1016/j.jobe.2021.102944

37. Li, L. G.; Zhuo, H. X.; Zhu, J.; and Kwan, A. K. H., "Packing Density of Mortar Containing Polypropylene, Carbon or Basalt Fibres Under Dry and Wet Conditions," *Powder Technology*, V. 342, 2019, pp. 433-440. doi: 10.1016/j.powtec.2018.10.005

ACI MATERIALS JOURNAL TECHNICAL PAPER

Title No. 121-M13

Influence of Type of Fibers on Fresh and Hardened Properties of Three-Dimensional-Printed Cementitious Mortars

by Yu Wang, Fabian B. Rodriguez, Jan Olek, Pablo D. Zavattieri, and Jeffrey P. Youngblood

Reinforcing strategies for three-dimensional printing (3DP) of cementitious materials (mostly mortars) have been extensively studied in recent years. Among various reinforcement strategies available for 3DP of cementitious materials, the use of fibers is frequently mentioned as a promising approach to enhance their mechanical performance. This work aims to evaluate the influence of four types of fibers (polyvinyl alcohol [PVA], nylon, rayon, and basalt) on the flowability and flexural strength of mortars used in 3DP. The flexural behavior of 3DP beams was compared with that of cast specimens, and the digital image correlation (DIC) technique was used to evaluate the development of the cracks. The fiber orientation in the reference (cast) and 3DP samples was examined using optical microscopy. The results revealed that, among four types of fibers used, the PVA fibers were most effective in increasing the flexural strength of both the cast and 3DP specimens. In addition, the results show that all fibers preferentially aligned parallel to the printing direction. 3DP specimens with filaments aligned in the direction perpendicular to the direction of the applied load showed superior flexural strength when compared to the cast specimens.

Keywords: fiber-reinforced cementitious composite; fiber orientation; mechanical performance; three-dimensional printing (3DP) of mortar.

INTRODUCTION

Additive manufacturing technology for cementitious materials has been developing rapidly in recent years.[1-5] Unlike conventional cast methods, which require formwork to control the geometry of the elements, three-dimensional printing (3DP) technology uses semiautomated processes to control the shape and geometry of the printed elements. Specifically, this technology gives the user the ability to control the spatial orientation of the filaments during the 3DP process, resulting in elements with so-called "internally architected microstructures." This approach allows for creation of elements which are lighter, yet tougher, than the cast elements.[6,7] The use of 3DP should ultimately lower the overall construction costs as this process requires fewer workers, minimizes the amount of wasted material, and often eliminates the need for formwork.[8-11]

Because concrete is inherently a brittle material, most structural members contain reinforcing bars to improve the load-carrying capacity and ductility of the structure. These reinforcing bars are typically preinstalled and subsequently encased in concrete during the construction process. However, due to the layer-by-layer manner of concrete deposition during the 3DP process, proper placement of the reinforcing bars in elements created using this technology is challenging.[12,13] In cases where the design calls for reinforcing bars to be oriented in the direction parallel to the printing direction, they can be manually (or automatically) placed between the subsequently printed layers.[14,15] However, concerns have been raised regarding the accuracy of such placements and the ability to obtain sufficient bond between reinforcing bars and the printed layers (filaments).[12,16] In cases where the design calls for reinforcement arranged perpendicularly to the printing direction, the challenge of inserting of reinforcing bars during the printing process is even greater.[13] Additionally, for elements with complex geometry, the reinforcing bars need to be pre-bent to match the shape of concrete filament. This, in connection with the often-complicated 3DP toolpath, leads to difficulties with reinforcing bar placement.[13]

In recent years, researchers have been developing alternative reinforcement systems for use in 3DP mortars.[17-21] One of these systems is based on the use of short, dispersed fibers as an alternative to inserting the reinforcing bars. In many cases, fiber-reinforced mortars have been proven to have outstanding strength, ductility, and durability.[22-30] As an example, Zhu et al.[27] developed ductile, 3DP cement composites based on polyethylene (PE) fibers. Ma et al.[29] studied the effect of basalt fibers on the fresh and mechanical properties of 3DP mortars. They reported that basalt acted as a pozzolanic material, resulting in the creation of additional calcium-silicate-hydrate (C-S-H) in the cement matrix as compared to basalt-free control mixtures, thereby improving the mechanical properties. Zhang et al.[30] found that the addition of polyvinyl alcohol (PVA) fibers can improve certain durability characteristics of the mortar, such as permeability and freezing-and-thawing resistance.

The current study used four different types of fibers: PVA, nylon, rayon, and basalt. The PVA and nylon fibers are synthetic fibers and have been reported to improve the mechanical performance and durability of mortars.[30-33] Rayon is a semi-synthetic, low-cost fiber[34] made from regenerated cellulose obtained from wood pulp or cotton. Basalt fibers, also considered to be low-cost material, are produced by melting basalt rocks and extruding the melt through spinning dies.[35]

The first part of this paper examines the effects of all four types of fibers on the flowability of mortars intended for 3DP applications. The second part of the paper compares the stress-strain responses and flexural strengths of 3DP and cast

ACI Materials Journal, V. 121, No. 2, March 2024.

MS No. M-2022-193.R1, doi: 10.14359/51740263, received June 8, 2022, and reviewed under Institute publication policies.

beams prepared from the fiber-reinforced mortars and tested using the four-point bending (4PB) method. These experiments were performed to quantify the potential changes in the flexural responses of the fiber-reinforced mortars resulting from the 3DP process. Digital image correlation (DIC) was used to analyze the crack development in the specimens. Optical microscopy was used to examine and to compare the orientation of the fibers in the cast and 3DP samples.

RESEARCH SIGNIFICANCE

This paper describes the study on the influence of four different types of fibers on the flowability and flexural behavior of cementitious mortars intended for 3DP applications. Specifically, to evaluate the effects of fibers on the rheological characteristics of freshly mixed mortars over time, flowability measurements were performed at 20-minute intervals for a period of 120 minutes (2 hours) after the completion of the mixing process. In addition to flexural strength, crack patterns and fiber orientation in both cast and 3DP specimens were also evaluated. The results demonstrate that the extrusion process promotes alignment of fibers in the direction of printing, which can lead to the enhancement of the flexural performance of 3DP mortars compared to cast mortars when the specimens are loaded perpendicular to the direction of printing. Thus, the test results revealed the benefits of using fiber-reinforced mortars in 3DP applications.

MATERIALS AND METHODS

Experimental program

In this study, experiments were conducted to evaluate the effect of short, chopped fibers on the flowability of fresh mortars and on flexural strength (f_t) of both cast and 3DP mortar beams. In addition, the distribution of fibers in 3DP beams was also examined and compared with the distribution of fibers in the cast beams.

Flowability is an important factor that affects the extrusion process of 3DP mortars. Flow table tests were conducted on mixtures containing four different types of fibers to evaluate their effect on the flowability and extrudability of the mortars. The effect of using different types of fibers on the flexural strength (f_t) was evaluated using both cast and 3DP beams. The dimensions of the cast beams were 40 x 40 x 160 mm (1.57 x 1.57 x 6.30 in.), whereas the dimensions of the 3DP beams were 40 x 40 x 140 mm (1.57 x 1.57 x 5.51 in.). The reason that 3DP specimens were shorter than the cast specimens was that the former were produced by extrusion of a mortar from a plastic syringe with a total capacity of 150 cm^3 (9.15 $in.^3$). That limited capacity of the syringe forced production of a shorter beam to facilitate printing one specimen using no more than two batches of material. All beams were subjected to a 4PB load with the same load span and the long dimension of the beam being perpendicular to the direction of the load. Because previous research has found that the 3DP process is likely to cause unidirectional (that is, parallel to the printing direction) alignment of the fibers,[29,36] all beams used in this study were printed with filaments parallel to the longitudinal axes of the beams to maximize the influence of the fibers on their flexural strength (when loaded in the direction perpendicular to the longitudinal axis).

Materials and mixtures

Four different types of fibers, each with a length of 6 mm, were used in this study (refer to Fig. 1). These included PVA, nylon, rayon, and basalt fibers.

While the length of all types of fibers was 6 mm (0.24 in.), their diameter varied depending on the type of the fiber. The aspect ratios (that is, the ratios of length to diameter) for nylon, PVA, basalt, and rayon fibers were, respectively, 250, 273, 300, and 333. The densities of the nylon, PVA, basalt, and rayon fibers were, respectively, 1.14, 1.3, 2.63, and 1.5 g/cm^3 (0.041, 0.047, 0.095, and 0.054 lb/$in.^3$).

In addition, the critical volume fraction of the fibers was determined by evaluating the extrudability of the mortar through a 6 mm (0.24 in.) diameter nozzle during the preliminary part of this study. Extrusion difficulties occurred during the printing process when the fiber content exceeded 0.4%. Thus, the volume fraction of the fibers used in this study was set at 0.4% (with respect to the total volume of the plain [that is, no fibers] mixture).

All mortars used in this study had the same basic composition (refer to Table 1) except for the type of fibers used in the individual mixtures. This composition was based on a previous study that focused on the assessment of printability, buildability, and open time of mortar mixtures intended for 3DP.[37] The weight percentages of water, silica fume, fine aggregate, high-range water-reducing admixture (HRWRA), and viscosity-modifying admixture (VMA) were calculated with respect to the mass of the total cementitious material. On the other hand, the amount of fibers added to each mixture was calculated as constant (0.4) percentage of the volume of the plain mixture.

Type I ordinary portland cement meeting the requirements of ASTM C150/C150M[38] was used as the hydraulic binder.

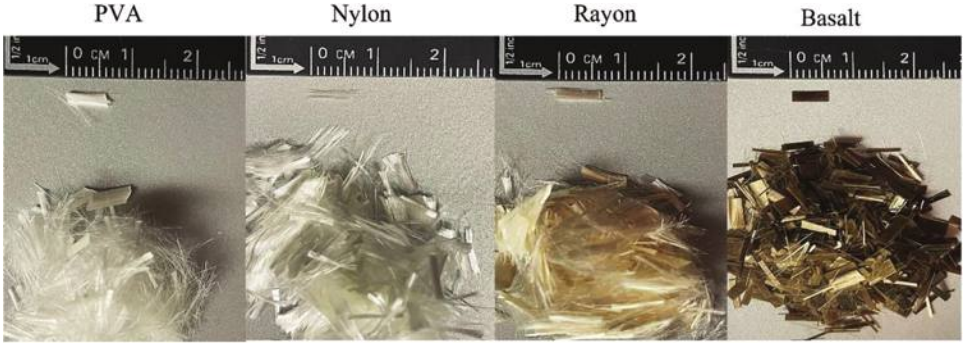

Fig. 1—Four types of fibers used in study.

The fine aggregate used was a natural siliceous sand with a maximum particle size of 0.6 mm (0.02 in.). The HRWRA and the VMA were used to adjust the flowability and consistency of the mixtures. Polycarboxylate-based HRWRA that met the requirements of ASTM C494/C494M[39] for Type F admixture and VMA that met the requirements of the ASTM C494/C494M[39] for Type S (specific performance) admixture were used in this study. Additionally, silica fume was used in all mixtures to improve the buildability and to enhance the bond strength between fibers and mortar.[40-42]

Preparation of fresh mortars and beam specimens

All mortars were batched using mixture proportions given in Table 1. When preparing the mortars, the liquid components (water, HRWRA, and VMA) were measured first and mixed manually in a plastic container to obtain a uniform blend of dispersed materials. In the second step, all solid materials (cement, sand, and silica fume) were measured and mixed in a mixer at medium speed for 2 minutes. Later, the premixed liquid materials were added to the solids and the entire assemblage of materials was mixed at medium speed for another 2 minutes. Then, the fibers were gradually added to the mortar by hand while the mixer was running at medium speed. The process of fiber addition took approximately 10 minutes. After the addition of fibers was completed, the mortars were mixed at high speed for another 5 minutes to ensure adequate dispersion of the fibers.

All 3DP beams were manufactured using an extrusion-based 3-D printer shown in Fig. 2. This printer was originally created for printing materials with high viscosity and high-solids content, such as plastics, clays, and cement-based materials. The printer used an electrical motor-operated printing head, which is mounted on a frame that controls the movement in X-Y directions. The motion in the Z-direction is controlled by the movement of the printing bed. The printer is controlled by software (Repetrel 5.1) that integrates the control of the head movement, flow rate, and so on.

During the printing process, the mortars were extruded from a plastic syringe with a capacity of 150 cm^3 (9.15 $in.^3$) attached to a stepper motor operating at a constant rate for continuous flow. The syringe used in this study had a nozzle opening of 6.0 mm (0.24 in.). The height of individual filaments was set to 4.0 mm (0.16 in.) and their length was 140 mm (5.51 in.). The layer height was selected based on a preliminary experiment to ensure printing quality and time efficiency. Each of the 3DP beams required 11 layers of filaments to achieve a height of 40 mm (1.57 in.). This is because one extra layer had to be added for each beam to account for the deformation of the layers during the printing process and dimensional variations due to printing system calibrations. A printing speed of 1000 mm/min (39.37 in./min) and a flow rate of approximately 20 cm^3/min (1.22 $in.^3$/min) were used during the fabrication of the beams.

The 3DP process started with a creation of the computer-aided design (CAD) model of a beam element. The CAD model was then imported to a slicer software to select the height and orientation of the filaments, the printing speed, and the flow rate. The slicer software generated the G-code commands that controlled the X-Y-Z movement and all other printing parameters. Once the G-code was uploaded to the printer, the syringe was charged with the mortar mixture and the printing process was initiated.

The cast beams were prepared by hand-placing the fresh mortars in a set of three-piece wooden molds, each with dimensions of 40 x 40 x 160 mm (1.57 x 1.57 x 6.30 in.). Both the printed and the cast beams were moist-cured for 14 days in an environmental chamber operating at a constant temperature of approximately 73°F (22.3°C) and relative humidity between 95 and 99%.

Table 1—Proportions of mortar mixtures

Water-cement ratio (*W*/*C*)*	Sand-cement ratio (*S*/*C*)*	Silica fume, %*	HRWRA, %*	VMA, %*	Fibers, %vol†
0.43	0.25	20	0.15	0.05	0.4

*With respect to weight of total cementitious material.

†Percentage of volume of plain (no fibers) mixture.

TESTING PROCEDURES

Flow table test

Flowability is an important property of fresh mortars that affects their extrusion during the 3DP process. Flow table testing has been extensively used in the past to evaluate the

Fig. 2—3DP process: (a) 3-D printer setup showing extrusion syringe mounted in printing head; and (b) examples of 3DP elements.

flowability of mixtures intended for 3DP.[37,43,44] In this study, the flow table test was performed in accordance with ASTM C1437.[45] As described in the sample preparation section, it took approximately 20 minutes to mix all the components of the mortar mixtures and to properly disperse the added fibers. Hence, the first measurement of flow was taken at approximately 20 minutes after the initial mixing of the cementitious materials and water. The resulting mortar was placed in the flow mold positioned in the center of the flow table. The mold was then lifted, and the table was dropped 25 times during the time span of 15 seconds. The diameter of the resulting mortar patch was then measured along the four lines scribed in the tabletop and the results of these measurements were used to calculate the average value of the flow. To ensure proper consistency throughout the entire 3DP process, the flow of the mortars was measured for up to 2 hours, at 20-minute intervals.

Four-point bending (4PB) test

The flexural behavior of the cast and 3DP mortar beams was evaluated using a 4PB test. To ensure the reliability of the results, three beams were tested for each type of mortars. After removal from the moist cabinet (at the end of the 14-day curing period), the surfaces of the beams were wiped off with a wet rag and stored in air. Once they achieved a surface-dry condition, the beams were prepped for DIC analysis and mounted in the testing machine. The top and bottom surfaces of the 3DP beams were quite flat and provided adequate contact with the loading and support fixers. As such, these specimens were tested in "as-printed" position. In contrast, the hand finishing of the cast specimens left the top surfaces relatively rough. As a result, for specimens tested in the "as-cast" position, the top surfaces had to be sanded off before testing. In some cases, the cast specimens were tested in the position rotated 90 degrees with respect to the direction of casting. The loading points at the top of the beam were 60 mm (2.36 in.) apart and the support points at the bottom of the beam were 120 mm (4.72 in.) apart.

The samples were tested using a universal testing machine with a capacity of 10 kN. ASTM C348[46] recommends applying the load at the rate of 2500 to 2800 N/min (562.02 to 629.47 lbf/min). In this study, the load was applied at a constant rate of 0.2 mm/min (0.008 in./min). Examination of the load-time curves revealed that this loading rate was roughly equivalent to approximately 1300 N/min (292.25 lbf/min). This relatively slow loading rate (compared to ASTM C348[46]) was used to ensure the ability to capture the processes of crack initiation and propagation by the DIC technique. The load-displacement curves were recorded to compare the effects of fibers on flexural and crack development characteristics of the tested beams specimens. The peak load was used to calculate the flexural stress (f_t), according to the following expression

$$f_t = \frac{3}{4}\frac{PL}{bd^2} \quad (1)$$

where P is the peak load; L is the support (bottom) span length; b is the width of the specimen, and d is the depth of the specimen.

DIC analysis

In this study, the DIC method was used to analyze the processes of crack initiation and propagation in the specimens. DIC is a noncontact measurement technique that can track (by comparing images of the surface at various states of testing) the displacement of discrete points on the surface of a sample during a mechanical test. These images are then compared to the reference image collected before any deformation has taken place to obtain the values of the strains and to detect the crack initiation and propagation events on the surfaces of the samples.

The DIC system consisted of two high-resolution cameras that photographed the surface of the specimens undergoing the tests at defined time intervals (that is, one picture every second). To use this method, the surface of the specimen needs to be covered with high-contrast speckle patterns. These speckle patterns were obtained by first panting the surface white, followed by spraying it with black paint. The captured images were analyzed by software (VIC-3D).

Optical microscopy analysis of fiber orientation

Fiber orientation in the cast and 3DP samples with PVA fiber was examined using a microscope. Specimens with PVA fibers were chosen for this evaluation because these types of fibers become fluorescent when exposed to the ultraviolet (UV) light. As a result, they can be more easily identified and photographed when observed in the optical microscope. The optical microscopy examination was performed on approximately 60 mm long segments of the beams cut off from a set of beams prepared in the same manner as the beams used for flexural testing. These segments were cut longitudinally, and the resulting cut surfaces were polished to a smooth finish. Several images were acquired at different distances between the microscope's objective and the objects, creating a stacked group of images. The resulting group of images was then processed (using an extended focus imaging [EFI] software) to select the sharply focused portion of each image and use it to produce a high-quality composite image of the entire surface.[47]

Because hydrated cementitious systems are highly alkaline (pH ~ 13), phenolphthalein solution (a common alkalinity indicator) was applied to the cut surfaces of the specimens, making them distinctively pink, and thus helping with identification of the fibers. Also, because, as mentioned earlier, the PVA fibers will become fluorescent when observed under the UV light, the examination of the surfaces in the optical microscope was performed under the UV light source.

EXPERIMENTAL RESULTS AND DISCUSSION

Flow test results

Figure 3 presents the results of the flow table tests for different fiber-reinforced mortars. It can be seen that, as time passes, the flow of mortar containing rayon fibers decreases faster than that of mortars with other fibers. Rayon is a cellulose fiber, with strong water absorption capacity.[48,49] The absorption of water by the fibers results in a reduction of available water to interact with cement particles and that leads to rapid reduction of flow. However, for the other types of fiber-reinforced mortars, the flow loss during the 2-hour measurement period is insignificant. In fact, these fiber-

reinforced mortars exhibit greater flow values than the plain mortar. This implies that all fibers used in this research, with the exception of rayon fibers, can be used to maintain the flowability of the mortar and to extend the open time during the 3DP process.

In general, the influence of fibers on the flowability will depend on both the characteristics of the fibers and the volume fraction used. Specifically, fiber-reinforced cementitious composites with relatively high volume fractions of fibers are likely to experience a decrease in flowability due to clumping of individual fibers, trapping of the water in the clumps, or due to interactions of the fibers with aggregate particles.[50] However, for a small volume fraction of fibers, especially short fibers, the probability of clumping is much reduced. In fact, it has been reported that in such situations, the fibers may actually promote the structural breakdown of the flocculated structure of the cementitious material, thus decreasing the viscosity of the mixture.[50] In the case of this study, due to the relatively low fiber-volume fraction, low sand-cement ratio, and small aggregate size, the breakdown (dispersion) of flocculated cement grains may have played a dominant role, thus increasing the flowability of the mixture. This phenomenon is beneficial for 3DP printing applications because it allows for the extrusion of the material over the longer period of time. Additionally, the ability to maintain the consistent levels of flowability can help control the shape and ensure the dimensional stability of the 3DP elements.

Flexural test results

All 3DP and cast beams prepared from plain and fiber-reinforced mortars were subjected to the 4PB test to evaluate their flexural behavior. Representative stress-displacement (f'-δ) curves obtained from these tests are shown in Fig. 4(a) and (b) for 3DP and cast samples, respectively. For both cast and 3DP reference specimens (that is, samples without fibers), the results show an expected brittle failure behavior (that is, the stress drops rapidly to zero immediately after reaching the flexural strength limit). The addition of fibers enhances the flexural strength (f_t) of both the cast and 3DP specimens. The stress-displacement curves show that most of the mortar samples with nylon, basalt, and rayon fibers exhibit a rapid stress drop after reaching the peak stress. However, all of these specimens were still resisting some level of stress as indicated by the gradual decay of the slope of the post-peak portions of the curves. In general, the pre-peak stress portions of the stress-displacement curves for mortars with nylon, basalt, and rayon fibers were continuous and smooth. However, the pre-peak stress portion of the curves for specimens with PVA fibers shows several instances of stress drops, typically of less than 0.40 MPa (58.02 psi). This suggests that several cracks developed during the pre-peak stress portion, but the PVA fibers could strongly bridge the cracks to resist higher stress after the cracks formed. The results indicate that specimens with the PVA fibers developed highest values of the peak stresses and (in the case of 3DP specimens) the largest overall deformation compared to specimens containing other fibers. Figure 4(c) compares the f_t values of cast and 3DP samples with and without fibers. The average values of the f_t for the cast specimens with nylon, basalt, rayon, and PVA fibers

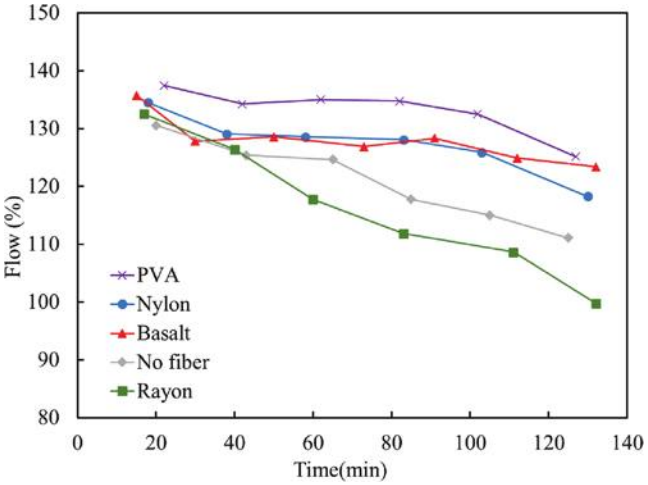

Fig. 3—Flow table test results for mortar with different types of fibers.

were, respectively, 10%, 31%, 58%, and 84% higher than those observed for the reference case (that is, cast specimens without fibers). On the other hand, the average f_t values for 3DP samples with nylon, basalt, rayon, and PVA fibers were, respectively, 28%, 28%, 92%, and 164% greater than the values observed for the reference case (that is, 3DP specimens without fibers). These results show that cast and 3DP samples with PVA fibers had the highest level of f_t improvement, whereas samples with nylon fiber had the lowest. The average values of the f_t for 3DP specimens with nylon, basalt, rayon, and PVA fibers were, respectively, 46%, 18%, 45%, and 74% higher than those obtained for cast specimens with the same types of fibers. The results indicate that flexural behavior of 3DP specimens was superior when compared to cast specimens. Additionally, the observed order of improvement of flexural strength of specimens associated with the use of different types of fibers did not correspond to the change in the order of aspect ratios of the fibers. This might be because other parameters, such as fiber strength and strength of the bond between the fiber and matrix, might have had a greater impact on the mechanical performance of the mortars than the aspect ratio for fibers of the same length.

Figure 5 summarizes the crack patterns observed in the 3DP and cast specimens with nylon, basalt, and rayon fibers. The behavior of one representative sample is presented herein and the crack patterns are represented by the contour of principal strains obtained from the DIC analysis. The color scale represents intensity of the principal strains in the vicinity of the cracks or other areas of stress concentration. The pictures shown herein were taken right after the sample reached peak stress. According to the DIC results, the cracks first appeared when the specimens reached the peak stress and continued to propagate upon further loading. All of the specimens shown in Fig. 5 failed as the result of formation and propagation of a single (critical) crack.

As shown in Fig. 6, the specimens containing the PVA fibers developed distinctively different crack patterns. Specifically, marked in Fig. 6(a) is a series of points (labeled P1, P2, P3, and P4 for 3DP specimen and labeled C1, C2, and C3 for the cast specimen) that correspond to particular stages of crack

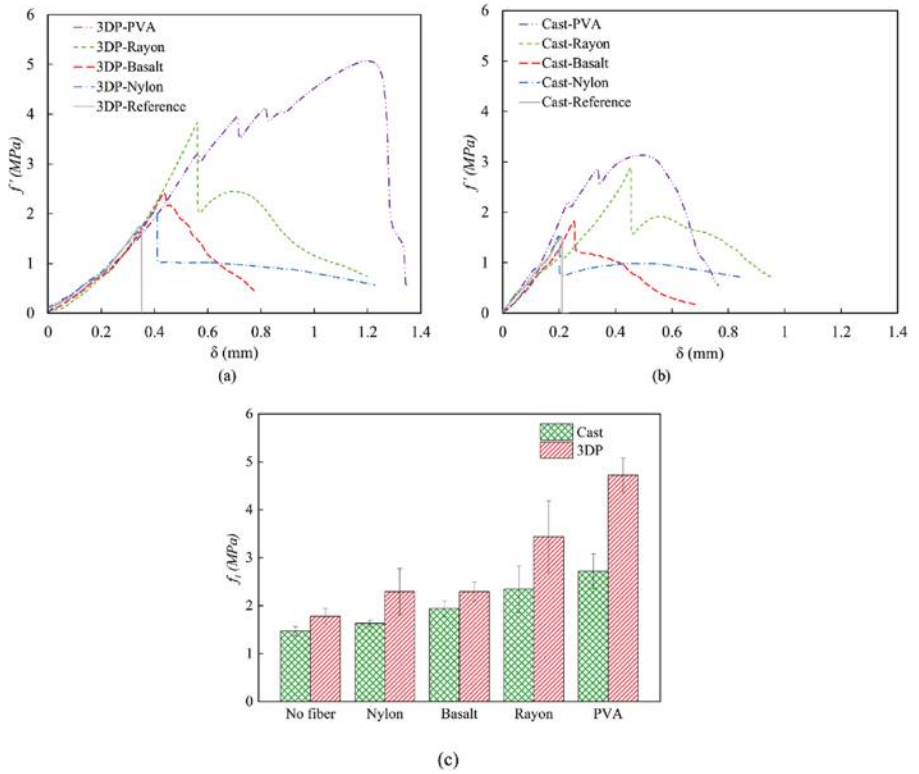

Fig. 4—Flexural test results: (a) representative stress-displacement curves for 3DP specimens; (b) representative stress-displacement curves for cast specimens; and (c) comparison of average values of flexural strength (f_t) for cast and 3DP specimens.

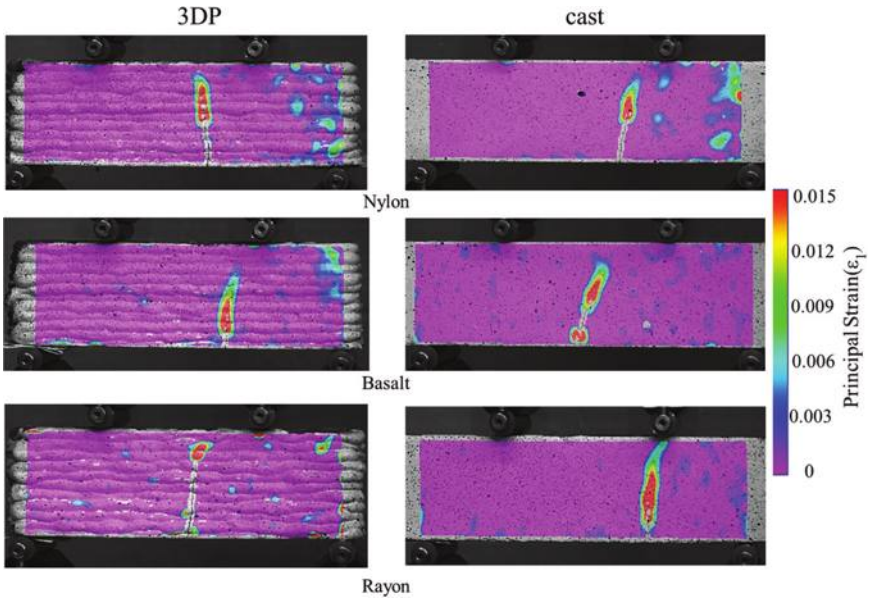

Fig. 5—DIC analysis of crack development in 3DP and cast specimens with nylon, basalt, and rayon fibers, represented by contour of principal strains obtained from DIC analysis (color scale represents intensity of principal strains in vicinity of crack or other areas of stress concentration; full-color PDF can be accessed at www.concrete.org).

development (shown in Fig. 6(b) and (c) respectively, for, 3DP and cast specimens). Comparing the stress-deformation curves with the DIC results, it can be seen that in each case, the initiation of the crack corresponded to the drop in the value of the corresponding stress. Figures 6(a), (b), and (c) also show that initial formation of the cracks did not result in immediate failure of the beam. Rather, the cracks were observed to gradually advance (or propagate) in response to increase in the load applied to the sample. It took approximately 6 to 7 minutes to complete the test. This observation may indicate the existence of a crack-bridging mechanism produced by the stronger bond between the PVA fibers and cement matrix, compared to the bond provided by other fiber types.[29,51] Specifically, after the crack is initiated, the fibers

can bridge the fractured surface to restrict further development of the crack.[29,52,53]

This crack-bridging mechanism might explain the development of multiple cracks in the PVA specimens. After the first crack was initiated, the PVA fibers maintained a strong bond with the matrix, allowing the specimens to resist higher stress up to the point of initiation of another crack. The spread of the damage and formation of multiple cracks in the PVA fiber-reinforced mortars led to the increase in the values of f_t and in the values of maximum displacement. It should also be noted that the 3DP PVA samples developed more cracks than cast PVA samples. Comparison of the stress-displacement curves for the cast and 3DP PVA beams reveals that the latter achieved greater strength and larger maximum displacement than the cast beam. Furthermore, as shown in Fig. 6(a), the 3DP specimens with PVA fibers were able to develop superior flexural behavior compared to flexural behavior of cast specimens with the same kind of fibers. Because the average values of the flexural strength for 3DP and cast specimens without fiber are comparable, the improvement in the flexural strength observed in 3DP specimens with PVA fibers is most likely the result of preferential alignment of fibers resulting from the 3DP process.[29,36]

For specimens prepared with other types of fibers, while the crack-bridging processes also likely took place, the effects of these processes on the values of peak stresses and the levels of deformations were not as pronounced as in the case of specimens with the PVA fibers. This is likely the result of weaker bonds between these types of fibers and the matrix.

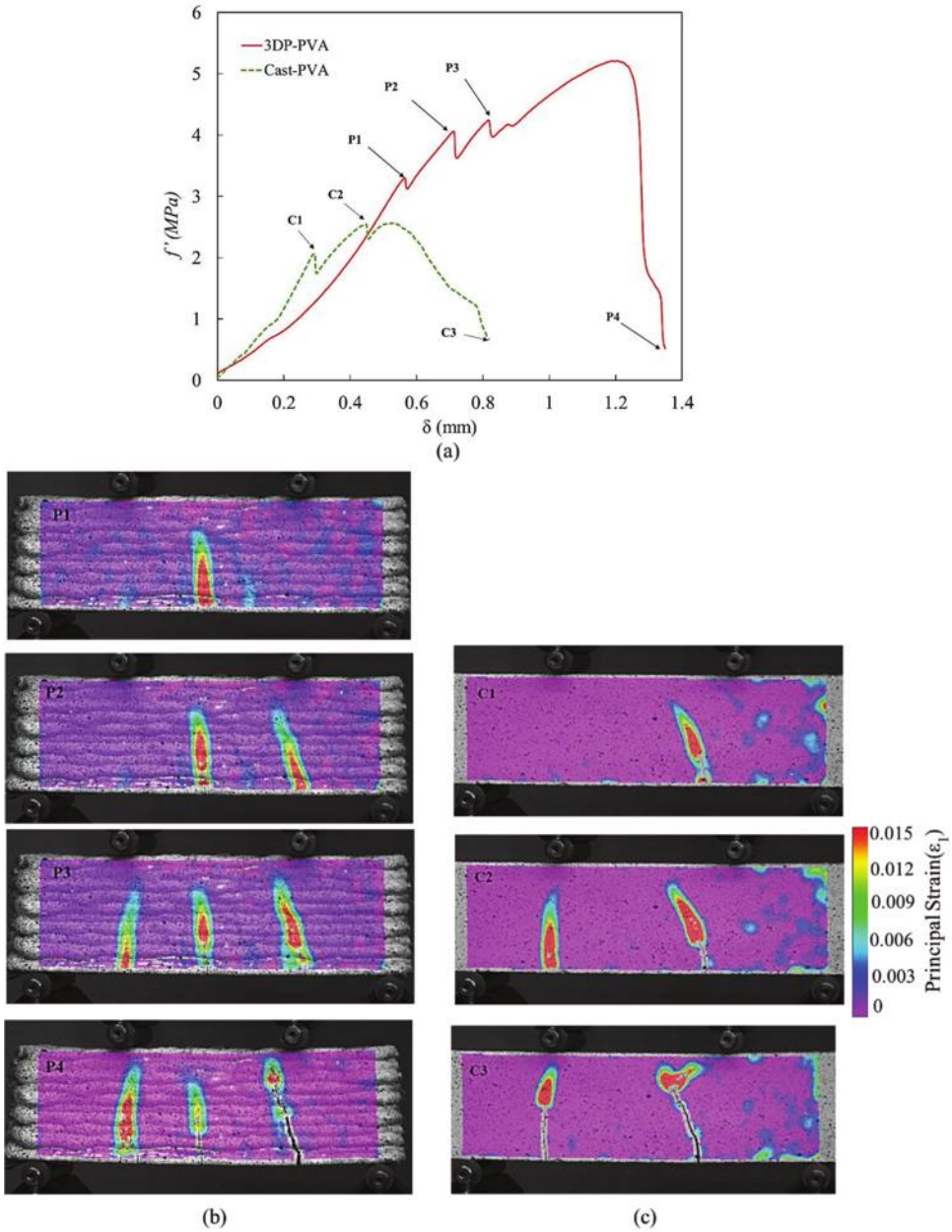

Fig. 6—(a) Representative stress-displacement curves of cast and 3DP specimens with PVA fibers; DIC analysis of crack development in: (b) 3DP specimen with PVA fibers showing formation of three cracks; and (c) cast specimen with PVA fibers showing formation of two cracks.

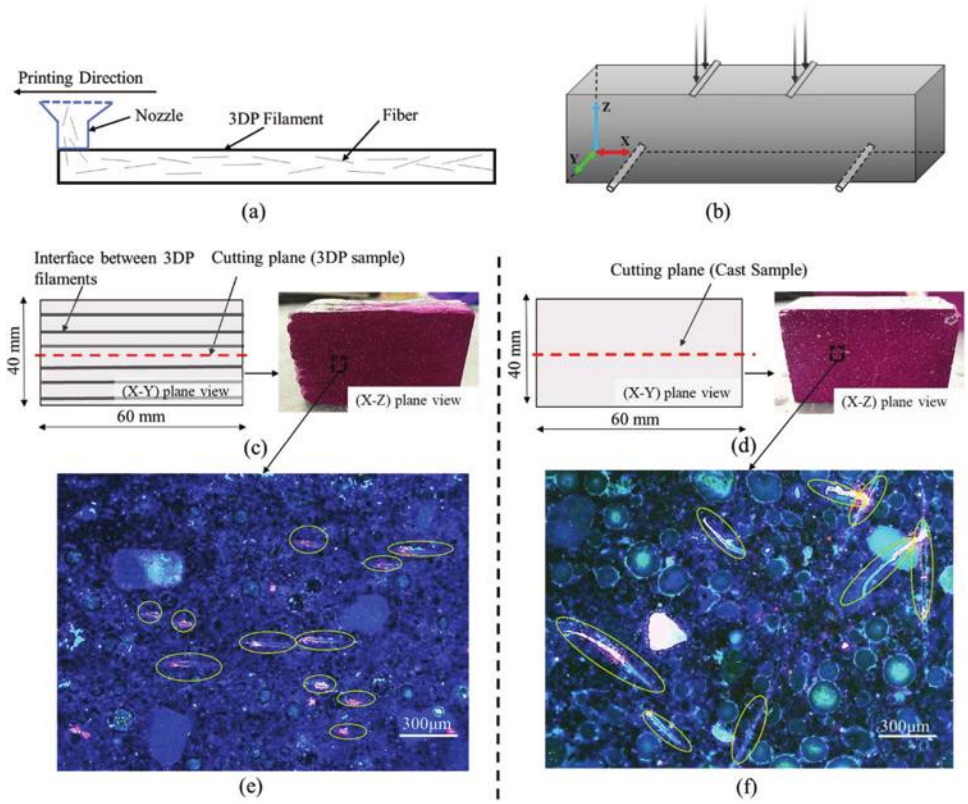

Fig. 7—(a) Schematic illustrating alignment of fibers resulting from 3DP process; (b) schematic of beam under 4PB test showing X-Y-Z axis; (c) view of top and cut planes of 3DP beam; (d) view of top and cut planes of cast beam; (e) optical microscope image of surface of 3DP specimen with PVA fibers; and (f) optical microscope image of surface of cast specimen with PVA fibers.

Optical microscopy test results

As mentioned earlier, the optical microscopy method was used to examine the dispersion and orientation of the fibers in both the cast and the 3DP samples with PVA fibers. For the 6 mm (0.24 in.) long PVA fibers and a 6 mm (0.24 in.) diameter circular nozzle used in this study, it was observed that the fibers are likely to align in the printing direction as the result of the movement of the nozzle during printing process (Fig. 7(a)). Figure 7(b) presents the schematic of a beam during a 4PB test showing the X-Y-Z axis. As shown in Fig. 7(c) and (d), shorter (roughly 60 mm long) segments of the beams, prepared the same way as the beams used for flexural testing, were cut longitudinally (along the vertical [X-Z] plane) and the resulting cut surfaces, parallel to the X-Z plane, were examined under the optical microscope. Figures 7(e) and (f) show optical microscopy images illustrating the orientation of the PVA fibers in, respectively, 3DP and cast specimens.

The optical microscopy images show that PVA fibers in 3DP samples are preferentially aligned in the direction parallel to the length of the filament orientation (Fig. 7(e)), whereas the PVA fibers in the cast samples are randomly oriented (Fig. 7(f)). Because the printing direction was parallel to the X-axis, this resulted in a higher number of PVA fibers becoming aligned perpendicular to the fracture surface. That preferential orientation, combined with (presumably) enhanced bond between the PVA fibers and the matrix, enhanced the crack-bridging effect, thus resulting in higher values of strength and maximum displacement observed in the 3DP specimens. Because all 3DP specimens manufactured from mixtures containing other types of fibers also exhibited improved flexural behavior compared to cast specimens, it is reasonable to assume that other fibers also experienced some degree of preferential alignment. It should be noted that the 6 mm (0.24 in.) long PVA fibers and a 6 mm (0.24 in.) diameter circular nozzle used in this study are not necessarily representing materials and equipment used in practice. In addition, one has to remember that there are some other factors that might influence the alignment of the fibers, including fiber stiffness, nozzle size, printing speed, and so on.[36]

Overall, the optical microscopy results suggest that the extrusion process associated with 3DP of fiber-reinforced mortars used in this study led to the preferential alignment of the fibers and, consequently, produced composite materials that were stronger and tougher than the materials of the same composition, but hand-cast.

SUMMARY AND CONCLUSIONS

The focus of this paper was on evaluation of the effects of four types of fibers (polyvinyl alcohol [PVA], basalt, nylon, and rayon) on the flowability and flexural behavior of the three-dimensional-printed (3DP) mortars. To reduce the number of variables that could obscure the analysis of the effects of the type of fibers, all fibers used in the study were of the same length (6 mm [0.24 in.]) and constituted the same volume percentage (0.4%) of the mortar. The

flexural behavior of 3DP beams was compared with that of cast beams and the processes of cracks formation and propagation were monitored using the digital image correlation (DIC) method. The fiber orientation in cast and 3DP samples was examined by optical microscopy. The results indicate that fiber-reinforced mortars represent a viable material type for 3DP manufacturing of cementitious components. The main conclusions and observations derived from the results of the study can be summarized as follows:

1. For the mixtures used in this study, the addition of all but one (rayon) fibers improved the flowability the mortars when compared to the plain (no fibers) mortar. These improvements are beneficial for 3DP applications because they extend the open time of the mixture and contribute to maintaining the dimensional consistency of the 3DP elements.

2. All fibers used in the study were observed to bridge the cracks, and thus improved the flexure strength of the specimens to some degree. However, the PVA fibers were most effective with respect to the enhancement of the aforementioned properties.

3. The optical microscopy images showed that PVA fibers in the 3DP beams were preferentially aligned in the direction parallel to movement of the nozzle (in this case, along the longitudinal axis of the beam). Because the beams were loaded in the direction perpendicular to the longitudinal axis, that preferential alignment strongly contributed to the enhancement of their flexural behavior.

AUTHOR BIOS

ACI member **Yu Wang** *is a PhD Student in the Lyles School of Civil Engineering at Purdue University, West Lafayette, IN. He received his BS in hydraulic and hydropower engineering from Northwest A&F University, Xianyang, China, and his MS in civil engineering from Northwestern University, Evanston, IL. His research interests include the development of functional architected cement-based materials using three-dimensional printing (3DP) technology, exploration of sustainable cementitious materials for 3DP, and multi-scale numerical simulations of cementitious composites.*

ACI member **Fabian B. Rodriguez** *is a Postdoctoral Researcher at National Renewable Energy Laboratory. He received his BS in civil engineering from Universidad Nacional de Colombia, Bogotá, Colombia, and his MS and PhD in civil engineering from Purdue University. He is a member of ACI Committee 564, 3-D Printing with Cementitious Materials. His research interests include the development of sustainable and low-carbon mixtures for 3DP, life-cycle assessment of construction materials, and durability of concrete structures.*

Jan Olek, *FACI, is the James H. and Carol H. Cure Professor in Civil Engineering at Purdue University. He received his BS, MS, and PhD in civil engineering from Cracow University of Technology, Kraków, Poland; The University of Texas at Austin, Austin, TX; and Purdue University, respectively. He is Chair of ACI Committee 552, Cementitious Grouting, and is a member of several other ACI committees. His research interests include mixture proportioning, characterization and use of supplementary cementitious materials, durability of concrete, and 3DP of concrete.*

Pablo D. Zavattieri *is the Jerry M. and Lynda T. Engelhardt Professor in Civil Engineering at Purdue University. He received his BS and MS from the Balseiro Institute, Bariloche, Argentina, and his PhD from Purdue University. Prior to joining Purdue, he worked at the GM R&D Center as a Staff Researcher for 9 years. His research interests include the interface between solid mechanics and materials engineering and bioinspired and architected materials.*

Jeffrey P. Youngblood *is a Professor in the School of Materials Engineering at Purdue University. He received his BS in chemistry and physics from Louisiana State University, Baton Rouge, LA, and his PhD in polymer science and engineering from the University of Massachusetts Amherst, Amherst, MA. His research interests include polymer and ceramics processing, sustainable nanotechnology, and functional coatings and additives.*

ACKNOWLEDGMENTS

Rayon and nylon fibers were obtained from MiniFIBERS Inc., the PVA fibers were supplied by Nycon Corporation, and the basalt fibers were obtained from Mafic Corporation. The authors acknowledge the generous support to this research by the National Science Foundation (Grant No. CMMI 1562927) awarded to Purdue University. The authors acknowledge the physical resources and support from the Pankow Materials Laboratory and Chemical Laboratory at Purdue University, where all the specimens were produced and the experimental tests were performed.

REFERENCES

1. Lim, S.; Buswell, R. A.; Le, T. T.; Austin, S. A.; Gibb, A. G. F.; and Thorpe, T., "Developments in Construction-Scale Additive Manufacturing Processes," *Automation in Construction*, V. 21, No. 1, 2012, pp. 262-268. doi: 10.1016/j.autcon.2011.06.010

2. Menna, C.; Mata-Falcón, J.; Bos, F. P.; Vantyghem, G.; Ferrara, L.; Asprone, D.; Salet, T.; and Kaufmann, W., "Opportunities and Challenges for Structural Engineering of Digitally Fabricated Concrete," *Cement and Concrete Research*, V. 133, 2020, p. 106079. doi: 10.1016/j.cemconres.2020.106079

3. Kazemian, A.; Yuan, X.; Cochran, E.; and Khoshnevis, B., "Cementitious Materials for Construction-Scale 3D Printing: Laboratory Testing of Fresh Printing Mixture," *Construction and Building Materials*, V. 145, 2017, pp. 639-647. doi: 10.1016/j.conbuildmat.2017.04.015

4. Zhang, C.; Hou, Z.; Chen, C.; Zhang, Y.; Mechtcherine, V.; and Sun, Z., "Design of 3D Printable Concrete Based on the Relationship between Flowability of Cement Paste and Optimum Aggregate Content," *Cement and Concrete Composites*, V. 104, 2019, p. 103406. doi: 10.1016/j.cemconcomp.2019.103406

5. Rodriguez, F. B.; Lopez, C. G.; Wang, Y.; Olek, J.; Zavattieri, P. D.; Youngblood, J. P.; Falzone, G.; and Cotrell, J., "Evaluation of Durability of 3D-Printed Cementitious Materials for Potential Applications in Structures Exposed to Marine Environments," *RILEM International Conference on Concrete and Digital Fabrication*, V. 37, 2022, pp. 175-181.

6. Moini, M.; Olek, J.; Youngblood, J. P.; Magee, B.; and Zavattieri, P. D., "Additive Manufacturing and Performance of Architectured Cement-Based Materials," *Advanced Materials*, V. 30, No. 43, 2018, p. 1802123. doi: 10.1002/adma.201802123

7. Nguyen-Van, V.; Tran, P.; Peng, C.; Pham, L.; Zhang, G.; and Nguyen-Xuan, H., "Bioinspired Cellular Cementitious Structures for Prefabricated Construction: Hybrid Design and Performance Evaluations," *Automation in Construction*, V. 119, 2020, p. 103324. doi: 10.1016/j.autcon.2020.103324

8. Hou, S.; Duan, Z.; Xiao, J.; and Ye, J., "A Review of 3D Printed Concrete: Performance Requirements, Testing Measurements and Mix Design," *Construction and Building Materials*, V. 273, 2021, p. 121745. doi: 10.1016/j.conbuildmat.2020.121745

9. Xiao, J.; Ji, G.; Zhang, Y.; Ma, G.; Mechtcherine, V.; Pan, J.; Wang, L.; Ding, T.; Duan, Z.; and Du, S., "Large-Scale 3D Printing Concrete Technology: Current Status and Future Opportunities," *Cement and Concrete Composites*, V. 122, 2021, pp. 104-115. doi: 10.1016/j.cemconcomp.2021.104115

10. Hossain, M. A.; Zhumabekova, A.; Paul, S. C.; and Kim, J. R., "A Review of 3D Printing in Construction and Its Impact on the Labor Market," *Sustainability (Basel)*, V. 12, No. 20, 2020, pp. 84-92. doi: 10.3390/su12208492

11. Mohan, M. K.; Rahul, A.; de Schutter, G.; and van Tittelboom, K., "Extrusion-Based Concrete 3D Printing From a Material Perspective: A State-of-the-Art Review," *Cement and Concrete Composites*, V. 115, 2021, p. 103855. doi: 10.1016/j.cemconcomp.2020.103855

12. Mechtcherine, V.; Grafe, J.; Nerella, V. N.; Spaniol, E.; Hertel, M.; and Füssel, U., "3D-Printed Steel Reinforcement for Digital Concrete Construction-Manufacture, Mechanical Properties and Bond Behavior," *Construction and Building Materials*, V. 179, 2018, pp. 125-137. doi: 10.1016/j.conbuildmat.2018.05.202

13. Mechtcherine, V.; Buswell, R.; Kloft, H.; Bos, F. P.; Hack, N.; Wolfs, R.; Sanjayan, J.; Nematollahi, B.; Ivaniuk, E.; and Neef, T., "Integrating Reinforcement in Digital Fabrication with Concrete: A Review and Classification Framework," *Cement and Concrete Composites*, V. 119, 2021, p. 103964. doi: 10.1016/j.cemconcomp.2021.103964

14. Hack, N., and Kloft, H., "Shotcrete 3D Printing Technology for the Fabrication of Slender Fully Reinforced Freeform Concrete Elements with High Surface Quality: A Real-Scale Demonstrator," *RILEM Bookseries*, V. 28, 2020, pp. 1128-1137. doi: 10.1007/978-3-030-49916-7_107

15. Neudecker, S.; Bruns, C.; Gerbers, R.; Heyn, J.; Dietrich, F.; Dröder, K.; Raatz, A.; and Kloft, H., "A New Robotic Spray Technology for Generative Manufacturing of Complex Concrete Structures without Formwork," *Procedia CIRP*, V. 43, 2016, pp. 333-338. doi: 10.1016/j.procir.2016.02.107

16. Baz, B.; Aouad, G.; Leblond, P.; Al-Mansouri, O.; D'hondt, M.; and Remond, S., "Mechanical Assessment of Concrete – Steel Bonding in 3D Printed Elements," *Construction and Building Materials*, V. 256, 2020, p. 119457. doi: 10.1016/j.conbuildmat.2020.119457

17. Wu, Z.; Memari, A. M.; and Duarte, J. P., "State of the Art Review of Reinforcement Strategies and Technologies for 3D Printing of Concrete," *Energies*, V. 15, No. 1, 2022, 360 pp. doi: 10.3390/en15010360

18. Caron, J.-F.; Demont, L.; Ducoulombier, N.; and Mesnil, R., "3D Printing of Mortar with Continuous Fibers: Principle, Properties And Potential For Application," *Automation in Construction*, V. 129, 2021, p. 103806. doi: 10.1016/j.autcon.2021.103806

19. Mechtcherine, V.; Buswell, R.; Kloft, H.; Bos, F. P.; Hack, N.; Wolfs, R.; Sanjayan, J.; Nematollahi, B.; Ivaniuk, E.; and Neef, T., "Integrating Reinforcement in Digital Fabrication with Concrete: A Review and Classification Framework," *Cement and Concrete Composites*, V. 119, 2021, p. 103964.

20. Mechtcherine, V.; Nerella, V. N.; Ogura, H.; Grafe, J.; Spaniol, E.; Hertel, M.; and Füssel, U., "Alternative Reinforcements for Digital Concrete Construction," *RILEM Bookseries*, V. 19, 2019, pp. 167-175. doi: 10.1007/978-3-319-99519-9_15

21. Müller, J.; Grabowski, M.; Müller, C.; Hensel, J.; Unglaub, J.; Thiele, K.; Kloft, H.; and Dilger, K., "Design and Parameter Identification of Wire and Arc Additively Manufactured (WAAM) Steel Bars for Use in Construction," *Metals*, V. 9, No. 7, 2019, p. 725. doi: 10.3390/met9070725

22. lo Monte, F., and Ferrara, L., "Tensile Behavior Identification in Ultra-High-Performance Fiber-Reinforced Cementitious Composites: Indirect Tension Tests and Back Analysis of Flexural Test Results," *Materials and Structures/Materiaux et Constructions*, V. 53, No. 6, 2020, pp. 1-12.

23. Cuenca, E.; Roig-Flores, M.; Garofalo, R.; Lozano-Násner, M.; Ruiz-Muñoz, C.; Schillani, F.; Borg, R. P.; Ferrara, L.; and Serna, P., "Mechanical and Durability Assessment of Concretes Obtained from Recycled Ultra-High-Performance Concretes," *RILEM Bookseries*, V. 36, 2022, pp. 947-957. doi: 10.1007/978-3-030-83719-8_81

24. Wang, W.; Liu, J.; Agostini, F.; Davy, C. A.; Skoczylas, F.; and Corvez, D., "Durability of an Ultra-High-Performance Fiber-Reinforced Concrete (UHPFRC) under Progressive Aging," *Cement and Concrete Research*, V. 55, 2014, pp. 1-13.

25. Teng, S.; Afroughsabet, V.; and Ostertag, C. P., "Flexural Behavior and Durability Properties of High-Performance Hybrid-Fiber-Reinforced Concrete," *Construction and Building Materials*, V. 182, 2018, pp. 504-515. doi: 10.1016/j.conbuildmat.2018.06.158

26. Niu, D.; Su, L.; Luo, Y.; Huang, D.; and Luo, D., "Experimental Study on Mechanical Properties and Durability of Basalt Fiber Reinforced Coral Aggregate Concrete," *Construction and Building Materials*, V. 237, 2020, p. 117628. doi: 10.1016/j.conbuildmat.2019.117628

27. Zhu, B.; Pan, J.; Nematollahi, B.; Zhou, Z.; Zhang, Y.; and Sanjayan, J., "Development of 3D Printable Engineered Cementitious Composites with Ultra-High Tensile Ductility for Digital Construction," *Materials & Design*, V. 181, 2019, p. 108088. doi: 10.1016/j.matdes.2019.108088

28. Yang, Y.; Wu, C.; Liu, Z.; Wang, H.; and Ren, Q., "Mechanical Anisotropy of Ultra-High-Performance Fiber-Reinforced Concrete for 3D Printing," *Cement and Concrete Composites*, V. 125, 2022, p. 104310. doi: 10.1016/j.cemconcomp.2021.104310

29. Ma, G.; Li, Z.; Wang, L.; Wang, F.; and Sanjayan, J., "Mechanical Anisotropy of Aligned Fiber Reinforced Composite for Extrusion-Based 3D Printing," *Construction and Building Materials*, V. 202, 2019, pp. 770-783. doi: 10.1016/j.conbuildmat.2019.01.008

30. Zhang, P.; Li, Q. F.; Wang, J.; Shi, Y.; and Ling, Y. F., "Effect of PVA Fiber on Durability of Cementitious Composite Containing Nano-SiO_2," *Nanotechnology Reviews*, V. 8, No. 1, 2019, pp. 116-127. doi: 10.1515/ntrev-2019-0011

31. Ling, Y.; Zhang, P.; Wang, J.; and Chen, Y., "Effect of PVA Fiber on Mechanical Properties of Cementitious Composite with and without Nano-SiO_2," *Construction and Building Materials*, V. 229, 2019, p. 117068. doi: 10.1016/j.conbuildmat.2019.117068

32. Song, P. S.; Hwang, S.; and Sheu, B. C., "Strength Properties of Nylon- and Polypropylene-Fiber-Reinforced Concretes," *Cement and Concrete Research*, V. 35, No. 8, 2005, pp. 1546-1550. doi: 10.1016/j.cemconres.2004.06.033

33. Qin, Y.; Li, M.; Li, Y.; Ma, W.; Xu, Z.; Chai, J.; and Zhou, H., "Effects of Nylon Fiber and Nylon Fiber Fabric on the Permeability of Cracked Concrete," *Construction and Building Materials*, V. 274, 2021, p. 121786. doi: 10.1016/j.conbuildmat.2020.121786

34. Westerlind, B.; Hirose, S.; Yano, S.; Hatekayama, H.; and Rigdahl, M., "Properties of Isoprene Rubber Reinforced with Treated Bleached Kraft Cellulosic Fibers or Rayon Fibers," *International Journal of Polymeric Materials*, V. 11, No. 4, 1987, pp. 333-353. doi: 10.1080/00914037808078670

35. Özkan, Ş., and Demir, F., "The Hybrid Effects of PVA Fiber and Basalt Fiber on Mechanical Performance of Cost-Effective Hybrid Cementitious Composites," *Construction and Building Materials*, V. 263, 2020, p. 120564. doi: 10.1016/j.conbuildmat.2020.120564

36. Arunothayan, A. R.; Nematollahi, B.; Ranade, R.; Bong, S. H.; Sanjayan, J. G.; and Khayat, K. H., "Fiber Orientation Effects on Ultra-High-Performance Concrete Formed by 3D Printing," *Cement and Concrete Research*, V. 143, 2021, p. 106384. doi: 10.1016/j.cemconres.2021.106384

37. Rodriguez, F. B.; Olek, J.; Moini, R.; Zavattieri, P. D.; and Youngblood, J. P., "Linking Solids Content and Flow Properties of Mortars to their Three-Dimensional Printing Characteristics," *ACI Materials Journal*, V. 118, No. 6, Nov. 2021, pp. 371-382.

38. ASTM C150/C150M-20, "Standard Specification for Portland Cement," ASTM International, West Conshohocken, PA, 2020.

39. ASTM C494/C494M-19, "Standard Specification for Chemical Admixtures for Concrete," ASTM International, West Conshohocken, PA, 2019.

40. Chan, Y. W., and Chu, S. H., "Effect of Silica Fume on Steel Fiber Bond Characteristics in Reactive Powder Concrete," *Cement and Concrete Research*, V. 34, No. 7, 2004, pp. 1167-1172. doi: 10.1016/j.cemconres.2003.12.023

41. Liu, Y.; Shi, C.; Zhang, Z.; Li, N.; and Shi, D., "Mechanical and Fracture Properties of Ultra-High Performance Geopolymer Concrete: Effects of Steel Fiber and Silica Fume," *Cement and Concrete Composites*, V. 112, 2020, p. 103665. doi: 10.1016/j.cemconcomp.2020.103665

42. Xie, J.; Zhang, Z.; Lu, Z.; and Sun, M., "Coupling Effects of Silica Fume and Steel-Fiber on the Compressive Behavior of Recycled Aggregate Concrete after Exposure to Elevated Temperature," *Construction and Building Materials*, V. 184, 2018, pp. 752-764. doi: 10.1016/j.conbuildmat.2018.07.035

43. Wi, K.; Hong, J.; and Wang, K., "Determining Printable Zone of Three-Dimensional-Printable Mortar Using Flow Table Tests," *ACI Materials Journal*, V. 118, No. 6, Nov. 2021, pp. 75-85.

44. Panda, B.; Sonat, C.; Yang, E. H.; Tan, M. J.; and Unluer, C., "Use of Magnesium-Silicate-Hydrate (M-S-H) Cement Mixes in 3D Printing Applications," *Cement and Concrete Composites*, V. 117, 2021, p. 103901. doi: 10.1016/j.cemconcomp.2020.103901

45. ASTM C1437-15, "Standard Test Method for Flow of Hydraulic Cement Mortar," ASTM International, West Conshohocken, PA, 2015.

46. ASTM C348-21, "Standard Test Method for Flexural Strength of Hydraulic-Cement Mortars," ASTM International, West Conshohocken, PA, 2021.

47. Finizio, A.; Javidi, B.; Alfieri, D.; Pierattini, G.; Coppola, G.; Ferraro, P.; de Nicola, S.; Grilli, S.; and Striano, V., "Extended Focused Image in Microscopy by Digital Holography," *Optics Express*, V. 13, No. 18, 2005, pp. 6738-6749.

48. Gupta, B. S., "Manufacture, Types and Properties of Biotextiles for Medical Applications," *Biotextiles as Medical Implants*, 2013, pp. 3-47.

49. Comnea-Stancu, I. R.; Wieland, K.; Ramer, G.; Schwaighofer, A.; and Lendl, B., "On the Identification of Rayon/Viscose as a Major Fraction of Microplastics in the Marine Environment: Discrimination between Natural and Manmade Cellulosic Fibers Using Fourier Transform Infrared Spectroscopy," *Applied Spectroscopy*, V. 71, No. 5, 2017, pp. 939-950. doi: 10.1177/0003702816660725

50. Kuder, K. G.; Ozyurt, N.; Mu, E. B.; and Shah, S. P., "Rheology of Fiber-Reinforced Cementitious Materials," *Cement and Concrete Research*, V. 37, No. 2, 2007, pp. 191-199. doi: 10.1016/j.cemconres.2006.10.015

51. Ding, T.; Xiao, J.; Zou, S.; and Zhou, X., "Anisotropic Behavior in Bending of 3D Printed Concrete Reinforced with Fibers," *Composite Structures*, V. 254, 2020, p. 112808 doi: 10.1016/j.compstruct.2020.112808

52. Ye, J.; Cui, C.; Yu, J.; Yu, K.; and Dong, F., "Effect of Polyethylene Fiber Content on Workability and Mechanical-Anisotropic Properties of 3D Printed Ultra-High Ductile Concrete," *Construction and Building Materials*, V. 281, 2021, p. 122586. doi: 10.1016/j.conbuildmat.2021.122586

53. Zahabizadeh, B.; Pereira, J.; Gonçalves, C.; Pereira, E. N. B.; and Cunha, V. M. C. F., "Influence of the Printing Direction and Age on the Mechanical Properties of 3D Printed Concrete," *Materials and Structures/Materiaux et Constructions*, V. 54, No. 2, 2021, pp. 1-22.

ACI MATERIALS JOURNAL TECHNICAL PAPER

Title No. 121-M14

Shoreline Resilience through Advanced Manufacturing

by Amin K. Akhnoukh and Mathew Campbell

The U.S. National Ocean Service estimates 95,741 miles (154,080 km) of shoreline in the United States, where 163 miles per year are hardened by bulkheads and riprap. These shoreline protection techniques are costly and require frequent maintenance. Different agencies are examining "nature-based" solutions that combine vegetation with traditional concrete. Digital construction, advanced manufacturing, and innovative cementitious composites have also been proposed as potential means to lower material use, cost, and environmental impact.

This paper presents a novel advanced manufacturing technique using a reactive-diffusion morphological process, called "dry-forming," to three-dimensionally (3-D) printed concrete structures of various shapes, sizes, and complexities with standard concrete mixtures.

This technology has reduced 60% of material use, enhanced local habitats, and increased the resiliency of the shoreline to sea level rise. The widespread use of this technology would increase the resiliency of coastal communities, protect aquatic life, and protect waterfront public and private real estate investments.

Keywords: advanced manufacturing; reactive-diffusion morphology; resiliency; shoreline protection; sustainable.

INTRODUCTION

The National Ocean Service (NOS) estimates the total length of the United States shoreline is 95,741 miles (154,080 km), including the continental United States as well as Hawaii and Alaska (Stoa 2019). Besides the coastal shorelines, other shorelines could include those associated with lakes, rivers, and creeks. During the twentieth century, climate changes resulted in a sea level rise of approximately 7 in. (18 cm). The continuous increase in temperature in the twenty-first century may result in additional sea level rise and a higher frequency and intensity of resulting storms (Church and White 2011). As a result, coastal communities are at increased risk of life-threatening events, land loss due to the shoreline's continuous erosion, significant economic losses due to property damage, and negative impact on tourism (Martyr-Koller et al. 2021).

Erosion mitigation techniques implemented in the United States include hard shorelines—such as the construction of bulkheads, rock breakwaters, and revetments—and living shorelines, which include native wetland plants and oyster reefs. Currently, 163 miles (263 km) are hardened every year by bulkheads, sea walls, concrete armor units, and riprap (Liew et al. 2020). These legacy shoreline protection techniques, shown in Fig. 1, are environmentally damaging, costly, require frequent maintenance, and have a negative impact on tourism. Thus, hardened shorelines are now being prohibited in multiple states and different countries across the globe (Tavares et al. 2020). Similarly, living shorelines are costly and require continuous maintenance intervention despite their efficiency in enhancing coastal sustainability, restoring ecosystems, and increasing shoreline sustainability (Smith et al. 2018).

This paper presents a novel advanced manufacturing technique's material use, cementitious material composition, and total carbon dioxide (CO_2) emissions. The material properties, material composition, and options for increased surface area, roughness, and improved performance are evaluated. This novel advanced manufacturing process uses a reactive-diffusion morphological process, called "dry-forming," (Campbell et al. 2018) to three-dimensionally (3-D) printed concrete structures of various shapes, sizes, and complexities with standard concrete mixtures. The injection of water (and chemicals) into a dry bed of cement and sand mixture is conducted using hollow needles spaced 2.0 in. (5.0 cm) apart in both directions. The needle depth is controlled by software to reflect the shape of the printed object, as shown in Fig. 2.

LITERATURE REVIEW

The global increase in coastal development and sea level rise resulted in increased coastal erosion in different countries, including the United States (IPCC 2019). Losses associated with coastal erosion include land losses, destruction of beachfront properties and real estate losses, and negative impact on tourism and marine/aquatic life. Under current circumstances, coastal erosion problems will develop into an unmanageable threat to the quality of life in coastal communities (Morton 2003). The coastal erosion problems are magnified due to population increase and wrong practices by beachfront community inhabitants (Barragán and de Andrés 2015). To sustainably mitigate erosion impact, shoreline protection techniques and practices are being standardized to ensure sufficient protection of lakes, streams, rivers, and along the coast without negatively impacting the surrounding environment (Miller et al. 2016). Basic principles followed to preserve the shoreline environment include nature imitation, maintaining a gentle shoreline slope to dissipate wave energy, and providing protection through live or dead protection techniques (Shows 2019). The aforementioned shoreline protection techniques, advantages, disadvantages, and limitations are provided in the following sections.

ACI Materials Journal, V. 121, No. 2, March 2024.

MS No. M-2022-217.R2, doi: 10.14359/51740264, received July 14, 2022, and reviewed under Institute publication policies.

Fig. 1—Types of hard shorelines: (a) riprap; (b) breakwater; and (c) bulkhead.

Fig. 2—Dry-bed technology for 3-D printing.

Fig. 3—Planted mangroves and oyster beds for coastal stabilization (photo by Linda Walters).

Nature imitation

Nature imitation is a natural shoreline protection technique where the shoreline can protect itself against erosion through the increased integrity of shoreline soils. Native vegetation around the shoreline can improve this integrity by reducing hydrodynamic forces and binding soil particles using plant roots. The vegetation's deep roots help protect shorelines against heavy rainfall, high-speed winds, and possible landslides, as shown in Fig. 3.

Shoreline slope

The shoreline slope is related to the shoreline grain particle size. Stable shoreline slopes depend on the particle size of the soils. Shorelines with larger-diameter particle sizes (that is, cobble) can adopt steeper slopes as compared to smaller fine-grain particles (that is, sand and silts). Shoreline slopes are also correlated to the hydrodynamic environment. The beach slope can become steeper during storm events and increase erosion rates (Bujan et al. 2019). These associated steeper-sloped shorelines tend to have increased run-up and overwash of waves that can cause flooding (Stockdon et al. 2006; Senechal et al. 2011). Traditionally, straw blankets, straw matting, and silt fences were used to maintain slopes in low-energy environments (Benik et al. 2000). Recently, erosion control blankets and superior compost erosion control blankets have been used to create a suitable environment for vegetation growth, which is beneficial in erosion control, as shown in Fig. 4.

Living shoreline protection

Living shoreline protection includes multiple techniques: 1) vegetation only—by providing a buffer region for upland areas, plants like mangroves, wetland grasses, shrubs, and trees are currently used for shoreline protection through vegetation; 2) edging, where a structure is added to protect the vegetated slope; and 3) sills, where a hard structure (that is, rock or concrete) is placed parallel to the shoreline to

protect coastal marshes from waves and currents. This technique, increasingly used on the East Coast of the United States, acts as a natural buffer to wave energy and inhibits erosion of coastal lands (Gittman et al. 2014; Barbier et al. 2008; Shepard et al. 2011).

Hard shoreline protection

"Hard" shoreline protection includes a variety of timber and/or concrete structures placed in shallow depths or by the shoreline to reflect wave energy, thus minimizing beach erosion. Despite their efficient wave-energy reflection, bulkheads may result in increased erosion along the toe of the structure (Bozek and Burdick 2005; National Research Council 2007). In addition, the use of bulkheads in shoreline hardening can cause an adverse impact on the ecological system and marine habitats and a significant decrease in the biodiversity of the region in which they are used (Douglass and Pickel 1999; Patrick et al. 2014; Seitz et al. 2006). Finally, treated timber-hardened shorelines may contain chemicals that can leach into the coastal environment and significantly harm marine life (Weis et al. 1998). A comparison of living and hard shorelines is shown in Fig. 5.

Due to the wide variation among shoreline protection techniques, associated hardships, and relevant advantages and disadvantages, the shoreline stabilization process is lengthy and requires multiple steps before the shoreline protection project starts. Table 1 presents the steps recommended for the shoreline protection process.

Fig. 4—Beach erosion control by using erosion control blankets.

RESEARCH SIGNIFICANCE

This research presents a novel advanced manufacturing technique to develop marine structures and artificial reefs through an advanced "dry-forming" (Campbell et al. 2018) technique to 3-D print structures and reefs of various shapes, sizes, and complexities with standard concrete mixtures. Structures produced could be used to protect shorelines from major hurricanes. Developed structures are environmentally

Table 1—Recommended shoreline design and construction process

Step	Activity description	Activity attributes/notes
1	Site analysis	Erosion rates (Thaler et al. 2022) Site elevation Wave energy (Ozkan et al. 2022) Hurricane activities (Camelo et al. 2020; Passeri et al. 2015) Wind Soil nature
2	Legal compliance and permit issuance	Federal regulations State regulations Local laws Permits
3	Project site preparation	Clearing debris Slope restoration Removing older/failing seawalls, bulkheads, and so on Addressing runoff issues
4	Main project activities/ construction	—
5	Monitoring and project maintenance	Debris removal Site and structural investigation Maintaining plantation Beach nourishment

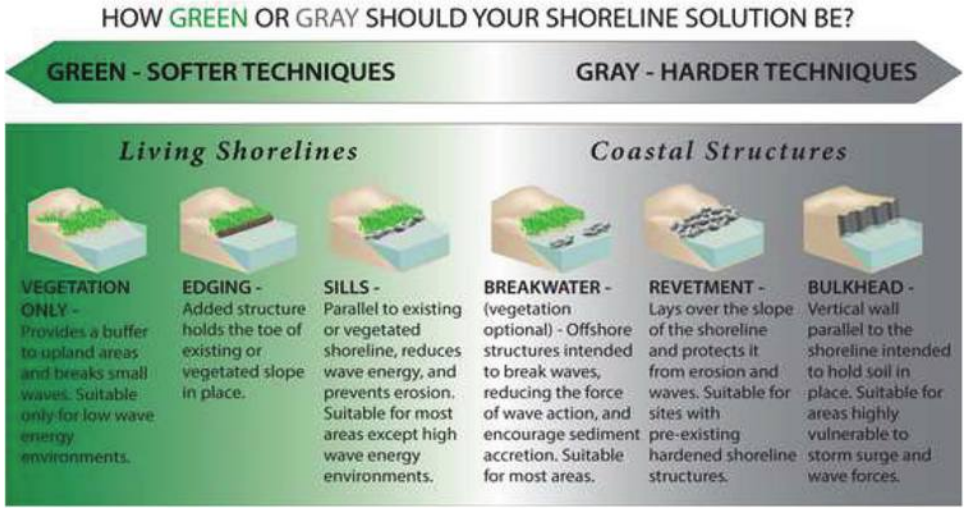

Fig. 5—Comparison of living and hardened shoreline protection techniques (NOAA Habitat Blueprint 2022; full-color PDF can be accessed at www.concrete.org).

friendly, reduce the carbon footprint, and are economical compared to current techniques. The widespread use of this technique in the construction market will positively impact social communities along shorelines globally.

EXPERIMENTAL INVESTIGATION AND REEF FABRICATION

The experimental phase and reef fabrication resulted from a two-phase experimental investigation. First, a material testing phase was conducted to evaluate the possible use of the new proposed "dry-forming" (Campbell et al. 2018) 3-D printing of reefs. Second, the equipment and process optimization phase was conducted to seamlessly produce reefs through a user-friendly and safe process.

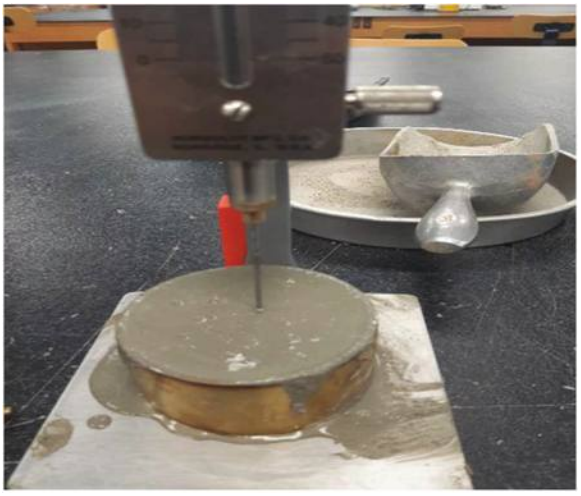

Fig. 6—Type M mortar initial setting test.

Material testing phase

Commercially available Type M mortar was used to conduct the experimental investigation to 3-D print reefs using the dry-forming process. The Type M mortar comprises four parts cement, one part lime, and 12 to 15 parts sand (by mass). The approximate compressive strength of Type M mortar mixtures ranges from 2500 to 3000 psi (17 to 21 MPa). In this research, Type M mortar was injected with water using a one-needle device. Several mortar specimens were tested according to ASTM C191 (2021) using moisture content ratios ranging from 0.19 to 0.24, as shown in Fig. 6.

The setting test results showed that the initial setting was not achieved after 1.0, 1.5, and 2.0 hours after concrete mixing. The lack of setting was validated by placing 2 x 2 in. (5 x 5 cm) cube specimens that collapsed upon stripping the mold, as shown in Fig. 7.

Based on the 2 x 2 in. (5 x 5 cm) cube results, larger specimens (3 x 6 in. [7 x 15 cm] cylinders) were used in placing additional specimens for setting time testing, as shown in Fig. 8.

Six cylinder specimens were placed with different accelerator content, as follows: a) three cylinders with 2% accelerator content (0.2 water-cement ratio [*w*/*c*]) at 90°F (32°C); and b) three cylinders with 4% accelerator content (0.2 *w*/*c*) at 90°F (32°C).

Cylinders were stripped after 1.5, 2.0, 2.5, and 3.0 hours of placing. The outcomes of cylinder stripping are shown in Table 2.

Fig. 7—Collapse of cube molds (setting time > 2 hours).

Table 2—Cylinder stripping results

Cylinder No.	Cylinder design	Test result	Notes
1	3 x 6 in., 2% accelerator, 90°F	Failed at mold strip after 1.5 hours of placing	2% chemicals are not adequate using Type M mortar only
2	3 x 6 in., 2% accelerator, 90°F	Failed at mold strip after 2.0 hours of placing	
3	3 x 6 in., 2% accelerator, 90°F	Failed at mold strip after 2.5 hours of placing	
4	3 x 6 in., 4% accelerator, 90°F	Failed at mold strip after 2.0 hours of placing	4% chemicals are not adequate at time less than 3 hours
5	3 x 6 in., 4% accelerator, 90°F	Partially failed at mold strip after 2.5 hours of placing	
6	3 x 6 in., 4% accelerator, 90°F	Succeeded at mold strip after 3.0 hours of placing	Strength of 100 psi attained

Note: 1 in. = 2.54 cm; °F = (°C × 1.8) + 32; 1 psi = 0.00689 MPa.

The outcome of cylinder setting time suggests that a 4% accelerator is recommended as a minimum dosage for chemicals at a *w*/*c* of 0.2 and 90°F (32°C). At this dosage, Type M mortar can sustain a total stress of 100 psi (0.689 MPa) after form removal when tested in compression, as shown in Fig. 9.

Full-scale case study

Random full-scale coral reefs are designed to be fabricated using Type M mortar and the dry-forming technique. A coral reef computer-aided design (CAD) simulation example is shown in Fig. 10.

Fig. 8—Cylinder molds for mortar setting time evaluation.

A dry bed with Type M mortar is conveyed to the printer location and placed below the printing needles. The printer's needles are controlled using the CAD-generated design and inserted into the dry bed to the required predetermined depth. Mixing water and chemicals are injected into the Type M dry mortar using the inserted needles. The needles are immediately retracted to avoid mortar hardening around the needles, as shown in Fig. 11. The produced 3-D-printed reefs are moved to shoreline locations and placed in position for erosion mitigation, as shown in Fig. 12.

RESULTS AND DISCUSSION

The outcome of this research project successfully produced 3-D-printed reefs using a novel reactive-diffusion morphological technique that injects an aqueous mixture (water and chemicals) through needles into a bin of dry mixture using a digitally controlled precise pumping system. The needles are robotically lifted so that each layer of the structure can be printed as the needle moves upward. Reacted materials are hardened to form a predesigned reef-shaped block, which is palletized and shipped to the designated location.

The developed technique is advantageous to current shoreline protection techniques due to the ability to 3-D print diverse shapes that are adapted for the local ecosystem and hydrodynamic environment. The ability to create internal voids that reduce weights and create interlocking at the same time allows for the reduction of materials while

Fig. 9—Mold stripping and compressive strength testing.

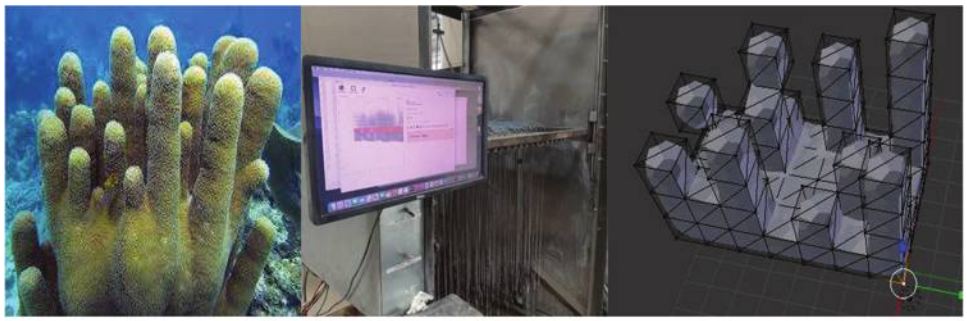

(a) (b) (c)

Fig. 10—(a) Pillar coral reefs; (b) CAD; and (c) CAD simulation of reefs.

creating hydrodynamical stable structures. This enables more cost-effective solutions for shoreline erosion mitigation that are also environmentally friendly.

RECOMMENDATIONS FOR FUTURE RESEARCH

The authors recommend the investigation of alkali-activated material (that is, geopolymers) use in the 3-D printing of concrete reefs using the developed dry-forming technique. The use of geopolymers will reduce cement consumption and result in an extensive reduction of the carbon footprint. In addition, some types of geopolymers are cost-effective, potentially reducing the final cost of shoreline protection projects.

AUTHOR BIOS

ACI member **Amin K. Akhnoukh** *is an Associate Professor at East Carolina University, Greenville, NC. He received his BS in civil engineering from Cairo University, Giza, Egypt; his MS in civil engineering from Kansas State University, Manhattan, KS; and his PhD in construction engineering from the University of Nebraska-Lincoln, Lincoln, NE. His research interests include the development of high-performance concrete mixtures and concrete construction using three-dimensional (3-D) printing additive manufacturing techniques.*

Mathew Campbell *is Co-Founder and President of Natrx, Inc. He received his BS and MS in biological engineering from Louisiana State University, Baton Rouge, LA, and his PhD in biological engineering from North Carolina State University, Raleigh, NC. He is also a licensed professional civil engineer with 20 years of experience. He invented and patented the "DryForming" process of creating concrete structures and industrialized the associated advanced manufacturing technology.*

Fig. 11—Dry bed water and chemical injection and diffusion through 3-D printer's needle.

ACKNOWLEDGMENTS

The authors would like to acknowledge the support and technical advice provided by North Carolina Department of Transportation personnel and the East Carolina University Coastal Studies Institute (CSI) in Outer Banks, NC. The authors would like to acknowledge the technical advice of R. Corbett, Dean of CSI.

REFERENCES

ASTM C191-21, 2021, "Standard Test Methods for Time of Setting of Hydraulic Cement by Vicat Needle," ASTM International, West Conshohocken, PA, 8 pp.

Barbier, E. B.; Koch, E. W.; Silliman, B. R.; Hacker, S. D.; Wolanski, E.; Primavera, J.; Granek, E. F.; Polasky, S.; Aswani, S.; Cramer, L. A.; Stoms, D. M.; Kennedy, C. J.; Bael, D.; Kappel, C. V.; Perillo, G. M. E.; and Reed, D. J., 2008, "Coastal Ecosystem-Based Management with Nonlinear Ecological Functions and Values," *Science*, V. 319, No. 5861, Jan., pp. 321-323. doi: 10.1126/science.1150349

Barragán, J. M., and de Andrés, M., 2015, "Analysis and Trends of the World's Coastal Cities and Agglomerations," *Ocean & Coastal Management*, V. 114, Sept., pp. 11-20. doi: 10.1016/j.ocecoaman.2015.06.004

Benik, S. R.; Biesboer, D. D.; Wilson, B. N.; and Hansen, B. J., 2000, "The Efficacy of Erosion Control Blankets and Soil Stabilizers," Final Report No. MN/RC - 2000-15, Minnesota Department of Transportation, St. Paul, MN, May, 135 pp.

Bozek, C. M., and Burdick, D. M., 2005, "Impacts of Seawalls on Saltmarsh Plant Communities in the Great Bay Estuary, New Hampshire USA," *Wetlands Ecology and Management*, V. 13, No. 5, Oct., pp. 553-568. doi: 10.1007/s11273-004-5543-z

Bujan, N.; Cox, R.; and Masselink, G., 2019, "From Fine Sand to Boulders: Examining the Relationship between Beach-Face Slope and Sediment Size," *Marine Geology*, V. 417, Nov., Article No. 106012. doi: 10.1016/j.margeo.2019.106012

Camelo, J.; Mayo, T. L.; and Gutmann, E. D., 2020, "Projected Climate Change Impacts on Hurricane Storm Surge Inundation in the Coastal United States," *Frontiers in Built Environment*, V. 6, Dec., Article No. 588049. doi: 10.3389/fbuil.2020.588049

Campbell, M. D.; Ortego, T. R.; Beine, R. L.; and Hall, S. G., 2018, Three-Dimensional Printing, US Patent No. 9,962,855 B2, filed Sept. 13, 2016, and issued May 8, 2018.

Church, J. A., and White, N. J., 2011, "Sea-Level Rise from the Late 19th to the Early 21st Century," *Surveys in Geophysics*, V. 32, No. 4-5, Sept., pp. 585-602. doi: 10.1007/s10712-011-9119-1

Douglass, S. L., and Pickel, B. H., 1999, "The Tide Doesn't Go Out Anymore – The Effect of Bulkheads on Urban Bay Shorelines," *Shore & Beach*, V. 67, No. 2-3, Apr./July, pp. 19-25.

Gittman, R. K.; Popowich, A. M.; Bruno, J. F.; and Peterson, C. H., 2014, "Marshes with and without Sills Protect Estuarine Shorelines from Erosion Better than Bulkheads during a Category 1 Hurricane," *Ocean & Coastal Management*, V. 102, Part A, Dec., pp. 94-102. doi: 10.1016/j.ocecoaman.2014.09.016

IPCC, 2019, "Special Report on the Ocean and Cryosphere in a Changing Climate," H.-O. Pörtner, D. C. Roberts, V. Masson-Delmotte, P. Zhai, M. Tignor, E. Poloczanska, K. Mintenbeck, A. Alegría, M. Nicolai, A. Okem, J. Petzold, B. Rama, and N. M. Weyer, eds., Intergovernmental Panel on Climate Change, Geneva, Switzerland, 755 pp.

Fig. 12—Examples of structures and techniques implemented by novel dry-forming technology: (a) pillar coral 3-D-printed structures; (b) porous coastal armoring units; and (c) living shoreline with oyster reefs fronting mangrove forest.

Liew, M.; Xiao, M.; Jones, B. M.; Farquharson, L. M.; and Romanovsky, V. E., 2020, "Prevention and Control Measures for Coastal Erosion in Northern High-Latitude Communities: A Systematic Review Based on Alaskan Case Study," *Environmental Research Letters*, V. 15, No. 9, Sept., Article No. 093002. doi: 10.1088/1748-9326/ab9387

Martyr-Koller, R.; Thomas, A.; Schleussner, C.-F.; Nauels, A.; and Lissner, T., 2021, "Loss and Damage Implications of Sea-Level Rise on Small Island Developing States," *Current Opinion in Environmental Sustainability*, V. 50, June, pp. 245-259. doi: 10.1016/j.cosust.2021.05.001

Miller, J. K.; Rella, A.; Williams, A.; and Sproule, E., 2016, "Living Shorelines Engineering Guidelines," Report No. SIT-DL-14-9-2942, New Jersey Department of Environmental Protection, Trenton, NJ, Feb., 102 pp.

Morton, R. A., 2003, "An Overview of Coastal Land Loss: With Emphasis on the Southeastern United States," USGS Open File Report No. 03-337, U.S. Geological Survey, Center for Coastal and Watershed Studies, St. Petersburg, FL, 29 pp.

National Research Council (NRC), 2007, "Mitigating Shore Erosion along Sheltered Coasts," National Academies Press, Washington, DC, 188 pp.

NOAA Habitat Blueprint, 2022, "Living Shorelines," National Oceanic and Atmospheric Administration, Washington, DC, https://www.habitatblueprint.noaa.gov/living-shorelines/. (last accessed Feb. 8, 2024)

Ozkan, C.; Mayo, T.; and Passeri, D. L., 2022, "The Potential of Wave Energy Conversion to Mitigate Coastal Erosion from Hurricanes," *Journal of Marine Science and Engineering*, V. 10, No. 2, Feb., Article No. 143. doi: 10.3390/jmse10020143

Passeri, D. L.; Hagen, S. C.; Medeiros, S. C.; Bilskie, M. V.; Alizad, K.; and Wang, D., 2015, "The Dynamic Effects of Sea Level Rise on Low-Gradient Coastal Landscapes: A Review," *Earth's Future*, V. 3, No. 6, June, pp. 159-181. doi: 10.1002/2015EF000298

Patrick, C. J.; Weller, D. E.; Li, X.; and Ryder, M., 2014, "Effects of Shoreline Alteration and Other Stressors on Submerged Aquatic Vegetation in Subestuaries of Chesapeake Bay and the Mid-Atlantic Coastal Bays," *Estuaries and Coasts*, V. 37, No. 6, Nov., pp. 1516-1531. doi: 10.1007/s12237-014-9768-7

Seitz, R. D.; Lipcius, R. N.; Olmstead, N. H.; Seebo, M. S.; and Lambert, D. M., 2006, "Influence of Shallow-Water Habitats and Shoreline Development on Abundance, Biomass, and Diversity of Benthic Prey and Predators in Chesapeake Bay," *Marine Ecology Progress Series*, V. 326, Nov., pp. 11-27. doi: 10.3354/meps326011

Senechal, N.; Coco, G.; Bryan, K. R.; and Holman, R. A., 2011, "Wave Runup during Extreme Storm Conditions," *Journal of Geophysical Research: Oceans*, V. 116, No. C7, July, Article No. C07032. doi: 10.1029/2010JC006819

Shepard, C. C.; Crain, C. M.; and Beck, M. W., 2011, "The Protective Role of Coastal Marshes: A Systematic Review and Meta-Analysis," *PLOS ONE*, V. 6, No. 11, Article No. e27374. doi: 10.1371/journal.pone.0027374

Shows, H., 2019, "Living Shorelines as Alternative Methods of Shoreline Protection," MS thesis, Louisiana State University, Baton Rouge, LA, 76 pp.

Smith, C. S.; Puckett, B.; Gittman, R. K.; and Peterson, C. H., 2018, "Living Shorelines Enhanced the Resilience of Saltmarshes to Hurricane Matthew (2016)," *Ecological Applications*, V. 28, No. 4, June, pp. 871-877. doi: 10.1002/eap.1722

Stoa, R. B., 2019, "The Coastline Paradox," *Rutgers University Law Review*, V. 72, No. 2, pp. 351-400.

Stockdon, H. F.; Holman, R. A.; Howd, P. A.; and Sallenger, A. H. Jr., 2006, "Empirical Parameterization of Setup, Swash, and Runup," *Coastal Engineering*, V. 53, No. 7, May, pp. 573-588. doi: 10.1016/j.coastaleng.2005.12.005

Tavares, K.-D.; Fletcher, C. H.; and Anderson, T. R., 2020, "Risk of Shoreline Hardening and Associated Beach Loss Peaks before Mid-Century: O'ahu, Hawai'i," *Scientific Reports*, V. 10, Article No. 13633. doi: 10.1038/s41598-020-70577-y

Thaler, E. A.; Kwang, J. S.; Quirk, B. J.; Quarrier, C. L.; and Larsen, I. J., 2022, "Rates of Historical Anthropogenic Soil Erosion in the Midwestern United States," *Earth's Future*, V. 10, No. 3, Mar., Article No. e2021EF002396. doi: 10.1029/2021EF002396

Weis, J. S.; Weis, P.; and Proctor, T., 1998, "The Extent of Benthic Impacts of CCA-Treated Wood Structures in Atlantic Coast Estuaries," *Archives of Environmental Contamination and Toxicology*, V. 34, No. 4, May, pp. 313-322. doi: 10.1007/s002449900324

ARE YOU A RESEARCHER?

SIGN UP FOR ORCID TODAY!

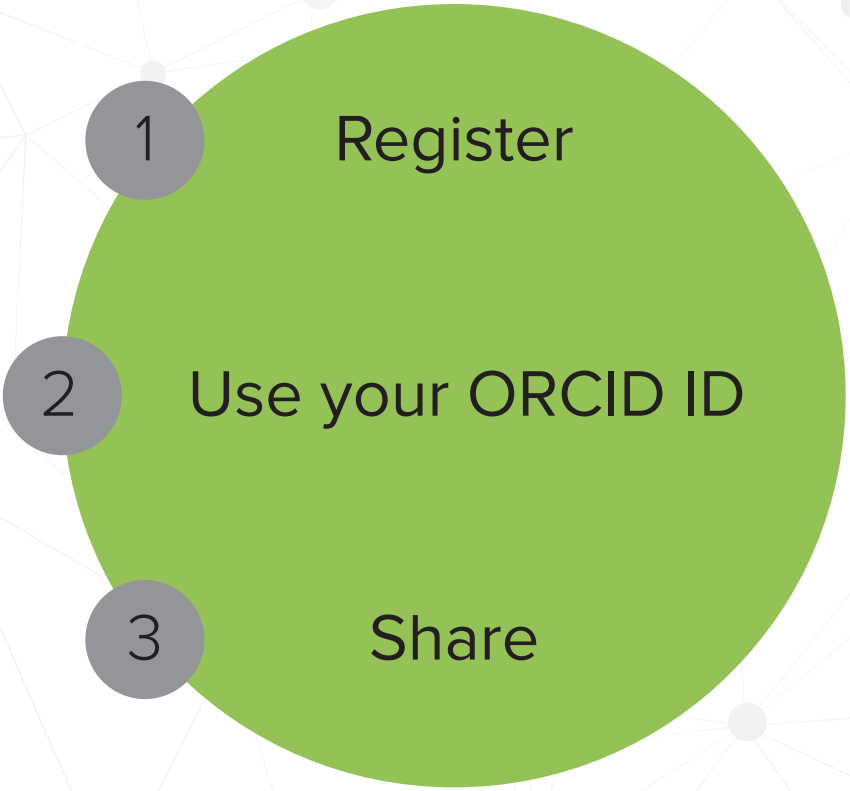

ORCID provides a digital identifier that distinguishes you from every other researcher and, through integration in key research workflows such as manuscript and grant submission, supports automated linkages between you and your professional activities, ensuring that your work is recognized.

ORCID services are FREE and it's as easy as **1-2-3**.

WWW.ORCID.ORG

ACI MATERIALS JOURNAL TECHNICAL PAPER

Title No. 121-M15

Fracture Behavior of Three-Dimensional-Printable Cementitious Mortars in Very Early Ages and Hardened States

by K. Sriram Kompella, Andrea Marcucci, Francesco Lo Monte, Marinella Levi, and Liberato Ferrara

The early-age material parameters of three-dimensional (3-D)-printable concrete defined under the umbrella of printability, namely, pumpability, extrudability, buildability, and the "printability window/open time," are subjective measures. The need to correlate and successively substitute these subjective measures with objective and accepted material properties, such as tensile strength, shear strength, and compressive strength, is paramount. This study validates new testing methodologies to quantify the tensile and shear strengths of printable fiber-reinforced concretes still in their fresh state. A tailored mixture with high sulfoaluminate cement and nonstructural basalt fibers has been assumed as a reference. The relation between the previously mentioned parameters and rheological parameters, such as yield strength obtained through International Center for Aggregates Research (ICAR) rheometer tests, is also explored. Furthermore, in an attempt to pave the way and contribute toward a better understanding of the mechanical properties of 3-D-printed concrete, to be further transferred into design procedures, a comparative study analyzing the work of fracture per unit crack width in three-point bending has been performed on printed and companion nominally identical monolithically cast specimens, investigating the effects of printing directions, position in the printed circuit, and specimen slenderness (length to depth) ratio.

Keywords: flexural strength and work of fracture; influence of layers; shear behavior; testing methods; three dimensional (3-D)-printable cementitious composites; very-early-age tensile constitutive behavior.

INTRODUCTION

Value-added labor productivity of the concrete construction industry has been lagging behind the rest of the manufacturing sectors for a long while. Upgrading the skill level of workers is crucial to increase the productivity of the industry worldwide, considering that the concrete industry is the most labor-intensive in the world.[1] Additive manufacturing of concrete provides a great solution to this problem while simultaneously addressing the challenges of lowering material use and cost of construction.[2-4] This makes the use of additive manufacturing in the concrete construction industry highly sought after. Among the available additive manufacturing concrete techniques, also widely referred to as three-dimensional (3-D) concrete printing, those based on concrete extrusion techniques have been the most intensively investigated to be further deployed for large-scale applications.[2,5-8]

Extrusion-based 3-D concrete printing allows the production of material-efficient structures with topologically optimized forms, without the need for formwork.[9] It employs a pump to transport a low-yield-strength material, which is placed by an extruder, depositing several layers to complete the structure. It also paves the way for technologies such as smart dynamic casting, which is a derivative of the layered extrusion process, as well as slipforming and self-consolidating concrete (SCC) technologies.[10] All these technologies are therefore dependent on the chemical hydration phenomenon of the controlled, structural buildup of concrete.[11-15]

Chronologically, extrusion-based 3-D concrete printing can be divided into three steps.[16] The first of these is to transport the low-yield-strength concrete through a mechanical pump. The ability to pump printable concrete is inherited from the self-consolidating technology of concrete construction and is known as "pumpability,"[17-19] and therefore has a set of rheological requirements.[20] This pumped concrete, for the purpose of deposition in layers, needs to be extruded through a nozzle and must retain the shape given to it by the nozzle. This ability of shape retention upon extrusion of concrete is called "extrudability."[21,22] This is correlated, on the one hand, to the evolution of rheological properties of the material, which allows the material to retain the extruded shape once laid. On the other hand, it is correlated to a rapid development of tensile and shear strength, which allow the filament to be continuously extruded without experiencing any breakage. Once deposited, the structural buildup allows the antecedent layers enough shear and normal strength to carry the weight of the latter deposited layers in the extrusion process. The study of the development of the strength of the layer is therefore of the utmost importance in understanding the printability of the mixture. This ability of printed concrete to withstand the weight of printing subsequent layers is loosely defined as "buildability."[23-26] The mechanics of pumping, extrusion, and layer-wise deposition of concrete therefore control the ability of any concrete mixture to be used for the extrusion-based 3-D concrete printing process, which can be defined under the umbrella term "printability." However, as can be seen from the definitions of those collated from various sources by Mohan et al.,[27] the parameters of pumpability, extrudability, buildability,

ACI Materials Journal, V. 121, No. 2, March 2024.

MS No. M-2022-286.R4, doi: 10.14359/51740302, received June 22, 2023, and reviewed under Institute publication policies.

and open time are very nebulous and qualitative. There is a need to translate these qualitative definitions into quantitative material characteristics to ease the industrial application of printable concrete technology. In summary, the pumpability of concrete depends on the rheological yield strength of the mixture, the extrudability of concrete depends on the early-age normal (both tensile and compressive) strengths of the mixture, and the buildability of concrete depends on the early-age shear and compressive strengths of the mixture.

These characteristics that govern the use of a mixture must also be compatible with the available robotics to ensure quality of printing. For example, the characteristics of the pumping equipment, including the pressure of pumping and the dimensions of the pump walls, must be compatible with the mixture being pumped to ensure there is no segregation during the pumping of concrete. The dimensions and shape of the nozzle, through which the concrete is extruded, need to be compatible with the concrete mixture to ensure that smooth and continuous filaments of the mixture are extruded. The rate of layer deposition must be coherent with the mixture to ensure sufficient interlayer bond in the elements printed. The printability of any mixture is also limited to a window of operation, as the structuration of concrete is a time-dependent process. This window of printability (also called open time) also limits the construction process, and its identification is of the utmost importance for the proper planning and handling of the overall printing process, from material concept and production to the selection of the equipment to its implementation into a "site-factory" practice.

From the aforementioned perspective, it is also of the utmost importance to understand the influence of these fabrication features on the mechanical performance of the material in the hardened state, which translates into structural performance. The literature shows that the maximum of these effects in the hardened state stems from the effect of interfaces between layers.[28-35] Some are also a direct effect of the anisotropy induced by the filament with extrusion direction.[29]

Moreover, the layer deposition process may induce a higher compression into the bottom layers than the top, owing to self-weight, while the material stiffness has not developed highly enough to make them able to withstand the stress without any significant deformation. This causes them to flatten more than the top layers, further resulting in varying section shapes and widths through the depth of the printed section, which needs to be incorporated into the design but through an appropriate evaluation of the section modulus. Moreover, because concrete specimens cast vertically tend to hydrate under varying pore pressure, combined with the fact that the rate of hydration of fast-setting cements is comparatively higher, a significant difference in the quantum and quality of hydration at the top and bottom of a vertically cast concrete element can arise. This is yet another challenge the 3-D-printing technology inherits from the slip-forming technology, whose effects on the overall mechanical and structural performance of printed materials and elements has to be appropriately evaluated to be coherently reflected into appropriate design algorithms and approaches.[14,36-38]

According to Menna et al.,[4] any new concrete technology faces four kinds of constraints before its widespread applicability and deployment—namely, fabrication, material, construction, and design constraints. In the case of 3-D concrete printing, the fabrication constraints include equipment and robotic technology required for layered extrusion. The material constraints include the development of printable concrete. The construction constraints include the challenge of compatible reinforcement, batching, and mixing procedures; printing of the material itself; time constraints of the open time and interlayer speed; and so on. The design constraints include the challenge of designing elements with anisotropic in-structure material properties, varying section moduli with depth, higher factors of safety associated with defects of construction, and the durability of printed elements. Unlike conventional reinforced concrete, printable concretes require attention to design in both the fresh and hardened states. The design requires testing methodologies that can give quantitative parameters and models developed based on these parameters. This paper aims to contribute to the material and construction constraints by validating a testing methodology, which enables the assessment of the fracture properties of a 3-D-printable mixture at its fresh/very early age, whose values could be translated into a quantitative assessment of the extrudability requirement. On the other hand, the tests done on the hardened-state printed elements aim to contribute to answering the design constraints through the assessment of the anisotropy and "position-dependence" of mechanical material properties. This will also be attempted through the definition of a suitable indicator of the performance, identified in the work of fracture per unit crack width, which, at the same time, could overcome some of the aforesaid limits and appropriately take into account the peculiarities of 3-D-printed concrete specimens as opposed to conventionally cast ones.

RESEARCH SIGNIFICANCE

As explained earlier, the qualitatively defined requirements of extrudability, pumpability, and buildability of a 3-D-printable/printed concrete mixture need to be associated to quantitatively identifiable material parameters. This study, extending to a 3-D-printable mixture the methodology also employed earlier by Mettler et al.[14] with reference to fresh SCC, aims at validating the use of direct tension and shear tests at very early ages (less than 2 hours from the contact of binder and water) as potentially valid to quantify the extrudability requirement and identify the open time through the identification of a fluid-to-solid state transition. Given the highly sophisticated nature of the printing process and its printer-dependent variability, it is necessary to develop performance-based tests at very early ages, which could then be transferred into appropriate standardization procedures. It should be noted that there are presently no standards for testing printable cementitious composites at very early ages. Moreover, to thoroughly validate the proposed mixture design and printing technology to address the needs of a design-oriented testing procedure for hardened-state properties, a comparative study of hardened-state mechanical properties was performed. The study is defined by the

work of fracture per unit crack width in three-point loading of specimens of varying sizes, layer orientations, and with varying effects of early-age consolidation.

MATERIALS AND EXPERIMENTAL PROCEDURE

Mixture details and protocol

A printable mixture was designed with a high proportion of calcium sulfoaluminates (CSA) along with a high volume of cement aimed at fast setting time and rapid strength gain. The fibers used in the cementitious mortar were nonstructural basalt fibers, added to improve the cohesion of the mixture in the fresh state to ensure printability. The composition and characteristics of the mixture are summarized in Table 1. The dry components of the mixture were first mixed at 120 rpm for 60 seconds before the addition of water and high-range water-reducing admixture (HRWRA). Next, the wet mixture was mixed for a further 3 minutes to ensure a degree of homogeneity. Then, nonstructural basalt fibers were added and the mixing was further resumed for 2 minutes to ensure their adequate dispersion.

Tensile and shear tests

Shear and tensile tests were performed on early-age samples of the employed mixture using specially designed molds, depicted in Fig. 1. The molds were made of transparent poly(methyl methacrylate) and consisted of both a fixed and movable half that slide across/away from each other. Fresh mixture was placed into the molds at the start of the very end of the mixing process and allowed to settle until the time at which the test was carried out. The molds were mounted on a table (as shown in Fig. 1) using screws, and the movable halves were pushed/pulled using a smart motor connected to a load cell of 600 N (135 lbf) capacity. Linear variable differential transformers (LVDTs) were connected to the movable halves to record the displacement, as also shown in Fig. 1. The tensile tests were performed at a constant displacement rate of 0.05 mm/s (≅0.002 in./s), while the shear tests were performed at a displacement rate of 0.1 mm/s (≅0.004 in./s). At least three tests each for shear and tension were performed at 30, 60, and 90 minutes from the end of mixing.

Rheometer tests

Twenty liters of the fresh mixture was placed into an International Center for Aggregates Research (ICAR) rheometer (a vane shear rheometer) immediately after mixing stopped. The minimum torque required to move the vane at 0.025 rps inside the rheometer filled with the mixture was calculated at different times as part of the grow tests. These recorded values of the torque are used to calculate the yield strength of the material using an analytical relation characteristic of the ICAR rheometer.

Three-point bending tests with printed and cast specimens

The fresh mixture was pumped into a robotic arm. The robotic arm had three directional degrees of freedom and a circular nozzle with a diameter of 25 mm (1 in.). Rectangular prismatic specimens were extruded at 50 mm/min up to a height of 450 mm (17.7 in.) and lengths of 200 cm (79 in.). Specimens of five different dimensions, shown in Table 2, were cut from these larger specimens, some with layer orientations along the length of the specimen and some with layer orientations along the depth of the specimen.

The fresh mixture was also cast into steel molds with dimensions of 750 x 750 x 60 mm (29.5 x 29.5 x 2.4 in.) up to an intended depth of 30 mm (1.2 in.). The hardened mixture was then cut into specimens of five different lengths and effective depths, as shown in Table 2.

At least three nominally identical specimens were cut for each dimension in the hardened state to ensure repeatability of the test. The specimens were also notched to a depth of 10 mm (0.4 in.) to localize the cracking. The specimens were then fitted with clips on either side of the notch at a distance of 5 mm (0.2 in.). A clip gauge of 3 mm (0.12 in.) range was fitted, which was connected to an electromechanical universal testing machine, as shown in the setup in Fig. 2. These specimens were thus tested in three-point bending under displacement control (crack-width control) at a rate of 0.015 mm/s (0.0006 in./s), and the load required was measured against the crack opening displacement (COD) until failure for each specimen.

Table 1—Mixture details

Components	Details	Description	Quantity
Fine aggregate	Silica sand	Maximum size of 0.5 mm	540 kg/m^3
	Ground recycled glass	Maximum size of 0.9 mm	440 kg/m^3
	Glass quartz fine compound	Maximum size of 0.45 μm	190 kg/m^3
Binder	White cement	CEM I – 52.5R	920 kg/m^3
	Calcium sulfoaluminate cement	CSA	80 kg/m^3
Water	Tap water	—	295 L/m^3
HRWRA	PCE	—	28 kg/m^3
Viscosity modifiers	Bentonite and cellulose ether	—	7 kg/m^3
Fibers	Basalt	16 mm (0.63 in.) length, 13 μm diameter, 2800 MPa (406.1 ksi) tensile strength, and 84 GPa (12,183 ksi) elastic modulus	20 kg/m^3 (0.7% V/V)

Note: 1 kg/m^3 = 0.06 lb/ft^3.

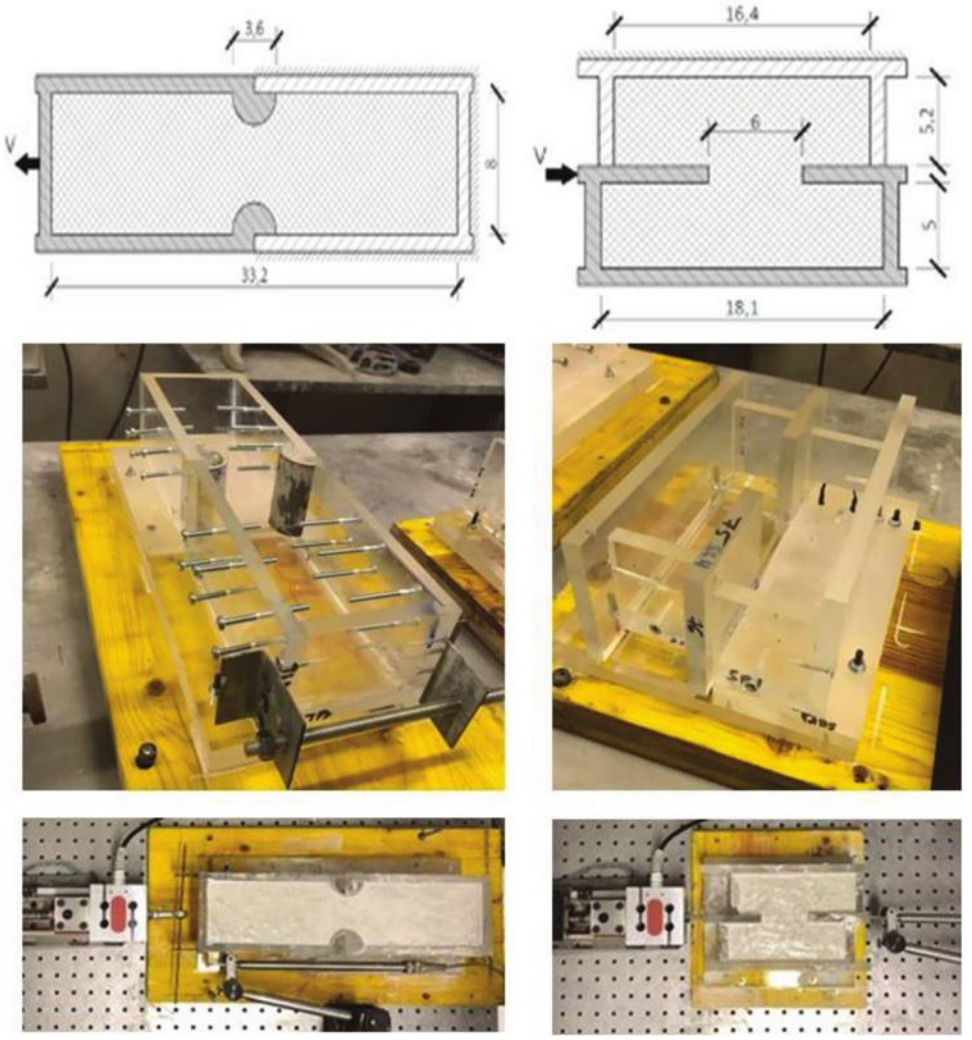

Fig. 1—Tensile (left) and shear (right) molds and test setup. (Note: Dimensions in cm; 1 cm = 0.39 in.)

DATA ANALYSIS PROCEDURE

Tensile and shear tests

As can be seen in Fig. 3, the failure patterns in tensile and shear tests are localized by means of stress concentration through a reduction in the cross-sectional area of the failure section. In the case of the tensile test, a kink was introduced in the center to induce higher stresses in the center of the specimen. In the shear test, a shear strut was induced at the interface of the two mold halves, localizing failure. However, a non-negligible frictional force acts on the specimen during the testing as the movable half of the mold slides away or across the fixed half. This frictional force was measured by calculating the force required to move the molds away/across the other half while carrying the equivalent and disconnected weight of the cementitious mixture placed in them during testing.

The load (P) in kN obtained through the load cell, after the subtraction of the frictional force, divided by this predetermined cross-sectional area of the failure section (either $A_{tension}$ or A_{shear}) in mm^2, gives the tensile (σ) and shear stresses (τ) in kPa at the location of failure. The stress (kPa) versus displacement (mm) for all the tested specimens is plotted, and the area under the curves is calculated as the energy release index per unit displacement (J) in kPa·mm/

Table 2—Experimental design of three-point bending tests on cast and printed specimens

Specimen No.	L/D	Effective length, mm	Specimen location	Layer orientation	Cast/Printed
1	2	160	Top	Perpendicular	Printed
2	3	200	Top	Perpendicular	Printed
3	3	300	Bottom	Perpendicular	Printed
4	4	320	Top	Perpendicular	Printed
5	4	320	Bottom	Perpendicular	Printed
6	4	180	—	Parallel	Printed
7	5	200	Top	Perpendicular	Printed
8	2	160	—	—	Cast
9	3	200	—	—	Cast
10	4	200	—	—	Cast
11	4	280	—	—	Cast
12	5	300	—	—	Cast

Note: 25.4 mm = 1 in.

mm. This energy release index per unit displacement is considered a more representative quantitative indicator than the peak stress values, as the mode of failure of the specimens in the tests varies with time. This means that the peak stress measured in these tests might not be the representative shear strength of the material, but would well represent the failure condition of a layer-wise additively manufactured element in the fresh state.

Three-point bending tests

The load (P) in kN, obtained through the load cell of the employed universal testing machine, is plotted against the crack width (COD) controlled by the clip gauge. The area under the load versus displacement curve is calculated as the work of fracture (kN·mm). The work of fracture per unit width of crack opening (kN·mm/mm) of each specimen is measured as an index of its mechanical performance. It is worth remarking that the calculations of the stresses in the specimens, and subsequently the strengths, require the considerations of Euler-Bernoulli beam-bending theories, which might not be easily applicable considering the layered structure of the printed specimens, and would otherwise be too significantly case-dependent. The nominal stresses calculated will also be affected by the consolidation of the bottom layers compared to the top layers in the calculation of the second moment of area. To study the effects in a more pronounced way, the area under the work of fracture per unit crack width calculated from the load versus crack-opening curve is considered more representative.

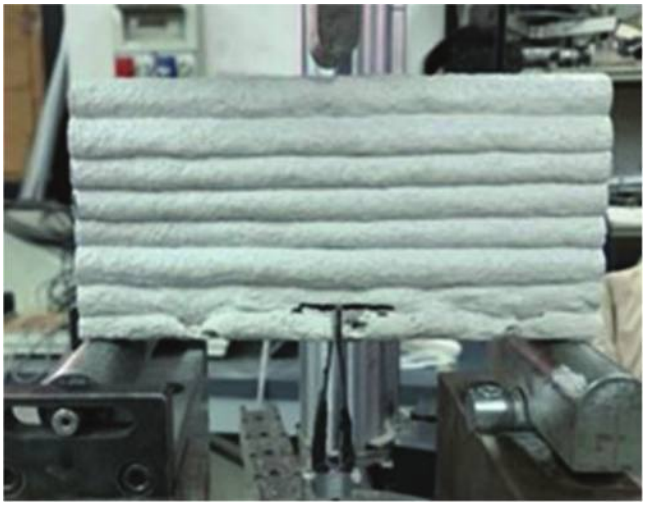

Fig. 2—3-D-printed specimen being tested in three-point bending under crack-width control.

EXPERIMENTAL RESULTS AND DISCUSSION

Tensile and shear tests

The average tensile stress values versus the displacement of the movable half of the mold for different times are plotted in Fig. 4. The same has been done for the shear stresses, as can be seen in Fig. 5. As is evident from the two graphs, the mixture is clearly still in its fluid state at 30 minutes. The fluidity can also be observed from the negative recorded stress values, indicating buoyancy of the material against the mold halves. At 60 minutes, the material still has a plastic fluid behavior, as is evident from the shear stress versus displacement graph. At 90 minutes, the material starts behaving as a hardened solid, with curves highlighting the development of the resistance of a compression strut, which can also be observed in the failure patterns, with significantly higher strengths and brittleness than at 30 and 60 minutes.

The maximum shear and tensile stresses in the specimens before failure are identified as the shear and tensile strength of the specimens, respectively. The peak stresses might not necessarily imply strength, as strength also necessitates a mode of failure that is either pure shear or pure tension. The peak shear and tensile stress evolution with time is plotted, as shown in Fig. 6. As discussed previously and is evident from the figure, the peak shear stress of the mixture increases significantly between 60 and 90 minutes, indicating a phase transition. While there is an initial setting happening at 60 minutes, the true strength gain is observed from the results of tests performed 90 minutes after the start of mixing. This is also corroborated by the energy released during fracture per unit displacement, as can be seen in Fig. 7.

Fig. 3—Typical failure patterns in tensile and shear tests.

ICAR rheometer tests

The results discussed previously for the very-early-age tension and shear tests were confirmed by the shear grow tests performed on the ICAR rheometer, whose results in Table 3 highlight that the yield strength increased almost by an order of magnitude between 45 and 90 minutes, the time when, in mechanical tests, a "solid-like" behavior of the material and specimens started being observed.

Three-point bending tests

The work of fracture per unit crack width for printed and cast elements of different sizes is shown in Fig. 8. As can be seen, the work of fracture per unit crack width follows the same pattern for printed and cast elements. It is higher for deeper specimens with low effective length to effective depth ratios (slenderness ratios). This is indicative of higher brittleness and a difference in the mode of failure compared to the ones with a higher slenderness. A closer observation

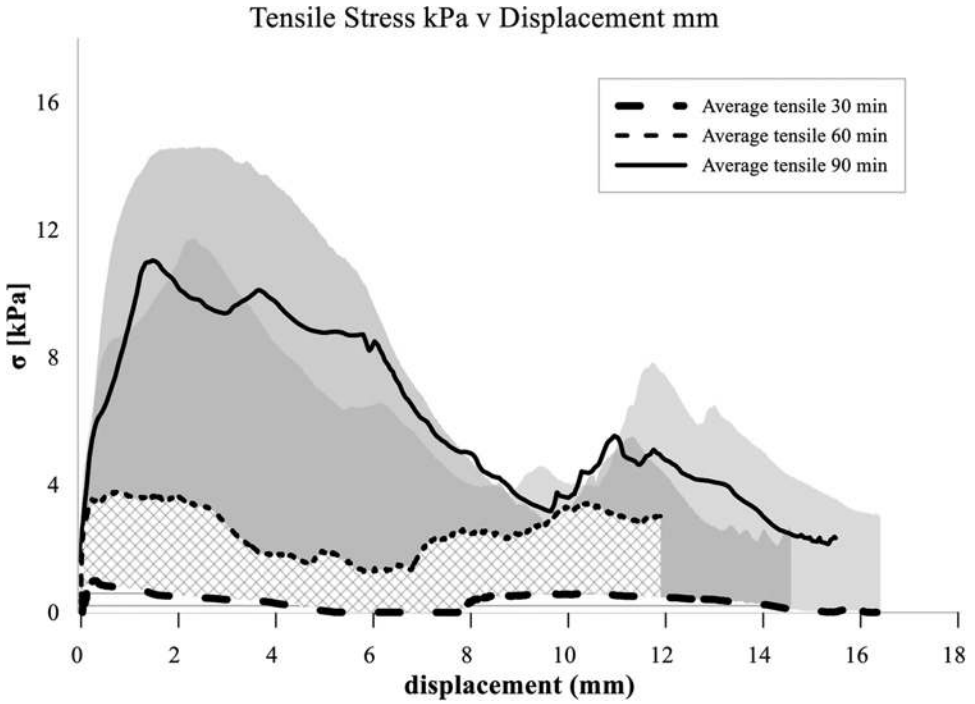

Fig. 4—Average tensile stress (kPa) versus displacement (mm) curves at different times. (Note: 1 kPa = 0.145 psi; 1 mm = 0.04 in.)

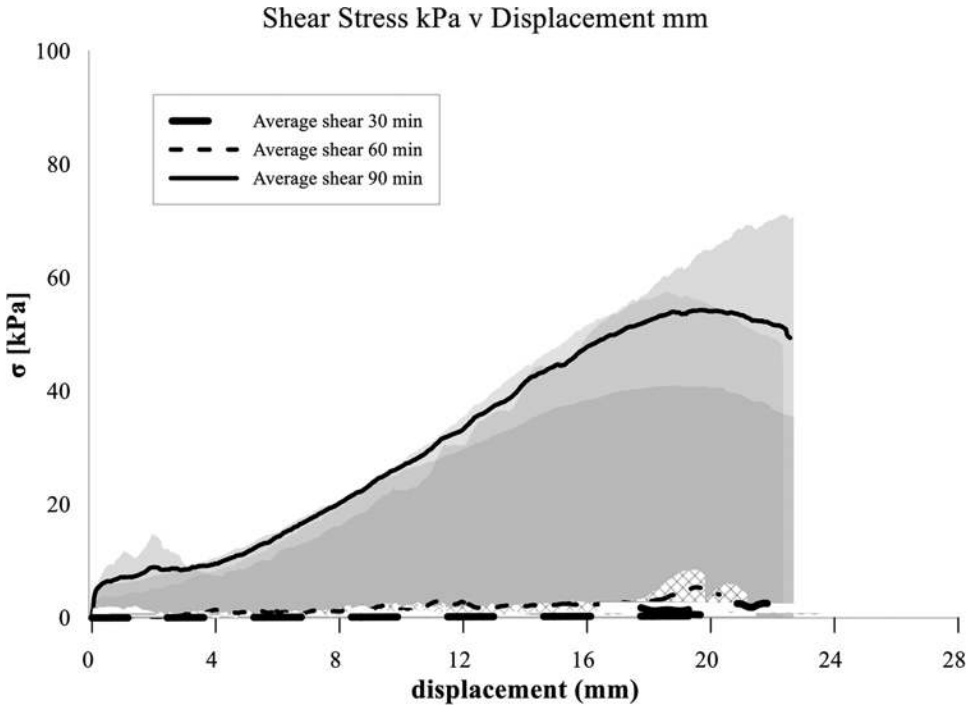

Fig. 5—Average shear stress (kPa) versus displacement (mm) curves at different times.

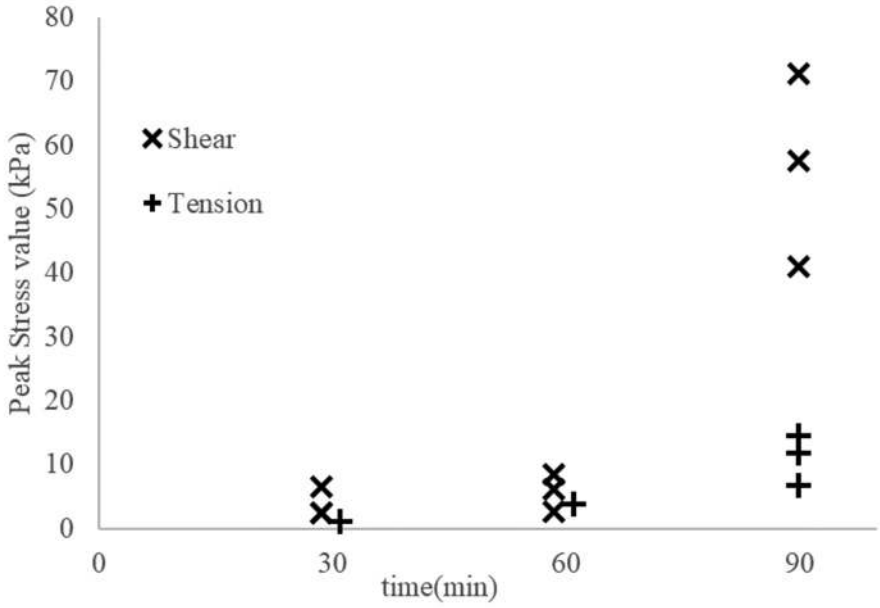

Fig. 6—Peak tensile and shear stress variation with time (minutes).

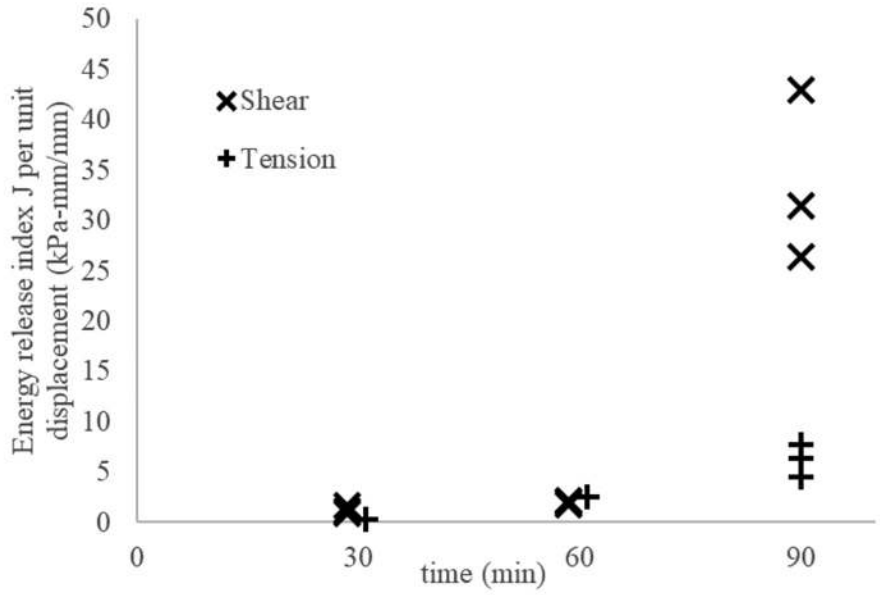

Fig. 7—Energy release index per unit displacement variation with time (minutes) for shear and tensile tests.

Table 3—Grow test yield strength at different times

Grow test, minutes	Yield strength, Pa	Peak torque, N·m
20	633.1	272
30	617	265
45	641.2	275
90	5249.3	2252

Note: 1 Pa = 0.000145 psi; 1 N·m = 0.74 lbf·ft.

indicates a higher scatter among the printed elements with low slenderness (l/d = 2) than the same specimens that are cast. The arch mechanism of load distribution in three-point bending of deep elements amplified by the orthotropic nature of layered printed elements could be a reason for this scatter in the results.

With reference to printed elements, it can be further observed that the elements with layer orientations parallel to the loading direction perform much poorer than those with layer orientations orthogonal to the loading direction.

A typical crack pattern in a monolithically cast specimen in three-point bending is depicted in Fig. 9. Figure 10 indicates the crack patterns in printed elements that are slender and deep with layer orientations perpendicular to the loading direction, while Fig. 11 depicts the typical crack patterns in printed elements with layer orientations parallel to the

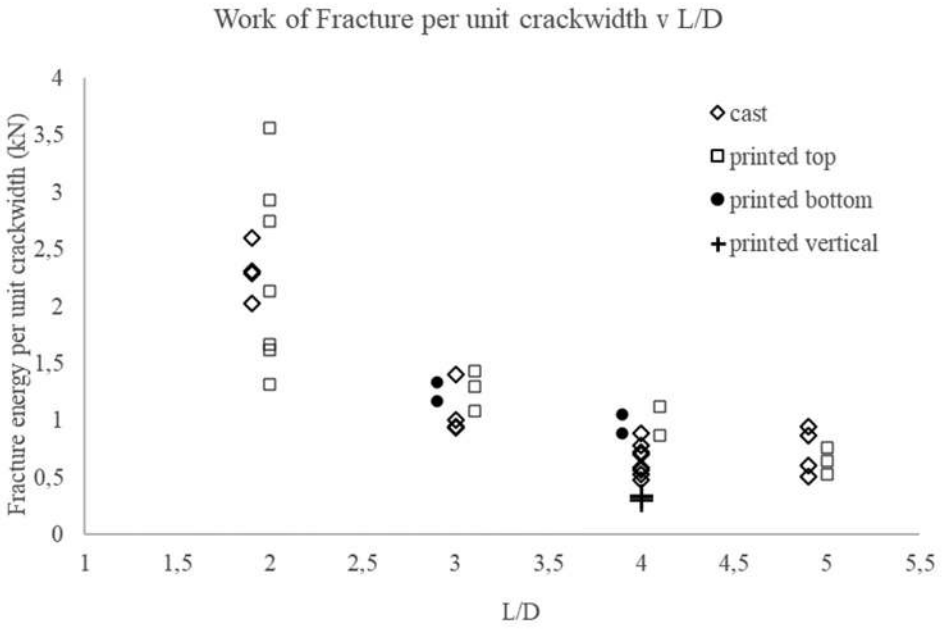

Fig. 8—Work of fracture per unit crack width (kN) at different sizes, comparison of monolithically cast and printed elements.

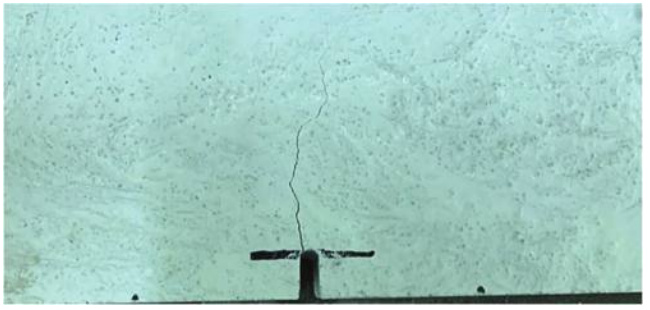

Fig. 9—Crack pattern in three-point bending in monolithically cast specimen.

loading direction. It can be noticed from the crack patterns that while there may be some refractive effects, the crack does not travel along the layer interface. This effect can be clearly noted in the case of elements tested with layer orientations parallel to the loading.

CONCLUSIONS

1. The testing procedure to identify the tensile and shear strengths at early ages provided information very relevant to mechanical properties, which could be correlated to extrudability as well as to the identification of the open time.

2. The average peak tensile and shear stress manifested a sudden increase between 60 and 90 minutes; this, implying a transition between fluid and granular behavior of the mixture, was corroborated by the measured increase in yield stress and the shape of the stress versus displacement curves and stands as an element of reliability of the tests to the purpose previously stated.

3. The aforementioned findings are also confirmed by the values of the average energy release indexes per unit displacement in tensile and shear tests. This energy, calculated from the tensile/shear stress versus displacement curves, is also a reliable indicator of material performance at very early ages and fluid-to-solid transition states, where "peak" stresses can be difficult to identify and hardly be associated with the concept of strength, which commonly holds for solid materials.

4. In the hardened state, the nominal flexural strength of specimens is not considered a representative quantitative parameter owing to the varying cross sections and dimensions. Instead, the work of fracture per unit crack width was defined and calculated. This energy parameter proved to be reliable in identifying the differences, if any, between printed and cast specimens, as well as, among printed specimens, those due to the local position of the specimens in a larger printed sample (in both cases, for the present study, the aforesaid differences were quite low).

5. The similarity of the flexural performance of monolithically cast and printed elements of different slenderness ratios indicates that the printing process executed with the given mixture yields a good bonding between layers. This can also be observed by the fact that there is no delamination of layers, as can be seen from the crack path. This successful execution of the printing was possible because of the study of the quantitative material properties of the mixture in the fresh state, thereby allowing the design of the printing parameters, such as the layer interval, open time, and the element depths.

6. The specimens tested with layer orientations parallel to the load had a very low average work of fracture per unit crack width at 0.32 MPa, as opposed to the 0.98 MPa of the specimens tested with layer orientations orthogonal to the load. This indicates a very high degree of orthogonal anisotropy in printed elements. This orthotropy is crucial for the design of printed concrete structures, especially considering the complex spatial design of topologically optimized structures. In considerations of funicular and no-tension struc-

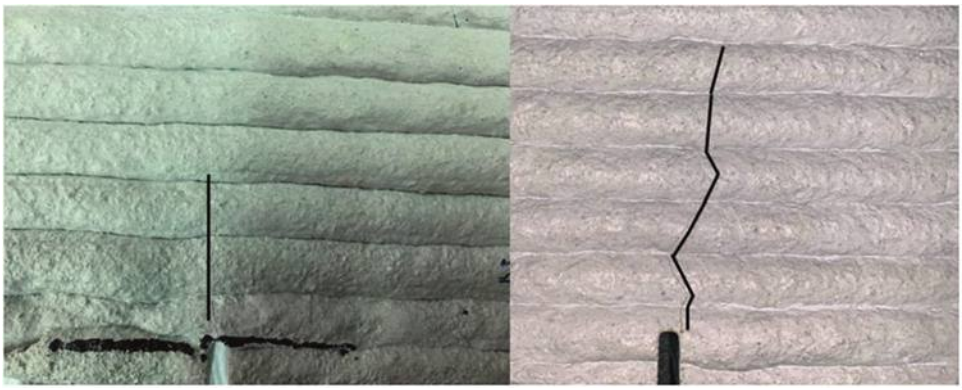

Fig. 10—Crack pattern in three-point bending in: (left) slender printed specimen; and (right) deeper printed specimen with layer orientations perpendicular to loading.

Fig. 11—Crack pattern in three-point bending in printed specimen with layer orientations parallel to loading.

tures, the print path also needs to be optimized to account for the orthotropy.

AUTHOR BIOS

ACI member **K. Sriram Kompella** *is a PhD Student in structural, seismic, and geotechnical engineering in the Department of Civil and Environmental Engineering at Politecnico di Milano, Milan, Italy. He is a member of ACI Committee 564, 3-D Printing with Cementitious Materials. His research interests include the structural performance and durability of printed concrete structures and the design of printed concrete.*

ACI member **Andrea Marcucci** *is a PhD Student in structural, seismic, and geotechnical engineering in the Department of Civil and Environmental Engineering at Politecnico di Milano. He is a member of ACI Committee 564, 3-D Printing with Cementitious Materials. His research interests include material and structural design for three-dimensional (3-D) concrete printing applications and nondestructive assessment of 3-D-printed concrete structures.*

Francesco Lo Monte *has been an Assistant Professor at Politecnico di Milano since 2018. He has been involved in different joint research projects with several international institutions, such as the Centre Scientifique et Technique du Bâtiment (CSTB), Paris, France; the Paul Scherrer Institute (PSI), Villigen, Switzerland; and the Swiss Federal Laboratories for Materials Science and Technology (Empa), Dübendorf, Switzerland. His research interests include high-/ultra-high-performance concrete mechanics, structural analysis (in ordinary, fire, or seismic conditions), and the development of new testing setups.*

Marinella Levi *is a Professor in the Department of Chemistry, Materials and Chemical Engineering "Giulio Natta" at Politecnico di Milano, and founded the Laboratory of Chemistry and Characterization of Innovative Polymeric Systems in that department. Her research interests include the design and characterization of hybrid polymeric micro- and nanocomposites and materials and technologies for Industry 4.0.*

Liberato Ferrara *is an Associate Professor of structural analysis and design and holds the Italian National qualification to be a full professor. He was a Fulbright Visiting Scholar at the Center for Advanced Cement-Based Materials, Northwestern University, Evanston, IL, and a Visiting Professor at Beijing Jiaotong University, Beijing, China. He is past Chair of ACI Committee 544, Fiber Reinforced Concrete, and a member of ACI Committees 130, Sustainability of Concrete; 237, Self-Consolidating Concrete; 238, Workability of Fresh Concrete; 239, Ultra-High-Performance Concrete; 241, Nanotechnology of Concrete; and 564, 3-D Printing with Cementitious Materials. He received the ACI Delmar L. Bloem Distinguished Service Award in 2021. His research interests include the material concept, experimental characterization, modeling and structural applications of advanced cement-based materials, with a special focus on durability, sustainability, and advanced manufacturing technologies, including 3-D printing and the use of artificial intelligence (AI) algorithms in civil engineering applications.*

ACKNOWLEDGMENTS

The second author acknowledges the support of the Italian national program PON Ricerca e Innovazione in funding his PhD scholarship. The authors also thank S. Guanziroli, Co-Founder and CEO of HINFRA Ltd., Milan, Italy, a company that focuses on the repair and retrofitting of tunnel structures using additive manufacturing techniques; and A. Bassani, IDeCOM Ltd., Erba, Italy, for providing the mixture design and raw materials and for their help in the 3-D concrete printing. The kind collaboration of the technicians of the Testing Laboratory for Materials, Buildings and Civil Structures, Politecnico di Milano, in the implementation of the experimental setup is also acknowledged.

REFERENCES

1. Dixit, S.; Mandal, S. N.; Sawhney, A.; and Singh, S., "Relationship between Skill Development and Productivity in Construction Sector: A Literature Review," *International Journal of Civil Engineering and Technology (IJCIET)*, V. 8, No. 8, 2017, pp. 649-665.

2. Bos, F.; Wolfs, R.; Ahmed, Z.; and Salet, T., "Additive Manufacturing of Concrete in Construction: Potentials and Challenges of 3D Concrete Printing," *Virtual and Physical Prototyping*, V. 11, No. 3, 2016, pp. 209-225. doi: 10.1080/17452759.2016.1209867

3. Bos, F. P.; Menna, C.; Pradena, M.; Kreiger, E.; Leal da Silva, W. R.; Rehman, A. U.; Weger, D.; Wolfs, R. J. M.; Zhang, Y.; Ferrara, L.; and Mechtcherine, V., "The Realities of Additively Manufactured Concrete Structures in Practice," *Cement and Concrete Research*, V. 156, 2022, Article No. 106746.

4. Menna, C.; Mata-Falcón, J.; Bos, F. P.; Vantyghem, G.; Ferrara, L.; Asprone, D.; Salet, T.; and Kaufmann, W., "Opportunities and Challenges for Structural Engineering of Digitally Fabricated Concrete," *Cement and Concrete Research*, V. 133, 2020, Article No. 106079.

5. Buswell, R. A.; Leal de Silva, W. R.; Jones, S. Z.; and Dirrenberger, J., "3D Printing Using Concrete Extrusion: A Roadmap for Research," *Cement and Concrete Research*, V. 112, 2018, pp. 37-49. doi: 10.1016/j.cemconres.2018.05.006

6. Wangler, T.; Lloret, E.; Reiter, L.; Hack, N.; Gramazio, F.; Kohler, M.; Bernhard, M.; Dillenburger, B.; Buchli, J.; Roussel, N.; and Flatt, R., "Digital Concrete: Opportunities and Challenges," *RILEM Technical Letters*, V. 1, 2016, pp. 67-75. doi: 10.21809/rilemtechlett.2016.16

7. Esposito Corcione, C.; Palumbo, E.; Masciullo, A.; Montagna, F.; and Torricelli, M. C., "Fused Deposition Modeling (FDM): An Innovative Technique Aimed at Reusing Lecce Stone Waste for Industrial Design and Building Applications," *Construction and Building Materials*, V. 158, 2018, pp. 276-284. doi: 10.1016/j.conbuildmat.2017.10.011

8. Lim, S.; Buswell, R. A.; Le, T. T.; Austin, S. A.; Gibb, A. G. F.; and Thorpe, T., "Developments in Construction-Scale Additive Manufacturing Processes," *Automation in Construction*, V. 21, 2012, pp. 262-268. doi: 10.1016/j.autcon.2011.06.010

9. Vantyghem, G.; De Corte, W.; Shakour, E.; and Amir, O., "3D Printing of a Post-Tensioned Concrete Girder Designed by Topology Optimization," *Automation in Construction*, V. 112, 2020, Article No. 103084.

10. Wangler, T.; Roussel, N.; Bos, F. P.; Salet, T. A. M.; and Flatt, R. J., "Digital Concrete: A Review," *Cement and Concrete Research*, V. 123, 2019, Article No. 105780.

11. Reiter, L.; Wangler, T.; Anton, A.; and Flatt, R. J., "Setting on Demand for Digital Concrete – Principles, Measurements, Chemistry, Validation," *Cement and Concrete Research*, V. 132, 2020, Article No. 106047.

12. Wolfs, R. J. M.; Bos, F. P.; and Salet, T. A. M., "Early Age Mechanical Behaviour of 3D Printed Concrete: Numerical Modelling and Experimental Testing," *Cement and Concrete Research*, V. 106, 2018, pp. 103-116. doi: 10.1016/j.cemconres.2018.02.001

13. Perrot, A.; Rangeard, D.; and Pierre, A. "Structural Built-Up of Cement-Based Materials Used for 3D-Printing Extrusion Techniques," *Materials and Structures*, V. 49, No. 4, 2016, pp. 1213-1220.

14. Mettler, L. K.; Wittel, F. K.; Flatt, R. J.; and Herrmann, H. J., "Evolution of Strength and Failure of SCC during Early Hydration," *Cement and Concrete Research*, V. 89, 2016, pp. 288-296. doi: 10.1016/j.cemconres.2016.09.004

15. Reiter, L.; Wangler, T.; Roussel, N.; and Flatt, R. J., "The Role of Early Age Structural Build-Up in Digital Fabrication With Concrete," *Cement and Concrete Research*, V. 112, 2018, pp. 86-95. doi: 10.1016/j.cemconres.2018.05.011

16. Mechtcherine, V.; Bos, F. P.; Perrot, A.; Leal da Silva, W. R.; Nerella, V. N.; Fataei, S.; Wolfs, R. J. M.; Sanebi, M.; and Roussel, N., "Extrusion-Based Additive Manufacturing with Cement-Based Materials – Production Steps, Processes, and Their Underlying Physics: A Review," *Cement and Concrete Research*, V. 132, 2020, Article No. 106037.

17. Río, O.; Rodríguez, A.; Nabulsi, S.; and Álvarez, M., "Pumping Quality Control Method Based on Online Concrete Pumping Assessment," *ACI Materials Journal*, V. 108, No. 4, July-Aug. 2011, pp. 423-431.

18. Kwon, S. H.; Jang, K. P.; Kim, J. H.; and Shah, S. P., "State of the Art on Prediction of Concrete Pumping," *International Journal of Concrete Structures and Materials*, V. 10, No. 3, 2016, pp. 75-85. doi: 10.1007/s40069-016-0150-y

19. Mohan, M. K.; Rahul, A. V.; De Schutter, G.; and Van Tittelboom, K., "Early Age Hydration, Rheology and Pumping Characteristics of CSA Cement-Based 3D Printable Concrete," *Construction and Building Materials*, V. 275, 2021, Article No. 122136.

20. Roussel, N., "Rheological Requirements for Printable Concretes," *Cement and Concrete Research*, V. 112, 2018, pp. 76-85. doi: 10.1016/j.cemconres.2018.04.005

21. Nerella, V. N.; Näther, M.; Iqbal, A.; Butler, M.; and Mechtcherine, V., "Inline Quantification of Extrudability of Cementitious Materials for Digital Construction," *Cement and Concrete Composites*, V. 95, 2019, pp. 260-270. doi: 10.1016/j.cemconcomp.2018.09.015

22. Perrot, A.; Rangeard, D.; Nerella, V. N.; and Mechtcherine, V., "Extrusion of Cement-Based Materials - An Overview," *RILEM Technical Letters*, V. 3, 2018, pp. 91-97. doi: 10.21809/rilemtechlett.2018.75

23. Bos, F. P.; Kruger, P. J.; Lucas, S. S.; and van Zijl, G. P. A. G., "Juxtaposing Fresh Material Characterisation Methods for Buildability Assessment of 3D Printable Cementitious Mortars," *Cement and Concrete Composites*, V. 120, 2021, Article No. 104024.

24. Nerella, V. N., Krause, M., and Mechtcherine, V., "Direct Printing Test for Buildability of 3D-Printable Concrete Considering Economic Viability," *Automation in Construction*, V. 109, 2020, Article No. 102986.

25. Kruger, J.; Zeranka, S.; and van Zijl, G., "3D Concrete Printing: A Lower Bound Analytical Model for Buildability Performance Quantification," *Automation in Construction*, V. 106, 2019, Article No. 102904.

26. Casagrande, L.; Esposito, L.; Menna, C.; Asprone, D.; and Auricchio, F., "Effect of Testing Procedures on Buildability Properties of 3D-Printable Concrete," *Construction and Building Materials*, V. 245, 2020, Article No. 118286.

27. Mohan, M. K.; Rahul, A. V.; De Schutter, G.; and Van Tittelboom, K., "Extrusion-Based Concrete 3D Printing from a Material Perspective: A State-of-the-Art Review," *Cement and Concrete Composites*, V. 115, 2021, Article No. 103855.

28. Ding, T.; Xiao, J.; Zou, S.; and Yu, J., "Flexural Properties of 3D Printed Fibre-Reinforced Concrete with Recycled Sand," *Construction and Building Materials*, V. 288, 2021, Article No. 123077. doi: 10.1016/j.conbuildmat.2021.123077

29. Le, T. T.; Austin, S. A.; Lim, S.; Buswell, R. A.; Law, R.; Gibb, A. G. F.; and Thorpe, T., "Hardened Properties of High-Performance Printing Concrete," *Cement and Concrete Research*, V. 42, No. 3, 2012, pp. 558-566. doi: 10.1016/j.cemconres.2011.12.003

30. Feng, P.; Meng, X.; Chen, J.-F.; and Ye, L., "Mechanical Properties of Structures 3D Printed with Cementitious Powders," *Construction and Building Materials*, V. 93, 2015, pp. 486-497. doi: 10.1016/j.conbuildmat.2015.05.132

31. Rahul, A. V.; Santhanam, M.; Meena, H.; and Ghani, Z., "3D Printable Concrete: Mixture Design and Test Methods," *Cement and Concrete Composites*, V. 97, 2019, pp. 13-23. doi: 10.1016/j.cemconcomp.2018.12.014

32. Rahul, A. V.; Santhanam, M.; Meena, H.; and Ghani, Z., "Mechanical Characterization of 3D Printable Concrete," *Construction and Building Materials*, V. 227, 2019, Article No. 116710. doi: 10.1016/j.conbuildmat.2019.116710

33. Nerella, V. N.; Hempel, S.; and Mechtcherine, V., "Effects of Layer-Interface Properties on Mechanical Performance of Concrete Elements Produced by Extrusion-Based 3D-Printing," *Construction and Building Materials*, V. 205, 2019, pp. 586-601. doi: 10.1016/j.conbuildmat.2019.01.235

34. Nerella, V. N.; Hempel, S.; and Mechtcherine, V., "Micro- and Macroscopic Investigations on the Interface between Layers of 3D-Printed Cementitious Elements," *Proceedings*, International Conference on Advances in Construction Materials and Systems (ICACMS 2017), Chennai, Tamil Nadu, India, 2017, 11 pp.

35. Zareiyan, B., and Khoshnevis, B., "Effects of Interlocking on Interlayer Adhesion and Strength of Structures in 3D Printing of Concrete," *Automation in Construction*, V. 83, 2017, pp. 212-221. doi: 10.1016/j.autcon.2017.08.019

36. Craipeau, T.; Toussaint, F.; Perrot, A.; and Lecompte, T., "Experimental Approach on a Moving Formwork," *Construction and Building Materials*, V. 270, 2021, Article No. 121472.

37. Lee, K. H.; Nam, S. Y.; Min, S. E.; Lee, H.-W.; Han, C.; and Ahn, J.-W., "Characterizations of High Early-Strength Type Shrinkage Reducing Cement and Calcium Sulfo-Aluminate by Using Industrial Wastes," *Journal of the Korean Ceramic Society*, V. 53, No. 2, 2016, pp. 215-221. doi: 10.4191/kcers.2016.53.2.215

38. Stefanoni, M.; Angst, U.; and Elsener, B., "Corrosion Challenges and Opportunities in Digital Fabrication of Reinforced Concrete," *First RILEM International Conference on Concrete and Digital Fabrication – Digital Concrete 2018*, T. Wangler and R. J. Flatt, eds., Springer, Cham, Switzerland, 2019, pp. 225-233.

ACI MATERIALS JOURNAL TECHNICAL PAPER

Title No. 121-M16

Development of In-Place Test Methods for Evaluating Printable Concretes

by Christian Negrón-McFarlane, Eric Kreiger, Lynette Barna, Peter Stynoski, and Megan Kreiger

*An experimental investigation was carried out using the volumetric proportioning approach to achieve printable portland cement concrete mixtures. The types of aggregates investigated were rounded pea gravel and coarse and fine sand. The test matrix of potential concrete mixtures was prepared based on water-cement ratios (*w/c*) of 0.46 to 0.48, sand-to-stone ratios (*sa/st*) of 1.18 to 1.91, and paste-aggregate ratios (*p/a*) of 0.74 to 0.81. The workability and early-age strength of fresh concrete were characterized by field-friendly flow-table and unconfined compressive strength (UCS) tests. Test results indicated that the* w/c*,* sa/st*, and* p/a *all significantly affect fresh concrete pumpability and early-age strength. The overall research results revealed that pumpability and buildability can be evaluated with these two tests. The results of these two tests together are used to define a printable region.*

Keywords: additive construction (AC); flow table; fresh concrete; three-dimensional (3-D) printing; unconfined compression; volumetric proportioning.

INTRODUCTION

Additive construction[1] (AC) (construction three-dimensional [3-D] printing) using concrete has been shown to provide a number of benefits, ranging from savings in cost, time of construction, and transportation logistics.[1-3] The common AC methods include print-in-place and preprint.[2] Much of the cost savings associated with additively constructed concrete (ACC) compared to cast concrete is the result of the elimination of formwork,[2] which requires the material to maintain shape and the components to remain stable with the active placement of successive layers.[4,5] Furthermore, in the case of extrusion-based ACC, the material must also exhibit pumpability.[4,5]

To ensure the successful completion of components, a fundamental understanding of material shape stability and print stability is required.[6] These properties are highly dependent on the material properties at placement and the time evolution of strength and elastic modulus.[7] Shape stability in concrete is achieved when concrete retains its shape after extrusion and can withstand the upper loads without deformation.[8] A stable component requires the material to have sufficient yield stress and elastic modulus to maintain the geometry of the print without failure.[6,7] The two primary failure mechanisms that dictate stability are plastic collapse and elastic buckling. Plastic collapse results from a loss of material shape stability due to insufficient material strength of a portion or portions of the ACC component during printing. Elastic buckling results from a loss of stability due to insufficient elastic stiffness of a portion or portions of the ACC component. A recent development in describing and predicting this behavior has been the modification of the uniaxial unconfined compression test for cohesive soils, ASTM D2166, to measure the early-age mechanical strength of printable concretes.[9-13] Kreiger et al.[14] also suggested a general elastic region plot to determine the "printability" of a mixture using layer stability tests obtained with a uniaxial unconfined compression test. Tripathi et al.[15] suggested that a bilinear curve could be used to model the elastoplastic behavior of fresh cementitious material used for AC.

The pumpability of materials depends on the rheology of those materials,[16] which depends on whether the printer system is considered to be a single-stage or two-stage material system.[17] A single-stage system simply pumps material from a hopper to the nozzle at the end of the pumping system, while a two-stage system has a mixing chamber that introduces an admixture, typically an accelerator, just before the nozzle. The one-stage system requires the material to be highly thixotropic to allow material flow in the pumping system and shape stability after extrusion. The two-stage system provides the ability to place a more workable material in the pump but relies on an admixture to provide the shape stability just before extrusion.

While much work has been done exploring the use of rheometers to determine rheological limits for ACC (3-D-printed concrete), the ability of these devices to provide material comparisons is limited as the results are highly dependent on shear history.[18] Because of this, the commercial sector has turned to more traditional tests like the slump test or flow-table test. The slump test may be applicable to two-stage materials that exhibit flow prior to the pump,[16] but this test does not provide a good measure of material strength at the time of placement. The flow-table test has been widely used to characterize the workability of the fresh printable materials.[19] This test measures the microstructural breakdown in the mixtures as a flow spread that can be related to the dynamic yield stress and pumpability.[20] The flow table is more suited for describing the flow characteristics of a material used in a single-stage system prior to pumping, as these materials are stiffer and have higher shape stability and thixotropy.[21]

There have been numerous approaches to evaluating the fresh material properties of printable cementitious

ACI Materials Journal, V. 121, No. 2, March 2024.

MS No. M-2022-288.R2, doi: 10.14359/51740265, received April 21, 2023, and reviewed under Institute publication policies.

materials.[22] Testing and development for fresh materials for printable cementitious materials have been primarily performed in laboratory spaces using equipment that is difficult to transport in the field. This may be applicable for performing quality control for components that are preprinted in a factory, but not for the quality control of near-site preprint or print-in-place applications. To develop a material that is printable, pumpable, and shape-stable, concrete professionals need to rely on combining standard practice, such as ACI 211.9R-18,[23] with the latest research. Print quality can be impacted by printer weight and stiffness, the material delivery system (one- or two-stage), and the material mixture proportions. The fresh material properties rely on the aggregate properties, paste content, water-cement ratio (*w*/*c*), and the effects of admixtures on the rheological properties.[24,25] These parameters then affect the buildability (shape stability and component stability) and pumpability of the cementitious materials.

This paper discusses the development of AC-specific quality assurance and quality control testing procedures for assessing printable concrete using a flow-table device and an unconfined compression device. The focus is on the material development of field-friendly equipment to characterize the pumpability and shape stability of fresh concrete. Several initial mixtures were assessed for flow, fresh material compressive strength, and elastic modulus. The mixture parameters explored were the *w*/*c*, paste-aggregate ratio (*p*/*a*), and sand-to-stone ratio (*sa*/*st*) of different potential mixtures to determine a range of parameters that indicate printability.

RESEARCH SIGNIFICANCE

Regarding cementitious AC, there have been numerous strategies developed to meet fresh property targets for achieving both pumpability and buildability (material shape stability and component stability). Currently, no standard test to measure and quantify these criteria exists, especially on the jobsite, where compact, portable, and accurate equipment is required. The study consisted of an initial assessment of the range of printability using portable test equipment that are candidates for in-place testing of single-stage materials, an evaluation of the proposed procedure for the unconfined compression test, and the limits of printing and results obtained from testing, followed by validation of printability in a quasi-deployed setting. The authors believe the use of the flow-table and unconfined compression tests will be useful for in-place measurement and quality control of the workability and buildability of printable mixtures. The mixtures and unconfined compression methodology were developed through validation using a deployable AC system.

EXPERIMENTAL INVESTIGATION

Materials

A volumetric proportioning approach was used to achieve printable portland cement concrete materials by incorporating binary and ternary aggregate blends and two ASTM-compliant admixtures. Type I portland cement meeting ASTM C150 was used throughout the experiments. Graded river sand meeting ASTM C33/C33M and mason sand meeting ASTM C144 were used as fine aggregates. The specific gravity was 2.60 for the river sand and 2.62 for the mason sand. Rounded pea gravel meeting ASTM C33/C33M with a specific gravity of 2.58 and a nominal maximum size (NMS) of 3/8 in. (9.5 mm) was used as coarse aggregate. For laboratory testing, all aggregates were oven-dried before use. The thixotropic modifier met API Specification 13A,[26] Section 9, and the high-range water-reducer met ASTM C494/C494M.

Variables of mixture proportions in this study were the gravimetric *w*/*c*, volumetric *p*/*a*, and volumetric *sa*/*st*. Binary and ternary aggregate combinations comprising the previously mentioned aggregates were also used. Binary mixtures consisted of the 3/8 in. (9.5 mm) pea gravel with either the graded river sand or the mason sand. The ternary mixture consisted of pea gravel with a 50:50 combination of river sand to mason sand. All other properties and proportions of the concrete mixture design remained constant. For comparison, a summary of the mixture proportions of traditional cementitious materials is included in Table 1.

More than 50 mixtures were performed in this study, but many were considered unsuitable for AC, as they were observably too dry or too wet. A total of 29 mixtures from this study are presented. Table 2 lists the grouping convention used for the different mixture types.

Material mixing for the initial evaluation was carried out at room temperature on a 5 qt (4.73 L) benchtop laboratory mixer. To prepare the specimens, stone and coarse sand were dry mixed, after which 50% of the water was added to the mixture. The mixing continued for an additional 30 seconds, and the ordinary portland cement (OPC) and thixotropic modifier were added with the remaining water. Last, the liquid admixture was added, and the mixing was continued until a homogeneous status was achieved. The mixtures evaluated are listed in Table 3.

Table 1—Volumetric mixture proportions of common cementitious materials

Material	*w*/*c*	*p*/*a*	*sa*/*st*	*st*/*c*	*sa*/*c*	NMS, in. (mm)
Stucco—base[27]	0.4 to 0.7	0.57 to 1.41	—	—	0.25 to 0.44	4.75
Stucco—finish[27]	0.4 to 0.7	0.75 to 2.15	—	—	0.33 to 0.67	4.75
Mortar[28]	0.4 to 0.7	0.63 to 1.41	—	—	0.28 to 0.44	4.75
Fine grout[29]	0.4 to 0.7	0.75 to 1.41	—	—	0.33 to 0.44	9.5
Coarse grout[29]	0.4 to 0.7	0.45 to 0.98	0.33 to 0.88	0.50 to 1.0	0.33 to 0.44	4.75
Concrete[30]	0.4 to 0.7	0.25 to 0.67	0.5 to 2	0.5 to 10	0.25 to 5	100

Note: *st*/*c* is stone-cement ratio; *sa*/*c* is sand-cement ratio.

Table 2—Nomenclature used for grouping mixtures

Group ID	Mixtures	Description
Binary base fine sand (Group 1)	B1, B2, B3	Increasing *p*/*a*
Ternary base (Group 2)	C2, C0, C1	Increasing *p*/*a*
Binary base coarse sand (Group 3)	A0, A1, A2	Increasing *p*/*a*
Binary coarse sand paste reduction (Group 4)	A0, A3, A4	Decreasing *w*/*c* and *p*/*a*
Binary coarse sand paste increase (Group 5)	A2, A5, A6	Increasing *w*/*c* and *p*/*a*
Binary coarse sand adjustment (Group 6)	A7, A8, A9	Increasing *sa*/*st*
Binary fine sand adjustment (Group 7)	B0, B4, B1	Decreasing *sa*/*st* and *sa*/*c*

Table 3—List of mixtures

Mixture ID	*w*/*c*	*p*/*a*	*sa*/*st*	*st*/*c*	*sa*/*c*	Sand ratio (coarse:fine)
A0	0.457	0.749	1.23	1.48	1.81	—
A1	0.457	0.764	1.23	1.45	1.78	—
A2	0.457	0.778	1.23	1.42	1.75	—
A3	0.467	0.759	1.23	1.48	1.81	—
A4	0.477	0.765	1.23	1.48	1.81	—
A5	0.467	0.789	1.23	1.42	1.75	—
A6	0.477	0.798	1.23	1.42	1.75	—
A7	0.455	0.787	1.66	1.48	1.81	—
A8	0.456	0.790	1.74	1.48	1.81	—
A9	0.456	0.793	1.91	1.48	1.81	—
B0	0.455	0.806	1.60	1.17	1.88	—
B1	0.455	0.792	1.18	1.42	1.68	—
B2	0.456	0.798	1.18	1.41	1.67	—
B3	0.456	0.802	1.18	1.41	1.66	—
B4	0.456	0.809	1.37	1.28	1.76	—
C0	0.456	0.771	1.61	1.23	1.97	51:49
C1	0.456	0.779	1.61	1.21	1.95	51:49
C2	0.457	0.743	1.61	1.27	2.04	51:49

Table 4—Mixture proportions for shape-stability plots

Label	*w*/*c*	*p*/*a*	*sa*/*st*	*st*/*c*	*sa*/*c*
D1	0.461	0.825	1.94	1.024	1.98
D2	0.462	0.826	1.94	1.024	1.98
D3	0.46	0.823	1.94	1.024	1.98
P1	0.47	0.834	1.94	1.024	1.98
P2	0.47	0.834	1.94	1.024	1.98
P3	0.47	0.834	1.94	1.024	1.98
P4	0.467	0.831	1.94	1.024	1.98
P5	0.476	0.840	1.94	1.024	1.98
W1	0.486	0.851	1.94	1.024	1.98
W2	0.495	0.860	1.94	1.024	1.98
W3	0.49	0.855	1.94	1.024	1.98

Material mixing for the evaluation of the unconfined compression test was carried out at room temperature in a 5 gal. (18.9 L) bucket using a handheld single-paddle mixer. The order and procedure for mixing were the same as that performed for the initial evaluation. The mixtures evaluated are listed in Table 4. Testing was performed on 11 mixtures: five mixtures considered to have good printability (P), three

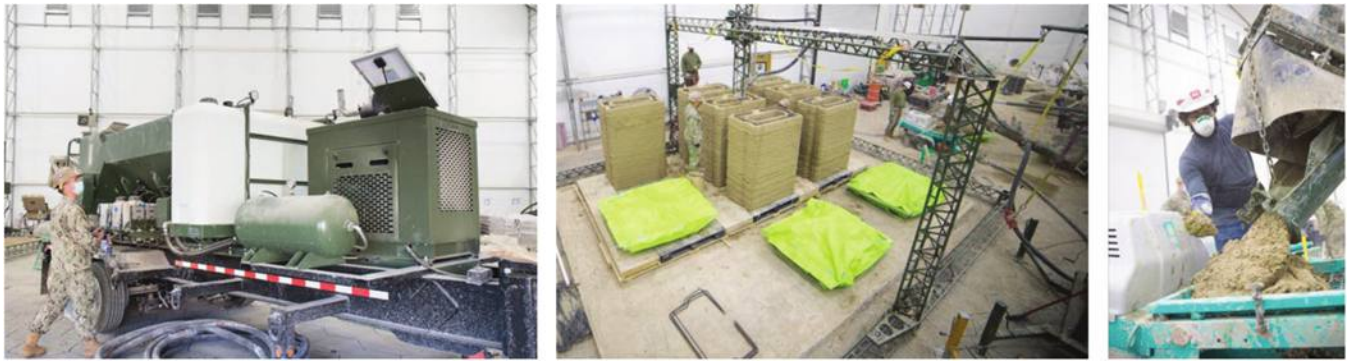

Fig. 1—(Left) Volumetric mixer; (center) deployable printer system; and (right) material delivery.

Fig. 2—Flow-table test experimental setup and storage in hard travel case.

dry printable mixtures (D), and three wet printable mixtures (W).

Material mixing for validation of printability was performed using a trailer-mounted automated volumetric mixer (refer to Fig. 1), set up to deliver mixtures that were developed as part of a quasi-deployed evaluation in a 70 x 100 ft (21.3 x 30.5 m) tent space. After mixing, the materials were evaluated using the flow-table and unconfined compression tests, as discussed in the following section. Once verified, the material was deposited using a deployable printer system developed by the U.S. Army Engineer Research and Development Center Construction Engineering Research Laboratory (ERDC-CERL). The deployable printer system uses a progressive cavity pump, hoses, and nozzle positioned in three dimensions using a computer-driven gantry printer, as shown in Fig. 1. The gantry printer was developed under a Cooperative Research and Development Agreement (CRADA).[14]

EXPERIMENTAL METHODS

This study investigates and develops two portable test methods, the flow-table test and uniaxial unconfined compression test, to determine the pumpability and very-early-age (at 0 minutes) strength, respectively, of fresh concrete to be used for a single-stage concrete AC process. It should be noted that multiple other fieldable test methods, including the slump test (ASTM C143/C143M), portable rheometer,[31] the Kelly ball penetration test (ASTM C360), and the Vebe consistometer (EN 12350-3), were considered. However, it was determined that the flow-table and unconfined compression tests could provide lightweight, low-volume portable solutions and the highest amount of directly measurable results to determine if the materials are pumpable, shape-stable, and will ensure component stability.

It is important to mention that two types of unconfined compression apparatuses were used to determine the material strength. Testing was performed using a commercial portable manual unconfined compression testing device to determine the range of printability and evaluate the device for performing in-place quality control testing of the concrete mixtures listed in Table 3. Any adjustments to mixtures were documented, and using an electrically driven load frame, the unconfined compression test procedure was evaluated and refined. From there, the best mixtures were evaluated using the deployable printing system mentioned in the previous section.

Portable flow-table test

The ability to determine the pumpability of the fresh concrete was found by evaluating the flow behavior of the mixture by performing a flow-table test as per ASTM C1437. To make this device portable, the table was mounted to a 12 x 12 x 1 in. (300 x 300 x 25 mm) thick steel plate, as shown in Fig. 2. In addition, it can be seen that the device is compact and can be packaged in a hard case to transport to the jobsite. The concrete was placed in two layers of the cone mold and rodded 20 times after each layer. After the top surface of the mold is leveled, the mold is pulled to form the

Fig. 3—Manual unconfined compression test experimental setup and storage in hard travel case.

standard cone shape. The material should retain the shape of the mold with no noticeable flow. Immediately after the mold was lifted, 25 flow-table drops in 15 seconds were imparted to the fresh material. The circular shape spread out of the material was measured in three directions—at 0-, 45-, and 90-degree angles—and averaged to get the flow reading.

Unconfined compression test—portable manual tester

Uniaxial unconfined compressive strengths (UCSs) were measured on cylindrical samples with a 3 in. (76 mm) diameter and 2 in. (51 mm) height. The specimen dimensions were chosen to mimic the width-to-height ratio dimensions of the beads of material deposited during the AC process. Fresh concrete was placed into a cylindrical plastic mold placed on the test equipment with minimal consolidation to mimic the unconsolidated printed material. Excess material was moved, and the mold was removed prior to testing. Testing was conducted using a commercially available hand-lever-operated unconfined compression soil tester (Fig. 3). Similar to the flow tester, the device can be packaged in a hard case to transport to the jobsite. Unconfined compression tests were performed in ambient conditions. Each test was conducted for close to 1 minute to neglect the effects of thixotropic buildup, and the value recorded is presented as the minimum load required to form the first crack on the specimen during loading.

Unconfined compression test—automated load frame

For the measurement of very-early-age strength, development testing was conducted using an electronically controlled load frame, as shown in Fig. 4. The tests were performed at a constant displacement rate of 1 in./min (25 mm/min) until 35% vertical strain had been attained, which was experimentally determined to be the best load rate. Vertical deformations were monitored with a linear variable differential transformer (LVDT), and vertical loads were monitored with a load cell mounted above the top platen.

Similar to the portable device, the test was performed on cylindrical samples with a 3 in. (76 mm) diameter and

Fig. 4—Automatic unconfined compression test experimental setup.

2 in. (51 mm) height created using a plastic mold that was removed prior to testing. A thin layer of release agent was applied on the inside of the mold before filling. The compaction procedure consisted of placing the material in two layers of the cylinder mold and compacting it using a rod with 25 evenly distributed strokes after each layer. After compaction, the top surface of the mold was leveled. Then, the mold was pulled from the material at the time of its corresponding test. These tests were performed at a fresh concrete age of $t = 0$. Herein, $t = 0$ is the earliest time possible considering mixing, consolidation, demolding, and placing of the specimens in the test setup and starting the test, which takes approximately 7 minutes after the cement is added to the mixture.

The values obtained are in terms of the stress and strain diagram. Yielding of concrete is determined when a change in the slope in the stress-strain plot is noticed. In addition, the lateral deformation of the sample was measured using an electronic digital caliper. The lateral area is assumed to change linearly during compression. Therefore, with the initial and final area of the specimen at its 35% strain, the change in cross-sectional area can be determined.

EXPERIMENTAL RESULTS AND DISCUSSION

Results are separated based on an initial test evaluation, an initial validation, test development, and a quasi-deployed validation. Initial testing was performed using the flow-table and the manual unconfined compression testers in a laboratory setting. Initial validation of the materials consisted of performing the test and running materials through the deployable printer system. The test development was done by performing the unconfined compression test using the automated load frame in a laboratory space to evaluate parameters and refine material limits. This was followed by using the in-place test equipment in a quasi-deployed setting

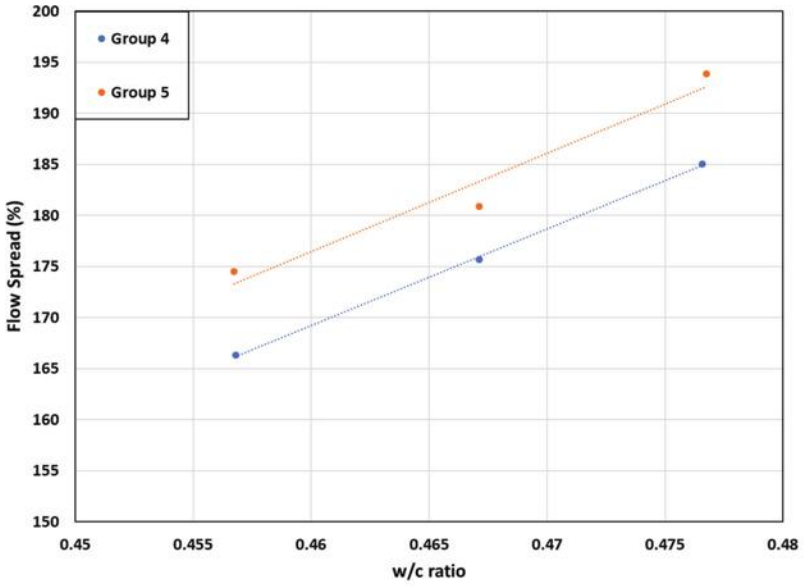

Fig. 5—Flow-table spread: w/c.

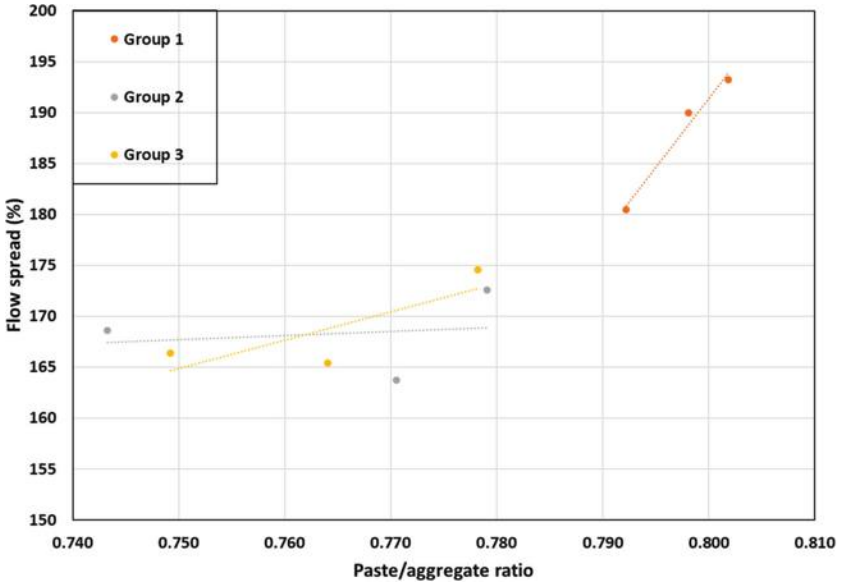

Fig. 6—Flow-table spread: p/a.

to evaluate the potential for using these tests for material quality control in a deployed setting.

INITIAL TEST EVALUATION

Flow properties

The percent flow was calculated according to ASTM C1437. Figure 5 shows the effect of the water content (variations of *w*/*c* and *p*/*a*) for Groups 4 and 5, where the paste content increases from Group 4 to 5. The results exhibited an almost linear correlation between the *w*/*c* and flow spread, as previously observed.[24] As the water content is increased, the flow of the fresh concrete increases. By adding more water to the mixtures, a higher flow was achieved. As established by previous studies, an increase in *w*/*c* causes a greater dispersion of cement particles; therefore, the mobility of the concrete increases with the mobility of the paste.[25]

Figure 6 shows a comparison of the flow to the *p*/*a* of Groups 1, 2, and 3 mixtures. Group 1 results show the flow increases when the *p*/*a* increases. With more cement paste, the paste coats the aggregates and fills the voids between them. Furthermore, the friction between aggregates is reduced and allows smoother movement. While these mixtures have different aggregate mixtures, the results are unclear regarding the fineness modulus and aggregate type. Therefore, more work is required to understand the results with variations in aggregates.

Unconfined compression test—portable manual tester

The compressive strength of fresh concrete was determined with the unconfined compression test, and results were compared to variations in *w*/*c*, *p*/*a*, and *sa*/*st*. Figure 7 presents the UCS of Group 3 and 4 concrete mixtures. The

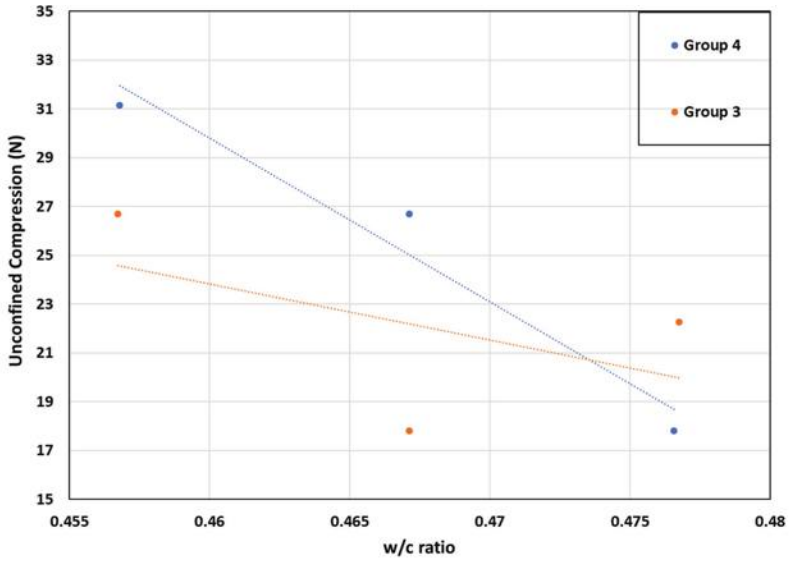

Fig. 7—Unconfined compressive strength: w/c.

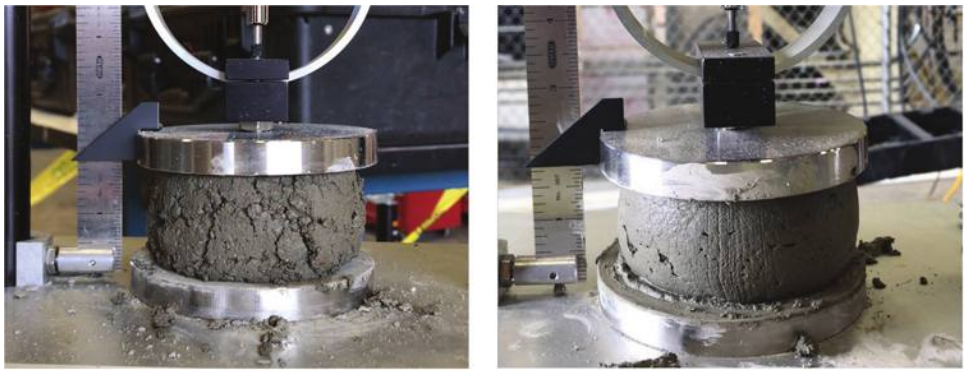

Fig. 8—Fresh concrete under compression: (left) dry concrete; and (right) good concrete.

results indicated that the UCS increased as the *w*/*c* decreased for both groups. An increase in *w*/*c* causes a greater dispersion of cement particles and, therefore, a lower UCS.

If the compressive strength of the mixture is too low, the material will have high mobility, resulting in the material having higher flow, being prone to failure, and exhibiting low shape stability. On the contrary, higher compressive strength values result in stiffer material with less mobility, which could result in the material tearing as it exits the nozzle, gaps in the print due to air pockets in the pump system, clogs in the pumping system, or overheating of the pump.[14] Figure 8 presents examples of good and dry unconfined compression samples.

Figure 9 shows the effect of the *p*/*a* on the UCS of the fresh concrete. When the *p*/*a* increases, more cement paste exists to coat aggregates and fill the voids between them. More paste reduces the friction between aggregates and allows a smoother movement. As a result, concrete with a higher *p*/*a* will develop lower UCS.

Figure 10 shows the UCS and *sa*/*st* relationship within two sets of mixtures: Groups 6 and 7. It is observed that increments in the *sa*/*st* increased the UCS of the fresh concrete. This phenomenon can be explained by the fact that the overall aggregate surface area increases when the *sa*/*st* increases. When less paste is available, the degree of friction and interlocking of the solid particles is increased, resulting in higher UCS.

In Fig. 10, it is worth noting that Group 7 exhibits higher strength than Group 6. This is a result of fine sand having a larger number of smaller particle sizes than its counterpart, increasing the surface area and leading to less paste and more friction between particles.

The relationship between the UCS and the flow spread of concrete mixtures is presented in Fig. 11. These results agreed with a previous study; the trend resulted in a linear inverse relationship on these plots.[12] Increasing the flow of the concrete mixture lowers its very-early-age strength. This is because more paste in the mixture results in more flow but lower UCS.

TEST METHOD DEVELOPMENT AND VALIDATION

Preliminary test validation

To ensure that the acceptance of mixtures was not solely based on laboratory testing, the mixtures underwent testing using the portable test devices before evaluating if the mixtures could be placed using an AC process before further developing the portable UCS test.

Figure 12 shows the quality of 3-D-printed concrete layers when the material meets/fails printability ranges of UCS and flow. The left figure depicts a dry concrete bead with obvious

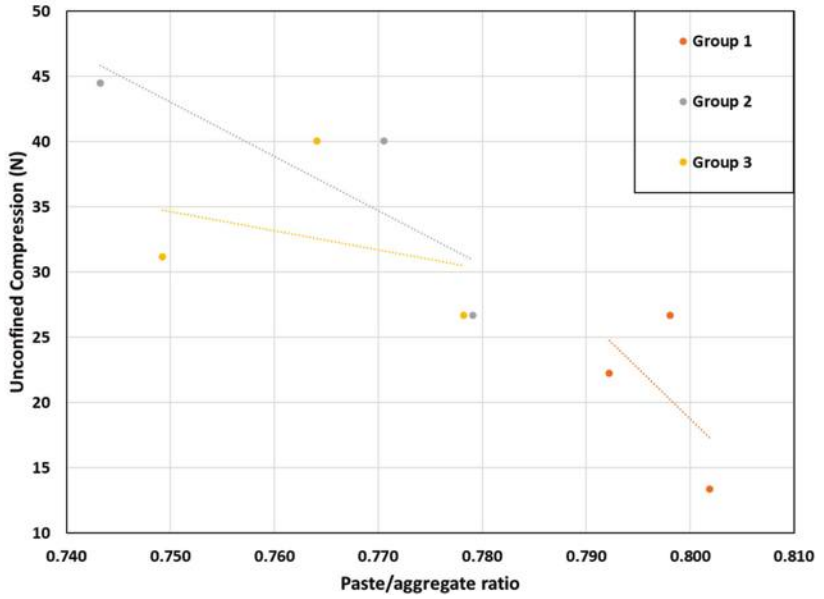

Fig. 9—Unconfined compressive strength: p/a.

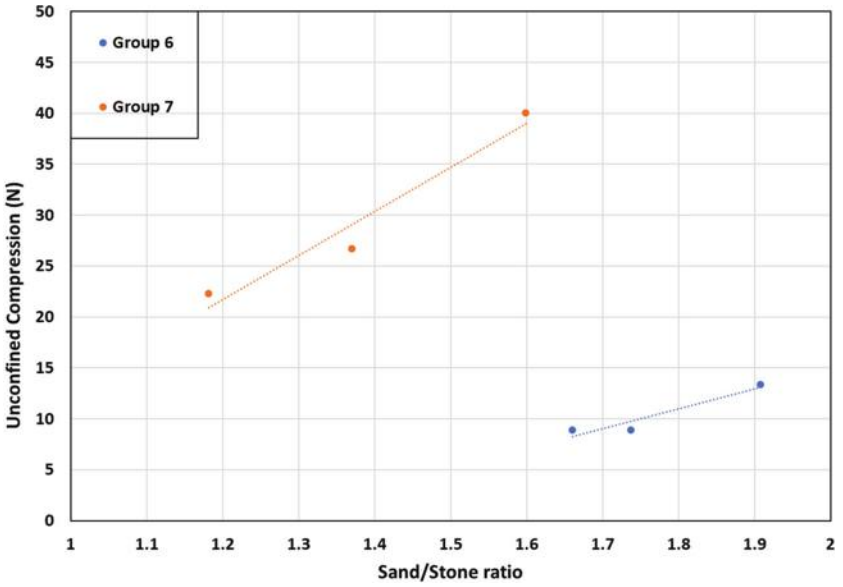

Fig. 10—Unconfined compressive strength: sa/st.

signs of tearing and splitting, the center figure depicts concrete layers that lie between the acceptable ranges, and the right figure represents a wet concrete bead that tends to show higher spread and deformation caused by the successive layers. Mixtures with low flow tend to exhibit rough texture on the surface of the beads. They possess high shape retention, large voids and cracks, and are difficult to pump. Conversely, mixtures with high flow spread appear to have a rippled surface and fewer voids and cracks. They are easier to pump; however, they also exhibit lower shape retention.[20]

Based on the results of running material in the deployable printer system, it has been determined that printable concrete mixtures should have a flow ranging from 157 to 177% and a UCS ranging between 3 and 7 lb (17.8 and 31.1 N) before cracking. These limits should ensure a mixture with a good compressive strength that can be pumped without having any placement problems. It should be noted that, at this time, the authors can only conclude these limits apply to the specific material studied until more mixture variations are studied.

Unconfined compression test—automated load frame

To determine the proper displacement rate, various strain rates were used on concrete samples at time 0 minutes and compared to the ASTM D2166 suggested maximum rate (2%/min). Figure 13 shows the evaluation of different strain rates on the unconfined compression test. It is observed that flocculation and structuration greatly influence the test. At a low rate, such as 0.02 in./min (0.5 mm/min), as suggested by ASTM D2166, the specimen exhibited a noticeable load gain. For accuracy, these tests should be performed fast enough to neglect the effects of structural buildup. As a

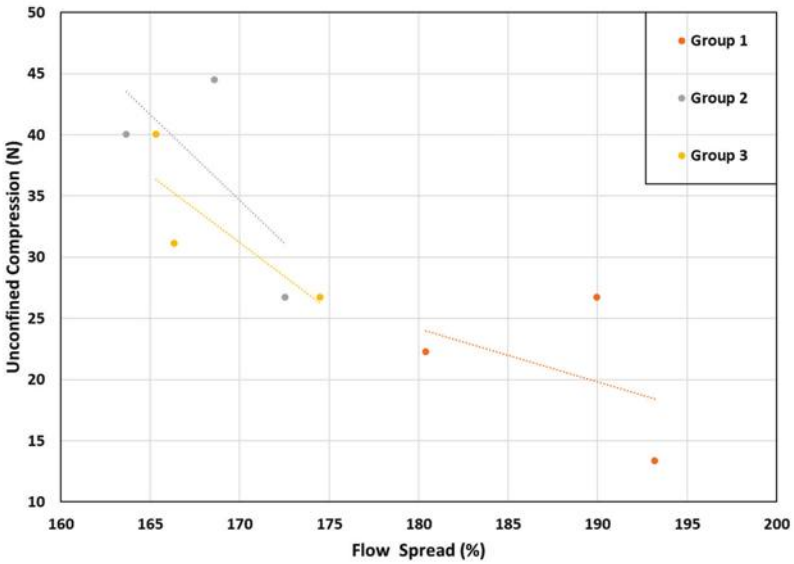

Fig. 11—Unconfined compressive strength and flow spread relationship.

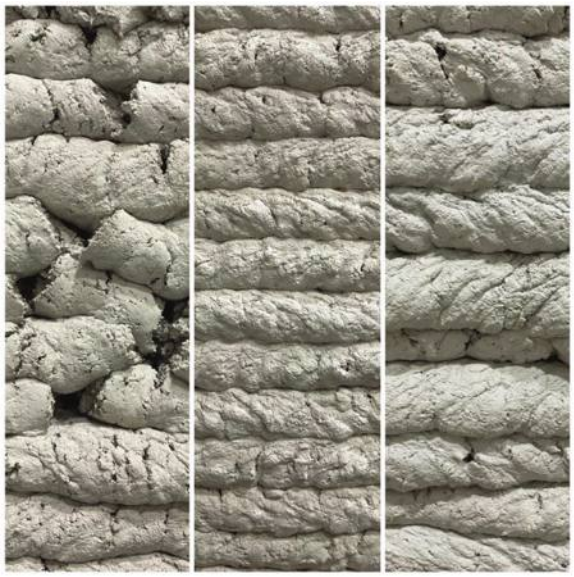

Fig. 12—Layer quality: (left) dry bead; (center) adequate; and (right) wet bead.

result, higher rates, such as 1.0 in./min (25.4 mm/min), are preferable. This rate agrees with the rate employed in other studies[9] and is preferable as it allows the operator to maintain a feasible crank rate while performing the test using the portable tester.

As mentioned earlier, Kreiger et al.[14] described a method to evaluate the layer shape-stability tests, as shown in Fig. 14. This "stability" plot serves as a quality control test that can be performed prior to the commencement of construction and at different times during construction. The shaded region corresponds to the stable zone. In this zone (gray zone), the material is strong enough to support the load of successive layers, is elastic enough not to tear, and yet not so elastic to displace excessively under load. Furthermore, it should be noted that this can be extended to describe the elastic and plastic regions of printable materials based on work by others[15] describing the elastoplastic behavior of printable materials as a bilinear model.

This region is constrained by the strain and stress limits of the mixture as well as the upper and lower elastic modulus limits. The upper and lower limits are obtained by determining the stiffness of the material and are associated with the elastic modulus when the material is too dry ($E_{E,D}$) and too wet ($E_{E,W}$). The strain limit is a strain value that relies on the linear range of the material and is associated with how much displacement the material will resist by the load (for example, layers or reinforcement) being placed on top of it. The stress limit is determined by the maximum force that the wet material can withstand without yielding, divided by the area of the specimen. This limit is obtained from the lower limit associated with the wet material. The intent of this plot is to determine if the yield point of the concrete at very early ages is inside or outside of the stability zone.

This methodology was explored through laboratory testing. The mixtures from Table 4 are representative of mixture variations that could be seen during the printing process. The mixtures consisting of the wet and dry materials are considered highly printable because they exhibit good flow, strength, and stiffness to hold successive layers with good surface quality after exiting the nozzle. The constituent amounts differ from those studied during the initial evaluation due to updates to the mixtures to meet the requirements of the deployable printer system. The yield point is determined by the sudden change in the slope in the stress-strain plot. If the material yields below the stress limit, the material will not be strong enough to support the load, and the component being constructed will be prone to plastic failure. If a material is below the lower limit associated with the material being too wet ($E_{E,W}$), then the component being constructed is prone to failure due to insufficient elastic modulus or strength. If a material is above the upper elastic limit associated with the materials being too dry ($E_{E,D}$), then

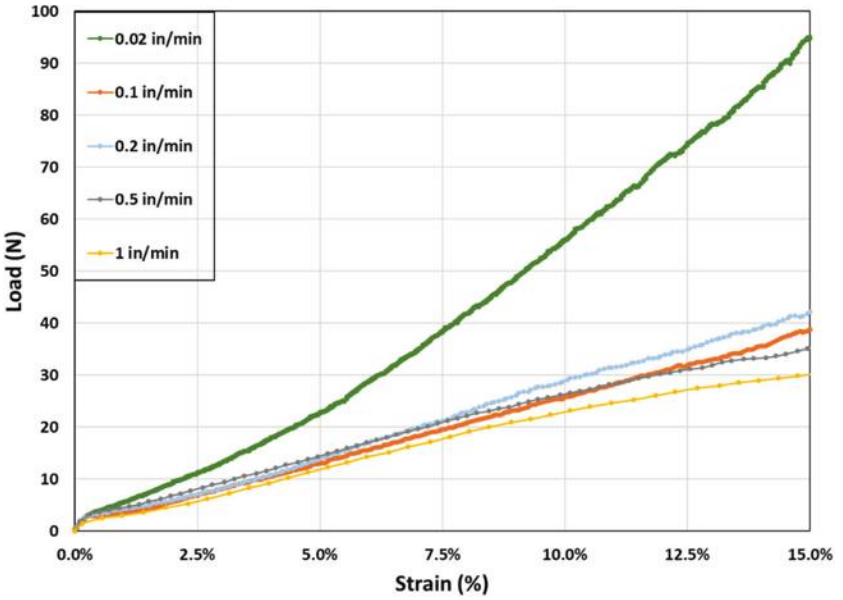

Fig. 13—Unconfined compression test strain rates of samples at time 0 minutes.

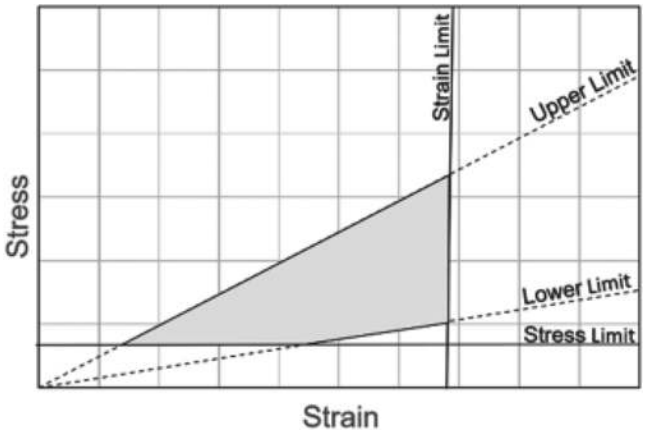

Fig. 14—General shape-stability plot.

the material will likely not be able to be pumped and, therefore, cannot be used for an AC application.

Figure 15 shows the elastoplastic stress-strain diagram of a printable concrete mixture at the age of 0 minutes after cross-sectional area correction. Using the three experiments for each limit, an average stress-strain relation can be determined, as indicated by the black (dry) and red (wet) solid lines (note: full-color PDF can be accessed at www.concrete.org). The other five plots correspond to the highly printable concrete mixtures. Figure 15 shows how the stress-strain plot changes by increasing the water amount in the concrete, resulting in a decrease in stress and stiffness with increased water.

It is clearly observed that the mixtures exhibit an elastoplastic behavior; the load initially increases approximately linearly as the vertical displacement increases up to the elastic limit, where it starts to transition to nonlinear behavior. Surface defects appear on the sample at approximately 18.5% strain. Although it can be appreciated that the curve is nonlinear after the elastic limit, the section up to 18.5% strain can be estimated as a linear curve. As a result, the plot can be defined as a bilinear elastoplastic material. Assuming the section is linear, it is possible to determine the upper and lower plastic stress limits. These limits, $\sigma_{P,D}$ and $\sigma_{P,W}$, represent the stress at the upper limit for the dry material and the lower limit for the wet material in the plastic state. Similarly, $\sigma_{E,D}$ and $\sigma_{E,W}$ can be defined for the upper and lower limits in the elastic portion of the plot. As for the plastic state, the modulus for the upper and lower limits can be defined as $E_{P,D}$ and $E_{P,W}$, respectively.

From this plot, the stress at these points was 0.70 and 0.28 psi (4.82 and 1.94 kPa) for $\sigma_{P,D}$ and $\sigma_{P,W}$, respectively. Similarly, the loads at these points were 7.0 and 2.9 lb (31.0 and 12.9 N).

The linearity of the plots of the averages of the dry, printable, and wet mixtures in the elastic portion was determined to be at 7.5% strain. By choosing 7.5% as the strain limit, the shape-stability plot can be determined, as shown in Fig. 16. The slope of the plots represents the stiffness (elastic modulus) of the material. With these stiffness values, the upper and lower limits can be obtained and form the shape-stability plot.

The average of the highly printable mixtures lies between the two dry and wet limits, according to the *w*/*c*; obviously, increasing the amount of water in the paste decreases the strength and stiffness of the material. In addition, the mixtures did not yield inside the stability zone. The stress limit was determined by the average of the yield points of the wet concrete mixtures. The stress limit determined by those mixtures was 0.07 psi (0.439 kPa), and the material can hold up to 1.74 lb (7.737 N). On the other hand, for dry mixtures at the strain limit, the stress was 0.41 psi (2.85 kPa), and the material can hold up to 3.4 lb (15.2 N). Last, the elastic moduli for the dry and wet printable mixtures were 5.74 and 2.64 psi (39.57 and 18.21 kPa), respectively. The upper and lower elastic limit equations were determined by a linear fit and are shown in Fig. 16.

It is critical to note that the five mixtures meet the stability criteria. The average load and stress (brown plot) for these five printable mixtures at the strain limit were 2.4 lb (10.9 N)

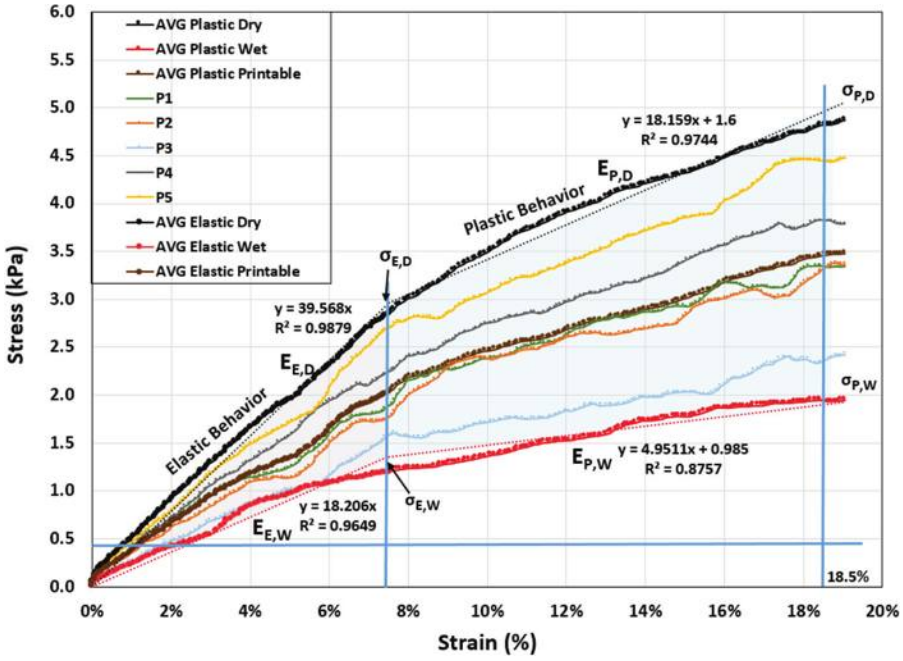

Fig. 15—Elastoplastic stress-strain plot at time = 0.

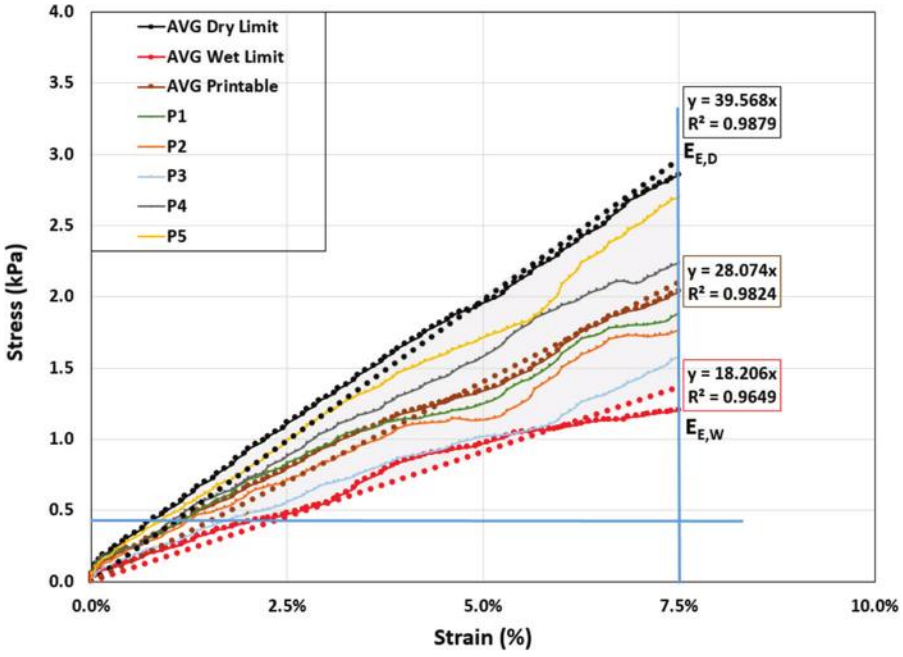

Fig. 16—Elastic shape-stability plot at time = 0.

and 0.30 psi (2.0 kPa), respectively. Similarly, the average elastic modulus for these mixtures was 4.07 psi (28.07 kPa). This stiffness is similar to previous studies in which having a low stiffness is desirable for the printing process because it reduces the internal friction and material fracture during extrusion.[9] Right after extrusion, the material has lost water due to this friction in the pump, resulting in a stiffer material extruding out of the nozzle.

Quasi-deployed validation

After the development of the UCS test procedure and stability plot, flow-table limits, and UCS limits, the tests were further verified during the production of several large wall samples (Fig. 17) in a quasi-deployed condition (conditioned tent, using the deployable printer system and a volumetric mixer). With the use of the portable flow-table and unconfined compression testers, it was possible to maintain quality control at the start of the printer operation and at different times during the AC process. Fresh concrete, after mixing, can be tested and verified to meet the stability plot. Any concrete material that does not meet the stability criteria was discarded to achieve or preserve a quality print. This shows that this printable material can be used for printing and that this plot serves as a quality control test that can reduce risk and increase suitability for AC operations.

This rate developed for the UCS provided reliable measurements of the fresh properties of the printable concrete, allowing for quality material and the completion of acceptable structures, as shown in Fig. 17. Table 5 shows the data on the UCS of printable concrete used during different quasi-deployed operations. It can be seen that during the December-B and January events, the material throughout the day was more consistent compared to other prints, with a coefficient of variation of 8 and 7%, respectively. In terms of confidence, the UCS test can meet the load requirements, with less than ±0.54 lb (2.37 N) for most days and under ±0.9 lb (3.98 N) for all 9 days, with 95% confidence for the results during each day. For the December-A print at 95% confidence, the proportion of obtaining a UCS of 5 lb (22.2 N) was between 4.8 and 5.6 lb (21.6 and 24.7 N). Overall, the average of these measurements throughout all prints lies between the range obtained from $\sigma_{P,D}$ and $\sigma_{P,W}$ of Fig. 15, where stable mixtures exhibited fracture on loads between 2.9 and 7.0 lb (12.9 and 31.0 N).

Fig. 17—8 ft (2.4 m) tall walls constructed in quasi-deployed conditions.

In the same way, Table 6 depicts the flow spread measurements obtained for the same quasi-deployed prints. The variance is low for all events, showing the apparatus is reliable during measurements.

The portable flow-table and UCS tests aid in the rapid evaluation of the fresh material flow and strength to determine pumpability and stability and have been determined to be reliable in the in-place quality control and evaluation of materials used for AC in a quasi-deployed condition. It should be noted that water content has a significant impact on both strength and stiffness; therefore, variations in water to achieve the properties must be used with care as they could impact material performance and strength. Additionally, variations in environmental conditions can impact the concrete performance. Therefore, variations in material performance may occur depending on the location, season, weather, and time of the day the concrete is mixed and placed/deposited. Material and operational considerations for AC have been previously discussed.[1,2,14] Materials considerations for concrete are also discussed in ACI 305R-20 and ACI 306R-16, which provide the minimum temperatures that guide hot weather and cold weather work, respectively.[32,33]

FURTHER RESEARCH

It is desirable to test specimens and create shape-stability plots for different mixtures at different ages to find out possible ways to maintain print stability during the printing process. The shape-stability plots at very early ages (0 to 120 minutes) can establish the rate of depositing of material during the actual printing of a structure in the field. Furthermore, it will be crucial to test out the test equipment in a field deployment to see how it performs; how temperature and humidity affect the results; and to consider the effects of aggregate type, gradation, and angularity, as well as the inclusion of manufactured/crushed aggregates of different mineralogical compositions, to prescribe initial guidelines for determining printable materials based on the available materials.

CONCLUSIONS

The pumpability and shape stability of fresh concrete used as potential material for single-stage printable concretes were measured according to two tests: flow table

Table 5—Unconfined compression test of multiple prints using 1.0 in./min rate

ID	Date	No. of samples	Mean, lb	STD	CV, %	Confidence interval (α = 0.05)
A	August	6	5	0.96	21.3	3.7 to 5.3
B	September	3	5	0.47	10.1	4.1 to 5.2
C	November	3	4	0.47	12.9	3.1 to 4.2
D	December-A	9	5	0.83	15.3	4.9 to 6.0
E	December-B	6	5	0.40	7.7	4.8 to 5.6
F	January	3	6	0.47	7.4	5.8 to 6.9
G	March-A	5	6	1.02	18.2	4.7 to 6.5
H	March-B	6	5	0.75	14.0	4.7 to 5.9

Note: STD is standard deviation; CV is coefficient of variation; 1.0 in./min = 25 mm/min; 1 lb = 4.448 N.

Table 6—Flow-table test of multiple prints

ID	Date	No. of samples	Mean (flow %)	STD	CV, %	Confidence interval (α = 0.05)
A	August	6	179.4	7.14	4.0	173.6 to 185.1
B	September	3	169.1	0.41	0.2	168.6 to 169.5
C	November	3	179.4	2.95	1.6	176.0 to 182.7
D	December-A	9	161.7	7.79	4.8	156.6 to 166.8
E	December-B	6	167.3	7.22	4.3	161.0 to 173.6
F	January	3	167.1	9.87	5.9	155.9 to 178.3
G	March-A	5	170.1	11.33	6.7	160.2 to 180.1
H	March-B	6	166.1	5.40	3.3	161.8 to 170.4

and unconfined compression. Printability windows were obtained by measuring a wide range of mixtures produced with various raw materials with different workability levels and setting criteria for accepting them as printable. The experiment demonstrated that these tests inform mixture design development and validation. The following conclusions are drawn:

1. The unconfined compressive strength (UCS) of the fresh concrete samples will decrease if the water-cement ratio (*w*/*c*) and paste-aggregate ratio (*p*/*a*) increase. UCS will only increase if the sand-to-stone ratio (*sa*/*st*) increases.

2. Flowability of fresh concrete is also affected by the *w*/*c* and *p*/*a*. Increasing either of these two parameters will result in a rise in the flow spread. Therefore, the relationship between UCS and flowability is inverse.

3. Layer shape-stability plots can be used as a quality control test for AC operations.

AUTHOR BIOS

Christian Negrón-McFarlane *is a Materials Research Engineer at the U.S. Army Engineer Research and Development Center Construction Engineering Research Laboratory (ERDC-CERL) in Champaign, IL. He received his BS and MS in chemical engineering and materials science and engineering from the University of Puerto Rico at Mayagüez, Mayagüez, PR, in 2016 and 2020, respectively. His research interests include early-age fresh concrete properties of additive construction materials.*

ACI member **Eric Kreiger** *is a Research Civil Engineer at the U.S. Army ERDC-CERL in Champaign, IL, and the Structural and Materials Lead for the ERDC's Additive Construction Program. He received his BS and MS in civil (structural) engineering from Michigan Technological University, Houghton, MI, in 2009 and 2012. He is Chair of ACI Subcommittee 564-B, Structural Design and Testing, and a member of ACI Committees 342, Evaluation of Concrete Bridges and Bridge Elements; 552, Cementitious Grouting; and 564, 3-D Printing with Cementitious Materials. His research interests include the evaluation of material properties, structural performance, and codes and standards for additive construction.*

Lynette Barna *is a Research Civil Engineer at the U.S. Army Engineer Research and Development Center Cold Regions Research and Engineering Laboratory in Hanover, NH. She received her bachelor of engineering from Dartmouth College, Hanover, NH, in 1996. Her research interests include cold weather concreting and laboratory testing of materials for additive construction.*

ACI member **Peter Stynoski** *is a Research Civil Engineer at the U.S. Army ERDC-CERL in Champaign, IL. He received his BS in engineering mechanics, MS in civil engineering, and PhD in civil engineering from the University of Illinois Urbana-Champaign, Champaign, IL, in 2009, 2011, and 2015, respectively. He is a member of ACI Committees 236, Material Science of Concrete; 241, Nanotechnology of Concrete; 242, Alternative Cements; and 564, 3-D Printing with Cementitious Materials; ACI Subcommittee 562-J, Material; and Joint ACI-ASCE Committee 446, Fracture Mechanics of Concrete. His research interests include the technology transition of structural fiber-reinforced polymer (FRP) composites, bio-based construction materials, and additive construction.*

Megan Kreiger *is a Research Mechanical Engineer at the U.S. Army ERDC-CERL in Champaign, IL. She received her BS and MS in mathematics and materials science and engineering from Michigan Technological University in 2009 and 2012. She is the Program Lead for the ERDC's Additive Construction Program. Her research interests include the development and technology transition of additive construction technologies.*

ACKNOWLEDGMENTS

This project was funded in part by the Office of the Under Secretary of Defense for Research and Engineering (OUSD(R&E)) for the Automated Construction of Expeditionary Structures (ACES) Joint Capability Technology Demonstration (JCTD) and the U.S. Army Environmental Technology Program. This research was supported in part by an appointment to the Department of Defense (DOD) Research Participation Program administered by the Oak Ridge Institute for Science and Education (ORISE) through an interagency agreement between the U.S. Department of Energy (DOE) and the DOD. ORISE is managed by Oak Ridge Associated Universities (ORAU) under DOE Contract No. DE-SC0014664. All opinions expressed in this paper are the authors' and do not necessarily reflect the policies and views of DOD, DOE, or ORAU/ORISE.

NOTATION

$E_{E,D}$ = elastic modulus of dry printable mixtures (upper limit)
$E_{E,W}$ = elastic modulus of wet printable mixtures (lower limit)
$E_{P,D}$ = plastic modulus of dry printable mixtures (upper limit)
$E_{P,W}$ = plastic modulus of wet printable mixtures (lower limit)
$\sigma_{E,D}$ = stress at elastic upper limit (dry)
$\sigma_{E,W}$ = stress at elastic lower limit (wet)
$\sigma_{P,D}$ = stress at plastic upper limit (dry)
$\sigma_{P,W}$ = stress at plastic lower limit (wet)

REFERENCES

1. Diggs-McGee, B. N., and Kreiger, E. L., "Using Isolated Temporal Analysis to Aid in the Assessment of Structural Element Quality for Additive Construction," *Standards Development for Cement and Concrete for Use in Additive Construction*, S. Z. Jones and E. L. Kreiger, eds., 2021, pp. 117-143.

2. Kreiger, E. L.; Kreiger, M. A.; and Case, M. P., "Development of the Construction Processes for Reinforced Additively Constructed Concrete," *Additive Manufacturing*, V. 28, Aug. 2019, pp. 39-49. doi: 10.1016/j.addma.2019.02.015

3. Jagoda, J. A., "An Analysis of the Viability of 3D-Printed Construction as an Alternative to Conventional Construction Methods in the Expeditionary Environment," master's thesis, Air Force Institute of Technology, Wright-Patterson Air Force Base, OH, 2020, 120 pp.

4. Buswell, R. A.; Leal de Silva, W. R.; Jones, S. Z.; and Dirrenberger, J., "3D Printing Using Concrete Extrusion: A Roadmap for Research," *Cement and Concrete Research*, V. 112, Oct. 2018, pp. 37-49. doi: 10.1016/j.cemconres.2018.05.006

5. Le, T. T.; Austin, S. A.; Lim, S.; Buswell, R. A.; Gibb, A. G. F.; and Thorpe, T., "Mix Design and Fresh Properties for High-Performance Printing Concrete," *Materials and Structures*, V. 45, No. 8, Aug. 2012, pp. 1221-1232. doi: 10.1617/s11527-012-9828-z

6. Suiker, A. S. J.; Wolfs, R. J. M.; Lucas, S. M.; and Salet, T. A. M., "Elastic Buckling and Plastic Collapse during 3D Concrete Printing,"

Cement and Concrete Research, V. 135, Sept. 2020, Article No. 106016. doi: 10.1016/j.cemconres.2020.106016

7. Roussel, N., "Rheological Requirements for Printable Concretes," *Cement and Concrete Research*, V. 112, Oct. 2018, pp. 76-85. doi: 10.1016/j.cemconres.2018.04.005

8. Wu, Y.; Liu, C.; Liu, H.; Zhang, Z.; He, C.; Liu, S.; Zhang, R.; Wang, Y.; and Bai, G., "Study on the Rheology and Buildability of 3D Printed Concrete with Recycled Coarse Aggregates," *Journal of Building Engineering*, V. 42, Oct. 2021, Article No. 103030. doi: 10.1016/j.jobe.2021.103030

9. Wolfs, R. J. M.; Bos, F. P.; and Salet, T. A. M., "Early Age Mechanical Behaviour of 3D Printed Concrete: Numerical Modelling and Experimental Testing," *Cement and Concrete Research*, V. 106, Apr. 2018, pp. 103-116. doi: 10.1016/j.cemconres.2018.02.001

10. Panda, B.; Lim, J. H.; and Tan, M. J., "Mechanical Properties and Deformation Behaviour of Early Age Concrete in the Context of Digital Construction," *Composites Part B: Engineering*, V. 165, May 2019, pp. 563-571. doi: 10.1016/j.compositesb.2019.02.040

11. Voigt, T.; Malonn, T.; and Shah, S. P., "Green and Early Age Compressive Strength of Extruded Cement Mortar Monitored with Compression Tests and Ultrasonic Techniques," *Cement and Concrete Research*, V. 36, No. 5, May 2006, pp. 858-867. doi: 10.1016/j.cemconres.2005.09.005

12. Zhang, Y.; Zhang, Y.; Liu, G.; Yang, Y.; Wu, M.; and Pang, B., "Fresh Properties of a Novel 3D Printing Concrete Ink," *Construction and Building Materials*, V. 174, June 2018, pp. 263-271. doi: 10.1016/j.conbuildmat.2018.04.115

13. Hou, S.; Duan, Z.; Xiao, J.; and Ye, J., "A Review of 3D Printed Concrete: Performance Requirements, Testing Measurements and Mix Design," *Construction and Building Materials*, V. 273, Mar. 2021, Article No. 121745. doi: 10.1016/j.conbuildmat.2020.121745

14. Kreiger, E.; Diggs-McGee, B.; Wood, T.; MacAllister, B.; and Kreiger, M., "Field Considerations for Deploying Additive Construction," *Second RILEM International Conference on Concrete and Digital Fabrication: Digital Concrete 2020*, F. P. Bos, S. S. Lucas, R. J. M. Wolfs, and T. A. M. Salet, eds., Springer, Cham, Switzerland, 2020, pp. 1147-1163.

15. Tripathi, A.; Nair, S. A.O.; and Neithalath, N., "A Comprehensive Analysis of Buildability of 3D-Printed Concrete and the Use of Bi-Linear Stress-Strain Criterion-Based Failure Curves Towards Their Prediction," *Cement and Concrete Composites*, V. 128, Apr. 2022, Article No. 104424.

16. Kaplan, D.; de Larrard, F.; and Sedran, T., "Avoidance of Blockages in Concrete Pumping Process," *ACI Materials Journal*, V. 102, No. 3, May-June 2005, pp. 183-191.

17. Wangler, T.; Pileggi, R.; Gürel, S.; and Flatt, R. J., "A Chemical Process Engineering Look at Digital Concrete Processes: Critical Step Design, Inline Mixing, and Scaleup," *Cement and Concrete Research*, V. 155, May 2022, Article No. 106782. doi: 10.1016/j.cemconres.2022.106782

18. Roussel, N., "A Thixotropy Model for Fresh Fluid Concretes: Theory, Validation and Applications," *Cement and Concrete Research*, V. 36, No. 10, Oct. 2006, pp. 1797-1806. doi: 10.1016/j.cemconres.2006.05.025

19. Rodriguez, F. B.; Olek, J.; Moini, R.; Zavattieri, P. D.; and Youngblood, J. P., "Linking Solids Content and Flow Properties of Mortars to Their Three-Dimensional Printing Characteristics," *ACI Materials Journal*, V. 118, No. 6, Nov. 2021, pp. 371-382.

20. Tay, Y. W. D.; Qian, Y.; and Tan, M. J., "Printability Region for 3D Concrete Printing Using Slump and Slump Flow Test," *Composites Part B: Engineering*, V. 174, Oct. 2019, Article No. 106968. doi: 10.1016/j.compositesb.2019.106968

21. Zhang, Y.; Zhang, Y.; She, W.; Yang, L.; Liu, G.; and Yang, Y., "Rheological and Harden Properties of the High-Thixotropy 3D Printing Concrete," *Construction and Building Materials*, V. 201, Mar. 2019, pp. 278-285. doi: 10.1016/j.conbuildmat.2018.12.061

22. Roussel, N.; Buswell, R.; Ducoulombier, N.; Ivanova, I.; Kolawole, J. T.; Lowke, D.; Mechtcherine, V.; Mesnil, R.; Perrot, A.; Pott, U.; Reiter, L.; Stephan, D.; Wangler, T.; Wolfs, R.; and Zuo, W., "Assessing the Fresh Properties of Printable Cement-Based Materials: High Potential Tests for Quality Control," *Cement and Concrete Research*, V. 158, Aug. 2022, Article No. 106836. doi: 10.1016/j.cemconres.2022.106836

23. ACI Committee 211, "Guide to Selecting Proportions for Pumpable Concrete (ACI 211.9R-18)," American Concrete Institute, Farmington Hills, MI, 2018, 51 pp.

24. Haach, V. G.; Vasconcelos, G.; and Lourenço, P. B., "Influence of Aggregates Grading and Water/Cement Ratio in Workability and Hardened Properties of Mortars," *Construction and Building Materials*, V. 25, No. 6, June 2011, pp. 2980-2987. doi: 10.1016/j.conbuildmat.2010.11.011

25. Hu, J., and Wang, K., "Effects of Size and Uncompacted Voids of Aggregate on Mortar Flow Ability," *Journal of Advanced Concrete Technology*, V. 5, No. 1, 2007, pp. 75-85. doi: 10.3151/jact.5.75

26. API Specification 13A, "Specification for Drilling Fluids Materials," 18th edition, American Petroleum Institute, Washington, DC, 2010.

27. ASTM C926-22, "Standard Specification for Application of Portland Cement-Based Plaster," ASTM International, West Conshohocken, PA, 2022, 14 pp.

28. ASTM C270-19, "Standard Specification for Mortar for Unit Masonry," ASTM International, West Conshohocken, PA, 2019, 14 pp.

29. ASTM C476-20, "Standard Specification for Grout for Masonry," ASTM International, West Conshohocken, PA, 2020, 4 pp.

30. Kosmatka, S. H., and Wilson, M. L., *Design and Control of Concrete Mixtures: The Guide to Applications, Methods, and Materials*, Engineering Bulletin 001, 15th edition, Portland Cement Association, Skokie, IL, 2011, 460 pp.

31. Koehler, E. P., and Fowler, D. W., "Development of a Portable Rheometer for Fresh Portland Cement Concrete," ICAR Report No. 105-3F, International Center for Aggregates Research, The University of Texas at Austin, Austin, TX, Aug. 2004, 328 pp.

32. ACI Committee 305, "Guide to Hot Weather Concreting (ACI 305R-20)," American Concrete Institute, Farmington Hills, MI, 2020, 28 pp.

33. ACI Committee 306, "Guide to Cold Weather Concreting (ACI 306R-16)," American Concrete Institute, Farmington Hills, MI, 2016, 24 pp.

ACI MATERIALS JOURNAL TECHNICAL PAPER

Title No. 121-M17

Ultra-High-Performance Concrete with Micro- to Nanoscale Reinforcement

by Zainab Hashim Abbas Alsalami and Fatima Hashim Abbas

Ultra-high-performance concrete (UHPC) is considered a sophisticated concrete construction solution for infrastructure and other structures because of its premium mechanical traits and superior durability. Fibers have a special effect on the properties of UHPC, especially as this type of concrete suffers from high autogenous shrinkage due to its high cementitious content, so the properties and volume fraction of fibers are more important in UHPC. This study will describe previous related works on the mechanical behavior of UHPC specimens reinforced with micro- and nanoscale fibers, and compare of the behavior of UHPC reinforced with microfibers to that reinforced with nanofibers. The compressive strength, flexural behavior, and durability aspects of UHPC reinforced with nano- and/or microscale variable types of fibers were studied to highlight the issues and make a new direction for other authors.

Keywords: compressive strength; durability; flexural strength; macro glass fiber (MGF); nano aluminum fiber; nano steel fiber; ultra-high-performance concrete (UHPC).

INTRODUCTION

Ultra-high-performance concrete (UHPC) has superior mechanical and durability properties in comparison with conventional concrete. Also, it is considered an advanced cement-based composite material (Russell and Graybeal 2013).

Researchers are widely interested in UHPC due to its commercial use. In other words, implementation of UHPC has been felicitously proven in different nations, but its extensive application is still restricted because of enormous hurdles, including scarceness of comprehension of the structural behavior, procedures on material characterization, and ordinarily agreeable design codes. The opportunity to develop low-weight and slender structures is one driving issue for greater use (Yoo and Banthia 2016). Also, maintenance costs and the environmental footprint are dramatically lowered.

Furthermore, researchers found that it is possible to produce eco-effective UHPC by the fractional alteration of silica fume (SF) and portland cement by fly ash (FA), ground-granulated blast-furnace slag (GGBS), metakaolin (MK), and rice husk ash (RHA) to compose UHPC with commensurate mechanical achievement and durability traits. Besides, the embodiment of these supplementary cementitious materials (SCMs) was perceived to be effective in reducing the high autogenous shrinkage of UHPC (Ghafari et al. 2015).

A major component in UHPC is noncontinuous fiber reinforcement. The embodiment of fibers is required for structural integrity by imposing the ductility in compression. Fibers control brittle behavior and might also promote various extra characteristics—for example, they provide employable tensile strength and raise the energy absorption range. Many types of fibers are employed, diverse in size, pattern, and substance. Several factors prompt fluctuations in the distribution and orientation of the fibers, including the rheological features of the fresh UHPC, the placement means, and the geometrical situations molded by the formwork. Alterations in fiber content, geometry, combination, distribution, and orientation are all central contributors to making the structural design of UHPC complex. Fibers are also one of the biggest contributors to the extraordinary unit cost and carbon footprint of UHPC. Consequently, shining light on the impacts of fiber reinforcement is an imperative step toward the advancement of regularly trusted design codes and the unrestricted use of UHPC (Larsen and Thorstensen 2020).

The incorporation of a sole sort of fiber as reinforcement in a cementitious composite has been widely demonstrated. Although the use of fibers in cement-based mixtures does not have much effect on their compressive strength, their remaining strength after a fire occurs is clearly enhanced by employing fiber as reinforcement (Al Qadi and Al-Zaidyeen 2014). On the other hand, investigators found that fibers had abilities to prevent and disconnect the mechanisms of split initiation and growth by working as stress-conveying bridges so that the use of fibers improves the plasticity of the crack tip, which raises the split toughness of the composite and prohibits the expansion of available and/or commenced cracks (Khan et al. 2014).

Numerous researchers explain the favored use of fiber hybridization in comparison to singular fibers, which have been assigned to the synergetic interactions of hybrid fibers. Khan et al. (2017) demonstrated that various artificial fibers have been integrated in hybrid or mono cases to promote several characteristics such as strain capacity, tensile strength, dimension stability, impact resistance, abrasion resistance, and modulus of elasticity.

In general, the ductility of a fiber-reinforced composite is lessened when the cementitious matrix's strength increases. Therefore, enhancing the ductility of fiber-reinforced composites is often claimed to reduce the strength of the cementitious matrix (Ranade et al. 2011). However, this decline in strength can lead to agreed durability traits.

ACI Materials Journal, V. 121, No. 2, March 2024.
MS No. M-2021-335.R3, doi: 10.14359/51740369, received March 30, 2023, and reviewed under Institute publication policies.

As a result, researchers have tried a different approach to boost ductility by increasing fiber volume; however, this can have a big effect on price and substance treatment. They also discovered that adding nanofibers to the cement matrix could increase the cement matrix's tensile strength, improving the composite's mechanical properties even further. An extra-powerful and extended-lasting highway mode can be accomplished by incorporating all of these corporealities and principles and employing the outcoming substance in essential infrastructure components (Muzenski et al. 2020a).

The use of nano-sized reinforcement was also investigated (Vera-Agullo et al. 2009; Zhao et al. 2020), primarily in the form of carbon nanofibers (CNFs) and nanotubes (CNTs) (Konsta-Gdoutos et al. 2010) and otherwise cellulose nanofibers, which have proven successful in contributing supplementary functionalities, such as increased resistance to corrosion (Konsta-Gdoutos et al. 2017), in addition to fulfilling their reinforcing effectiveness at the scale of the powerful crystalline composition of the material capacity to self-cure and self-sense (Materazzi et al. 2013; D'Alessandro et al. 2016), as well as improving durability in the cracked condition (Cuenca et al. 2021a)—in other words, promoting and improving autogenous self-healing ability (Cuenca et al. 2021b).

The mechanical properties of UHPC are covered in a few review articles (Yoo and Banthia 2016; Shi et al. 2015, 2019; Shaikh et al. 2020); also, there has been little research concern on the impact of micro- or nanofibers on the features of concrete or mortar. On the other hand, there were a few researchers concentrated on the effect of micro- or nanoscale fiber on the properties of UHPC.

RESEARCH SIGNIFICANCE

The target of this paper is to manifest the more modern research outcomes about the effect of incorporating various types of micro- and nanoscale fibers in UHPC on the mechanical properties of this type of concrete. Also, this paper compares the behavior of using micro- and nanoscale fibers in UHPC to make new direction for future authors.

RELATED WORKS

Studies were performed on the compressive strength, flexural response, bond strength, and some durability properties of micro-/nanofiber UHPC. A summary of materials, reinforcement properties, fiber-volume fraction, and tests in the studies is explained in Table 1.

Compressive strength

Researchers (Muzenski et al. 2020a; Meng and Khayat 2016; Hisseine et al. 2020; Mohammed et al. 2021; Song et al. 2020) studied the effect of micro- or nanofibers on the compressive strength of UHPC; they observed, as explained in Table 2, that the compressive strength of a specimen increased with a rise in the volume of fibers up to a certain limit. That behavior could be attributed to some types of nanofibers, such as alumina (Al_2O_3) nanofiber (ANF) and CNF, acting as seeding and promoting nucleation, thus creating a calcium-silicate-hydrate (C-S-H) with a thick structure. This is also due to the bridging effect of the nano- or microfibers on microcracks. Despite that, the high dose of nano- or microfibers led to fiber agglomeration and reduced slump flow, requiring more high-range water-reducing admixture (HRWRA) to produce a more workable mixture—but that can cause the problem of entrapped air released by the interaction of HRWRA with some types of nanofibers, such as nano-cellulose fiber (CF).

Jung et al. (2020) estimated the impact of curing methods on the compressive strength of UHPC reinforced with CNT fiber; they found that the compressive strength of UHPFRC/CNT-EC specimens—that is, those cured by electrical curing—was higher than the strength of specimens cured by steam curing (UHPFRC-SC).

Figure 9 illustrates the difference between the effect of nano- and microscale fibers of variable types on UHPC's compressive strength from numerous authors. Nearly identical percentages of volume fraction of nanofibers, as well as that of microscale fiber, were chosen to be a more suitable comparison. It was clear that the nanoscale fibers at small dosages had a more positive effect on strength than microscale fibers at a higher volume fraction, even if the raw materials of nanoscale fibers have less strength than microscale fibers. Furthermore, the highest strength was for UHPC reinforced with CNTs with 0.244% by weight of cementitious materials at 28 days of electrical curing, which was equal to 188 MPa.

Flexural behavior and bond strength

Researchers (Muzenski et al. 2020a; Meng and Khayat 2016; Hisseine et al. 2020; Mohammed et al. 2021; Chun and Yoo 2019; Yoo et al. 2014) studied the effect of micro- or nanofibers on the flexural behavior of UHPC; they observed, as shown in Table 3, that the flexural capacity of specimens increased with the rising volume of fibers up to a certain limit. Furthermore, some described that UHPC without or with a very small amount of nanomaterials shows softening behavior, but with a sufficient amount of nanofiber, the UHPC had hardening behavior under tensile load. This trend might be due to nanofibers enhancing the density of the matrix while also disrupting fissure replication at the C-S-H stage, allowing for the formation of larger cracks to be delayed. Others (Meng and Khayat 2016) found that using graphite nanoplatelets (GNPs) in UHPC could enhance the pullout strength and pullout energy of steel fiber in that concrete. That behavior could be attributed to the existence of nanoplatelets, which may serve as additional sources for hydrate nucleation. The slipping of steel fibers in UHPC patterns can allow particle scratch in the fiber tunnel, particle wedging, fiber scraping, and partial or complete delamination of the brass covering, which can improve coarseness and bonding between steel fibers and the UHPC pattern. This is in agreement with Yoo et al. (2014), who also declined that the bond strength increases with the increase in micro steel fiber amount through an upgrade in the fiber bridging function.

Figure 19 illustrates the difference between the effect of nano- and microscale fibers of variable types on the flexural strength of UHPC from different authors. The volume fraction of nano- and microscale fibers was chosen at nearly the same percentages to provide a more suitable comparison. The

Table 1—Summary of experimental programs of research studies

Authors	Structure	Reinforcement properties	Volume fractions	Materials	Parameter studied
Muzenski et al. (2020a)	50.8 mm cubes for compressive strength, 160 x 14 x 40 mm beams for flexural strength	Pure crystalline ANFs with surface area of 155 m^2/g were used in the study. Tensile strength of the fiber's single crystal and modulus are 12 and 400 GPa, respectively. Average fiber diameter is 10 to 20 nm, and fibers are sold in 50 mm lengths. Density, length, diameter, tensile strength, and modulus of polyethylene fibers was 970 kg/m^3, 12 mm, 12 to 21 mm, 3.6 GPa, and 116 GPa, respectively. Polyvinyl alcohol (PVA) fibers measured 8 mm in length, 15 dtex in thickness, 40 µm in diameter, 40 GPa in Young's modulus, and 1.6 GPa in tensile strength.	ANFs, 0.5% by mass of cementitious materials (CM); 2% by vol. PVA or HDPE	Cement, SF, silica sand, HRWRA, superhydrophobic admixtures (polymethylhydrosiloxane [PMHS]-based admixtures), and water	Compressive strength based on ASTM C109/C109M with a 1.4 kN/s loading rate; flexural behavior based on ASTM D7264/D7264M with 1.2 mm/min displacement rate.
Meng and Khayat (2016)	50 mm cubes; 76 x 76 x 305 mm beams for flexural test	CNFs with 100 nm diameter and 50 to 200 nm length; GNP-C (graphite nanoplatelets) with 25 nm diameter and 2 to 10 nm thickness; GNP-M with 30 nm diameter and 2 to 10 nm thickness; tensile strength of 30, 5, and 5 GPa for CNF, GNP-C, and GNP-M, respectively; 0.5% steel microfibers	0.05, 0.1, 0.15, 0.2, and 0.3	Cement, river sand, SF, FA, HRWRA, and water	Compressive strength based on ASTM C109/C109M at 1.8 kN/min; flexural behavior based on ASTM C1609/C1609M with a 0.05 mm/min displacement rate and single-fiber pullout strength: a steel fiber with a definite length was entrenched in 50 mm cube samples (tested mixtures were UHPC with 0.15% GNP-C, 0.30% GNP-C, and reference mixture), which were firmly confined by special arrangement of steel frame. Half of steel fiber was inside cube and other half of fiber was held by the frame to supply tensile load. Moreover, displacement rate of test was 0.05 mm/min.
Hisseine et al. (2020)	50 x 50 x 50 mm cubes for compressive strength; 100 x 100 x 400 mm prisms for flexural strength; 80 x 80 x 350 mm prisms for autogenous shrinkage	CFs made up of mechanistically treated cellulose fibers with 30 to 400 nm and 100 to 2000 µm length, aspect ratio of 100 to 1000, and surface area greater than 80 m^2/g	Nanoscale CFs (at 0, 0.15, and 0.30% per cement mass)	High-sulfate-resistant cement, SF, quartz sand, high-alkali ground-glass pozzolan, HRWRA, and water	Compressive strength based on ASTM C109/C109M, flexural strength based on ASTM C78/C78M with displacement rate of 0.05 mm/min, and autogenous shrinkage based on ASTM C157/C157M.
Mohammed et al. (2021)	Mechanical characteristics and ductility behavior were measured with 50 mm cube, 70 mm cube, 150 mm cube, and 70 x 70 x 280 mm prism	Micro glass with length of 13 mm, diameter of 18 mm, aspect ratio of 722, and tensile strength of 2000 MPa	0, 0.5, 1,1.5, 2, 2.5, and 3	Cement, SF, quartz sand, HRWRA, and water	Compressive strength test based on BS 1881-116, tensile strength test based on BS 1881-117, and fracture energy based on RILEM (1985).
Chun and Yoo (2019)	Specimens with dog-bone shape had a cross-sectional area of 25 x 25 mm for pullout measurement. Specimens with 30 x 13 mm cross section were used for measuring direct tensile strength	SS, S, H, and T represented micro and macro straight steel fiber, macro hooked steel fiber, and macro twisted steel fiber, respectively, and their aspect ratios were 65, 100, 80, and 100, respectively, with tensile strengths of 2788, 2580, 2900, and 2428 MPa, respectively.	At a constant total volume portion of 2%, microfibers were used to supplant some of the macrofibers. Ultra-high-performance hybrid fiber-reinforced concrete (UHP-HFRC) was created using macro-to-micro fiber substitution ratios of 0, 0.5, 1.0, 1.5, and 2.0%.	SF, silica flour, silica sand, cement, HRWRA, and water	Bond strength (pullout test) was tested by applying a uniaxial pullout load on dog-bone-shaped paradigms by employing a universal testing machine (UTM) with a 0.018 mm/s rate of displacement. Post-cracking strength was based on JSCE (2004) by employing a UTM with a 0.4 mm/min rate of displacement. Moreover, to identify microcracks with the naked eye, polyurethane was sprayed two to three times on specimens at the end of tensile inspections (Park et al. 2012).

Table 1 (cont.)—Summary of experimental programs of research studies

Authors	Structure	Reinforcement properties	Volume fractions	Materials	Parameter studied
Song et al. (2020)	1 cm cube for X-ray diffraction (XRD) test. Mercury intrusion porosimetry (MIP) test has pore size range of 6 nm to 360 μm.	0.2 mm diameter and 13 mm length straight steel fiber.	Steel-fiber ratios were 0, 0.5, 1.0, 1.5, 2.0, 2.5, and 3.0% by volume	River sand, SF, cement, and FA	Compressive rate loss based on EN 196-1 (2005), XRD with an X-ray diffractometer, and pore distribution with a mercury porosimeter.
Yoo et al. (2014)	150 x 150 x 150 mm specimens for free shrinkage, pullout test on 150 mm cubic samples with unique reinforcing bar inserted vertically along centerline, and 100 x 100 x 400 mm notched beam specimens for flexural strength	Smooth fiber with 0.2 x 13 mm diameter x length, aspect ratio of 65, and 2500 MPa tensile strength.	1, 2, 3, and 4% steel microfibers	Cement, SF, sand, silica flour, HRWRA, and water	Shrinkage was inspected with strain gauge placed in middle of form; a layer of polytetrafluoroethylene (PTFE) was placed inside form to diminish the friction of interfaces between concrete and form; bond strength based on RILEM TC (1983) and flexural strength based on JCI-S-001-2003 (2003).
Muzenski et al. (2020b)	Compressive test with 50.8 mm cube and flexural test with 14 x 40 x 160 mm prism	Chemically pure crystalline alumina fibers with surface area of 155 m^2/g were used as ANFs. Fibers' single crystal tensile strength was 12 GPa, and its modulus was 400 GPa. The fiber diameter was usually 10 to 20 nm.	Nanofibers 0.5% by mass of cementitious material	Type I and Type V portland cement, SF, MK, HRWRA, and water	Compressive strength based on ASTM C109/C109M with 1.4 kN/s loading rate and flexural behavior per ASTM D7264/D7264M with 1.2 mm/min displacement rate.
Jung et al. (2020)	50 mm cubic molds. Two copper panels with dimensions of 20 x 60 x 0.4 mm were installed into the specimens as electrodes to assess variations in electrical resistance during the curing process.	CNTs with diameter of 1 to 8 nm, length of 0.1 to 5 mm, and specific surface area of 180 $\mu m^2/g$.	CNTs 0.245 wt. of cement, 2 vol % steel fiber	Silica sand, SF, silica powder, cement, HRWRA, and water	Compressive strength was inspected with UTM based on ASTM C109/C109M. Two strain gauges were attached to specimen surface, one on each side, and were connected to data logger to measure compressive strain.
Cuenca et al. (2021c)	100 mm cubes for compressive strength; 500 mm length x 100 mm width beams with thicknesses of 100 and 25 mm for deep and thin beams, respectively, were used for four-point bending tests	Calcium, oxygen, silicon, magnesium, aluminum, and potassium, among other chemical constituents, are found in CAs, which is made up of irregularly shaped particles of sizes varying from 1 to 20 μm. ANFs used in this study were supplied in an aqueous suspension at a concentration of 10%. Their lengths ranged from 100 to 900 nm and diameters ranged from 4 to 11 nm, with a surface area of 155 m^2/g.	0.25% by cement mass of ANFs, 4.8 kg/m^3 of CA, 1.5% by vol. straight steel fibers with 20 x 0.22 mm length and diameter, respectively	Cement, slag, crushed sand, HRWRA, and water	Self-healing performance was investigated by inspection of mechanical performance, water permeability, and by analyzing crack closure image.

Table 2—Compressive strength

Authors	Parameter studied	Results
Muzenski et al. (2020a)	Compressive strength	Figure 1 illustrates the compressive capacity effects. Samples with ANFs had compressive strength exceeding 150 MPa after 270 days. It could also be shown that even a small quantity of nanofibers can result in a substantial increase in compressive strength at whole hardening age. The rise in compressive strength could be due to the nanofibers' seeding influence (Muzenski et al. 2019). This impact would encourage the nucleation and construction of C-S-H with a denser structure. Consequently, nanofibers can elaborate as reinforcement for the C-S-H, mitigating microcracking and flexibility of the C-S-H layers (He and Shi 2008).
Meng and Khayat (2016)	Compressive strength	From Fig. 2, the compressive strength of the UHPC increases mildly (5 to 8 MPa) as the nanomaterial content increases. The rise in compressive strength can be assigned to the function of CNFs and GNPs in the bridging of micro-fissures and the filling of pores, as well as speeding the hydration processes of cementitious substances (Han et al. 2015). GNP-C had significantly better compressive strength of the UHPC than the CNFs and GNP-M.
Hisseine et al. (2020)	Compressive strength	From Fig. 3, compressive strength increased with an increase in nanoscale CFs up to 0.3%, which led to a negative influence on the strength. This negative effect can be attributed to the complexity of ensuring sufficient dispersion when CF loading is high. The study found that a percolated network of nanoscale filaments was established by increasing the CF loading (Hisseine et al. 2018a). To reach the objective slump flow, this network raises the mixture requirement in HRWRA. A greater HRWRA content in CF systems can cause interactions between CFs and HRWRA, causing more air to be trapped and negatively affecting the compressive strength.
Mohammed et al. (2021)	Compressive strength	Figure 4 shows that increasing fiber content until 1.5% results in an efficient increase in strength; however, above this fiber content, strength enhancement remains constant, regardless of water-binder ratio (*w*/*b*) or age. There was no impact on compressive strength when the amount of micro glass fiber (MGF) was raised by more than 1.5%. The aforementioned operation may be due to elevated fiber pieces. In other words, a huge magnitude of fibers could lead to microvoid formation in the concrete throughout the mixing process, resulting in a decline in strength enhancement due to the presence of more fibers.
Song et al. (2020)	Compressive strength	The compressive strength degradation rate (*Ks*) of UHPFRC samples subjected to three distinct marine environments for 3 months as depicted in Fig. 5. To begin, the *Ks* of the UHPFRC cured in raised-temperature seawater was found to be larger than that of the samples cured in wetting-and-drying cycles in seawater. Even so, the *Ks* raised due to an increase in the amount of added fiber. The increase in *Ks* was particularly noticeable when there was an increase in fiber bulk from 1.5 to 2 vol %. This finding, however, did not match the UHPFRC samples subjected to wetting-and-drying cycles in seawater. The *Ks* value was almost constant when the bulk of additional fibers was lighter than 2%. On the contrary, when the bulk of attached fibers was greater than 2 vol %, the *Ks* proportion noticeably improved. The level of ion erosion in the UHPFRC samples could explain the aforementioned phenomena. The compressive strength of the UHPFRC samples was reduced proportionally when the ion erosion degree was relatively high. First, as opposed to wetting-and-drying cycles and standard seawater, raised-temperature seawater had the greatest effect on ion promulgation, resulting in compressive strength retrogression for the UHPFRC samples. Besides this, the addition of steel fiber, which was conductive to the intrusion of ions, would disrupt and deteriorate the dense system of UHPFRC samples. As a result, a rise in the number of added fibers will lower the *Ks* of UHPFRC after treatment in raised-temperature seawater. Furthermore, based on the findings of the previous research (Song et al. 2018), it was observed that as the fiber volume increased, the linked steel fiber increased as well, resulting in electrochemical corrosion in the UHPFRC with comparatively altitudinal steel-fiber material. This may explain why, after treatment in wetting-and-drying cycles in seawater, the *Ks* of UHPFRC increased significantly when the bulk of attached fiber was comparably altitudinal (>2 vol %).
Muzenski et al. (2020b)	Compressive strength	The authors (Muzenski et al. 2020a) demonstrated that replacing large amounts of SF in UHPC with small amounts of ANFs will result in a more cost-effective and thus more effective UHPC material. The established material has a compressive strength of 160 MPa, according to the researchers. In other words, it is demonstrated that with very low amounts of SF, such as 1% by mass of cementitious materials, a fiber-reinforced composite with properties similar to traditional UHPC can be made. Based on previous work (Sanchez and Sobolev 2010), the ANFs are thought to serve as seeds, facilitating the nucleation of C-S-H and resulting in a denser microstructure with encased void space between the hydrating cement particles. Otherwise, more SF will have to be introduced into this vacuum.
Jung et al. (2020)	Compressive strength	Regardless of the treatment process, the UHPFRC/CNT had a higher compressive strength than the reference sample (UHPFRC-SC), as shown in Fig. 6. The UHPFRC/CNT-EC exhibited the strongest strength of 196.6 MPa, which was 8.6% higher than the UHPFRC-SC. The intense conductive route administered by electronic flow was created in the UHPFRC/CNT because the CNTs were evenly scattered across the pattern, as exhibited in Fig. 7, and obscurely associated with steel fibers in the composite (Fig. 8(b)). As a result, the matrix's initial resistance was significantly lower than the UHPFRC's and stayed relatively fixed during curing. When comparing UHPFRC/CNT cured by electrical curing (EC) to UHPFRC/CNT treated by steam curing (SC), the EC-cured UHPFRC/CNT showed even more structural improvements. During EC, the electrical scope generated in the composite possibly aroused ionic polarization as well as intensified the chemical reaction between ions, leading to a superior degree of hydration (DOH). The microscale and mesoscale fabrication of the calcium-aluminate-silicate-hydrate (C-(A)-S-H) (for example, more cross-linking places and greater fractal proportions) was further modified as a result of the electrically driven improvements in the chemical reaction of UHPFRC, resulting in augmented architectural capabilities of the UHPFRC/CNT composite.

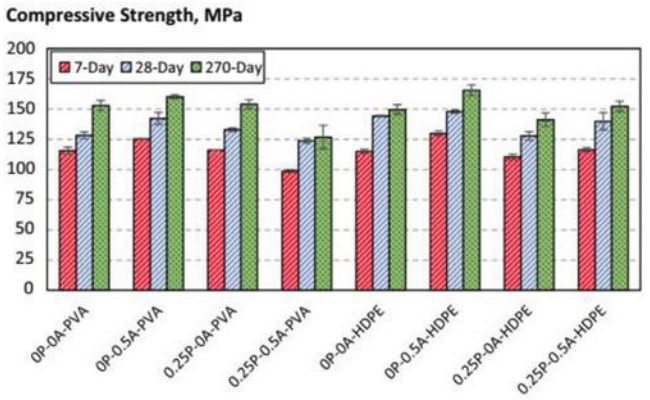

Fig. 1—Impacts of fiber reinforcement on cement-based composites' compressive strength (Muzenski et al. 2020a).

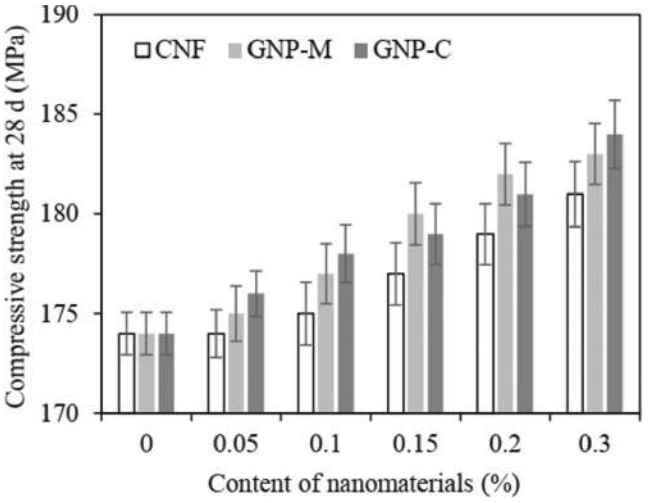

Fig. 2—Compressive strengths at 28 days (Meng and Khayat 2016).

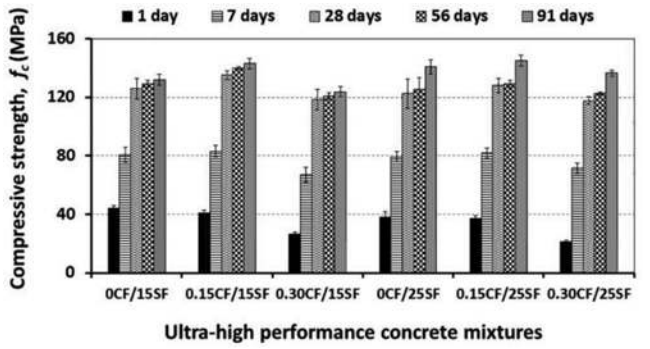

Fig. 3—Upshots of compressive strength for multiple UHPCs (Hisseine et al. 2020).

same behavior of compressive strength was noticed, but the ratio of enhancing flexural strength for nano- or microscale fibers was more valuable than that observed for compressive strength. Moreover, the highest strength was for UHPC reinforced with ANFs with a dose of 0.5% by weight of cementitious materials and 2% high-density polyethylene (HDPE) by volume at 28 days of moist curing, equal to 32 MPa.

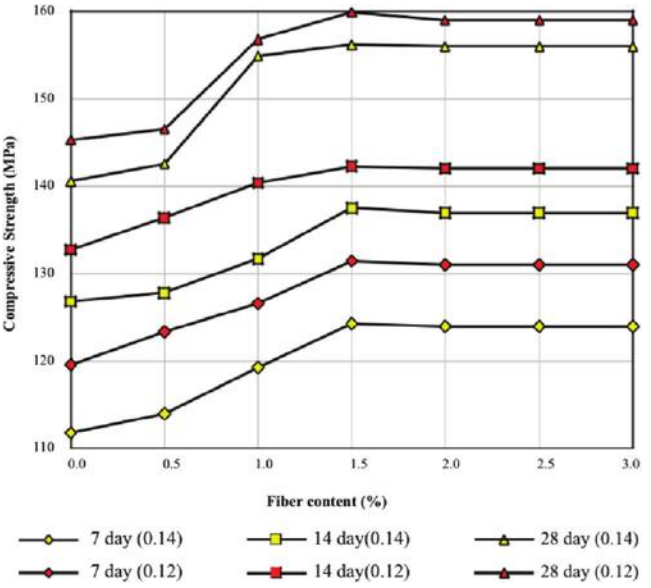

Fig. 4—Variation of compressive strength with micro glass fibers of 0.12 and 0.14 w/b UHPC at variable ages (Mohammed et al. 2021).

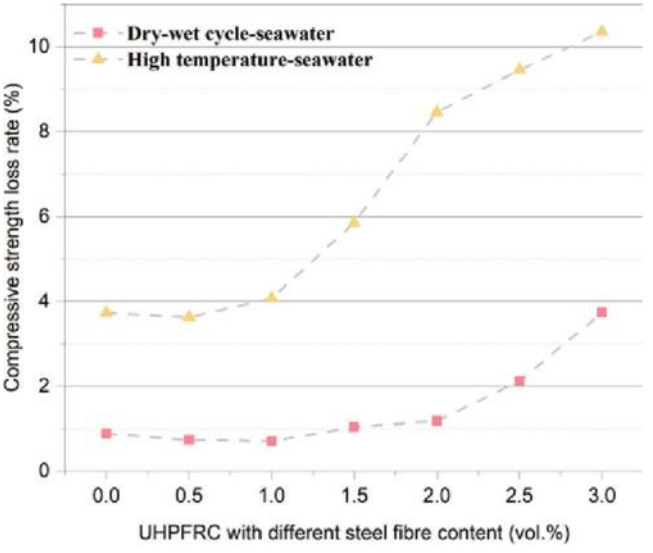

Fig. 5—Rate of compressive strength declining in UHPFRC with increasing micro steel fiber amount (Song et al. 2020).

Some durability properties

From Table 4, some authors (Cuenca et al. 2021c; Song et al. 2020; Yoo et al. 2014; Hisseine et al. 2020) demonstrated the effect of nano- or microfibers on some durability properties; they discovered that nano- or microfibers could reduce shrinkage and lead to quicker healing, both with respect to crack filling and mechanical characteristics restoration. Thus, there will be future aspirations to produce ultra-high-durability concrete by nanotechnology.

The cracking occurrence could be controlled from their initiation by the nature of very-small-size of nanofibers, which can act as reinforcement promotors. Besides, the hydrophilic nature of ANFs has enhanced the hydration of cementitious materials, thus encouraging the crack-sealing and healing retrieval processes of the interface between fibers and matrix at both macroscopic and mesoscopic

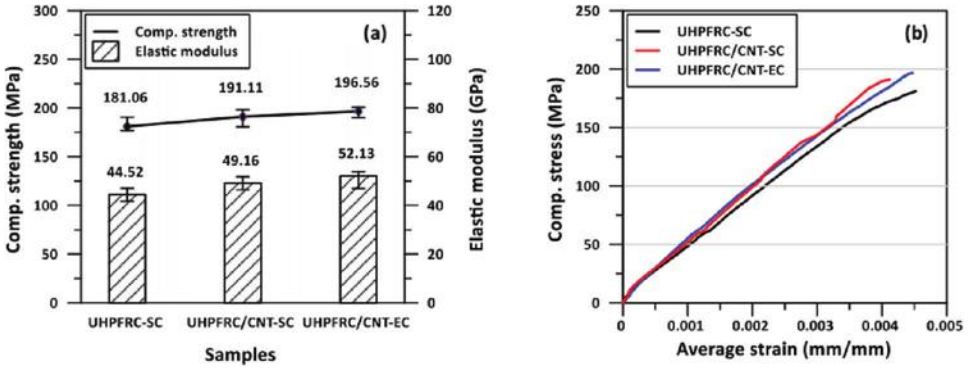

Fig. 6—Compressive strength and elastic modulus of samples: (a) synopsis of upshots; and (b) stress-strain curves (Jung et al. 2020).

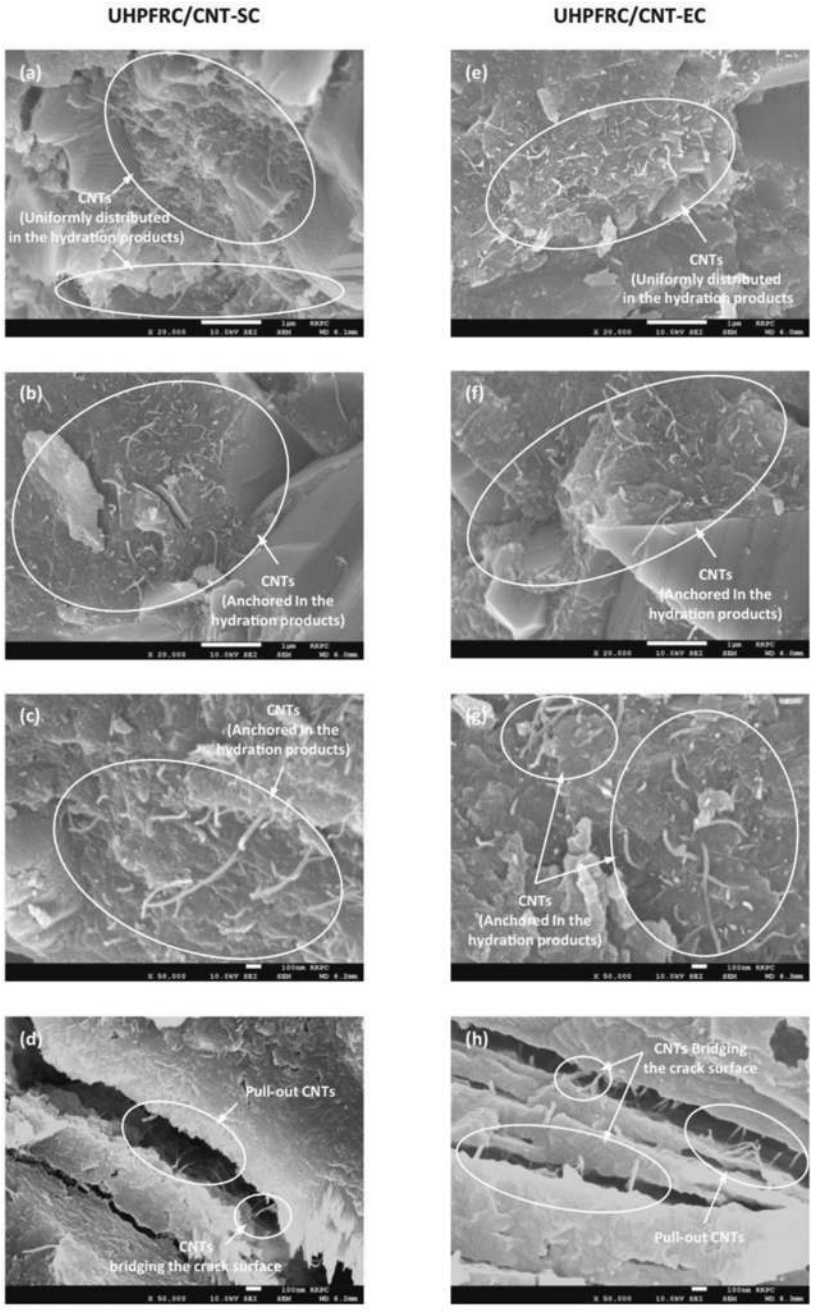

Fig. 7—SEM photographs of experiments after 28 days: (a) to (d) UHPFRC/CNT-SC; and (e) to (h) UHPFRC/CNT-EC (Jung et al. 2020).

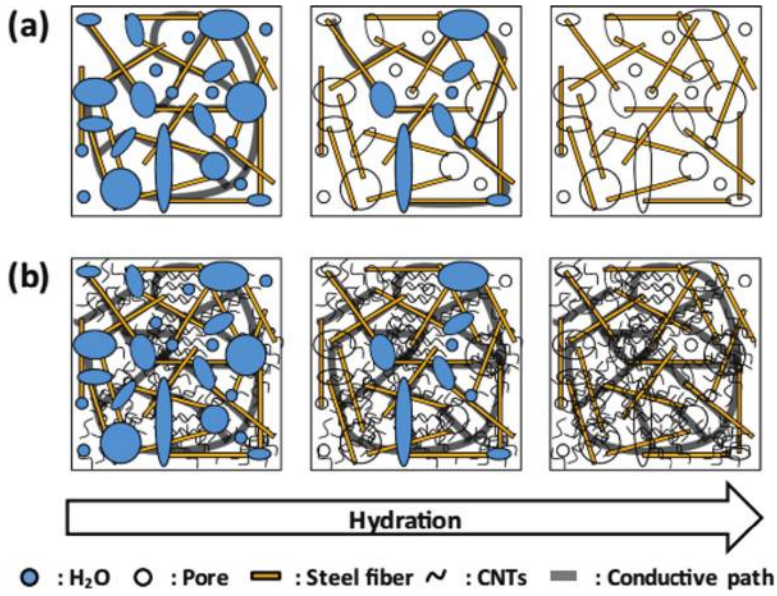

Fig. 8—Diagram of conduction variance in UHPFRC patterns throughout treatment: (a) UHPFRC; and (b) UHPFRC/CNT (Jung et al. 2020).

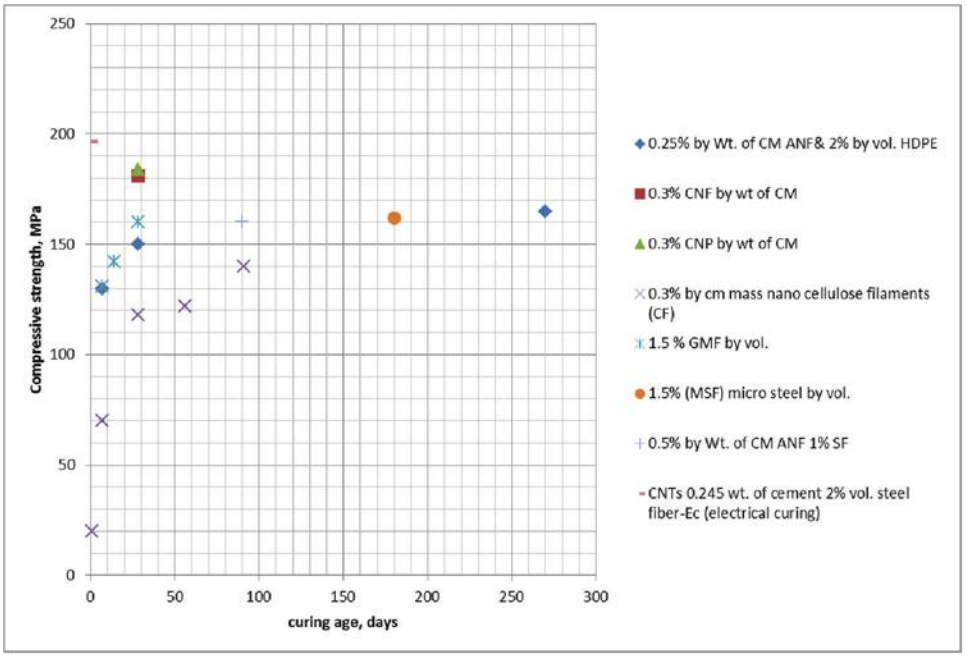

Fig. 9—Effect of different types of nano- or microscale fibers on compressive strength of UHPC from various research.

Table 3—Flexural behavior and bond strength

Authors	Parameter studied	Results
Muzenski et al. (2020a)	Flexural behavior	Figure 10 displays the flexural response of fiber-reinforced cement-based composites. Owing to the significant variations in strain, the scales vary. The UHPC pattern forms a close ligature with the fiber, and the fibers are capable of bridging the crack once it forms. A lower-strength matrix can have a weaker link between the cement pattern and the fiber, making them less capable of moving loads through cracks and having the same strain-hardening behavior. With samples containing ANFs, the improved flexural behavior is particularly noticeable. This effect could be due to the nanofibers raising the density of the pattern also stopping fissure formation at the C-S-H stage, allowing larger cracks to form for longer. The strain-hardening behavior of composites made with HDPE fibers and ANFs will be applicable to a variety of engineering applications.

Table 3 (cont.)—Flexural behavior and bond strength

Authors	Parameter studied	Results
Meng and Khayat (2016)	Flexural behavior	Figure 11 shows flexural test results, which clearly show that a softening condition was identified in UHPC samples, which created external nanomaterials or a small concentration of nanomaterials. When the GNP content in UHPC samples containing GNP-M or GNP-C reached 0.20%, a "hardening" pattern was reported. In Fig. 12, the dropout charge-gliding curves of three UHPC samples of diverse GNP-C accounts were contrasted. The implementation of nanoplatelets increases bond strength, which is linked to the alteration of the interface caused by the nanoplatelets, which can provide additional opportunities for hydrate nucleation. The chemical adhesive bond is broken when debonding occurs at the interface, so fiber pullout action is mainly determined by attrition and mechanical overlap impacts. As shown in Fig. 13(b), abrasion of particles in the fiber path caused by the gliding of steel fiber in the UHPC sample, particle squeezing, fiber tearing, and partial or complete delamination of the brass coating (Wille and Naaman 2013), which can reinforce the roughness of the steel fibers and the bond between them and the UHPC matrix. The drawn capacity, which rises with the amount of nanomaterials, is represented by the region beneath the drawn intensity-gliding curve. The various coarseness statuses of the exterior face of steel fibers and the fiber duct in the paradigm are blamed for the curve fluctuations. Figures 14(a) to (d) display a microstructure view of the rupture interfaces of samples containing 0.3% nanomaterials. In the UHPC mixture (Fig. 14(a)), fiber lumps were discovered after the CNFs were applied exclusively to the mix water without any preparation for improved dissipation. CNFs are more evenly distributed in the matrix following treatment (Fig. 14(b)). As manifested in Fig. 14(b) to (d), partly inserted CNFs and GNPs were found in the sample. The CNFs and GNPs will link the fissure interfaces as soon as microcracks appear in the matrix. The CNFs and GNPs were gradually extracted from the sample as the applied load increased, scattering energy at the nanomaterial-matrix interfaces. Linkage effects for flaws at the nano- or microscale significantly increase the cracking loads of UHPC samples, which may compensate for the connection influences of steel fibers at the mesoscale.
Hisseine et al. (2020)	Flexural strength	From Fig. 15, the behavior of flexural strength was similar to the behavior of the compressive strength. As for the impact of CF, it is more noticeable at 0.15% CF, where a 10% increase in flexural capacity (f_{fl}) was noticed, than at 0.30%, where no meaningful benefit was observed. The stronger f_{fl} in samples containing 0.15% CF could be due to matrix nanomodification caused by CF incorporation, while the subaltern impact at 0.30% CF could be due to intervention between CF's intensification effect and its downside on compressive strength caused by trapped air. CF has been shown to improve the tensile strength of concrete in other places (Hisseine et al. 2018b). Furthermore, nanoindentation assessments suggested that using CF improved the microstructure mode (Hisseine et al. 2019). According to the findings, adding CF to low-w/b mixtures (w/b = 0.30) improved the microstructure process and micromechanical features, resulting in stronger flexural efficiency and elastic modulus.
Mohammed et al. (2021)	Flexural behavior (flexural strength and fracture energy)	When MGF was applied to UHPC, it made it more ductile. The breakage intensity *Gf* raised as the amount of the MGF increased, irrespective of the w/b as illustrated in Fig. 16. The superior performance of MGFs could be traced to their interesting characteristics, such as super tensile capacity and aspect ratio, which rendered it difficult to break the patterns due to stopping fissures without a lot of energy. Also, the results demonstrated that the compressive and flexural strength increase with an MG content increase up to 1.5%. The outcomes of the mechanical attributes, on the other hand, suggested that there was no more strength gain. This may be due to the large amount of fibers per unit of bulk concrete as the fiber content rises. Furthermore, it was clear that the impact of an increasing MG fiber amount on UHPC resistance is much more advantageous than the influence of decreasing water amount. For instance, attaching 3% of fibers to explicit UHPC improved net flexural strength by 60.1% for the 0.12 w/b category, while decreasing the w/b from 0.14 to 0.12 improved net flexural strength by just 10.7% with the comparable level of MGF injection. In other words, with the introduction of 3% MGF, the net flexural strength of UHPFRC raised to 17.7 and 16 MPa, respectively, after 28 days of water treatment for the 0.12 and 0.14 w/b. The use of thin, well-distributed glass fibers to improve the relation between cement sample aggregate pieces can be referred to as increasing the modulus of rupture.

levels (Cuenca et al. 2021c). Furthermore, the incorporation of ANFs and cellulose nanocrystals (CNCs) together in UHPFRC could considerably enhance the self-healing capacity of UHPFRC submerged in geothermal water by both waterproofing retrieval (sealing of crack) and self-redress of cracks (crack rehabilitation) (Cuenca et al. 2022). Finally, Indhumathi et al. (2022) demonstrated that the combination of ANFs with crystalline admixtures in the concrete mixtures had the ability to heal cracks up to 1 mm wide.

To sum, the initiation and expansion of cracks at the nano-level were controlled by ANF additions (Muzenski et al. 2019). Besides, these nanofiber additions in the concrete worked as promoter agents to improve the cement paste matrix (Muzenski et al. 2019; Li et al. 2006). In other words, the existence of hydroxyl groups on the surface of ANFs could quicken the hydration process of cement, thus providing greater volumes of reaction outcomes. Moreover, they were working as filler agents, compacting the microstructure, thus reducing the porosity of the mixture (Gopalakrishnan and Jeyalakshmi 2018; Sanchez and Sobolev 2010; Li et al. 2006).

Table 3 (cont.)—Flexural behavior and bond strength

Authors	Parameter studied	Results
Chun and Yoo (2019)	Post-cracking strength and bond strength (pullout test)	From Fig. 17 and 18, in macro straight fiber situations, increasing the replacement ratio resulted in a reduction in post-crushing strength, thus increasing the average fastening power. Furthermore, although the *g*-value was decreased, the normalized drawn energy was enhanced. In the case of straight fibers, the fastening territory between the fiber and matrix was the most important assistant that influenced the tensile and adhesive strengths. The tilt angle of the fiber was artificially anchored to zero in the pullout experiments, and the amount of fibers was measured solely by the volume portion, which was originally thought to be 2%. It was well-prepared; nevertheless, it did not accurately represent the conduct of composites under tension stress. Because the genuine number of fibers present at the shattered surface was not equivalent to the volume fraction due to manifold means, including fiber length, aspect ratio, orientation, and scattering, the actual bonding area in the tensile explorations vary from that in the pullout tests. Based on the substitution proportion of macro upright fibers to microfibers, negative associations between tensile and pullout operations were witnessed. In the issue of the hooked fibers, on the other hand, extending the replacement ratio increased the post-crushing tensile strength and *g*-magnitude, but it decreased the average fastening power and normalized drawn energy. This suggested that the hooked fiber sample resulted in negative replacement ratio connections between tensile and fiber-drawn achievements. As examined in macro upright fibers, it was more awkward to have identical fiber scattering in the matrix because the hooked fibers were balled at first. In addition, the hooked fibers in the UHP-HFRC samples handled for flexural tests were randomly oriented, whereas the fibers in the drawn tests were regulated in the course of the pullout force. The average fastening power of macro direct fibers developed 112% when 1.5% of them were replaced with microfibers in the pullout experiment with UHPC mixtures.
Yoo et al. (2014)	Bond strength and flexural strength	Because of the improvement in compressive strength, the bond strength and gliding at peak drawn charge progressed with progressing bulk fiber up to 3%. Owing to an improvement in the fiber bridging effect, the flexural strength, as well as the analogous displacement and crack mouth opening displacement (CMOD), extended pseudo-linearly with raising fiber material. The pattern with 4 vol % fibers had the highest flexural capacity, which was 14 to 114% stronger than the patterns with 1 to 3 vol % fibers. In addition, as the fiber content increased, the coarseness of the fissure surface, matrix spalling, and crack tortuosity progressed. A larger percentage of steel fibers increased ultimate load and elastic modulus under stress up to 3 vol %, but the sample with 4 vol % of fibers had the deepest charges due to poor fiber diffusion.

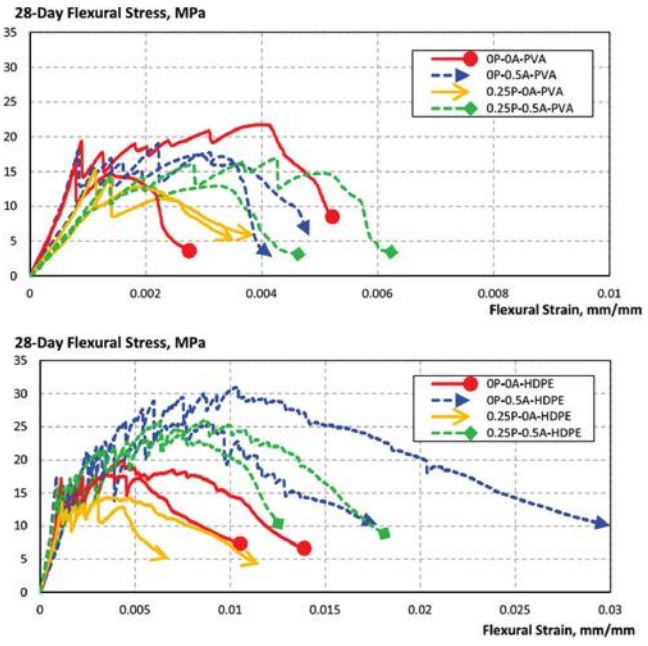

Fig. 10—Flexural features of PVA fibers in topmost portion and HDPE fibers in nethermost portion of cement-based composites (Muzenski et al. 2020a).

Performance of UHPC exposure to aggressive solution—Xi et al. (2022) studied the self-healing features of UHPC with crystalline admixtures (CAs) attacked by aggressive environments such as salt water and salt water and geothermal water. They demonstrated that a period of 7 days was considerably adequate for sealing the small crack in the samples inundated in salt water, as shown in Fig. 26(a). In other words, there was no well sealing for the larger cracks, as obvious in Fig. 26(b), because the crystal's particle size was smaller. Besides, numerous needle-shaped fibrous crystals were noticed in the cracks, as presented in Fig. 26(c). On the other hand, for the samples attacked by the chloride solution, it was troublesome to notice these fibrous crystals on their surface after 7 days.

At any status of environmental exposure, cracks with small widths have been shown to provide quicker and more considerable healing than cracks with larger widths. Furthermore, the achievement of fundamental crack closure could be difficult for cracks larger than 150 µm width (Xi et al. 2023).

Qian et al. (2019) proposed that the average of $CaCO_3$ crystallization declined due to NaCl. Moreover, NaCl caused a decline in the thermodynamic and kinetic potential of $CaCO_3$ crystallization.

The impacts of the incorporation of nano-sized particles of Al_2O_3 on the behavior of the UHPC subjected to aggressive environments such as sodium hydroxide, sodium hypochlorite, and ammonium hydroxide attacks were investigated by Preeth and Mahendran (2019). They demonstrated that the incorporation of nano-Al_2O_3 particles prevented the entrance of aggressive solutions into the UHPC samples; also, this inclusion diminished the feature of leaching of the

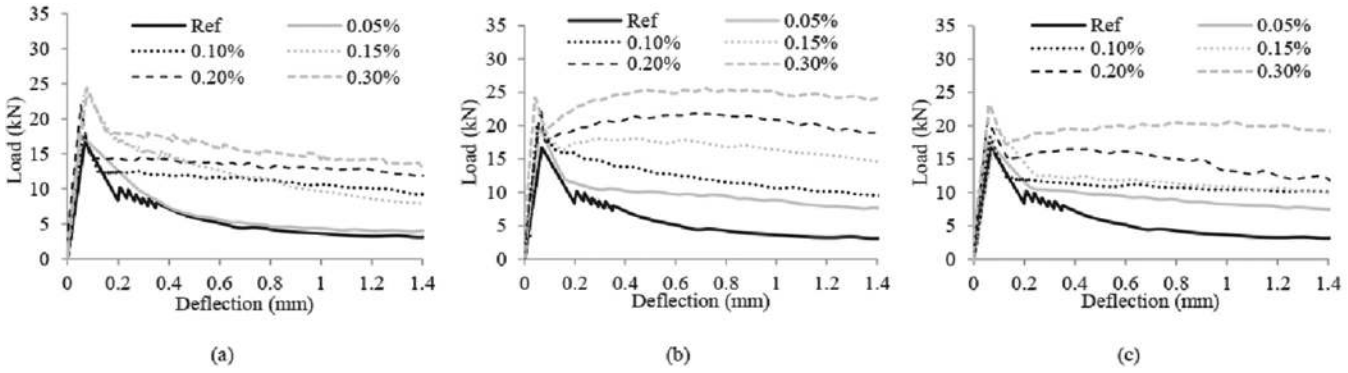

Fig. 11—Flexural examination outcomes of paradigm inserting: (a) CNF; (b) GNP-C; and (c) GNP-M (Meng and Khayat 2016).

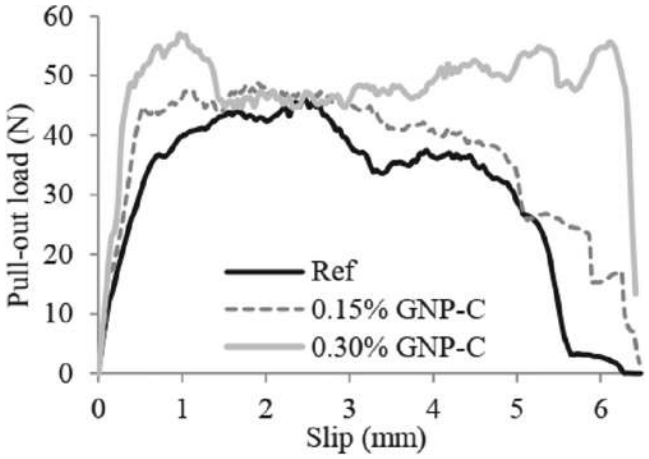

Fig. 12—Outcomes of drawn alone fiber experiment (Meng and Khayat 2016).

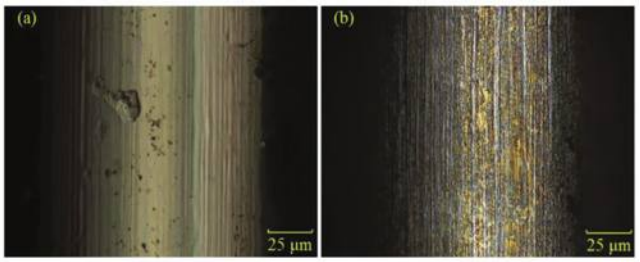

Fig. 13—Optical microscopy of steel fibers: (a) prior to; and (b) after pullout evaluation (Meng and Khayat 2016).

cement matrix. Besides, the maximum confinement in the weight and strength losses was noticed in the samples with 2% inclusion of Al_2O_3 nanoparticles. In other words, the reasons for this behavior could be due to:

- The pore-filling role of nano-Al_2O_3 particles.
- The provision of seeding spots for creation of C-S-H gel by these nanoparticles.
- The creation of aluminosilicate gel in the cement matrix.

There was good resistance of UHPFRC containing CNCs and ANF to the accelerated Cl transportation due to the roles of CNCs and ANF in providing dense and compacted microstructures with less porosity, which also made the resistance of UHPFRC to geothermal water considerably high (Cuenca et al. 2022).

The reaction of penetrated CO_2 with $Ca(OH)_2$ in the presence of water to produce water-insoluble $CaCO_3$ products is called carbonation of concrete. That is, $CaCO_3$ products could drop inside the pores of concrete, resulting in reduced porosity, sealed microcracks, and a denser concrete microstructure. Therefore, the mechanical properties of carbonated concrete could be enhanced (Zheng et al. 2022). On the other hand, the carbonation of concrete is considered a popular cause of retrogradation of concrete. In other words, the carbonation of concrete could result in shrinkage and cracking of the concrete matrix, declining concrete ductility, corrosion of reinforcing steel bars or fibers, and diminishing service life of a concrete structure (Tam et al. 2021; ACI Committee 544 2008).

The carbonation resistance of UHPC is considered superior in comparison with normal-strength concrete because of the nature of UHPC, which is characterized by a dense, compacted microstructure with less porosity and fewer microcracks (Piérard et al. 2012). In other words, Li et al. (2022) found that the carbonation depth of UHPC samples was zero after 14 days of carbonation exposure.

Microstructure performance

A comparison of the microstructure of UHPC with and without ANFs cured in a climate room and in geothermal water is presented in Fig. 25. The involvement of ANFs obviously appeared in the images. Furthermore, their reinforcement role among the elementary crystal aggregate of the material microstructure was clear. Moreover, the effect of uninterrupted water availability in the geothermal inundation treatment setting could be seen in the more elegant composition of crystals, with more extensive crystals overlaid by smaller ones, indicating that hydration reactions were likely to continue (Cuenca et al. 2021c).

The mechanisms of conduct improvement owing to the ANF incorporation was interpreted into two patterns (Cuenca et al. 2021c):

- The first pattern: the free hydroxyl groups on the surface of ANFs could work as nucleation place for processes of cement particles hydration.
- The second pattern: nano-sized aluminum oxide could make them work as reinforcement for the C-S-H layered structure, thus supplying a nanostructural strengthening impact and diminishing the deformation of shrinkage.

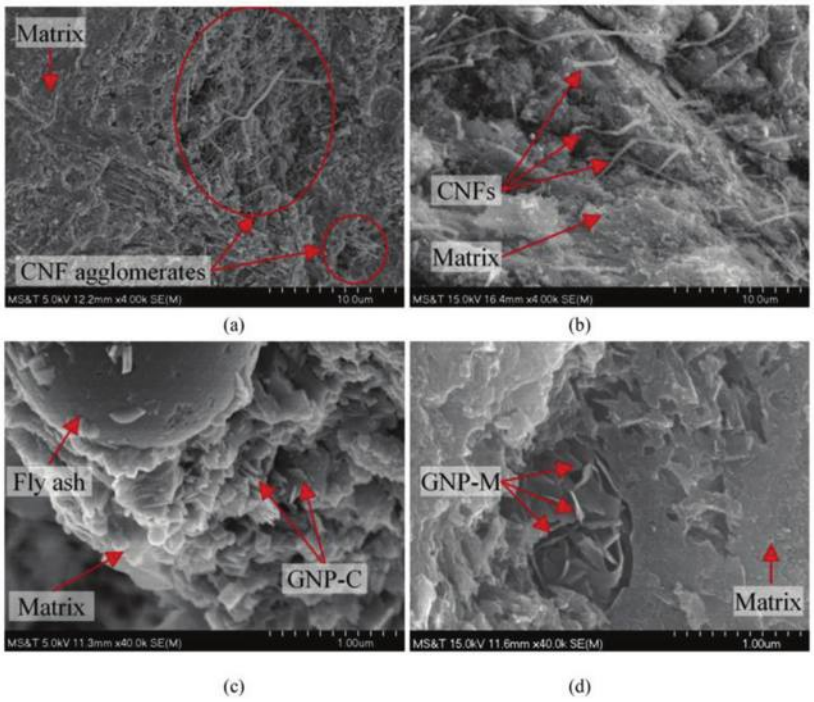

Fig. 14—Microstructures at UHPC shattered interfaces with various nanomaterials: (a) CNF at 4000×; (b) CNF at 40,000×; (c) GNP-C at 40,000×; and (d) GNP-M at 40,000× (Meng and Khayat 2016).

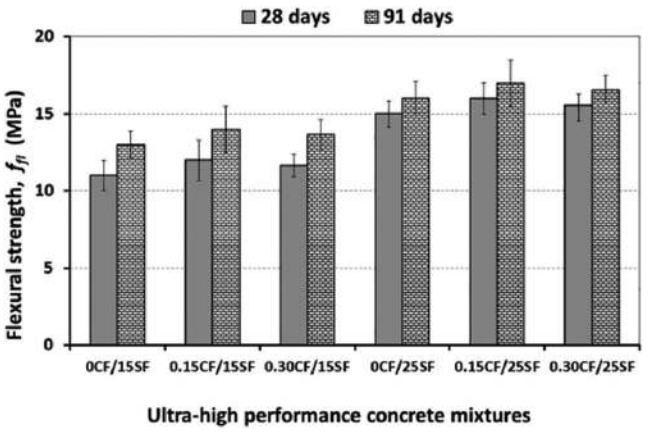

Fig. 15—Performance of flexural strength for numerous UHPCs (Hisseine et al. 2020).

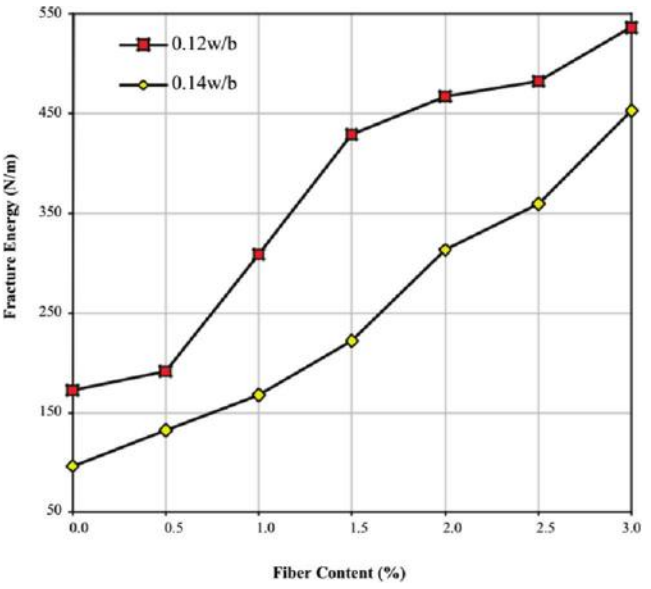

Fig. 16—At 28 days, fracture energy versus specific MGF rates of UHPFRC (Mohammed et al. 2021).

The use of ANFs accompanied by HDPE fibers in UHPC led to a denser matrix, particularly the region close to the interface between fibers and matrix, as offered in Fig. 27. In other words, the interpretation of this behavior could be due to the seeding influence of ANFs (Muzenski et al. 2020b).

From Fig. 28, it was clear that the microstructure of UHPC with no ANFs (NA0) had no perspicuous cracks. However, it had an interfacial transition zone (ITZ) with less compactness and uniformity when compared with UHPC with 1% and 2% nano-Al_2O_3 (NA). In other words, the microstructure of UHPC was obviously enhanced and the ITZ had a superior regular and compact micromorphology with the injection of NA. Furthermore, no perspicuous interface relationship could be observed with the incorporation of NA in UHPC (Chu et al. 2022).

The interpretation of this behavior could be due to the nanofibers' seeding influence, which would encourage the nucleation and construction of C-S-H with a denser structure, as mentioned by Muzenski et al. (2019). Consequently, nanofibers can elaborate as reinforcement for the C-S-H, mitigating microcracking and flexibility of the C-S-H layers (He and Shi 2008).

Supporting the nucleation position supposition, Fig. 29 offered scanning electron microscope (SEM) images of ultra-high-strength diluted cement-based composites with ANF incorporation, where it appeared that the hydration outcomes were collecting around the nanofibers (Muzenski et al. 2019).

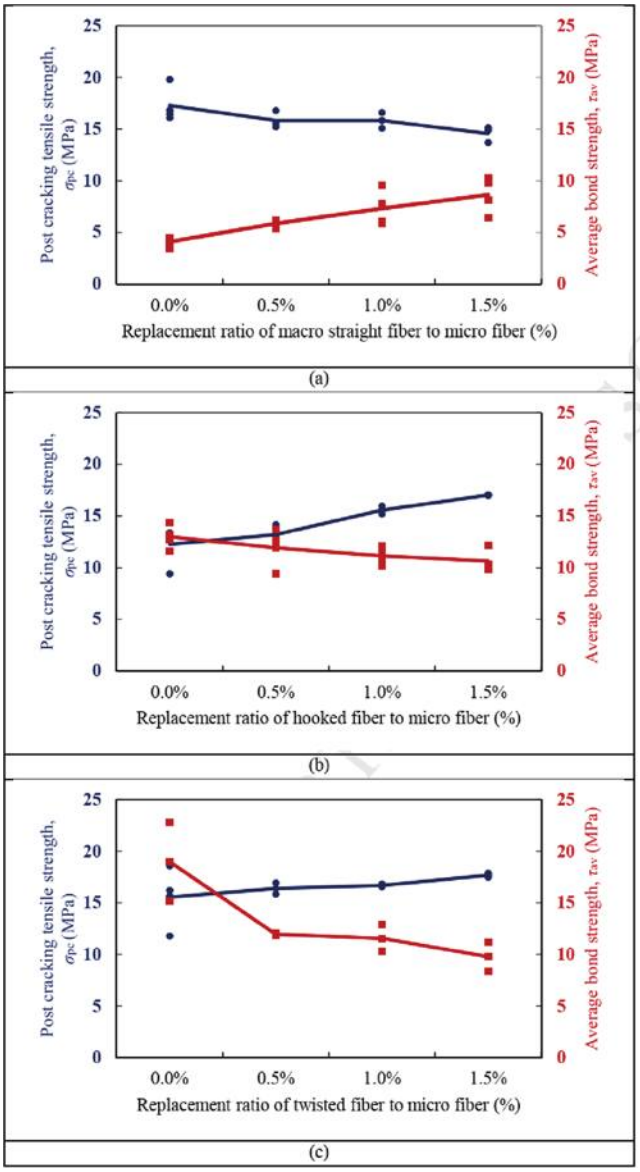

Fig. 17—Association between both post-crushing stretching power and average fastening power: right fiber, hooked fiber, and twisted fiber are three kinds of fiber (Chun and Yoo 2019).

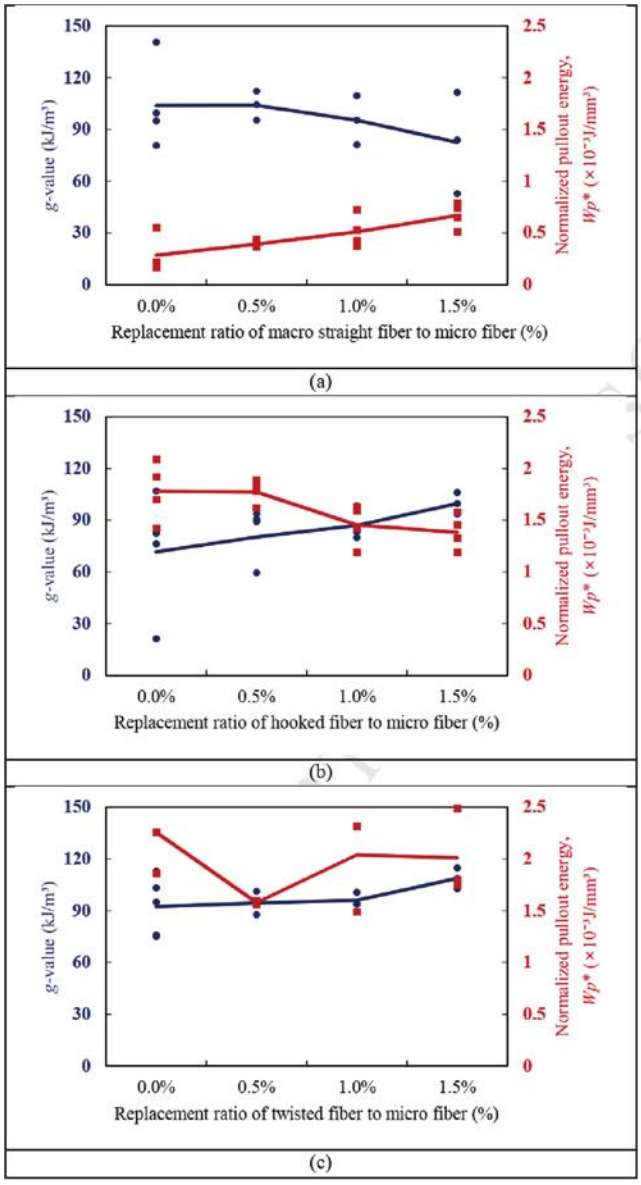

Fig. 18—Association between both g-magnitude and normalized drawn energy: (a) right fiber; (b) hooked fiber; and (c) twisted fiber (Chun and Yoo 2019).

CONCLUSIONS

1. The addendum of a small value of Al_2O_3 nanofibers (ANFs) with a small amount of silica fume (SF) to future building projects has the potential to create prospective high-performance or ultra-high-performance concrete (UHPC). To put it another way, by replacing large amounts of SF in UHPC with small amounts of ANFs, a more cost-effective and thus more effective UHPC material can be produced.

2. A substantial rise in compressive and flexural strength in common periods of hardening obtained by the addition of just a slight amount of ANFs might be due to the nucleation and creation of the calcium-silicate-hydrate (C-S-H)'s rather dense structure. Furthermore, the nanofibers can act as reinforcement to the C-S-H, limiting the bulk of microcracking and flexibility of C-S-H strata, as well as arresting the

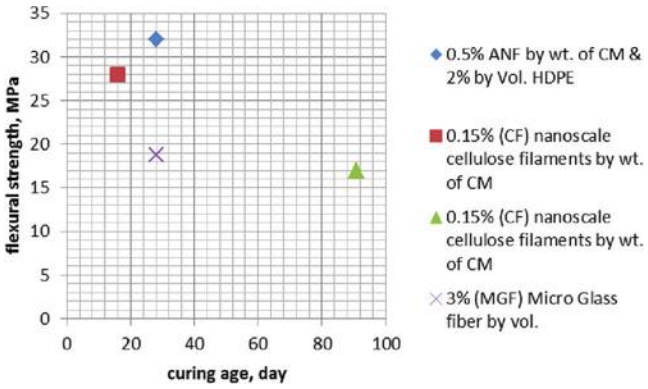

Fig. 19—Effect of different types of nano- or microscale fibers on flexural strength of UHPC from various research.

Table 4—Durability properties

Authors	Parameter studied	Results
Hisseine et al. (2020)	Autogenous shrinkage	CF has a huge impact on the autogenous shrinkage behavior of UHPC, especially at very young ages (after placement to the primary 7 days). CF caused autogenous expansions that were not seen in counterpart samples. This is due to a time-dependent deliverance of water from the hydrophilic and hygroscopic CF, which helps refresh the emptying matrix pores. Thus, adding CF to the mixture minimized autogenous shrinkage by 45 to 75% after 1 day, before stabilizing at 22 to 53% after 7 days. This may help reduce the chances of cracking in concrete that has not yet established proper tensile strength.
Song et al. (2020)	Compressive rate loss, XRD, and pore distribution beyond 180 days of curing in three different marine environments	Compressive rate loss increased with increased fiber volume for UHPC cured in marine environments, as previously explained in the "Compressive strength" section of this paper. Figure 20 shows the XRD trends of UHPFRC patterns after 180 days of treatment in three marine environments. After curing in raised-temperature seawater, Friedel's salt can clearly be seen in all the UHPFRC samples' XRD patterns. Furthermore, the Friedel's salt step can be seen in the XRD pattern for the UHPFRC treated in wetting-and-drying cycles in seawater with proportionately strong (3.0 vol %) steel fibers. Furthermore, no Friedel's salt step can be established in UHPFRC cured in regular seawater. These results show that dense UHPFRC can be corroded in a harsh marine setting, chiefly in cases where the temperature is high, the number of fibers is high, and there is a high proportion of steel fibers. Figures 21(a), (b), and (c) depict the pore distribution of UHPFRCs after 180 days of treating in raised-temperature seawater (with 1.0, 2.0, and 3.0 vol % fiber, respectively). The different pore colors denote the various sizes of pores, with red representing macropores and blue representing micropores (full-color PDF can be accessed at www.concrete.org). It was discovered that as the amount of added fiber increases, the color indicators of pore size change. The explanation is as follows: 1) as the added fiber volume increased, so did the linkage of fibers, improving the likelihood of electrochemical corrosion in UHPFRCs; and 2) as the attached fiber value increased, the compactness of UHPFRCs decreased, allowing ions to seep more easily into the UHPFRCs.
Yoo et al. (2014)	Shrinkage	The shrinkage of the fiber-reinforced sample reduced as the fiber volume expanded, according to Zhang and Li's analytical method (Zhang and Li 2001). However, as shown in Fig. 22, a raise in fiber volume only led to an abatement in shrinkage up to a fiber value of 3%. The shrinkage strain of the specimen with 4% fibers was almost identical to that of the pattern with 3% fibers. This finding is in line with the findings of a previous study (Chern and Young 1990), which found that adding 4% of fibers did not reduce shrinkage. As a result, it was determined that raising fiber content has no impact on UHPFRC shrinkage beyond a fiber value of 3 vol %.
Cuenca et al. (2021c)	Self-healing	A UHPFRC sample containing ANFs and CA as a self-healing prompter was reviewed for its autogenous self-healing ability. The self-healing capability was examined in terms of mechanical efficiency and water permeability recovery as measures of resilience in the cracked state—that is, the material's ability to maintain its planned scale of rendering for the duration of the structure's service life. The addition of ANFs to the mixture, made possible by a tailored elaboration technique to attain the desired concentricity in the suspension, results in a superior dispersion of stress aptitude in the injured status, as evidenced by the increased number and narrower width of cracks that develop over the prior-summit stable stretch process. This, combined with the hydrophilic character of the identical fibers, which promotes belated binder hydration reactions, led to better and quicker crack sealing and mechanical characteristics restoration, even when exposed to highly hostile conditions such as geothermal water, which is rich in chlorides and sulfates. Figure 23 illustrates the permeability recovery trend and shows that there is a 50 μm threshold for initial crack opening. Below this threshold, complex three-dimensional closing of the crack—both at its exterior and internally—can guarantee the full recovery of the permeability conduct after a little healing duration, while larger cracks require longer healing times to heal the material conduct. The mechanical and stability efficiency indexes of recovery are associated with crack sealing performance in Fig. 23. The measurements' accuracy is confirmed by a strong association between (im)permeability recovery and crack wrapping. In terms of the mechanical performance recovery indexes, the observed trends are consistent with previous observations by the inventor team in equivalent realizations, which show that injury rehabilitation requires a fissure stamp rate of at least 60% to begin to be noticeable, progressing even faster for superior stamp proportion in the future. Recovery of load-bearing capability, on the other hand, is stationary upon gradual reocclusion of the cracks, and is also based on the rift-seamstress leverage of the scattered fiber reinforcement, because pre-cracking and recracking transpired during the regime of pre-peak deformation hardening. Figure 24 emphasizes the significance of ANFs in encouraging greater stamp and even more salutary restoration of mechanical efficiency, but most importantly, it ensures that fissures resided within a very narrow aperture range during the pre-cracking stage. It may be due to a synergy between the nano-reinforcement impact created by ANFs and the hydrophilic impression of the identical nanofibers, which may also allow them to function as seeds of curing reactions due to the occupation of hydroxyl series on their surface. After 84 days of treating in both environments, SEM photos of the microstructure of the investigated composites are displayed in Fig. 25. The involvement of ANFs is clearly visible in the SEM images, which also show their role as reinforcement among the elementary crystal aggregates of the material microstructure. The effect of uninterrupted water availability in the geothermal inundation treating setting can be seen in the more elegant composition of crystals, with more extensive crystals overlaid by junior ones, indicating that hydration reactions are likely to continue. Analog SEM photographs of reference representations originated with the primary mixture without ANFs subjected to an identical treatment background to support this.

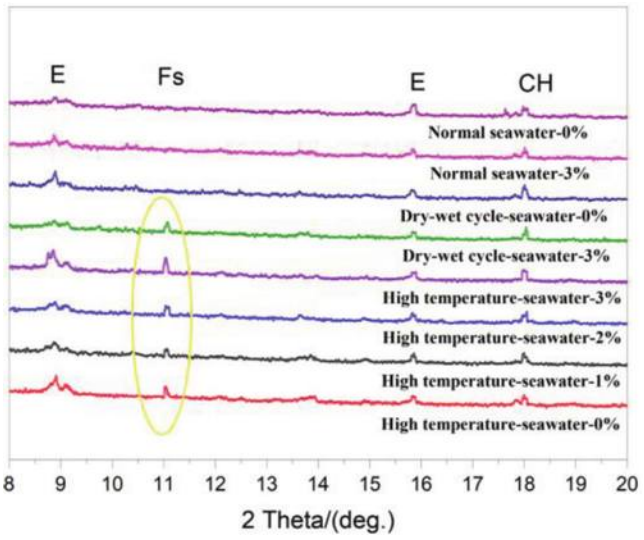

Fig. 20—XRD pattern of UHPFRC specimens after 180 days of treatment in various marine environments (Song et al. 2020).

formation of cracks at the C-S-H stage, thereby furthering the formation of larger cracks.

3. The existence of graphite nanoplatelets (GNPs), which work as nucleation sites of hydrates, could strengthen the interface between fiber and matrix, resulting in enhanced fastening power. Thus, the drawn energy (the territory beneath the drawn load-slip curve) increased with the rise in content of nanomaterials.

4. The incorporation of nanoscale cellulose fibers (CFs) in UHPC provided higher flexural capacity due to enhancing the microstructure-phase micromechanical properties. However, despite using nanoscale CFs at a high level in UHPC, a reduction in compressive and flexural strength occurred due to the interaction between the high-range water-reducing admixture (HRWRA) and CFs, which caused the release of entrapped air in the mixture.

5. The presence of CF in UHPC played a good role in limiting the danger of cracking at a young age while the concrete did not yet have an adequate tensile strength by reducing autogenous shrinkage by recharging the emptying

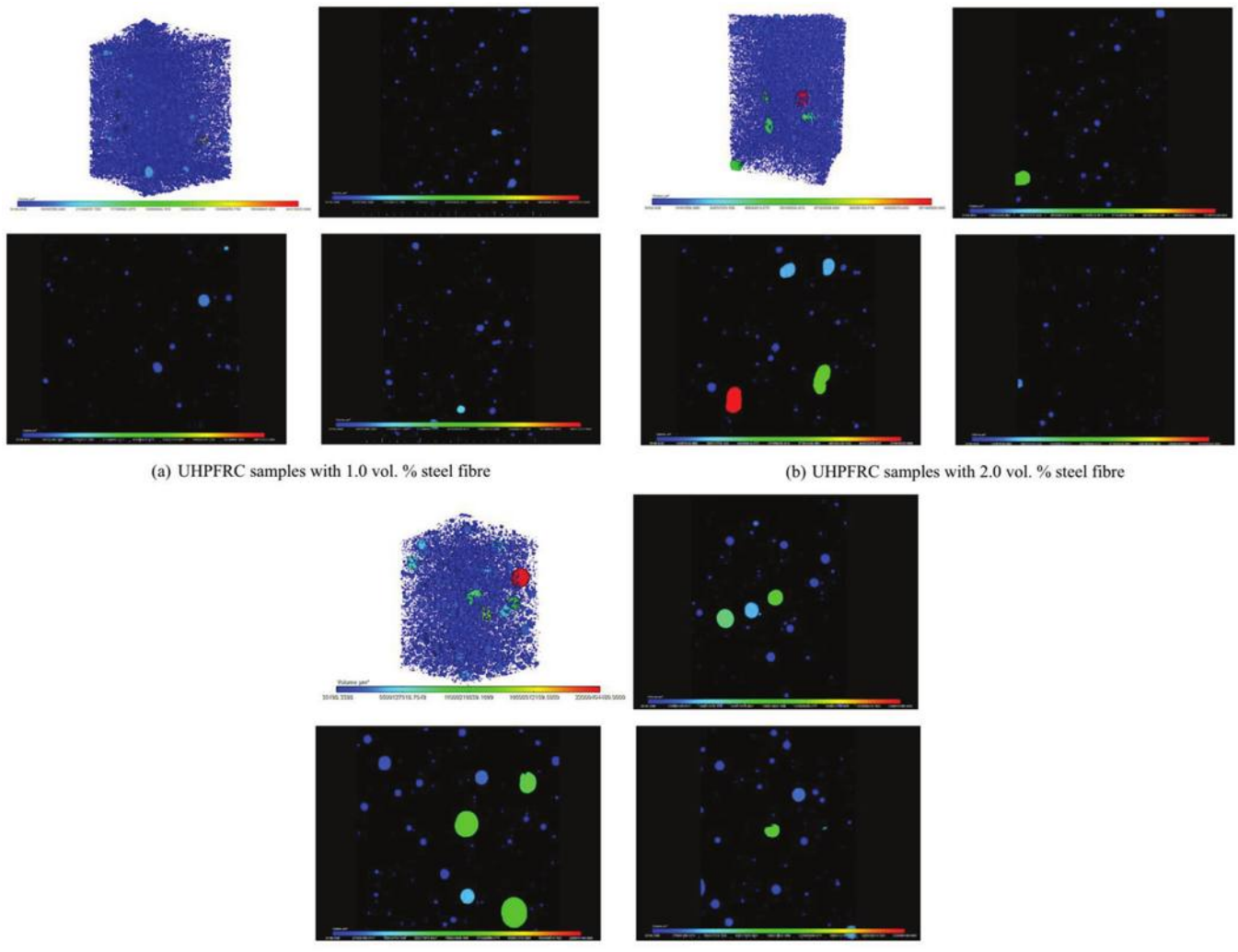

Fig. 21—Three-dimensional pore dispersion of UHPFRC specimens after 180 days of treatment in high-temperature seawater: (a) UHPFRC specimens with 1.0 vol % steel fiber; (b) UHPFRC specimens with 2.0 vol % steel fiber; and (c) UHPFRC specimens with 3.0 vol % steel fiber (Song et al. 2020).

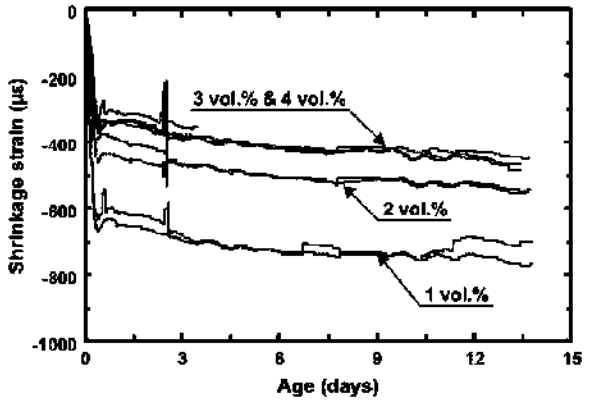

Fig. 22—Effect of fiber content on shrinkage behavior (Yoo et al. 2014).

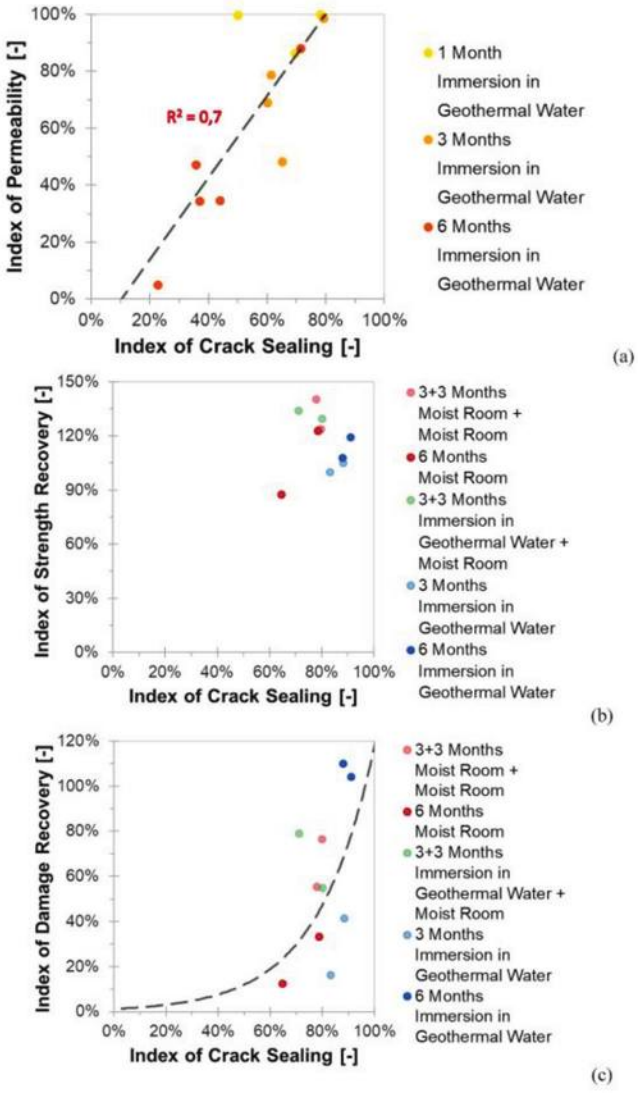

Fig. 23—Correlation of: (a) permeability restoration; (b) strength; and (c) stiffness indexes versus fissure closure index (Cuenca et al. 2021c).

matrix pore spaces through the release of water from the hydrophilic and hygroscopic CF.

6. The addition of micro glass fibers (MGFs) in UHPC resulted in more ductile UHPC due to their high aspect ratio and tensile strength, which strongly arrested cracks, so higher fracture energy was needed. Moreover, the positive effect of MGFs was more noticeable on UHPC strength than on reduction in the water content.

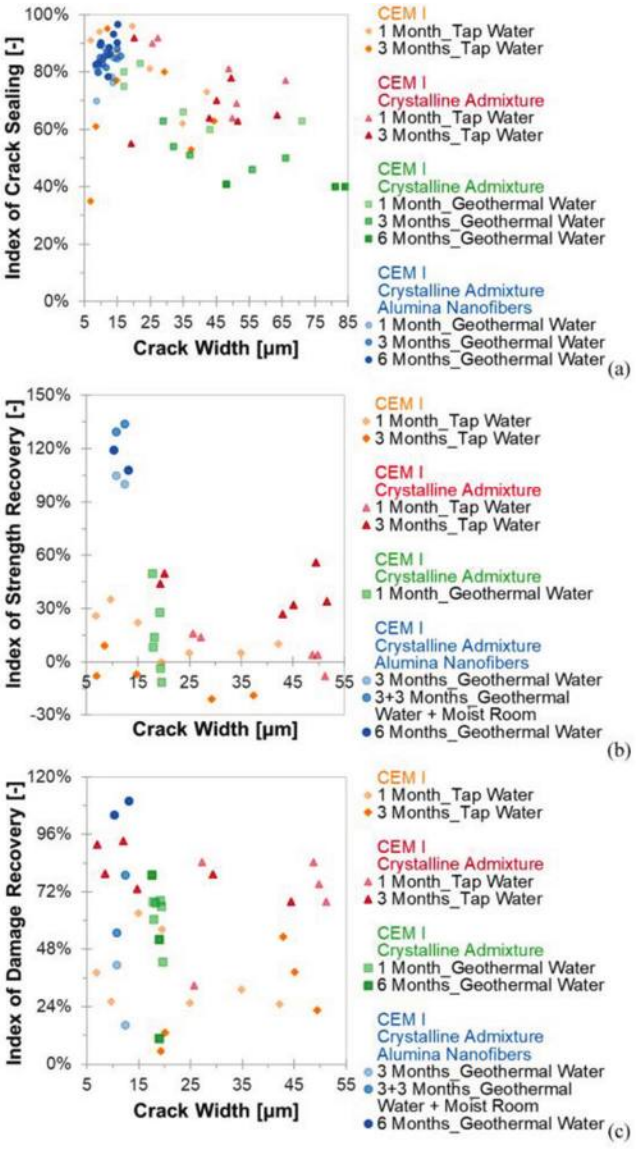

Fig. 24—Correlation of: (a) permeability restoration; (b) strength; and (c) stiffness indexes against fissure width for various experimental operations (Cuenca et al. 2021c).

7. Dense ultra-high-performance fiber-reinforced concrete (UHPFRC) could suffer corrosion in serious marine environments, particularly in a situation with elevated temperatures (high-temperature seawater could highly affect ion spreading) and comparatively at a high steel fiber level, resulting in difficult compaction of UHPC, which led to the easy entrance of ions into the concrete. Furthermore, at a high steel fiber level, the fibers' connection increased, leading to the appearance of electrochemical corrosion in the comparatively high-steel-fiber-level UHPFRC.

8. The incorporation of micro steel fiber in UHPC resulted in a reduction of the shrinkage strain up to a specific volume fraction of fibers. In other words, the increase of micro steel fiber above 3% by volume had no effect on shrinkage strain when compared with a lower level of fiber content.

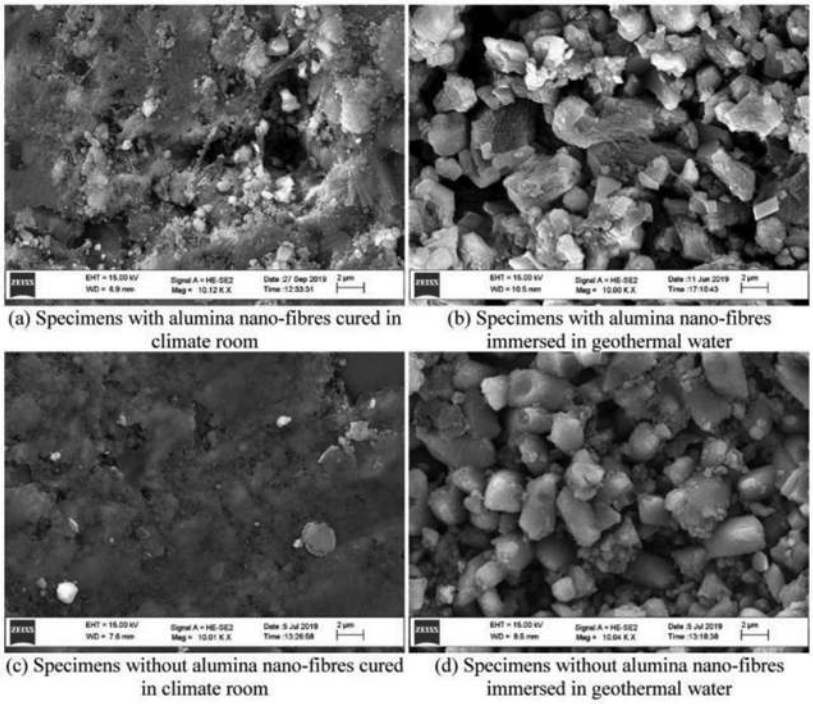

Fig. 25—SEM photos of cementitious composites cured in: (a) and (c) a climate room, or (b) and (d) in geothermal water; (a) and (b) with, and (c) and (d) without ANFs (Cuenca et al. 2021c).

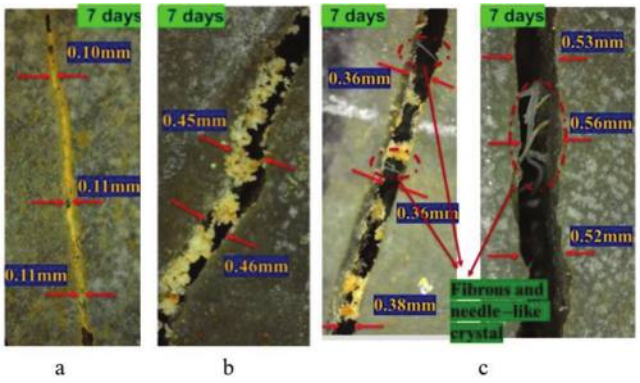

Fig. 26—Monitoring of self-healing outcomes after 7 days of saltwater exposure: (a) shutting of small cracks; (b) shutting of large cracks; and (c) crystal morphology (Xi et al. 2022).

9. Based on the results of researchers, it is suggested that by adding carbon nanotubes (CNTs) and using electrical curing (EC) in on-site field installation, UHPFRC can be accurately assembled. Thus, the mechanical and electrical behavior of construction materials could be further improved.

10. The concept of "conventional" UHPFRC could be upgraded to ultra-high-durability concrete through "nano-functionalization". For example, the addition of ANFs to the mixture could result in a superior redistribution of stress in the cracked stage and the noticeably slimmer size of cracks that formed during the pre-peak level of steady propagation. Moreover, the fibers could induce accelerated hydration of the delayed binder materials through the hydrophilic nature of these fibers, as well as induce superior and rapid healing for recovery of both mechanical properties and crack sealing, even under extremely aggressive exposure conditions, such as geothermal water, which is filled with sulfates and chlorides.

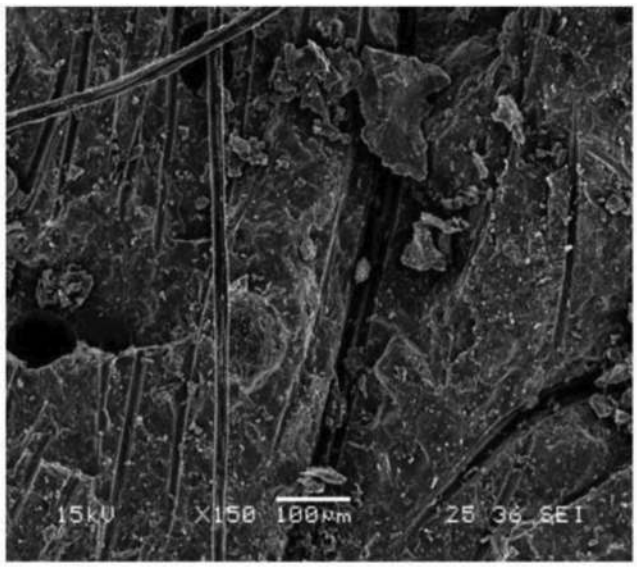

Fig. 27—SEM of broken UHPC matrix with ANFs and HDPE fiber injection (Muzenski et al. 2020b).

RECOMMENDATION FOR FUTURE RESEARCH

1. The high manufacturing cost of UHPC has confined its use to the general works sector, although it has superior mechanical properties as compared to conventional concrete. In other words, the concrete materials, mixture proportions, and the addition of fibers elevate the manufacturing cost of UHPC. Consequently, a future guide to manufacturing UHPC may involve finding sustainable, environmentally friendly, and cost-reducing methods. For example, the use of

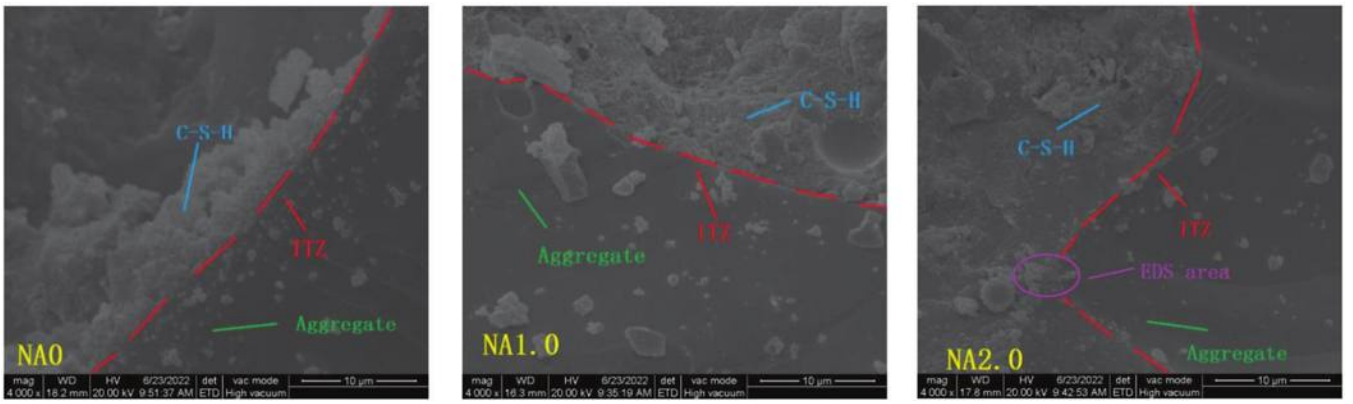

Fig. 28—SEM of UHPC with different ANF percentages at 28 days' curing age (Chu et al. 2022).

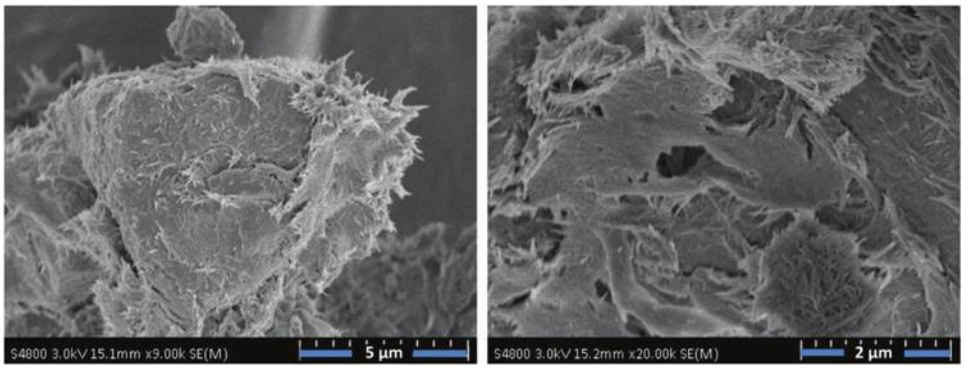

Fig. 29—SEM of diluted cement pastes with ANFs at 9000× (left) and 20,000× (right) magnification (Muzenski et al. 2019).

recycled materials or fibers from recycled material or high-range supplementary cementitious materials could be future research in the production of UHPC.

2. Research on the behavior of UHPC in aggressive environmental media is still limited. Therefore, the application of UHPC (that is, its mechanical properties and durability) in extreme environmental media needs to be assessed.

3. Compressive studies on hybrid fibers in UHPC is needed.

4. Internal sulfate attack on concrete is a big problem, especially in Iraq and neighboring countries due to the high sulfate content in natural raw materials there. For example, the content of sulfate in the sand from natural quarries in Iraq highly exceeds the limit of sulfate content in specifications. Thus, the behavior of UHPC with high internal sulfate attack needs to be studied.

AUTHOR BIOS

Zainab Hashim Abbas Alsalami *is a PhD Student in building materials engineering science at the University of Technology, Iraq, Baghdad, Iraq, and an Assistant Professor in construction materials in the College of Engineering at Al-Qasim Green University, Al-Qasim, Iraq. She received her bachelor's degree in civil engineering in 2010 and her master's degree in civil engineering/construction materials in 2014 from the University of Babylon, Hillah, Iraq. Her research interests include curing regimes and properties of high-performance concrete, lightweight concrete, and self-consolidating concrete.*

Fatima Hashim Abbas *is a Lecturer at Al-Mustaqbal University, Hillah, Iraq.*

REFERENCES

ACI Committee 544, 2008, "Guide for Specifying, Proportioning, and Production of Fiber-Reinforced Concrete (ACI 544.3R-08)," American Concrete Institute, Farmington Hills, MI, 14 pp.

Al Qadi, A. N. S., and Al-Zaidyeen, S. M., 2014, "Effect of Fibre Content and Specimen Shape on Residual Strength of Polypropylene Fibre Self-Compacting Concrete Exposed to Elevated Temperatures," *Journal of King Saud University. Engineering Sciences*, V. 26, No. 1, pp. 33-39. doi: 10.1016/j.jksues.2012.12.002

ASTM C78/C78M-16, 2016, "Standard Test Method for Flexural Strength of Concrete (Using Simple Beam with Third-Point Loading)," ASTM International, West Conshohocken, PA.

ASTM C109/C109M-99, 1999, "Standard Test Method for Compressive Strength of Hydraulic Cement Mortars (Using 2-in. or [50-mm] Cube Specimens)," ASTM International, West Conshohocken, PA.

ASTM C157/C157M-08(2014)e1, 2008, "Standard Test Method for Length Change of Hardened Hydraulic-Cement Mortar and Concrete," ASTM International, West Conshohocken, PA.

ASTM C1609/C1609M-05, 2005, "Standard Test Method for Flexural Performance of Fiber-Reinforced Concrete (Using Beam with Third-Point Loading)," ASTM International, West Conshohocken, PA.

ASTM D7264/D7264M-07, 2007, "Standard Test Method for Flexural Properties of Polymer Matrix Composite Materials," ASTM International, West Conshohocken, PA.

BS 1881-116:1983, 1983, "Testing Concrete. Method for Determination of Compressive Strength of Concrete Cubes," British Standards Institution, London, UK.

BS 1881-117:1983, 1983, "Testing Concrete. Method for Determination of Tensile Splitting Strength," British Standards Institution, London, UK.

Chern, J. C., and Young, C. H., 1990, "Study of Factors Influencing Drying Shrinkage of Steel Fiber Reinforced Concrete," *ACI Materials Journal*, V. 87, No. 2, Mar.-Apr., pp. 123-129.

Chu, H.; Wang, Q.; Gao, L.; Jiang, J.; and Wang, F., 2022, "An Approach of Producing Ultra-High-Performance Concrete with High Elastic Modulus by Nano-Al_2O_3: A Preliminary Study," *Materials (Basel)*, V. 15, No. 22, p. 8118. doi: 10.3390/ma15228118

Chun, B., and Yoo, D. Y., 2019, "Hybrid Effect of Macro and Micro Steel Fibers on the Pullout and Tensile Behaviors of Ultra-High-Performance Concrete," *Composites Part B: Engineering*, V. 162, pp. 344-360. doi: 10.1016/j.compositesb.2018.11.026

Cuenca, E.; Criado, M.; Giménez, M.; Alonso, M. C.; and Ferrara, L., 2022, "Effects of Alumina Nanofibers and Cellulose Nanocrystals on Durability and Self-Healing Capacity of Ultrahigh-Performance Fiber-Reinforced Concretes," *Journal of Materials in Civil Engineering*, ASCE, V. 34, No. 8, p. 04022154. doi: 10.1061/(ASCE)MT.1943-5533.0004375

Cuenca, E.; D'Ambrosio, L.; Lizunov, D.; Tretjakov, A.; Volobujeva, O.; and Ferrara, L., 2021c, "Mechanical Properties and Self-Healing Capacity of Ultra High-Performance Fibre Reinforced Concrete with Alumina Nano-Fibres: Tailoring Ultra High Durability Concrete for Aggressive Exposure Scenarios," *Cement and Concrete Composites*, V. 118, p. 103956. doi: 10.1016/j.cemconcomp.2021.103956

Cuenca, E.; Mezzena, A.; and Ferrara, L., 2021b, "Synergy between Crystalline Admixtures and Nano-Constituents in Enhancing Autogenous Healing Capacity of Cementitious Composites under Cracking and Healing Cycles in Aggressive Waters," *Construction and Building Materials*, V. 266, p. 121447. doi: 10.1016/j.conbuildmat.2020.121447

Cuenca, E.; Rigamonti, S.; Gastaldo Brac, E.; and Ferrara, L., 2021a, "Crystalline Admixture as Healing Promoter in Concrete Exposed to Chloride-Rich Environments: Experimental Study," *Journal of Materials in Civil Engineering*, ASCE, V. 33, No. 3, p. 04020491. doi: 10.1061/(ASCE)MT.1943-5533.0003604

D'Alessandro, A.; Rallini, M.; Ubertini, F.; Materazzi, A. L.; and Kenny, J. M., 2016, "Investigations on Scalable Fabrication Procedures for Self-Sensing Carbon Nanotube Cement-Matrix Composites for SHM Applications," *Cement and Concrete Composites*, V. 65, pp. 200-213. doi: 10.1016/j.cemconcomp.2015.11.001

EN 196-1:2005, 2005, "Methods of Testing Cement—Part 1: Determination of Strength," European Committee for Standardization, Brussels, Belgium.

Ghafari, E.; Costa, H.; and Júlio, E., 2015, "Critical Review on Eco-Efficient Ultra-High-Performance Concrete Enhanced with Nano-Materials," *Construction and Building Materials*, V. 101, pp. 201-208. doi: 10.1016/j.conbuildmat.2015.10.066

Gopalakrishnan, R., and Jeyalakshmi, R., 2018, "Strength Deterioration of Nano-Silica Contained in Ordinary Portland Cement Concretes in Aggressive Sulfate Environments," *The European Physical Journal Plus*, V. 133, No. 9, p. 351. doi: 10.1140/epjp/i2018-12162-3

Han, B.; Sun, S.; Ding, S.; Zhang, L.; Yu, X.; and Ou, J., 2015, "Review of Nanocarbon-Engineered Multifunctional Cementitious Composites," *Composites Part A: Applied Science and Manufacturing*, V. 70, pp. 69-81. doi: 10.1016/j.compositesa.2014.12.002

He, X., and Shi, X., 2008, "Chloride Permeability and Microstructure of Portland Cement Mortars Incorporating Nanomaterials," *Transportation Research Record: Journal of the Transportation Research Board*, V. 2070, No. 1, pp. 13-21. doi: 10.3141/2070-03

Hisseine, O. A.; Basic, N.; Omran, A. F.; and Tagnit-Hamou, A., 2018a, "Feasibility of Using Cellulose Filaments as a Viscosity Modifying Agent in Self-Consolidating Concrete," *Cement and Concrete Composites*, V. 94, pp. 327-340. doi: 10.1016/j.cemconcomp.2018.09.009

Hisseine, O. A.; Omran, A. F.; and Tagnit-Hamou, A., 2018b, "Influence of Cellulose Filaments on Cement Paste and Concrete," *Journal of Materials in Civil Engineering*, ASCE, V. 30, No. 6, p. 04018109. doi: 10.1061/(ASCE)MT.1943-5533.0002287

Hisseine, O. A.; Soliman, N. A.; Tolnai, B.; and Tagnit-Hamou, A., 2020, "Nano-Engineered Ultra-High-Performance Concrete for Controlled Autogenous Shrinkage Using Nanocellulose," *Cement and Concrete Research*, V. 137, p. 106217. doi: 10.1016/j.cemconres.2020.106217

Hisseine, O. A.; Wilson, W.; Sorelli, L.; and Tagnit-Hamou, A., 2019, "Nanocellulose for Improved Concrete Performance: A Macro-to-Micro Investigation for Disclosing the Effects of Cellulose Filaments on Strength of Cement Systems," *Materials & Design*, V. 206, pp. 84-96.

Indhumathi, S.; Dinesh, A.; and Pichumani, M., 2022, "Diverse Perspectives on Self-Healing Ability of Engineered Cement Composite–All-Inclusive Insight," *Construction and Building Materials*, V. 323, p. 126473. doi: 10.1016/j.conbuildmat.2022.126473

JCI-S-001-2003, 2003, "Method of Test for Fracture Energy of Concrete by Use of Notched Beam," Japan Concrete Institute, Tokyo, Japan.

JSCE, 2004, "Recommendations for Design and Construction of Ultra-High-Performance Fiber Reinforced Concrete Structures (Draft)," Japan Society of Civil Engineers, Tokyo, Japan.

Jung, M.; Park, J. S.; Hong, S. G.; and Moon, J., 2020, "Micro- and Meso-Structural Changes on Electrically Cured Ultra-High-Performance Fiber-Reinforced Concrete with Dispersed Carbon Nanotubes," *Cement and Concrete Research*, V. 137, p. 106214. doi: 10.1016/j.cemconres.2020.106214

Khan, M. I.; Abbas, Y. M.; and Fares, G., 2014, "Development of Sustainable, Ultra High-Performance Hybrid Fiber Reinforced Cementitious Composites Utilizing Locally Available Materials for Applications in Harsh Saudi Arabian Environment," King Saud University, Riyadh, Saudi Arabia.

Khan, M. I.; Abbas, Y. M.; and Fares, G., 2017, "Review of High and Ultrahigh Performance Cementitious Composites Incorporating Various Combinations of Fibers and Ultrafines," *Journal of King Saud University. Engineering Sciences*, V. 29, No. 4, pp. 339-347. doi: 10.1016/j.jksues.2017.03.006

Konsta-Gdoutos, M. S.; Batis, G.; Danoglidis, P. A.; Zacharopoulou, A. K.; Zacharopoulou, E. K.; Falara, M. G.; and Shah, S. P., 2017, "Effect of CNT and CNF Loading and Count on the Corrosion Resistance, Conductivity and Mechanical Properties of Nanomodified OPC Mortars," *Construction and Building Materials*, V. 147, pp. 48-57. doi: 10.1016/j.conbuildmat.2017.04.112

Konsta-Gdoutos, M. S.; Metaxa, Z. S.; and Shah, S. P., 2010, "Highly Dispersed Carbon Nanotube Reinforced Cement-Based Materials," *Cement and Concrete Research*, V. 40, No. 7, pp. 1052-1059. doi: 10.1016/j.cemconres.2010.02.015

Larsen, I. L., and Thorstensen, R. T., 2020, "The Influence of Steel Fibers on Compressive and Tensile Strength of Ultra-High-Performance Concrete: A Review," *Construction and Building Materials*, V. 256, p. 119459. doi: 10.1016/j.conbuildmat.2020.119459

Li, C.; Li, J.; and Gong, S., 2022, "Experimental Study on Carbonation Resistance of Ultra-High-Performance Concrete for Electric Pole," 2nd International Conference on Mechanical, Electronics, and Electrical and Automation Control (METMS 2022), Guilin, China.

Li, Z.; Wang, H.; He, S.; Lu, Y.; and Wang, M., 2006, "Investigations on the Preparation and Mechanical Properties of the Nano-Alumina Reinforced Cement Composite," *Materials Letters*, V. 60, No. 3, pp. 356-359. doi: 10.1016/j.matlet.2005.08.061

Materazzi, A. L.; Ubertini, F.; and D'Alessandro, A., 2013, "Carbon Nanotube Cement-Based Transducers for Dynamic Sensing of Strain," *Cement and Concrete Composites*, V. 37, pp. 2-11. doi: 10.1016/j.cemconcomp.2012.12.013

Meng, W., and Khayat, K. H., 2016, "Mechanical Properties of Ultra-High-Performance Concrete Enhanced with Graphite Nanoplatelets and Carbon Nanofibers," *Composites Part B: Engineering*, V. 107, pp. 113-122. doi: 10.1016/j.compositesb.2016.09.069

Mohammed, B. H.; Sherwani, A. F.; Faraj, R. H.; Qadir, H. H.; and Younis, K. H., 2021, "Mechanical Properties and Ductility Behavior of Ultra-High Performance Fiber Reinforced Concretes: Effect of Low Water-to-Binder Ratios and Micro Glass Fibers," *Ain Shams Engineering Journal*, V. 12, No. 2, pp. 1557-1567. doi: 10.1016/j.asej.2020.11.008

Muzenski, S.; Flores-Vivian, I.; Farahi, B.; and Sobolev, K., 2020b, "Towards Ultrahigh Performance Concrete Produced with Aluminum Oxide Nanofibers and Reduced Quantities of Silica Fume," *Nanomaterials*, V. 10, No. 11, p. 2291. doi: 10.3390/nano10112291

Muzenski, S.; Flores-Vivian, I.; and Sobolev, K., 2019, "Ultra-High Strength Cement-Based Composites Designed with Aluminum Oxide Nano-Fibers," *Construction and Building Materials*, V. 220, pp. 177-186. doi: 10.1016/j.conbuildmat.2019.05.175

Muzenski, S.; Flores-Vivian, I.; and Sobolev, K., 2020a, "Hydrophobic Modification of Ultra-High-Performance Fiber-Reinforced Composites with Matrices Enhanced by Aluminum Oxide Nano-Fibers," *Construction and Building Materials*, V. 244, p. 118354. doi: 10.1016/j.conbuildmat.2020.118354

Park, S. H.; Kim, D. J.; Ryu, G. S.; and Koh, K. T., 2012, "Tensile Behavior of Ultra-High Performance Hybrid Fiber Reinforced Concrete," *Cement and Concrete Composites*, V. 34, No. 2, pp. 172-184. doi: 10.1016/j.cemconcomp.2011.09.009

Piérard, J.; Dooms, B.; and Cauberg, N., 2012, "Evaluation of Durability Parameters of UHPC Using Accelerated Lab Tests," *Proceedings of the 3rd International Symposium on UHPC and Nanotechnology for High Performance Construction Materials*, Kassel, Germany, pp. 371-376.

Preeth, S. K., and Mahendran, K., 2019, "Aggressive Alkaline Attack on Nano Al_2O_3 Blended Ultra High-Performance Concrete," *International Journal of Advanced Scientific Research and Management*, V. 4, No. 4, pp. 436-440.

Qian, M.; Zuo, Y.; Chen, Z.; Yin, X.; Liu, Y.; Yang, W.; and Chen, Y., 2019, "Crystallization of $CaCO_3$ in Aqueous Solutions with Extremely High Concentrations of NaCl," *Crystals*, V. 9, No. 12, p. 647. doi: 10.3390/cryst9120647

Ranade, R.; Stults, M. D.; Li, V. C.; Rushing, T. S.; Ronth, J.; and Heard, W. F., 2011, "Development of High Strength High Ductility Concrete," 2nd International RILEM Conference on Strain Hardening Cementitious Composites, Rio de Janeiro, Brazil.

RILEM, 1985, "Determination of the Fracture Energy of Mortar and Concrete by Means of Three-Point Bend Tests on Notched Beams," *Materials and Structures*, V. 18, No. 4, pp. 287-290. doi: 10.1007/BF02472918

RILEM TC, 1983, "RILEM Recommendations for the Testing and Use of Constructions Materials. RC 6 Bond Test for Reinforcement Steel. 2. Pull-Out Test," E & FN Spon, London, UK, pp. 218-220.

Russell, H. G., and Graybeal, B. A., 2013, "Ultra-High-Performance Concrete: A State-of-the-Art Report for the Bridge Community," Report No. FHWA-HRT-13-060, Federal Highway Administration, Washington, DC.

Sanchez, F., and Sobolev, K., 2010, "Nanotechnology in Concrete–A Review," *Construction and Building Materials*, V. 24, No. 11, pp. 2060-2071. doi: 10.1016/j.conbuildmat.2010.03.014

Shaikh, F. U. A.; Luhar, S.; Arel, H. Ş.; and Luhar, I., 2020, "Performance Evaluation of Ultrahigh Performance Fiber Reinforced Concrete–A Review," *Construction and Building Materials*, V. 232, p. 117152. doi: 10.1016/j.conbuildmat.2019.117152

Shi, C.; Wu, Z.; Xiao, J.; Wang, D.; Huang, Z.; and Fang, Z., 2015, "A Review on Ultra High-Performance Concrete: Part I. Raw Materials and Mixture Design," *Construction and Building Materials*, V. 101, pp. 741-751. doi: 10.1016/j.conbuildmat.2015.10.088

Shi, R. J.; Xiang, Z.; Liu, S. G.; Wang, D. H.; and Ju, Y. Z., 2019, "Mechanical Properties of Reactive Powder Concrete: A Review," *IOP Conference Series: Materials Science and Engineering*, V. 629, No. 1, p. 012009. doi: 10.1088/1757-899X/629/1/012009

Song, Q.; Yu, R.; Shui, Z.; Rao, S.; Fan, D.; and Gao, X., 2020, "Macro/Micro Characteristics Variation of Ultra-High Performance Fiber Reinforced Concrete (UHPFRC) Subjected to Critical Marine Environments," *Construction and Building Materials*, V. 256, p. 119458. doi: 10.1016/j.conbuildmat.2020.119458

Song, Q.; Yu, R.; Shui, Z.; Rao, S.; Wang, X.; Sun, M.; and Jiang, C., 2018, "Steel Fibre Content and Interconnection Induced Electrochemical Corrosion of Ultra-High Performance Fiber Reinforced Concrete (UHPFRC)," *Cement and Concrete Composites*, V. 94, pp. 191-200. doi: 10.1016/j.cemconcomp.2018.09.010

Tam, V. W.; Butera, A.; and Le, K. N., 2021, "Mechanical Properties of CO_2 Concrete Utilizing Practical Carbonation Variables," *Journal of Cleaner Production*, V. 294, p. 126307. doi: 10.1016/j.jclepro.2021.126307

Vera-Agullo, J.; Chozas-Ligero, V.; Portillo-Rico, D.; García-Casas, M. J.; Gutiérrez-Martínez, A.; Mieres-Royo, J. M.; and Grávalos-Moreno, J., 2009, "Mortar and Concrete Reinforced with Nanomaterials," *Nanotechnology in Construction*, Springer, Berlin, Germany, pp. 383-388

Wille, K., and Naaman, A. E., 2013, "Effect of Ultra-High-Performance Concrete on Pullout Behavior of High-Strength Brass-Coated Straight Steel Fibers," *ACI Materials Journal*, V. 110, No. 4, July-Aug., pp. 451-462.

Xi, B.; Al-Obaidi, S.; and Ferrara, L., 2023, "Effect of Different Environments on the Self-Healing Performance of Ultra High-Performance Concrete–A Systematic Literature Review," *Construction and Building Materials*, V. 374, p. 130946. doi: 10.1016/j.conbuildmat.2023.130946

Xi, B.; Huang, Z.; Al-Obaidi, S.; Monte, F. L.; and Ferrara, L., 2022, "Investigation of Self-Healing Property of UHPC with Sustained Loads under Aggressive Exposure Environments," *Proceedings of the 14th PhD Symposium in Civil Engineering*, Rome, Italy, pp. 329-336.

Yoo, D. Y., and Banthia, N., 2016, "Mechanical Properties of Ultra-High-Performance Fiber-Reinforced Concrete: A Review," *Cement and Concrete Composites*, V. 73, pp. 267-280. doi: 10.1016/j.cemconcomp.2016.08.001

Yoo, D. Y.; Shin, H. O.; Yang, J. M.; and Yoon, Y. S., 2014, "Material and Bond Properties of Ultra-High Performance Fiber Reinforced Concrete with Micro Steel Fibers," *Composites Part B: Engineering*, V. 58, pp. 122-133. doi: 10.1016/j.compositesb.2013.10.081

Zhang, J., and Li, V. C., 2001, "Influences of Fibers on Drying Shrinkage of Fiber-Reinforced Cementitious Composite," *Journal of Engineering Mechanics*, ASCE, V. 127, No. 1, pp. 37-44. doi: 10.1061/(ASCE)0733-9399(2001)127:1(37)

Zhao, Z.; Qi, T.; Zhou, W.; Hui, D.; Xiao, C.; Qi, J.; Zheng, Z.; and Zhao, Z., 2020, "A Review on the Properties, Reinforcing Effects, and Commercialization of Nanomaterials for Cement-Based Materials," *Nanotechnology Reviews*, V. 9, No. 1, pp. 303-322. doi: 10.1515/ntrev-2020-0023

Zheng, W.; Wang, S.; Quan, X.; Qu, Y.; Mo, Z.; and Lin, C., 2022, "Carbonation Resistance and Pore Structure of Mixed-Fiber-Reinforced Concrete Containing Fine Aggregates of Iron Ore Tailings," *Materials (Basel)*, V. 15, No. 24, p. 8992. doi: 10.3390/ma15248992

ACI MATERIALS JOURNAL TECHNICAL PAPER

Title No. 121-M18

Automated Piecewise Linear Regression for Analyzing Structural Health Monitoring Data

by H. Garg, K. Yang, A. G. Cohn, D. Borman, S. V. Nanukuttan, and P. A. M. Basheer

The recent increased interest in structural health monitoring (SHM) related to material performance has necessitated the application of advanced data analysis techniques for interpreting the real-time data in decision-making. Currently, an accurate and efficient approach for the timely analyses of large volumes of uncertain sensor data is not well-established. This paper proposes an automated clustering-based piecewise linear regression (ACPLR)-SHM methodology for handling, smoothing, and processing large data sets. It comprises two main stages, where the gaussian weighted moving average (GWMA) filter is used to smooth noisy data obtained from electrical resistance sensors, and piecewise linear regression (PLR) predicts material properties for assessing the performance of concrete in service. The obtained values of stabilized resistance and derived values of diffusion coefficients using this methodology have clearly demonstrated the benefit of applying ACPLR to the sensor data, thereby classifying the performance of different types of concrete in service environments.

Keywords: artificial intelligence (AI); automated clustering-based piecewise linear regression (ACPLR); diffusion coefficient; electrical resistance; in-service performance; structural health monitoring (SHM).

INTRODUCTION

The extensive demand for a reliable estimation of the material performance during the service life of structures, along with the prediction of their current and future conditions in the service environment, has expedited innovations in structural health monitoring (SHM) systems (McCarter et al. 2012; Frangopol and Kim 2014). They use the data obtained from the specifically designed sensors and sensing technologies installed in a structure to continuously monitor either the changes in materials or structural characteristics of members, thereby assessing the structure's performance in service. They notify any defects in the structure so that necessary remedial and timely repairs can be carried out and perform real-time maintenance, with the ultimate objective of ensuring the structure's safety and serviceability (Farrar and Worden 2012).

SHM is generally used for two purposes. First, SHM can be used to monitor the changes in structural behavior or conditions of the structure such as acceleration, displacement, or rotation that would indicate the integrity and structural damage and assess the performance of the structure during its service life (Brownjohn et al. 2011; Dong and Catbas 2021). Second, SHM can be used to identify physical and/or chemical changes in material properties caused by the interaction between the material in structural members and the exposure environment, including corrosion of the embedded steel in reinforced concrete members, delamination or cracking, and void formation, all of which affect the performance of the whole structure (Bungey et al. 2006; ACI Committee 444 2021). Thus, an accurate diagnosis of the structural behavior or material properties from the SHM data can be used for decision-making processes, including cost-effective repair and maintenance strategies.

With recent developments in both types of monitoring strategies, the installation of multiple sensors for long-term monitoring of structures normally generates a huge amount of complex, uncertain sensor data (Smarsly et al. 2016). Hence, data handling, smoothing, and analyzing large amounts of sensor data from structures to properly decide on structural repair and maintenance is currently a challenge (Nanukuttan et al. 2017a; Yavuz and Safak 2019). In addition, a wrong diagnosis due to inaccurate data analysis may trigger untimely maintenance or repair, resulting in an increased cost of maintenance (Chandrasekaran 2019) or premature failure. These concerns have led to the implementation of advanced computational techniques, such as artificial intelligence (AI) algorithms, for analyzing the SHM data, thereby resolving any issues related to data processing and decision-making.

The rising trend of the application of AI algorithms in SHM has the potential to revolutionize the concrete industry (Ahmed et al. 2019). AI uses machine learning (ML) algorithms such as those based on statistics, probability, and neural networks to train models and provides a way to access massive amounts of information, process it, analyze it, and implement solutions to various problems (Pan and Zhang 2021; Flah et al. 2021).

RESEARCH SIGNIFICANCE

A review of the literature highlighted that considerable research has been undertaken in the field of analyzing SHM data using ML algorithms to capture changes in natural vibration frequencies, mode shape, modal strain energy, dynamic flexibility, and strain measurements (Yu et al. 2011; Karbassi et al. 2014; Aydin and Kisi 2015; Diez et al. 2016). However, an accurate and efficient approach for the timely analysis of large volumes of noisy and uncertain data to capture material properties is not well established. Therefore, this paper explicitly focuses on SHM undertaken for assessing changes in material performance and thus proposes an automated AI-based SHM methodology to effectively extract

ACI Materials Journal, V. 121, No. 2, March 2024.

MS No. M-2022-399.R2, doi: 10.14359/51740370, received October 13, 2023, and reviewed under Institute publication policies.

and interpret knowledge on changes in material properties obtained from SHM data for predicting the in-service performance of concrete structures.

SENSING METHODOLOGIES FOR ASSESSING CONCRETE PERFORMANCE IN SERVICE

SHM is used to assess the material characteristics of structures and thereby determine their current condition and predict the in-service performance of the structure (Dong and Catbas 2021). Degradation mechanisms such as chloride ion ingress, carbonation, corrosion of steel reinforcement, freezing-and-thawing damage, and alkali-aggregate reaction are some of the principal causes affecting the performance of materials in structures (Bungey et al. 2006; ACI Committee 201 2016). Researchers and practitioners have developed and used many sensors and sensing technologies to identify and measure changes in materials that may have an adverse effect on the future performance of structures. A list of various sensors or sensing techniques used to assess changes in material properties is provided in Table 1. These sensors measure the physical changes in the concrete due to environmental and loading conditions, as well as monitor the ambient environmental conditions where the material is exposed. Among the sensors listed in Table 1, the electrical resistance sensor is one of the most reliable types of sensors for use in concrete structures.

Electrical resistance monitoring

It is known that electrical resistance is a property that can be used to analyze early-age variations in cement hydration, the effect of temperature and moisture content, ingress of chloride ions that could induce corrosion of the embedded reinforcing steel, carbonation, and performance of material with time (Basheer et al. 2002; Nokken and Hooton 2007; Nanukuttan et al. 2017b). As diffusion and permeability are the primary mechanisms of transporting chloride ions or carbon dioxide in the concrete, these parameters cannot be monitored regularly but can be measured intermittently (Garboczi and Bentz 1992; Nanukuttan et al. 2015). On the other hand, the rate of corrosion can be monitored. Still, as this data is obtained after the initiation of corrosion, it is ineffective for carrying out preventative maintenance. However, these parameters are related to electrical resistance; thus, they can be determined from the steady-state resistance values for predicting the performance of concrete. However, electrical resistance is also affected by ambient environmental conditions and changes in the hydration of cement, and, as a result, interpretation becomes difficult due to these variations in most of the measurements.

Therefore, the focus of this paper is to demonstrate the methodology to smooth noisy and uncertain electrical resistance sensor data and analyze it using an automated clustering-based automated piecewise linear regression (ACPLR). The steady-state resistance values obtained are used to determine the diffusion coefficient values for assessing the performance of concrete for prognosis.

EXPERIMENTAL PROCEDURE

Materials, concrete mixtures, and site conditions

The study used three high-performance concrete mixtures manufactured with portland cement (PC), pulverized fuel ash (PFA), and microsilica (MS), as reported in Table 2. The experiment used CEM-I cement, 10 and 20 mm size crushed basalt as the coarse aggregate (CA), and medium-graded natural sand as the fine aggregate (FA). A polycarboxylic acid-based polymer was used as a high-range water-reducing admixture (HRWRA) that was added to the mixtures to ensure the consistency of the mixture was satisfactory while the water-binder ratio (w/b) remained at 0.3 (Yang et al. 2014).

Two concrete blocks of dimensions 410 x 100 x 250 mm were cast for each mixture and were cured in a constant-temperature water tank (20 ± 2°C) for 3 days. These blocks were kept at a constant room temperature (20 ± 1°C) for 90 days before relocating them to an open area 1 m from a three-story building (Latitude 54° 39’ N, Longitude 6° 12’ W). The two 410 x 250 mm sides were exposed, and the remaining sides were sealed with two coats of epoxy-based paint to ensure a uniaxial moisture movement. The exposed side of the specimen was placed vertically to let rain flow freely on the surface (Yang et al. 2014). Further details on materials, preparation of specimens and testing were detailed by Yang et al. (2014).

Sensors and monitoring

The concrete blocks were embedded with a multielectrode array within the cover zone of specimens for acquiring electrical resistance and temperature. A resistance meter was used to measure the electrical resistance between the electrode pairs (stainless steel pins, Fig. 1(a)) at three depths: 15, 25, and 45 mm from the surface of the blocks. Three thermistors were also embedded at 15, 25, and 45 mm depths to measure changes in temperature in the concrete cover zone. The monitoring started after 3 days of curing, and the data were recorded using a portable data logging system (Fig. 1(b)) for 6 months. The data were captured at a 10-minute frequency for a period of 172 days, and over 24,000 sets of data were reported in the study.

As-measured resistance measurements inside concrete specimens

The average as-measured resistance data for the two concrete blocks at 15 mm depth from the concrete surface for the three concrete mixtures are shown in Fig. 2. It can be seen that, overall, the resistance increased over the period for the three concrete mixtures. In comparison, the rate of increase in resistance in MS was the fastest, rising from 10 to 190 kΩ, followed by PC and PFA, rising from 5 to 30 kΩ in 6 months. It can be observed that concrete blocks were sensitive to the natural environment. After exposing them to the natural condition (day 90), there were substantial diurnal variations in the data set, especially for the MS blocks. No major difference can be seen between PFA and PC. However, it can be observed that the resistance of PFA rose steadily, while PC can be seen as stable after 100 days. The 6-month data shown in Fig. 2 depicts that the presence of a

Table 1—Types of sensors used for assessing material performance

Sensors	Measurands	Purpose	Limitations
Corrosion sensors, electrical resistance probes, half-cell potential	Corrosion (Perveen et al. 2014)	Used to monitor corrosion rate in structure due to changes in concrete chemical environment.	These are not recommended to monitor corrosion with epoxy-coated reinforcing bars, as this creates barrier between metals and alters results.
Electrical resistance sensors, chloride ion sensors	Chloride content (Montemor et al. 2006)	Used to detect presence of chemicals such as chloride ions in reinforced concrete (RC) structures to prevent premature corrosion.	They are only used for local measurement; hence, prior knowledge of likely locations where chloride values could increase is needed for positioning sensors.
Humidity sensor, weather station, fiber Bragg grating (FBG) sensors	Humidity (Tanner 1990; Zhang et al. 2010)	Used to measure relative humidity (RH) in concrete and determine moisture content in and around the concrete.	They are sensitive to thermal and environmental conditions and may result in wrong measurements.
Load cell, weigh-in-motion sensors	Load (Hernandez 2006; Ballo et al. 2014)	Used to measure deformations caused due to external force applied to structure.	They are bulky and require expensive electronic devices along with them.
pH sensors, fiber-optic sensor (FOS)	pH (Basheer et al. 2004)	Used to measure pH values of the concrete, which determines level of acidic or basic nature.	FOS are currently not suitable for long-term monitoring of pH and require careful handling.
Piezometers	Pressure (Kalkani 1992)	Used to measure changes in water table or pore water pressure.	They are sensitive to temperature and moisture conditions.
Temperature sensors, thermistors, FOS, thermocouples	Temperature (Rai 2007)	Used to monitor temperature changes in concrete structure due to hydration and pore structure changes.	Self-heating in sensor may cause errors in measurement. No linear relationship between the two variables.
Weather station, rain gauges	Precipitation (Fabo et al. 2020)	Used to measure precipitation.	They are only used to measure ambient environmental conditions.

Table 2—Mixture proportions and compressive strength of concretes

Types of concrete	Proportions of binder material, % by mass	Material quantities, kg/m^3								Compressive strength, N/mm^2	
		PC	PFA	MS	Water	FA	CA	*w/b*	HRWRA	28 days	56 days
PC	100% PC	485	0	0	145	689	1150	0.3	1.3	81.8	87.3
PFA	80:20 PC:PFA	388	97	0	145	689	1150	0.3	1.4	81.3	90.7
MS	73:7:20 PC:MS:PFA	352	97	36	145	689	1150	0.3	1.5	84.2	94.6

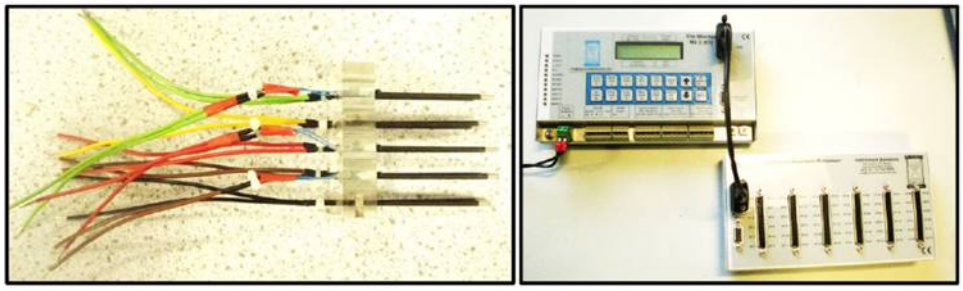

(a) (b)

Fig. 1—(a) Sensor block used for embedding in specimen; and (b) monitoring system.

large amount of uncertain data meant there are challenges that require handling, smoothing, and processing SHM data to identify the standard steady-state resistance values of the three mixtures for decision-making. Thus, the authors aim to use all the available data sets and present an AI-based SHM methodology to handle, smoothen, and analyze the electrical resistance data.

METHODOLOGY USED FOR AI-BASED SHM DATA ANALYSIS

In this section, an AI-based SHM methodology is presented to smooth noisy data obtained from the electrical resistance sensors and analyze it to predict the performance of the concretes. The workflow of the AI-based SHM methodology is illustrated in Fig. 3, followed by a detailed analysis in later sections.

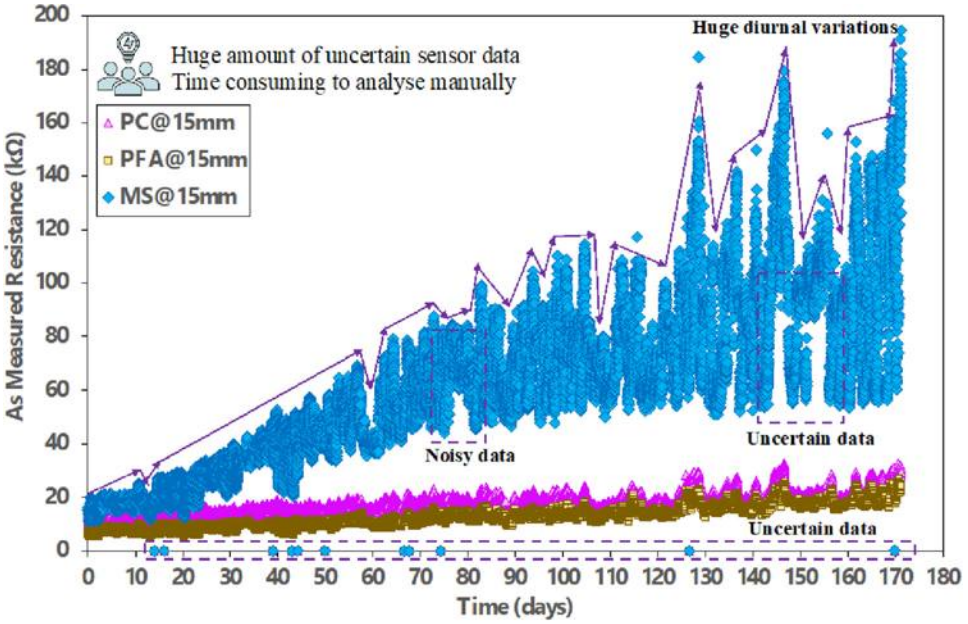

Fig. 2—Average as-measured resistance data at 15 mm depth for three mixtures.

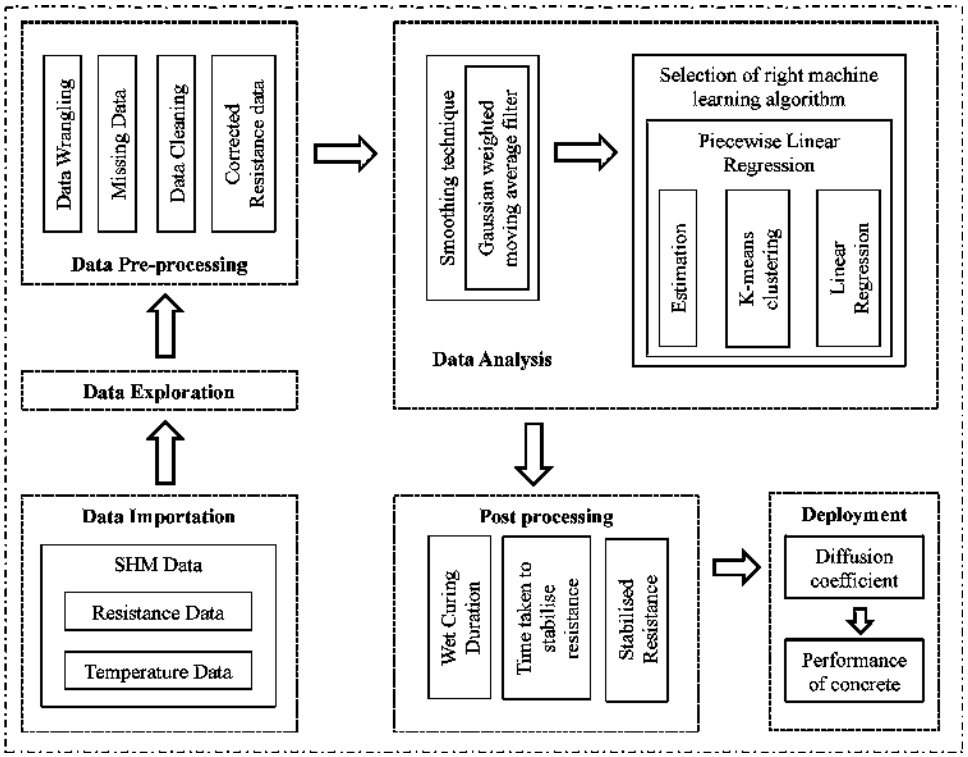

Fig. 3—Methodology used to clean, analyze, and process SHM data.

Data preprocessing

The measurements from the thermistors were converted to temperature (°C) using the Steinhart-Hart equation (Steinhart and Hart 1968)

$$T = 1/[A + B \ln R + C (\ln R)^3] - 273.1 \quad (1)$$

where T is the temperature in °C; R is the measured resistance in ohms (Ω); ln is the natural logarithm; and A, B, and C are coefficients, 1.28×10^{-3} K^{-1}, 2.36×10^{-4} K^{-1}, and 9.31×10^{-8} K^{-1}, respectively, based on the type of thermistor used.

The data set thus obtained was re-examined, and it was observed that there were missing values, duplication of data, and invalid data, presumably due to sensor connection issues while moving the specimens from one place to another after 90 days. These points were identified and eliminated from the data to reduce their influence on the analysis and to improve the signal-to-noise ratio. Further, the temperature variations were very high for the data captured every 10 minutes, and hence, daily average diurnal variations were considered for further data analysis.

Correction of resistance data for temperature variations

The measured electrical resistance is affected by the changes in temperature and moisture content of the concrete (McCarter et al. 2005; Nanukuttan et al. 2017a; Demircilioğlu et al. 2019). The effect of variations in temperature on the measured electrical resistance could be removed by expressing the resistance at a reference temperature—say, 25°C. For this, an Arrhenius relationship (Eq. (2)) was used (McCarter et al. 2012)

$$\rho_x = \rho_y e E_a/R_g[1/T_{k,x} - 1/T_{k,y}] \quad (2)$$

where ρ_y is the resistance (kΩ) recorded at the temperature at $T_{k,x}$ (K) is used to obtain equivalent resistance ρ_x at reference temperature ($T_{k,y}$); R_g is the universal gas constant (8.3141×10^{-3} kJ/mole/K); and E_a is the activation energy (kJ/mol). As both ρ_x and ρ_y have the same geometrical factors, resistivity was replaced by resistance for the analysis (Nanukuttan et al. 2017a).

The activation energy was determined by following the procedure suggested by McCarter et al. (2012), as described herein. The values of E_a/R_g for all concrete mixtures can be determined from Eq. (3). The equation linearizes the data by plotting the natural log of resistance (ρ) against $1000/T$, and the slope thus obtained is E_a/R_g with ρ_0 as pre-exponential constant (kΩ). E_a at each electrode pair for concrete can then be calculated by multiplying the slope with the value of R_g, which, when substituted in Eq. (3), would remove the temperature effects from the field measurements (McCarter et al. 2012)

$$\ln \rho = \ln \rho_0 + \frac{E_a}{R_g T} \quad (3)$$

McCarter et al. (2012) depicted a linear relationship from the equation by plotting every 15th set of data points from 1 to 150 days. Nanukuttan et al. (2017a) plotted all data obtained from the measurement period and observed that there were multiple parallel lines and for each line, the value R^2 was similar. Thus, it was suggested that one of these lines could be used to determine the activation energy. However, for the data reported in this paper, when all the available data were plotted, a significant scatter of data during the initial 45 days was observed for both PFA and MS concretes, indicating no clear relationship, which was not observed for the PC concrete (Fig. 4). The slope values obtained using all the data for PFA and MS were three times higher than that determined by McCarter et al. (2012) and Nanukuttan et al. (2017a). However, after 45 days, a linear relationship was obtained for both these concretes, giving similar results to those reported by McCarter et al. (2012). This is potentially the case because the total cementitious material content and the reactivity of SiO_2, CaO, Al_2O_3, and Fe_2O_3 might have influenced the rate of hydration and, hence, the total heat generated at an early age (Nehdi and Soliman 2011; Jansen et al. 2012; Schöler et al. 2017).

Up to approximately 50% hydration of PC is completed within 1 day of adding water to the cement, 80% within 28 days, and the remaining hydration gradually occurs within the next 3 to 4 months. At this stage, the hydrated portland cement paste is considered to have reached a stable state (Scrivener and Nonat 2011). On adding supplementary cementitious materials (SCMs), the pozzolanic reaction normally starts after 3 days of the hydration of portland cement and continues beyond 28 days, depending on the type of SCM, curing condition, and proportion of the binder materials (Zelić et al. 2000). Therefore, for further analysis, the matured concrete data after 45 days were considered for

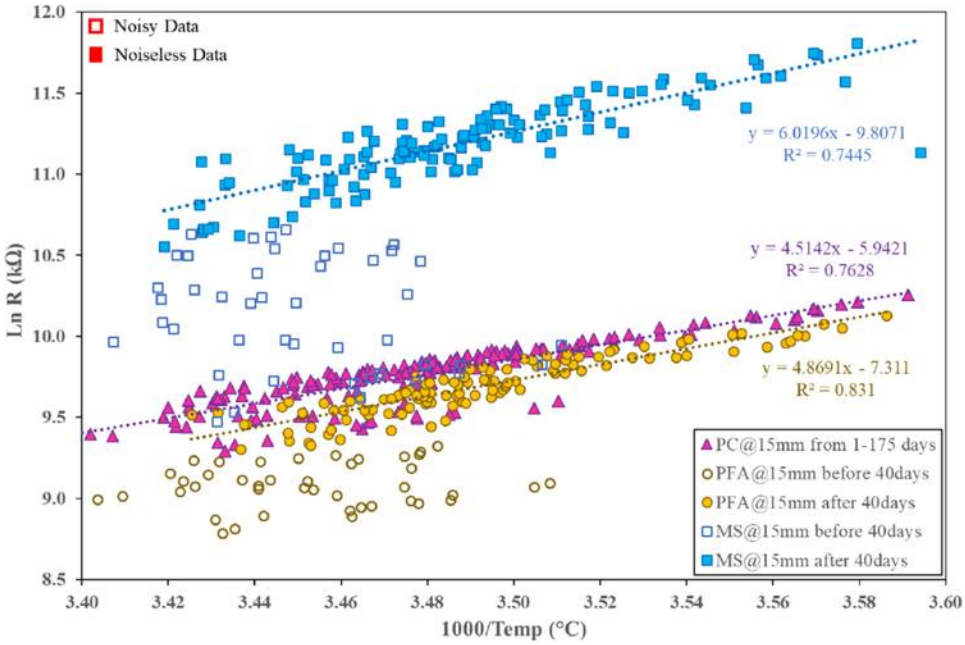

Fig. 4—Removal of noise from 25 mm depth data for establishing Arrhenius equation for PC, PFA, and MS. (Note: Noisy data presented herein for PFA and MS are from first 45 days of reaction; thereafter, trend becomes linear, whereas noise is absent for PC.)

estimating the activation energy and reducing the effect of cement hydration and pozzolanic reactions on the calculated activation energy.

When the activation energy was estimated using the aforementioned procedure, it is interesting to note that the graph now depicts a linear correlation, as shown in Fig. 4. The estimated activation energy, E_a, for each electrode pair for all concrete mixtures of each sample from Eq. (3) is reported in Table 3. It shows that not much variation is seen in PC and PFA and lies within the range of 35 to 47, while MS lies in the 50 to 57 kJ/M range. The results of PC and PFA are within the same range as reported by McCarter et al. (2012) and Nanukuttan et al. (2017a). It highlights that the presence of microsilica in MS concrete altered the pore structure (McCarter et al. 2012). Further, not much variation is observed in the two samples for each mixture, nor at each depth of the three concrete mixtures, as was reported by McCarter et al. (2012). Therefore, the calculated values for E_a/R_g for each mixture can be used to correct the resistance data to a reference temperature of 25°C using Eq. (2). The standardized resistance (SR) values for each concrete mixture were then averaged for the two concrete blocks and presented in Fig. 5.

It can be seen from the SRs in Fig. 5(a) to (c) that the huge fluctuations of the as-measured resistance in Fig. 2 are now slightly reduced, which indicates the removal of temperature effects from the measurement, as established by McCarter et al. (2012). However, from Fig. 5(c), it can be observed that there are still diurnal variations occurring after 80 days. Electrical resistance is also affected by other environmental interactions, such as ambient temperature, rainfall, and

Table 3—E_a/R_g determined from Eq. (3) and activation energy, E_a

	Mixtures											
	PC1		PC2		PFA1		PFA2		MS1		MS2	
Depth	E_a/R_g, K	E_a, kJ/M	E_a/R_g, K	E_a, kJ/M	E_a/R_g, K	E_a, kJ/M	E_a/R_g, K	E_a, kJ/M	E_a/R_g, K	E_a, kJ/M	E_a/R_g, K	E_a, kJ/M
15 mm	3.92	32.61	4.87	40.48	5.70	47.42	4.51	37.53	6.42	53.41	6.02	50.04
25 mm	4.50	37.38	5.43	45.15	5.44	45.24	5.24	43.57	6.87	57.10	6.67	55.48
45 mm	5.40	44.86	5.40	44.90	5.69	47.31	5.33	44.33	6.29	52.26	6.42	53.38
Average	4.60	38.28	5.23	43.51	5.61	46.66	5.03	41.81	6.53	54.26	6.37	52.97

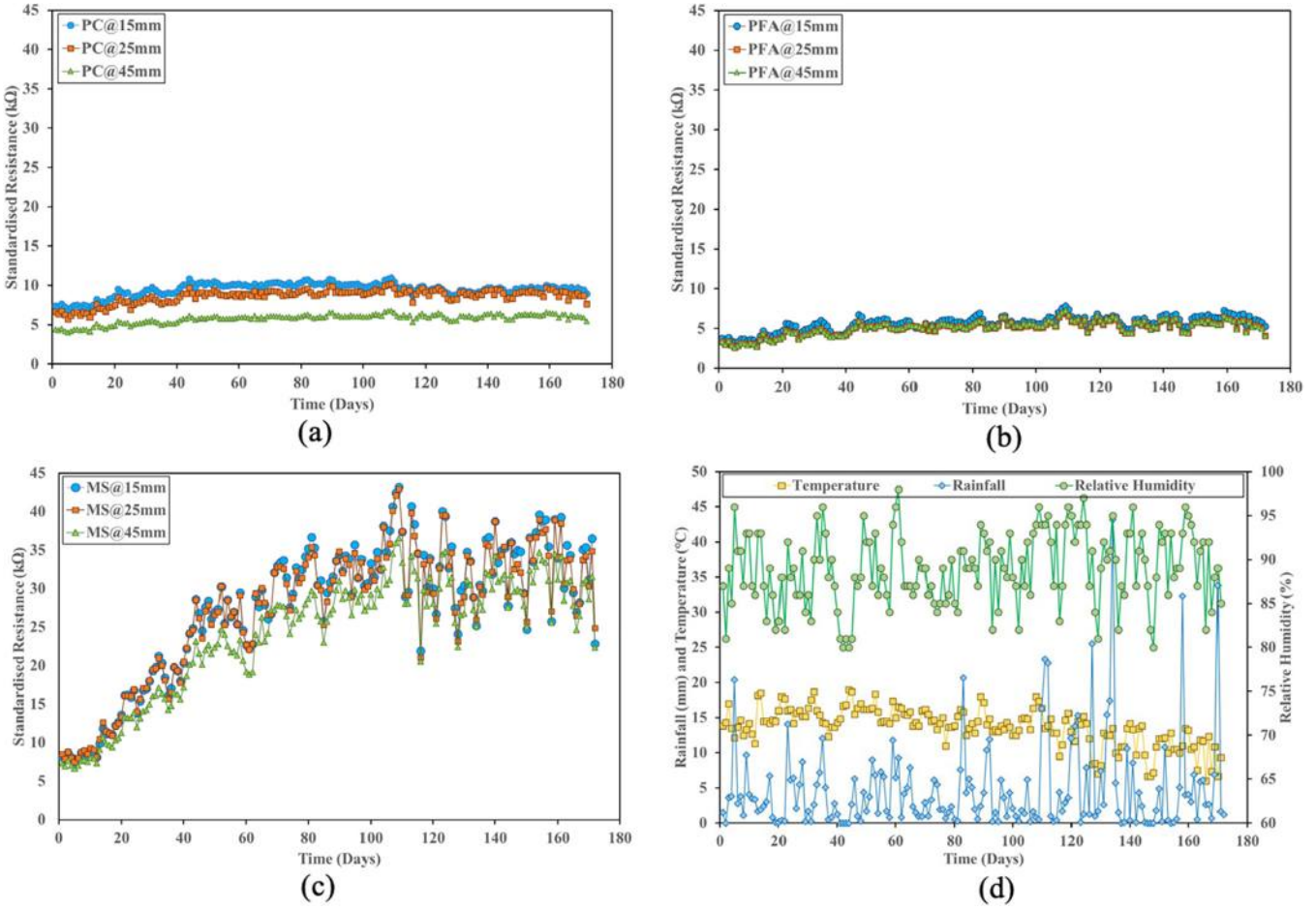

Fig. 5—Standardized resistance (kΩ) to reference temperature of 25°C for: (a) PC concrete mixture; (b) PFA concrete mixture; (c) MS concrete mixture; (d) rainfall, RH, and ambient temperature data during studied period as per UK met office.

relative humidity (RH) (Azarsa and Gupta 2017). Figure 5(d) shows the rainfall and ambient temperature data from the UK Met Office (metoffice.gov.uk). When comparing these data with the MS data in Fig. 5(c), it is clear that the resistance decrease can be attributed to the increase in rainfall and the associated possible increase in the moisture uptake. However, with no RH sensors installed in the concrete specimen, the effect of moisture variation on electrical resistance could not be fully quantified.

Determination of diffusion coefficient D_e

As discussed in the previous section, the performance of concrete can be assessed based on electrical resistance, chloride diffusion, and permeability. However, the electrical resistance of the saturated concrete can be used to determine the diffusivity (Hossain and Lachemi 2004; McCarter et al. 2012; Basnayake et al. 2020). Garboczi and Bentz (1992) presented an inverse relationship between the diffusion coefficient of a porous material and the bulk resistivity of the saturated material

$$\frac{D_e}{D_0} = \frac{\rho}{\rho_{bulk}} \tag{4}$$

where D_0 is the diffusion coefficient of the desired ion in pure water (for chloride, $D_0 = 2.032 \times 10^{-9}$ m^2/s); ρ is the resistivity of pore fluid (estimated using the NIST model); and ρ_{bulk} is the bulk resistivity of the saturated material. ρ_{bulk} can be obtained from the steady-state condition of the SR for the three concretes. Therefore, it is necessary to determine the steady-state electrical resistance values for the three concretes from a large number of data sets.

Automated piecewise linear regression for SHM data

It can be observed from Fig. 5 that the resistance increases with time for the three concrete types. It can also be observed that there is a change in the slope of resistance with time. For example, in the case of PC at 15 mm depth from the exposed surface, the resistance increases from 8 to 10 kΩ in the first 15 days, and then there is a drop in resistance. Again, the resistance starts to increase at a faster rate, rising from 8 to 12 kΩ during the initial 110 days, and subsequently, it nearly stabilizes. In the case of PFA at 15 mm depth, there is a drop in resistance after day 12, and then it starts to increase at a faster rate, rising from 5 to 8 kΩ in 110 days, and it nearly stabilizes in the remaining days. Similarly, it can be observed for MS at 15 mm depth that the resistance drops at approximately 14 days and then starts increasing significantly. The resistance increases from 10 to 35 kΩ in 80 days, and later, it increases at a slower rate. A similar trend can be seen for all the depths plotted in Fig. 5 for PC, PFA, and MS. During the cement hydration process, there are significant changes in the concrete microstructure as the liquid state of cement is changed to a hardened state. As a result, there are changes in mechanical properties and behavioral patterns in the early age of concrete (Glišić and Simon 2000). In addition, the increase in resistance with time is also a result of the microstructural changes due to the hydration of PC and the pozzolanic reactions of PFA and MS. The resistance increases initially with these reactions and either increases at a slower rate or stabilizes when these reactions either slow down or stop (McCarter et al. 2012). After this stage, the resistance decreases only when the concrete starts to deteriorate (Neville 2011; Cosoli et al. 2020). Therefore, in the current study, the SR graphs for each mixture are studied to determine the rate of change in resistance, the time taken to stabilize the resistance, and the stabilized resistance value. It is also necessary to understand and identify the changes in the early age of concrete from the data and its influence on the long-term service life performance.

It is interesting to note that the resistance data is subdivided into smaller disjointed regions, showing the change in the behavior of the resistance data. One of the solutions for addressing this situation was to divide the data into *k*-many clusters and fit a continuous linear regression to different clusters and, thus, perform a PLR (Ferrari-Trecate and Muselli 2002). PLR is used to partition the independent variables into smaller regions and fit a separate segment for each region to define the change in the behavior of the variables (Muhammad et al. 2014). The breakpoint of these regions could determine the change in the gradient of the resistance and the time taken to stabilize the resistance. Therefore, to proceed with the analysis, an ACPLR approach was used to understand and interpret the SR data and reach the solution to the problem, as described in the following.

Step 1: Gaussian weighted moving average (GWMA) filter—One of the main problems with analyzing SHM data using PLR was the noise in the data. As the concrete specimens were exposed to the outdoor environment, they were subjected to rain, humidity, temperature, and other environmental effects. Although the influence of temperature was reduced from the resistance measurements, the data still seem noisy and, hence, can affect the predictions. A GWMA filter was used to compress the noise level of the original data, thereby smoothing the noisy data and reflecting the trend of the original data. This was done by selecting a window of a few data points to extract the noise and then assuming that for the distribution, the mean is zero with standard deviation σ to scale the noise level (Yavuz and Safak 2019). However, there is no straightforward rule for selecting a smoothing window. A short window size is usually selected to extract high-frequency data, while a long smoothing window is selected to extract low-frequency data and may eliminate high-frequency data points (Takatoi et al. 2020). This is explained by considering one data set for MS concrete at 15 mm depth, as shown in Fig. 6(a). As only a few noisy points can be seen in the data, a short window size was chosen to smooth noisy data and maintain an optimum signal-to-noise ratio, as shown in Fig. 6(a).

Step 2: k-*means clustering*—It is an unsupervised ML algorithm that identifies patterns within the data sets without any training data or manual input and provides exploratory analysis (Hearty 2016). The main objective of using a *k*-means clustering algorithm is to separate the data set into clusters, find optimal coefficients, and predict the best possible outcome corresponding to a large number of data points that were difficult to predict manually. The algorithm was selected due to its advantage of dealing with large data

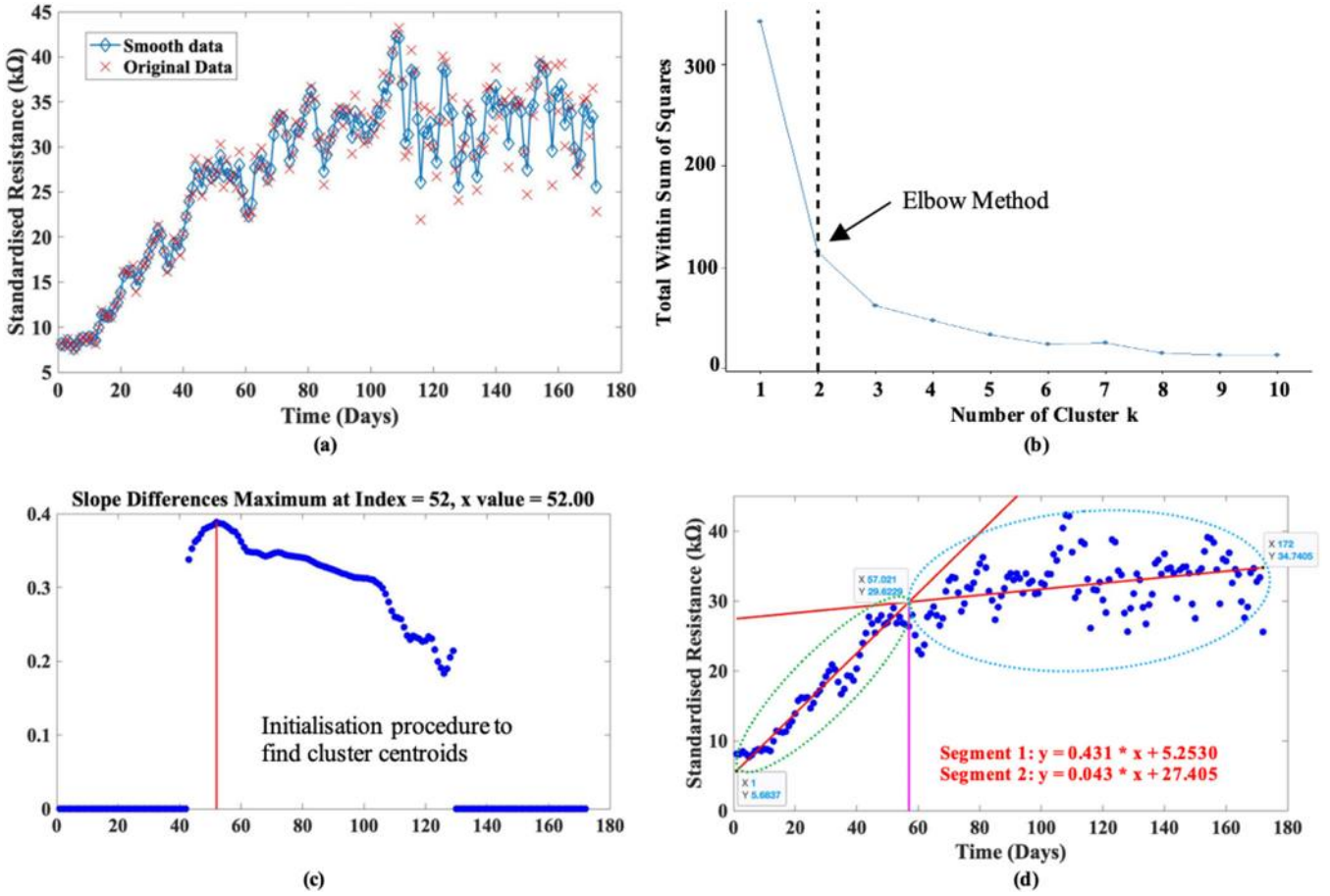

Fig. 6—Steps for ACPLR: (a) original data versus smoothed data (GWMA filter) for MS at 15 mm depth; (b) identifying number of optimal clusters using elbow method; (c) identification of maximum slope difference to find final clusters; and (d) piecewise linear regression on two clusters and breakpoint showing change in resistance, stabilized resistance, and time taken to stabilize resistance. (Note: Process was carried out 18 times [nine times each for short-term and long-term data analysis] in the study.)

sets and running multiple clustering configurations to extract key content (Hearty 2016).

First, the elbow curve method was also used to identify the optimal number of clusters *k*. The algorithm was run for different values of *k* ranging from 1 to 10, and then the sum of squared distances to the centroid across all data points for each value of *k* was calculated. After plotting these points, the point where the average distance from the centroid falls suddenly was identified to find the optimal *k* clusters, as shown in Fig. 6(b). Thus, two clusters were specified for the analysis.

The next step was to provide an approximate location of the breakpoint such that there are at least 25% of the points in one cluster to have a good estimate of the line. The algorithm divided the data into approximate clusters from the approximate location of the breakpoint to get the accurate location of the breakpoint. After initializing the algorithm, new cluster centroids were redefined by extracting the slope difference from the structure array. Based on this, the maximum slope difference was identified, as shown in Fig. 6(c), and thus, the two accurate clusters were found such that the data points were then kept to either side of the maximum slope difference.

Step 3: Piecewise linear regression—After obtaining the accurate location of the clusters, the algorithm estimated the position of the breakpoint and performed piecewise linear regression for each cluster simultaneously to have minimal absolute deviation (Yang et al. 2016). The linear coefficients and the intercept of linear functions were obtained by solving linear regression for each cluster, as shown in Fig. 6(d). Finally, the interaction point for the segments was identified and considered as the ultimate breakpoint for the change in resistance. The intersection point (x, y) was considered as the time taken to stabilize the resistance value (x-axis = 57 days) and the stabilized resistance (y-axis = 29.63 kΩ). Figure 6(d) shows the change in the resistance through two new clusters and linear regression for the two clusters via ACPLR for MS at a depth of 15 mm from the surface.

This paper uses the developed ACPLR-based SHM methodology in two phases for an effective and reliable interpretation of the resistance data. In the first phase, short-term (early-age) resistance data up to 21 days were used to see the early change in resistance due to curing and identify the time taken to develop a discontinuous capillary pore structure during wet curing. The second phase used the complete resistance data to determine the standard steady-state conditions for resistance and diffusion coefficient to predict concrete performance.

RESULTS AND DISCUSSION

Phase 1—Short-term data analysis using ACPLR

As discussed in the last section, there was a change in the resistance during the initial few days of curing, and then the resistance started to increase at a faster rate for all depths in all three types of concrete. The change in resistance at an early age depicts the time taken for the concrete to develop its pore structure and start influencing the physical and mineralogical characteristics; both would contribute to the development of a discontinuous pore structure. According to Basnayake et al. (2020), the time taken to develop this discontinuous capillary pore structure can be identified from the change in slope of the resistance with time. That is, the intersection point of the two segments is considered to demonstrate the minimum time at which the wet curing influences the microstructure of the three concretes. The ACPLR is performed for the initial 21 days to study the change in behavior of concrete due to early-age hydration and curing effect. Table 4 shows both the intersection point at which the resistance starts to increase again and the change in the gradient of resistance.

It can be seen that the intersection point is at 5.18 days for PC, 5.85 days for PFA, and 6.31 days for MS. As the water content for the three concretes is the same (145 kg/m^3), at least 5.5, 6, and 7 days, respectively, are required for PC, PFA, and MS concretes to begin to develop a discontinuous pore structure to satisfy durability requirements. These results are in agreement with Basnayake et al. (2020) that there is a change in resistance before and after obtaining a discontinuous pore structure, and wet curing should be continued for at least 7 days until the pore structure develops discontinuous pores. However, it is important to recognize that this suggested minimum wet curing duration is not universally applicable and may vary for different cementitious materials. In addition, Table 4 shows that MS takes the largest time to obtain a discontinuous pore structure, followed by PFA and PC. However, there is not much difference in the minimum wet curing duration for the three concretes, suggesting that all concretes started developing discontinuous pores almost simultaneously. This is likely because, during the very early stage of portland cement hydration, there is little effect of the pozzolanic reaction (Zelić et al. 2000).

Phase 2—Long-term data analysis using ACPLR

The second phase of the analysis was done to determine the steady-state conditions for the three concrete types and, thereby, to estimate diffusion coefficients to predict the concretes' performance. The ACPLR was performed for the complete data set. Table 5 shows the initial rate of increase in resistance, the value of stabilized resistance, and the time taken to stabilize resistance based on the outputs from the program. The diffusion coefficient values were then calculated using the stabilized resistance values as ρ_{bulk} in the relationship described by Garboczi and Bentz (1992) in Eq. (4).

Overall trends—It is observed that, overall, the resistance increased with time for all concrete types, showing that the pore structure is getting less conductive with time. Figure 7(a) presents the change in resistance with time for the three concretes at 15, 25, and 45 mm depths from the concrete surface. The rate of increase in resistance is the highest for MS, followed by PFA and PC. The data in Table 5 shows that at 15 mm depth, MS has the highest initial resistance, which is approximately five times that of the PFA. The initial resistance values varied for the three concretes and are within the range of one to five times that of the PC. Similarly, MS took more time to stabilize when compared to both PFA and PC, as shown in Fig. 7(b). The addition of SCMs such as microsilica and PFA alters the pore structure

Table 4—Change in resistance at early age and intersection point for two segments

Concrete mixture	Depth of sensor, mm	Change in resistance, %	Intersection point, days	Resistance, kΩ
PC	15	16.6	5.18	8.21
	25	13.4	4.95	5.71
	45	10.9	4.62	4.03
PFA	15	26.4	5.85	3.33
	25	18.8	4.84	2.81
	45	16.8	4.76	2.79
MS	15	65.9	6.31	7.05
	25	57.7	5.63	7.68
	45	52.5	5.54	6.47

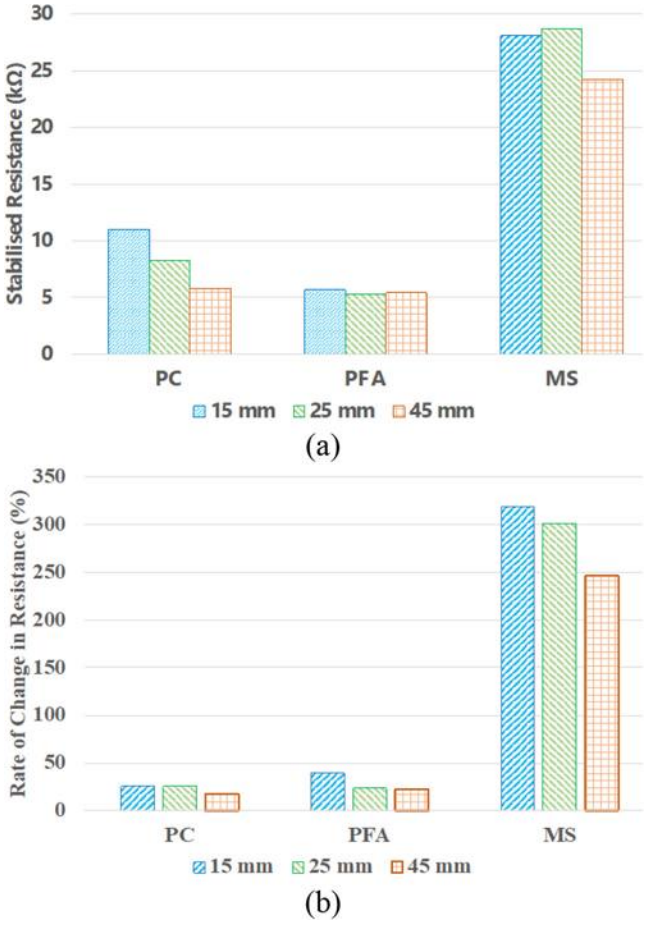

Fig. 7—(a) Rate of change in resistance; and (b) stabilized resistance for three concretes at three different depths determined using ACPLR.

Table 5—Determination of steady-state resistance/diffusion coefficient values using ACPLR

Concrete mixture	Depth, mm	Rate of increase in resistance, %	Time taken to stabilize resistance, days	Stabilized resistance value, kΩ	Diffusion coefficient, $\times 10^{-12}$ m^2/s	Average diffusion coefficient, $\times 10^{-12}$ m^2/s
PC	15	25.6	49.62	11.02	1.11	1.56
	25	25.8	49.77	8.32	1.46	
	45	17.4	50.77	5.78	2.11	
PFA	15	39.1	43.76	5.68	2.45	2.55
	25	23.5	49.76	5.28	2.64	
	45	22.6	52.32	5.42	2.57	
MS	15	318.5	56.09	28.10	1.08	1.12
	25	3301.2	56.91	28.72	1.05	
	45	246.2	58.52	24.27	1.24	

due to the continued pozzolanic reactivity of the binder material in all concrete and increases the rate of change in resistance for MS (Safiuddin et al. 2007; Nanukuttan et al. 2015). Further, microsilica is a denser material and quickly reacts with the portland cement hydration products in a pozzolanic reaction than PFA once the discontinuous capillary pore structure starts to develop. Therefore, it leads to a significant reduction in the porosity of concrete, resulting in a substantial increase in resistance (Sellevold and Radjy 1983; Berke 1988).

Depth effect—Figure 7(b) shows that the resistance at the deeper concrete (45 mm) is lower than at the exposed surface (15 mm) for the three concretes. Similarly, all concretes took more time to stabilize at the deeper part. This is primarily due to the drying and wetting effects of the concretes. Resistance is strongly affected by the interaction occurring between the surface layer of concrete and the atmosphere (McCarter et al. 2005). While the deeper part of the concrete is saturated, the surface releases more moisture, so the evaporation of moisture increases the surface layer's resistance. However, in the case of MS, the resistance nearer to the surface at a depth of 15 mm is lower than at a depth of 25 mm. This may be due to the decrease in resistance caused by water being trapped during the pozzolanic reaction of the binder material in the MS concrete.

Diffusion coefficient—Table 5 shows the estimated diffusion coefficient values for the three mixtures using the stabilized resistance values. It is observed that the diffusion coefficients have a trend opposite to that of the resistance values, as is expected. The continued hydration and pozzolanic reactions reduce both the porosity and the connected porosity in concrete; thus, the overall diffusion coefficient reduces with time (Oslakovic et al. 2008). The calculated values of the diffusion coefficient can then be used to predict the performance of concrete and thereby the service life. Table 5 shows that the best performance among the three concretes is observed for MS. However, confirming this requires further research to determine their durability performance, which is outside the scope of this paper.

Advantages of using ACPLR-based SHM methodology

a) The ACPLR-SHM methodology used for the analysis is an easy and understandable approach to interpret large amounts of complex data by identifying the best aspects of segmented regression. Each line segment identified from the algorithm is balanced against the noise such that it reduces the influence of short-term fluctuations to show long-term results in smooth data. The algorithm efficiently analyzed a large amount of noisy electrical resistance sensor data (24,000 data points) to obtain a steady-state condition of resistance.

b) This approach is more efficient than the conventional method for different types of concrete and exposure conditions to calculate the value of the diffusion coefficient. The value of the diffusion coefficient is either determined by performing nondestructive testing of concretes in the lab or using an assumed diffusion coefficient value from the literature for service life modeling. Thus, this proposed methodology provides valuable knowledge on stabilized resistance values that can be used to calculate diffusion coefficient values.

c) The proposed methodology provides reliable interpretations of the resistance/diffusion coefficient values. The obtained values of diffusion coefficient for the three concretes are in the range of 1 to 3 $\times 10^{-12}$ m^2/s, which is at the high end of the spectrum for good-quality and high-performance concrete as per the literature to measure the performance of the concrete (Bjegović et al. 1995; Yang et al. 2018). Therefore, this criterion can be used as a measure of the performance of the concrete and thereby reinforce the reliability of the proposed methodology.

CONCLUSIONS

The novelty of the proposed methodology lies in its ability to smooth noisy data and perform automated clustering-based piecewise linear regression (ACPLR) on the data set to obtain the time taken to develop a discontinuous pore structure, time taken to stabilize resistance, the stabilized resistance value, and the rate of change in resistance. Based on the results obtained from the application of ACPLR to electrical resistance sensor data, it can be concluded that the proposed methodology diminished the challenges of handling, smoothing, and analyzing large data sets manually.

The methodology is robust enough to provide some valuable insights on the steady-state condition of the resistance, which means interpretability is of importance and thereby can be further used for calculating the diffusion coefficient values. The stabilized resistance and diffusion coefficient values obtained from the structural health monitoring (SHM) data also demonstrated the benefit of using supplementary cementitious materials (SCMs) to improve the durability of concrete. Overall, practitioners and researchers can use the proposed ACPLR-based SHM methodology to interpret resistance sensor data for different types of concrete structures for monitoring and determining the resistance/diffusion coefficient values and thereby predict the performance of concrete in structures.

FURTHER RESEARCH

The results from the study highlighted that even after reducing the influence of temperature on resistance measurements, other environmental conditions, such as ambient temperature, RH, and rainfall also had an impact on the resistance measurements. Therefore, it is suggested that future work should use RH sensors inside and outside the concrete and temperature sensors outside the concrete during SHM and consider their effect on reducing the influence of ambient environmental conditions.

The proposed ACPLR-based SHM methodology was applied to the resistance sensor data from the concrete blocks exposed to environmental conditions for only 6 months. To conduct a more thorough evaluation of the methodology, it is suggested that a long-term study should be conducted across a wider set of locations with marine conditions.

AUTHOR BIOS

ACI member **Harshita Garg** *is a Doctorate Student at the School of Civil Engineering, University of Leeds, Leeds, UK. She received her bachelor's degree in architecture from India and her MSc. (Eng.) in international construction management and engineering from the University of Leeds. Her research interests include structural health monitoring, performance of concrete structures, service life prediction, and maintenance management of civil infrastructure.*

Kai Yang *is an Associate Professor in the College of Materials Science and Engineering, Chongqing University, Chongqing, China. He received his bachelor's and master's degrees from Chongqing University, and his PhD from Queen's University Belfast, Belfast, UK. His research interests include durability assessment of structures, structural health monitoring, alkali-activated cementitious materials, and the development of nondestructive tests for assessing concrete.*

Anthony G. Cohn *is a Professor at the School of Computing, University of Leeds. He received his BSc and PhD from the University of Essex, Essex, UK. His research interests include artificial intelligence, knowledge representation and reasoning, data and sensor fusion, cognitive vision, spatial representation and reasoning, and robotics.*

Duncan Borman *is an Associate Professor at the University of Leeds, where he received his MSc and PhD. His research interests include computational fluid dynamics and mathematical modeling of environmental and multiphase flows, particularly those with industrial applications.*

Sreejith V. Nanukuttan *is a Senior Lecturer at the School of Natural and Built Environment, Queens University Belfast, where he received his PhD. His research interests include testing and monitoring of structures, durability of structures, and service-life prediction.*

P. A. Muhammed Basheer, *FACI, is a Professor of civil engineering and the Executive Dean of the School of Energy, Geoscience, Infrastructure and Society at Heriot-Watt University, Edinburgh, UK. He received his PhD and DSc from Queen's University Belfast. He is a member of ACI Committees 130, Sustainability of Concrete; 201, Durability of Concrete; 211, Proportioning Concrete Mixtures; 236, Material Science of Concrete; 365, Service Life Prediction; and 444, Structural Health Monitoring. His research interests include the durability of concrete, nondestructive tests, structural health monitoring, performance of materials in structures, and service life prediction.*

NOTATION

D_0	=	diffusion coefficient of chloride ion in pure water
E_a	=	activation energy, kJ/mol
R_g	=	universal gas constant, 8.3141×10^{-3} kJ/mole/K
ρ	=	resistivity of pore fluid
ρ_0	=	pre-exponential constant, kΩ
ρ_{bulk}	=	bulk resistivity of saturated material
ρ_x	=	equivalent resistance, kΩ, at reference temperature 25°C
ρ_y	=	resistance, kΩ, recorded at the temperature at $T_{k,x}$

REFERENCES

ACI Committee 201, 2016, "Guide to Durable Concrete (201.2R-16)," American Concrete Institute, Farmington Hills, MI, 84 pp.

ACI Committee 444, 2021, "Structural Health Monitoring Technologies for Concrete Structures—Report (ACI PRC-444.2-21)," American Concrete Institute, Farmington Hills, MI, 110 pp.

Ahmed, Z.; Ali, J. S. M.; Rafeeq, M.; and Hrairi, M., 2019, "Application of Machine Learning with Impedance Based Techniques for Structural Health Monitoring of Civil Infrastructure," *International Journal of Innovative Technology and Exploring Engineering (IJITEE)*, V. 8, No. 6S4, pp. 1139-1148.

Aydin, K., and Kisi, O., 2015, "Damage Diagnosis in Beam-Like Structures by Artificial Neural Networks," *Journal of Civil Engineering and Management*, V. 21, No. 5, pp. 591-604. doi: 10.3846/13923730.2014.890663

Azarsa, P., and Gupta, R., 2017, "Electrical Resistivity of Concrete for Durability Evaluation: A Review," *Advances in Materials Science and Engineering*, pp. 1-30. doi: 10.1155/2017/8453095

Ballo, F.; Gobbi, M.; Mastinu, G.; and Previati, G., 2014, "Advances in Force and Moments Measurements by an Innovative Six-Axis Load Cell," *Experimental Mechanics*, V. 54, No. 4, pp. 571-592. doi: 10.1007/s11340-013-9824-4

Basheer, P. A. M.; Gilleece, P. R. V.; Long, A. E.; and Mc Carter, W. J., 2002, "Monitoring Electrical Resistance of Concretes Containing Alternative Cementitious Materials to Assess Their Resistance to Chloride Penetration," *Cement and Concrete Composites*, V. 24, No. 5, pp. 437-449. doi: 10.1016/S0958-9465(01)00075-0

Basheer, P. A. M.; Grattan, K. T.; Sun, T.; Long, A. E.; McPolin, D.; and Xie, W., 2004, "Fiber Optic Chemical Sensor Systems for Monitoring pH changes in Concrete," *Advanced Environmental, Chemical, and Biological Sensing Technologies II*, International Society for Optics and Photonics, Bellingham, WA, pp.144-153.

Basnayake, K.; Mazumder, A. F.; Attanayake, U.; and Berke, N. S., 2020, "Assessment of Concrete Curing Duration using Bulk Electrical Conductivity and Porosity," *Transportation Research Record: Journal of the Transportation Research Board*, V. 2674, No. 10, pp. 261-268. doi: 10.1177/0361198120935114

Berke, N. S., 1988, "Microsilica and Concrete Durability," *Transportation Research Record: Journal of the Transportation Research Board*, V. 1204, pp. 21-26.

Bjegović, D.; Krstić, V.; Mikulić, D.; and Ukrainczyk, V., 1995, "C-D-c-t Diagrams for Practical Design of Concrete Durability Parameters," *Cement and Concrete Research*, V. 25, No. 1, pp. 187-196. doi: 10.1016/0008-8846(94)00126-J

Brownjohn, J. M. W.; de Stefano, A.; Xu, Y. L.; Wenzel, H.; and Aktan, A. E., 2011, "Vibration-Based Monitoring of Civil Infrastructure: Challenges and Successes," *Journal of Civil Structural Health Monitoring*, V. 1, No. 3-4, pp. 79-95.

Bungey, J. H.; Millard, S. G.; and Grantham, M. G., 2006, *Testing of Concrete in Structures*, fourth edition, Taylor & Francis, New York, 352 pp.

Chandrasekaran, S., 2019, "Structural Health Monitoring: An Overview," *Structural Health Monitoring with Application to Offshore Structures*, World Scientific, pp. 1-50.

Cosoli, G.; Mobili, A.; Tittarelli, F.; Revel, G. M.; and Chiariotti, P., 2020, "Electrical Resistivity and Electrical Impedance Measurement in Mortar and Concrete Elements: A Systematic Review," *Applied Sciences,* Basel, Switzerland, V. 10, No. 24, pp. 1-42. doi: 10.3390/app10249152

Demircilioğlu, E.; Teomete, E.; Schlangen, E.; and Baeza, F. J., 2019, "Temperature and Moisture Effects on Electrical Resistance and Strain Sensitivity of Smart Concrete," *Construction and Building Materials*, V. 224, No. 11, pp. 420-427. doi: 10.1016/j.conbuildmat.2019.07.091

Diez, A.; Khoa, N. L. D.; Makki Alamdari, M.; Wang, Y.; Chen, F.; and Runcie, P., 2016, "A Clustering Approach for Structural Health Monitoring on Bridges," *Journal of Civil Structural Health Monitoring*, V. 6, No. 3, pp. 429-445. doi: 10.1007/s13349-016-0160-0

Dong, C. Z., and Catbas, F. N., 2021, "A Review of Computer Vision-Based Structural Health Monitoring at Local and Global Levels," *Structural Health Monitoring*, V. 20, No. 2, pp. 692-743. doi: 10.1177/1475921720935585

Fabo, P.; Sedivy, S.; Kuba, M.; Buchholcerova, A.; Dudak, J.; and Gaspar, G., 2020, "PLC Based Weather Station for Experimental Measurements," *19th International Conference on Mechatronics – Mechatronika (ME)*, Prague, Czech Republic, pp. 1-4.

Farrar, C. R., and Worden, K., 2012, *Structural Health Monitoring: A Machine Learning Perspective*, first edition, John Wiley & Sons, Ltd, Chichester, UK, 631 pp.

Ferrari-Trecate, G., and Muselli, M., 2002, "A New Learning Method for Piecewise Linear Regression," J. R. Dorronsoro, ed., *Artificial Neural Networks – ICANN 2002, International Conference*, Springer Verlag, Madrid, Spain, pp. 444-449.

Flah, M.; Nunez, I.; Ben Chaabene, W.; and Nehdi, M. L., 2021, "Machine Learning Algorithms in Civil Structural Health Monitoring: A Systematic Review," *Archives of Computational Methods in Engineering*, V. 28, No. 4, pp. 2621-2643. doi: 10.1007/s11831-020-09471-9

Frangopol, D. M., and Kim, S., 2014, "Prognosis and Life-Cycle Assessment Based on SHM Information," *Sensor Technologies for Civil Infrastructures. Volume 2 - Applications in Structural Health Monitoring*, M. L. Wang, J. P. Lynch, and H. Sohn, eds., Woodhead Publishing, Netherlands, pp. 145-171.

Garboczi, E. J., and Bentz, D. P., 1992, "Computer Simulation of the Diffusivity of Cement-Based Materials," *Journal of Materials Science*, V. 27, No. 8, pp. 2083-2092. doi: 10.1007/BF01117921

Glišić, B., and Simon, N., 2000, "Monitoring of Concrete at Very Early Age Using Stiff SOFO Sensor," *Cement and Concrete Composites*, V. 22, No. 2, pp. 115-119. doi: 10.1016/S0958-9465(99)00037-2

Hearty, J., 2016, *Advanced Machine Learning with Python*, first edition, Packt Publishing, Birmingham, UK, 278 pp.

Hernandez, W., 2006, "Improving the Response of a Load Cell by Using Optimal Filtering," *Sensors (Basel)*, V. 6, No. 7, pp. 697-711. doi: 10.3390/s6070697

Hossain, K. M. A., and Lachemi, M., 2004, "Corrosion Resistance and Chloride Diffusivity of Volcanic Ash Blended Cement Mortar," *Cement and Concrete Research*, V. 34, No. 4, pp. 695-702. doi: 10.1016/j.cemconres.2003.10.021

Jansen, D.; Goetz-Neunhoeffer, F.; Lothenbach, B.; and Neubauer, J., 2012, "The Early Hydration of Ordinary Portland Cement (OPC): An Approach Comparing Measured Heat Flow with Calculated Heat Flow from QXRD," *Cement and Concrete Research*, V. 42, No. 1, pp. 134-138. doi: 10.1016/j.cemconres.2011.09.001

Kalkani, E. C., 1992, "Ambient Temperature Effect in Concrete Dam Foundation Seepage," *Journal of Geotechnical Engineering*, ASCE, V. 118, No. 1, pp. 1-11. doi: 10.1061/(ASCE)0733-9410(1992)118:1(1)

Karbassi, A.; Mohebi, B.; Rezaee, S.; and Lestuzzi, P., 2014, "Damage Prediction for Regular Reinforced Concrete Buildings using the Decision Tree Algorithm," *Computers and Structures*, V. 130, pp. 46-56. doi: 10.1016/j.compstruc.2013.10.006

McCarter, W. J.; Chrisp, T. M.; Starrs, G.; Adamson, A.; Owens, E.; Basheer, P. A. M.; Nanukuttan, S. V.; Srinivasan, S.; and Holmes, N., 2012, "Developments in Performance Monitoring of Concrete Exposed to Extreme Environments," *Journal of Infrastructure Systems*, ASCE, V. 18, No. 3, pp. 167-175. doi: 10.1061/(ASCE)IS.1943-555X.0000089

McCarter, W. J.; Chrisp, T. M.; Starrs, G., Basheer, P. A. M.; and Blewett, J., 2005, "Field Monitoring of Electrical Conductivity of Cover-Zone Concrete," *Cement and Concrete Composites*, V. 27, No. 7-8, pp. 809-817.

Montemor, M. F.; Alves, J. H.; Simões, A. M.; Fernandes, J. C. S.; Lourenço, Z.; Costa, A. J. S.; Appleton, A. J.; and Ferreira, M. G. S., 2006, "Multiprobe Chloride Sensor for In-Situ Monitoring of Reinforced Concrete Structures," *Cement and Concrete Composites*, V. 28, No. 3, pp. 233-236. doi: 10.1016/j.cemconcomp.2006.01.005

Muhammad, Y., S.; Afgan, N.; Iqbal, M.; and Hussain, I., 2014, "Modeling Non-linear Behavior of Independent Variables," *International Journal of Business and Social Science*, V. 5, No. 13, pp. 192-200.

Nanukuttan, S. V.; Basheer, P. A. M.; McCarter, W. J.; Tang, L.; Holmes, N.; Chrisp, T. M.; Starrs, G.; and Magee, B., 2015, "The Performance of Concrete Exposed to Marine Environments: Predictive Modelling and Use of Laboratory/On-Site Test Methods," *Construction and Building Materials*, V. 93, pp. 831-840. doi: 10.1016/j.conbuildmat.2015.05.083

Nanukuttan, S. V.; Campbell, N.; Mccarter, J.; Basheer, M.; Mcrobert, J.; and McBurney, P., 2017a, "State of Health Assessment of Concrete Repair using Electrical Sensors," *2nd International RILEM/COST Conference on Early Age Cracking and Serviceability in Cement-Based Materials and Structures*, S. Staquet, and D. Aggelis, eds., RILEM Publications SARL, Brussels, pp. 149-154.

Nanukuttan, S. V.; Yang, K.; McCarter, J.; and Basheer, P. A. M., 2017b, "Methods of Assessing the Durability and Service Life of Concrete Structures," *Annual Technical Symposium of the Institute of Concrete Technology (ICT)*, Leeds, UK, pp. 1-14.

Nehdi, M. L., and Soliman, A. M., 2011, "Early-Age Properties of Concrete: Overview of Fundamental Concepts and State-of-the-Art Research," *Construction Materials*, V. 164, No. 2, pp. 57-77.

Neville, A. M., 2011, *Properties of Concrete*, fifth edition, Pearson Education Limited, London, UK, 846 pp.

Nokken, M. R., and Hooton, R. D., 2007, "Using Pore Parameters to Estimate Permeability or Conductivity of Concrete," *Materials and Structures*, V. 41, No. 1, pp. 1-16. doi: 10.1617/s11527-006-9212-y

Oslakovic, I. S.; Serdar, M.; Bjegovic, D.; and Mikulic, D., 2008, "Modeling of Time Depended Changes of Chloride Diffusion Coefficient," *11DBMC International Conference on Durability of Building Materials and Components*, Istanbul, Turkey, pp. 203-2112.

Pan, Y., and Zhang, L., 2021, "Roles of Artificial Intelligence in Construction Engineering and Management: A Critical Review and Future Trends," *Automation in Construction*, V. 122, No. 2, pp. 1-21. doi: 10.1016/j.autcon.2020.103517

Perveen, K.; Bridges, G. E.; Bhadra, S.; and Thomson, D. J., 2014, "Corrosion Potential Sensor for Remote Monitoring of Civil Structure based on Printed Circuit Board Sensor," *IEEE Transactions on Instrumentation and Measurement*, V. 63, No. 10, pp. 2422-2431. doi: 10.1109/TIM.2014.2310092

Rai, V. K., 2007, "Temperature Sensors and Optical Sensors," *Applied Physics B: Lasers and Optics*, V. 88, No. 2, pp. 297-303. doi: 10.1007/s00340-007-2717-4

Safiuddin, M.; Raman, S. N.; and Zain, M. F. M., 2007, "Effect of Different Curing Methods on the Properties of Microsilica Concrete," *Australian Journal of Basic and Applied Sciences*, V. 1, No. 2, pp. 87-95.

Schöler, A.; Lothenbach, B.; Winnefeld, F.; Haha, M. B.; Zajac, M.; and Ludwig, H.-M., 2017, "Early Hydration of SCM-Blended Portland Cements: A Pore Solution and Isothermal Calorimetry Study," *Cement and Concrete Research*, V. 93, pp. 71-82. doi: 10.1016/j.cemconres.2016.11.013

Scrivener, K. L., and Nonat, A., 2011, "Hydration of Cementitious Materials, Present and Future," *Cement and Concrete Research*, V. 41, No. 7, pp. 651-665. doi: 10.1016/j.cemconres.2011.03.026

Sellevold, E. J., and Radjy, F. F., 1983, Condensed Silica fume (Microsilica) in Concrete: Water Demand and Strength Development, *Symposium Paper*, V. 79, pp. 677-694.

Smarsly, K.; Dragos, K.; and Wiggenbrock, J., 2016, "Machine Learning Techniques for Structural Health Monitoring," *8th European Workshop on Structural Health Monitoring (EWSHM)*, Bilbao, Spain, pp. 1522-1531.

Steinhart, J. S., and Hart, S. R., 1968, "Calibration Curves for Thermistors," *Deep-Sea Research and Oceanographic Abstracts*, V. 15, No. 4, pp. 497-503. doi: 10.1016/0011-7471(68)90057-0

Takatoi, G.; Sugawara, T.; Sakiyama, K.; and Li, Y., 2020, "Simple Electromagnetic Analysis against Activation Functions of Deep Neural Networks," J. Zhou, ed., *International Conference on Applied Cryptography and Network Security*, Springer, Cham, pp.181-197.

Tanner, B. D., 1990, "Automated Weather Stations," *Remote Sensing Reviews*, V. 5, No. 1, pp. 73-98. doi: 10.1080/02757259009532123

Yang, K.; Basheer, P. A. M.; Bai, Y.; Magee, B. J.; and Long, A. E., 2014, "Development of a New In-Situ Test Method to Measure the Air Permeability of High-Performance Concretes," *NDT & E International*, V. 64, pp. 30-40. doi: 10.1016/j.ndteint.2014.02.005

Yang, K.; Nanukuttan, S. V.; McCarter, W. J.; Long, A.; and Basheer, P. A. M., 2018, "Challenges and Opportunities for Assessing Transport Properties of High-performance Concrete," *Revista ALCONPAT*, V. 8, No. 3, pp. 246-263. doi: 10.21041/ra.v8i3.301

Yang, L.; Liu, S.; Tsoka, S.; and Papageorgiou, L. G., 2016, "Mathematical Programming for Piecewise Linear Regression analysis," *Expert Systems with Applications*, V. 44, pp. 156-167. doi: 10.1016/j.eswa.2015.08.034

Yavuz, K., and Safak, E., 2019, "Structural Health Monitoring: Real-Time Data Analysis and Damage Detection," *Seismic Structural Health Monitoring*, M. P. Limongelli and M. Çelebi, eds., Springer, Cham, pp. 171-197.

Yu, C.; Wang, J.; Tan, L.; and Tu, X., 2011, "A Bridge Structural Health Data Analysis Model Based on Semi-supervised Learning," *IEEE International Conference on Automation and Logistics (ICAL)*, Chongqing, China, IEEE, pp. 30-34.

Zelić, J.; Rušić, D.; Veža, D.; and Krstulović, R., 2000, "Role of Silica Fume in the Kinetics and Mechanisms During the Early Stage of Cement Hydration," *Cement and Concrete Research*, V. 30, No. 10, pp. 1655-1662. doi: 10.1016/S0008-8846(00)00374-4

Zhang, C.; Zhang, W.; Webb, D. J.; and Peng, G. D., 2010, "Optical Fibre Temperature and Humidity Sensor," *Electronics Letters*, V. 46, No. 9, pp. 643-644. doi: 10.1049/el.2010.0879

ACI MATERIALS JOURNAL TECHNICAL PAPER

Title No. 121-M19

Relation between Strength and Yield Stress in Fiber-Reinforced Mortar

by Ronan Chometon, Maxime Liard, Pascal Hébraud, and Didier Lootens

The need to constantly improve the quality and properties of manufactured products leads to the development of hybrid materials that combine different elements, complementing one another. Fiber-reinforced mortar is one of those products, as the fibers are used to improve cementitious materials' flexural weakness. Experimental data on different metallic fibers dispersed in mortar demonstrate the correlation between early-age rheological properties and long-term mechanical strength. Both quantities depend on the ratio of the solid volume fraction of the fiber to a critical solid volume fraction characteristic of the form factors of the fiber. It is demonstrated that both effects arise from the packing stress of the fibers in the mortar when their concentrations are close to their maximum packing fraction. Geometrical arguments are used to explain how this critical volume fraction is related to the fiber form factor. Then, it enables the building of master curves using geometrical arguments.

Keywords: critical volume fraction; fiber-reinforced mortar; flexural strength; master curves; mortar; rheology.

INTRODUCTION

The need to reduce the quantity of construction materials drives the industry to develop new materials with more diverse and advanced properties. Most construction materials should be kept affordable as the amount needed is significant and essentially obtained from cheap local raw materials. Most of the time, these materials fulfill one property—such as structural, acoustic, or thermal—and should be used in combination with several other materials glued together to build sandwich walls. Developing composite or hybrid materials whose properties are a combination of their constitutive components' properties could then be a solution to limit the number of layers required for the sandwich walls, reducing the number of materials and simplifying the recycling process. The main difficulty of a hybrid formulation is ensuring the positive interactions between its different elements: the aim is to collect the best of each material and avoid any property conflict. This is particularly relevant for the concrete industry as cementitious materials display a very high compressive strength—up to 230 MPa[1]—but a relatively weak flexural strength—approximately 10 times weaker than the compressive strength. This weakness makes standard concrete unsuitable for structural applications required for slabs or bridges; therefore, metallic reinforcing bars are mandatory according to the norms.[2] Over the last decades, numerous studies have been carried out to improve cementitious materials' flexural strength to reduce the systematic use of metallic reinforcing bars. Different strategies have been explored, such as the development of epoxy-modified concrete,[3] the addition of latex suspensions,[4] or crushed tires,[5] but the most promising option is the addition of fibers.[6,7] Fiber-reinforced material is an example of such a hybrid: the fibers are added and mixed with the original cementitious slurry to improve its mechanical properties. This method is not restricted to concrete but is also used in different industries, such as ceramics.[8] Adding a high concentration of fibers in concrete leads to the creation of ultra-high-performance concrete (UHPC), whose flexural strength can reach up to 50 MPa.[9] The main drawbacks of a fiber-reinforced material are: 1) the degradation of the rheological properties of the original paste with the addition of fibers,[10,11] leading to such issues as pumping or casting difficulties; and 2) the price increases of the formulation generated by the addition of fibers.

Fiber-reinforced cementitious composites (FRCC) have been studied regarding rheological and mechanical properties.[12] The fiber's nature impacts the fracture toughness of the composite,[12] mainly depending on the interaction or bond of the fibers with the cementitious matrix. The microcrack formations can be delayed with an increase in the toughness of the composite with polyvinyl alcohol (PVA), refined cellulose (RC),[13] metallics,[14,15] or glass.[16] On the other hand, polypropylene (PP) or polyethylene fibers are not chemically binding to the cementitious matrix. Other natural fibers[17] are now used to reinforce mortar and concrete.

The impact of the fiber aspect ratio, which is defined as the ratio of the length of the fiber to its thickness, on mechanical properties has been studied on PVA fibers,[18] PP,[19,20] and steel.[21] The conclusions differ depending on the type of fiber, demonstrating that for steel fiber at a given concentration, the larger aspect ratio exhibits better performance in terms of either the flexural strength or toughening effect, and for the polymer-type fiber, an optimal form factor has been observed.[22] Several empirical models[23] and machine learning algorithms have been built to predict the impact of the flexural strength on the fiber volume fraction and aspect ratio.[24]

The influence of the fiber volume fraction, rigidity, length, and diameter on the rheological and mechanical properties is described by the fiber factor (*FF*), which can be obtained by multiplying the fiber volume fraction by its aspect ratio.[19]

ACI Materials Journal, V. 121, No. 2, March 2024.

MS No. M-2022-409.R3, doi: 10.14359/51740371, received August 14, 2023, and reviewed under Institute publication policies.

Table 1—Mass concentration per weight and percentage of different components of mortar equivalent concrete

Components	OPC	Limestone	Sand	Water	PCE	Total
Mass, %	22	21.5	44	12	0.5	100
Mass, g	440	430	880	240	12	2000

Table 2—Form factors and maximum packing fraction ϕ_0 of metallic fibers

Fiber types	*L*30	*L*20-2	*L*20-1	*L*15	*L*10	*L*5
Length *L*, mm	30	20	20	15	10	5
Width *w*, mm	1.6	1.6	1	1	1	1
Thickness *d*, μm	29	29	24	24	24	24

Table 3—Equivalent between mass fiber added and solid volume fraction of metallic fibers in standard mortar

Mass fiber, g, added in 2 kg of mortar	15	30	45	60	75	112	150	187	225
Equivalent solid volume fraction, %	0.2	0.4	0.6	0.8	1	1.5	2	2.5	3

The *FF* impact on the rheological properties is the same for all types of fibers, with an increase in the yield stress or decrease in the slump spread as well as an increase in the plastic viscosity.[19,21] The influence of the fiber on the mechanical properties is defined with two critical limits of the *FF*: below a critical factor called *Fc*, the influence of the fiber on the mechanical properties is negligible, and above a density factor called *Fd*, the rheological and mechanical properties are worsened due to the nonuniform dispersal of the fibers. The limits of *Fc* and *Fd* depend on the nature and rigidity of the fibers: 30 and 80, respectively, for glass fibers; 100 and 300 for PP; or 100 and 400 for PVA fibers.[19] There is a further need to understand the mechanism of the flexural strength and viscosity increases with the addition of fibers. This would rationalize the optimization of the concrete formulations. To this goal, the correlations between the composite performances, either mechanical or rheological, are then always made with dimensionless parameters to establish such a correlation based on pure geometrical considerations, linking the rheological and mechanical properties with critical volume fractions, which can be calculated from the fiber form factor.

RESEARCH SIGNIFICANCE

This paper aims to link the mechanical and rheological properties of metallic fiber-reinforced mortar with the organization of the fibers. The characterization of the metallic fibers' concentration is made based on the flexural strength, and the rheological properties of the fresh mixture are made and rescaled on geometrical parameters with a series of six different metallic fibers. The impact of the fiber form factor and concentration on the material's physical properties is studied in a fresh and hardened state, showing that the paste's yield stress evolution and the set mortar's flexural strength are linked with the relative fiber volume fractions.

EXPERIMENTAL INVESTIGATION

Materials and formulations

The rheological and mechanical impacts of the fiber addition are studied on a mortar prepared with a binary binder made of ordinary portland cement (OPC) type CEM I 52.5N and limestone having the same particle-size distribution. Natural siliceous sand with a particle size ranging from 0.1 to 0.5 mm with a specific gravity of 2.6 kg/L and water absorption of 1% was used. Finally, a noncommercial plasticizer of the type of polycarboxylate high-range water-reducing admixture (PCE) with a solid content of 40% and a density of 1.08 kg/L was added at a concentration of 0.5% to obtain a self-leveling mortar. The formulation of the reference mortar is shown in Table 1 in terms of percentage and mass used. A 2 kg mortar mixture was prepared with a water-cement ratio (*w*/*c*) of 0.56 and a water-binder ratio (*w*/*b*) of 0.28. The mixing protocol consists of mixing for 1 minute in a mixer at speed one, then letting the paste rest for 30 seconds, and mixing again at speed two for 2 minutes. The resulting mortar is self-leveling with a density of 2 kg/L.

The fibers used are commercial; they are amorphous metallic fibers for concrete and mortar reinforcement with a density of 7.25 kg/L.[25] A series of six different fibers were tested to study the impact of the form factor on the fibers' rheological and mechanical properties of the mixture. The reference names of the fibers with their equivalent length *L*, width *w*, and thickness *d* are summarized in Table 2.

The different fibers were incorporated in a second step into the self-leveling mortar with a second mixture of 1 minute at speed one. A noncommercial deformer was used to keep the air content below 2% for all the mixtures to avoid the air's negative impact on the mechanical properties. All the fiber concentrations are given in percentage per volume. Table 3 gives the equivalence between mass concentration and volume fraction of the fibers in the mortar mixtures. Due to the high density of the fiber, the mass added for 3% is 223 g for 2 kg of mortar. No sedimentation of the fibers was observed, as confirmed by tomography measurements.

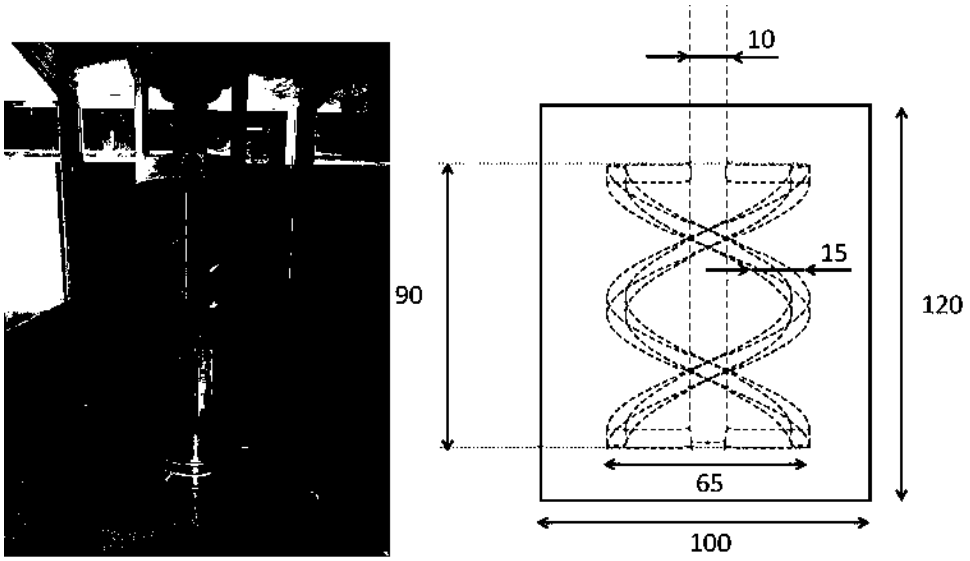

Fig. 1—Concrete rheometer used for measurement of rheological properties of mortar pastes: (left) picture of rheometer with measuring cell; and (right) dimensions of geometry.

Rodlike PVA fiber was used for complementary rheological measurements and validation of theory building on the metal fibers. The ductile monfilament PVA fiber has a diameter of 38 μm, a length of 8 mm, and a density of 1.3 g/cm^3. The PVA fibers are also used to improve the strength properties of concrete and mortar.

Rheological measurements

To compare the rheological and mechanical properties, two different tests have been conducted: 1) rheological with a concrete rheometer; and 2) mechanical, with a three-point flexural test. The rheological properties of the fresh reinforced mortar are measured with a custom-made concrete rheometer represented in the left picture of Fig. 1. It is equipped with a double-helicoidal geometry designed for the rheological measurement of a cement paste, as described in former works,[26-28] and with the dimensions given in the right picture of Fig. 1. The rheometer was calibrated with a calibration oil developed by the National Institute of Standards and Technology (NIST).[29] This calibration allows the quantification of the shear rate and shear stress directly from the measurement of the geometry rotation speed and torque. The measurement protocol is as such: after a pre-shear of 60 seconds at a shear rate $\dot{\gamma}$ of 100 s^{-1} is first applied, the shear stress τ is measured as a function of the shear rate $\dot{\gamma}$, with 30 points evenly distributed in a logarithmic scale from 100 to 0.1 s^{-1}. The measurement is run three times to ensure good reproducibility.

Flexural strength measurements

The mechanical properties of the mortars are measured on prisms of standard dimensions of 4 x 4 x 16 cm. The prisms are stored in a chamber with controlled curing conditions of 68% relative humidity and 23°C for 7 days. After 7 days of curing, the flexural strength σ_f is measured with the three-point bending test method.

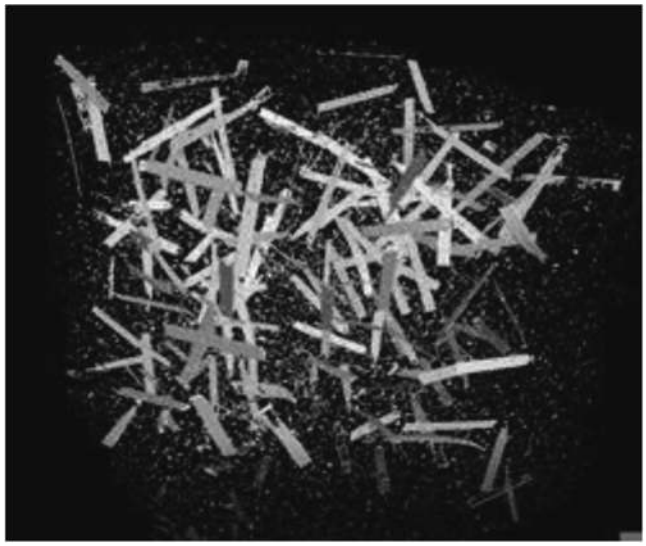

Fig. 2—X-ray tomography of mortar prepared with 1% of L*30. Probe is cube of 40 mm side.*

X-ray tomography

The X-ray tomography imaging was performed with a three-dimensional (3-D) X-ray micro-computed tomography system. The illumination is realized with an X-ray generator with a tungsten filament and a tungsten target, and the detector is a matrix plane sensor consisting of 1920 x 1536 pixels of size 127 x 127 μm. A representation of a 40 mm side sample prepared with 1% of the *L*30 fiber is shown in Fig. 2.

It is very easy to see the metallic fibers. Much smaller objects can also be seen, which are a few microns in size, probably metal oxide particles from the cement, which absorb approximately as much as metal fibers. The metal fibers are not deformed and do not form clusters and appear to be anisotropic without any visible sedimentation, which confirms that the mortar matrix can be reasonably regarded as uniform in nature.

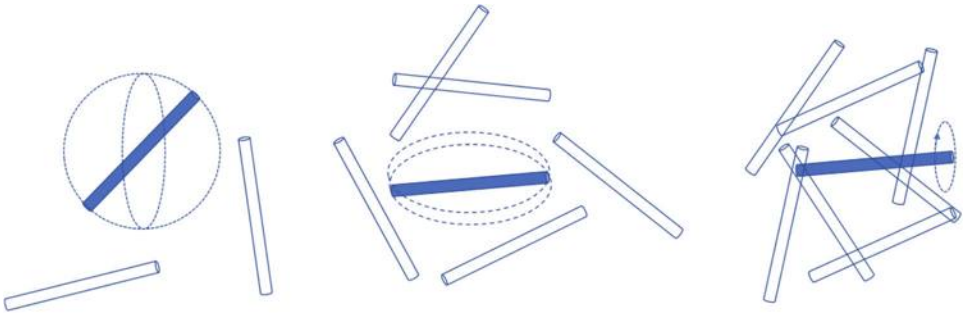

Fig. 3—Three regimes of fibers in solution, from left to right: dilute; semi-dilute, less rotational movement is allowed; and entangled, only rotation on cylindrical axis is possible. (Adapted from Evans and Gibson.[30])

ANALYTICAL INVESTIGATION

The critical flexural strength σ_f is calculated following Eq. (1), with the maximum force applied Fc where the facture of the prism occurs, and with the dimensions of the prism: A = 40 mm and L = 160 mm.

$$\sigma_f = \frac{3FcL}{2A^3} \quad (1)$$

The toughness of the prism, which is the energy the material can absorb by deforming plastically before its rupture, is also calculated using an integral of the force along its displacement δ, as described in Eq. (1).

$$U = \int_0^{\delta_\infty} F(\delta) d\delta \quad (2)$$

All the results shown in the next section are the mean values of the three probes used to measure either the rheological properties or the flexural strength. Error bars correspond to the standard deviation calculated from the experimental data.

To characterize quantitatively the impact of the fiber form factors on the rheological and mechanical properties, the work of Evans and Gibson[30] is adapted, who studied the packing of randomly oriented fibers. This is done by assimilating the metallic fibers to a rodlike fiber with the same length l and an equivalent circular surface with a diameter d_e, calculated by assimilating the rectangular section of the fiber to a circle and defined in Eq. (3).

$$d_e = \sqrt{\frac{4dw}{\pi}} \quad (3)$$

A theoretical packing of the fiber can be calculated if a fiber concentration is considered by unit volume c, which is the number of fibers per unit of volume. Then, according to fiber conservation, the fiber volume fraction ϕ, being the volume occupied by the fibers, is equal to

$$\phi = \frac{\pi d_e^2 lc}{4} \quad (4)$$

Evans and Gibson[30] made a parallel with the liquid-crystal transition, where the particles are constrained by their neighbors. There are three concentration regimes described in Fig. 3: a) the dilute one, where $c \leq l^{-3}$ and each fiber can be rotated freely around all axes without touching the others; b) the semi-dilute regime $l^{-3} \leq c \leq l^{-2}d_e^{-1}$, where a fiber can only rotate in a plane without any contact; and c) the entangled regime $l^{-2}d_e^{-1} \leq c \leq l^{-1}d_e^{-2}$, where the fibers are only free to rotate around its cylindrical axis of symmetry without touching its neighbors. This corresponds to a nematic ordering.

Table 4—Maximum fiber volume fraction ϕ_0 of different metallic fibers used, as computed from Eq. (5) with k_{th} = 4

Fiber types	*L*30	*L*20-2	*L*20-1	*L*15	*L*10	*L*5
ϕ_0, %	3.3	5.0	3.6	4.8	7.2	14.4

Nevertheless, in this study's system, where the fibers are dispersed in a complex media, they cannot self-organize in a fully nematic state, and their maximum volume fraction will be lower than the maximum volume fraction of the nematic ordering. One needs to consider the maximum volume fraction of randomly oriented fibers, which may be evaluated by considering fibers at low volume fractions and then compressing the system up to the point where it cannot be compressed further without deformation of the fibers. This leads to the result[31] that the maximum number fraction of the rods is

$$\phi_0 = \frac{kd_e}{l} \quad (5)$$

where k is a numerical refactor, which has been numerically evaluated as k_{th} = 4. Experiments show this expression is valid, but experiments disagree on the numerical prefactor when a k_{exp} = 5.3 is measured.[32] It should be noted that both the maximum packing and the transition between disordered and nematic states scale as the inverse of the form factor, FF.

The list of ϕ_0 calculated with the theoretical coefficient k_{th} for all the types of fibers used is given in Table 4.

EXPERIMENTAL RESULTS AND DISCUSSION

Effect of fiber content on flexural strength

The effect of fiber concentration on the flexural strength of the fiber-reinforced mortar was tested, and the evolution of the strength as a function of the applied deformation for different concentrations of the fiber type *L*30 is shown in Fig. 4. One can observe that below a given fiber volume fraction, in the case of the *L*30, ϕ = 0.4%v, the fibers do

not have any significant effect on the mechanical properties, as has already been observed.[33] Above this concentration, the addition of fibers increases the mortar critical flexural strength σ_f, which is doubled with an addition of 1%v of *L*30 fibers, demonstrating the toughening effect of the metallic fibers.

The quantification of the impact of the concentration and form factors of the six different fibers on the critical flexural strength σ_f is analyzed with its representation as a function of the fiber volume fraction, as shown in Fig. 5. The effect of the mechanical performances is highly dependent on the fiber form factors: the shortest fibers (*L*5) have the least effect, and the increase in the critical flexural strength occurs only above concentration 1.5%v, whereas the same increase can be seen at a volume fraction of 0.5%v for the larger fiber (*L*30). It is interesting to notice that while their lengths are different, the duos *L*30 and *L*20-1 and *L*20-2 and *L*15 display very similar behaviors, which means that the relevant parameter is the fiber's form factor and not its length.[34]

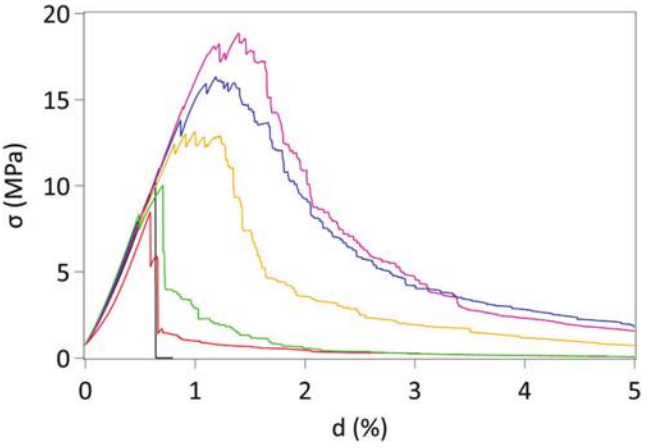

Fig. 4—Strength of reinforced mortar as function of flexural strain for different fiber concentrations at 0, 0.2, 0.4, 0.6, 0.8, and 1% volume fraction from left to right in order of appearance of peak. Tested fiber is L*30, described in Table 2. Maximum strength is taken as critical flexural strength* σ_f *of composite.*

The evolution of the flexural strength confirms that there is a minimum volume fraction required to impact the mechanical properties, which depends on the fiber form factor. The fiber network then affects the mechanical properties as the mechanical effort is transmitted in both the fiber and mortar networks.[35,36]

To identify the mechanisms at play in the increase in the strength of the system, the data of Fig. 5 were rescaled by the maximum packing fraction ϕ_0 displayed in Table 4 to correlate the packing influence of the fibers on the mechanical properties. As ϕ_0 is a function of the ratio d_e/l, each curve is shifted differently according to its form factor, and the evolution of the critical flexural strength as well as the toughness of the samples are represented in Fig. 6 (left). The flexural strength starts to kick off for a ratio of $\phi/\phi_c \approx 0.15$: below this ratio, the fibers do not have any significant effect on the mechanical properties.

Remarkably, all data from the different fibers collapse on a master curve under this rescaling by the maximum packing volume fraction ϕ_0. In particular, the increase in the flexural strength occurs at a similar rescaled volume fraction. This implies that the transition toward the strong reinforcement regime is controlled by the same scaling factor as the maximum packing volume fraction. According to the preceding discussion, it may be identified with the volume fraction transition between the semi-dilute and the entangled regime.

Therefore, according to Eq. (4) and (5), the ratio between ϕ_c and ϕ_0 can be written as

$$\frac{\phi_c}{\phi_0} = \frac{\pi}{4k} \tag{6}$$

The ratio ϕ_c/ϕ_0 is approximately equal to 0.2 and 0.15 with $k_{th} = 4$ and $k_{exp} = 5.3$, respectively. Those values are very close to the experimental values of Fig. 6 and confirm that the fibers start to have a significant impact when their orientational motion in both angular directions is constrained by their neighbors. The same observations are confirmed by the values of the toughness: the effect of the fibers is only controlled by the ratio ϕ_c/ϕ_0, as shown in Fig. 6 (right). The

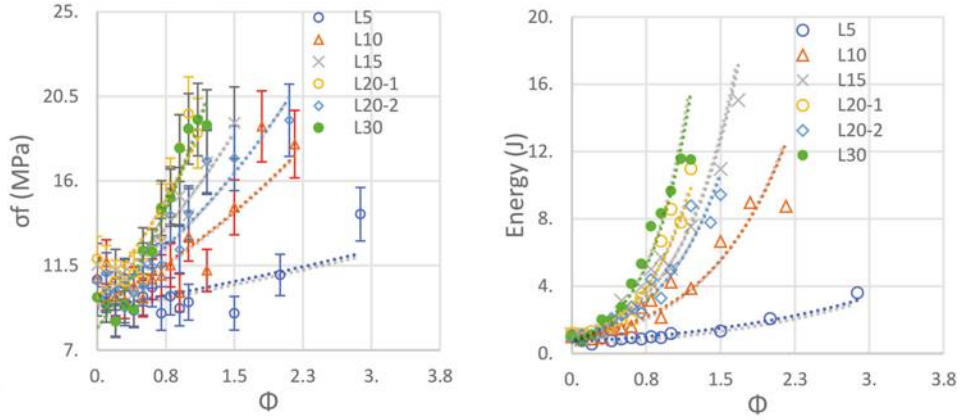

Fig. 5—(Left) Evolution of mean critical flexural strength σ_f *of reinforced mortar has function of solid volume fraction of six different kinds of fibers, described in Table 2; and (right) evolution of total energy, as calculated in Eq. (2) for same fibers. Colors are associated with same fiber, lines are giving trends, and error bars are calculated with average of 10%.*

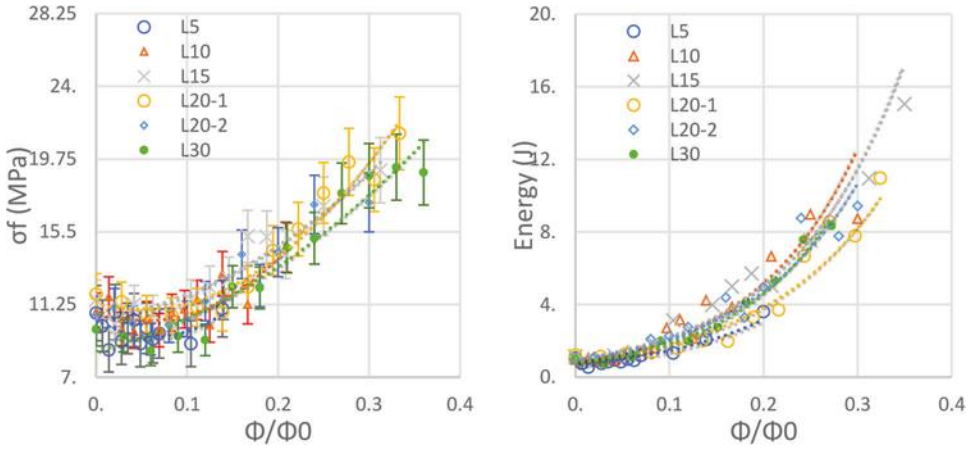

Fig. 6—(Left) Evolution of mean flexural strength of reinforced mortar has function of ratio ϕ/ϕ_0 for six different kinds of fibers, described in Table 2; and (right) evolution of total energy or toughness, as calculated in Eq. (2). Colors are associated with same fiber, lines are giving trends, and error bars are calculated with average of 10% from flexural strength.

toughness curves also collapse in a master curve when the unit ϕ/ϕ_0 is used to rescale the data.

Rheological measurements

As the fiber concentration has been proved to be close to when the hybrid mechanical properties drastically increase, the rheology of the mixture is also supposed to diverge when its volume fraction ϕ tends to some maximum packing fraction that may not be identical to the previously defined ϕ_0, and that this study calls ϕ_m. The increase in the viscosity η with the volume fraction has been widely studied,[37] and the theoretical solution is known for a dilute sphere suspension in a Newtonian fluid of viscosity[38] η_0

$$\eta = \eta_0(1 + 2.5\phi) \tag{7}$$

The problem becomes rapidly difficult to model when the volume fraction increases and becomes close to the maximum packing fraction ϕ_m as the viscosity diverges at the limit.[39] Among all the models, the most commonly used is the Krieger-Dougherty relationship[40]

$$\eta(\phi) = \eta_0(1 - \phi/\phi_m)^{-B\phi_m} \tag{8}$$

with $B = 2.5$ for the hard-sphere Maron-Pierce model,[41] which has the advantage of fixing the power-law exponent and easing the determination of ϕ_m

$$\eta(\phi) = \eta_0(1 - \phi/\phi_m)^{-2} \tag{9}$$

Those models allow the estimation of the maximum packing of a sphere suspension by fitting the experimental data of the evolution of the viscosity with the sphere volume fraction. For the hard sphere, which is the simplest system,[42] $\phi_m \approx 0.64$, but higher experimental values have also been reported.[43] The system becomes even more complex when the suspension is not made out of spheres but rodlike objects: the values of both η_0 and ϕ_m are different from the hard-sphere model.[44,45] Another level of complexity is added to the system as the suspending fluid is non-Newtonian.[39]

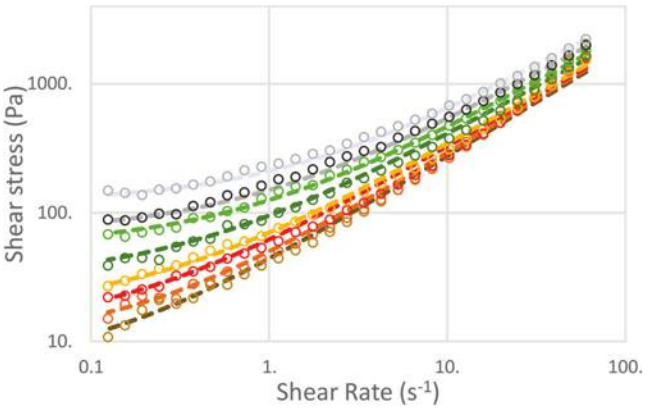

Fig. 7—Evolution of shear stress τ as function of shear rate $\dot{\gamma}$ for fiber-reinforced mortar made with L30 fiber at different fiber concentrations, from bottom to top: ϕ = 0, 0.16, 0.33, 0.5, 0.66, 0.82, 0.99, and 1.15%v. Points are experimental data and dotted lines are Herschel-Bulkley fits.

An example of the evolution of the mortar rheological properties with the amount of *L*30 fibers is represented in Fig. 7. A strong increase in the yield stress τ_y can be observed with the fiber concentrations but also a weaker increase at a high shear rate, which means that the plastic viscosity η_∞ is less dependent on the fiber concentration. It can be explained by a possible fiber alignment with the flow field.[10]

As the mortar is a yield-stress fluid, a Herschel-Bulkley relationship describes the shear stress evolution with the shear rate[46]

$$\tau(\dot{\gamma}) = \tau_y + K\dot{\gamma}^n \tag{10}$$

where K is the consistency index; and n is the flow index. The raw rheological data were fitted with the previous equation to obtain a more precise estimation of the yield stress τ_y, whose mean value was averaged over three experiments. Most of the previously published studies[47-49] focused on the concentration impact on the viscosity and slump flow rather than a direct measure of the yield stress; nevertheless,

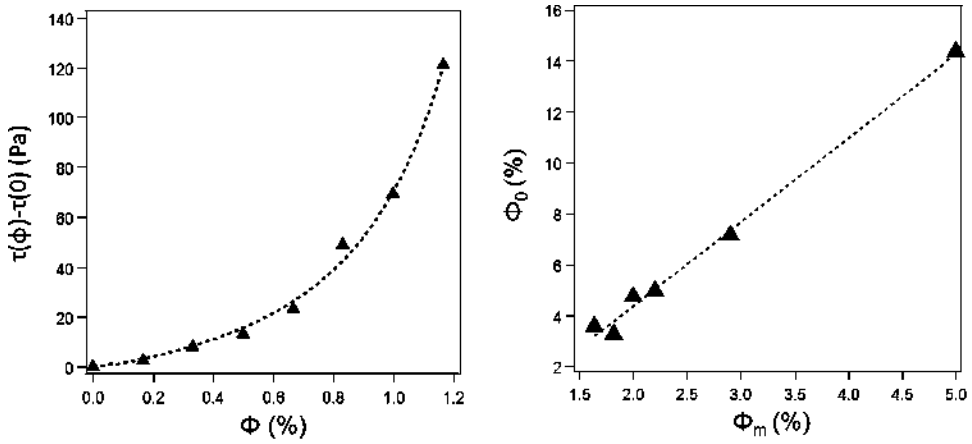

Fig. 8—(Left) Evolution of yield-stress increases $\tau(\phi) - \tau(0)$ as function of L*30 fiber concentration ϕ. Data have been fitted using Eq. (11) with $\tau^* = 18.3$ Pa and $\phi_m = 1.2\%$v. (Right) Calculated value ϕ_0 as function of value deduced from rheological measurement ϕ_m for all fibers tested. Dotted line is linear fit of data.*

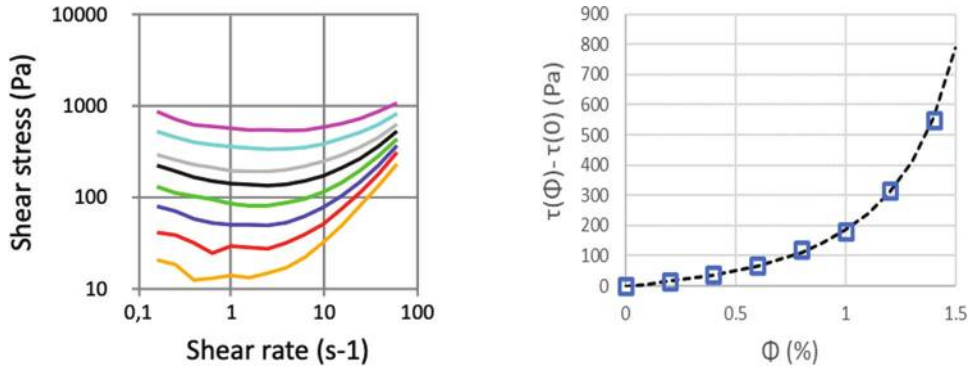

Fig. 9—(Left) Shear stress as function of shear rate for reference mortar made at different concentrations of PVA fibers, from bottom to top: $\phi = 0$, 0.2, 0.4, 0.6, 0.8, 1, 1.2, and 1.4%v; and (right) evolution of yield-stress increases $\tau(\phi) - \tau(0)$ as function of PVA fiber concentration ϕ. Points are extrapolated from experimental data and dotted line from Eq. (11) with τ^* of 70 Pa and ϕ_m of 2.1%.

a derived Maron-Pierce equation has been proposed for its evolution with the particle volume fraction[50]

$$\tau(\phi) = \tau^* \left(\left(1 - \frac{\phi}{\phi_m} \right)^{-2} - 1 \right) \quad (11)$$

This equation has been used to fit the experimental data, and because the previous equation assumed that $\tau(0) = 0$, the fit has been done using $\tau(\phi) = \tau_y(\phi) - \tau_y(0)$, which is represented as a function of the volume fraction on the left side of Fig. 8 for the *L*30 fibers. The points correspond to the experimental data, and the line is the model that perfectly describes the experimental data, demonstrating that the model can be generalized to the complex system. The maximum packing fraction ϕ_m deduced from the fit $\phi_m(L30) = 1.2\%$v appears to be much lower than the maximum packing fraction $\phi_0(L30) = 3.33\%$v obtained from the form factor packing calculation. The same measurements were made for all types of fibers to compare the values of the maximum packing fraction ϕ_m obtained from the rheological measurements and the volume fraction ϕ_0 obtained from the geometrical calculation. The representation of the ϕ_0 as a function of ϕ_m is made in Fig. 8 (right).

Nevertheless, it should be noted that the maximum volume fraction, corresponding to the viscosity divergence ϕ_m, is approximately three times smaller than the theoretical maximum packing fraction of randomly oriented spheres ϕ_0.

To test the generality of the results, experiments were done with other kinds of fibers, in shape and nature, with rodlike PVA fibers. Fibers of diameter 38 μm and length of 8 mm have theoretical maximum packing fractions ϕ_0 of 1.9%v and 2.5%v, calculated with Eq. (5) and with a *k*-factor of 4 and 5.3, respectively. The shear stress evolution as a function of the shear rate in the mortar matrix is represented in Fig. 9 (left), and the measured yield stress is plotted as a function of the volume fraction of the PVA fibers in Fig. 9 (right).

The fitting of the rheological measurements with Eq. (9) (Fig. 9) allows the determination of the experimental critical volume fraction, which is approximately $\phi_m = 2.1\%$v, in between the calculated values of the maximum packing fractions of 1.9%v and 2.5%v. The results obtained with the rodlike fibers are then in the range of the values obtained with Eq. (5), confirming the generality of the results.

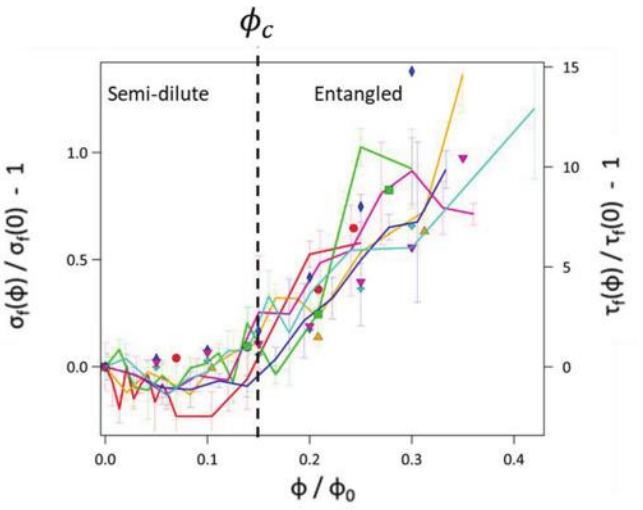

Fig. 10—(Left scale) Evolution of mean normalized flexural strength as function of ϕ/ϕ_0 and maximum packing for six different kinds of fibers, described in Table 2 (line); and (right scale) evolution of mean normalized yield stress as function of ϕ/ϕ_0 (symbol), colors are associated with same fiber. Red: L*5, green:* L*10, orange:* L*15, blue:* L*20-1, green* L*20-2, and pink:* L*30. (Note: Full-color PDF can be accessed at www.concrete.org.)*

Strength-rheology relationship

The data of Fig. 5, 8, and 9 show that both the yield stress τ_y and the critical flexural strength σ_f start to increase drastically around the same volume fraction (ϕ = 0.4%v for the *L*30 fibers). This observation could be a hint that each effect arises from the same phenomenon, which is the outbreak of a fiber network within the mortar sample. To check the similitude between those and make the correlation between the rheological and mechanical properties, the normalized structural strength ($\sigma_f(\phi)/\sigma_f(0) - 1$) and the normalized yield stress ($\tau_f(\phi)/\tau_f(0) - 1$) are represented as a function of the ratio between the volume fraction and the maximum packing ϕ_m calculated from Eq. (5). The results displayed in Fig. 10 show that a similar evolution is observed for both the yield stress and the flexural properties as a function of the ratio between the solid volume fraction and critical volume fraction. A factor of 10 between the scale for the normalized structural strength and the yield stress is observed, meaning that the impact of the relative slope is, therefore, different. This result highlights another remark previously made: the maximum packing fraction deduced from the rheological data using Eq. (11) is always lower than the calculated value from Eq. (5), as can be observed in Fig. 8 (right).

Experimentally, it was nearly impossible to mix and reach fiber volume fractions larger than $0.4\phi/\phi_0$, while it is very easy to prepare hard-sphere suspension up to $0.9\phi/\phi_0$. This could be an argument to advance that the value of the maximum packing deduced from the experimental rheological measurement is closer to the true maximum packing fraction of fibers. Thus, the minimum fiber concentration to trigger their effect can be explained by the theory[30] that has been verified in the experiments: both effects are triggered when $\phi/\phi_0 \approx 0.15$, which corresponds to the transition between the semi-dilute to the entangled regimes represented in Fig. 3. The prediction of the maximum packing fraction of fibers is incorrect because of the modeling of the fibers, which are rectangular cuboids, by rodlike objects, which, as a consequence, could overestimate the real maximum packing fraction. The factor of three for the fiber diameter, obtained between theory and experiment, can be explained with an orientation of the cuboids, leading to an apparent diameter smaller than the one calculated theoretically. The rheological experiments thus allow a quick determination of the fiber form factor, which is needed to determine its impact on the mechanical reinforcement.

CONCLUSIONS

In this paper, the impact of the addition of metallic fibers on both the flexural properties and the rheological properties of a mortar were studied. It was shown experimentally that below a critical concentration, which is only a function of the fiber geometry and defined as the transition between the semi-dilute and entangled regimes, the addition of fibers does not have any significant effect on the improvement of flexural strength. These results were explained by the fact that this critical concentration corresponds to the beginning of an organized network of fibers. Above this critical concentration, both the flexural strength and the yield stress of the fiber-reinforced mortar increase quickly and similarly with the fiber concentration, making the link between flexural properties and rheological properties. No correlation could be made with the plastic viscosity, as the effect of fiber addition is lower at a high shear rate due to their trend to align with the flow but also on the impact of the fibers on the shear thinning of the constitutive paste matrix.

The flexural strength and yield stress increase in parallel as they appear to arise from a common phenomenon based only on the form factor of the fibers. This correlation allows the choosing of the optimal fiber aspect ratio, allowing a quantitative extrapolation and estimation of the flexural properties from the measurement of the yield stress by the calculation of the maximum solid fraction, which is a function of the fiber form factors. The theory was tested with polyvinyl alcohol (PVA) fibers, which have different chemistry and form factors than metal fibers. The maximum packing fractions calculated from the form factor are near the value obtained from the evolution of the yield stress as a function of the fiber volume fraction. Those results could be interesting to ease the formulation of fiber-reinforced mortars as one can calculate the minimum concentration required to improve mechanical properties directly from rheological measurements. This work demonstrates that simple rheological measurements can be performed early to predict and optimize the flexural strength of fiber-reinforced mortar. Further work performed on concrete and highly flexible fiber would allow the generalization of this theory on a more global use of fibers for concrete.

AUTHOR BIOS

Ronan Chometon *received his double engineering degree from ESPCI Paris, Paris, France, in chemical physics, and École Nationale Supérieure des Mines de Paris (MINES Paris – PSL), Paris, France, in materials*

science. He currently works on the development of hybrid interfaces between Li-metal and the electrolyte for solid-state batteries.

Maxime Liard *is a Senior Scientist for Sika Technology AG, Zürich, Switzerland. He received his PhD in physics and chemistry from the Université de Strasbourg, Strasbourg, France, in 2015. His research interests include soft matter, rheology of suspensions, three-dimensional (3-D) printing, and cementitious materials.*

Pascal Hébraud *is a National Centre for Scientific Research (CNRS) Senior Researcher and works at the Institute of Physics and Chemistry of Materials at the Université de Strasbourg. He received his PhD in physics from the Université de Strasbourg in 1998. His research interests include colloids and particle flow and aggregation, which he studies by means of rheology and light scattering techniques.*

Didier Lootens *is a Physico-Chemist and Principal Scientist at Sika Technology. He received his MSc in physico-chemistry from ESPCI Paris, and his PhD in materials science from the Université Pierre et Marie Curie, Paris, France, in 2004. His research interests include early-age characterization of construction materials, rheology, reduction of carbon footprint with supplementary cementitious materials, and formulation optimization.*

ACKNOWLEDGMENTS

The authors thank D. Favier (Institut Charles Sadron [CNRS], Strasbourg, France) for the realization of the X-ray tomography imaging.

NOTATION

A	=	prism width equal to 40 mm
B	=	constant for hard-sphere model of Maron-Pierce,[41] equal to 2.5
c	=	fiber number concentration by unit volume
d	=	thickness of fiber
d_e	=	equivalent diameter of fiber corresponding to circular section
Fc	=	critical factor
F_c	=	maximum flexion force at failure for prism
Fd	=	density factor
FF	=	fiber factor
$F(\delta)$	=	force applied at given displacement
K	=	consistency index
k	=	numerical prefactor[30] for calculation of maximum fiber packing fraction
k_{exp}	=	experimental numerical prefactor k equal to 5.3
k_{th}	=	theoretical numerical prefactor k equal to 4
L	=	prism length equal to 160 mm and section width equal to 40 mm
l	=	equivalent length of fiber
n	=	flow index
U	=	toughness of prism, which is energy material can absorb by deforming plastically before its rupture
w	=	width of fiber
δ	=	displacement or deformation of prism
ϕ	=	fiber volume fraction
ϕ_c	=	fiber volume fraction at dilute/semi-dilute transition
ϕ_m	=	volume fraction corresponding to divergence of viscosity
ϕ_0	=	fiber volume fraction at semi-dilute/tangle transition
	=	shear rate
η	=	viscosity of suspension with or without fiber
η_0	=	Newtonian fluid of viscosity
σ_f	=	critical flexural strength
τ	=	shear stress
τ^*	=	shear stress constant
τ_y	=	yield stress

REFERENCES

1. de Larrard, F., and Sedran, T., "Optimization of Ultra-High-Performance Concrete by the Use of a Packing Model," *Cement and Concrete Research*, V. 24, No. 6, 1994, pp. 997-1009. doi: 10.1016/0008-8846(94)90022-1

2. MacGregor, J. G., *Reinforced Concrete: Mechanics and Design*, third edition, Prentice Hall, Upper Saddle River, NJ, 1997, 939 pp.

3. El-Hawary, M. M., and Abdul-Jaleel, A., "Durability Assessment of Epoxy Modified Concrete," *Construction and Building Materials*, V. 24, No. 8, Aug. 2010, pp. 1523-1528. doi: 10.1016/j.conbuildmat.2010.02.004

4. Shaker, F. A.; El-Dieb, A. S.; and Reda, M. M., "Durability of Styrene-Butadiene Latex Modified Concrete," *Cement and Concrete Research*, V. 27, No. 5, May 1997, pp. 711-720. doi: 10.1016/S0008-8846(97)00055-0

5. Topçu, I. B., "The Properties of Rubberized Concretes," *Cement and Concrete Research*, V. 25, No. 2, Feb. 1995, pp. 304-310. doi: 10.1016/0008-8846(95)00014-3

6. Sivakumar, A., and Santhanam, M., "Mechanical Properties of High Strength Concrete Reinforced with Metallic and Non-Metallic Fibres," *Cement and Concrete Composites*, V. 29, No. 8, Sept. 2007, pp. 603-608. doi: 10.1016/j.cemconcomp.2007.03.006

7. Wafa, F. F., and Ashour, S. A., "Mechanical Properties of High-Strength Fiber Reinforced Concrete," *ACI Materials Journal*, V. 89, No. 5, Sept.-Oct. 1992, pp. 449-455.

8. Bansal, N. P., ed., *Handbook of Ceramic Composites*, Kluwer Academic Publishers, New York, 2005, 554 pp.

9. Acker, P., and Behloul, M., "Ductal® Technology: A Large Spectrum of Properties, A Wide Range of Applications," *Proceedings of the International Symposium on Ultra High Performance Concrete*, M. Schmidt, E. Fehling, and C. Geisenhanslüke, eds., Kassel, Germany, Sept. 2004, pp. 11-23.

10. Petrie, C. J. S., "The Rheology of Fibre Suspensions," *Journal of Non-Newtonian Fluid Mechanics*, V. 87, No. 2-3, Nov. 1999, pp. 369-402. doi: 10.1016/S0377-0257(99)00069-5

11. Maschmeyer, R. O., and Hill, C. T., "Rheology of Concentrated Suspensions of Fibers in Tube Flow. II. An Exploratory Study," *Transactions of The Society of Rheology*, V. 21, No. 2, July 1977, pp. 183-194. doi: 10.1122/1.549453

12. Alrawashdeh, A., and Eren, O., "Mechanical and Physical Characterisation of Steel Fibre Reinforced Self-Compacting Concrete: Different Aspect Ratios and Volume Fractions of Fibres," *Results in Engineering*, V. 13, Mar. 2022, Article No. 100335. doi: 10.1016/j.rineng.2022.100335

13. Nelson, P. K.; Li, V. C.; and Kamada, T., "Fracture Toughness of Microfiber Reinforced Cement Composites," *Journal of Materials in Civil Engineering*, ASCE, V. 14, No. 5, Oct. 2002, pp. 384-391.

14. Ku, D.-O.; Kim, S.-D.; Kim, H.-S.; and Choi, K.-K., "Flexural Performance Characteristics of Amorphous Steel Fiber-Reinforced Concrete," *Journal of the Korea Concrete Institute*, V. 26, No. 4, Aug. 2014, pp. 483-489. doi: 10.4334/JKCI.2014.26.4.483

15. Shin, H.-O.; Kim, K.; Oh, T.; and Yoo, D.-Y., "Effects of Fiber Type and Specimen Thickness on Flexural Behavior of Ultra-High-Performance Fiber-Reinforced Concrete Subjected to Uniaxial and Biaxial Stresses," *Case Studies in Construction Materials*, V. 15, Dec. 2021, Article No. e00726. doi: 10.1016/j.cscm.2021.e00726

16. Pannirselvam, N., and Manivel, S., "Influence of Addition of Glass Fibre on Concrete," *IOP Conference Series: Materials Science and Engineering*, V. 1026, 2021, Article No. 012008. doi: 10.1088/1757-899X/1026/1/012008

17. Araya-Letelier, G.; Antico, F. C.; Carrasco, M.; Rojas, P.; and García-Herrera, C. M., "Effectiveness of New Natural Fibers on Damage-Mechanical Performance of Mortar," *Construction and Building Materials*, V. 152, Oct. 2017, pp. 672-682. doi: 10.1016/j.conbuildmat.2017.07.072

18. Si, W.; Cao, M.; and Li, L., "Establishment of Fiber Factor for Rheological and Mechanical Performance of Polyvinyl Alcohol (PVA) Fiber Reinforced Mortar," *Construction and Building Materials*, V. 265, Dec. 2020, Article No. 120347. doi: 10.1016/j.conbuildmat.2020.120347

19. Pu, B.-C.; Liu, B.; Li, L.; Pang, W.; and Wan, Z., "Influence of Polypropylene Fibre Factor on Flowability and Mechanical Properties of Self-Compacting Geopolymer," *Materials*, V. 14, No. 17, Sept. 2021, Article No. 5025. doi: 10.3390/ma14175025

20. Ibragimov, R.; Bogdanov, R.; Miftakhutdinova, L.; Fediuk, R.; Vatin, N. I.; and de Azevedo, A. R. G., "Effect of Polydisperse Reinforcement on the Fresh and Physical-Mechanical Properties of Self-Compacting Concrete," *Case Studies in Construction Materials*, V. 17, Dec. 2022, Article No. e01188. doi: 10.1016/j.cscm.2022.e01188

21. Hameed, R.; Turatsinze, A.; Duprat, F.; and Sellier, A., "Metallic Fiber Reinforced Concrete: Effect of Fiber Aspect Ratio on the Flexural Properties," *ARPN Journal of Engineering and Applied Sciences*, V. 4, No. 5, July 2009, pp. 67-72.

22. Rao, M. M.; Chowhan, L. N.; and Patro, S. K., "Effect of Aspect Ratio of Fiber in HDPE Reinforced Concrete," *International Journal of Engineering Research & Technology (IJERT)*, V. 8, No. 9, Sept. 2019, pp. 164-171.

23. Teng, L.; Meng, W.; and Khayat, K. H., "Rheology Control of Ultra-High-Performance Concrete Made with Different Fiber Contents," *Cement and Concrete Research*, V. 138, Dec. 2020, Article No. 106222. doi: 10.1016/j.cemconres.2020.106222

24. Kang, M.-C.; Yoo, D.-Y.; and Gupta, R., "Machine Learning-Based Prediction for Compressive and Flexural Strengths of Steel Fiber-Reinforced Concrete," *Construction and Building Materials*, V. 266, Part B, Jan. 2021, Article No. 121117. doi: 10.1016/j.conbuildmat.2020.121117

25. FIBRAFLEX® Documentation, Saint-Gobain, Chalon-sur-Saône, France, www.fibraflex.fr/documents. (last accessed Feb. 16, 2024)

26. Liard, M.; Oblak, L.; Hachim, M.; Vachon, M.; and Lootens, D., "Impact of Viscosity on Hydration Kinetics and Setting Properties of Cementitious Materials," *Advances in Civil Engineering Materials*, V. 3, No. 2, 2014, pp. 117-126. doi: 10.1520/ACEM20130096

27. Toussaint, F.; Roy, C.; and Jézéquel, P.-H., "Reducing Shear Thickening of Cement-Based Suspensions," *Rheologica Acta*, V. 48, No. 8, Oct. 2009, pp. 883-895. doi: 10.1007/s00397-009-0362-z

28. Fabbris, F.; De Carvalho, W.; and Lootens, D., "A Concrete Rheometer: Features and Industrial Applications," *Rheology and Processing of Construction Materials: Proceedings of the 7th RILEM International Conference on Self-Compacting Concrete and 1st RILEM International Conference on Rheology and Processing of Construction Materials*, N. Roussel and H. Bessaies-Bey, eds., Paris, France, 2013, pp. 99-106.

29. Olivas, A.; Ferraris, C. F.; Martys, N. S.; George, W. L.; Garboczi, E. J.; and Toman, B., "Certification of SRM 2493: Standard Reference Mortar for Rheological Measurements," NIST Special Publication 260-187, National Institute of Standards and Technology, Gaithersburg, MD, 2017, 192 pp.

30. Evans, K. E., and Gibson, A. G., "Prediction of the Maximum Packing Fraction Achievable in Randomly Oriented Short-Fibre Composites," *Composites Science and Technology*, V. 25, No. 2, 1986, pp. 149-162. doi: 10.1016/0266-3538(86)90040-0

31. Toll, S., "Packing Mechanics of Fiber Reinforcements," *Polymer Engineering and Science*, V. 38, No. 8, Aug. 1998, pp. 1337-1350. doi: 10.1002/pen.10304

32. Milewski, J. V., "A Study of the Packing of Milled Fibreglass and Glass Beads," *Composites*, V. 4, No. 6, Nov. 1973, pp. 258-265. doi: 10.1016/0010-4361(73)90392-3

33. Lok, T.-S., and Pei, J.-S., "Flexural Behavior of Steel Fiber Reinforced Concrete," *Journal of Materials in Civil Engineering*, ASCE, V. 10, No. 2, May 1998, pp. 86-97. doi: 10.1061/(ASCE)0899-1561(1998)10:2(86)

34. Banthia, N., "A Study of Some Factors Affecting the Fiber–Matrix Bond in Steel Fiber Reinforced Concrete," *Canadian Journal of Civil Engineering*, V. 17, No. 4, Aug. 1990, pp. 610-620. doi: 10.1139/l90-069

35. Johnston, C. D., "Steel Fiber Reinforced Mortar and Concrete: A Review of Mechanical Properties," *Fiber Reinforced Concrete*, SP-44, American Concrete Institute, Farmington Hills, MI, 1974, pp. 127-142.

36. Shannag, M. J.; Brincker, R.; and Hansen, W., "Interfacial (Fiber-Matrix) Properties of High-Strength Mortar (150 MPa) from Fiber Pullout," *ACI Materials Journal*, V. 93, No. 5, Sept.-Oct. 1996, pp. 480-485.

37. Mewis, J., and Wagner, N. J., *Colloidal Suspension Rheology*, Cambridge University Press, Cambridge, UK, 2012.

38. Einstein, A., "Eine neue Bestimmung der Moleküldimensionen," *Annalen der Physik*, V. 324, No. 2, 1906, pp. 289-306. doi: 10.1002/andp.19063240204

39. Mueller, S.; Llewellin, E. W.; and Mader, H. M., "The Rheology of Suspensions of Solid Particles," *Proceedings of the Royal Society A: Mathematical, Physical and Engineering Sciences*, V. 466, No. 2116, Apr. 2010, pp. 1201-1228. doi: 10.1098/rspa.2009.0445

40. Krieger, I. M., and Dougherty, T. J., "A Mechanism for Non-Newtonian Flow in Suspensions of Rigid Spheres," *Transactions of the Society of Rheology*, V. 3, No. 1, 1959, pp. 137-152. doi: 10.1122/1.548848

41. Maron, S. H., and Pierce, P. E., "Application of Ree-Eyring Generalized Flow Theory to Suspensions of Spherical Particles," *Journal of Colloid Science*, V. 11, No. 1, Feb. 1956, pp. 80-95. doi: 10.1016/0095-8522(56)90023-X

42. Rintoul, M. D., and Torquato, S., "Computer Simulations of Dense Hard-Sphere Systems," *The Journal of Chemical Physics*, V. 105, No. 20, Nov. 1996, pp. 9258-9265. doi: 10.1063/1.473004

43. Rutgers, I. R., "Relative Viscosity of Suspensions of Rigid Spheres in Newtonian Liquids," *Rheologica Acta*, V. 2, No. 3, Sept. 1962, pp. 202-210. doi: 10.1007/BF01983952

44. Jeffery, G. B., "The Motion of Ellipsoidal Particles Immersed in a Viscous Fluid," *Proceedings of the Royal Society of London. Series A, Containing Papers of a Mathematical and Physical Character*, V. 102, No. 715, Nov. 1922, pp. 161-179. doi: 10.1098/rspa.1922.0078

45. Brenner, H., "Rheology of a Dilute Suspension of Axisymmetric Brownian Particles," *International Journal of Multiphase Flow*, V. 1, No. 2, Apr. 1974, pp. 195-341. doi: 10.1016/0301-9322(74)90018-4

46. Herschel, W. H., and Bulkley, R., "Konsistenzmessungen von Gummi-Benzollösungen," *Colloid and Polymer Science*, V. 39, No. 4, Aug. 1926, pp. 291-300. doi: 10.1007/BF01432034

47. Gwon, S.; Han, S. H.; Vu, T. D.; Kim, C.; and Shin, M., "Rheological and Mechanical Properties of Kenaf and Jute Fiber-Reinforced Cement Composites," *International Journal of Concrete Structures and Materials*, V. 17, No. 1, Dec. 2023, Article No. 5. doi: 10.1186/s40069-022-00565-1

48. De La Rosa, Á.; Ruiz, G.; Castillo, E.; and Moreno, R., "Probabilistic Assessment of the Dynamic Viscosity of Self-Compacting Steel-Fiber Reinforced Concrete through a Micromechanical Model," *Materials*, V. 15, No. 8, Apr. 2022, Article No. 2763. doi: 10.3390/ma15082763

49. Teng, L.; Huang, H.; Du, J.; and Khayat, K. H., "Prediction of Fiber Orientation and Flexural Performance of UHPC Based on Suspending Mortar Rheology and Casting Method," *Cement and Concrete Composites*, V. 122, Sept. 2021, Article No. 104142. doi: 10.1016/j.cemconcomp.2021.104142

50. Heymann, L.; Peukert, S.; and Aksel, N., "On the Solid-Liquid Transition of Concentrated Suspensions in Transient Shear Flow," *Rheologica Acta*, V. 41, No. 4, Jan. 2002, pp. 307-315. doi: 10.1007/s00397-002-0227-1

ACI MATERIALS JOURNAL TECHNICAL PAPER

Title No. 121-M20

Study on Effect of Curing Regimes on Ultra-High-Performance Concrete by Nuclear Magnetic Resonance Spectroscopy

by Hao Qian, Gaozhan Zhang, Jun Yang, Qingjun Ding, Chundong Geng, and Sudong Hua

As one of the key factors influencing the hydration process, as well as the microstructure formation and evolution of ultra-high-performance concrete (UHPC), the action mechanism of different curing regimes have been studied to some extent. However, the current knowledge of the underlying mechanisms that control the different effects of different curing regimes is limited. In this study, the composition of hydration products, micromorphology, and migration and evolution of aluminum-phase hydration products of UHPC under three combined curing regimes (standard curing, steam curing + standard curing, and autoclave curing + standard curing) were investigated in depth. Micromorphology observation shows that heat treatment promoted the formation of higher-stiffness hydration products (tobermorite and xonotlite) in UHPC, and the higher the polymerization degree, the higher the Si/Ca ratio of the hydration product. Meanwhile, ^{29}Si and ^{27}Al nuclear magnetic resonance (NMR) spectroscopy shows that specimens with higher strength had higher Al[4]/Si and a lower amount of ettringite and AFm at the early curing stage. The elevated curing temperature reduced the formation of ettringite and AFm and allowed more Al^{3+} to replace Si^{4+} into the structure and interlayer of the calcium-(alumino)silicate-hydrate (C-(A)-S-H) gel, which increased the mean chain length (MCL) and polymerization degree of the C-(A)-S-H gel. However, the polymerization effect of Al ions is limited, so the provision of the silicon source to improve the Si/Ca ratio of the system is important.

Keywords: calcium-(alumino)silicate-hydrate (C-(A)-S-H) gel; curing regime; nuclear magnetic resonance (NMR) spectroscopy; microstructure; ultra-high-performance concrete (UHPC).

INTRODUCTION

Ultra-high-performance concrete (UHPC) has been used in various construction applications because of its excellent permeability resistance, outstanding mechanical properties as well as durability, and superior ductility.[1-4] In bridge engineering, compared with ordinary concrete construction, UHPC could significantly reduce the volume and weight of piers, bridge girders, and other construction products and save a large amount of natural material.[5] However, due to the large amount of cementitious materials, low water-cement ratio, and compact design of UHPC, mineral admixtures with low reaction activity do not react immediately well in UHPC. Accordingly, the mechanical strength gain rate and hardening process of UHPC with standard curing are slow, which restricts the production rate construction activities and precast industries. Customized autoclaves are usually used for heat treatment in the factory production process. Although heat treatments such as autoclaved curing and steam curing have the disadvantage of limitation of specimen scale and the high cost of curing plant, heat treatment is essential to ensure the quality of products and improve production efficiency.[6-8] It was found that the heat treatment process in the production of precast UHPC products can greatly improve their early strength and volume stability.[9,10]

To provide guidance for the choice of appropriate curing regime and enhance the mechanical performance of UHPC, it is profound to study the influence of different curing regimes on the microstructure and hydration process of UHPC. The mechanisms of standard curing, steam curing, and autoclave curing, as the most commonly used curing regimes, have been studied in previous papers.[11-13] Shen et al.[14] investigated the effect of standard curing, steam curing, and autoclave curing on the mechanical properties and microstructure of UHPC. The results show that heat treatment could promote the generation of additional hydration products in UHPC. When the curing temperature reaches 90°C, the added silica fume/quartz powder could participate in the reaction with cementitious material in UHPC and generate fibrous or foiled tobermorite.[14,15] On continued increase of the curing temperature and pressure to 210°C and 2 MPa, respectively, the formed tobermorite ($Ca_{4+x}(H_{2-2x}Si_6O_{17})\cdot 5H_2O$)) is transformed into xonotlite ($Ca_6(Si_6O_{17})(OH)_2$).[11,16] However, the improved properties could not be obtained by simply prolonging the curing time and increasing the curing temperature. Higher curing temperature would harm the strength of UHPC at a later age.[17] Helmi et al.[18] found that heat curing alone (240°C) could accelerate the propagation of microcracks, which would make the 28-day compressive strength 5% lower than the 7-day compressive strength. Yazıcı et al.[19] also studied the effect of different curing conditions on UHPC, and the results show that curing temperature, pressure, and duration are all significant in the design of the curing regime. There was a specific curing time for each temperature and pressure. While the duration of heat treatment was short, the high-stiffness hydration product (such as tobermorite) was unstable. However, too long a curing time also had a negative influence due to the excessive crystallization. Moreover,

ACI Materials Journal, V. 121, No. 2, March 2024.

MS No. M-2022-418.R3, doi: 10.14359/51740372, received July 20, 2023, and reviewed under Institute publication policies.

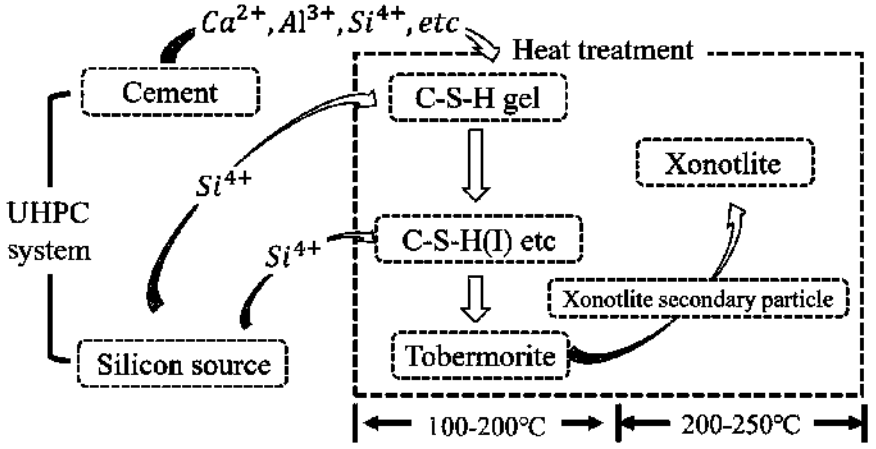

Fig. 1—Schematic diagram of hydration products' changes in UHPC under heat treatment.

the researches[19-21] found that an increase of curing pressure is helpful to improve the polymerization degree of hydration products and reduce curing time. Tobermorite could be detected at 6 hours of autoclaving at 1, 2, and 3 MPa and 10 hours of autoclaving at 0.5, 1, and 1.5 MPa. Although pressure treatment could result in an increase of specific gravity, the pressurization of entrapped air voids would promote the propagation of microcracks and reduce the strength. The Ca/Si ratio of calcium-silicate-hydrate (C-S-H) gel could reflect the polymerization degree of C-S-H gel in UHPC to some extent and evaluate the curing time of different curing regimes.[22,23] The Ca/Si ratio of C-S-H gel is usually between 0.8 and 2.5. When the Ca/Si ratio of the C-S-H structure reaches 0.8 to 1.0, C-S-H gel of this composition tends to convert to tobermorite first at temperatures between 100 and 200°C, and then to xonotlite at temperatures between 200 and 250°C.[14,19,24] To improve the polymerization degree of UHPC, the provision of an external silicon source is also important in the hydration process.[16] C_3S and C_2S could only convert to α-dicalcium silicate in the absence of silica fume/quartz powder (external SiO_2). Due to the higher porosity and smaller volume of α-dicalcium silicate, it is harmful to the strength of UHPC.

Generally, the evolution mechanism of hydration products in UHPC is shown in the schematic diagram in Fig. 1. Heat treatment promotes Al^{3+} to replace Si^{4+} in bridge sites of the silicate chains of C-S-H gel, which increases the mean chain length (MCL) and polymerization of silicate chains. The most predominant silicate chains in C-S-H gel transform from dimers to pentamers.[25,26] Before the formation of tobermorite, intermediate products such as C-S-H (I), C-S-H (II), and α-C_2SH are formed, which are harmful to the mechanical strength of UHPC due to their porous structures. With the increase in curing temperature and pressure, the pozzolanic reaction of the silicon source is intensified, and more Si^{4+} is released. The depolymerized Si^{4+} helps to convert the intermediate products into higher-stiffness hydration products (such as tobermorite and xonotlite).[27] The average stiffness of tobermorite and xonotlite are 77 and 106 GPa, respectively, which is much higher than that of C-S-H.[14,24] The higher stiffness of hydration products is beneficial to the improvement of mechanical properties of UHPC. Moreover, compared with intermediate hydration products, the tobermorite/xonotlite phase formed from the pozzolanic reaction has larger structural volume.[19] The pore-filling effect by tobermorite/xonotlite could reduce the porosity and drying shrinkage of UHPC and improve its compressive strength and resistance to chemical attack. As a result, although the role of curing pressure cannot be ignored, the enhancement effect of different curing regimes on the mechanical properties of UHPC is related to curing temperature.[14,28]

Many previous studies have shown the change of mechanical performance, microstructure, and hydration process of UHPC under different curing regimes. The reasons for the improvement of the mechanical properties of UHPC have been investigated from the perspective of microstructure. However, the current knowledge of the underlying mechanisms of long-term microstructural change with combined curing regimes is still limited. Presently, there are many researches on the difference between standard curing, steam curing, and water curing. There is little deep analysis of the composition of hydration products, C-S-H gel microstructure, and migration and evolution of aluminum-phase hydration products of cement/silica fume-quartz powder system UHPC under three curing regimes (standard curing at 20°C, steam curing at 90°C, and pressure steam curing at 210°C and 2 MPa). Therefore, it is necessary to pay attention to the study of the microstructural change behind different combined curing regimes. In this study, three types of typical combined curing regimes (standard curing, steam curing + standard curing, and autoclave curing + standard curing) were performed on UHPC specimens. The mechanical properties, microstructure, and the difference in improvement of three combined curing regimes were investigated. The microstructure development as well as migration and evolution of aluminum-phase hydration products of UHPC with different curing regimes is the research focus of this paper. The mechanical properties were characterized by testing the compressive strength of samples of different ages. Meanwhile, X-ray diffraction (XRD) and scanning electron microscopy (SEM) were used to investigate the hydration product and microstructure of specimen. The migration and evolution of Si and Al ions in UHPC were determined by ^{29}Si nuclear magnetic resonance (NMR) and

Table 1—Mixture proportions of cement, silica fume, and quartz powder

Constituent, wt%	SiO_2	Al_2O_3	Fe_2O_3	CaO	MgO	SO_3	K_2O	Na_2O	LOI
Cement	20.87	4.87	3.59	64.47	2.13	2.52	0.65	0.11	0.79
Silica fume	96.34	0.61	0.16	0.54	0.25	0.13	0.21	0.008	1.68
Quartz powder	98.75	0.73	0.11	0.06	—	—	0.16	—	0.19

Note: LOI is loss on ignition.

Table 2—Mixture proportions of UHPC, kg/m³

Cement	Silica fume	Quartz powder	River sand	Steel fiber	Water	HRWRA
880	265	325	1030	158	264	44.9

^{27}Al NMR spectroscopy, and the following main parameters were obtained: hydration degree of cement and silica fume/quartz powder, MCL, Al[4]/Si ratio.

RESEARCH SIGNIFICANCE

In this study, the composition of hydration products, micromorphology, and migration and evolution of aluminum-phase hydration products of UHPC under three combined curing regimes (standard curing, steam curing + standard curing, and autoclave curing + standard curing) were investigated in depth. By analyzing the underlying mechanism that controls the different effects of different curing regimes, it is expected to provide a reference for the selection of UHPC curing system. Moreover, it also provides a theoretical basis for the application of UHPC and further study of hydration reaction of UHPC.

MATERIALS AND EXPERIMENTAL METHODOLOGY

Materials

Raw materials—Portland cement (P.I 52.5) and mineral admixtures (silica fume and quartz powder) used in this study are all produced by domestic manufacturers. The specific surface area of silica fume and quartz powder were 19,500 and 445 m^2/kg, respectively. The chemical composition of portland cement, silica fume, and quartz powder are all shown in Table 1. Fine river sand with a fineness modulus of 1.87, derived from Yueyang Dongting Lake Yellow Sand, was used as aggregate in UHPC. Moreover, high-range water-reducing admixture (HRWRA) (water-reducing ratio of 30%, solid content of 20%), steel fiber (length = 13 mm, diameter = 0.18 mm, modulus of elasticity = 200 GPa) were also used. Tap water was used for mortar preparation and deionized water was used for UHPC paste preparation.

Mixture proportion—The main mixture proportion of UHPC analyzed in this study for investigation is shown in Table 2.

Specimen preparation

Mortar preparation—Fine river sand, cementitious material, and mineral admixture were first added into the dry mixer and mixed for 1 minute. Then, the mixture was mixed with water and HRWRA for 4 minutes. Finally, steel fiber was slowly added into and mixed together for 3 minutes. The prepared mortar was placed in a 40 x 40 x 160 mm mold.

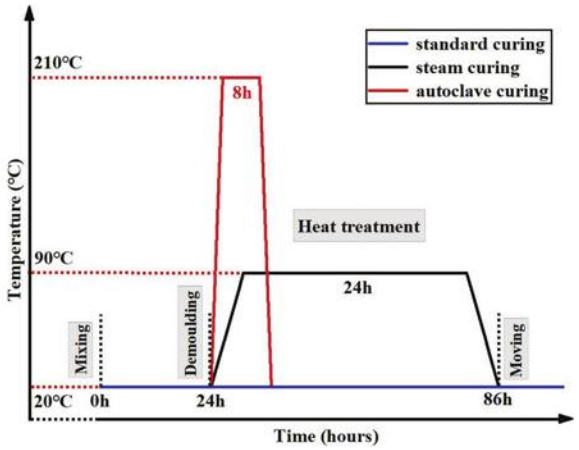

Fig. 2—Different curing regimes of UHPC.

After being vibrated and smoothed to shape, the molds were covered with impermeable film in the standard environment for 24 hours.

Paste preparation—First, cement and mineral admixture were added into a dry mixer and mixed for 1 minute. Then the water and HRWRA were added together and continued to be stirred for more than 4 minutes. Finally, the prepared paste was placed into a ϕ10 x 50 mm plastic pipe. After standard curing for 24 hours, the specimens were detached from the mold.

Curing regimes

Three types of curing regimes, shown in Fig. 2, were used in this study. The curing temperature, curing pressure, and curing time are found in the references.[14,17,19,29,30]

Standard curing—The specimens detached from the mold were cured under the standard environment (20 ± 3°C, relative humidity > 95%) to the corresponding curing age.

Steam curing—The specimens detached from the mold were first moved into a rapid concrete curing box (constant temperature: 90°C, heating rate: 10°C/h) and cured at 90°C for 48 hours. After natural cooling, the specimens were moved into standard curing environment and cured until the test curing age (3, 7, and 28 days).

Autoclave curing—The specimens detached from the mold were first moved into the autoclave (constant temperature: 210°C, pressure: 2 MPa, temperature and pressure reached within 2.5 hours) and cured under 210°C, 2 MPa condition for 8 hours. After natural cooling, the specimens were moved to the standard curing environment and cured to the corresponding test age.

EXPERIMENTAL METHODOLOGY

Mechanical properties

According to GB/T 50081-2019, the mechanical strength of specimens was tested at specific curing ages. There are three samples in each group, and the average value is calculated after testing the compressive strength.

X-ray diffraction analysis

In aspect to the treatment of test samples, the ϕ10 x 50 mm specimens cured to the specific curing age were processed through the following steps: 1) the specimens were cracked to a particle size of approximately 2 to 3 mm granular samples and soaked in anhydrous ethanol solution to terminate hydration; and 2) the no-longer-hydrated granular samples were dried at 40°C under vacuum for 2 hours, then ground and passed through a mesh sieve. The crystal structures and phase composition of specimens obtained through the aforementioned steps were tested by a diffractometer with CuKα1 radiation. The test was carried out using a 2θ angle range of 5 to 70 degrees with a step size of 0.02 degrees. The scanning speed of the test ws 5 deg/min.

Scanning electron microscopy (SEM)

The no-longer-hydrated granular samples, obtained through the steps mentioned previously, were used as test samples. A field-emission environmental scanning electron microscope was used to characterize the microstructure and micromorphology of the specimens. Moreover, an X-ray energy spectrometer (EDS) was also used to analyze the microzone composition of the samples.

Nuclear magnetic resonance (NMR) spectroscopy

The samples used in ^{29}Si NMR and ^{27}Al NMR were the same as those used in XRD analysis. The magic-angle rotation speeds were 8 and 12 kHz. The resonant frequencies of ^{29}Si and ^{27}Al were 79.3 and 104 MHz, the pulse widths were 4.0 and 0.5 μs, and the number of scans were all 12,000. The relative intensity values (I) of characteristic peaks of ^{29}Si NMR and ^{27}Al NMR spectra were calculated through PeakFit software. Meanwhile, the obtained relative intensity values (I) could be further calculated, according to Eq. (1) to (4), to obtain the hydration degree, the MCL of silicate chains in calcium (alumino)silicate hydrate (C-(A)-S-H) gels, and the degree of Al^{3+} substitution for Si^{4+} (Al[4]/Si)[31-33]

$$\alpha_C = 1 - I(Q^0)/I_0(Q^0) \quad (1)$$

$$\alpha_{SF+Q} = 1 - I(Q^3 + Q^4)/I_0(Q^3 + Q^4) \quad (2)$$

$$\mathrm{MCL} = 2[I(Q^1) + I(Q^2) + 1.5Q^2(1\mathrm{Al})]/I(Q^1) \quad (3)$$

$$\mathrm{Al[4]/Si} = 0.5I(Q^2(1\mathrm{Al}))/[I(Q^1) + I(Q^2(0\mathrm{Al})) + I(Q^2(1\mathrm{Al}))] \quad (4)$$

where α_C and α_{SF+Q} denote the hydration degree of cement and the hydration degree of silica fume/quartz powder in UHPC, respectively; $I_0(Q^0)$ denotes the relative intensity of the Q^0 integral area in the cement when the cementitious material of UHPC is unhydrated; $I(Q^0)$ denotes the relative intensity of the Q^0 integral area of residual unhydrated cement in the hardened paste; $I_0(Q^4)$ and $I(Q^4)$ denote the relative intensity of the Q^4 integrated area in the unhydrated silica fume/quartz powder and the hardened paste, respectively; and $I(Q^1)$, $I(Q^2)$, and $I(Q^2(1\mathrm{Al}))$ denote the relative intensities of the Q^1, Q^2, and $Q^2(1\mathrm{Al})$ integrated areas in the hardened paste, respectively.

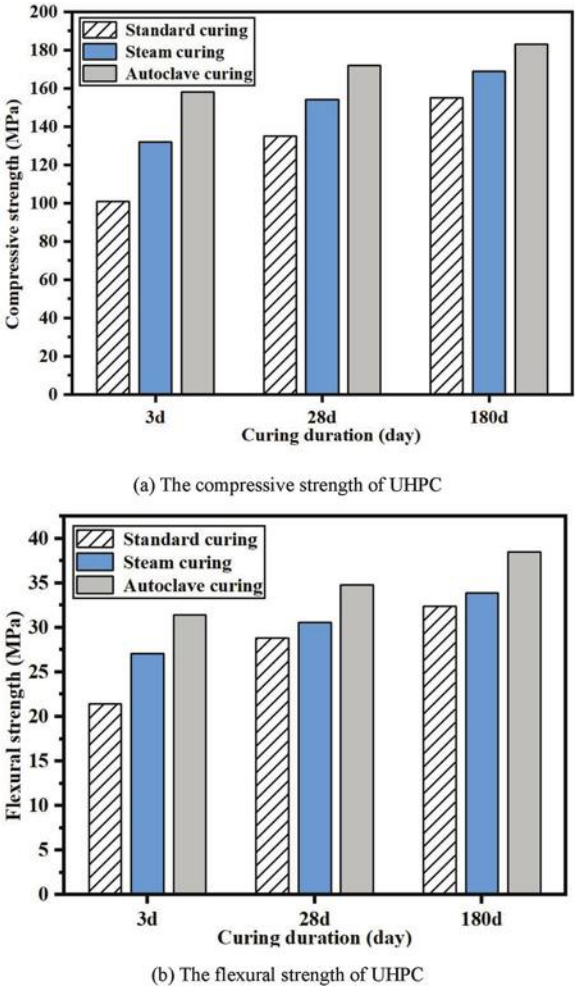

Fig. 3—Mechanical properties of UHPC under different curing regimes.

EXPERIMENTAL RESULTS AND DISCUSSION

Effect of curing regimes on mechanical properties of UHPC

Figure 3 shows the compressive strength and flexural strength of UHPC cured to 3, 28, and 180 days under three different curing regimes (standard curing, steam curing at 90°C, and autoclave curing at 210°C and 2 MPa).

From Fig. 3, it can be seen that the compressive and flexural strength of specimens increased with the increase of curing temperature at the same curing age. Compared with that of specimens with standard curing, the 3-day compressive strength of specimens with steam curing and autoclave curing increased by 30.69% and 56.44%, respectively, and the 3-day flexural strength of specimens with steam curing and autoclave curing increased by 26.64% and 46.73%, respectively. When the curing age reached 180 days, the compressive strength of specimens with steam curing and

autoclave curing increased by 9.03% and 18.06%, respectively, and the flexural strength increased by 4.63% and 18.83%, respectively. This phenomenon could be attributed to the fact that the high temperature and pressure of curing regimes promoted the hydration of cement and pozzolanic reaction of silica fume/quartz powder. The higher hydration degree resulted in more hydration products and a higher crystallization degree, which improved the mechanical performance of UHPC.[12] Moreover, it can also be found that the strength growth rate with the increased curing age for different curing regimes is: standard curing > steam curing > autoclave curing. This may be attributed to the fact that for the standard curing samples, the hydration process of cement and mineral admixtures is a long-term and slow process. Although the amount of early hydration products is relatively small and the porosity is large, the hydration products and the compactness continue to increase with the increase of the age, which made the mechanical properties improve greatly in the later stage. For the steam and autoclave curing specimens, heat treatment increased the hydration degree of cement and silica fume/quartz powder in the early curing age. A large amount of formed hydration products built around the cementitious material, affecting the diffusion process of subsequent hydration and resulting in reduced increase in compressive strength and flexural strength in later stages.[12]

Phase composition

The XRD patterns of specimens under three different curing regimes are shown in Fig. 4. As can be seen from Fig. 4(a), under the standard curing regime, the hydration products of specimens at different curing ages all mainly contained ettringite, $Ca(OH)_2$, and unhydrated C_3S and β-C_2S phases. With the extension of the curing age, the diffraction peak intensity of C_3S and β-C_2S phases gradually decreased and were consumed in the process of hydration. Meanwhile, the $Ca(OH)_2$ content also decreased with the extension of curing age, which could be attributed to the fact that $Ca(OH)_2$ generated by cement hydration was consumed by the pozzolanic reaction of silica fume/quartz powder in the specimen. However, no matter how long the curing age, the diffraction peak intensity of ettringite (AFt) was always in a low state, which is the same as in previous studies.[16,34] This may be due to the fact that the dense structure of UHPC influenced the growth of AFt.

From Fig. 4(b) and (c), it can be seen that the varied patterns of hydration products of UHPC under different curing regimes are similar. Compared with specimens under standard curing regimes, the intensity of diffraction peaks of AFt and $Ca(OH)_2$ decreased significantly with the increase of curing temperature and pressure. When the curing temperature and pressure reached 210°C and 2 MPa, the presence of both AFt and $Ca(OH)_2$ was no longer detected in the XRD pattern. This is because high temperature and high pressure could not only effectively promote the hydration of cement and the pozzolanic reaction in UHPC, but also made AFt decompose and convert to other phases.[35] Moreover, it can be seen that there is another peak of tobermorite (T) in the XRD pattern of the autoclave curing specimens, which does

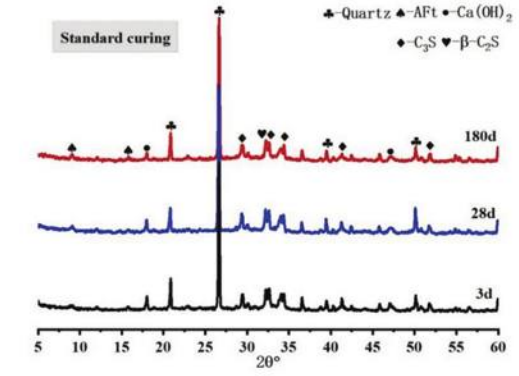

(a) The XRD pattern of specimen with standard curing

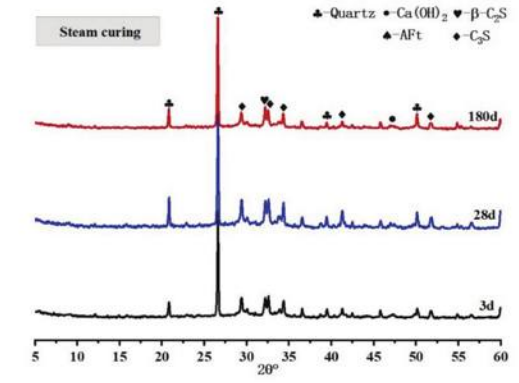

(b) The XRD pattern of specimen with steam curing

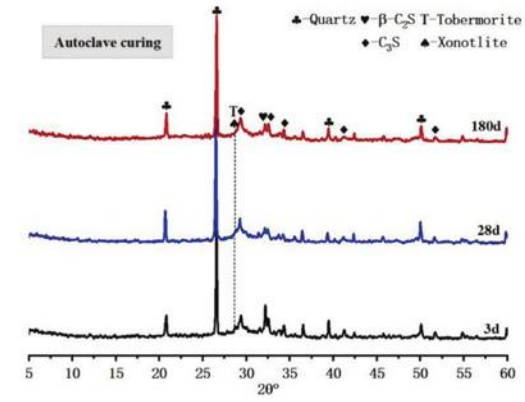

(c) The XRD pattern of specimen with autoclave curing

Fig. 4—XRD patterns of specimens under different curing regimes.

not appear in the XRD pattern of the standard curing specimens and steam curing specimens. As mentioned in peer literature,[14,18] this phenomenon could be attributed to the fact that the high curing temperature and pressure of autoclaved curing involved more Al^{3+}, as well as Si^{4+}, in the silicate chain and improved the polymerization degree of the hydration product (tobermorite). The high packing density and stiffness of tobermorite could also explain the higher compressive strength of autoclaved cured samples to some extent.

Micromorphology

The microstructure of specimens cured under three different curing regimes are shown in Fig. 5. It can be seen from

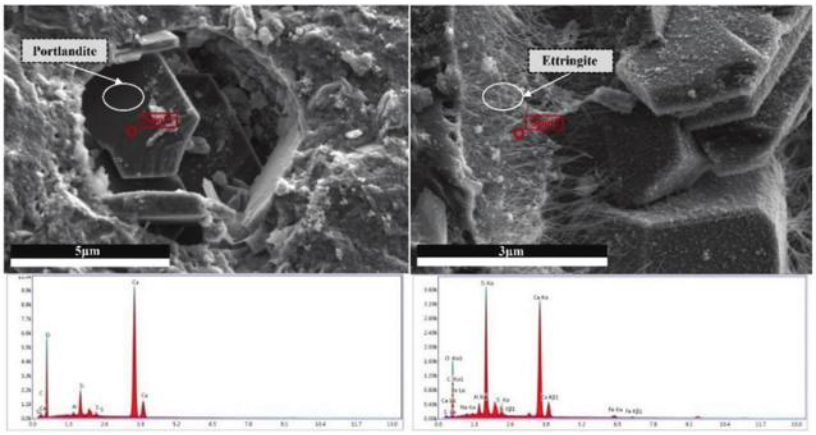

(a) SEM spectra of hydration products in specimen with standard curing

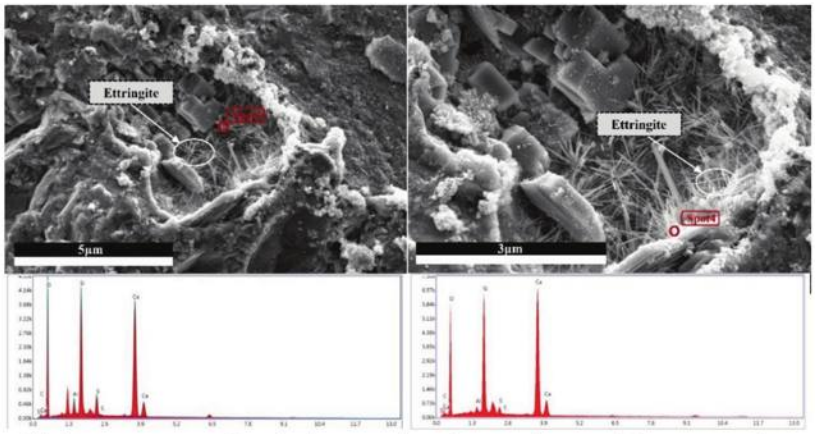

(b) SEM spectra of hydration products in specimen with steam curing

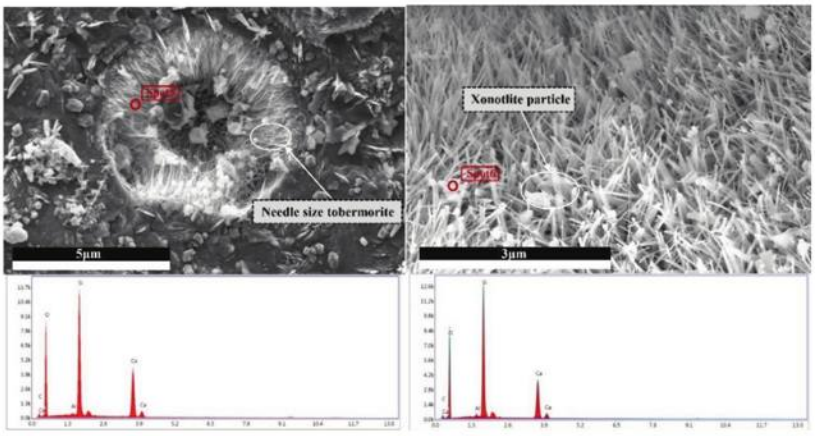

(c) SEM spectra of hydration products in specimen with autoclave curing

Fig. 5—SEM-EDS spot analysis of UHPC under different curing regimes.

Fig. 5(a) that there was a large amount of portlandite as well as needle-like AFt in the sample standard cured for 180 days. When the curing temperature increased to 90°C, the amount of portlandite and AFt gradually decreased. This phenomenon is the same as described in the "Phase composition" section, which confirms that the steam curing regime promoted the hydration reaction in UHPC. When the curing temperature and curing pressure increased further to 210°C and 2 MPa, respectively, the portlandite content is further reduced. Needle-size tobermorite began to appear in the micromorphology of UHPC. Moreover, some xonotlite particles transformed from tobermorite can even be observed in the SEM image. This can verify that high curing temperature increased the crystallization and polymerization of the gel.

From the EDS spectra of specimens under the different curing regimes, it can be found that the Si/Ca ratio of needle hydration products at point 1 and point 3 is approximately 0.70, which is ettringite, and the Si/Ca ratio of needle hydration products increased to 1.81 for the specimen with autoclave curing.[11,36] This phenomenon clarifies that: 1) higher curing temperature enhanced the pozzolanic reaction of silica fume/quartz powder, which provided more Si^{4+} for the

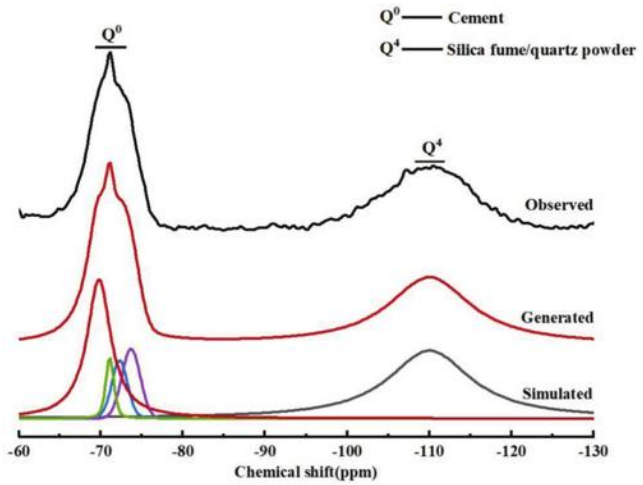

Fig. 6—^{29}Si NMR spectra of cementitious material.

formation of C-S-H gel and increased the Si/Ca ratio as well as the polymerization degree of the gel; and 2) a high Si/Ca ratio is necessary to improve the polymerization degree of hydration products, which could promote Al^{3+} incorporation into C-S-H gel and increase the MCL.[37] Generally, the autoclave curing regime promoted the pozzolanic reaction of silica fume/quartz powder in specimens, which incorporated more Si^{4+} in the gel structure and formed higher-stiffness hydration products (such as tobermorite and xonotlite).[38]

^{29}Si NMR

To characterize the hydration degree of specimens with different curing regimes, ^{29}Si NMR was used in this paper. Meanwhile, to analyze the ^{29}Si NMR spectra more accurately, ^{29}Si NMR was also performed on the raw cementitious material. As shown in Fig. 6 and 7, the ^{29}Si NMR spectra of different specimens are carried on according to the Q_n-Quotation, where Q represents the silicon-oxygen tetrahedron unit and n represents the degree of connectivity. The resonance peak Q^0, located at –71.0 ppm, corresponds to tricalcium silicate and dicalcium silicate in the cement. The amorphous SiO_2 in the silica fume/quartz powder exhibits Q^4 at approximately –110.5 ppm. $Q_0(H)$ represents the hydrated silicon-oxygen tetrahedral monomer, displaying peak at approximately –75.7 ppm. The C-S-H phase presents Q^1, Q^2(1Al), Q^{2B}, and Q^{2P} units from its chain structure at approximately –78.7, –80.1, –82.2, and –84.2 ppm, respectively. Q^1, Q^{2B}, Q^{2P}, and Q^2(1Al) denote the silicate tetrahedra in the C-(A)-S-H gel chain terminals, chain bridging places, and paired sites with an aluminate tetrahedron coordination.[27]

The deconvolution results of specimens with different curing regimes are shown in Table 3. Combined with Fig. 7, it can be seen that under the same curing age, the relative strength value of Q^0 and Q^1 of different curing regimes shows the trend that autoclave curing < steam curing < standard curing. C-S-H gel under standard curing mainly exists as dimer (Q^1),[39,40] as shown in Fig. 8. With the increase of curing temperature and pressure, the ion diffusion rate of cementitious materials during hydration was improved, which promoted the

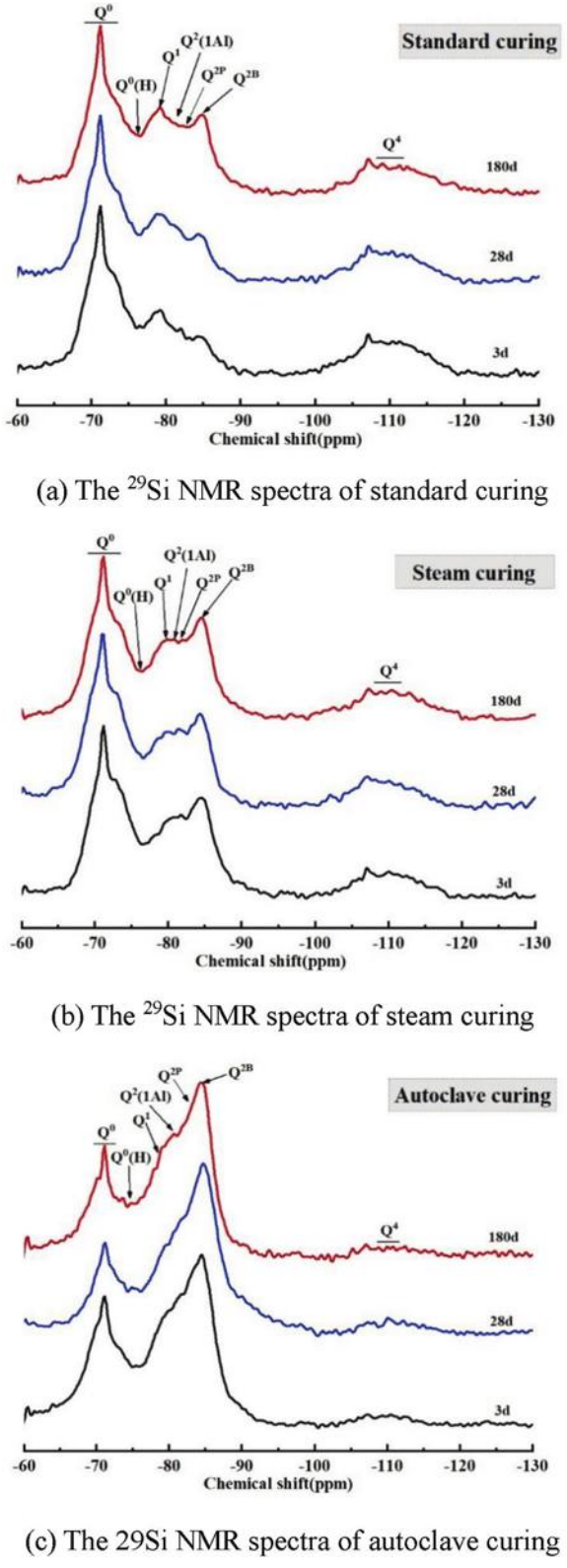

Fig. 7—^{29}Si NMR spectra of UHPC under different curing regimes.

hydration kinetics of cement and silica fume/quartz powder. Thus, the relative strength value of Q^0 and Q^4 in the specimens decreased and more Al^{3+} and Si^{4+} worked as bridging tetrahedra between silicate units. AlO_4 and SiO_4 bridging tetrahedra increased the MCL and polymerization degree of C-S-H gel,[40] which could be verified by the decreased relative

Table 3—Deconvolution results of ^{29}Si NMR spectra

Curing regimes	Curing age, days	Relative strength value of Q^n, %							α_C, %	α_{SF+Q}, %	MCL	Al[4]/Si
		Q^0	$Q^0(H)$	Q^1	Q^2(1Al)	Q^{2B}	Q^{2P}	Q^4				
Standard curing	3	44.3	1.0	19.6	0	2.5	5.0	36.6	28.5	3.6	2.8	0
	28	33.1	3.3	19.8	1.8	3.1	6.3	32.6	46.6	14.2	3.2	0.03
	180	30.1	5.2	19.4	3.4	3.9	7.8	29.8	51.5	21.6	3.7	0.05
Steam curing	3	36.5	8.7	12.9	11.9	4.1	8.1	27.3	41.1	28.2	6.5	0.16
	28	31.6	6.6	12.2	8.5	5.3	10.6	25.2	49.0	33.7	6.7	0.11
	180	27.9	5.7	11.9	7.3	8.2	16.4	22.6	55	40.5	8.0	0.08
Autoclave curing	3	27.3	1.5	12.7	18.2	9.2	18.4	13.6	57.4	64.2	10.3	0.16
	28	26.4	1.0	12.0	14.2	12.8	25.6	10.7	61.8	71.8	12.0	0.11
	180	20.3	0.8	11.8	13.4	15.1	30.2	8.4	67.2	77.9	13.1	0.10

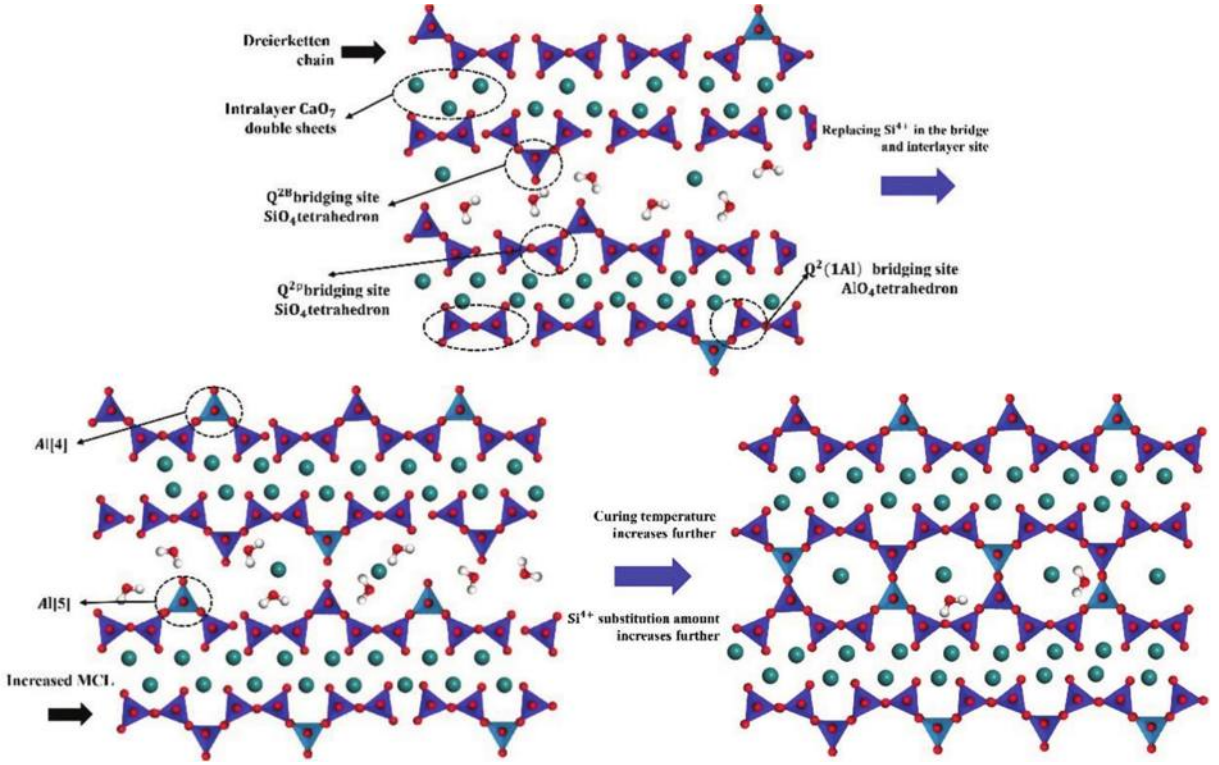

Fig. 8—Variation of silicate chain with increased curing temperature.

strength value of Q^1. Moreover, from Table 3, it can also be seen that the change trend of Q^2(1Al), Q^{2B}, and Q^{2P} units of different curing regimes is contrary to that of Q^0, Q^1, and Q^4, which could be attributed to the fact that Q^2(1Al), Q^{2B}, and Q^{2P} were transformed from Q^0, Q^1, and Q^4. Thus, the higher relative strength value of Q^1, Q^2(1Al), Q^{2B}, and Q^{2P} signify the presence of a higher amount of C-S-H gel and crystal hydration products in the specimens with autoclave curing and steam curing. For further discussion, the hydration degree of cement (α_C), hydration degree of silica fume + quartz powder (α_{SF+Q}), MCL, and ratio of tetracoordinated aluminum to silicon (Al/Si) of the specimens with different curing regimes are calculated and listed in Table 3.

Hydration degree—From Table 3, it can be found that the α_C of the specimens with autoclave curing is 51.0% at 3 days, 55.8% at 28 days, and 62.6% at 180 days, which is much higher than those of the specimens with standard curing and steam curing at the same curing age. Meanwhile, it can be seen that the α_{SF+Q} of specimens with different curing regimes show the same change trend. Thus, it confirmed that the increased curing temperature and the exerted curing pressure promoted the hydration kinetics of cement and silica fume/quartz powder. However, it could also be seen from Table 3 that the α_C and α_{SF+Q} long-term growth rate of the specimen with autoclave curing was slower than those of the other curing regimes. When the curing age of the autoclave curing specimens increased from 3 to 180 days, the growth rates of α_C and α_{SF+Q} were only 9.8% and 13.7%, respectively, which is the same with the change trend of compressive strength. This may be attributed to the fact that the formation of a large amount of hydration products wrapped around the cementitious particles impeded the diffusion of ions and affected the subsequent hydration of the cement. The lower the amount of $Ca(OH)_2$ generated from the hydration of cement, the

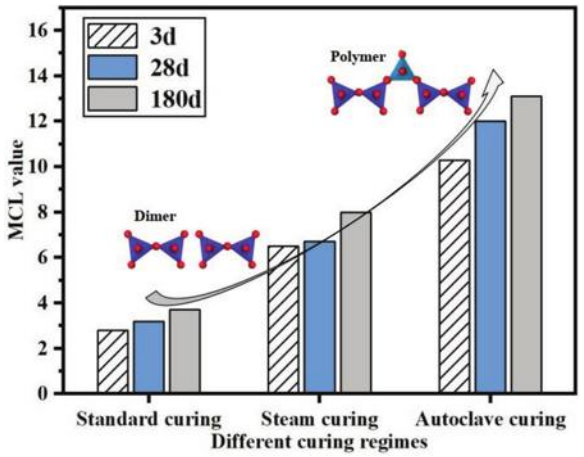

Fig. 9—MCL of specimens with different curing regimes.

lower the hydration degree of silica fume/quartz powder. Thus, the strength growth at later stages was slowed down. Accordingly, it could be concluded that the increased curing temperature and pressure promote the hydration reaction of cement and silica fume/quartz powder at the early stage, but had a negative effect on the long-term hydration process.

MCL—It can be found from Table 3 that the MCL of the specimens with standard curing, steam curing, and autoclave curing at 3 days' curing age are 2.5, 4.1, and 9.2, respectively. As shown in peer literature,[40,41] the MCL of the specimens with standard curing is small, which confirms that the silicate chain in traditional cement-based material is mainly dimer. Meanwhile, according to the linear relationship between MCL and curing temperature, it can also be concluded that a higher curing temperature could promote more Al^{3+} and Si^{4+} working as bridging tetrahedra between silicate units and increase the MCL of the specimens, as depicted in Fig. 9. Moreover, from Table 3, it can also be seen that the MCL of specimens with different curing regimes all increased with curing age. When the curing age reached 180 days, the MCL of specimens with standard curing, steam curing, and autoclave curing are 3.9, 8.2, and 15.1, respectively. This phenomenon confirms that although a longer curing age could increase the hydration and polymerization degree of hydration products, the MCL of the tested specimens do not change greatly, and high-stiffness hydration products (such as tobermorite) in the autoclave curing samples did not appear in the standard curing samples. This confirms the value of heat treatment in UHPC curing.

Al[4]/Si ratio—When the curing age is the same, the relationship of the Al[4]/Si ratio of different specimens is autoclave curing > steam curing > standard curing. Increased curing temperature involved more Al^{3+} in the bridging site of the silicate chain, which contributed to the increased MCL. Meanwhile, considering that the total amount of aluminum ions is constant, this phenomenon could also verify that a higher curing temperature decreased the formation of aluminum-phase hydration products at the early stage. Although the Al[4]/Si ratio of the steam curing specimen at 3 days' curing age is similar to that of the autoclave curing specimen, no tobermorite was detected in the steam curing sample. From the combined MCL calculation data shown in Table 3, it can be inferred that the hydration product with a higher polymerization degree in steam curing samples mainly exists in intermediate products such as C-S-H(I), C-S-H(II), and α-C_2SH.[41,42] Thus, it can be concluded that although the incorporation of Al could extend the MCL of the specimens, its function is limited, and the Si/Ca ratio of gel is a necessary condition for further improving the polymerization degree of hydration products.

Moreover, it can also be found from Table 3 that apart from the specimens with standard curing, the Al[4]/Si ratio of specimens with steam curing and autoclave curing decreased (from 0.16 at 3 days' curing age to 0.08 and 0.10 at 180 days' curing age). This phenomenon could be attributed to the fact that the material containing a large amount of active Al^{3+} (such as C_3A) reacted faster in the early reaction stage and more Al^{3+} was released and absorbed into the gel. This phenomenon made the Al[4]/Si ratio of specimens with steam curing and autoclave curing higher at the early stage. With the extension of the curing age, the unhydrated cement and active SiO_2 in the silica fume/quartz powder continued to hydrate and generate increasing amounts of silica-oxygen tetrahedra, making the Al[4]/Si of the C-S-H gel lower. As a previous study reported,[43] the strength of the Si-O-Si bonds is higher than those of Si-O-Al and Al-O-Al, which accounts for continued growth in long-term strength. Nevertheless, it can be concluded that during the early reaction stage, the C-S-H gel with higher Al[4]/Si had a higher reaction degree and crystallization degree. As the reaction proceeds, more Si^{4+} is involved in the C-S-H gel construction, reducing the Al[4]/Si ratio of C-S-H and improving the long-term stability of the gel.

^{27}Al NMR

The composition of Al-phase products of different specimen are characterized by the ^{27}Al NMR spectrum to explore the effect of different curing regimes on the properties of UHPC. Figure 10 shows the ^{27}Al NMR spectra of specimens with different curing regimes, and the deconvolution results of these specimens are shown in Table 4. The resonance peaks, located at 13.1, 9.8, and 3.9 ppm, are attributed to AFt (Al[6]-E), AFm (Al[6]-M), and TAH (Al[6]-T), respectively. TAH is an amorphous octahedral coordination aluminate phase in the form of $OxAl(OH)_{6-x}^{(3+x)-}$.[32,44] The chemical shift at 35.4 ppm peak is related to Al[5] in the interlayer of C-(A)-S-H gel. The broad resonance centered at approximately 67.2 ppm is attributed to Al[4] in the C-(A)-S-H structure. Moreover, the resonance peak Al[4] in the unhydrated cement is mainly located at approximately –81.0 ppm. Combined with Fig. 10 and Table 4, it can be seen that for the specimens with standard curing and steam curing, Al^{3+} is mainly presented as Al[4] in the C-(A)-S-H gel structure. Meanwhile, for the autoclave curing specimen at 3 days' curing age, Al[4] and Al[5] reached 51.3 and 6.6, respectively. It manifests that Al^{3+} began to be present as Al[5] in the interlayer of C-(A)-S-H gel, which decreased the layer spacing of the gel and balanced the negative charge caused by the replacement of Si^{4+} with Al^{3+}.[32,44,45] Accordingly, the polymerization degree and crystallization degree of C-S-H gel was enhanced, as illustrated in Fig. 8.

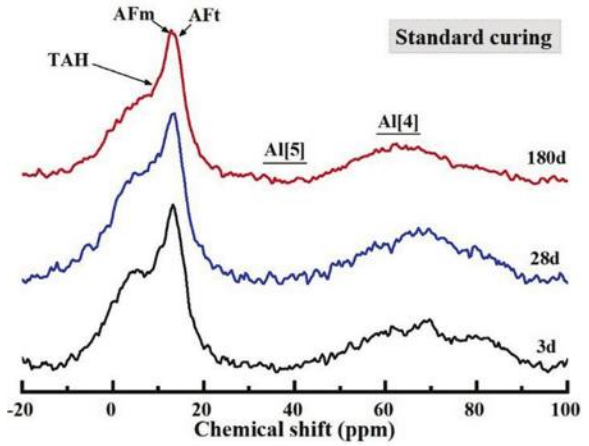

(a) The ^{27}Al NMR spectra of standard curing

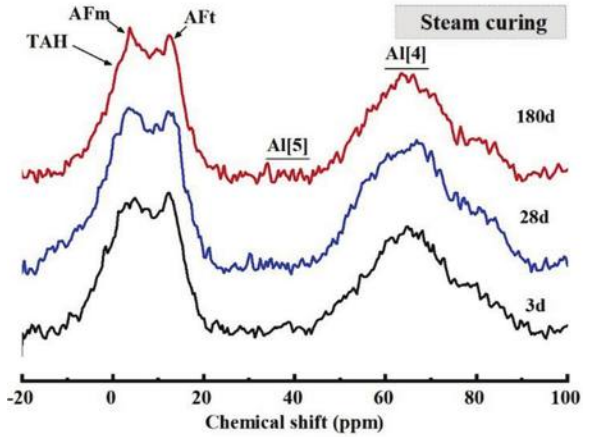

(b) The ^{27}Al NMR spectra of steam curing

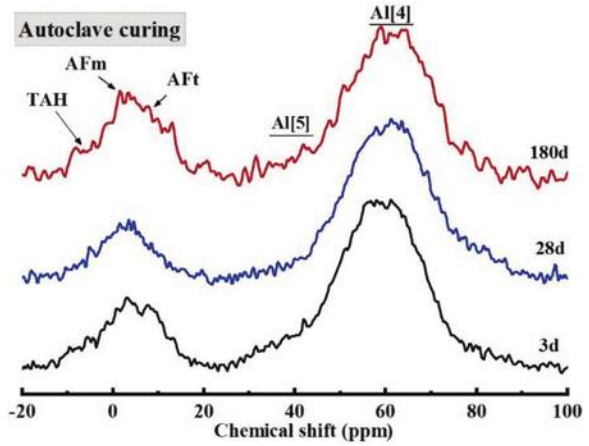

(c) The ^{27}Al NMR spectra of autoclave curing

Fig. 10—^{27}Al NMR spectra of UHPC under different curing regimes.

From Table 4 and Fig. 10, it can also be seen that for the specimens with different curing regimes, the relative content of AFt and AFm increased with the rise of curing age. However, the relative content of TAH shows a different change trend: it decreased with the increase of curing age. It could be concluded that with the extension of curing age,

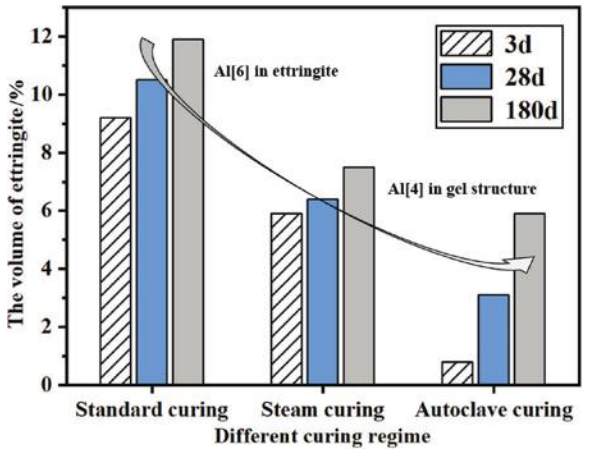

Fig. 11—Volume of ettringite change with curing regime.

TAH gradually converted to AFt and AFm. Moreover, as shown in Fig. 11, it can be seen that the relative content of AFt and AFm at the same curing age decreased with the increase of curing temperature. Combined with the increase of Al[4] and Al[5], this phenomenon could be attributed to the fact that: 1) higher curing temperature affected the formation of AFt and AFm; and 2) the higher polymerization and crystallization degree of cementitious material absorbed large amount of Ca^{2+} and Al^{3+} into the gel structure (Al[4] in aluminum hydration product transformed to Al[4] in gel structure). Compared with specimens under the standard curing regime, on the basis of no other aluminum source material, it can be concluded that Al, Ca, and other ions decomposed from AFt are beneficial to the formation of hydation products with a higher polymerization degree (such as tobermorite or xonotilite).

CONCLUSIONS

A comprehensive investigation was carried out on the composition of hydration products, calcium-silicate-hydrate (C-S-H) gel microstructure, and migration and evolution of aluminum-phase hydration products of cement/silica fume-quartz powder system ultra-high-performance concrete (UHPC) under three curing regimes (standard curing at 20°C, steam curing at 90°C, and pressure steam curing at 210°C and 2 MPa). The following conclusions could be drawn:

1. Heat treatment promotes the hydration of cement and pozzolanic reaction of mineral admixtures, which results in the improvement of compressive strength and flexural strength. The early increase in compressive and flexural strength of the specimen with heat treatment was large, and the 3-day compressive and flexural strengths of the autoclave curing samples were 56.44 and 46.73% higher than those of standard curing specimens. However, the large amount of formed hydration products affected the further hydration of the cementitious material, which slowed down the growth of long-term strength.

2. Compared with the hydration products with a low Si/Ca ratio of standard cured products, the Si/Ca ratio of hydration specimens and the specimens with autoclave curing was increased to 1.81. With the increase of curing temperature

Table 4—Deconvolution results of ^{29}Si NMR spectra

Curing regimes	Curing age, days	Al^{3+} relative strength, %					
		Al[6]-T	Al[6]-M	Al[6]-E	Al[5]	Al[4]	Al[4] in unhydrated cement
Standard curing	3	39.3	3.9	9.2	0	22.7	25.1
	28	35.1	5.2	10.5	0	28.5	22.2
	180	32.2	7.1	11.9	0	34	14.7
Steam curing	3	42.4	0.8	5.9	0	25.5	17.4
	28	39.3	1	6.4	0	29.4	16.4
	180	36.9	1.5	7.5	0	31.3	15.8
Autoclave curing	3	35.7	0.8	0.8	6.6	51.3	4.1
	28	27.3	1.2	3.1	7.1	58.6	2.7
	180	19.7	1.7	5.9	7.6	66.1	1.1

and curing pressure, the polymerization degree of the hydration products of the samples continued to increase, and more silicon and aluminum ions participated in construction of the gel structure.

3. The increased curing temperature and pressure resulted in the higher degree of hydration. More Si^{4+} entered as Q^1, Q^2(1Al), Q^{2B}, and Q^{2P} into the C-S-H gel, which is beneficial to the formation of hydration products. Moreover, the mean chain length (MCL) and Al[4]/Si of the C-S-H gel also increased with the increased curing temperature, implying that the increased temperature allows more Al^{3+} to replace Si^{4+} into the C-S-H gel structure, resulting in growing chain length and increased polymerization of the early C-S-H gel. However, the polymerization effect of Al ions is limited, so the provision of the silicon source to improve the Si/Ca ratio of the system is also important.

4. With the increase of curing temperature, Al^{3+}, originally formed as Al[6] in UHPC, transformed to Al[4] and Al[5] in the gel structure. With the extension of curing age, more and more Si^{4+} decomposed from raw material and became involved in the formation of calcium-(alumino)silicate-hydrate (C-(A)-S-H), which resulted in the decrease of Al[4]/Si of UHPC. The ever-decreasing Al[4]/Si (the strength of Si-O-Si is higher that Al-O-Al or Al-O-Si) explains the long-term increase in mechanical strength of UHPC.

AUTHOR BIOS

Hao Qian *is a Researcher at Anhui Jianzhu University, Hefei, Anhui, China. He received his master's degree from Nanjing Tech University, Nanjing, Jiangsu, China, in 2022. His research interests include three-dimensional (3-D) construction printing materials and ultra-high-performance concrete.*

Gaozhan Zhang *is a Professor at Anhui Jianzhu University. He received his PhD in materials science from Wuhan University of Technology, Wuhan, Hubei, China, in 2017. His research interests include basic theoretical research and engineering application research of advanced cementitious composites.*

Jun Yang *is a Lecturer at Anhui Jianzhu University. He received his PhD in materials science from Wuhan University of Technology in 2019. His research interests include high-performance cement-based materials and radiation-resistant concrete.*

Qingjun Ding *is a Professor at Wuhan University of Technology, where he received his PhD in materials science in 2009, and is a member of the expert group of the Building Materials Science and Technology Engineering Consulting Department of Hubei Science and Technology Consulting Service Center.*

Chundong Geng *is a Researcher at Wuhan University of Technology. His research interests include the planning, consulting, survey, and design of water conservancy and hydropower projects.*

Sudong Hua *is a Professor at Nanjing Tech University. His research interests include the recycling of industrial solid waste and study of 3-D construction printing materials.*

ACKNOWLEDGMENTS

Financial support from the National Natural Science Foundation of China under Grant U21A20149; the Ecological Environment Scientific Research Project of Anhui Province (Grant No. 2023hb0014); the Research Reserve of Anhui Jianzhu University under Grant 2022XMK01; and the Excellent Scientific Research and Innovation Team in Colleges and Universities of Anhui Province under Grant 2022AH010017 is gratefully acknowledged.

REFERENCES

1. Jung, M.; Park, J.-S.; Hong, S.-G.; and Moon, J., "Micro- and Meso-Structural Changes on Electrically Cured Ultra-High-Performance Fiber-Reinforced Concrete with Dispersed Carbon Nanotubes," *Cement and Concrete Research*, V. 137, 2020, p. 106214. doi: 10.1016/j.cemconres.2020.106214

2. Shen, P.; Lu, J.-X.; Lu, L.; He, Y.; Wang, F.; and Hu, S., "An Alternative Method for Performance Improvement of Ultra-High-Performance Concrete by Internal Curing: Role of Physicochemical Properties of Saturated Lightweight Fine Aggregate," *Construction and Building Materials*, V. 312, 2021, p. 125373. doi: 10.1016/j.conbuildmat.2021.125373

3. Hannawi, K.; Bian, H.; Prince-Agbodjan, W.; and Raghavan, B., "Effect of Different Types of Fibers on the Microstructure and the Mechanical Behavior of Ultra-High-Performance Fiber-Reinforced Concretes," *Composites Part B: Engineering*, V. 86, 2016, pp. 214-220. doi: 10.1016/j.compositesb.2015.09.059

4. Yoo, D.-Y., and Yoon, Y.-S., "A Review on Structural Behavior, Design, and Application of Ultra-High-Performance Fiber-Reinforced Concrete," *International Journal of Concrete Structures and Materials*, V. 10, No. 2, 2016, pp. 125-142. doi: 10.1007/s40069-016-0143-x

5. Yazıcı, H.; Yardımcı, M. Y.; Aydın, S.; and Karabulut, A. Ş., "Mechanical Properties of Reactive Powder Concrete Containing Mineral Admixtures under Different Curing Regimes," *Construction and Building Materials*, V. 23, No. 3, 2009, pp. 1223-1231. doi: 10.1016/j.conbuildmat.2008.08.003

6. Matte, V., and Moranville, M., "Durability of Reactive Powder Composites: Influence of Silica Fume on the Leaching Properties of Very Low Water/Binder Pastes," *Cement and Concrete Composites*, V. 21, No. 1, 1999, pp. 1-9. doi: 10.1016/S0958-9465(98)00025-0

7. Yu, R.; Spiesz, P.; and Brouwers, H. J. H., "Mix Design and Properties Assessment of Ultra-High Performance Fibre Reinforced Concrete (UHPFRC)," *Cement and Concrete Research*, V. 56, 2014, pp. 29-39. doi: 10.1016/j.cemconres.2013.11.002

8. Heinz, D.; Urbonas, L.; and Gerlicher, T., "Effect of Heat Treatment Method on the Properties of UHPC," *3rd International Symposium on UHPC and Nanotechnology for High Performance Construction Materials*, Kassel University, Kassel, Germany, 2012, pp. 283-290.

9. Li, W.; Huang, Z.; Hu, G.; Duan, W. H.; and Shah, S. P., "Early-Age Shrinkage Development of Ultra-High-Performance Concrete under Heat Curing Treatment," *Construction and Building Materials*, V. 131, 2017, pp. 767-774. doi: 10.1016/j.conbuildmat.2016.11.024

10. Wille, K.; Naaman, A. E.; El-Tawil, S.; and Parra-Montesinos, G. J., "Ultra-High-Performance Concrete and Fiber Reinforced Concrete: Achieving Strength and Ductility without Heat Curing," *Materials and Structures*, V. 45, No. 3, 2012, pp. 309-324. doi: 10.1617/s11527-011-9767-0

11. Hiremath, P. N., and Yaragal, S. C., "Effect of Different Curing Regimes and Durations on Early Strength Development of Reactive Powder Concrete," *Construction and Building Materials*, V. 154, 2017, pp. 72-87. doi: 10.1016/j.conbuildmat.2017.07.181

12. Prem, P. R.; Bharatkumar, B. H.; and Iyer, N. R., "Influence of Curing Regimes on Compressive Strength of Ultra-High-Performance Concrete," *Sādhanā*, V. 38, No. 6, 2013, pp. 1421-1431. doi: 10.1007/s12046-013-0159-8

13. Yazıcı, H., "The Effect of Curing Conditions on Compressive Strength of Ultra-High Strength Concrete with High Volume Mineral Admixtures," *Building and Environment*, V. 42, No. 5, 2007, pp. 2083-2089. doi: 10.1016/j.buildenv.2006.03.013

14. Shen, P.; Lu, L.; He, Y.; Wang, F.; and Hu, S., "The Effect of Curing Regimes on the Mechanical Properties, Nano-Mechanical Properties and Microstructure of Ultra-High-Performance Concrete," *Cement and Concrete Research*, V. 118, 2019, pp. 1-13. doi: 10.1016/j.cemconres.2019.01.004

15. Courtial, M.; de Noirfontaine, M.-N.; Dunstetter, F.; Signes-Frehel, M.; Mounanga, P.; Cherkaoui, K.; and Khelidj, A., "Effect of Polycarboxylate and Crushed Quartz in UHPC: Microstructural Investigation," *Construction and Building Materials*, V. 44, 2013, pp. 699-705. doi: 10.1016/j.conbuildmat.2013.03.077

16. Wang, D.; Shi, C.; Wu, Z.; Xiao, J.; Huang, Z.; and Fang, Z., "A Review on Ultra-High-Performance Concrete: Part II. Hydration, Microstructure and Properties," *Construction and Building Materials*, V. 96, 2015, pp. 368-377. doi: 10.1016/j.conbuildmat.2015.08.095

17. Hamada, H.; Alattar, A.; Tayeh, B.; Yahaya, F.; and Almeshal, I., "Influence of Different Curing Methods on the Compressive Strength of Ultra-High-Performance Concrete: A Comprehensive Review," *Case Studies in Construction Materials*, V. 17, 2022, p. e01390. doi: 10.1016/j.cscm.2022.e01390

18. Helmi, M.; Hall, M. R.; Stevens, L. A.; and Rigby, S. P., "Effects of High Pressure/Temperature Curing on Reactive Powder Concrete Microstructure Formation," *Construction and Building Materials*, V. 105, 2016, pp. 554-562. doi: 10.1016/j.conbuildmat.2015.12.147

19. Yazıcı, H.; Deniz, E.; and Baradan, B., "The Effect of Autoclave Pressure, Temperature and Duration Time on Mechanical Properties of Reactive Powder Concrete," *Construction and Building Materials*, V. 42, 2013, pp. 53-63. doi: 10.1016/j.conbuildmat.2013.01.003

20. Yang, K. H.; Moon, G. D.; and Jeon, Y. S., "Implementing Ternary Supplementary Cementing Binder for Reduction of the Heat of Hydration of Concrete," *Journal of Cleaner Production*, V. 112, 2016, pp. 845-852. doi: 10.1016/j.jclepro.2015.06.022

21. Ahmed, S.; Al-Dawood, Z.; Abed, F.; Mannan, M. A.; and Al-Samarai, M., "Impact of Using Different Materials, Curing Regimes, and Mixing Procedures on Compressive Strength of Reactive Powder Concrete-A Review," *Journal of Building Engineering*, V. 44, 2021, p. 103238. doi: 10.1016/j.jobe.2021.103238

22. Zhu, Y.; Zhang, Y.; Hussein, H. H.; Liu, J.; and Chen, G., "Experimental Study and Theoretical Prediction on Shrinkage-Induced Restrained Stresses in UHPC-RC Composites under Normal Curing and Steam Curing," *Cement and Concrete Composites*, V. 110, 2020, p. 103602. doi: 10.1016/j.cemconcomp.2020.103602

23. Li, W.; Huang, Z.; Hu, G.; Duan, W. H.; and Shah, S. P., "Early-Age Shrinkage Development of Ultra-High-Performance Concrete under Heat Curing Treatment," *Construction and Building Materials*, V. 131, 2017, pp. 767-774. doi: 10.1016/j.conbuildmat.2016.11.024

24. Manzano, H.; Moeini, S.; Marinelli, F.; Van Duin, A. C. T.; Ulm, F.-J.; and Pellenq, R. J.-M., "Confined Water Dissociation in Microporous Defective Silicates: Mechanism, Dipole Distribution, and Impact on Substrate Properties," *Journal of the American Chemical Society*, V. 134, No. 4, 2012, pp. 2208-2215. doi: 10.1021/ja209152n

25. Cong, X., and Kirkpatrick, R. J., "^{29}Si MAS NMR Study of the Structure of Calcium Silicate Hydrate," *Advanced Cement Based Materials*, V. 3, No. 3-4, 1996, pp. 144-156. doi: 10.1016/S1065-7355(96)90046-2

26. Zhang, G.; Li, Y.; Yang, J.; Ding, Q.; and Sun, D., "Insight into the Strengthening Mechanism of the Al-Induced Cross-Linked Calcium Aluminosilicate Hydrate Gel: A Molecular Dynamics Study," *Frontiers in Materials*, V. 7, 2021, p. 611568. doi: 10.3389/fmats.2020.611568

27. Zou, J.; Guo, C.; Jiang, Y.; Wei, C.; and Li, F., "Structure, Morphology and Mechanism Research on Synthesizing Xonotlite Fiber from Acid-Extracting Residues of Coal Fly Ash and Carbide Slag," *Materials Chemistry and Physics*, V. 172, 2016, pp. 121-128. doi: 10.1016/j.matchemphys.2016.01.050

28. Ipek, M.; Yilmaz, K.; Sümer, M.; and Saribiyik, M., "Effect of Presetting Pressure Applied to Mechanical Behaviors of Reactive Powder Concrete During Setting Phase," *Construction and Building Materials*, V. 25, No. 1, 2011, pp. 61-68. doi: 10.1016/j.conbuildmat.2010.06.056

29. Abdulkareem, O. M.; Ben Fraj, A.; Bouasker, M.; and Khelidj, A., "Effect of Chemical and Thermal Activation on the Microstructural and Mechanical Properties of More Sustainable UHPC," *Construction and Building Materials*, V. 169, 2018, pp. 567-577. doi: 10.1016/j.conbuildmat.2018.02.214

30. Wu, Z.; Shi, C.; and He, W., "Comparative Study on Flexural Properties of Ultra-High-Performance Concrete with Supplementary Cementitious Materials under Different Curing Regimes," *Construction and Building Materials*, V. 136, 2017, pp. 307-313. doi: 10.1016/j.conbuildmat.2017.01.052

31. Zhang, G.; Yang, Q.; Hou, D.; Zhou, P.; and Ding, Q., "Unraveling the Microstructural Properties of Cement-Slag Composite Pastes Incorporated with Smart Polymer-Based Corrosion Inhibitors: From Experiment to Molecular Dynamics," *Cement and Concrete Composites*, V. 125, 2022, p. 104298. doi: 10.1016/j.cemconcomp.2021.104298

32. Zhang, G.; Wu, C.; Hou, D.; Yang, J.; Sun, D.; and Zhang, X., "Effect of Environmental pH Values on Phase Composition and Microstructure of Portland Cement Paste under Sulfate Attack," *Composites Part B: Engineering*, V. 216, 2021, p. 108862. doi: 10.1016/j.compositesb.2021.108862

33. Girão, A. V.; Richardson, I. G.; Taylor, R.; and Brydson, R. M. D., "Composition, Morphology and Nano-Structure of C–S–H in 70% White Portland Cement–30% Fly Ash Blends Hydrated at 55°C," *Cement and Concrete Research*, V. 40, No. 9, 2010, pp. 1350-1359. doi: 10.1016/j.cemconres.2010.03.012

34. Chong, W.; Yang, C.; Fang, L.; Wan, C.; and Pu, X., "Preparation of Ultra-High-Performance Concrete with Common Technology and Materials," *Cement and Concrete Research*, V. 26, No. 4, 2004, pp. 538-544.

35. Kim, S.; Lee, N.; Lee, H. K.; and Park, S., "Experimental and Theoretical Studies of Hydration of Ultra-High-Performance Concrete Cured under Various Curing Conditions," *Construction and Building Materials*, V. 278, No. 7, 2021, p. 122352. doi: 10.1016/j.conbuildmat.2021.122352

36. Chen, T.; Gao, X.; and Ren, M., "Effects of Autoclave Curing and Fly Ash on Mechanical Properties of Ultra-High-Performance Concrete," *Construction and Building Materials*, V. 158, 2018, pp. 864-872. doi: 10.1016/j.conbuildmat.2017.10.074

37. Kapeluszna, E.; Kotwica, Ł.; Różycka, A.; and Gołek, Ł., "Incorporation of Al in C-A-S-H Gels with Various Ca/Si and Al/Si Ratio: Microstructural and Structural Characteristics with DTA/TG, XRD, FTIR and TEM Analysis," *Construction and Building Materials*, V. 155, 2017, pp. 643-653. doi: 10.1016/j.conbuildmat.2017.08.091

38. Hesse, C.; Goetz-Neunhoeffer, F.; and Neubauer, J., "A New Approach in Quantitative In-Situ XRD of Cement Pastes: Correlation of Heat Flow Curves with Early Hydration Reactions," *Cement and Concrete Research*, V. 41, No. 1, 2011, pp. 123-128. doi: 10.1016/j.cemconres.2010.09.014

39. Battocchio, F., and Paulo, J. M., "Rietveld Refinement of the Structures of 1.0 CSH and 1.5 C-S-H," *Cement and Concrete Research*, V. 42, No. 11, 2012, pp. 1534-1548. doi: 10.1016/j.cemconres.2012.07.005

40. Dong, Y.; Feng, C.; Zhao, Q.; and Liang, X., "Study on the Structure of C-S-H Gels of Slag–Cement Hardened Paste by ^{29}Si, ^{27}Al MAS NMR," *Applied Magnetic Resonance*, V. 50, No. 12, 2019, pp. 1345-1357. doi: 10.1007/s00723-019-01152-6

41. Oh, J. E.; Clark, S. M.; and Monteiro, P. J. M., "Does the Al Substitution in C–S–H (I) Change its Mechanical Property?" *Cement and Concrete Research*, V. 41, No. 1, 2011, pp. 102-106. doi: 10.1016/j.cemconres.2010.09.010

42. Dharmawardhana, C. C.; Misra, A.; and Ching, W. Y., "Theoretical Investigation of C-(A)-S-H(I) Cement Hydrates," *Construction and Building Materials*, V. 184, 2018, pp. 536-548. doi: 10.1016/j.conbuildmat.2018.07.004

43. Duxson, P.; Provis, J. L.; Lukey, G. C.; Mallicoat, S. W.; Kriven, W. M.; and van Deventer, J. S. J., "Understanding the Relationship between Geopolymer Composition, Micro-Structure and Mechanical Properties," *Colloids and Surfaces A: Physicochemical and Engineering Aspects*, V. 269, No. 1-3, 2005, pp. 47-58. doi: 10.1016/j.colsurfa.2005.06.060

44. Andersen, M. D.; Jakobsen, H. J.; and Skibsted, J., "A New Aluminum Hydrate Species in Hydrated Portland Cements Characterized by ^{27}Al and ^{29}Si MAS NMR Spectroscopy," *Cement and Concrete Research*, V. 36, No. 1, 2006, pp. 3-17. doi: 10.1016/j.cemconres.2005.04.010

45. Pardal, X.; Pochard, I.; and Nonat, A., "Experimental Study of Si–Al Substitution in Calcium-Silicate-Hydrate (C-S-H) Prepared under Equilibrium Conditions," *Cement and Concrete Research*, V. 39, No. 8, 2009, pp. 637-643. doi: 10.1016/j.cemconres.2009.05.001

ACI MATERIALS JOURNAL TECHNICAL PAPER

Title No. 121-M21

Statistical Process Control of Fiber-Reinforced Concrete Precast Tunnel Segments

by C. Pleesudjai, D. Patel, K. A. Williams Gaona, M. Bakhshi, V. Nasri, and B. Mobasher

Statistical process control (SPC) procedures are proposed to improve the production efficiency of precast concrete tunnel segments. Quality control test results of more than 1000 ASTM C1609/C1609M beam specimens were analyzed. These specimens were collected over 18 months from the fiber-reinforced concrete (FRC) used for the production of precast tunnel segments of a major wastewater tunnel project in the Northeast United States. The Anderson-Darling (AD) test for the overall distribution indicated that the data are best described by a normal distribution. The initial residual strength parameter for the FRC mixture, f^D_{600}, is the most representative parameter of the post-crack region. The lower 95% confidence interval (CI) values for 28-day flexural strength parameters of f_1, f^D_{600}, and f^D_{300} exceeded the design strengths and hence validated the strength acceptability criteria set at 3.7 MPa (540 psi).

A combination of run chart, exponentially weighted moving average (EWMA), and cumulative sum (CUSUM) control charts successfully identified the out-of-control mean values of flexural strengths. These methods identify the periods corresponding to incapable manufacturing processes that should be investigated to move the processes back into control. This approach successfully identified the capable or incapable processes. The study also included the Bootstrap Method to analyze standard error in the test data and its reliability to determine the sample size.

Keywords: Bootstrap Method; fiber-reinforced concrete; flexure; lining; precast; quality control; statistical process control; time-series control process; tunnel segment.

INTRODUCTION

Precast segmental tunnel lining is an important component of tunnel infrastructure needed for the operation of tunnel boring machines (TBMs) and providing permanent ground support. The functionality of tunnels depends on the structural and durability performance of these lining systems as protective barriers against large overburden loads and complex geotechnical exposure conditions. The precast linings are suitable for tunneling in both soft ground and fractured hard rock and serve as initial and final support. They are used as the dominant lining option due to their efficiency, construction speed, and economics in comparison to conventional cast-in-place lining systems.[1]

Steel fiber-reinforced concrete (SFRC) is known for improving concrete's ductility by bridging cracks and resisting their propagation and opening. The ductility and strength offered by steel fibers allow a partial or complete replacement of traditional reinforcing steel cages. In many structural applications, using a hybrid design with steel fiber and reinforcing bar has shown significant structural and economic advantages.[2-4] It is also known that the dispersion of steel fibers, especially in the reinforcement cover region, improves the durability and delays the onset and extent of corrosion.[5] Steel fiber use in tunnel linings has considerably increased during the past decade.[6] Moreover, fiber reinforcement mitigates the bursting and spalling of concrete at segment joints in both circumferential joints (under TBM thrust jack forces) and longitudinal joints (under hoop forces due to embedment loads).[7,8] Also, segment joint cracks are inevitable due to joint misalignment under strict production and construction tolerances.[9] By reinforcing the edges or corners, SFRC further resists premature deterioration of the segments during the construction phase.

The random nature of short fibers used as primary or secondary reinforcement requires a reliable set of estimates for quality control (QC) during manufacturing. The residual strength offered by the fiber-reinforced concrete (FRC) is a function of the number of fibers crossing the cracked section and is often used as a measure of variability in the post-crack performance.[10,11] Other parameters include the strength, geometry, type, and orientation of fibers in a bridged cracked section, as well as interfacial shear strength during fiber pullout,[12] structural size, and the test setup.[13-16] The treatment of FRC as an isotropic material is not directly applicable because cracking is inevitable under certain conditions and the residual strength of an FRC member depends on the variability of the material.[17] The contribution of steel fibers to the residual strength is measured by using the load-deflection curve obtained from the ASTM C1609/C1609M flexural tests[18] to back-calculate the apparent tension and compression stress-strain responses.[19] The idealized stress-strain relationships derived from the load-deflection response, allowing for the design of sections with different sizes, shapes, and reinforcements.[20]

RESEARCH SIGNIFICANCE

The use of TBMs in the construction of tunnels using precast FRC segments has resulted in significant economic advantages in terms of quality, economic aspects, and speed of construction. Due to the interlocking nature of the precast segments, QC and tolerance aspects of section dimensions, strength, and ductility affect the serviceability significantly. Unanticipated problems with durability and watertightness

ACI Materials Journal, V. 121, No. 2, March 2024.

MS No. M-2022-424.R2, doi: 10.14359/51740373, received July 28, 2023, and reviewed under Institute publication policies.

could lead to costly repair and significant downtime of essential infrastructure elements. Better identification of the trends in data and understanding the variations causing outlier samples through statistical process control (SPC) provide acceptable risk levels and are important aspects of the design process. Monitoring the potential problems before field installation, when combined with the necessary number of samples tested, is also an important aspect of process control.

The purpose of this paper is to address the QC aspects of the flexural data by the proposed SPC procedures adopted in daily tests on the FRC used in different production cycles during the segment fabrication phase of a major wastewater tunnel project. The objective is to correlate the interrelationship of the measured properties with the acceptance criteria and to determine if, by monitoring the deviations observed, the knowledge could be identified to avoid out-of-control trends and control the production schedule. Furthermore, an extensive investigation into the minimum sampling requirements for ASTM C1609 testing was conducted by the Bootstrap Method approach to obtain statistical data from a limited number of random samples. The findings provide valuable insights into the variability of results obtained through ASTM C1609 and, consequently, propose minimum sampling requirements. By adhering to these recommended sampling guidelines, FRC users can minimize the number of tests, leading to considerable time and cost savings while ensuring the reliability of FRC properties.

EXPLORATORY BACKGROUND DATA

The data set used for this study was obtained from the construction production data of South Hartford Conveyance and Storage Tunnel over 18 months from mid-2018 to late 2019.[21,22] Project specification required portland cement Type I/II, calcareous aggregates, and air content of 3 to 6%. Specified properties include minimum compressive strengths of 14 and 45 MPa (2000 and 6500 psi) at stripping time and 28 days, respectively; maximum water-cementitious materials ratio (*w*/*cm*) of 0.35; silica fume content of 5% of cementitious materials; maximum aggregate size of 19 mm (3/4 in.); and maximum chloride-ion penetrability of 1000 coulombs. The reinforcement was a double hooked-end steel fiber with a tensile strength of 1800 MPa (260 ksi), length of 60 mm (2.36 in.), and an aspect ratio of 80, with a minimum dosage of 40 kg/m^3 (67 lb/yd^3). These specifications were used satisfactorily in a preconstruction trial and the mixture presented in Table 1. As a part of the QC requirements, ASTM C1609 beam specimens were tested daily during the production days. Multiple specimens were tested at two curing ages of formwork stripping and 28 days. The design parameter (residual flexural strength) was 2.3 MPa (340 psi) for stripping age. For serviceability design, a parameter of 3.7 MPa (540 psi) was specified as characteristic 28-day flexural strength at the first crack (f_1) and residual flexural strength at a deflection of 0.75 mm (0.03 in.) as f^D_{600} when tested following the test procedures.[18] Using these data, the equivalent tensile strength values were calculated from these specifications using back-calculation methods.[11] The limit state design strength criteria at 28 days were specified as 4 MPa (580 psi) characteristic residual flexural strength at a deflection of 1.5 mm (f^D_{300}) or 3 mm (f^D_{150}). This characteristic strength was specified as 2.5 MPa (360 psi) for stripping age. The total number of ASTM C1609 test results accounted for 1060 specimens, with 243 specimens tested at stripping age and 817 specimens at 28 days during the period from June 2018 to October 2019. Figure 1 shows the load-deflection results of the standard four-point bending (ASTM C1609[18]) test for both the stripping age (a few hours up to 1 day) and 28 days of curing. The variation in the range of the test data for the entire production cycle is noted. After the initial loading and first cracking, a nonlinear response is expected that is demonstrated by either deflection softening or hardening in the post-crack zone. Most test results showed a sudden drop after the first crack load. The maximum level of post-cracking load at stripping age

Table 1—Concrete mixture proportions of precast tunnel segments

	SI units, kg/m^3	Imperial units, lb/yd^3
Total cementitious materials	373.8	630
Portland cement Type I/II	355.1	598.5
Silica fume (SF)	18.7	31.5
Fine aggregate	842.5	1420
Coarse aggregate	1154.6	1946
Water	131.2	221
High-range water-reducing admixture	2.1	3.6 (57 fl oz)
Steel fiber	42.1	71
Unit weight	2545	4291
w/*cm*	0.35	
SF/*cm*	5%	
Steel fiber-volume fraction (V_f)	0.54%	
Air content	3.9%	

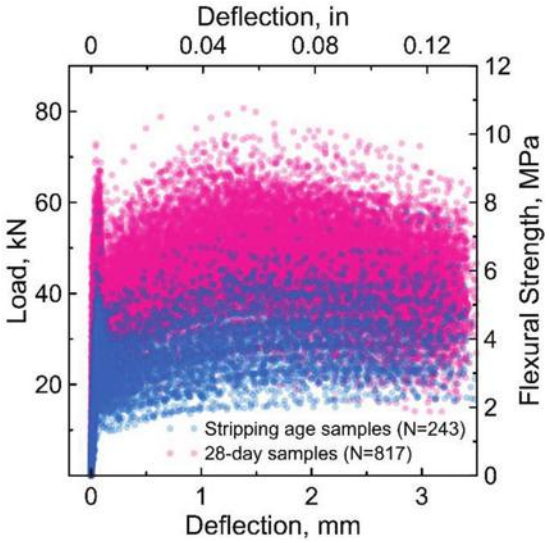

Fig. 1—Scatter plot of four-point bending ASTM C1609 tests at stripping age and 28 days.

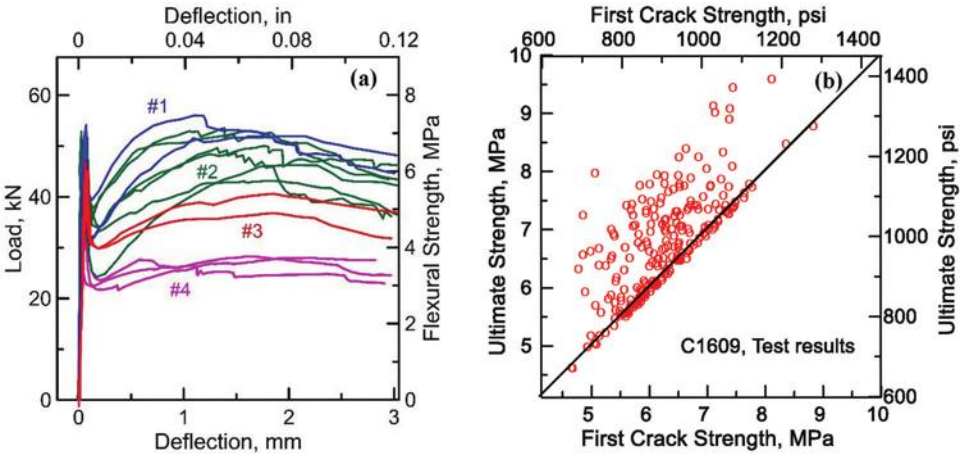

Fig. 2—(Left) Representative samples of different response categories; and (right) correlation of first crack strength (f_1) with peak strength (f_p) at 28 days, showing evidence of deflection hardening.

occurred near a deflection of 2 to 3 mm (0.08 to 0.12 in.), while the maximum residual load observed in 28-day specimens was in the early stage of deflection—that is, 1 to 2 mm (0.04 to 0.08 in.). The enhanced behavior and post-crack hardening could be attributed to improved bond strength between the fibers and cementitious matrix after 28 days of curing. Moreover, the scatter plot of 28-day specimens ranges from a minimum of 14 kN (3108 lb) to a peak load of 77 kN (17,232 lb), which, in terms of equivalent flexural stress, is 1.87 to 10.27 MPa (271 to 1489 psi), respectively, representing approximately 1.4 times the scatter at stripping age (refer to Fig. 1).

The load-deflection responses were categorized and separated into several ranges covering the deflection-softening to deflection-hardening responses. Figure 2(a) shows these four ranges as representative plots of behavior that span the post-cracking responses. Group 1 represents typical specimens in the deflection hardening. Between Groups 2, 3, and 4, the response of FRC gradually changes toward deflection softening such that, as shown in Fig. 2(a), Group 4 represents a constant stress deflection-softening. It is reasonable to expect that within each range the results will vary as well. Figure 2(b) shows the correlation of first crack strength (f_1) with the peak strength (f_p) of the 28-day specimens, indicating that for most samples, the flexural peak strength exceeds the first crack strength. The points falling on the 1:1 line exhibit deflection softening, and those above the line are deflection hardening. Most of the specimens show deflection hardening.

Descriptive measures of statistics

The ASTM C1609[18] test measures the apparent flexural strength at first crack, peak strength, and at certain prescribed deflection values by using Eq. (1). Parameter P is the applied load; L is the span length; and b and h are the width and depth of the beam section, respectively. Typical parameters are b = 152 mm (6 in.), h = 152 mm (6 in.), and L = 457 mm (18 in.). The apparent residual flexural stress, f, is calculated using the elastic section modulus at deflections corresponding to L/600 (0.75 mm [0.03 in.]), L/300 (1.5 mm [0.06 in.]), and L/150 (3 mm [0.12 in.])

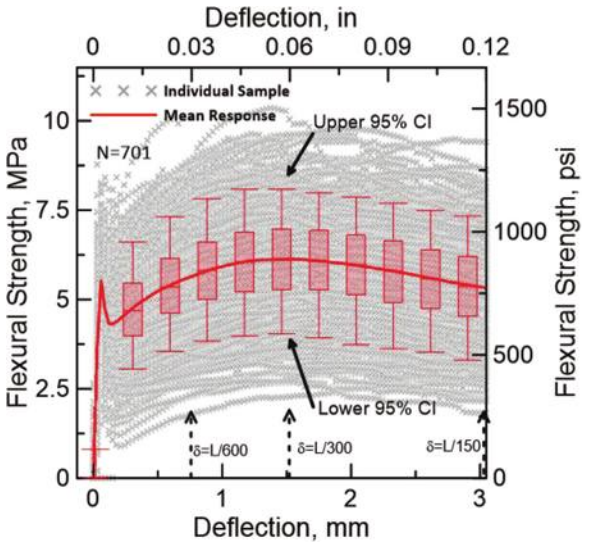

Fig. 3—Scatter plot of all data with mean curve and box and whisker plot of flexural response of individual data for 28-day specimens.

$$f = \frac{PL}{bh^2} \quad (1)$$

The individual load-deflection response of specimens up to a 3 mm (0.12 in.) deflection level was used for the evaluation of the descriptive statistics. Figure 3 shows the mean value of apparent flexural stress and its box and whisker plot through the range of deflections. Only the 28-day results are presented in Fig. 3. Individual 28-day test results that failed to meet the deflection level of L/150 were eliminated from pooled data, resulting in a total of 701 data sets. The whiskers extend a distance of 95% two-sided confidence interval (CI) from the ends of the box, while the box encloses the interquartile range with a lower line at the first quartile (Q1) and an upper line at the third quartile (Q3). The line drawn through the box in the middle is the 50th percentile. The variation of residual strength observed on the box and whisker plot at different deflection levels was not significant throughout the entire testing range. The data beyond the whiskers were flagged as outliers. Table 2 presents with N = 701 the descriptive statistics, including mean, standard

Table 2—Descriptive statistics of flexural strength parameters and deflections

Parameter / Descriptive statistic	First crack strength, f_1, MPa (psi)	Deflection at f_1, δ_1, mm (in. × 10^{-3})	Peak strength f_P, MPa (psi)	Deflection at f_P, δ_P, mm (in. × 10^{-3})	f^D_{600}, MPa (psi)	f^D_{300}, MPa (psi)	f^D_{150}, MPa (psi)	$f^D_{e,150}$, MPa (psi)
Mean	6.36 (923)	0.068 (2.67)	6.79 (985)	0.78 (30.65)	5.65 (819)	6.1 (886)	5.32 (772)	5.60 (813)
SD	0.88 (128)	0.025 (0.99)	1.00 (146)	0.85 (33.34)	1.19 (173)	1.22 (177)	1.23 (179)	1.10 (159)
Minimum	3.33 (483)	0.12 (0.48)	3.31 (480)	0.012 (0.48)	1.78 (259)	2.29 (332)	1.82 (264)	2.10 (306)
Maximum	9.51 (1379)	2.89 (11.38)	10.32 (1497)	3.28 (129)	8.96 (1300)	9.90 (1436)	9.40 (1364)	9.00 (1306)
95% lower CI	4.87 (707)	0.031 (1.24)	5.17 (750)	0.049 (1.93)	3.73 (541)	3.98 (577)	3.23 (469)	3.70 (536)
95% upper CI	7.72 (1119)	0.095 (3.74)	8.52 (1235)	2.25 (88.56)	7.66 (1111)	8.07 (1171)	7.27 (1055)	7.33 (1064)

deviation (SD), minimum, maximum, and 95% two-sided CI for major flexural parameters. These parameters include the flexural strength at the first crack (f_1); the peak stress (f_P); residual flexural strengths at $L/600$ (f^D_{600}), $L/300$ (f^D_{300}), $L/150$ (f^D_{150}); the equivalent flexural strength ($f^D_{e,150}$); and deflections at first crack and peak strength (δ_1 and δ_P). The equivalent flexural strength ($f^D_{e,150}$) of ASTM C1609 is the average stress value obtained from the absorbed energy of the beam—that is, the area under the load-deflection curve from deflection 0 to $L/150$ (3 mm [0.12 in.]).

The mean flexural strength at the first crack (f_1) was 6.36 MPa (923 psi) with 95% two-sided CI values of 4.87 and 7.72 MPa (707 and 1119 psi), respectively. While many of the specimens demonstrated deflection softening, the deflection-hardening response was more noticeable with the mean peak strength (f_P) of 6.79 MPa (985 psi) and its 95% two-sided CI values of 5.17 and 8.52 MPa (750 and 1235 psi). The mean value of first-crack deflection (δ_1) was 0.068 mm (2.67 × 10^{-3} in.) with 95% two-sided CI values determined as 0.031 mm (1.24 × 10^{-3} in.) and 0.095 mm (3.74 × 10^{-3} in.). Because of the deflection-hardening effect, mean peak-strength deflections (δ_P) were higher at 0.78 mm (30.65 × 10^{-3} in.) as well as the 95% two-sided CI values at 0.049 mm (1.93 × 10^{-3} in.) and 2.25 mm (88.56 × 10^{-3} in.). Among residual strength parameters, f^D_{300} had the highest mean value of 6.10 MPa (886 psi), followed by f^D_{600} and f^D_{150} of 5.65 (819 psi) and 5.32 MPa (772 psi). This is also evident from the shape of the stress-deflection curve with a vertex around the middle of the curve near $L/300$ (1.5 mm [0.06 in.]) deflection range.

The SD and coefficient of variation (COV) of residual strengths f^D_{600}, f^D_{300}, and f^D_{150} range from 1.19 to 1.23 MPa (173 to 179 psi), 20 to 23%, respectively, and are almost identical. All of minimum, maximum, and two-sided 95% CI values for these residual strength parameters are within 2 to 13% of each other, except for the minimum value of f^D_{300}, which is 28% higher than the minimum value of f^D_{600}. The similarity of residual flexural strength parameters indicates that no significant differences among the parameters are observed. The mean value of ASTM C1609's equivalent flexural strength ($f^D_{e,150}$) was calculated based on the total toughness (area under the load-deflection curve) and compared with the three residual parameters. Results indicate that f^D_{600} is the most representative residual strength parameter of the post-crack region, especially with less than a 1% difference from the mean value of $f^D_{e,150}$. In addition, the box and whisker plot in Fig. 3 presents similar variations through the range of deflections, with some results identified as outliers. Using a 95% lower confidence bound for f_1, f^D_{600}, and f^D_{300}, 28-day strength values of the FRC mixture were 4.87, 3.73, and 3.98 MPa (707, 541, and 577 psi). All these values validate and exceed the design parameters. To classify this FRC mixture according to *fib* Model Code (MC) 2010,[23] characteristic residual strengths were determined at crack mouth opening dimensions (CMOD) of 0.5 mm (0.02 in.) (f_{R1k}) and 2.5 mm (0.1 in.) (f_{R3k}). Because the CMOD was not directly measured, the deflection-CMOD relationship proposed by Conforti et al.[24] was used, which resulted in f_{R1k} as the characteristic stress f at a deflection of 0.38 mm (0.015 in.) and f_{R3k} as the characteristic stress f at a deflection of 1.72 mm (0.068 in.). Because *fib* MC 2010[23] requires the characteristic parameters (and not the mean) corresponding to a probability of 5% failure, the 95% lower confidence bound curve was used for determination. f_{R1k} and f_{R3k} were obtained as 3.05 and 3.88 MPa (435 and 563 psi), respectively. f_{R1k} represents a strength interval of 3 MPa (435 psi) and f_{R3k}/f_{R1k} =1.29 represents the letter *d*, which refers to a strength ratio class of $1.1 \le f_{R3k}/f_{R1k} \le 1.3$. Therefore, the FRC mixture according to *fib* MC 2010 is classified as 3*d*.

Table 3—*p*-value and AD values of different probability distribution functions

	Normal		Weibull		Lognormal	
	AD	*p*-value	AD	*p*-value	AD	*p*-value
f_1	0.529	0.176	2.346	<0.010	3.372	<0.005
f^D_{600}	0.487	0.223	2.584	<0.010	3.149	<0.005
f^D_{300}	0.441	0.289	1.137	<0.010	5.033	<0.005
f^D_{150}	0.333	0.509	0.540	0.186	5.209	<0.005

Flexural strength distribution of 28-day specimens

Three distributions—including the normal, Weibull, and lognormal—were tested to determine their applicability to adequately describe the ASTM C1609 first crack and residual strengths results. The *p*-values of the strength distributions were used to determine the appropriateness of the distribution. Results are reported in Table 3 for the 95% confidence interval as the level of hypothesis acceptance. If the *p*-value was lower than or equal to 0.05, the given distribution function was rejected from the null hypothesis, indicating that it was not suitable for describing the data. Table 3 shows that the normal distribution is acceptable for the flexural strength

distribution of the first crack, f^D_{600}, f^D_{300}, and f^D_{150}. This observation shows a good correlation with another study by Dean et al.[25] The highest *p*-value of a normal distribution was in flexural strength at *L*/150, accounting for 0.509, and the lowest was 0.176 in first crack strength. The Weibull distribution is only applicable for residual strength at *L*/150 (f^D_{150}), while the lognormal distribution function was rejected for all groups. The smallest value of Anderson-Darling (AD) test also compared the fit of several distributions to determine the suitability. The AD value of normal distribution in Table 3 is significantly lower than the lognormal and Weibull distributions. This confirmed that a normal distribution is the best fit for ASTM C1609 experimental data, with the normal distribution function addressing f_1 and residual flexural strength f^D_{150} with a normal probability function shown in Fig. 4. The narrow bell-shaped curve of f_1 in this figure confirmed the lower SD compared to f^D_{150}, as previously presented in Table 2.

STATISTICAL PROCESS CONTROL

A methodology to evaluate FRC quality is by using SPC. This procedure for QC is beneficial for producers, contractors, owners, and construction management. The ASTM C1609 test is known to have a high variation in the data, as measured by the COV, which can range from 2 to 25%.[15,24,26] The residual strength variability is attributed to the concrete mixture formulation and type, size, strength, dosage, and geometry of the fiber. In particular batches, the rheology affects the fiber orientation, placement direction, compaction procedures, self-compaction, vibrating-compaction, and the formwork wall-side effect.[15] Regardless of how carefully maintained and well-designed a mixture is, a natural level of variability always exists. Nevertheless, such natural variability is considered small and should not shift the mean values of FRC strength or result in out-of-control events. In the context of design, the natural variability in residual strength can be addressed by limiting the design criteria at a certain CI level when population characteristics were assumed unchanged. Variability due to temperature and climatic conditions affecting the curing and conditioning of the test specimens, mixing, batching, and placing machinery, or operator errors are considered as assignable causes of variation that may shift the mean and SD of the process. These production uncertainties must be evaluated and eliminated to confirm that FRC product properties are applicable for the design framework. SPC is a tool for early detection of spurious shifts and provides the necessary detection and warning for out-of-control FRC manufacturing. Cumulative sum (CUSUM) and exponentially weighted moving average (EWMA) are two well-known SPC methods to capture the production variability. These methods are fundamentally similar in monitoring the variations of the time-based data. The difference is that the CUSUM approach uses a constant weight factor for all the data, while the EWMA applies an exponential weight factor, giving recent observations more weight than the older data set. Laungrungrong et al.[27] suggested that by combining the control charts such as the CUSUM and EWMA with the run chart, small shifts (1.5 SD or less) in the concrete production line can be monitored,

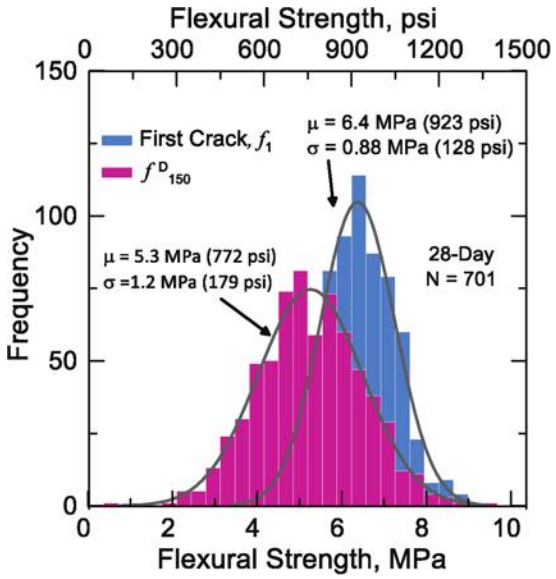

Fig. 4—Probability distribution plot and normal probability distribution function of first crack strength f_1 *and residual flexural strength* f^D_{150}.

thus allowing concrete producers and precast plant manufacturers to identify the problems beforehand.

The production variability investigated in this section is applicable only for the specimens at 28 days, and the ultimate deflection has to meet *L*/150 (3 mm [0.12 in.]). Therefore, the total number of individual ASTM C1609 tests is 701 out of 843 samples that were studied in this section. This SPC procedure was applied to the first crack strength, f_1, the ultimate strength, f_P, and the residual strengths f^D_{600}, f^D_{300}, and f^D_{150}. The interpolation of run charts and control charts is described to provide insight into distinguishing between QC and SPC and comparing signals in CUSUM and EWMA methods.

Run chart

A run chart illustrates the progression of the data throughout the time of observation. Horizontal lines represent the minimum required strengths of 4 MPa (580 psi) for f_1 and f^D_{600} and 3.7 MPa (540 psi) for f^D_{300} and f^D_{150}. These lines were added to the run chart, as shown in Fig. 5, to identify the unacceptable level of flexural strength values falling below the criteria. It is observed that more f^D_{600} data fail to meet the strength criteria than the first crack (f_1) and peak strength (f_P) (refer to Fig. 5(a)). The number of unqualified observations corresponding to f^D_{150} is considerably higher than f^D_{600} due to the residual strength decreasing at large deflections, which is more conducive to the peak-strength level (refer to Fig. 5(b)). Although the run chart detects the specimens that fail to meet the quality requirement, it cannot mathematically determine the stability and variability in the process compared to the neighbor observations such as CUSUM and EWMA.

Control charts

CUSUM—CUSUM control measure detects the cumulative sum of deviations of individual observations from the target value. If the target value and SD are unknown, the

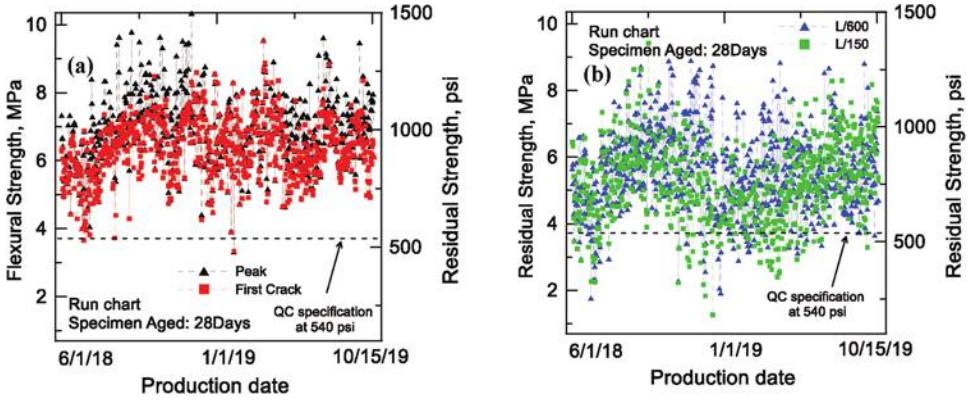

Fig. 5—Run chart of strength results over 18-month production period: (left) peak strength and first crack strength; and (right) residual flexural strength at L/*150 (f^D_{150}) and* L/*600 (f^D_{600}).*

sample population's properties can be used. The general form of the CUSUM is given by

$$\begin{aligned} C_i^+ &= \max[0, x_i - (\mu_0 + K) + C_{i-1}^+] \\ C_i^- &= \max[0, (\mu_0 + K) - x_i + C_{i-1}^-] \end{aligned} \quad (2)$$

where C_i presents the CUSUM of the deviation from target values (μ_0) over the domain. A one-sided upper and lower CUSUM (above and below μ_0, respectively) are designated as C^+ and C^-. The constant $K = k\sigma$ is the reference value expressed as the SD unit adjusted by k, representing the expected sensitivity of detecting out-of-control signals in the process. The upper and lower control limits (UCL and LCL, respectively) are the horizontal lines plotted in CUSUM, defined by the decision interval term called $H = h\sigma$. In other words, the out-of-control signal is determined when C^+ exceeds UCL or C^- is below LCL. Using $k = 0.5$ and $h = 4$ provides good average run length (ARL) properties, as recommended by Montgomery.[28] Details on the evaluation of suitable values of k and h are extensively explained in earlier publications.[27,28]

The CUSUM method with resetting C^+ and C^- was used. In this study, the mean flexural strength for each scheme was assigned as the target value μ_0. The design specified strengths of 3.7 and 4 MPa (540 and 580 psi) as target values are unreasonable because the concrete was designed with a safety factor to be superior to the required residual strength. Therefore, most of the data exceeded the specified value. Use of the design-specified strength as the target value results in many out-of-control results overestimating the target value, or a large C^+ value compared to the mean value.

A key feature of the process is to reset the CUSUM every time the out-of-control signal is triggered. This is because a misleading signal may occur when the previous CUSUM was not reset to zero (that is, $C_{i-1}^- = 0$, $C_{i-1}^+ = 0$) after an out-of-control signal detection in an earlier observation. The comparison between the CUSUM chart with and without resetting the signal for the peak strength (f_p) is in Fig. 6. When $i = 7$, C^- was below UCL, and C^- at $i = 8$ was calculated without reset $C_{i-1}^- = 0$, the CUSUM in observations between 8 and 20 determined biased results below LCL. In comparison, the signal with zero resets can indicate the stability in the process independently from the process data before an earlier outbreak signal. More discussion on using a CUSUM chart in production can be consulted in ACI 214R-11,[29] which provides examples of applying the CUSUM chart and discusses some of the difficulties with the CUSUM analysis.

EWMA—The EWMA control chart is another approach to monitoring small shifts in the data. By using an exponential weight function, EWMA gives a higher priority to a signal based on the nearby (newer) observations rather than farther neighbors (older). A typical equation is given by

$$z_i = \lambda \sum_{j=0}^{i-1} (1-\lambda)^j x_{i-j} + (1-\lambda)^i z_0 \quad (3)$$

where $\lambda \sum_{j=0}^{i-1} (1-\lambda)^j x_{i-j}$ is the weight assigned to the neighbor observations; and the second term represents the most recent sample. The weight factor for each observation is illustrated in Fig. 7 with the value of λ used to weigh an average from neighbor observations. When $\lambda = 0.3$, a higher contribution is assigned to the closer (newer) observations, while farther (older) observations have less contribution compared to $\lambda = 0.1$ and 0.2. The smaller shift corresponds to the smaller λ assigned. UCL and LCL of the EWMA chart are identified in Eq. (4). In this study, L was defined as 3 and $\lambda = 0.3$. The appropriate values of the λ and L parameters for the control chart can be determined by ARL, which is explained in past studies.[27,28] The process detects an out-of-control signal when the EWMA exceeds the UCL and LCL.

$$\begin{aligned} &\text{UCL} = \mu_0 + L\sigma\beta \text{ and LCL} = \mu_0 - L\sigma\beta; \\ &\text{where } \beta = \sqrt{\frac{\lambda}{2-\lambda}\left[1-(1-\lambda)^{2i}\right]} \end{aligned} \quad (4)$$

Interpolation of control charts—A preliminary analysis presented earlier in this paper confirmed that flexural strength at the first crack (f_1) and residual flexural strengths of f^D_{600}, f^D_{300}, and f^D_{150} all follow a normal distribution trend. An analytical investigation was conducted based on hybrid CUSUM and EWMA control chart methodology. For CUSUM, the constant values were taken as $h = 4$ and $k = 0.5$. The CUSUM method with resetting C^+ or C^- was adopted. The EWMA control chart was applied with the constant

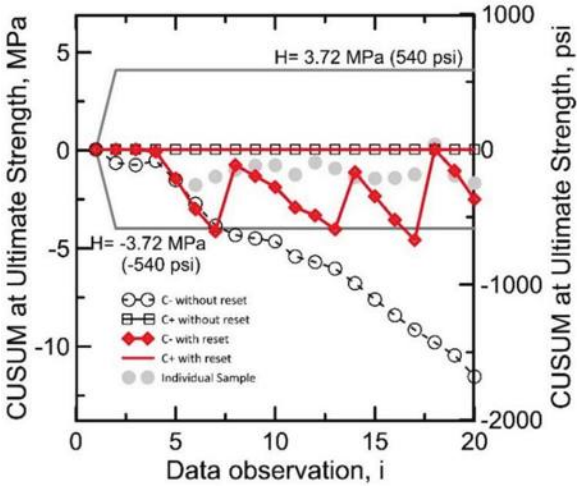

Fig. 6—CUSUM with and without reset when signal exceeds limit for peak strength, f_p.

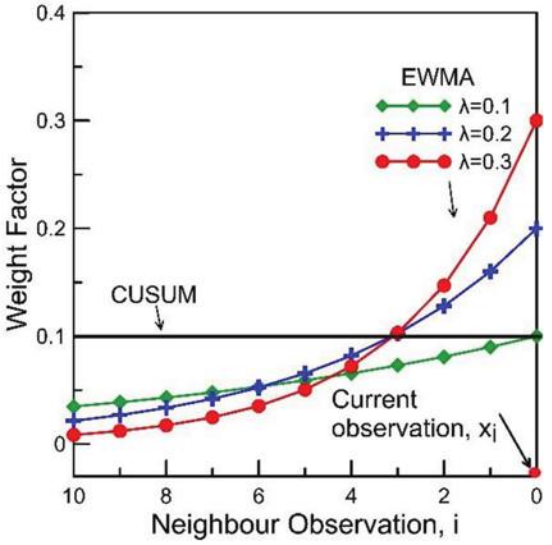

Fig. 7—Comparison of weight factor of CUSUM and EWMA.

value of $L = 3$ and $\lambda = 0.3$. The mean value of flexural strength for each scheme was assigned as the target value μ_0.

The control charts are investigated in Fig. 8 to 12 by adopting the constant parameters described earlier for flexural strength at various stages. Several aspects of the control chart in addressing the variations in the process become apparent by evaluating it in conjunction with the run chart in the form of CUSUM or EWMA. The constant (horizontal) lines represent the minimum specified strength of 3.7 MPa (540 psi) for f_1 and f^D_{600}, and 4 MPa (580 psi) for f_p, f^D_{300}, and f^D_{150}. Out-of-control signals were detected in the first crack strength, f_1, from observations 1 to 150 on CUSUM and EWMA control charts, but no individual f_1 data failed to meet the required strength of 3.7 MPa (540 psi). EWMA charts do not present any out-of-control signal for other strength parameters in this observation range. CUSUM charts, except for one or two sporadic out-of-control signals for f_p and f^D_{600}, show similar results. Also, except for one single unqualified f^D_{150} test result, all other data meet specified strength in this observation range. In this case, the manufacturing process is unstable, but the concrete batch is acceptable as there is no need to be rejected. However, an investigation may be required to address the assignable causes of instability in the production process.

For observations 450 to 550, parameters f_1 and f_p indicate the out-of-control signals. While no single f_1 and f_p datum in this observation range fell under the specified strength level, f^D_{600}, f^D_{300}, and f^D_{150} reveal several unqualified strengths data. The largest number of unqualified strength specimens was found for parameter f^D_{150}. This can be explained by the fact that the flexural strength of SFRC in a conventional fiber dosage gradually decreases after f_p, and f^D_{150} is typically lower than f^D_{300} and f^D_{600}. This attributes those batches to an incapable process at an unacceptable level of strength. Similarly, observations 300 to 450 indicate out-of-control signals concerning the LCL on EWMA charts for f^D_{600}, f^D_{300}, and f^D_{150}. Also, the largest number of unqualified f^D_{600}, f^D_{300}, and f^D_{150} parameters can be seen in this observation range. The manufacturing process during such periods should be further investigated for the assigned causes and corrected to be back into control before the continuous production operation may proceed. Considering out-of-control signals in observations 450 to 550 were detected for f_1 and in the observation range of 300 to 450 were detected for residual strength parameters (f^D_{600}, f^D_{300}, and f^D_{150}), it can be speculated that the assignable causes for the former range can be related to concrete and for the latter to the fiber reinforcement.

The control chart cannot be independently used as a measure of quality. Observations in the range of 200 to 300 in the EWMA control chart did not present an out-of-control signal in f_1 and f_p (refer to Fig. 8 and 10). However, several unqualified samples in residual strength fell below the required strength. This scenario shows that the manufacturing process is stable, but the samples are unqualified and need to be rejected. However, a small range of out-of-control signals was still detected within an observation range of 200 to 300 in the CUSUM chart (refer to Fig. 8 to 12), while EWMA did not support such a decision. A similar investigation found that other CUSUM charts are more sensitive to indicating the out-of-control signal compared to EWMA. This can be due to the parameters employed in the applicable formulas. It is noted that the control chart also results in a false alarm. The ARL is technically adopted to evaluate the performance of constant parameters used in the control chart. This topic is beyond the purpose of the present study and the details of ARL can be found elsewhere.[28]

MINIMUM SAMPLING REQUIREMENTS FOR ASTM C1609 TESTING

The method of random sampling can be used to estimate the minimum required sample size with an acceptable design variability. The distribution of fibers is a random process and primarily a function of orientation and the number of fibers at the cracked section. This leads to varying post-crack strength and causes a high COV. These characteristic values of FRC may require testing of a higher number of samples to gain a reliable distribution of flexural strength parameters representing the population data set.

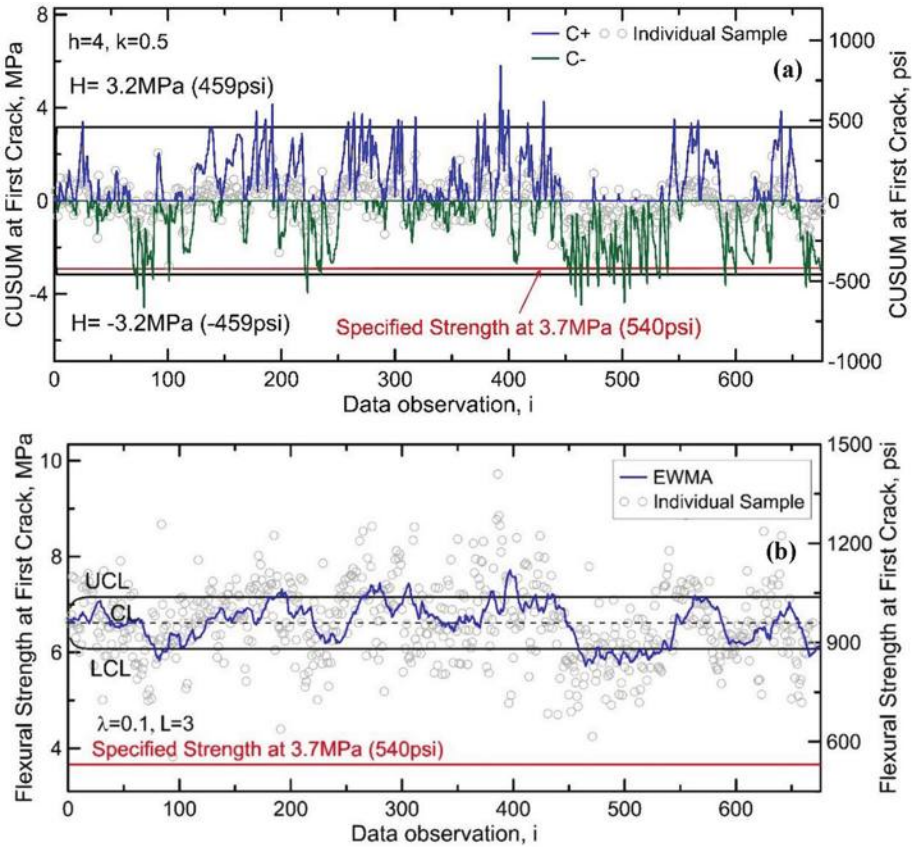

Fig. 8—Control charts of first crack strength (f_1) at 28 days collected from June 2018 to October 2019: (top) CUSUM; and (bottom) EWMA.

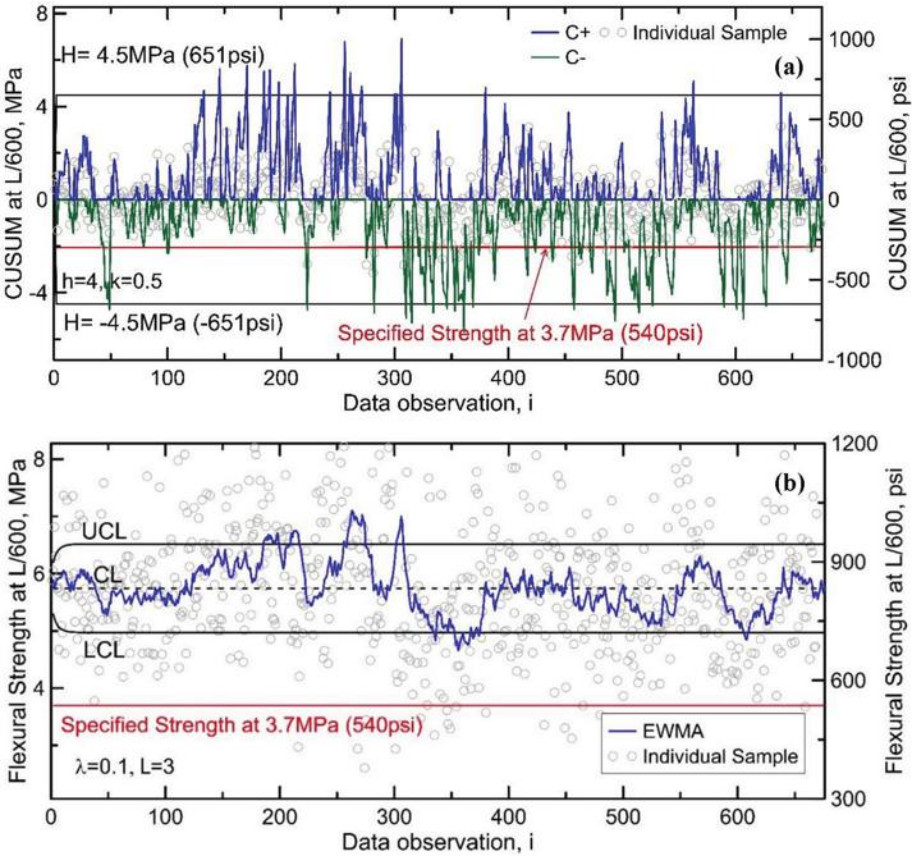

Fig. 9—Control charts of residual strength at L*/600 (f^D_{600}) at 28 days collected from June 2018 to October 2019: (top) CUSUM; and (bottom) EWMA.*

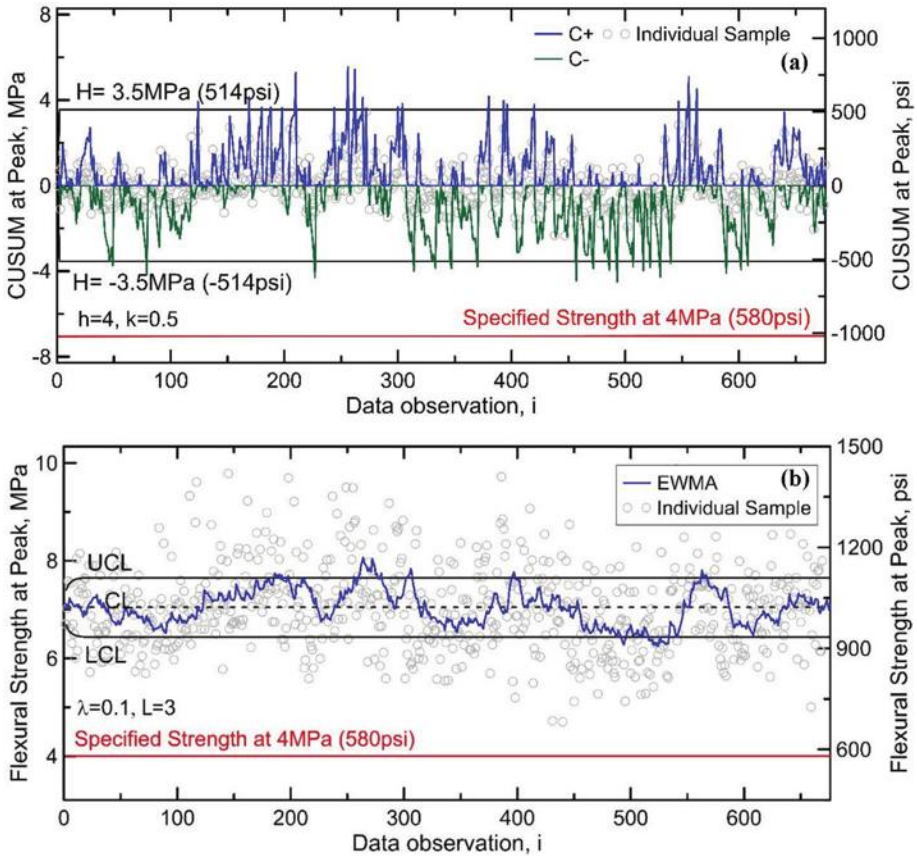

Fig. 10—Control charts of residual strength at peak strength (f_p) at 28 days collected from June 2018 to October 2019: (top) CUSUM; and (bottom) EWMA.

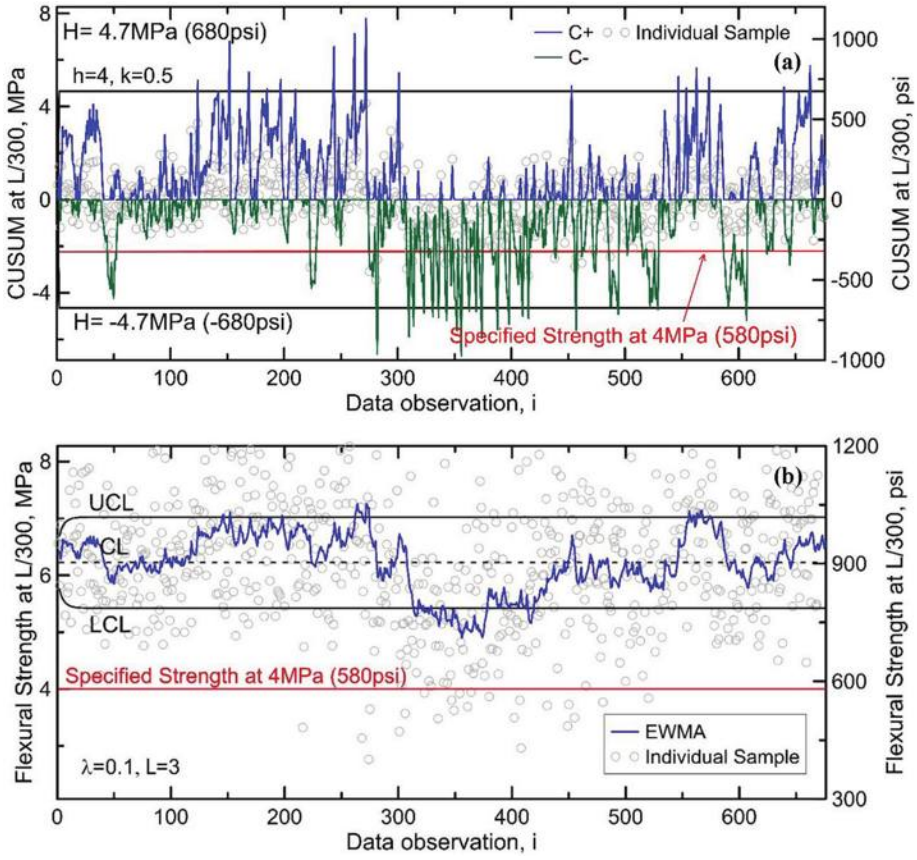

Fig. 11—Control charts of residual strength at L/300 (f^D_{300}) *at 28 days collected from June 2018 to October 2019: (top) CUSUM; and (bottom) EWMA.*

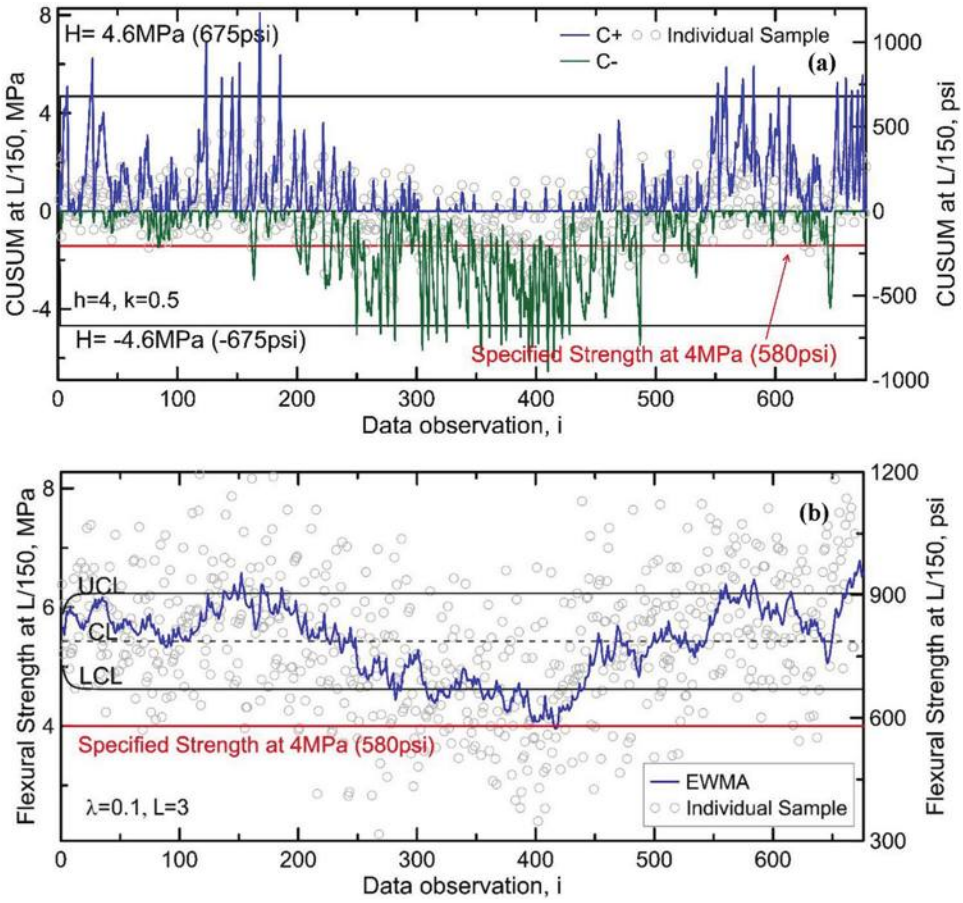

Fig. 12—Control charts of residual strength at L*/150 (*f^D_{150}*) at 28 days collected from June 2018 to October 2019: (top) CUSUM; and (bottom) EWMA.*

Among the entire data, a method by random resampling of the data with replacement, known as the Bootstrap Method, was adopted for simulation and assigning accuracy measures of the statistical estimates. This method evaluates the standard error in any statistical measure such as the mean, median, and SD by randomly sampling from a pool of sample data that are a part of the same population.[30] This method ensures that the variability measure is independent of the date or process of manufacturing and can have wider implications in terms of expected error in a sample size considering limited testing capabilities. The Bootstrap approach could also be used to measure errors in other statistical estimates for which analytical equations are not available.

A test data recorded for $N = 701$ beams at the production of every batch was selected as the population data set. The beam data excludes the 116 beam samples that did not reach $L/150$ deflection point from the total 817 beams. The flexural strength at first cracking, f_1, and the residual strengths f^D_{600}, f^D_{300}, and f^D_{150} were selected as primary parameters of interest. The process requires the selection of "n" random samples from the population data, referred to the Bootstrap sample set and denoted by a vector $X_m = (x_1, x_2, \ldots, x_n)$, where n is the sample size and m denotes the trial set. The sampling of each data point is done independently with replacement from the population data pool, meaning every one of n values has an equal probability of $1/N$. The sample mean $\bar{x}$ and sample SD s of each Bootstrap sample set are recorded at every trial. This process can be conducted for any number of trials, and in this case, was repeated for $m = 50$ trial sets. The process was then repeated with higher and higher sample sizes, with n ranging from 3 to 500.

Figure 13 presents the 95% two-sided CIs of the Bootstrap samples of size n with the bond lines and the mean of the sample means ($\bar{x}$) of all $m = 50$ trials with solid lines, as well as the tracks line of population mean. The CI can be interpreted as, 95% of the time, the variation in the sample means will fall under the shaded area. As the number of samples n in the Bootstrap sample increases, the variability in the sample means decreases as expected. It was observed that moving from a sample size of three to five, the 95% CI reduces by 20 to 28%, and a further reduction of approximately 20 to 40% is observed when moving from sample size five to 10. It is also observed that the 95% two-sided CI reaches stability near the Bootstrap sample size of $n = 100$. Compared to the first-crack strength (f_1) and other residual strength parameters in Fig. 13(b), f^D_{150} shows a wider scatter of 95% CI when a sample size of 10 or less is selected, showing lower reliability on measured strength parameters when a small sample size is available. This study provides an insight into the accuracy of the sample mean as the size varies and shows that given the type of distribution, a smaller sample can represent the mean as accurately as the entire population, considering that the measured average

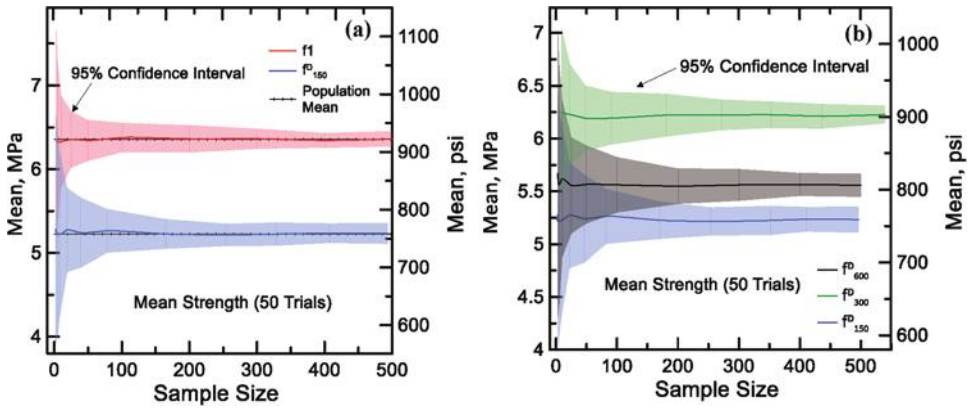

Fig. 13—Interval plots of sample size versus mean using random sampling and Bootstrap analysis of ASTM C1609 strength parameters: (left) 95% CIs for first crack strength and residual strength at L*/150 deflection; and (right) 95% CIs for various residual strength parameters.*

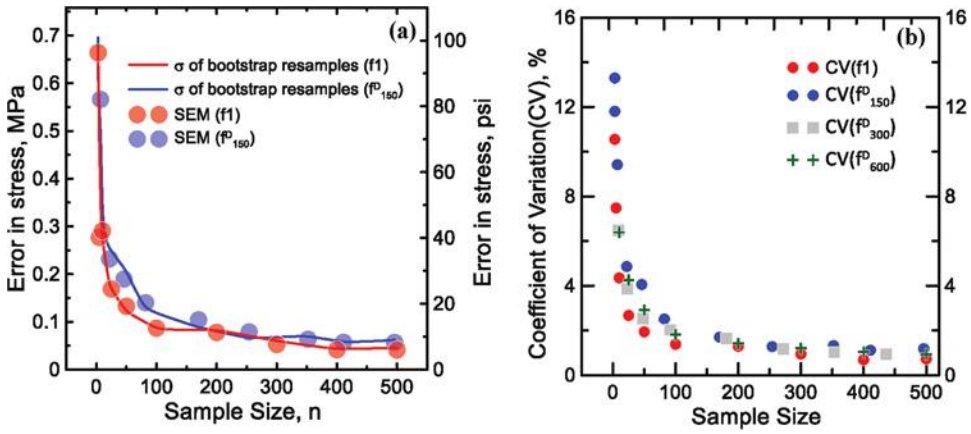

Fig. 14—(left) Comparison of SD from Bootstrap analysis versus analytical SEM; and (right) comparing coefficient of variation in bootstrap samples.

value should be factored for expected error, also referred to as "standard error". The study also provides estimates of the number of samples required for higher accuracy in test data with the associated errors.

A simpler and traditional analytical method is referred to as standard error of mean (SEM) as the statistical estimate of accuracy, and defined as $s/\sqrt{n}$, with s as the sample SD of sample size and n as the number of samples. Figure 14(a) compares the traditional approach with the simulated resampling approach of bootstrapping. Both approaches show similar accuracies in mean strength deviations and estimating errors as a function of sample size.

The COV, defined as COV = σ/μ, is another statistical parameter used with the bootstrapping method. The COV for all residual strength parameters is plotted in Fig. 14(b). The COV in parameter f^D_{150} is 13.2% for a sample size of $n = 3$, and 11.8% for a sample size of $n = 5$. Around $n = 25$ samples are required for COV to become 5% or lower, and as the sample size increases above 100, the COV reduces significantly to 2.5%, and remains stable below 1.5% for sample sizes greater than 200. Appropriate variability factors can be derived from the COV for specific sample size and strength parameters. The other strength parameters (f^D_{600} and f^D_{300}) indicated a similar tendency of COV, as illustrated in Fig. 14(b).

The COV and confidence interval charts can be used to select the minimum required sample size to characterize the entire population of FRC or to evaluate QC parameters for different suppliers. It can be used to determine the required number of standard ASTM C1609 or EN 14651 tests to meet the design properties of FRC. Note that the measured variation of strength is specific for a single fiber type as well as dosage in this study, and the measured errors with respect to sample size may change with different fiber types and their properties. The presented study, however, can be easily extended to other groups of fibers, and similar conclusions are expected to be drawn.

CONCLUSIONS

Residual flexural strength is primarily a design parameter that controls the serviceability and strength of structural fiber-reinforced concrete (FRC) elements such as precast tunnel segments. High variability in the manufacturing process is inevitable in FRC structures, especially in full-scale specimens; therefore, suitable safety for the manufacturing process needs to be implemented. The descriptive statistics were calculated, and the highlighted information was drawn here. The Anderson-Darling (AD) approach fit of the distribution indicated that the data is best described by a normal distribution as compared to lognormal and Weibull

distribution. The scatter range of 28-day specimens ranged from a minimum load of 14 kN (3108 lb) to a maximum load of 77 kN (17,232 lb). The disparity between the first crack strength and the peak strength is due to the presence of both deflection softening and deflection hardening. The deflection hardening was recorded with the mean peak strength f_P noted at 6.8 MPa (985 psi) with 95% two-sided confidence intervals (Cls) being 5.2 and 8.5 MPa (750 and 1235 psi). The mean flexural strength at first crack f_1 was 6.36 MPa (923 psi) with 95% two-sided CI values of 4.87 and 7.72 MPa (707 and 1119 psi). The similar results of residual flexural strength parameters indicate that when using basic statistics on the tested mixtures, no significant differences among the parameters are observed. Comparison of ASTM C1609's average equivalent flexural strength ($f^D_{e,150}$), calculated based on total toughness (area under load-deflection curve) with three major residual parameters at various deflection stages, indicates that f^D_{600} is the most representative residual strength parameter of the post-crack region, especially with less than a 1% difference from the mean value of $f^D_{e,150}$. The 95% lower confidence bound for all of the 28-day residual strength values f^D_{600}, f^D_{300}, and f^D_{150} of the FRC mixtures were 4.87, 3.73, and 3.98 MPa (707, 541, and 577 psi). Because these values are larger than the design parameters, they validate the selection of FRC mixture.

The statistical process control (SPC) procedures used a combination of the run chart, exponentially weighted moving average (EWMA), and cumulative sum (CUSUM) control charts to identify spurious shifts (or out-of-control signal) in the mean values of flexural strengths. Results show that the tendency in the residual strength parameters is to decrease at large deflections; hence, the number of unqualified observations corresponding to the end deflection stage is considerably higher than the strength reported at early stages of post-crack response, which are more conducive to the peak strength levels. Periods with incapable manufacturing processes at an unacceptable level of strength were identified for further examination to move the process back into control before the continuous production operation may proceed.

The Bootstrap Method applied to the data determined the minimum required number of samples to test for a specific level of variance to match the population variance. The coefficient of variation (COV) and CI charts were introduced and show that a sample set of 25 specimens could provide a reasonable level of estimation for flexural strength parameters with COV = 5% or less. The 95% two-sided CI was observed to reach stability after selecting a sample close to 100. This indicates that the frequency of the quality control (QC) data collection can be reduced significantly without a significant impact on the overall analysis of the results.

AUTHOR BIOS

Chidchanok Pleesudjai *was a Graduate Research Assistant at the School of Sustainable Engineering and the Built Environment, Arizona State University (ASU), Tempe, AZ. She received her BEng in civil engineering from Chulalongkorn University, Bangkok, Thailand, in 2015 and her MS in structural and materials engineering from ASU in 2021. Her research interests include analytical solutions for serviceability-based flexural design of fiber-reinforced concrete.*

Devansh Patel *is a Graduate Research Assistant at the School of Sustainable Engineering and the Built Environment at ASU. He received his BS in civil engineering from University of Pune, Pune, India, in 2017 and his MS in structural and materials engineering from ASU in 2020. His research interests include fiber-reinforced cement composites and their application in tunnel linings.*

Kenneth A. Williams Gaona *was a Graduate Research Assistant at the School of Sustainable Engineering and the Built Environment at ASU. He received his BS in civil engineering from Santa María La Antigua Catholic University, Panama City, Panama, in 2017 and his MS in structural and materials engineering from ASU in 2020. His research interests include fiber-reinforced cement composites and their application in tunnel linings.*

ACI member **Mehdi Bakhshi** *is a Lead Tunnel Engineer at AECOM. He received his BS and MS in civil and structural engineering from the University of Tehran, Tehran, Iran, and his PhD in civil, environmental and sustainable engineering from ASU. He is a member of ACI Committees 305, Hot Weather Concreting; 350, Environmental Engineering Concrete Structures; 506, Shotcreting; 533, Precast Panels; and 544, Fiber Reinforced Concrete. His research interests include structural design and tunnel engineering.*

ACI member **Verya Nasri** *is Chief Tunnel Engineer at AECOM. He received his BS and MS in structural engineering from Sharif University of Technology, Tehran, Iran, and his PhD in geotechnical engineering from École Centrale Paris, Châtenay-Malabry, France. His research interests include geotechnical, structural, and tunnel engineering, including design and construction support for major tunneling projects.*

Barzin Mobasher, *FACI, is a Professor of structural materials at ASU. His publications include two books on fiber- and textile-reinforced concrete, four edited books, and more than 200 research papers. He is a past Chair and member of ACI Committee 544, Fiber Reinforced Concrete, and is a member of the ACI Technical Activities Committee; ACI Committee 549, Thin Reinforced Cementitious Products and Ferrocement; ACI Subcommittee 239-C, Structural Design on UHPC; and Joint ACI-ASCE Committee 446, Fracture Mechanics of Concrete.*

REFERENCES

1. ACI Committee 544, "Report on Design and Construction of Fiber-Reinforced Precast Concrete Tunnel Segments (ACI 544.7R-16)," American Concrete Institute, Farmington Hills, MI, 2016, 36 pp.

2. Plizzari, G. A., and Tiberti, G., "Steel Fibers as Reinforcement for Precast Tunnel Segments," *Tunnelling and Underground Space Technology*, V. 21, No. 3-4, 2006, pp. 438-439. doi: 10.1016/j.tust.2005.12.079

3. Yao, Y.; Bakhshi, M.; Nasri, V.; and Mobasher, B., "Interaction Diagrams for Design of Hybrid Fiber-Reinforced Tunnel Segments," *Materials and Structures*, V. 51, No. 1, 2018, p. 35. doi: 10.1617/s11527-018-1159-2

4. Meda, A.; Rinaldi, Z.; Spagnuolo, S.; De Rivaz, B.; and Giamundo, N., "Hybrid Precast Tunnel Segments in Fiber Reinforced Concrete with Glass Fiber Reinforced Bars," *Tunnelling and Underground Space Technology*, V. 86, 2019, pp. 100-112. doi: 10.1016/j.tust.2019.01.016

5. ACI Committee 544, "Guide for Design with Fiber-Reinforced Concrete (ACI 544.4R-18)," American Concrete Institute, Farmington Hills, MI, 2018, 44 pp.

6. Molins, C., and Arnau, O., "Experimental and Analytical Study of the Structural Response of Segmental Tunnel Linings based on an In Situ Loading Test. Part 1: Test Configuration and Execution," *Tunnelling and Underground Space Technology*, V. 26, No. 6, 2011, pp. 764-777. doi: 10.1016/j.tust.2011.05.002

7. Bakhshi, M., and Nasri, V., "Design of Precast Concrete Segmental Lining for the Montreal Express Link (REM) Airport Tunnel," *ITA-AITES World Tunnel Congress and 46th General Assembly*, Kuala Lumpur, Malaysia, May 15-21, 2020.

8. Bakhshi, M., and Nasri, V., "Crack Width Simulation and Nonlinear Finite Element Analysis of Bursting and Spalling Stresses in Precast FRC Tunnel Segments Under TBM Thrust Jack Forces," *Fibre Reinforced Concrete: Improvements and Innovations: RILEM-fib International Symposium on FRC (BEFIB) in 2020*, P. Serna, A. Llano-Torre, J. R. Martí-Vargas, and J. Navarro-Gregori, eds., Springer, Cham, Switzerland, 2021, pp. 621-638. doi: 10.1007/978-3-030-58482-5_56

9. Cavalaro, S. H. P.; Blom, C. B. M.; Aguado, A.; and Walraven, J. C., "New Design Method for the Production Tolerances of Concrete Tunnel Segments," *Journal of Performance of Constructed Facilities*, ASCE, V. 26, No. 6, 2012, pp. 824-834. doi: 10.1061/(ASCE)CF.1943-5509.0000291

10. Buratti, N.; Ferracuti, B.; and Savoia, M., "Concrete Crack Reduction in Tunnel Linings by Steel Fibre-Reinforced Concretes," *Construction and Building Materials*, V. 44, 2013, pp. 249-259. doi: 10.1016/j.conbuildmat.2013.02.063

11. Bakhshi, M.; Barsby, C.; and Mobasher, B., "Back-Calculation of Tensile Properties of Strain Softening and Hardening Cement Composites," *High Performance Fiber Reinforced Cement Composites 6*, G. J. Parra-Montesinos, H. W. Reinhardt, and A. E. Naaman, eds., Springer, Dordrecht, the Netherlands, 2012, pp. 83-90. doi: 10.1007/978-94-007-2436-5_11

12. Mobasher, B., *Mechanics of Fiber and Textile Reinforced Cement Composites*, first edition, CRC Press, Boca Raton, FL, 2011.

13. Nguyen, D.-L.; Thai, D.; Ngo, T.; Tran, T.; and Nguyen, T., "Weibull Modulus from Size Effect of High-Performance Fiber-Reinforced Concrete under Compression and Flexure," *Construction and Building Materials*, V. 226, Nov, 2019, pp. 743-758. doi: 10.1016/j.conbuildmat.2019.07.234

14. Yoo, D.; Banthia, N.; Yang, J.; and Yoon, Y., "Size Effect in Normal- and High-Strength Amorphous Metallic and Steel Fiber Reinforced Concrete Beams," *Construction and Building Materials*, V. 121, Sept. 2016, pp. 676-685. doi: 10.1016/j.conbuildmat.2016.06.040

15. Tiberti, G.; Germano, F.; Mudadu, A.; and Plizzari, G. A., "An Overview of the Flexural Post-Cracking Behavior of Steel Fiber Reinforced Concrete," *Structural Concrete*, V. 19, No. 3, 2018, pp. 695-718. doi: 10.1002/suco.201700068

16. Conforti, A.; Tiberti, G.; Plizzari, G. A.; Caratelli, A.; and Meda, A., "Precast Tunnel Segments Reinforced by Macro-Synthetic Fibers," *Tunnelling and Underground Space Technology*, V. 63, 2017, pp. 1-11. doi: 10.1016/j.tust.2016.12.005

17. Galeote, E.; Picazo, Á.; Alberti, M. G.; de la Fuente, A.; Enfedaque, A.; Gálvez, J. C.; and Aguado, A., "Statistical Analysis of an Experimental Database on Residual Flexural Strengths of Fiber Reinforced Concretes: Performance-Based Equations," *Structural Concrete*, V. 23, No. 5, 2022, pp. 3140-3153. doi: 10.1002/suco.202100416

18. ASTM C1609/C1609M-19, "Standard Test Method for Flexural Performance of Fiber-Reinforced Concrete (Using Beam With Third-Point Loading)," ASTM International, West Conshohocken, PA, 2019.

19. ACI Committee 544, "Report on Indirect Method to Obtain Stress Strain Response of Fiber-Reinforced Concrete (FRC) (ACI 544.8R-16)," American Concrete Institute, Farmington Hills, MI, 2016, 22 pp.

20. Mobasher, B.; Yao, Y.; and Soranakom, C., "Analytical Solutions for Flexural Design of Hybrid Steel Fiber Reinforced Concrete Beams," *Engineering Structures*, V. 100, Oct, 2015, pp. 164-177. doi: 10.1016/j.engstruct.2015.06.006

21. Sullivan, J., and Perham, A., "Design and Construction of the South Hartford CSO Tunnel," *Pipelines 2018: Planning and Design - Proceedings of Sessions of the Pipelines 2018 Conference*, 2018, pp. 69–80. doi: 10.1061/9780784481646.008

22. Bakhshi, M., and Nasri, V., "Design of Steel Fiber-Reinforced Concrete Segmental Lining for the South Hartford CSO Tunnel," *Proceedings, Rapid Excavation Tunneling Conference*, San Diego, CA, 2017, pp. 706-717.

23. *fib*, "*fib* Model Code for Concrete Structures 2010," Fédération Internationale du Béton, Lausanne, Switzerland, 2013.

24. Conforti, A.; Minelli, F.; Plizzari, G. A.; and Tiberti, G., "Comparing Test Methods for the Mechanical Characterization of Fiber Reinforced Concrete," *Structural Concrete*, V. 19, No. 3, 2018, pp. 656-669. doi: 10.1002/suco.201700057

25. Dean, S. W.; Bernard, E. S.; and Xu, G. G., "Statistical Distribution of Fiber-Reinforced Concrete Beam Test Data," *Journal of ASTM International*, V. 4, No. 3, 2007, p. 100774. doi: 10.1520/JAI100774

26. Alberti, M. G.; Enfedaque, A.; Gálvez, J. C.; and Agrawal, V., "Reliability of Polyolefin Fibre Reinforced Concrete beyond Laboratory Sizes and Construction Procedures," *Composite Structures*, V. 140, Apr, 2016, pp. 506-524. doi: 10.1016/j.compstruct.2015.12.068

27. Laungrungrong, B.; Mobasher, B.; and Montgomery, D., "Development of Rational Pay Factors Based on Concrete Compressive Strength Data," Arizona Department of Transportation, Phoenix, AZ, 2008.

28. Montgomery, D. C., "Introduction to Statistical Quality Control," *The Statistician*, V. 35, No. 1, 1986, pp. 81-82. doi: 10.2307/2988304

29. ACI Committee 214, "Guide to Evaluation of Strength Test Results of Concrete (ACI 214R-11)," American Concrete Institute, Farmington Hills, MI, 2011, 16 pp.

30. Efron, B., and Tibshirani, R. J., *An Introduction to the Bootstrap*, Chapman and Hall/CRC, Boca Raton, FL, 1994.

ACI in Your Classroom

Integrate ACI into your classroom!

To support future leaders, ACI has launched several initiatives to engage students in the Institute's activities and programs – select programs that may be of interest to Educators are:

- **Free student membership –** encourage students to sign up
- **Special student discounts on *ACI 318 Building Code Requirements for Structural Concrete*, *ACI 530 Building Code Requirements and Specification for Masonry Structure*, & *Formwork for Concrete* manual.**
- **Access to *Concrete International* –** free to all ACI student members
- **Access to *ACI Structural Journal* and *ACI Materials Journal* –** free to all ACI student members
- **Free sustainability resources –** free copies of Sustainable Concrete Guides provided to universities for use in the classroom
- **Student competitions –** participate in ACI's written and/or team-based competitions
- **Scholarships and fellowships –** students who win awards are provided up to $15,000 and may be offered internships and paid travel to attend ACI's conventions
- **ACI Award for University Student Activities –** receive local and international recognition for your University's participation in concrete-related activities
- **Free access to the *ACI Collection of Concrete Codes, Specifications, and Practices* –** in conjunction with ACI's chapters, students are provided free access to the online ACI Collection
- **ACI online recorded web sessions and continuing education programs –** online learning tools ideal for use as quizzes or in-class study material

https://www.concrete.org/educatorsandresearchers/aciinyourclassroom.aspx

ACI MATERIALS JOURNAL TECHNICAL PAPER

Title No. 121-M22

Chemical Detection of Expansion Susceptibility of Concrete

by Ronald Lichtenwalner and Joseph T. Taylor

This experimental study evaluated the correlation between measured concrete expansion from a modified version of the miniature concrete prism test (MCPT) with the concentration of chemical markers leached from the prisms into an alkaline soak solution. Fifteen concrete mixture designs were tested for expansion and soak solution concentrations over time. The changes in expansion and soak solution concentrations were found to correlate well even with variations in alkali loading and substitution of cement with Class F fly ash. A model was developed to estimate the expansion potential of concrete based on an expansion reactivity index (ERI) that incorporated the concentrations of silicon, sulfate, calcium, and aluminum. The relationship between ERI and expansion was then used to identify potentially expansive concrete mixtures using the ERI of cores taken from a structure exhibiting potential alkali-silica reaction (ASR) expansion and concrete cylinders matching the mixture designs of the MCPT specimens.

Keywords: alkali-silica reaction; concrete expansion; delayed ettringite formation; miniature concrete prism test; Turner-Fairbank Alkali-Silica Reaction Aggregate Susceptibility Test (T-FAST).

INTRODUCTION

Deleterious concrete expansion is a significant source of premature deterioration of concrete infrastructure worldwide.[1] Expansion may be caused by a variety of factors, through physical mechanisms such as freezing-and-thawing, or through chemical mechanisms. Two notable chemical causes of expansion are alkali-silica reaction (ASR) and delayed ettringite formation (DEF).[1,2] ASR is a reaction between aggregates with reactive silica and alkali hydroxides that form a gel within concrete that swells in the presence of sufficient moisture, causing the concrete to expand.[1] For ASR to occur in concrete, three conditions must be met: sufficient moisture, an aggregate with a reactive form of silica, and sufficient alkali hydroxides to trigger the dissolution of the reactive silica from the aggregate.[1] The alkali hydroxide concentration within the concrete pore solution is largely determined by the alkali content of the cement. However, aggregates, supplementary cementitious materials (SCMs), and external alkalis from environmental sources can also contribute to the pore solution alkali concentration. DEF shares the requirement of sufficient moisture that ASR requires, but also requires sufficient sulfate (SO_4^{2-}) provided from external or internal sources.[2] The formation of delayed ettringite in localized voids and cracks can ultimately result in the expansion of the concrete.[2] Various mitigation strategies, primarily for the prevention of ASR, are employed throughout the industry, including substitution of cement with SCMs, inhibiting admixtures, restrictions on the alkali content of cement, restrictions on aggregate sources, and/or blending of aggregates.[1,3]

Current physical expansion testing and limitations

Most current laboratory tests for expansion focus on determining the ASR potential of a specific aggregate by measuring physical expansion and experience several limitations.[4] These tests of expansion include the miniature concrete prism test (MCPT, AASHTO T 380),[5] the accelerated mortar bar test (AMBT, ASTM C1260), and the concrete prism test (CPT, ASTM C1293).[6] The CPT is considered the most reliable of the expansion test methods; however, the test requires an extended time of at least a year to classify material as deleteriously reactive.[7] Additionally, CPT samples exhibit alkali leaching, which can yield results that diverge from concrete exposed to natural conditions.[8-10] The AMBT is the most accelerated of currently available tests, yielding results in 28 days, and has become the most widely used test method.[7] However, the AMBT suffers from poor accuracy, yielding both false negatives and false positives due to unrealistically aggressive conditions.[10,11] The MCPT lies between the two extremes of the CPT and AMBT tests. The MCPT is an accelerated version of the CPT that provides results within 84 days and has shown broad correlation with the CPT.[12,13] In one study, the MCPT was found to correlate better with exposure site block expansion compared to the CPT.[10] All of the expansion tests discussed thus far require significant preparation of the aggregates and are restricted to mixtures made using specific ingredients under highly controlled conditions not representative of the variety in field concrete mixture designs. To address these shortcomings, the accelerated concrete cylinder test (ACCT) has been developed.[14] The ACCT involves soaking a cylinder in alkaline solution at 60°C (140°F) within a volumetric change measuring device (VCMD) and recording length change measurements automatically. The ACCT has shown some promise in being used to test a wide array of mixtures that correlate well with the CPT.[14] However, the test is still new and there is little data on correlation with exposure site block expansion, which the CPT does not always agree with.[8-10]

Chemical testing of expansion susceptibility

Chemical tests for expansion of concrete are potentially capable of more explanatory power in revealing how and why concrete experiences expansion, however, chemical tests for expansion are much less common. One of these tests, ASTM C289, was withdrawn due to the method being

ACI Materials Journal, V. 121, No. 2, March 2024.

MS No. M-2023-152.R1, doi: 10.14359/51740374, received October 11, 2023, and reviewed under Institute publication policies.

overly severe with poor reliability.[1] Recently, the Turner-Fairbank Alkali-Silica Reaction Aggregate Susceptibility Test (T-FAST, provisional standard AASHTO TP 144) has been developed. The T-FAST has provided rapid results in 21 days that have shown good correlation with standard expansion test methods, field cases, and long-term block farm expansion data.[15-17] The three elements used in T-FAST to assess expansion susceptibility are silicon (Si), calcium (Ca), and aluminum (Al). The Si measured is primarily present from the dissolution of silica from reactive aggregates. An increase in Al in the simulated pore solution corresponds with a mitigation of expansion potential and has shown mitigation in other studies.[18-20] The final component of the T-FAST results is the Ca concentration, which has generally exhibited more mixed data regarding its role in ASR expansion, but in the T-FAST model is shown to reduce the expansion potential.[3,15,16,21-24] Combined, these concentrations form a chemical reactivity index, shown in Eq. (1)

$$RI = \frac{[Si]}{[Al] + [Ca]} \quad (1)$$

where the concentrations are given in mol/m^3. The T-FAST test in the current state does share some of the drawbacks of expansion testing, such as requiring substantial preparation of coarse aggregates and testing only the isolated aggregate.

Ideal expansion test method

Each of the current standard test methods have some drawbacks and are unable to test concrete mixtures placed in the field or test complicated mixture designs representative of field concrete mixtures. Thomas et al.[7] proposed that the ideal test for expansion would be reliable, simple, rapid, and capable of assessing the susceptibility of an unmodified sample representing a concrete mixture proposed for a specific use. Such a test could be used for complex mixtures and potentially used to assess in-place structures for expansion potential.[7]

RESEARCH SIGNIFICANCE

Current expansion tests are not designed to predict the susceptibility and estimation of expansion in complex field concrete mixtures. This study describes a chemical model for concrete samples that can be used to determine the susceptibility of a concrete mixture to expansion using a modified MCPT. From the correlation of expansion and chemical reactivity markers in concrete soak solution, the potential expansion of laboratory-made concrete cylinders and field-obtained concrete cores are estimated. This correlation provides a potential approach to accurately and rapidly determine the expansion susceptibility of true job-specific concrete mixtures sampled from the field.

EXPERIMENTAL INVESTIGATION

Modified miniature concrete prism test

Concrete prisms were prepared with varying coarse aggregates, alkali loading, and replacement of cement with fly ash. A variety of aggregates were chosen to assess a broad spectrum of ASR reactivities. Several alkali loadings were used for two of the most reactive aggregates to determine if the expansion and chemical reactivity would correlate as the alkali content was adjusted. Concrete prisms of a specific mixture were placed in a polypropylene container with a soak solution that was adjusted with sodium hydroxide (NaOH) to match the estimated alkalinity of the concrete pore solution. The alkalinity of the soak solution in terms of NaOH concentration was estimated assuming all alkali from the cement was soluble using the weight and % Na_2O_{Eq} of the cement in the mixture as demonstrated in Eq. (2)

$$[NaOH] = \frac{\frac{\%\ Na_2O_{Eq}}{100} \times W_{Cement} \times 32.2691}{V_{Water}} \quad (2)$$

where [NaOH] is the sodium hydroxide concentration in mol/m^3; %Na_2O_{Eq} is the percent of sodium alkali equivalent of the cement; W_{Cement} is the weight of the cement in kg; 32.2691 is the conversion factor to convert from kg of Na_2O_{Eq} to moles of NaOH; and V_{Water} is the volume of mixture water in m^3.

Concrete cylinders

To compare the feasibility of testing concrete cylinders with this method, concrete cylinders were cast for a subset of 10 out of the 15 MCPT mixtures and soaked in alkaline soak solutions calculated using Eq. (2).

Field concrete cores

To ascertain whether the test method in this study could potentially be used to assess in place structures, concrete cores from a North Carolina roadway exhibiting potential ASR were also soaked in alkaline solutions.

Materials

The chemical compositions of the cementitious materials used are listed in Table 1. Ten coarse aggregate sources were used, and the ASR reactivity of each source was estimated using a modified T-FAST with only conditions 2 and 4 performed. The reactivity classification of the aggregates and historical field record are summarized in Table 2. Moderately reactive aggregates are ordered based on the estimated reactivity from T-FAST testing, with the expected reactivity in decreasing order from MR-1 to MR-6. Graded Ottawa sand conforming to ASTM C778 was used as the fine aggregate in all the MCPT mixtures. A local fine aggregate was used in the concrete cylinder specimens and tested as nonreactive using a modified AASHTO TP 144 suitable for fine aggregates wherein the fine aggregate is dried, but no sieving is performed.[16]

Specimens

MCPT—Concrete prisms measuring 50 x 50 x 285 mm (2 x 2 x 11.25 in.) were cast and cured according to AASHTO T 380 specification with the following exceptions: prisms were made in duplicate instead of triplicate due to MCPT mold capacity and laboratory oven capacity; the alkali loading of the mixture water and the soak solution

Table 1—Composition of cementitious materials used in mixtures

Oxide, % wt	CEM-VHA	CEM-HA	CEM-LA	FA
SiO_2	20.62	19.99	20.28	44.60
Al_2O_3	3.76	4.85	4.91	21.90
CaO	62.09	63.58	63.96	4.21
Fe_2O_3	3.09	3.18	3.40	19.19
MgO	3.18	2.18	1.27	0.78
SO_3	3.42	2.63	2.80	1.44
LoI	2.20	2.60	2.78	2.16
Na_2O	0.31	0.14	0.12	1.53
K_2O	1.11	0.80	0.56	1.87
Na_2O_{Eq}	1.04	0.67	0.49	2.76

Note: LoI is loss on ignition.

Table 2—Aggregate reactivity classification

Aggregate ID	AASHTO TP 144 (T-FAST) ASR reactivity classification	Evidence of field ASR reactivity
HR-1	Highly reactive	Yes
HR-2	Highly reactive	No
MR-1	Moderately reactive	Yes
MR-2	Moderately reactive	No
MR-3	Moderately reactive	Yes
MR-4	Moderately reactive	No
MR-5	Moderately reactive	No
MR-6	Moderately reactive	No
NR-1	Nonreactive	No
NR-2	Nonreactive/slow reactive	No

Table 3—Concrete mixture designs used for MCPT and cylinder specimens

		Cementitious materials			Aggregate		
Mixture design ID	Alkali loading, kg/m^3	Cement used	Cement, kg/m^3	Class F fly ash, kg/m^3	Coarse, kg/m^3	Fine, kg/m^3	*w/c*
NR-1-1.55%	6.4	CEM-HA	415	0	804	982	0.48
NR-2-1.55%*	6.2	CEM-HA	402	0	778	951	0.49
HR-1-0.49%†	2.0	CEM-LA	410	0	794	970	0.47
HR-1-0.67%†	2.7	CEM-HA	405	0	784	958	0.50
HR-1-1.25%†	5.3	CEM-HA	427	0	1141	620	0.45
HR-2-0.67%	2.9	CEM-HA	431	0	1151	625	0.45
MR-1-1.55%*	6.5	CEM-HA	421	0	1125	611	0.45
MR-1-1.55%-FA*	6.5	CEM-HA	333	83	1114	605	0.45
MR-1-1.04%-A	4.4	CEM-VHA	421	0	1125	611	0.45
MR-1-1.04%-B*	4.4	CEM-HA	421	0	1125	611	0.45
MR-2-1.25%†	5.4	CEM-HA	429	0	1147	623	0.45
MR-3-1.55%†	6.6	CEM-HA	427	0	1141	620	0.45
MR-4-1.04%	4.4	CEM-VHA	426	0	1137	618	0.45
MR-5-1.55%†	6.6	CEM-HA	426	0	1139	619	0.45
MR-6-1.55%	6.5	CEM-HA	420	0	1121	609	0.45

*Matching cylinder made in duplicate.

†Matching cylinder made.

varied from the specified 1.25% Na_2O_{Eq} to determine the effectiveness of MCPT and the proposed test devised in this study at reflecting the variety of alkali levels seen in field concrete mixtures; the No. 78 aggregate was dried, but otherwise used as provided by the producer with no additional gradation or preparation to more realistically reflect concrete cast in the field; and the volume fraction for the coarse aggregate was 0.70 in most mixtures. The higher volume fraction of coarse aggregate matches the CPT test and was used to potentially induce more expansion from a larger reservoir of reactive silica being available. However, there is some evidence that the volume fraction of coarse aggregate has minimal influence on MCPT results, as Latifee[13] found "no clear relationship" between 0.65 and 0.70 volume fraction of coarse aggregate and the expansion of concrete prisms. The concrete mixture proportions as batched for the MCPT and cylinder specimens are given in Table 3. The air content is not measured per AASHTO T 380, but was assumed to be 2.5% per the original MCPT research.[13] The mixture design ID schematic (XX-X-Y.YY%) indicates the aggregate identity (XX-X) and alkali in terms of Na_2O_{Eq} of cement (Y.YY%). The mixtures HR-0.49%, HR-0.67%, NR1-1.55%, and NR2-1.55% have designs notably different from the rest, as they were the first four mixtures batched as trials before a standardized mixture was decided upon. They were still included because the intent of this study was to correlate concrete expansion and the chemistry of the corresponding soak solution, rather than classify the reactivity of a standardized mixture. For MR-1-1.55%-FA, the estimated alkali content of the soak solution was made without considering the dilution effect and it was assumed to have the same alkali loading as the straight cement mixture. This was done

to isolate the mitigation effect due to the material properties of the fly ash from the dilutive effect of soluble alkalis that result from fly ash substitution.

Concrete cylinders—Cylinders measuring 76 x 152 mm (3 x 6 in.) were cast as noted in Table 3. Following the steps in ASTM C192, the cylinders were hand mixed and then rodding was used for consolidation; however, there was no preparation of the No. 78 sized aggregates beyond oven drying. The cylinders were demolded after 24 hours of curing at 21°C (70°F) and then placed into 100 x 200 mm (4 x 8 in.) concrete cylinder molds that had 800 mL of solution matching the estimated alkalinity of the cylinder pore solution from Eq. (2). One difference in the experimental setup for the cylinders from the MCPT is that a lower oven temperature of 55°C (131°F) was used, matching the temperature of the T-FAST. This change in temperature was done to assess whether the reactivity at similar ages would be significantly affected compared to the MCPT.

Concrete cores—Two 100 x 200 mm (4 x 8 in.) concrete cores from a North Carolina jointed plain concrete pavement constructed in 1984 that appeared to be exhibiting deleterious expansion were tested using a version of this test at 60°C (140°F). Companion cores to these were also sent out for petrography analysis and the results compared.

Items of investigation

Approximately every week, concrete prisms were measured for change in length expansion per AASHTO T 380. At the time of the expansion measurement, the temperature of each prism container's soak solution was also measured, and 20 mL of the soak solution was collected and filtered with a glass microfiber syringe filter. The filtered soak solution was then measured for Si, Ca, Al, sulfur (S), potassium (K), and sodium (Na) concentrations by wavelength-dispersive X-ray fluorescence (WDXRF). WDXRF is incapable of determining the exact form of elemental species, and in the case of sulfur, the sulfur was assumed to be present as SO_4^{2-}. To measure filtered solution concentrations by WDXRF, a nylon membrane was soaked in the solution for 1 minute, dried in an oven at 110°C (230°F), and then analyzed under vacuum on a 1.2kW WDXRF. The blank nylon membranes were also analyzed by WDXRF before being soaked to ensure there was no contamination present. Initial MCPT samples were tested for expansion and soak solution concentrations until 84 days. Later prisms were kept beyond 84 days to monitor the long-term expansion and corresponding concentrations of the soak solution. The concrete cylinder specimen and field-core soak solutions followed the same filtering and WDXRF procedure, except that analysis was only performed every 28 days.

ANALYTICAL INVESTIGATION

Development of a model correlating MCPT soak solution composition to expansion

The T-FAST reactivity index (RI) parameter was initially used to correlate the degree of reactivity of each concrete mixture with concrete specimen expansion. As more data from the study was collected, other parameters were trialed for inclusion in the equation to improve the correlation to the expansion measurements, as there exist other chemical mechanisms that also contribute to concrete expansion, such as DEF.[2,11,25] Therefore, dissolved sulfur, assumed to be present as SO_4^{2-}, was also added to the RI equation to determine if the correlation with expansion would improve. This new index, titled the expansion reactivity index (ERI), is given by Eq. (3)

$$\text{ERI} = \frac{[\text{Si}] + [\text{SO}_4^{2-}]}{[\text{Al}] + [\text{Ca}]} \quad (3)$$

where the concentration is given in mol/m^3 for each analyte. The ERI was then correlated with the expansion of the prisms produced from the concrete mixtures from 14 until 84 days. By the end of the testing period, an overall model was developed to estimate the level of concrete prism expansion based on the analyte concentrations leached into the soak solutions from the mixture. The developed ERI regression model was then used to determine a corresponding ERI threshold based on the generally agreed upon deleterious expansion threshold of 0.040%.[26]

Concrete cylinders

The ERI determined from soak solution concentrations was used to estimate the expansion for the concrete cylinders and results compared to the measured MCPT specimen expansion.

Field concrete cores

For the two cores received from the field and partitioned, one quarter was placed in a 1.25% Na_2OEq solution, one quarter was placed in a 0.80% Na_2OEq solution, and one was placed in distilled water only. Because the true mixture designs for these cores were unknown, the alkali solution concentrations using Eq. (2) were based on an estimated mixture that used 420 kg/m^3 of cement with a 0.40 water-cement ratio (*w*/*c*). This could be considered typical of pavement mixtures approved for use in North Carolina. The ERI measured from the core soak solutions were used to estimate expansion and compared to petrography results.

EXPERIMENTAL RESULTS AND DISCUSSION

Expansion measurements

The results for the 56- and 84-day expansions or the closest day measured for each mixture design are shown in Fig. 1, including the range of the prism measurements of the two bars at 84 days. As expected, based on the behavior of the aggregates from their field history and testing with T-FAST, the expansion of most mixtures exceeded 0.040% by day 56. The mixtures that did not exceed 0.040% expansion were: the two mixtures containing assumed nonreactive aggregates (NR-1 and NR-2); the low alkali loading mixture of HR-1; the moderate alkali loading mixtures of HR-1 and HR-2; and the MR mixtures on the lower end of T-FAST reactivity, MR-5-1.55% and MR-6-1.55%. These results largely match the expected outcome, as HR-1-0.49% is considered a low-alkali mixture and included a lower coarse aggregate content than the other mixtures. HR-1-0.67% and HR-2-0.67% are mixtures with lower alkali loadings and

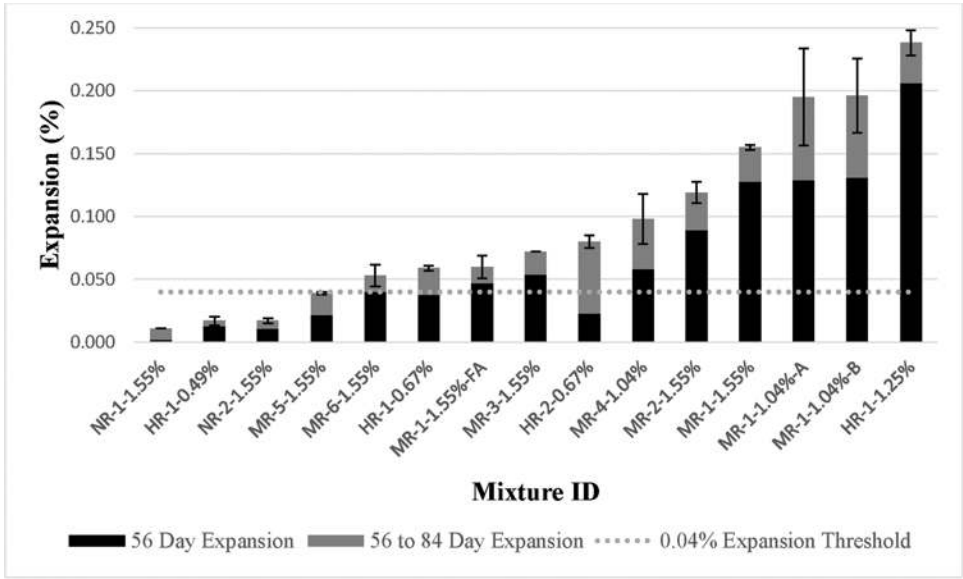

Fig. 1—MCPT specimen expansion.

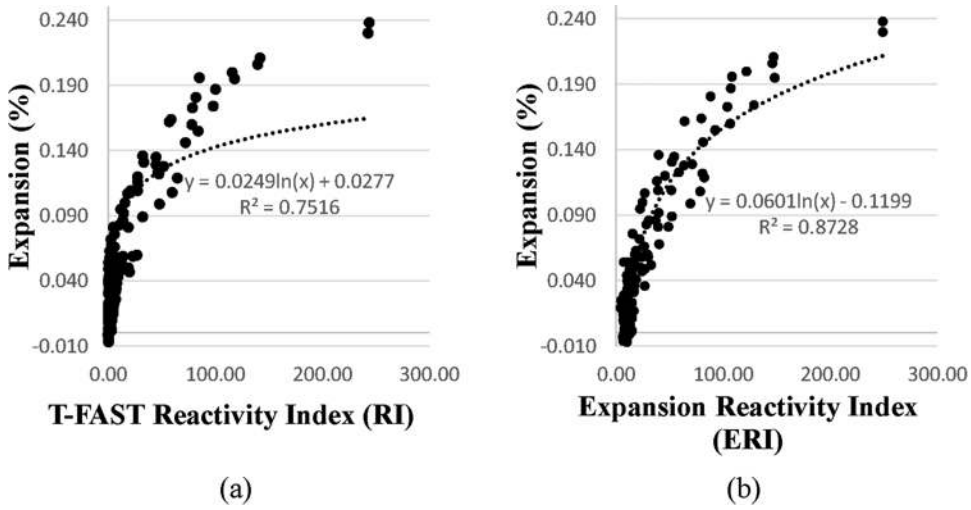

Fig. 2—Models of expansion: (a) T-FAST reactivity index equation; and (b) addition of sulfate to RI model equation.

would be expected to expand slower if deleterious expansion were to occur. Based on the T-FAST classification of the aggregates, MR-5-1.55% and MR-6-1.55% are the only mixtures that failed to reach the expected 0.04% threshold for deleterious expansion by 56 days. The trends from the 56-day readings were largely followed by the 84-day expansions and all mixtures surpassed 0.04% expansion, except for MR-5-1.55%, HR-1-0.49%, and the mixtures containing nonreactive aggregates (NR-1 and NR-2).

ERI results

Initially, the RI as used in T-FAST was used to correlate expansion to soak solution composition. As indicated by Fig. 2, when SO_4^{2-} was added to the equation as an indicator of deleterious expansion, the R^2 improved from 0.75 to 0.87. Subsequently, the ERI was then used to analyze and predict expansion susceptibility of samples. Figure 2(b) illustrates the overall strong relationship of expansion and the ERI across all days. The ERI from the prisms provides some illumination on the mechanism of the expansions measured. On the extreme end, the lack of expansion of NR-1-1.55% and NR-2-1.55% can be attributed to the lack of available Si in solution for ASR gel to form. The initial classification of aggregates by the T-FAST indicated both aggregates had very little Si leaching into the alkaline solution that would be available to form ASR gel, which is reflected in the low ERI seen in this study. Similarly, the most reactive aggregates classified by the T-FAST (that is, HR-1, MR-1, and MR-2) show large expansions, owing to the abundant availability of Si to form ASR gel in highly alkaline solutions.

To test concrete mixtures obtained from the field, a determination of values of the ERI that correspond to deleterious expansion needs to be formulated. From the nonlinear relationship between ERI and expansion (Fig. 2), a logarithmic transformation of the ERI was performed, and a linear regression developed from this transformation. The results of the logarithmic transformation and subsequent linear regression performed on the data from Fig. 2(b) is shown in Fig. 3. The resulting linear regression equation is given by Eq. (4)

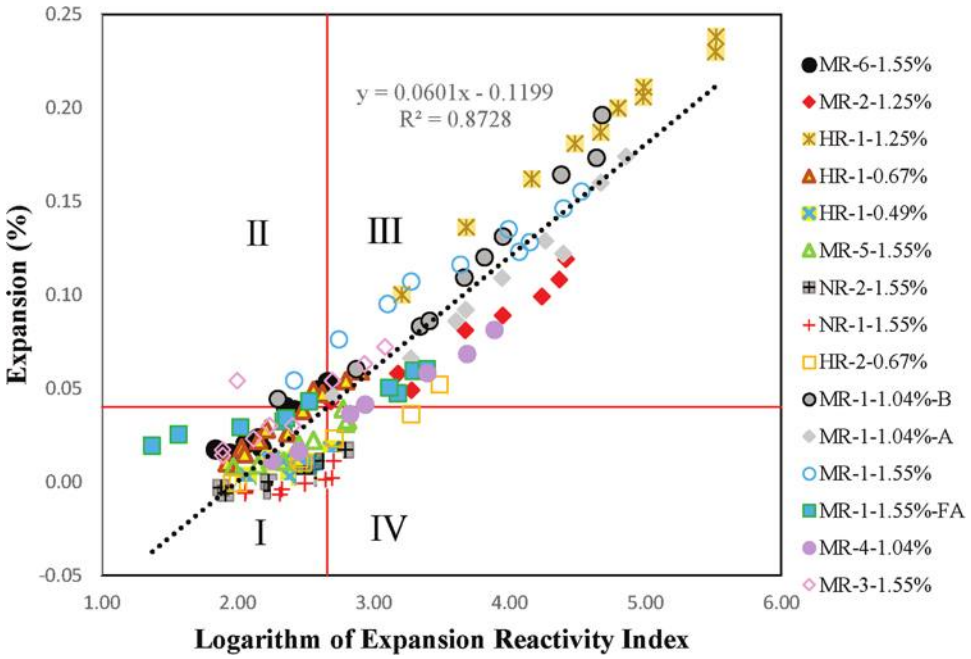

Fig. 3—Logarithmic transformation of MCPT results from 14 until 84 days.

$$Exp_{Pred} = 0.0601 \times \ln(ERI) - 0.1199 \quad (4)$$

where Exp_{Pred} is the predicted percent expansion based on the natural logarithm of the ERI calculated from Eq. (3). Substituting 0.040% expansion into Eq. (4) results in a calculated ln(ERI) threshold level of 2.66. The horizontal and vertical lines in Fig. 3 indicate an ERI false negative or false positive when points lie in the second or fourth quadrant, respectively. There are a few false negative points in which the concrete had expanded beyond 0.040%, yet the ERI did not reach the equivalent threshold value. For the mixtures with large expansion at early measurement times, the probable cause is the lag between the concrete reaching chemical equilibrium with the soak solution. In these mixtures, the ASR gel formation is likely occurring rapidly within the concrete prisms and the concentrations, particularly Si, have not yet reached equilibrium with the soaking solution. This is particularly evident by the point in quadrant II of Fig. 3 for MR-1-1.55% and MR-1-1.04%-B, which occurred within the first 15 days of soaking.

Deviations in correlation for slowly and moderately reactive mixtures

Reaction equilibrium may also explain the deviation for MR-3-1.55% and MR-6-1.55%, as the ERI did not cross the threshold indicating deleterious expansion until later stages, well after expansion exceeded 0.040%. In these cases, a potential cause may be a masking of the Si dissolution in soak solution due to the presence of available Ca. As evidenced in Eq. (3), the ERI is highly dependent on the Si concentration. Prior to the exhaustion of Ca^{2+} in the solution, reactive silica that dissolves into solution from the aggregate is being readily consumed, forming calcium-silicate-hydrates and ASR products. Once the Ca^{2+} reserve has been exhausted, then the Si builds up in excess in the solution.[3,23,24] Figure 4 displays the relationship between the Si, Ca, and expansion from all the mixtures where Ca did not reach below 0.06 mol/m^3 until after 56 days in the soaking solution. As seen in Fig. 4, once the Ca content in solution is nearly exhausted, the Si content measured in solution increases rapidly. The overall rate of Si dissolution before this point may be greater than would be indicated by the Si detected in the soak solution due to the consumption of Si by available Ca in solution.[24] This suppression of excess Si in solution by Ca supports the lag seen between the ERI and expansion in the slow to moderate reactive mixtures. Once the Ca concentration in solution reaches low levels, approximately 0.06 mol/m^3, the apparent rate of Si dissolution increased and then remained largely constant after that time. For a specific example, MR-3-1.55% exceeded 0.040% expansion at 56 days, yet did not reach the ERI value corresponding to deleterious expansion until day 70 of testing, when the Ca concentration in solution reached below 0.06 mol/m^3. In another case, MR-6-1.55% solution tested beyond 84 days did not reach below 0.06 mol/m^3 of Ca until 109 days, at which point the ERI crossed the threshold indicating deleterious expansion as determined by Eq. (4).

Variation of ERI and expansion with changes in alkali loading for HR-1

The expansion and ERI results for the mixtures containing the reactive aggregate HR-1 with varied alkali loading were evaluated (Table 3). Figure 5 shows how the ERI and expansion varied under different alkali loadings, establishing that the ERI reflects the reduction in expansion measured under lower alkali loadings than typically used in standardized ASR expansion testing. The reduction in ERI at lower alkali loadings is primarily due to a large decrease in Si dissolution as the concentration of hydroxide in the soaking solution decreases.

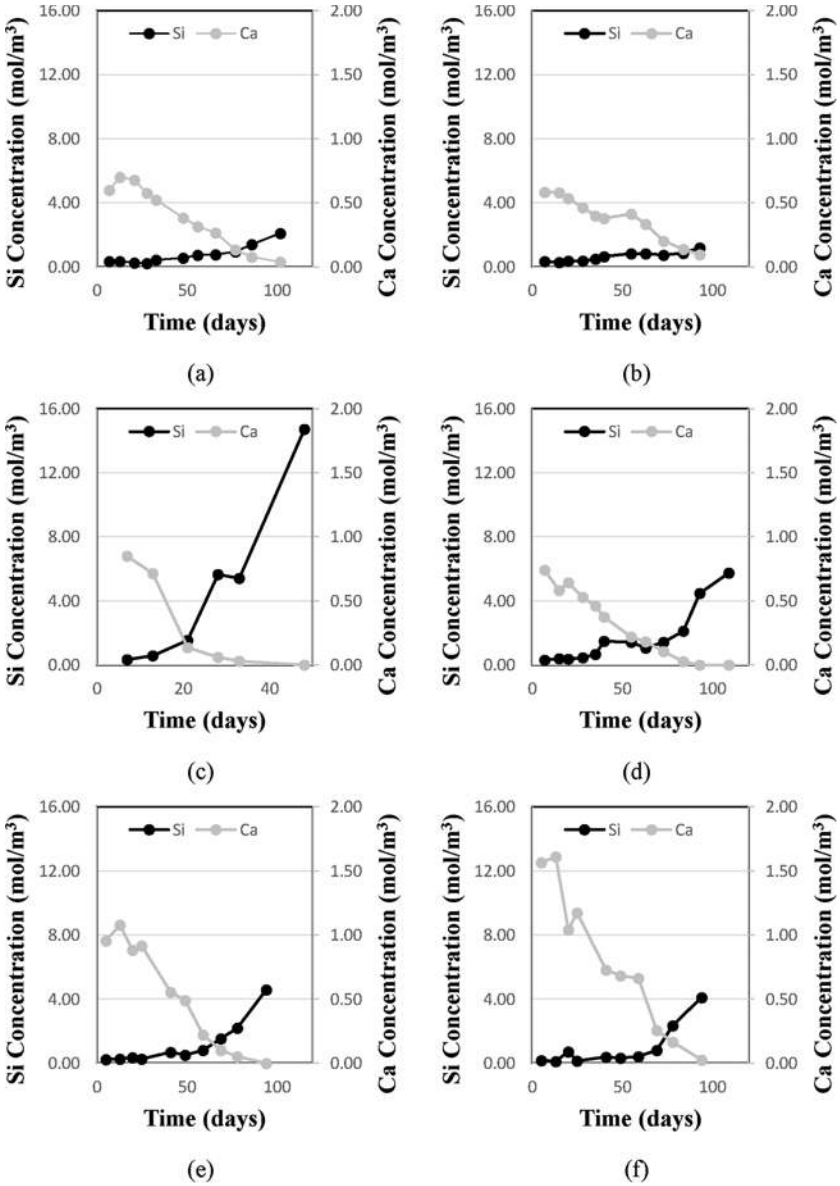

Fig. 4—Solution concentrations of calcium and silicon over time for: (a) MR-5-1.55%; (b) MR-6-1.55%; (c) MR-2-1.25%; (d) MR-3-1.55%; (e) MR-4-1.04%; and (f) HR-2-0.67%.

Variation of ERI and expansion with changes in alkali loading for MR-1

Three alkali loading variation mixtures were made for MR-1, two sets of prisms made with 1.04% Na_2O_{Eq} alkali content and one set of prisms at 1.55% $Na_2O_{Eq.}$ The two sets of 1.04% Na_2O_{Eq} prisms differed in the source of cement, where MR-1.04%-A used a high-alkali cement that required no boosting of alkali content in the mixture water, while MR-1.04%-B used a 0.67% Na_2O_{Eq} cement and required NaOH to be added to the mixture water. This test was done to illuminate the assumption that the soak solution alkali content is more important than the small contribution the cement alkalis will provide. Latifee's[13] original research on the MCPT showed a 10% reduction in expansion when low-alkali cement boosted with NaOH in the mixture water was used versus a cement with $0.90 \pm 0.10\%$ Na_2O_{Eq} cement. However, this was done on only a single set of comparison specimens, and the standardized MCPT currently has no estimated precision.[5] The CPT, which is wholly reliant on internal alkalis for expansion, has an estimated within-laboratory precision of 12% at expansion greater than 0.02% expansion; thus, it is possible that the MCPT variation seen with alkali boosting may be within the expected variation of the standardized test.[3,6]

The expansion and ERI data for the MR-1 alkali variation mixtures for up to 84 days of testing are displayed in Fig. 6. The two MR-1 mixtures containing 1.04% $Na2O_{Eq}$ displayed similar expansion, though slightly different ERI results, supporting the expectation that the alkali soak solution is likely the primary factor in expansion versus the internal alkalis. Interestingly, the ERI and the expansion both agree that this lower-alkali loading is more expansive than the MR-1-1.55% mixture. Thus, MR-1 may be an aggregate that displays a pessimum effect of higher reactivity at lower-alkali loadings that is seen in some reactive aggregates.[11] The increased ERI for MR-1-1.04% at 84 days is not due to an increase in the concentration of Si leaching into solution, which is nearly half the concentration leached from

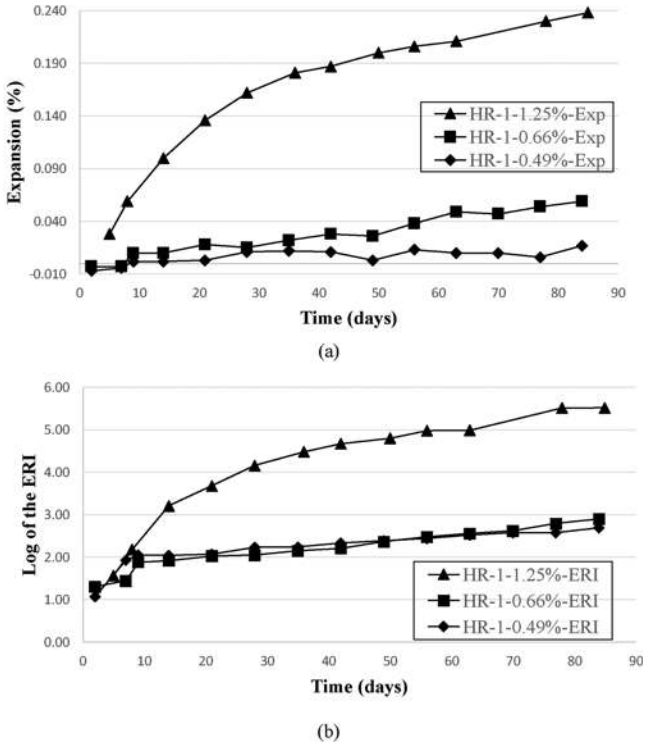

Fig. 5—Effect of alkali loading on HR-1 reactivity: (a) change in expansion; and (b) change in ln(ERI).

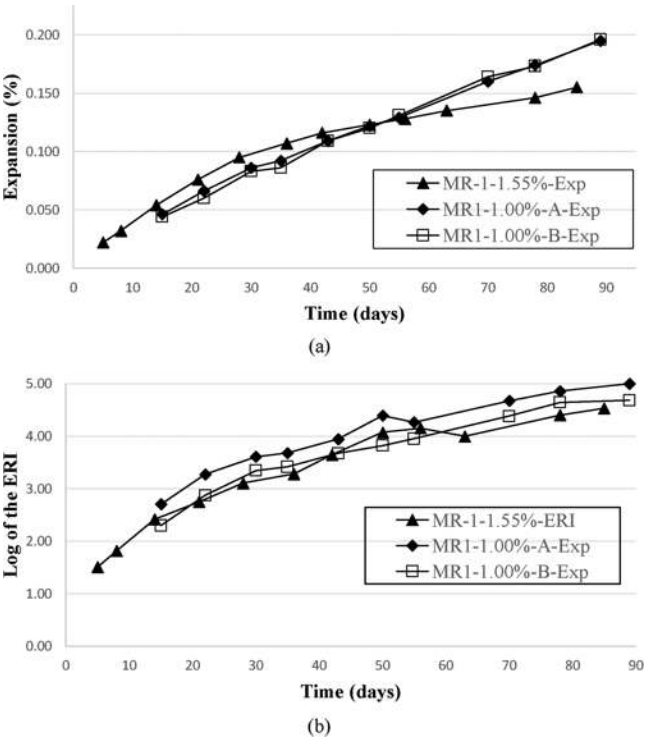

Fig. 6—Effect of alkali loading on MR-1 reactivity: (a) change in expansion; and (b) change in ln(ERI).

MR-1-1.55%. Rather, the increase is due to the decrease in the concentration of Al and an increase in the concentration of SO_4^{2-}. With the decrease in Al in solution, one effect that would be expected is less protection of Si dissolution; however, as measured here, the overall concentration of Si leached is less than the higher alkali mixture of MR-1. This

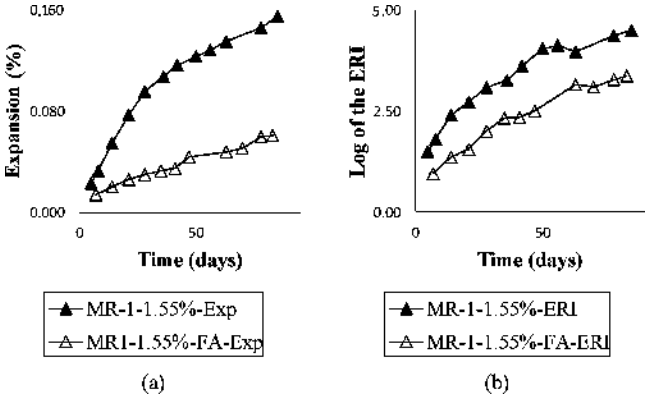

Fig. 7—Effect of 20% fly ash substitution on MR-1 reactivity: (a) change in expansion; and (b) change in ln(ERI).

Table 4—MR-1 reactivity results with mixture design variations at 84 days

Mixture design	Si, mol/m^3	Al, mol/m^3	SO_4^{2-}, mol/m^3	ERI	Expansion, %
MR-1-1.04%-A	44.55	0.38	11.33	148.4	0.195
MR-1-1.04%-B	33.64	0.40	9.25	108.3	0.196
MR-1-1.55%	76.95	0.91	7.95	92.86	0.155
MR-1-1.55%-FA	40.79	1.53	1.54	27.0	0.060

implies there may be other factors causing optimum expansion, such as the ratio of alkali to Al in the pore solution.[18]

Mitigation of expansion and reduction in ERI with cement replacement by fly ash

Mixture MR1-1.55%-FA showed a marked drop in the expansion and the ERI compared to the straight cement mixture (Fig. 7). This indicates the solution chemistry and thus the ERI reflects some degree of expansion mitigation that occurs with the substitution of Class F fly ash. The expansion and ERI are still substantial, with an expansion greater than 0.040% at 56 days, indicating a likely lack of adequate substitution of Class F fly ash to completely mitigate the ASR reaction. Table 4 shows how the reduction in the ERI at day 84 compared to the straight cement mixture is a result of an increase in the Al and reduction of the Si and SO_4^{2-} concentrations. The decrease in Si available is likely due to the suppression of reactive silica by the additional Al in solution contributed by the fly ash.[18-20] Although the results show the mitigation of fly ash substitution in both the expansion and ERI, the ERI for MR-1-1.55%-FA is larger than would be expected based on Eq. (4). More research will need to be performed with mixtures containing fly ash to see if this is due to an interaction occurring in the mixture not modelled by the ERI, perhaps due to a pozzolanic reaction, or if it is indicative of latent expansion.

Comparison of concrete cylinders and MCPT ERI

Results comparing the ERI of the cylinders and MCPT specimens at equal ages of measurement are provided by Fig. 8. As the temperature and soak solution volume to concrete ratio differed between the two sets of specimens, the

comparison between cylinders and MCPT mixture reactivity merely provides a first step in the broader goal of classifying reactive concrete field mixtures. The expansion prediction equation from Eq. (4) was applied to the ERI of the cylinders to provide an estimate of the expansion. Note that MR-2-1.25%, MR-3-1.55%, and MR-5-1.55% were compared at 56 days and the remainder were at 84 days. This was due to scheduling conflicts where some measurements were missed for the cylinders.

The predicted cylinder expansion from Eq. (4) and the measured expansion in the MCPT mixture at the same ages are similar in most instances and duplicate cylinders agree well with each other. The largest deviation is by NR-2-1.55%, which indicates deleterious expansion from the cylinder ERI, but did not expand significantly in the MCPT test. NR-2 did exhibit borderline slow reactivity in the T-FAST test of the aggregate alone. HR-1-0.67% also shows some significant deviation, although both predicted and measured expansion indicate deleterious expansion. More testing is required to determine whether these discrepancies are due to test variations between cylinders and prisms, natural reactivity variation from the aggregate, or another factor.

Analysis of highway concrete cores suspected of ASR

Table 5 summarizes the soak solution measurements of field cores C-1 and C-5. The core portions soaked in 1.25% Na_2O_{Eq} solution were only tested until 32 days due to the early indication of a high degree of reactivity from the ERI. The estimated expansions given from the ERI and Eq. (4) for the core pieces soaked in alkaline solutions are well above 0.040% and would indicate the mixtures are susceptible to expansion with as little as 0.80% Na_2O_{Eq} and have similar reactivity to each other. The availability of reactive silica to dissolve from the aggregate even after decades in the field supports the possibility of identifying potentially expansive mixtures in field concrete. To support the findings from the soak solution testing, two cores taken near C-1 and C-5 were sent to an independent petrographer for assessment of ASR and general composition of the cores by ASTM C856. These cores submitted for petrography are referred to as C-1S and C-5S. Petrography noted the two cores had the same coarse and fine aggregate, were well graded, and had similar estimated *w*/*c*. Both cores exhibited microcracking, though C-5S was more extensive, extending to a depth of 61 mm, compared to 15 mm in core C-1S. Evidence of moderate ASR was observed in C-5S, including secondary deposits of ASR gel in reaction rims, subvertical microcracks, and air voids at various depths. In contrast, little evidence of ASR or deterioration was noted for core C-1S and only secondary deposits of ettringite were observed lining air voids and filling smaller air voids. The overall similarity in composition of cores C-1S and C-5S and the similarity in residual expansion of cores C-1 and C-5 determined by this study would suggest the most likely difference in the visible ASR in the cores is due to the environmental conditions at C-5S. The chemical identification of expansive potential corroborated by the petrography report shows promise for this method to be used on cores to identify the expansion potential of existing structures.

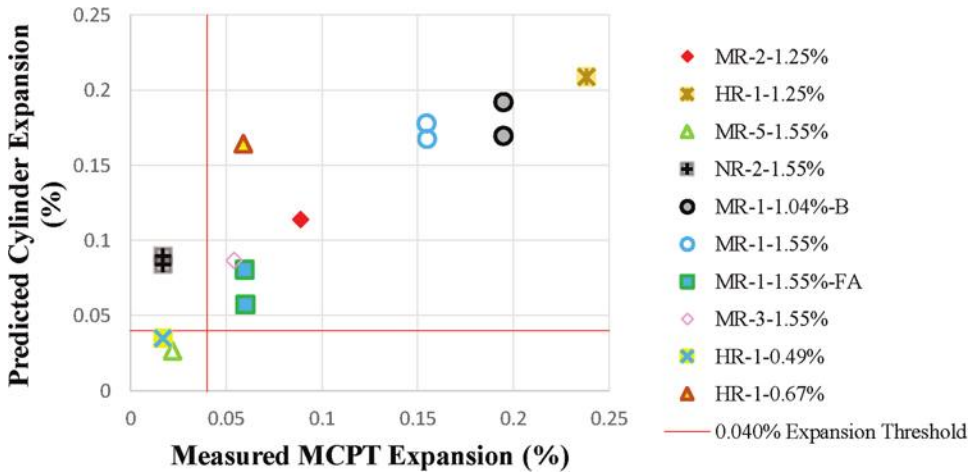

Fig. 8—Correlation of predicted cylinder mixture expansion with measured MCPT expansion.

Table 5—Field concrete core reactivity results

Core sample	Na_2O_{Eq} solution, %	Time, days	Si, mol/m^3	Al, mol/m^3	SO_4^{2-}, mol/m^3	Ca, mol/m^3	ln(ERI)	Estimated expansion, %
C-1	0	56	4.00	0.12	1.03	1.38	1.21	–0.047
C-1	0.80	61	31.55	0.58	7.43	0.00	4.21	0.133
C-1	1.25	32	14.00	0.89	5.75	0.00	3.10	0.066
C-5	0	56	1.85	0.11	1.36	1.00	1.06	–0.056
C-5	0.80	61	16.19	0.91	10.61	0.00	3.38	0.083
C-5	1.25	32	15.39	0.84	10.01	0.00	3.41	0.085

FURTHER RESEARCH

While these initial results are promising, more extensive testing will need to be performed to refine and validate the model relating ERI to expansion. Potential areas of further research include:

1. Optimizing testing conditions to provide a test that is as accelerated as possible while maintaining strong correlation with expansion.

2. Further validate the model linking ERI to expansion by matching mixture designs from long-term exposure site blocks and comparing the ERI of the replicated mixtures to the block expansion.

3. Testing of concrete specimens of varying sizes and mixture designs, including mixtures reflective of field concrete that contain concrete admixtures.

4. Verify that the reduction of ERI reflects the reduced expansion when other common ASR-mitigating materials are used, such as ground-granulated blast-furnace slag, Class C fly ash, silica fume, and lithium admixtures.

5. Testing of additional structures affected by expansion as well as control cores from structures unlikely to be experiencing expansion could be compared. Cores could be pinned, and residual expansion measured to further validate the ERI prediction model for existing structures.

CONCLUSIONS

The chemical model for expansion susceptibility developed in this study provides a potential pathway for the identification of expansive concrete mixtures and insights into the underlying mechanism of the expansion. The specific findings of this study that support this are:

1. Test results from this study showed a strong correlation between miniature concrete prism test (MCPT) expansion and the concentrations of Si, SO_4^{2-}, Al, and Ca leached into the MCPT alkaline soak solution. Concrete specimens that displayed deleterious expansion had elevated levels of Si and SO_4^{2-}, indicating the possible detection of the chemical triggers of alkali-silica reaction (ASR) and delayed ettringite formation (DEF) expansion. The increase in Al and Ca dissolved into solution from the concrete indicated lower expansion. In the case of Al, the likely cause is due to the reduction of reactive silica dissolution from aggregates.

2. The expansion reactivity index (ERI) correlated with expansion when the alkalinity of the mixture and soaking solution varied. For MR-1, a lower-alkali concentration resulted in an average 26% increase in expansion for two sets of MCPT specimens with an average increase of 38% ERI. For HR-1, the reduction of mixture alkalinity from 1.25% Na_2O_{Eq} to 0.67% Na_2O_{Eq} resulted in a 75% reduction in expansion and 93% reduction of the ERI. For the same highly reactive aggregate, the reduction of mixture alkalinity from 1.25% Na_2O_{Eq} to 0.49% Na_2O_{Eq} resulted in a 93% reduction in MCPT expansion and a 94% reduction in the ERI at 84 days.

3. The ERI indicated sensitivity to substitution with Class F fly ash. The partial substitution of cement with fly ash in a mixture with a moderately reactive aggregate showed a decrease in expansion of 61% at 84 days with a decrease of 71% in the ERI at the same alkali loading.

4. Nine out of 10 concrete cylinders matching MCPT mixtures were classified with the same broad reactivity when measured solely by ERI compared to MCPT expansion of the same mixtures.

5. The measured ERI of concrete cores from an ASR-affected structure were indicative of expansion susceptibility based on the model developed in this study. Petrographic analysis of cores from the same structure identified ASR as present in the concrete, agreeing with the assessment of the ERI model of an ASR susceptible mixture.

These findings relating the chemical ERI model to measured expansion provide the potential for a test method that would be accurate, fast, require minimal sample preparation, test job-specific concrete mixtures, and illuminate the underlying cause of expansion.

AUTHOR BIOS

Ronald Lichtenwalner *is a Chemist at the North Carolina Department of Transportation, Materials and Tests Unit, in Raleigh, NC. He received his BA in chemistry from North Carolina State University, Raleigh, NC, in 2013. His research interests include long-term durability and deleterious expansion of concrete structures.*

ACI member **Joseph T. Taylor** *is a Chemist at the North Carolina Department of Transportation, Materials and Tests Unit. He received his BS in meteorology, BS in marine science, and MS in soil science from North Carolina State University in 2013 and 2016, respectively. His research interests include alkali-silica reaction in concrete and temporal-spatial variability of concrete components from NC cement and aggregate plants.*

ACKNOWLEDGMENTS

The authors would like to express their gratitude to the North Carolina Department of Transportation for their support. The authors recognize the helpful correspondence with J. Muñoz at the FHWA Turner-Fairbank Highway Research Center during the initial conception of this research. The authors would also like to express gratitude to T. Cavalline at the University of North Carolina at Charlotte and R. Ghantous for insightful commentary and editing of the manuscript.

REFERENCES

1. Thomas, M. D.; Fournier, B.; and Folliard, K. J., "Alkali-Aggregate Reactivity (AAR) Facts Book," *Technical Report No. FHWA-HIF-13-019*, Office of Pavement Technology, Federal Highway Administration, Washington, DC, 2013.

2. Collepardi, M., "A State-of-the-Art Review on Delayed Ettringite Attack on Concrete," *Cement and Concrete Composites*, V. 25, No. 4-5, 2003, pp. 401-407. doi: 10.1016/S0958-9465(02)00080-X

3. Rajabipour, F.; Giannini, E.; Dunant, C. F.; Ideker, J. H.; and Thomas, M. D. A., "Alkali-Silica Reaction: Current Understanding of the Reaction Mechanisms and the Knowledge Gaps," *Cement and Concrete Research*, V. 76, 2015, pp. 130-146. doi: 10.1016/j.cemconres.2015.05.024

4. Fanijo, E. O.; Kolawole, J. T.; and Almakrab, A., "Alkali-Silica Reaction (ASR) in Concrete Structures: Mechanisms, Effects and Evaluation Test Methods Adopted in the United States," *Case Studies in Construction Materials*, V. 15, 2021, p. e00563. doi: 10.1016/j.cscm.2021.e00563

5. AASHTO T 380, "Standard Method of Test for Potential Alkali Reactivity of Aggregates and Effectiveness of ASR Mitigation Measures (Miniature Concrete Prism Test, MCPT)," American Association of State Highway and Transportation Officials, Washington, DC, 2022.

6. ASTM C1293-20, "Standard Test Method for Determination of Length Change of Concrete Due to Alkali-Silica Reaction," ASTM International, West Conshohocken, PA, 2020.

7. Thomas, M.; Fournier, B.; Folliard, K.; Ideker, J.; and Shehata, M., "Test Methods for Evaluating Preventive Measures for Controlling Expansion due to Alkali-Silica Reaction in Concrete," *Cement and Concrete Research*, V. 36, No. 10, 2006, pp. 1842-1856. doi: 10.1016/j.cemconres.2006.01.01410.1016/j

8. Fournier, B.; Chevrier, A. B.; Nkinamubanzi, P.-C.; and Bouzoubaa, N., "Comparative Field and Laboratory Investigations on the Use of Supplementary Cementing Materials (SCMs) to Control Alkali-Silica Reaction (ASR) in Concrete," *Proceedings*, 15th International Conference on Alkali-Aggregate Reaction in Concrete, São Paulo, Brazil, 2016.

9. Ideker, J. H.; Bentivegna, A. F.; Folliard, K. J.; and Juenger, M. C. G., "Do Current Laboratory Test Methods Accurately Predict Alkali-Silica Reactivity?" *ACI Materials Journal*, V. 109, No. 4, July-Aug. 2012, pp. 395-402. doi: 10.14359/51683914

10. Tanesi, J.; Drimalas, T.; Chopperla, K. S. T.; Beyene, M.; Ideker, J. H.; Kim, H.; Montanari, A.; and Ardani, A., "Divergence between Performance in the Field and Laboratory Test Results for Alkali-Silica Reaction," *Transportation Research Record: Journal of the Transportation Research Board*, V. 2674, No. 5, 2020, pp. 120-134. doi: 10.1177/0361198120913288

11. Folliard, K. J.; Barborak, R.; Drimalas, T.; Du, L.; Garber, S.; Ideker, J.; Ley, T.; Williams, S.; Juenger, M.; Fournier, B.; and Thomas, M. D. A., "Preventing ASR/DEF in New Concrete: Final Report," Texas Department of Transportation, Austin, TX, 2006.

12. Rangaraju, P. R.; Afshinnia, K.; Enugula, S. S. R.; and Latifee, E. R., "Evaluation of Alkali-Silica Reaction Potential of Marginal Aggregates Using Miniature Concrete Prism Test (MCPT)," *Proceedings*, 15th International Conference on Alkali-Aggregate Reaction in Concrete, São Paulo, Brazil, 2016.

13. Latifee, E., "Miniature Concrete Prism Test - A New Test Method for Evaluating the ASR Potential of Aggregates, the Effectiveness of ASR Mitigation and the Job Mixture," doctoral dissertation, Clemson University, Clemson, SC, 2013.

14. Liu, K.-W., and Mukhopadhyay, A. K., "Accelerated Concrete-Cylinder Test for Alkali-Silica Reaction," *Journal of Testing and Evaluation*, V. 44, No. 3, 2016, pp. 1229-1238. doi: 10.1520/JTE20140334

15. Muñoz, J. F.; Balachandran, C.; and Arnold, T. S., "New Chemical Reactivity Index to Assess Alkali–Silica Reactivity," *Journal of Materials in Civil Engineering*, ASCE, V. 33, No. 4, 2021, p. 04021037. doi: 10.1061/(ASCE)MT.1943-5533.0003640

16. Muñoz, J. F.; Balachandran, C.; and Arnold, T. S., "New Turner-Fairbank Alkali-Silica Reaction Susceptibility Test for Aggregate Evaluation," *Transportation Research Record: Journal of the Transportation Research Board*, V. 2675, No. 9, 2021, pp. 798-808. doi: 10.1177/03611981211004584

17. Munoz, J. F.; Balachandran, C.; Beyene, M.; and Arnold, T. S., "A Novel Approach for the Assessment of ASR Susceptibility of Concrete Mixtures in Airfield Pavements and Infrastructure," *Technical Report No. FHWA-HRT-22-103*, Office of Research, Development, and Technology, Federal Highway Administration, Washington, DC, 2021. doi: 10.21949/1521689

18. Wei, S.; Zheng, K.; Zhou, J.; Prateek, G.; and Yuan, Q., "The Combined Effect of Alkalis and Aluminum in Pore Solution on Alkali-Silica Reaction," *Cement and Concrete Research*, V. 154, 2022, p. 106723. doi: 10.1016/j.cemconres.2022.106723

19. Szeles, T.; Wright, J.; Rajabipour, F.; and Stoffels, S., "Mitigation of Alkali-Silica Reaction by Hydrated Alumina," *Transportation Research Record: Journal of the Transportation Research Board*, V. 2629, No. 1, 2017, pp. 15-23. doi: 10.3141/2629-04

20. Chappex, T., and Scrivener, K. L., "The Influence of Aluminium on the Dissolution of Amorphous Silica and its Relation to Alkali Silica Reaction," *Cement and Concrete Research*, V. 42, No. 12, 2012, pp. 1645-1649. doi: 10.1016/j.cemconres.2012.09.009

21. Duchesne, J., and Bérubé, M. A., "Relationships between Portlandite Depletion, Available Alkalies and Expansion of Concrete Made with Mineral Admixtures," *Proceedings*, 9th International Conference on Alkali-Aggregate Reaction in Concrete, Westminster, UK, 1992.

22. Wang, H., and Gillott, J. E., "Mechanism of Alkali-Silica Reaction and the Significance of Calcium Hydroxide," *Cement and Concrete Research*, V. 21, No. 4, 1991, pp. 647-654. doi: 10.1016/0008-8846(91)90115-X

23. Kim, T.; Olek, J.; and Jeong, H., "Alkali-Silica Reaction: Kinetics of Chemistry of Pore Solution and Calcium Hydroxide Content in Cementitious System," *Cement and Concrete Research*, V. 71, 2015, pp. 36-45. doi: 10.1016/j.cemconres.2015.01.017

24. Hou, X.; Struble, L. J.; and Kirkpatrick, R. J., "Formation of ASR Gel and the Roles of C-S-H and Portlandite," *Cement and Concrete Research*, V. 34, No. 9, 2004, pp. 1683-1696. doi: 10.1016/j.cemconres.2004.03.026

25. Collepardi, M., "Ettringite Formation and Sulfate Attack on Concrete," *Fifth CANMET/ACI Conference on Recent Advances in Concrete Technology-Proceedings, Fifth International Conference*, SP-200, V. M. Malhotra, ed., American Concrete Institute, Farmington Hills, MI, 2001, pp. 21-38. doi: 10.14359/1056910.14359/10569

26. Thomas, M. D. A.; Fournier, B.; and Folliard, K. J., "Selecting Measures to Prevent Deleterious Alkali-Silica Reaction in Concrete: Rationale for the AASHTO PP65 Prescriptive Approach," *Technical Report No. FHWA-HIF-13-002*, Office of Pavement Technology, Federal Highway Administration, Washington, DC, 2012.

aci Foundation

Building the Future

We're Building the Future

OUR MISSION

We make strategic investments in ideas, research, and people to create the future of the concrete industry.

Through its councils and programs, the ACI Foundation helps to keep the concrete industry at the forefront of advances in material composition, design, and construction.

OUR FOCUS

- Identifying technologies and innovations which provide needed solutions for the concrete industry
- Seeking concrete research projects that further the knowledge and sustainability of concrete materials, construction, and structures
- Supporting our future concrete innovators and leaders by administering fellowships and scholarships
- Helping honorably discharged veterans with our Veterans Rebate for ACI Certification program

www.acifoundation.org

REVIEWERS IN 2023

In 2023, the individuals listed on these pages served as technical reviewers of papers offered for publication in ACI periodicals. A special "thank you" to them for their voluntary assistance in helping ACI maintain the high quality of its publication program.

A. Abbas, Waleed
University of Technology Iraq
Al-Sinaa Street, Baghdad, Iraq

Abdeldjalil, Mhammed
University of Science and Technology of Oran Mohamed-Boudiaf
El Mnaouar, Algeria

Abdellatef, Mohammed
The University of New Mexico
Albuquerque, NM, United States

Abdulla, Nwzad
Salahaddin University-Erbil
Erbil, Iraq

Abdullah, Saman
University of California, Los Angeles
Los Angeles, CA, United States

Abdul-Razzaq, Khattab
University of Diyala
Diyala, Iraq

Abed, Ziyad
University of Technology Iraq
Baghdad, Baghdad, Iraq

Abellan-García, Joaquin
Universidad del Norte
Barranquilla, Colombia

Abousnina, Rajab
University of Southern Queensland
Toowoomba, QLD, Australia

Abraham, Sarah Mariam
Birla Institute of Technology and Science Pilani
Pilani, Rajasthan, India

Abu Obeidah, Adi
Rutgers, The State University of New Jersey
Piscataway, NJ, United States

Abuzeid, Al-Tuhami
Badr for Consulting and Retrofitting
Cairo, Nasr City, Egypt

Accornero, Federico
Shantou University
Shantou, China

Acun, Bora
UBC Okanagan
Kelowna, BC, Canada

Adak, Dibyendu
National Institute of Technology Meghalaya
Shillong, Meghalaya, India

Adekunle, Saheed
King Fahd University of Petroleum and Minerals
Dhahran, Saudi Arabia

Afif, Rahma
Damascus University Faculty of Civil Engineering
Damascus, Syrian Arab Republic

Aghamohammadi, Omid
Isfahan University of Technology
Isfahan, Islamic Republic of Iran

Aguayo, Federico
University of Washington
Seattle, WA, United States

Agustiningtyas, Rudi
Ministry of Public Works and Public Housing
Bandung, Indonesia

Ahani, Elshan
Sahand University of Technology
Tabriz, Islamic Republic of Iran

Ahmad, Subhan
Aligarh Muslim University Faculty of Engineering and Technology
Aligarh, Uttar Pradesh, India

Ahmadi Nedushan, Behrooz
Yazd University
Yazd, Yazd, Islamic Republic of Iran

Ahmed, Afaf
Sohar College of Applied Sciences
Sohar, Oman

Ahmed, Mohamed
Université de Sherbrooke
Sherbrooke, QC, Canada

Ahmed, Mshtaq
King Saud University
Riyadh, Riyadh, Saudi Arabia

REVIEWERS IN 2023

Ahmed, Saddam
Anna University
Chennai, Tamil Nadu, India

Ahn, Seong Ryong
Seoul National University
Seoul, Seoul, Republic of Korea

Aire, Carlos
National Autonomous University of Mexico
Mexico, DF, Mexico

Akakin, Tumer
Aggregate and Ready Mix Association of Minnesota
Eagan, MN, United States

Akalin, Ozlem
PLUSTECHNO Ltd
Istanbul, Turkey

Akhlaghi, Alireza
Isfahan, Islamic Republic of Iran

Akkaya, Yildir
İstanbul Teknik Üniversitesi
Maslak, Sarıyer, Istanbul, Turkey

Al Mansouri, Omar
CSTB
Marne-la-Vallée, France

Alam, A.K.M. Jahangir
Bangladesh University of Engineering and Technology (BUET)
Dhaka, Bangladesh

Al-Ani, Moustafa
Auckland, New Zealand

Alcocer, Sergio
Institute of Engineering, UNAM
Mexico City, DF, Mexico

Aldea, Corina-Maria
St. Catharines, ON, Canada

Aldwaik, Mais
Russeifa, Zarqa, Jordan

Al-Harthy, Ali
Sultan Qaboos University
Al-Khaudh, Oman

Ali, Elias
Case Western Reserve University
Cleveland, OH, United States

Ali, Yahia
Nanjing, Jiangsu, China

Alimrani, Naser
Budapest University of Technology and Economics
Budapest, Budapest, Hungary

Aljewifi, Hana
Université de Cergy-Pontoise
Elbeida, Libya

Al-Kamal, Mustafa
Al-Nahrain University
Baghdad, Baghdad, Iraq

Alkhairi, Fadi
Magna MEP
Dubai, United Arab Emirates

Alkhrdaji, Tarek
Structural Technologies
Columbia, MD, United States

Almasabha, Ghassan
The Hashemite University
Sahab, Amman, Jordan

Almbaidheen, Khalil
Mapei SpA
Dubai, United Arab Emirates

Almuhsin, Bayrak
University of Technology Iraq
Karrada, Baghdad, Iraq

Al-Najmi, AbdulQader
Amman, Jordan

Al-Nasra, Moayyad
American University of Ras Al Khaimah School of Engineering
Ras Al Khaimah, United Arab Emirates

Al-Qaralleh, Mohammad
Mutah University
Karak, Jordan

Al-Sadoon, Zaid
University of Sharjah College of Engineering
Sharjah, United Arab Emirates

Al-Tameemi, Mohamed
University of Wisconsin–Madison
Madison, WI, United States

Al-Zuheriy, Ahmed
University of Technology - Iraq
Baghdad, Baghdad, Iraq

Amir, Sana
Delft University of Technology
Delft, South Holland, Netherlands

Anaokar, Manoj
NMIMS Deemed to be University - Mumbai Campus
Mumbai, Maharashtra, India

Antoni, Antoni
Petra Christian University
Surabaya, Indonesia

Anwari, Qareeb Ullah
NUST Institute of Civil Engineering
Islamabad, Islamabad, Pakistan

Anyaoha, Uchenna
University of British Columbia Okanagan
Kelowna, BC, Canada

Arabzadeh, Abolfazl
Tarbiat Modares University
Tehran, Islamic Republic of Iran

Arafa, Ahmed
Université de Sherbrooke
Sherbrooke, QC, Canada

Araghi, Hassan
Islamic Azad University, South Tehran
Karaj, Tehran, Islamic Republic of Iran

Aras, Murat
Bilecik Şeyh Edebali University
Bilecik, Bilecik, Turkey

Arce, Gabriel
Virginia Transportation Research Council
Charlottesville, VA, United States

Arcine, Maicon de Freitas
Universidade Federal de São Carlos
São Carlos, São Paulo, Brazil

Aristizabal-Ochoa, Jose
National University of Colombia
Medellín, Antioquia, Colombia

Arito, Philemon
University of Namibia
Ongwediva, Oshana, Namibia

Asadian, Alireza
Concordia University
Montreal, QC, Canada

Ashish, Deepankar Kumar
Yonsei University
Seodaemun-gu, Seoul, Republic of Korea

Ashrafy, Mohammad
Islamic Azad University – Arak Branch
Kermanshah, Islamic Republic of Iran

Assaad, Joseph
University of Balamand
Balamand, Lebanon

Assi, Lateef
Al-Mustaqbal University College
Hillah, Babylon, Iraq

Attia Ahmed, Mohamed
Ain Shams University Faculty of Engineering
Cairo, Egypt

Attiogbe, Emmanuel
Discovery Bay, CA, United States

Attiyah, Ali
University of Kufa
Kufa, Iraq

Awida, Tarek
SQC International Consultants
Kuwait, Kuwait, Kuwait

Aydin, Ertug
Lefke Avrupa Üniversitesi
Lefke, Cyprus

Aziminejad, Armin
Islamic Azad University Science and Research Branch
Tehran, Tehran, Islamic Republic of Iran

Aziz, Ali
Al-Mustansiriyah University-College of Engineering
Baghdad, Baghdad, Iraq

B S, Sindu
CSIR Structural Engineering Research Centre
Chennai, India

Babatola, Oluwatosin
Akure, Ondo, Nigeria

Bacinskas, Darius
Vilnius Gediminas Technical University
Vilnius, Lithuania

Bahij, Sifatullah
King Fahd University of Petroleum and Minerals
Dhahran, Dammam, Saudi Arabia

Bai, Shaoliang
Chongqing University
Chongqing, China

Balouch, Sana
University of Dundee
Dundee, United Kingdom of Great Britain and Northern Ireland

REVIEWERS IN 2023

Banjara, Nawal
CSIR Structural Engineering Research Centre
Chennai, Tamil Nadu, India

Bao, Chao
Ningxia University
Yinchuan, China

Basereh, Sina
Mar Structural Design
Berkeley, CA, United States

Bassuoni, Mohamed T.
University of Manitoba
Winnipeg, MB, Canada

Baty, James
Concrete Foundations Association
Mount Vernon, IA, United States

Behnoud, Ali
Aurecon Australia Group Ltd Sydney
Neutral Bay, NSW, Australia

Bektas, Fatih
Minnesota State University, Mankato
Mankato, MN, United States

Benaicha, Mouhcine
AMU
Marseille, France

Benítez, Pablo
Universidad Nacional de Itapúa
Encarnación, Itapúa, Paraguay

Benliang, Liang
Shanghai, China

Berenguer, Romildo
Universidade Federal de Pernambuco Centro de Ciências Exatas e da Natureza
Recife, Brazil

Beyene, Mengesha
Turner-Fairbank Highway Research Center
McLean, VA, United States

Bharadwaj, Keshav
Indian Institute of Technology Delhi
New Delhi, India

Bhojaraju, Chandrasekhar
St Joseph Engineering College
Mangalore, Karnataka, India

Bilek, Vlastimil
ŽPSV a.s.
Brno, Czech Republic

Bilisik, Kadir
Erciyes University
Kayseri, Central Anatolia, Turkey

Billah, AHM Muntasir
University of Calgary
Calgary, AB, Canada

Blandón Valencia, John
National University of Colombia Medellin
Medellín, Antioquia, Colombia

Bonacci, John
Karins Engineering Group
Sarasota, FL, United States

Borzovič, Viktor
Slovak University of Technology in Bratislava, Faculty of Civil Engineering
Bratislava, Slovakia

Boulifa, Ridha
Mohamed-Cherif Messaadia University-Souk Ahras
Souk Ahras, Algeria

Bouzid, Haytham
Université Ibn Khaldoun Tiaret
Tiaret, Algeria

Braestrup, Mikael
Rambøll Group A/S
Copenhagen, Denmark

Brahma, Abdelmalek
Université Saad Dahlab Blida
Blida, Algeria

Brena, Sergio
University of Massachusetts
Amherst, MA, United States

Browning, JoAnn
University of Kansas-Civil, Environmental & Architectural Engineering
Lawrence, KS, United States

Buitrago, Manuel
Universitat Politècnica de València
Valencia, Spain

Bujnak, Jan
Peikko Group Corporation
Kráľová nad Váhom, Slovakia

Burak Bakir, Burcu
Orta Doğu Teknik Üniversitesi
Ankara, Turkey

Buttignol, Thomaz Eduardo
Universidade Estadual de Campinas - Campus Cidade Universitária Zeferino Vaz
Campinas, SP, Brazil

C, Akin
KCG College of Technology
Chennai, India

Cafarelli, Renato
Politecnico di Torino
Turin, Italy

Cai, Jingming
Southeast University
Nanjing, Jiangsu, China

Calderon, Victor
North Carolina State University
Raleigh, NC, United States

Campos, Claudia
Universidade Federal Fluminense
Rio de Janeiro, Rio de Janeiro, Brazil

Cao, Jian
Nanchang Institute of Technology
Nanchang, Jiangxi, China

Carloni, Christian
Case Western Reserve University
Cleveland, OH, United States

Carlton, Aerik
Exponent
Warrenville, IL, United States

Carpio, Víctor
Escuela Politécnica Nacional
Quito, Pichincha, Ecuador

Carrette, Jordan
Crosier Kilgour and Partners Ltd
Winnipeg, MB, Canada

Cascudo, Oswaldo
Universidade Federal de Goiás
Goiânia, GO, Brazil

Chakkamalayath, Jayasree
Kuwait Institute for Scientific Research
Safat, Kuwait

Chakraborty, Arun
Bengal Engineering and Science University
Howrah, West Bengal, India

Chang, Jeremy
Holmes Aus & NZ
Christchurch, New Zealand

Chang, Wei
Harbin, China

Chao, Shih-Ho
The University of Texas at Arlington
Arlington, TX, United States

Chapirom, Aphai
Suranaree University of Technology Institute of Science
Nakhon Ratchasima, Nakhon Ratchasima, Thailand

Chellappan, C. Selin Ravikumar
Malla Reddy Engineering College
Secunderabad, Telangana, India

Chen, Xu
University of Colorado Boulder
Boulder, CO, United States

Cheng, Jianwei
China University of Mining and Technology
Xuzhou, Jiangsu, China

Cheng, Min-Yuan
National Taiwan University of Science and Technology
Taipei, Taiwan, China

Chidambaram, R. Siva
CSIR-Central Building Research Institute
Roorkee, Uttarakhand, India

Cho, Soon-Ho
Gwangju University
Gwangju, Republic of Korea

Choi, Yoon Suk
Korea Conformity Laboratories
Seoul, Republic of Korea

Choong, Kokkeong
Universiti Sains Malaysia
Penang, Seberang Perai Selatan, Malaysia

Chorzepa, Migeum
Park Ridge, IL, United States

Chowdhury, Sharmin
Boğaziçi University
Istanbul, Turkey

Chu, S. H.
Columbia University
New York, NY, United States

Ciggelakis, William
Professional Service Industries
San Antonio, TX, United States

REVIEWERS IN 2023

Cladera, Antoni
University of the Balearic Islands
Palma, Balearic Islands, Spain

Clementino, Fabio
IFPI
Teresina, Piauí, Brazil

Climent, Miguel
University of Alicante
Alicante, Spain

Cuenca, Estefania
Politecnico di Milano
Milan, Italy

da Silveira, Rodrigo
Universidade Federal de Santa Maria
Santa Maria, Rio Grande do Sul, Brazil

Dadvar, Sayyed Ali
University of Sherbrooke
Sherbrooke, QC, Canada

Dave, Shemal
Marwadi Education Foundation's Group of Institutions
Jamnagar, Gujarat, India

Davila, Jose
University of Huelva, Escuela Técnica Superior de Ingeniría
Palos de la Frontera, Huelva, Spain

DC, Mitra
College of Engineering Trivandrum
Thiruvananthapuram, Kerala, India

De Brito, Jorge
IST / TUL
Lisbon, Portugal

de Oliveira, Gabriel
Unicamp
Campinas, São Paulo, Brazil

De Rooij, Mario
TNO
Delft, Netherlands

Degtyarev, Vitaliy
Lexington, SC, United States

del Rey Castillo, Enrique
University of Auckland
Auckland, Auckland, New Zealand

Delalibera, Rodrigo
University of São Paulo
São Carlos, São Paulo, Brazil

Dhole, Rajaram
Katy, TX, United States

Dhonde, Hemant
University of Houston
Houston, TX, United States

Dias, WPS
University of Moratuwa
Moratuwa, Sri Lanka

Diniz, Sofia Maria
Federal University of Minas Gerais School of Engineering
Belo Horizonte, Minas Gerais, Brazil

Dogan, Unal
Istanbul Technical University
Istanbul, Turkey

Dolan, Charles
University of Wyoming
Laramie, WY, United States

Dong, Jiangfeng
Sichuan University
Chengdu, China

Dongell, Jonathan
Pebble Technology International
Scottsdale, AZ, United States

Donmez, Abdullah
İstanbul Teknik Üniversitesi
Istanbul, Turkey

Du, Lianxiang
The University of Alabama at Birmingham
Birmingham, AL, United States

Du, Yingang
Anglia Ruskin University
Chelmsford, United Kingdom of Great Britain and Northern Ireland

Dugvekar, Mitali
MANIT
Bhopal, Madhya Pradesh, India

Dundar, Cengiz
Cukurova University
Adana, Turkey

Dwairi, Hazim
The Hashemite University
Zarqa, Zarqa, Jordan

Ekenel, Mahmut
International Code Council-Evaluation Service
Los Angeles, CA, United States

El-Ariss, Bilal
United Arab Emirates University
Al Ain, United Arab Emirates

Elbady, Ahmed
Université de Sherbrooke
Sherbrooke, QC, Canada

El-Dash, Karim
College of Technological Studies
Kuwait, Kuwait

El-Gendy, Mohammed
Winnipeg, MB, Canada

El-Hassan, Hilal
United Arab Emirates University Faculty of Engineering
Al Ain, United Arab Emirates

Elkafrawy, Mohamed
American University of Sharjah
Sharjah, United Arab Emirates

El-Maaddawy, Tamer
United Arab Emirates University
Al Ain, Abu Dhabi, United Arab Emirates

Elmasry, Mohamed
Arab Academy for Science, Technology and Maritime Transport
Alexandria, Egypt

Elmenshawi, Abdelsamie
University of Calgary
Calgary, AB, Canada

Elnady, Mohamed
Mansoura University
Vancouver, BC, Canada

El-Refaie, Sameh
El-Gama City, Mataria, Cairo, Egypt

El-Salakawy, Ehab
University of Manitoba
Winnipeg, MB, Canada

El-Sayed, Ahmed
University of Sherbrooke
Sherbrooke, QC, Canada

Elsayed, Tarek
Cairo, Egypt

Eltahawy, Reham
Ain Shams University
Cairo, Egypt

Ercolino, Marianna
University of Greenwich Faculty of Engineering and Science
Chatham Maritime, United Kingdom of Great Britain and Northern Ireland

Eskandari, Rasoul
Kashmar, Khorasan Razavi, Islamic Republic of Iran

Etman, Emad
El-Mahalla El-Kubra, Egypt

Ewis, Ahmed
Cairo, Egypt

Ezeldin, Samer
The American University in Cairo
Cairo, Egypt

Faleschini, Flora
University of Padova
Padua, Italy

Fan, Shengxin
Nanyang Technological University
Singapore, Singapore

Fanella, David
Concrete Reinforcing Steel Institute
Schaumburg, IL, United States

Fantilli, Alessandro Pasquale
Politecnico di Torino
Turin, Italy

Faraone, Gloria
San Diego State University
San Diego, CA, United States

Fargier, Luis
Kiewit Infrastructure Engineers
Englewood, CO, United States

Faria, Duarte
Faculdade de Ciências e Tecnologia
Caparica-Lisbon, Portugal

Farshadfar, Omid
Thornton Tomasetti
Lawrence, KS, United States

Farzadnia, Nima
Missouri University of Science and Technology
Rolla, MO, United States

Farzam, Masood
Structural Engineering
Tabriz, Islamic Republic of Iran

Fatemi, Hassan
Montreal, QC, Canada

REVIEWERS IN 2023

Fernandes, Fernando Antonio da Silva
Federal University of Pará - Campus Salinópolis - Faculty of Engineering
Salinópolis, Pará, Brazil

Fernandez Montes, David
Madrid, Madrid, Spain

Fick, Damon
Bozeman, MT, United States

Fikry, Ahmed
Helwan University
Cairo, Egypt

Fitik, Birol
Hochschule für Technik Stuttgart
Stuttgart, Germany

Folino, Paula
University of Buenos Aires
Buenos Aires, Argentina

Franco-Lujan, Victor
Tecnológico Nacional de México
Mexico City, Mexico City, Mexico

Fu, Tengfei
Fuzhou, Fujian, China

G D R N, Ransinchung
Roorkee, Uttarakhand, India

Gąćkowski, Roman
Częstochowa University of Technology
Częstochowa, Poland

Gadkar, Shubhada
Ontario, CA, United States

Galati, Nestore
Structural Technologies
Columbia, MD, United States

Gallandorm, Edith
PCI
Chicago, IL, United States

Gan, Dan
Chongqing, China

Ganesan, N.
National Institute of Technology Calicut
Calicut, India

Gao, Peng
Hefei University of Technology
Hefei, China

Gao, Xiangling
Tongji University
Shanghai, China

Garcia Troncoso, Natividad Leonor
ESPOL
Guayaquil, Ecuador

Gayed, Ramez
University of Calgary
Calgary, AB, Canada

Geng, Yan
MCC Central Research Institute of Building and Construction Co. Ltd.
Beijing, Beijing, China

Getaz, James
Shockey Precast Group
Winchester, VA, United States

Ghannoum, Wassim
The University of Texas at Austin
Austin, TX, United States

Gheni, Ahmed
Komar University of Science and Technology
Sulaymaniyah, Iraq

Ghiami Azad, Amir Reza
University of Tehran
Boston, MA, United States

Ghimire, Krishna
Kansas State University
Manhattan, KS, United States

Ghoddousi, Parviz
Iran University of Science and Technology
Tehran, Tehran, Islamic Republic of Iran

Ghugal, Yuwaraj
Government College of Engineering, Karad
Karad, Maharashtra, India

Giduquio, Marnie
National Taiwan University of Science and Technology
Taipei, Taiwan, China

Girgin, Canan
Yıldız Technical University
Istanbul, Turkey

Glegorio, Marcio
Portland, OR, United States

Goel, Rajeev
CSIR-Central Road Research Institute
Delhi, India

González, Javier
University of the Basque Country
Bilbao, Basque Country, Spain

Govan, G. Elangovan
Civil Engg
Chennai, Tamil Nadu, India

Guades, Ernesto
Technical University of Denmark
Lyngby, Denmark

Guan, Bowen
Xi'an, China

Gujar, Abhay
Dr. Babasaheb Ambedkar Technological University
Satara, Maharashtra, India

Guo, Honglei
Wuhan Polytechnic University
Wuhan, Hubei, China

Guo, Liping
Southeast University
Nanjing, Jiangsu, China

Habulat, Afifudin
Universiti Teknologi MARA
Permatang Pauh, Penang, Malaysia

Haddadin, Laith
United Nations
New York, NY, United States

Hadje-Ghaffari, Hossain
John A. Martin & Associates, Inc.
Los Angeles, CA, United States

Haggag, Hesham
Haggag Consultancy for Construction
Cairo, Cairo, Egypt

Hamed, Ehab
The University of New South Wales
Sydney, NSW, Australia

Han, Baoguo
Dalian University of Technology
Dalian, China

Haneefa Kolakkadan, Mohammed
SSN College of Engineering
Kalavakkam, Tamil Nadu, India

Harith, Iman
Babylon, Iraq

Hassan, Mostafa
University of Connecticut
Storrs, CT, United States

Hassanpour, Sina
Sharif University of Technology
Tehran, Tehran, Islamic Republic of Iran

Henigal, Ashraf
Suez University
Suez, Egypt

Hentges, Tatiane
Unisinos
São Leopoldo, Rio Grande do Sul, Brazil

Heras Murcia, Daniel
University of New Mexico
Albuquerque, NM, United States

Himawan, Aris
Singapore, Singapore

Ho, Johnny
The University of Hong Kong
Hong Kong, Hong Kong, China

Horowitz, Bernardo
Recife, PE, Brazil

Hosseini, Seyed Mohammad
University of Sherbrooke
Sherbrooke, QC, Canada

Hoult, Neil
Toronto, ON, Canada

Hu, Nan
South China University of Technology
Guangzhou, Guangdong, China

Hu, Zhong-Wei
Nanjing, China

Huang, Chung-Ho
National Taipei University of Technology
Taipei, Taiwan, China

Huang, Jianwei
Southern Illinois University Edwardsville
Edwardsville, IL, United States

Huang, Xiaobao
Oakland University
Rochester, MI, United States

Huang, Yuan
Hunan University
Changsha, Hunan, China

REVIEWERS IN 2023

Huo, Jingsi
Huaqiao University
Xiamen, Fujian, China

Hurtado, Pablo E.
Simpson Gumpertz & Heger Inc.
Atlanta, GA, United States

Hussain, Safdar
MS Ramaiah University of Applied Sciences
Bangalore, Karnataka, India

Huts, Andriy
Politechnika Rzeszowska im. Ignacego Łukasiewicza
Rzeszów, Poland

Hwang, Hyeon Jong
Seoul National University
Seoul, Republic of Korea

Hwang, Shyh-Jiann
National Taiwan University
Taipei, Taiwan, China

Ibrahim, Ayoob
University of Wollongong
Wollongong, NSW, Australia

Ibrahim, Izni
Universiti Teknologi Malaysia
Johor Bahru, Johor, Malaysia

Ichinose, Toshikatsu
Meijo University
Nagoya, Aichi, Japan

Idrees, Maria
University of Engineering and Technology Lahore
Lahore, Punjab, Pakistan

Idrisi, Amir Hussain
Michigan Technological University
Houghton, MI, United States

Ilki, Alper
Istanbul Technical University
Istanbul, Turkey

Ioannou, Sokrates
Higher Colleges of Technology
Abu Dhabi, United Arab Emirates

Irassar, Edgardo
Dep. Ingeniería Civil - UNCPBA
Olavarría, Buenos Aires, Argentina

Isik, Ercan
Bitlis Eren Üniversitesi
Bitlis, Turkey

Islam, Mohammad Momeen Ul
RMIT University
Melbourne, VIC, Australia

Ismail, Kamaran
The University of Sheffield
Sheffield, United Kingdom of Great Britain and Northern Ireland

Ismail, Mohamed
Memorial University of Newfoundland
St. John's, NL, Canada

Jagad, Gaurav
Sardar Vallabhbhai National Institute of Technology
Surat, Gujarat, India

Jahami, Ali
University of Balamand Faculty of Engineering
El-Koura, Lebanon

Jang, Bong
K-water
Deajeon, Republic of Korea

Jang, Seung Yup
Korea National University of Transportation
Uiwang, Gyeonggi-do, Republic of Korea

Jansen, Daniel
California Polytechnic State University
San Luis Obispo, CA, United States

Janssen, Donald
Seattle, WA, United States

Januzzi, Rafael
Universidade Federal de Ouro Preto
Ouro Preto, Minas Gerais, Brazil

Javed, Ali
Florida International University
Miami, FL, United States

Jędrzejewska, Agnieszka
Silesian Technical University
Gliwice, Poland

Jensen, Elin
Lawrence Technological University
Southfield, MI, United States

Jensen, James
San Mateo, CA, United States

Jeyan Sudhakar, Alein
SRM Institute of Science and Technology
Kattankulathur, India

Jiang, Hua
McDermott International Inc.
Plainfield, IL, United States

Jiang, Liying
Jensen Hughes Inc.
Lexington, MA, United States

John. V, Thomas
CUSAT
Kochi, Kerala, India

Johnston, David
North Carolina State University
Raleigh, NC, United States

Jozić, Dražan
Faculty of Chemical Technology
Split, Croatia

K, K B Prakash
Government Engineering College, Haveri
Haveri, Karnataka, India

K, Sargunan
Malla Reddy Engineering College
Secunderabad, India

Kadima Lukanu Lwa Nzambi, Aaron
Universidade Federal do Pará
Belém, Brazil

Kaliyavaradhan, Senthil
Hunan University
Changsha, Hunan, China

Kalliontzis, Dimitrios
University of California, San Diego
San Diego, CA, United States

Kamath, Muralidhar
Manipal Academy of Higher Education
Dakshima Kannada, Karnataka, India

Kan, Yu-Cheng
Chaoyang University of Technology
Taichung County, Taiwan, China

Kanaan, Dima
Concordia University - Sir George Williams Campus
Montreal, QC, Canada

Kanagaraj, Ramadevi
Kumaraguru College of Technology
Coimbatore, Tamil Nadu, India

Kandasami, Sivakumar
Larsen and Toubro Ltd.
Chennai, Tamil Nadu, India

Kankam, Charles
Kwame Nkrumah University of Science & Technology
Kumasi, Ghana

Kanta Rao, Velidandi
Central Road Research Institute
New Delhi, Delhi, India

Kar, Arkamitra
Birla Institute of Technology and Science Pilani
Hyderabad, Telangana, India

Karade, Sukhdeo
CSIR-Central Building Research Institute
Roorkee, Uttarakhand, India

Karakale, Vail
Marmara Üniversitesi
Istanbul, Turkey

Karayannis, Christos
Democritus University of Thrace
Xanthi, Greece

Karimi, Hossein
Eindhoven University of Technology
Eindhoven, Netherlands

Kaya, Osman
Muğla Sıtkı Koçman Üniversitesi
Muğla, Turkey

Kazemi, Mohammad
Sharif University of Technology
Tehran, Tehran, Islamic Republic of Iran

Ke, Guo-Ju
Research Institute of Highway Ministry of Transport
Beijing, China

Keskin, Süleyman
Muğla Sıtkı Koçman Üniversitesi
Muğla, Turkey

Khabaz, Amjad
Hasan Kalyoncu University
Gaziantep, Turkey

Khajehdehi, Rouzbeh
SJCA P. C.
Indianapolis, IN, United States

Khaliq, Wasim
National University of Sciences and Technology
Islamabad, ICT, Pakistan

Khan, Sadaqat Ullah
NED University of Engineering and Technology
Karachi, Sindh, Pakistan

REVIEWERS IN 2023

Khatib, Jamal
University of Wolverhampton
Wolverhampton, United Kingdom of Great Britain and Northern Ireland

Khennane, Amar
UNSW @ ADFA
Canberra, ACT, Australia

Khorramian, Koosha
Dalhousie University
Halifax, NS, Canada

Kim, Chulgoo
Seoul National University
Seoul, Republic of Korea

Kim, Kil-Hee
Kongju National University
Kongju, Chungnam, Republic of Korea

Kim, Tae-Hoon
Korea Railroad Research Institute
Uiwang, Republic of Korea

Kim, Taehwan
University of New South Wales
Sydney, NSW, Australia

Kisicek, Tomislav
Civil Engineering Faculty
Zagreb, Croatia

Koehler, Eric
Titan America
Norfolk, VA, United States

Kopiika, Nadiia
Lviv Polytechnic National University
Lviv, Ukraine

Kotecha, Payal
The University of Texas at Arlington
Daytona Beach, FL, United States

Kreiger, Eric
U.S. Army Corps of Engineers Construction Engineering Research Laboratory
Champaign, IL, United States

Krstulovic-Opara, Neven
ExxonMobil Production Co.
Houston, TX, United States

Kumar, Mayank
NIT Kurukshetra
Kurukshetra, Haryana, India

Laco, Jan
D-Phase a.s.
Bratislava, Slovakia

Lai, James
Sacramento, CA, United States

Lai, Jianzhong
Nanjing University of Science and Technology
Nanjing, Jiangsu, China

Lakavath, Chandrashekar
Indian Institute of Technology Hyderabad
Hyderabad, Telangana, India

Lakshmi, R
Kamaraj College of Engineering and Technology
Virudhunagar, Tamil Nadu, India

Lantsoght, Eva
Delft University of Technology
Delft, Netherlands

Lapi, Massimo
Università degli Studi di Firenze
Florence, Italy

Lederle, Rita
University of St. Thomas
Saint Paul, MN, United States

Lee, Chadon
Chung-Ang University
Anseong, Gyeonggi, Republic of Korea

Lee, Chang Hoon
Cornell University
Ithaca, NY, United States

Lee, Deuckhang
Chungbuk National University
Cheongju, Republic of Korea

Lee, Heui Hwang
HNTB Corporation - Oakland
Oakland, CA, United States

Lee, Hung-Jen
National Yunlin University of Science and Technology
Douliou, Taiwan

Lee, Ju Dong
Texas A&M Transportation Institute
Bryan, TX, United States

Lehman, Dawn
University of Washington
Seattle, WA, United States

Lequesne, Rémy D.
University of Kansas
Lawrence, KS, United States

Li, Bo
The Hong Kong Polytechnic University
Kowloon, Hong Kong, China

Li, Fumin
China University of Mining and Technology
Xuzhou, Jiangsu, China

Li, Genfeng
Chongqing University of Arts and Sciences
Chongqing, China

Li, Ning
Tianjin University
Tianjin, Tianjin, China

Liao, Wen-Cheng
National Taiwan University
Taipei, Taiwan, China

Libre, Nicolas Ali
Missouri University of Science and Technology
Rolla, MO, United States

Lignola, Gian Piero
Università degli Studi di Napoli Federico II Scuola Politecnica e delle Scienze di Base
Naples, Italy

Lin, Wei-Ting
Dept. of Civil Engineering
Yilan, Taiwan, China

Liu, Chengqing
Southwest Jiaotong University
Chengdu, Sichuan, China

Liu, Kai-Wei (Victor)
Prairie View A&M University
Prairie View, TX, United States

Liu, Peng
Changsha, China

Liu, Wenguang
Shanghai University
Shanghai, Shanghai, China

Liu, Xuejian
The University of Texas at Arlington
Arlington, TX, United States

Liu, Zhengyu
Iowa State University of Science and Technology
Ames, IA, United States

Lizarazo Marriaga, Juan
Universidad Nacional de Colombia - Sede Bogotá
Bogotá, Colombia

Looi, Daniel
Swinburne University of Technology - Sarawak Campus
Kuching, Malaysia

Lopes, Sergio
University of Coimbra
Coimbra, Portugal

Lu, Tingting
Xi'an, Shaanxi, China

Luan, Yao
Saitama University
Saitama, Japan

Lubell, Adam
Read Jones Christoffersen Ltd.
Vancouver, BC, Canada

Lutomirska, Marta
Warsaw University of Technology Faculty of Civil Engineering
Warsaw, Poland

Lv, Henglin
Xuxhou, Jiangsu, China

Ma, Zhongguo
University of Tennessee
Knoxville, TN, United States

Maage, Magne
Skanska Norge AS
Trondheim, Norway

MacDougall, Colin
Queen's University
Kingston, ON, Canada

Maganti, Ravindra Krishna
Guntur Engineering College
Guntur, Andhra Pradesh, India

Mahadik, Vinay
University of Stuttgart
Stuttgart, Germany

Maheswaran, Chellapandian
Mepco Schlenk Engineering College
Sivakasi, Tamil Nadu, India

Mahfouz, Ibrahim
Cairo, Egypt

Mander, John
Texas A&M University
College Station, TX, United States

REVIEWERS IN 2023

Mardi, Sahand
QIAU
Qazvin, Islamic Republic of Iran

Marikunte, Shashi
Southern Illinois University
Carbondale, IL, United States

Marques, Marília
Rio Paranaíba, Minas Gerais, Brazil

Martinez Andino, Marcos
DeSimone Consulting Engineers
Atlanta, GA, United States

Mata, Luis
University of Toledo
Toledo, OH, United States

Mata-Falcón, Jaime
ETH Zurich, Institute of Structural Engineering
Zurich, Zurich, Switzerland

Matta, Fabio
University of South Carolina
Columbia, SC, United States

Mazzotti, Claudio
University of Bologna
Bologna, Bologna, Italy

McCall, W
Concrete Engineering Consultants
Charlotte, NC, United States

Medallah, Khaled
Saudi Aramco IKPMS
Al Khobar, Saudi Arabia

Meydanli Atalay, Hilal
Kocaeli University
Kocaeli, Turkey

Mirrashid, Masoomeh
Semnan University
Semnan, Islamic Republic of Iran

Mirzaee, Alireza
Shiraz, Islamic Republic of Iran

Mitrofanov, Vitalii
Center for Advanced Design Methods of Concrete Structures
Poltava, Ukraine

Miura, Taito
Nagoya University
Nagoya, Aichi, Japan

Mogili, Srinivas
National Taiwan University
Taipei, Taiwan, China

Mohamed, Ashraf
Alexandria University
Alexandria, Egypt

Mohamed, Nayera
Assiut University
Assiut, Egypt

Mohammed, Tarek
Islamic University of Technology
Gazipur, Dhaka, Bangladesh

Mohee, Fai
TMBN Extrados Inc.
Toronto, ON, Canada

Mondal, Bipul
Chittagong University of Engineering & Technology
Chattogram, Bangladesh

Montoya Coronado, Luis Alberto
Palma, Spain

Moradi, Hiresh
Amirkabir University of Technology
Tehran, Islamic Republic of Iran

Moreno, Carlos
Instituto Politécnico de Bragança
Bragança, Bragança, Portugal

Morgese, Maurizio
University of Illinois Chicago
Chicago, IL, United States

Mostafa, Ibrahim
University of Sherbrooke
Sherbrooke, QC, Canada

Mostafa, Mostafa M. A.
Al-Azhar University - Assiut Branch
Qena, Egypt

Mostofinejad, Davood
Isfahan University of Technology
Isfahan, Islamic Republic of Iran

Motaref, Sarira
University of Connecticut
Storrs, CT, United States

MS, Sandeep
Muthoot Institute of Technology and Science
Cochin, Kerala, India

Mubin, Sajjad
University of Engineering and Technology, Lahore
Lahore, Punjab, Pakistan

Mukai, David
University of Wyoming
Laramie, WY, United States

Musselman, Eric
Villanova University
Villanova, PA, United States

Mutsuddy, Rupak
Bangladesh University of Engineering and Technology
Dhaka, Bangladesh

N, Pannirselvam
SRM Institute of Science and Technology
Kanchipuram, Tamil Nadu, India

Nabavi, Seyed Esrafil
Rezvanshahr, Islamic Republic of Iran

Nabil, Mohamed
Heriot-Watt University - Dubai Campus
Dubai, United Arab Emirates

Naganathan, Sivakumar
Universiti Tenaga Nasional
Kajang, Selangor, Malaysia

Nair, Sooraj
United States Gypsum Corporation
Libertyville, IL, United States

Najimi, Meysam
Iowa State University
Ames, IA, United States

Namakiaraghi, Parsa
Philadelphia, PA, United States

Narayanan, Subramanian
Gaithersburg, MD, United States

Naser, M. Z.
Clemson University
Clemson, SC, United States

Nazarimofrad, Ebrahim
Bu-Ali Sina University
Hamedan, Islamic Republic of Iran

Neithalath, Narayanan
Clarkson University
Potsdam, NY, United States

Nguyen, Hai
Huntington, WV, United States

Nguyen, Tan
Ton Duc Thang University
Ho Chi Minh City, Viet Nam

Nguyen, Thi Thu Dung
Shimizu Corporation
Chuo-ku, Tokyo, Japan

Nili, Mahmoud
Bu-Ali Sina University
Hamedan, Islamic Republic of Iran

Nishiwaki, Tomoya
Tohoku University
Sendai, Japan

Nishiyama, Minehiro
Kyoto University
Kyoto, Japan

Noshiravani, Talayeh
EPFL
Lausanne, Switzerland

Obla, Karthik
National Ready Mixed Concrete Association
Silver Spring, MD, United States

Okeil, Ayman
Louisiana State University
Baton Rouge, LA, United States

Okumus, Pinar
University at Buffalo
Buffalo, NY, United States

Ombres, Luciano
University of Calabria
Cosenza, Italy

Oritola, Sikiru
Universiti Teknologi Malaysia
Skudai, Malaysia

Orta, Luis
ITESM
Zapopan, Jalisco, Mexico

Ortiz-Lozano, Jose
Autonomous University of Aguascalientes
Aguascalientes, Aguascalientes, Mexico

Ou, Yu-Chen
National Taiwan University
Taipei, Taiwan, China

Oukaili, Nazar
University of Baghdad
Baghdad, Iraq

REVIEWERS IN 2023

Oz, Hatice Oznur
Niğde Ömer Halisdemir University
Niğde, Turkey

Ozyildirim, H. Celik
Virginia Transportation Research Council
Charlottesville, VA, United States

P, Mary
Indian Institute of Technology Madras
Chennai, Tamil Nadu, India

Pacheco, Alexandre
Universidade Federal do Rio Grande do Sul (UFRGS)
Porto Alegre, RS, Brazil

Pacheco, Jose
MJ2 Consulting, PLLC
Chicago, IL, United States

Palazzo, Gustavo
National Technological University
Ciudad Mendoza, Mendoza, Argentina

Palieraki, Vasiliki
National Technical University of Athens
Zografou, Athens, Greece

Pan, Wang Fook
SEGi University
Petaling Jaya, Selangor, Malaysia

Panchmatia, Parth
Kansas State University
Manhattan, KS, United States

Pandit, Poornachandra
Manipal Institute of Technology
Manipal, India

Pantazopoulou, Stavroula
York University - Keele Campus
Toronto, ON, Canada

Parastesh, Hossein
University of Science and Culture
Tehran, Tehran, Islamic Republic of Iran

Park, Min-Kook
Delft University of Technology
Delft, Netherlands

Parsekian, Guilherme
UFSCar
São Carlos, Brazil

Parthasarathy, Pavithra
Hong Kong University of Science and Technology
Kowloon, Hong Kong, China

Patil, Sagar
Tatyasaheb Kore Institute of Engineering & Technology
Warananagar, Maharashtra, India

Paul, Alvaro
Universidad de los Andes
Santiago, Las Condes, Chile

Paulson, Conrad
Wiss, Janney, Elstner Associates, Inc.
Pasadena, CA, United States

Peng, Fei
Hunan University
Changsha, China

Perceka, Wisena
Parahyangan Catholic University Faculty of Engineering
Bandung, West Java, Indonesia

Persson, Bertil
Bara, Sweden

Piccinin, Roberto
Hilti, Inc.
Tulsa, OK, United States

Pierott, Rodrigo
Universidade Estadual do Norte Fluminense Darcy Ribeiro
Campos dos Goytacazes, RJ, Brazil

Pincheira, Jose
University of Wisconsin–Madison
Madison, WI, United States

Pocesta, Ylli
Debar, North Macedonia

Pourazin, Khashaiar
Pars AB Tadbir Consulting Engineering Company
Tehran, Islamic Republic of Iran

Pourbaba, Masoud
Islamic Azad University, Maragheh
Maragheh, East Azerbaijan, Islamic Republic of Iran

Prakash, M N
J.N.N. College of Engineering
Shimoga, Karnataka, India

Praul, Michael
FHWA
Augusta, ME, United States

Presuel-Moreno, Francisco
Florida Atlantic University
Dania Beach, FL, United States

Principallo, Antonio
Heidelberg Materials Italia Cementi S.p.A
Peschiera Borromeo, Milan, Italy

Pugliaro, Andrea
Senior Materials and Laboratory Engineer (Civil and Geotechnical)
Savona, Italy

Putra Jaya, Ramadhansyah
Universiti Teknologi Malaysia
Gambang, Pahang, Malaysia

Pv, Premalatha
CARE School of Engineering
Tiruchirappalli, India

Qian, Chen-Hui
Shanghai Jiao Tong University
Shanghai, China

Qian, Kai
NTU
Singapore, Singapore

Qissab, Musab
Al-Nahrain University
Baghdad, Iraq

Quach, Phillip
RJC Engineers
Toronto, ON, Canada

Quintana Gallo, Patricio
Czech Technical University in Prague
Prague, Czech Republic

Quiroga, Pedro
Escuela Colombiana de Ingeniería Julio Garavito
Bogotá, Colombia

Rafi, Muhammad
NED University of Engineering and Technology
Karachi, Sindh, Pakistan

Raghavendra, T.
R.V. College of Engineering, Visvesvaraya Technological University
Bangalore, Karnataka, India

Ragheb, Wael
Alexandria University
Windsor, ON, Canada

Rahal, Khaldoun
Kuwait University
Safat, Kuwait

Ramaswamy, Ananth
Indian Institute of Science
Bangalore, Karnataka, India

Ramirez, Julio
Purdue University
West Lafayette, IN, United States

Rasul, Mehboob
Sumitomo Mitsui Construction Co Ltd
Chuo, Japan

Razaqpur, A. Ghani
McMaster University
Hamilton, ON, Canada

Rezaifar, Omid
Semnan, Semnan, Islamic Republic of Iran

Ridha, Maha (Lianne)
Melbourne, VIC, Australia

Rizwan, Syed Ali
National University of Computer and Emerging Sciences - Lahore Campus
Lahore, Punjab, Pakistan

Rodrigues, Publio
LPE Engenharia e Consultoria
São Paulo, Brazil

Rodriguez, Mario
National Autonomous University of Mexico
Mexico City, Mexico

Rojas Aguero, Rosangel
Universidade Federal do Rio Grande
Rio Grande, Rio Grande do Sul, Brazil

Roy, Arunabha Mohan
University of Michigan
Ann Arbor, MI, United States

Rughooputh, Reshma
University of Mauritius
Moka, Mauritius

S, Kumaravel
Annamalai University
Cuddalore, Tamil Nadu, India

S A, Jaffer Sathik
CSIR-SERC
Chennai, Tamil Nadu, India

Saedi, Houman
Tarbiat Modares & Tabriz University and TSML Co.
Tehran, Islamic Republic of Iran

REVIEWERS IN 2023

Saeed, Yasir
Portland State University
Portland, OR, United States

Saeki, Tatsuhiko
Niigata University
Niiagta, Japan

Safiuddin, Md.
George Brown College
Toronto, ON, Canada

Sahoo, Kirtikanta
Rourkela, India

Said, Shwan
Erbil, Iraq

Sakban, Haider
Piscataway, NJ, United States

Saleh Ahari, Reza
Ege University
İzmir, Turkey

Salib, Sameh
Markham, ON, Canada

Sánchez, Isidro
University of Alicante
Alicante, Alicante, Spain

Santos, Daniel
Polytechnic School of the University of São Paulo
São Paulo, São Paulo, Brazil

Santos, Jose
University of Madeira
Funchal, Portugal

Santos, Sérgio
SBS Engineering Consultancy
Goiânia, Goiás, Brazil

Sapp, James
ATMI Precast
Aurora, IL, United States

Sartaji, Parisa
Ardabil, Islamic Republic of Iran

Sato, Yuichi
Kyoto University
Kyoto, Kyoto, Japan

Sayed Ahmed, Mahmoud
Toronto Metropolitan University
Toronto, ON, Canada

Sayın, Barış
Engineering Faculty
Istanbul, Turkey

Schlicke, Dirk
Graz University of Technology
Graz, Austria

Seco, Laura
Coimbra, Portugal

Semelawy, Mohamed
Western University
London, ON, Canada

Sengupta, Amlan
Indian Institute of Technology Madras
Chennai, Tamil Nadu, India

Serry, Mohamed
The Arab Contractors
Cairo, Egypt

Sezen, Halil
Ohio State University
Columbus, OH, United States

Sha, Fei
Shandong University
Jinan, Shandong, China

Shabana, Islam
University of Sherbrooke
Sherbrooke, QC, Canada

Shafigh, Payam
Kuala Lumpur, Malaysia

Shafiq, Nasir
Universiti Teknologi PETRONAS
Tronoh, Perak, Malaysia

Shaik, Madeena Imam Shah
Advanced Construction Technology Services SAL
Riyadh, Saudi Arabia

Sharifzad, Shayan
The University of Texas at Arlington College of Engineering
Arlington, TX, United States

Sharma, Akanshu
Institute of Construction Materials
Stuttgart, Germany

Shehata, Medhat
Toronto Metropolitan University
Toronto, ON, Canada

Shekarchi, William
Austin, TX, United States

Shen, Yin
Tongji University
Shanghai, China

Shete, Vivek
TKIET Warananagar
Panhala, Maharashtra, India

Shetty, Kiran
Manipal Institute of Technology
Manipal, Karnataka, India

Shi, Caijun
Hunan University
Changsha, Hunan, China

Shi, Xianming
Washington State University
Pullman, WA, United States

Shin, Hyeongyeop
Seoul National University
Gwanak-gu, Seoul, Republic of Korea

Shumuye, Eskinder Desta
Shenzhen University College of Civil and Transportation Engineering
Shenzhen, GD, China

Shuraim, Ahmed
King Saud University
Riyadh, Saudi Arabia

Siddique, Mohammad
Bangladesh University of Engineering and Technology
Dhaka, Bangladesh

Silfwerbrand, Johan
KTH Royal Institute of Technology
Stockholm, Sweden

Silva, Marcos
Campinas, Brazil

Simplício, Marcos
Universidade Federal de Sergipe
Aracaju, Sergipe, Brazil

Singh, Brijesh
Faridabad, Haryana, India

Singh, Harvinder
Guru Nanak Dev Engineering College
Ludhiana, Punjab, India

Singh, Navdeep
Jalandhar, Punjab, India

Singh, Surender
Indian Institute of Technology Madras
Chennai, Tamil Nadu, India

Sivey, Paul
Sivey Enterprises
Hilliard, OH, United States

Smadi, Mohammad
Jordan University of Science and Technology
Irbid, Jordan

Soares, Renan
Universidade Federal de Pernambuco
Recife, Pernambuco, Brazil

Soliman, Ahmed
Western University
London, ON, Canada

Solnosky, Ryan
Penn State University Park
University Park, PA, United States

Soltani, Mahmoodreza
Bradley University Caterpillar College of Engineering and Technology
Peoria, IL, United States

Sonkusare, Hemantkumar
G H Raisoni College of Engineering
Nagpur, Maharashtra, India

Sonyal, Muhammad
University of Engineering and Technology, Lahore
Lahore, Punjab, Pakistan

Sorensen, Taylor
Brigham Young University
Provo, UT, United States

Spinella, Nino
University of Catania Faculty of Engineering
Catania, Italy

Spyridis, Panagiotis
Institute for Structural Engineering
Vienna, Austria

Sreekala, R
Structural Engineering Research Centre
Chennai, Tamil Nadu, India

Sreenivasappa, Nandeesh
Ramaiah Institute of Technology
Bangalore, Karnataka, India

Stalin Anto, Karthiga
Bannari Amman Institute of Technology
Sathyamangalam, Tamil Nadu, India

REVIEWERS IN 2023

Stojadinovic, Bozidar
Swiss Federal Institute of Technology
Zurich, Switzerland

Stucchi, Fernando
Polytechnic School of the University of São Paulo
Adamantina, SP, Brazil

Su, Yu-Min
National Kaohsiung University of Science and Technology
Kaohsiung, Taiwan, China

Suda, Vijaya
Vardhaman College of Engineering
Shamshabad, Telangana, India

Sultan, Mohamed
Al-Azhar University
Cairo, Egypt

Sun, Jing
Beijing, China

Sun, Qiaorong
Hohai University
Nanjing, Jiangsu, China

Suryawanshi, Yogesh
JSPM's Imperial College of Engineering and Research, Wagholi
Pune, Maharashtra, India

Swamy, H C
Bangalore, Karnataka, India

Tabkhi Wayghan, Amir Reza
Carleton University Faculty of Engineering and Design
Ottawa, ON, Canada

Tabsh, Sami
American University of Sharjah
Sharjah, United Arab Emirates

Tadros, Maher
e.construct.USA, LLC
Omaha, NE, United States

Tajaddini, Abbas
University of Bath Faculty of Engineering and Design
Bath, United Kingdom of Great Britain and Northern Ireland

Tan, Kiang Hwee
National University of Singapore
Singapore, Singapore

Tang, Chao-Wei
Cheng Shiu University
Niaosong District, Kaohsiung City, Taiwan, China

Tang, Fujian
Dalian University of Technology
Dalian, Liaoning, China

Tang, Xiusheng
Nanjing Hydraulic Research Institute
Nanjing, China

Tawfic, Yasser
Minia University
Minia, Minia, Egypt

Teodoro, Rodrigo
Goiânia, Goiás, Brazil

Thokchom, Suresh
Manipur Institute of Technology
Imphal, Manipur, India

Tian, Ying
University of Nevada, Las Vegas
Las Vegas, NV, United States

Tiznobaik, Mohammad
The University of British Columbia | Okanagan Campus
Kelowna, BC, Canada

Tkach, James
Largo Concrete, Inc.
San Diego, CA, United States

Tognonvi, Tohoue Monique
Université de Sherbrooke
Sherbrooke, QC, Canada

Tomas, Antonio
Technical University of Cartagena
Cartagena, Spain

Topuzi, Dritan
Schöck Bauteile GmbH
Toronto, ON, Canada

Torabian, Ala
Isfahan, Islamic Republic of Iran

Tore, Erkan
Balıkesir University
Balıkesir, Balıkesir, Turkey

Tosun, Kamile
Dokuz Eylül University
İzmir, Turkey

Tran, Mien
Ho Chi Minh City University of Technology
Ho Chi Minh City, Viet Nam

Trejo, David
Oregon State University
Corvallis, OR, United States

Tripathi, Deep
University of Sherbrooke Faculty of Engineering
Sherbrooke, QC, Canada

Tuchscherer, Robin
Northern Arizona University
Flagstaff, AZ, United States

Ueda, Naoshi
Kansai University
Suita, Osaka, Japan

Umipig, Jorge
Vista Land & Lifescapes, Inc.
Mandaluyong City, Metro Manila, Philippines

Ungermann, Jan
RWTH Aachen University
Aachen, Germany

Uzel, Almıla
Yeditepe University
Istanbul, Turkey

Vaz Rodrigues, Rui
Universidade de Lisboa Instituto Superior Técnico
Lisbon, Portugal

Venkataraman, Jayakumar
IFET College of Engineering
Viluppuram, Tamil Nadu, India

Vollum, Robert
Department of Civil and Environmental Engineering
London, United Kingdom of Great Britain and Northern Ireland

Vosahlik, Jan
ICON
Austin, TX, United States

Vosoughi, Payam
Caltrans
Rancho Cordova, CA, United States

Vu, Ngoc Son
Hanoi University of Civil Engineering
Hanoi, Viet Nam

Wally, Gustavo
Universidade Federal do Rio Grande do Sul
Porto Alegre, Brazil

Wang, Ben
University of Houston
Houston, TX, United States

Wang, Dun
Research Institute of Structural Engineering & Disaster Reduction, Tongji University
Shanghai, China

Wang, Hongze
Inner Mongolia University of Technology
Hohhot, Inner Mongolia, China

Wang, Kejin
Iowa State University
Ames, IA, United States

Wang, Xiao-Yong
Kangwon National University
Chuncheon, Republic of Korea

Wardhono, Arie
The State University of Surabaya
Surabaya, East Java, Indonesia

Wei-Jian, Yi
Changsha, China

Werner, Anne
SIUE
Edwardsville, IL, United States

Windisch, Andor
Karlsfeld, Germany

Witwit, Jaafar
Baghdad, Iraq

Won, Moon
Texas Tech University
Lubbock, TX, United States

Wong, Sook Fun
Nanyang Technological University
Singapore, Singapore

Wu, Chao
Wuhan University of Technology
Wuhan, Hubei, China

Wu, Kai
Nanjing, Jiangsu, China

Wu, Ruoyang
University of Utah
Herriman, UT, United States

Wu, Yu-You
Foshan University
Foshan, Guangdong, China

Wu, Zhimin
Dalian University of Technology
Dalian, Liaoning, China

REVIEWERS IN 2023

Xi, Xun
University of Strathclyde
Glasgow, United Kingdom of Great Britain and Northern Ireland

Xia, Jin
Zhejiang University
Hangzhou, Zhejiang, China

Xie, Guoshuai
Wuhan University
Wuhan, Hubei, China

Xie, Jun
Ministry of Transport Research Institute of Highways
Beijing, China

Xie, Tianyu
RMIT University
Melbourne, VIC, Australia

Xu, Aimin
ARRB Group
Melbourne, VIC, Australia

Yan, Peiyu
Tsinghua University
Beijing, China

Yang, Junlong
Dalian University of Technology
Dalian, China

Yang, Keun-Hyeok
Kyonggi University
Suwon, Gyeonggi-do, Republic of Korea

Yang, Rick
SNC-Lavalin Engineers and Constructors Inc
Houston, TX, United States

Yang, Shuyan
Yinchuan City, China

Yang, Sung Chul
Hongik University
Mapo-gu, Republic of Korea

Yang, Yunyun
Guanghan, China

Yankelevsky, David
National Building Research Institute
Haifa, Israel

Yapa, Hiran
University of Peradeniya Faculty of Engineering
Peradeniya, Sri Lanka

Yaqub, Muhammad
University of Engineering and Technology, Taxila
Taxila, Punjab, Pakistan

Yassein, Mohamed
Abu Dhabi, Abu Dhabi, United Arab Emirates

Yasso, Samir
University of Mosul
Mosul, Nineveh, Iraq

Yazbeck, Fouad
360 TANGENT Engineering Consultancy
Abu Dhabi, United Arab Emirates

Yazdani, Nur
The University of Texas at Arlington
Arlington, TX, United States

Yekrangnia, Mohammad
Shahid Rajaee Teacher Training University
Tehran, Islamic Republic of Iran

Yerramala, Amarnath
University of Dundee
Dundee, United Kingdom of Great Britain and Northern Ireland

Yi, Yousun
The University of Texas at Austin
Austin, TX, United States

Yildirim, Salih
Columbia University
New York, New York, United States

Yindeesuk, Sukit
University of Illinois Urbana-Champaign
Urbana, IL, United States

Yingjie, Shan
Central South University
Changsha, Hunan, China

Youdong, Xing
Guilin, China

Yousefpour, Hossein
The University of Texas at Austin
Austin, TX, United States

Youssef, Ahmed
Giza, Giza, Egypt

Youzhi, Liu
China Institute of Water Resources and Hydropower Research
Beijing, China

Yuan, Qiang
Central South University
Changsha, China

Yüksel, Isa
Bursa Technical University
Bursa, Turkey

Yuniarsyah, Eko
Institut Teknologi Bandung
Bandung, Indonesia

Zaki, Adel
SNC-Lavalin
Montreal, QC, Canada

Zandparsa, Kumars
California State University, Long Beach
Long Beach, CA, United States

Zanuy, Carlos
Universidad Politécnica de Madrid
Madrid, Madrid, Spain

Zapata, Luis
Universidad Industrial de Santander
Bucaramanga, Santander, Colombia

Zega, Claudio
CONICET
La Plata, Argentina

Zeidan, Mohamed
Southeastern Louisiana University College of Science and Technology
Hammond, LA, United States

Zeris, Christos
National Technical University of Athens
Zografou, Greece

Zhang, Changhui
Zhengzhou University
Zhengzhou, Henan, China

Zhang, Feng
Nanjing Hydraulic Research Institute
Nanjing, China

Zhang, Hongen
Tongji University
Shanghai, China

Zhang, Peng
Karlsruhe Institute of Technology (KIT)
Karlsruhe, Germany

Zhang, Qian
Nanjing, China

Zhang, Qin
Dalian University of Technology
Dalian, Liaoning, China

Zhang, Wei
University of Tsukuba
Tsukuba, Japan

Zhao, Tiejun
Qingdao, China

Zhao, Xingzhuang
University of Maryland College Park
College Park, MD, United States

Zhao, Xin-Yu
South China University of Technology
Guangzhou, China

Zheng, Dafeng
Guangzhou, Guangdong, China

Zheng, Herbert
Gammon Construction Limited
Hong Kong, Hong Kong, China

Zheng, Yu
Dongguan University of Technology
Dongguan, Guangdong, China

Zheng, Yulong
Jiangsu University
Zhenjiang, China

Zhenhong, Wang
China Institute of Water Resources and Hydropower Research
Beijing, China

Zhong, Rui
Southeast University
Nanjing, China

Zhu, Hai
Charlotte, NC, United States

Zhu, Wenjun
L'Institut National des Sciences Appliquées de Toulouse
Toulouse, Toulouse, France

Zhu, Yanping
Missouri University of Science and Technology
Rolla, MO, United States

Zornoza, Emilio
University of Alicante
Alicante, Alicante, Spain

Zych, Mariusz
Politechnika Krakowska im. Tadeusza Kościuszki
Krakow, Poland

CALL FOR ACTION

ACI Invites You To...

Share your expertise

Do you have EXPERTISE in any of these areas?

- BIM
- Chimneys
- Circular Concrete Structures Prestressed by Wrapping with Wire and Strand
- Circular Concrete Structures Prestressed with Circumferential Tendons
- Concrete Properties
- Demolition
- Deterioration of Concrete in Hydraulic Structures
- Electronic Data Exchange
- Insulating Concrete Forms, Design, and Construction
- Nuclear Reactors, Concrete Components
- Pedestal Water Towers
- Pipe, Cast-in-Place
- Strengthening of Concrete Members
- Sustainability

Then become a REVIEWER for the *ACI Structural Journal* or the *ACI Materials Journal*.

Become a Reviewer for the ACI Journals

How to become a Reviewer:

1. Go to: **http://mc.manuscriptcentral.com/aci**;
2. Click on "Create Account" in the upper right-hand corner; and
3. Enter your E-mail/Name, Address, User ID and Password, and Area(s) of Expertise.

Update your Manuscript Central user account information

Did you know that the database for MANUSCRIPT CENTRAL, our manuscript submission program, is separate from the ACI membership database?

How to update your user account:

1. Go to **http://mc.manuscriptcentral.com/aci**;
2. Log in with your current User ID & Password; and
3. Update your E-mail/Name, Address, User ID and Password, and Area(s) of Expertise.

QUESTIONS?

E-mail any questions to Journals.Manuscripts@concrete.org.

American Concrete Institute

Always advancing

American Concrete Institute

This joint special issue of the *ACI Structural Journal* and *ACI Materials Journal* contains nine manuscripts focused on construction aspects of additive construction using cement-based materials. These papers cover structural topics including testing reinforced beams and modeling the construction process, and materials topics including characterizing extrusion, enhancing and testing mechanical properties, shoreline resiliency, fracture behavior, and quality control methods.

The American Concrete Institute (ACI) is a leading authority and resource worldwide for the development and distribution of consensus-based standards and technical resources, educational programs, and certifications for individuals and organizations involved in concrete design, construction, and materials, who share a commitment to pursuing the best use of concrete.

Individuals interested in the activities of ACI are encouraged to explore the ACI website for membership opportunities, committee activities, and a wide variety of concrete resources. As a volunteer member-driven organization, ACI invites partnerships and welcomes all concrete professionals who wish to be part of a respected, connected, social group that provides an opportunity for professional growth, networking, and enjoyment.